



McGill

**Advancing Biomedical Applications with Functional Polymers**

by Hui Wen Yong

Department of Chemistry  
McGill University, Montreal

April 2024

*A thesis submitted to McGill University in partial fulfillment of the  
requirements of the degree of Doctor of Philosophy*

© Hui Wen Yong, 2024

## Table of Contents

Table of Contents .....	ii
Abstract .....	vi
Résumé.....	vii
Acknowledgements.....	viii
Contribution of Authors .....	x
Copyright .....	xii
List of Figures .....	xv
List of Tables .....	xxiv
List of Schemes.....	xxv
List of Abbreviations .....	xxvi
Chapter 1: Introduction.....	1
1.1 Nanoengineering Branched Star Polymer-based Formulations: Scope, Strategies and Advances.....	2
1.1.1. Abstract.....	2
1.1.2. Introduction.....	3
1.1.3. Emerging Potential of Branched Star Polymers as Nanocarriers .....	4
1.1.4. Polymer Self-assembly: Methods .....	8
1.1.5. Key Parameters of Self-assemblies.....	12
1.1.6. Strategies to Design Branched Star Copolymers for Drug Delivery .....	15
1.1.6.1. Polymer Composition .....	18
1.1.6.2. Polymer Architecture.....	22
1.1.6.3. Core/ Shell-Cross-linked Micelles.....	27
1.1.6.4. Stereocomplexation and Mixed Micelles.....	29

1.1.6.5. Compatibility between the Drug and Core-forming Block.....	30
1.1.6.6. Chemical Conjugation of the Drug to Polymer .....	32
1.1.6.7. Polymer: Drug Feed Ratio .....	34
1.1.6.8. Choice of Solvent for Self-Assembly .....	35
1.1.7. Biological Evaluations .....	36
1.1.8. Conclusions and Future Outlook .....	40
1.2. The Unexplored Potential of Gas-responsive Polymers in Drug Delivery: Progress, Challenges and Outlook.....	43
1.2.1 Abstract.....	43
1.2.2. Introduction.....	44
1.2.2.1. Gas-responsive Polymers.....	44
1.2.2.1.1. Nitric Oxide (NO).....	48
1.2.2.1.2. Carbon Monoxide (CO) .....	49
1.2.2.1.3. Hydrogen Sulfide (H <sub>2</sub> S).....	50
1.2.2.1.4. Sulfur Dioxide (SO <sub>2</sub> ).....	51
1.2.2.1.5. Oxygen (O <sub>2</sub> ).....	52
1.2.2.1.6. Carbon Dioxide (CO <sub>2</sub> ) .....	53
1.2.3. Challenges and Outlook with Gas-responsive Polymers .....	54
1.2.4. Conclusions.....	56
1.3. Stimuli-responsive Polymeric Nanoparticles.....	57
1.3.1. CO <sub>2</sub> -responsive Polymeric Nanoparticles.....	60
1.3.2. pH-responsive Polymeric Nanoparticles.....	61
1.3.3. ROS-responsive Polymeric Nanoparticles.....	63
1.4. Antibacterial Nanoparticles .....	65
1.5. Thermoresponsive Polymeric Nanoparticles .....	71

1.6. Scope of Thesis and Contribution to Original Knowledge.....	76
1.7. References.....	78
Chapter 2: Single Functional Group Platform for Multi-Stimuli Responsivities: Tertiary Amine for CO <sub>2</sub> /pH/ROS-Triggered Cargo Release in Nanocarriers.....	124
2.1. Opening Remarks.....	124
2.2. Abstract.....	125
2.3. Introduction.....	125
2.4. Experimental Section.....	128
2.5. Results and Discussion .....	134
2.6. Conclusions.....	153
2.7. References.....	153
2.8 Appendix A: Supporting Information for Chapter 2.....	164
Chapter 3: Soft Nanoparticles as Antimicrobial Agents and Carriers of Microbiocides for Enhanced Inhibition Activity.....	193
3.1. Opening remarks.....	193
3.2. Abstract.....	194
3.3. Introduction.....	194
3.4. Experimental Section.....	197
3.5. Results and Discussion .....	202
3.6. Conclusions.....	222
3.7. References.....	222
3.8 Appendix B: Supporting Information for Chapter 3.....	233
Chapter 4: Soft Nanoparticles with Induced Reversible Morphological Transitions through Upper Critical Solution Temperature for Controlled Drug Release .....	255
4.1. Opening Remarks.....	255
4.2. Abstract.....	256

4.3. Introduction.....	256
4.4. Experimental Section.....	260
4.5. Results & Discussion.....	264
4.6. Conclusions.....	284
4.7. References.....	285
4.8. Appendix C: Supporting Information for Chapter 4.....	298
Chapter 5: Conclusions and Outlook .....	306
5.1. Conclusions.....	306
5.2. Outlook .....	308
5.3. References.....	312

## Abstract

---

Functional polymers have offered a viable platform in designing smart nanoformulations for a variety of applications. However, development of well-defined nanocarriers through efficient design of their polymer precursors, still remains a significant challenge. This thesis research contributes towards the field of nanomedicine by simplifying the design of smart amphiphilic polymeric precursors, and a detailed evaluation of their aqueous nanoformulations. We describe a versatile methodology to multi-stimuli responsive soft nanoparticles from branched star polymers of AB<sub>2</sub> composition, in which the core forming biocompatible and biodegradable polycaprolactone (PCL) arm (A) is functionalized with a tertiary amine. These nanoparticles respond to multiple stimuli (varying CO<sub>2</sub> concentrations, pH, ROS, and a combination of CO<sub>2</sub> + ROS) prevalent at disease sites, using a single chemical entity, for controlled and sustained cargo release. This design strategy streamlines and enables effective delivery of active pharmaceutical agents in diverse biological environments. In a reverse strategy, amine groups are chemically linked to polyethylene glycol (PEG) hydrophilic arms (B), yielding cationic nanoparticles with positively charged hydrophilic shell and hydrophobic core. Such drug loaded nanoformulations exhibit dual therapeutic effects: intrinsic biocidal activity and delivery of potent small molecule antibacterial agents. Subsequently, by leveraging on the existing polymerization and post-polymerization techniques, we have developed a smart platform for inducing temperature-regulated morphological transitions in soft nanoparticles. By strategic location of upper critical solution temperature responsive poly(acrylamide-*co*-acrylonitrile), hydrophilic PEG and hydrophobic PCL arms in an ABC block copolymer, reversible *in situ* transformations are easily facilitated. It offers tailored delivery of a model drug (curcumin) through sustained morphological changes without nanoparticle disassembly. This thesis research signifies the importance of structural design in regulating stimuli-responsive properties in nanoformulations for desired spatiotemporal control in drug delivery. It demonstrates how synthetic design can help craft efficient formulations for diverse biomedical applications.

## Résumé

---

Les polymères fonctionnels ont offert une plate-forme viable pour la conception de nanoformulations intelligentes pour une variété d'applications. Cependant, le développement de nanotransporteurs bien définis grâce à la conception efficace de leurs précurseurs polymères reste un défi important. Cette thèse de recherche contribue au domaine de la nanomédecine en simplifiant la conception de précurseurs polymères amphiphiles intelligents et en évaluant en détail leurs nanoformulations aqueuses. Nous décrivons une méthodologie polyvalente pour des nanoparticules souples réactives à plusieurs stimuli à partir de polymères en étoile ramifiés de composition AB<sub>2</sub>, dans lesquels le bras polycaprolactone (PCL) biocompatible et biodégradable formant le noyau (A) est fonctionnalisé avec une amine tertiaire. Ces nanoparticules répondent à de multiples stimuli (concentrations variables de CO<sub>2</sub>, pH, ROS et une combinaison de CO<sub>2</sub> + ROS) prévalents sur les sites de la maladie, en utilisant une seule entité chimique, pour une libération contrôlée et soutenue de la cargaison. Cette stratégie de conception rationalise et permet une administration efficace d'agents pharmaceutiques actifs dans divers environnements biologiques. Dans une stratégie inverse, les groupes amines sont chimiquement liés aux bras hydrophiles de polyéthylène glycol (PEG) (B), produisant des nanoparticules cationiques avec une coque hydrophile chargée positivement et un noyau hydrophobe. De telles nanoformulations chargées de médicaments présentent un double effet thérapeutique: une activité biocide intrinsèque et la délivrance d'agents antibactériens puissants à petites molécules. Par la suite, en s'appuyant sur les techniques de polymérisation et de post-polymérisation existantes, nous avons développé une plate-forme intelligente pour induire des transitions morphologiques régulées par la température dans des nanoparticules molles. Grâce à l'emplacement stratégique des bras poly(acrylamide-*co*-acrylonitrile) sensibles à la température critique supérieure de la solution, du PEG hydrophile et du PCL hydrophobe dans un copolymère à blocs ABC, les transformations *in situ* réversibles sont facilement facilitées. Il offre une délivrance sur mesure d'un médicament modèle (curcumine) par le biais de changements morphologiques soutenus sans désassemblage des nanoparticules. Cette recherche de thèse souligne l'importance de la conception structurelle dans la régulation des propriétés de réponse aux stimuli dans les nanoformulations pour le contrôle spatiotemporel souhaité dans l'administration de médicaments. Il démontre comment la conception synthétique peut aider à élaborer des formulations efficaces pour diverses applications biomédicales.

## Acknowledgements

---

First of all, I would like to thank my supervisor, Prof. Ashok Kakkar for his continuous guidance throughout these few years. He has been opened to establishing new collaborations and venturing into new research directions, which have undoubtedly shaped my growth as a scientist.

I am also immensely thankful to all the contributions from our collaborators. It has been an absolute pleasure working with everyone from the Montréal Heart Institute, including Dr. Marine Ferron, Mélanie Mecteau, Teodora Mihalache-Avram, Sylvie Lévesque, Gabriel Théberge-Julien, Dr. Éric Rhéaume and Dr. Jean-Claude Tardif. Not forgetting Dr. Seyed Mohammad Amin Ojagh for his guidance with the bacterial studies. The hardwork and dedication that everybody has shown truly motivated me to bring out my best and make meaningful contributions to science.

I would also like to thank the help of many facility managers at McGill, namely, Dr. Violeta Toader, Nadim Saadé, Dr. Hatem Titi, Dr. Mohini Ramkaran, Petr Fiurasek, Dr. Kelly Sears, Dr. Jeannie Mui, Dr. David Liu, and Weawkamol Leelapornpisit. Their consistent support and help has been instrumental in guiding me to prepare my samples and understanding my results critically.

Fellow lab members, past and present, who have also made my Ph.D. journey more pleasant: Victor Lotocki, Laura McKay, Fei Rui Long, Samaneh Yousefi Adlsadabad, Anjali Saini, as well as all the graduate and undergraduate research trainees. Also not missing our friends from the Bohle group with whom we share the office and lab space. I also want to acknowledge the efforts from my undergraduate research assistants Natali Joma and Laura Sofia Reyes Castellanos.

Across the Atlantic Ocean, Dr. Barbara Güttler, Stefan Buchalik-Bopp, Angelika Streich, Nasirzade Tabrizi Mohamadreza, Petra Volk, Claudius Pirro, and many others welcomed me warmly during my short stay at the Leibniz-Institut für Verbundwerkstoffe. I am truly grateful for this opportunity to delve into new research areas and experience a different work culture.

I am grateful to my review committee, Prof. Theo van de Ven and Prof. Christopher Barrett for their invaluable suggestions to my research.

In addition, huge gratitude to Ms. Chantal Marotte for her assistance in various matters even before the start of my Ph.D.

Last but not least, I would like to thank my Pa, Ma, Gor, and Victor for their unwavering love and support in all my endeavours.

## Contribution of Authors

---

The details of author contributions are listed as follows:

**Chapter 1:** (A) Yong, H. W.; Kakkar, A., Nanoengineering Branched Star Polymer - based Formulations: Scope, Strategies, and Advances. *Macromol. Biosci.* **2021**, *21*, 2100105.

(B) Yong, H. W.; Kakkar, A., The Unexplored Potential of Gas - responsive Polymers in Drug Delivery: Progress, Challenges and Outlook. *Polym. Int.* **2022**, *71* (5), 514-520.

Yong, H. W.: writing-original draft, review, editing; Kakkar, A.: writing, review, editing.

**Chapter 2:** Yong, H. W.; Ferron, M.; Mecteau, M.; Mihalache-Avram, T.; Lévesque, S.; Rhéaume, E.; Tardif, J.-C.; Kakkar, A. Single Functional Group Platform for Multistimuli Responsivities: Tertiary Amine for CO<sub>2</sub>/pH/ROS-Triggered Cargo Release in Nanocarriers. *Biomacromolecules* **2023**, *24* (9), 4064-4077.

Yong, H. W.: methodology, investigation, formal analysis, writing-original draft, review, editing; Ferron, M., Mecteau, M., Mihalache-Avram, T.: *in vitro* studies, writing-original draft, review, editing; Lévesque, S.: statistical analyses of *in vitro* studies; Rhéaume, E.: writing-original draft, review, editing; Tardif, J. C.: review, editing, supervision; Kakkar, A.: supervision, writing-original draft, review, editing.

**Chapter 3:** Yong, H. W.; Ojagh, S. M. A.; Théberge-Julien, G.; Castellanos, L. S. R.; van de Ven, T. G. M; Rhéaume, É.; Tardif, J.-C.; Kakkar, A. Soft Nanoparticles as Antimicrobial Agents and Carriers of Microbiocides for Enhanced Inhibition Activity. *J. Mat. Chem. B* **2024**, DOI: 10.1039/D4TB01200C.

Yong, H. W.: methodology, investigation, formal analysis, writing-original draft, review, editing; Ojagh, S. M. A.: guidance in antibacterial studies, writing-review & editing; Castellanos, L. S. R.: assistance in drug release experiments; Kakkar, A.: supervision, writing-original draft, review, editing.

**Chapter 4:** Yong, H. W.; Kakkar, A. Soft Nanoparticles with Induced Reversible Morphological Transitions through Upper Critical Solution Temperature for Controlled Drug Release.

Yong, H. W.: conceptualization, methodology, investigation, formal analysis, writing-original draft, review, editing; Kakkar, A.: supervision, writing-original draft, review, editing.

## Copyright

---

# JOHN WILEY AND SONS LICENSE TERMS AND CONDITIONS

Apr 10, 2024

---

---

This Agreement between Ms. Hui Wen Yong ("You") and John Wiley and Sons ("John Wiley and Sons") consists of your license details and the terms and conditions provided by John Wiley and Sons and Copyright Clearance Center.

License Number	5765510849377
License date	Apr 10, 2024
Licensed Content Publisher	John Wiley and Sons
Licensed Content Publication	Macromolecular Bioscience
Licensed Content Title	Nanoengineering Branched Star Polymer-Based Formulations: Scope, Strategies, and Advances
Licensed Content Author	Ashok Kakkar, Hui Wen Yong
Licensed Content Date	Jun 12, 2021
Licensed Content Volume	21
Licensed Content Issue	8
Licensed Content Pages	20
Type of Use	Dissertation/Thesis
Requestor type	Author of this Wiley article
Format	Print and electronic
Portion	Full article
Will you be translating?	No
Title of new work	Advancing Biomedical Applications with Functional Polymers
Institution name	McGill University
Expected presentation date	Apr 2024
Requestor Location	Ms. Hui Wen Yong 801 Sherbrooke Street West OM230  Montreal, QC H3A 0B8 Canada Attn: Ms. Hui Wen Yong
Publisher Tax ID	EU826007151
Total	<b>0.00 CAD</b>
Terms and Conditions	

# JOHN WILEY AND SONS LICENSE TERMS AND CONDITIONS

Apr 09, 2024

This Agreement between Ms. Hui Wen Yong ("You") and John Wiley and Sons ("John Wiley and Sons") consists of your license details and the terms and conditions provided by John Wiley and Sons and Copyright Clearance Center.

License Number	5761471040174
License date	Apr 03, 2024
Licensed Content Publisher	John Wiley and Sons
Licensed Content Publication	Polymer International
Licensed Content Title	The unexplored potential of gas-responsive polymers in drug delivery: progress, challenges and outlook
Licensed Content Author	Hui Wen Yong, Ashok Kakkar
Licensed Content Date	Nov 18, 2021
Licensed Content Volume	71
Licensed Content Issue	5
Licensed Content Pages	7
Type of Use	Dissertation/Thesis
Requestor type	Author of this Wiley article
Format	Print and electronic
Portion	Full article
Will you be translating?	No
Title of new work	Advancing Biomedical Applications with Functional Polymers
Institution name	McGill University
Expected presentation date	Apr 2024
Requestor Location	Ms. Hui Wen Yong 801 Sherbrooke Street West OM230  Montreal, QC H3A 0B8 Canada Attn: Ms. Hui Wen Yong
Publisher Tax ID	EU826007151
Total	<b>0.00 CAD</b>



### Single Functional Group Platform for Multistimuli Responsivities: Tertiary Amine for CO<sub>2</sub>/pH/ROS-Triggered Cargo Release in Nanocarriers

**Author:** Hui Wen Yong, Marine Ferron, Mélanie Mecteau, et al

**Publication:** Biomacromolecules

**Publisher:** American Chemical Society

**Date:** Sep 1, 2023

*Copyright © 2023, American Chemical Society*

#### PERMISSION/LICENSE IS GRANTED FOR YOUR ORDER AT NO CHARGE

This type of permission/license, instead of the standard Terms and Conditions, is sent to you because no fee is being charged for your order. Please note the following:

- Permission is granted for your request in both print and electronic formats, and translations.
- If figures and/or tables were requested, they may be adapted or used in part.
- Please print this page for your records and send a copy of it to your publisher/graduate school.
- Appropriate credit for the requested material should be given as follows: "Reprinted (adapted) with permission from {COMPLETE REFERENCE CITATION}. Copyright {YEAR} American Chemical Society." Insert appropriate information in place of the capitalized words.
- One-time permission is granted only for the use specified in your RightsLink request. No additional uses are granted (such as derivative works or other editions). For any uses, please submit a new request.

If credit is given to another source for the material you requested from RightsLink, permission must be obtained from that source.

BACK

CLOSE WINDOW

## List of Figures

---

<b>Figure 1.1:</b> Symmetrical and asymmetrical star copolymers, where A, B/B' and C/C' are incompatible polymeric arms.....	6
<b>Figure 1.2:</b> Key highlights of some of the parameters and variables of significance in designing star polymer-based nanoformulations.....	8
<b>Figure 1.3:</b> Polymers commonly employed in nanocarriers for drug delivery.....	19
<b>Figure 1.4:</b> Schematic illustration of hydrodynamic radii differences based on different hydrophilic lengths in star polymers; PCL = polycaprolactone and PEG = polyethylene glycol.	21
<b>Figure 1.5:</b> Schematic illustration of hydrodynamic radii changes based on the packing of (A) linear, and (B) star PCL- <i>b</i> -PDMAEMA copolymers; PCL = polycaprolactone, and PDMAEMA = poly(2-(dimethylamino)ethyl methacrylate).....	24
<b>Figure 1.6:</b> Schematic illustration of hydrodynamic radii based on the packing of (A) 3-arm, and (B) 4-arm PCL-PEGMA star copolymers; PCL = polycaprolactone and PEGMA = poly(ethylene glycol) methyl ether methacrylate. ....	25
<b>Figure 1.7:</b> Schematic illustration of hydrodynamic radii changes upon packing of (A) linear, and (B) star PCL- <i>b</i> -PDMAEMA copolymers; PCL = polycaprolactone and POEGMA = poly(oligo(ethylene glycol) methyl ether methacrylate).....	27
<b>Figure 1.8:</b> Schematic illustration of hydrodynamic radii differences based on the packing of (A) non-crosslinked linear, and (B) cross-linked H-type star copolymers; HPTB = hydroxyl-terminated polybutadiene, and PMAA = poly(methacrylic acid).....	28
<b>Figure 1.9:</b> Structure of PEG <sub>2</sub> -PCL miktoarm polymer that had been loaded with (B) nimodipine and (E) curcumin; PEG = poly(ethylene glycol) methyl ether and PCL = polycaprolactone, and structure of all the drugs that were summarized in Table 1. 2.....	31
<b>Figure 1.10:</b> Schematic illustration of changes in drug loading from (A) physical encapsulation, and (B) physical encapsulation, and chemical conjugation of ibuprofen at the core to PEG <sub>7</sub> -PCL <sub>14</sub> ; PEG = poly(ethylene glycol) and PCL = polycaprolactone. ....	33
<b>Figure 1.11:</b> Schematic illustration of changes in drug loading from (A) physical encapsulation (SP-DTX-C), and (B) physical encapsulation at the core and chemical conjugation at corona (SP-DTX) of DTX; PHPMA = poly( <i>N</i> -(2-hydroxypropyl)methacrylamide) and POSS-PDS = pyridyldisulfanyl-functionalized polyhedral oligomeric silsesquioxane.....	34

<b>Figure 1. 12:</b> Publications reporting studies on star polymers in drug delivery from 1992-2021. .....	41
<b>Figure 1. 13:</b> <i>O</i> -phenylenediamine (NO-responsive) and Pd-bridged (CO-responsive) functionalities for gas-responsive polymers-based drug delivery systems.....	49
<b>Figure 1. 14:</b> Azido (H <sub>2</sub> S-responsive) and levulinate (SO <sub>2</sub> -responsive) functionalities gas-responsive polymers-based drug delivery systems. ....	51
<b>Figure 1. 15:</b> Aliphatic fluorine (O <sub>2</sub> -responsive) and tertiary amine/ amidine (CO <sub>2</sub> -responsive) functionalities gas-responsive polymers-based drug delivery systems. ....	53
<b>Figure 1. 16:</b> Schematic representation of P(AnMA <sub>3-co</sub> -MMA <sub>87</sub> )- <i>b</i> -PDEAEMA <sub>77</sub> polymer with reversible polymersome-micelle morphologies controllable by CO <sub>2</sub> and UV light. Reproduced with permission from reference 221; Copyright 2019, Royal Society of Chemistry. ....	54
<b>Figure 1. 17:</b> Illustration of main components in Gram-positive and Gram-negative bacteria. Figure adapted from reference 320; Copyright 2020, American Chemical Society, used under Creative Commons CC-BY license. ....	66
<b>Figure 1. 18:</b> Schematic representation of both vancomycin-mediated bacterial targeting and antibiotics release. <sup>344</sup> Reproduced with permission from Chen, M.; Xie, S.; Wei, J.; Song, X.; Ding, Z.; Li, X. Antibacterial Micelles with Vancomycin-Mediated Targeting and pH/Lipase-Triggered Release of Antibiotics. <i>ACS Appl. Mater. Interfaces</i> <b>2018</b> , <i>10</i> (43), 36814-36823. Copyright 2018, American Chemical Society. ....	69
<b>Figure 1. 19:</b> Schematic illustrating a potential multimechanistic approach to treat bacterial infections using a phosphonium-functionalized micelle loaded with antibiotic. <sup>345</sup> Reproduced with permission from Hisey, B.; Ragogna, P. J.; Gillies, E. R. Phosphonium-Functionalized Polymer Micelles with Intrinsic Antibacterial Activity. <i>Biomacromolecules</i> <b>2017</b> , <i>18</i> (3), 914-923 reference. Copyright 2017, American Chemical Society. ....	70
<b>Figure 1. 20:</b> Representative phase diagram for polymers exhibiting (A) LCST and (B) UCST behavior. Yellow shaded regions denote biphasic regions, whereas white areas represent one-phase regions. $\chi_{\text{polymer}}$ indicates polymer fraction.....	72
<b>Figure 2. 1:</b> Cur-release from (A) Cur-MP1 and (B) Cur-TA-MP2 in the absence and presence of CO <sub>2</sub> . All studies were conducted in 0.01 M PBS buffer with 1% v/v Tween 80 at pH 7.4. Error bars represent a standard deviation of n=3. ....	140

**Figure 2. 2:** TEM of Cur-TA-MP2 showing small increments in size after continuous CO<sub>2</sub> bubbling: (A) CO<sub>2</sub> 0 h, D= 40 nm; (B) CO<sub>2</sub> 0.5 h, D= 53 nm; (C) CO<sub>2</sub> 6.5 h, D= 68 nm; (D) CO<sub>2</sub> 12 h, aggregation..... 143

**Figure 2. 3:** Cur-release profiles from Cur-TA-MP2 (A) at room temperature under different pH: pH 7.4 (in 0.01 M PBS), pH 6.5 (in 0.01 M PBS), pH 5.5 (in 0.01 M PBS), and pH 4.0 (in 0.01 M sodium acetate buffer); (B) in the absence and presence of H<sub>2</sub>O<sub>2</sub>; (C) with the combination of CO<sub>2</sub> + H<sub>2</sub>O<sub>2</sub> + tertiary amine. All studies were conducted in buffers with 1% v/v Tween 80. Error bars represent a standard deviation of n=3. .... 144

**Figure 2. 4:** Upper panels A and B: MTT assessment of cell viability of THP-1 human macrophages following (A) 1 h or (B) 24 h exposure of Cur or Cur-TA-MP2 at 10, 50 or 100 μM. Lower panels C-E: Flow cytometry assessment using propidium iodide and Annexin V labeling of (C) viable cells and (D) apoptotic cell percentages of the THP-1 human macrophages following 24 h exposure of Cur or Cur-TA-MP2 at 50 μM. (E) Dot plot graphs of flow cytometry. Results are expressed as mean ± SEM of 3 to 9 biological replicates. aaa: comparison with control, bbb: comparison with the same concentration of Cur when p<0.001, \*\*\*: p<0.001. .... 149

**Figure 2. 5:** Upper panels A-C: Anti-inflammatory activity of Cur assessed by quantification of interleukin-1β (IL-1β) secretion using western blotting analysis after (A) 1 h or (B) 24 h exposure of THP-1 cells to Cur and Cur-TA-MP2 at 50 μM and inflammasome activation using nigericin (Figure 2. 41). THP-1 cells were treated with Cur or Cur-TA-MP2 for 1 h or 24 h before nigericin 10 μM exposure for 30 minutes. (C) Nigericin induced THP-1's secretion of IL-1β in culture media. Lower panels D-F: (D) Anti-inflammatory activity of Cur and Cur-TA-MP2 assessed by polarization of THP-1 macrophages into CD68<sup>+</sup>HLA-DR<sup>+</sup> (M1 phenotype) or (E) CD68<sup>+</sup>HLA-DR<sup>-</sup> (M2-like phenotype) cells using flow cytometry analysis as represented by dot plots (F). To induce M1 polarization, THP-1 cells were co-treated with LPS-IFNγ and Cur or Cur-TA-MP2 at 10, 30 or 50 μM for a 24 h exposure. Results are expressed as mean ± SEM of 4 to 5 biological replicates. a: comparison with control, b: comparison with the same concentration of Cur when p<0.05, c: comparison with nigericin-exposed control when p<0.05. \*\*\*: p<0.001, aa: p<0.01, aaa: p<0.001. .... 151

**Figure 2. 6:** <sup>1</sup>H NMR spectrum of 3,5-bis(prop-2-ynyloxy)benzyl methanol (1)..... 170

**Figure 2. 7:** <sup>13</sup>C NMR spectrum of 1. .... 170

**Figure 2. 8:** <sup>1</sup>H NMR spectrum of 3,5- bis(prop-2-ynyloxy)benzyl polycaprolactone (2)..... 171

<b>Figure 2. 9:</b> $^{13}\text{C}$ NMR spectrum of 2. ....	171
<b>Figure 2. 10:</b> MALDI-TOF MS spectrum of 2. ....	172
<b>Figure 2. 11:</b> $^1\text{H}$ NMR spectrum of tosyl PEG <sub>2000</sub> monomethyl ether (MePEG <sub>2000</sub> -OTs).....	172
<b>Figure 2. 12:</b> $^{13}\text{C}$ NMR spectrum of MePEG <sub>2000</sub> -OTs. ....	173
<b>Figure 2. 13:</b> $^1\text{H}$ NMR spectrum of azido PEG <sub>2000</sub> monomethyl ether (3). ....	173
<b>Figure 2. 14:</b> $^{13}\text{C}$ NMR spectrum of 3. ....	174
<b>Figure 2. 15:</b> FTIR spectrum of (A) MePEG <sub>2000</sub> monomethyl ether and (B) 3. The presence of the azide in 3 was confirmed by the appearance of a peak at 2120 $\text{cm}^{-1}$ . ....	174
<b>Figure 2. 16:</b> $^1\text{H}$ NMR spectrum of (MePEG <sub>2000</sub> ) <sub>2</sub> -PCL <sub>3600</sub> (MP1). ....	175
<b>Figure 2. 17:</b> $^{13}\text{C}$ NMR spectrum of MP1. ....	175
<b>Figure 2. 18:</b> $^1\text{H}$ NMR spectrum of MABr. ....	176
<b>Figure 2. 19:</b> $^{13}\text{C}$ NMR spectrum of MABr. ....	176
<b>Figure 2. 20:</b> $^1\text{H}$ NMR spectrum of TA-MP2. ....	177
<b>Figure 2. 21:</b> $^{13}\text{C}$ NMR spectrum of TA-MP2. ....	177
<b>Figure 2. 22:</b> GPC traces of 3 (blue $D=1.06$ ), 2 (red, $D=1.15$ ), MP1 (orange, $D=1.20$ ), and TA-MP2 (black, $D=1.19$ ). ....	178
<b>Figure 2. 23:</b> Size changes of MP1-micelles and TA-MP2-micelles upon bubbling $\text{CO}_2$ . ....	178
<b>Figure 2. 24:</b> TEM images and analyses of (A) MP1-micelles and (B) TA-MP2-micelles. ....	179
<b>Figure 2. 25:</b> CMC determination of (A) MP1 and (B) TA-MP2. (Pyrene (6 $\mu\text{M}$ ) was used as the fluorescent probe. Error bars represent a standard deviation of $n=3$ . ....	179
<b>Figure 2. 26:</b> $^1\text{H}$ NMR analysis of TA-MP2 with (A) $\text{CO}_2 + \text{H}_2\text{O}_2$ , (B) $\text{CO}_2$ , and (C) no stimulus. ....	180
<b>Figure 2. 27:</b> TEM images and analyses of (A) MP1-micelles and (B) TA-MP2-micelles after $\text{CO}_2$ bubbling for 0.5 h. ....	180
<b>Figure 2. 28:</b> Size distribution upon Cur loading into (A) MP1-micelles and (B) TA-MP2-micelles. ....	181
<b>Figure 2. 29:</b> TEM image and analysis of Cur-MP1. ....	181
<b>Figure 2. 30:</b> pH (black) and $\text{CO}_2$ concentrations (red/blue) measurements of: (A) Milli-Q water + $\text{CO}_2$ ; (B) Milli-Q water + $\text{CO}_2 + \text{H}_2\text{O}_2$ ; (C) PBS + $\text{CO}_2$ ; and (D) PBS + $\text{CO}_2 + \text{H}_2\text{O}_2$ . Values of pH and $\text{CO}_2$ concentrations are listed in Table S1. Error bars represent a standard deviation of $n=3$ ....	182

.....	182
<b>Figure 2. 31:</b> DLS analysis of Cur-TA-MP2 upon treatment with CO <sub>2</sub> over time: 0 h (no CO <sub>2</sub> , black, 57 nm), 0.5 h (purple, 71 nm), 6.5 h (green, 134 nm), and 12 h (blue, 188 nm). .....	184
<b>Figure 2. 32:</b> TEM analysis of Cur-TA-MP2 with CO <sub>2</sub> over time: (A) 0 h (no CO <sub>2</sub> ), (B) 0.5 h, (C) 6.5 h, and (D) 12 h. ....	184
<b>Figure 2. 33:</b> DLS study of Cur-TA-MP2 after 12 h in varied pH media: pH 7.4 (black, 57 nm), pH 6.5 (blue, 72 nm), pH 5.5 (red, 79 nm), and pH 4.0 (purple, 87 nm).....	185
<b>Figure 2. 34:</b> TEM of Cur-TA-MP2 solution after 12 h in varied pH media: (A) pH 6.5; (B) pH 5.5; and (C) pH 4.0. ....	186
<b>Figure 2. 35:</b> TEM grid upon depositing Cur-TA-MP2 solution containing H <sub>2</sub> O <sub>2</sub> . ....	187
<b>Figure 2. 36:</b> DLS of Cur-TA-MP2 in 200 mM H <sub>2</sub> O <sub>2</sub> solution at various time intervals: 0 h (black, 57 nm), 0.5 h (blue, 67 nm), 6.5 h (red, 69 nm), and 12 h (purple, 84 nm).....	187
<b>Figure 2. 37:</b> Drug release data of Cur-TA-MP2 fitted to zero-order model. (A) No stimuli (pH 7.4), (B) high CO <sub>2</sub> conc, (C) low CO <sub>2</sub> , (D) pH 6.5, (E) pH 5.5, (F) pH 4.0, (G) H <sub>2</sub> O <sub>2</sub> , (F) low CO <sub>2</sub> + H <sub>2</sub> O <sub>2</sub> . ....	188
<b>Figure 2. 38:</b> Drug release data fitted to first-order model. (A) No stimuli (pH 7.4), (B) high CO <sub>2</sub> conc, (C) low CO <sub>2</sub> , (D) pH 6.5, (E) pH 5.5, (F) pH 4.0, (G) H <sub>2</sub> O <sub>2</sub> , (F) low CO <sub>2</sub> + H <sub>2</sub> O <sub>2</sub> . ....	189
<b>Figure 2. 39:</b> Drug release data fitted to Higuchi model. (A) No stimuli (pH 7.4), (B) high CO <sub>2</sub> conc, (C) low CO <sub>2</sub> , (D) pH 6.5, (E) pH 5.5, (F) pH 4.0, (G) H <sub>2</sub> O <sub>2</sub> , (F) low CO <sub>2</sub> + H <sub>2</sub> O <sub>2</sub> . ....	190
<b>Figure 2. 40:</b> Drug release data fitted to Korsmeyer-Peppas model. (A) No stimuli (pH 7.4), (B) high CO <sub>2</sub> conc, (C) low CO <sub>2</sub> , (D) pH 6.5, (E) pH 5.5, (F) pH 4.0, (G) H <sub>2</sub> O <sub>2</sub> , (F) low CO <sub>2</sub> + H <sub>2</sub> O <sub>2</sub> . ....	191
.....	191
<b>Figure 2. 41:</b> Raw images for Western blot data. ....	192
<b>Figure 3. 1:</b> (A) TEM image and (B) DLS analyses of P6-micelles, (C) TEM image and (D) DLS analyses of P7-micelles. Growth curves of (E) <i>E. coli</i> and (F) <i>B. subtilis</i> incubated with P6-micelles, growth curves of (G) <i>E. coli</i> and (H) <i>B. subtilis</i> treated with P7-micelles. Graph legends: P6 represents P6-micelles whereas P7 represents P7-micelles. Letter following sample represents bacterial strains, while the numbers that follow suit represent concentration of micellar solutions (e.g., P6E2500 contains 2500 µg mL <sup>-1</sup> of P6-micelle added to <i>E. coli</i> , P7B2500 contains 2500 ug mL <sup>-1</sup> of P6-micelle added to <i>B. subtilis</i> ). For additional concentrations tested, see Appendix B (Figure 3. 24-27). ....	204

**Figure 3. 2:** SEM images of untreated (A) *E. coli* and (B) *B. subtilis*, *E. coli* incubated with (C) P6-micelles, (E) P7-micelles, and *B. subtilis* with (D) P6-micelles, (F) P7-micelles. Bacteria were incubated with P6-/P7-micelles (2500  $\mu\text{g mL}^{-1}$ ) for 24 h prior to fixing. .... 208

**Figure 3. 3:** DLS analyses of (A) P6-CUR and P6-TBF, and (B) P7-CUR and P7-TBF. TEM images of (C) P6-CUR, (D) P6-TBF, (E) P7-CUR, and (F) P7-TBF..... 211

**Figure 3. 4:** (A) CUR release from P6-CUR and P7-CUR, (B) TBF release from P6-TBF and P7-TBF. All studies were conducted at 37 °C in 1X PBS buffer (pH 7.4, +1% v/v Tween 80). Error bars represent a standard deviation of n = 3. .... 213

**Figure 3. 5:** Growth curves of *E. coli* treated with (A) CUR and (B) TBF, *B. subtilis* treated with (C) CUR and (D) TBF, *E. coli* treated with (E) P7-CUR and (F) P7-TBF, and *B. subtilis* treated with (G) P7-CUR and (H) P7-TBF. Graph legends: P7C represents P7-CUR whereas P7T represents P7-TBF. Letter following sample represents bacterial strains, while the numbers that follow suit represent concentration of micellar solutions (e.g., P7CE2500 contains 2500  $\mu\text{g mL}^{-1}$  of P7-CUR added to *E. coli*, P7TB2500 contains 2500  $\mu\text{g mL}^{-1}$  of P7-TBF added to *B. subtilis*). For additional concentrations tested, see Appendix B (Figure 3. 34-37). .... 216

**Figure 3. 6:** SEM images of *E. coli* incubated with (A) CUR, (B) P7-CUR, (C) TBF, (D) P7-TBF and *B. subtilis* incubated with (E) CUR, (F) P7-CUR, (G) TBF, (H) P7-TBF. Bacteria were incubated with samples (2500  $\mu\text{g mL}^{-1}$ ) for 24 h prior to fixing. .... 220

**Figure 3. 7:**  $^1\text{H}$  NMR spectrum of P1. .... 236

**Figure 3. 8:**  $^{13}\text{C}$  NMR spectrum of P1. .... 237

**Figure 3. 9:**  $^1\text{H}$  NMR spectrum of P2. .... 237

**Figure 3. 10:**  $^{13}\text{C}$  NMR spectrum of P2. .... 238

**Figure 3. 11:**  $^1\text{H}$  NMR spectrum of P3. .... 238

**Figure 3. 12:**  $^{13}\text{C}$  NMR spectrum of P3. .... 239

**Figure 3. 13:**  $^1\text{H}$  NMR spectrum of P5. .... 239

**Figure 3. 14:**  $^{13}\text{C}$  NMR spectrum of P5. .... 240

**Figure 3. 15:** MALDI-Tof spectrum of P5. .... 240

**Figure 3. 16:**  $^1\text{H}$  NMR spectrum of P6. .... 241

**Figure 3. 17:**  $^{13}\text{C}$  NMR spectrum of P6. .... 241

**Figure 3. 18:**  $^1\text{H}$  NMR spectrum of P7. .... 242

**Figure 3. 19:**  $^{13}\text{C}$  NMR spectrum of P7. .... 242

<b>Figure 3. 20:</b> GPC traces of P3 (blue $D=1.11$ ), P5 (brown, $D=1.26$ ), P6 (green, $D=1.38$ ), and P7 (purple, $D=1.54$ ). .....	243
<b>Figure 3. 21:</b> FTIR spectrum of (A) P2, (B) P3 and (C) P6. The presence of the azide in P2 and P3 was confirmed by the appearance of a peak at $2120\text{ cm}^{-1}$ . .....	243
<b>Figure 3. 22:</b> TEM analyses of (A) P6-micelles and (B) P7-micelles. ....	244
<b>Figure 3. 23:</b> The CMC of (A) P6-micelles and (B) P7-micelles derived from the plot of fluorescence intensity of pyrene at 338 nm and 333 nm against polymer concentration. ....	244
<b>Figure 3. 24:</b> Growth curve analyses of <i>E. coli</i> in the presence of P6-micelles. Graph legends: P6 represents P6-micelles. Letter E following sample represents <i>E. coli</i> , while the numbers that follow suit represent concentration of micellar solutions (e.g., P6E1250 contains $1250\text{ }\mu\text{g mL}^{-1}$ of P6-micelle added to <i>E. coli</i> ). .....	245
<b>Figure 3. 25:</b> Growth curve analyses of <i>B. subtilis</i> in the presence of P6-micelles. Graph legends: P6 represents P6-micelles. Letter B following sample represents <i>B. subtilis</i> , while the numbers that follow suit represent concentration of micellar solutions (e.g., P6B1250 contains $1250\text{ }\mu\text{g mL}^{-1}$ of P6-micelle added to <i>B. subtilis</i> ). .....	245
<b>Figure 3. 26:</b> Growth curve analyses of <i>E. coli</i> in the presence of P7-micelles. Graph legends: P6 represents P7-micelles. Letter E following sample represents <i>E. coli</i> , while the numbers that follow suit represent concentration of micellar solutions (e.g., P7E1250 contains $1250\text{ }\mu\text{g mL}^{-1}$ of P7-micelle added to <i>E. coli</i> ). .....	246
<b>Figure 3. 27:</b> Growth curve analyses of <i>B. subtilis</i> in the presence of P7-micelles. Graph legends: P7 represents P7-micelles. Letter B following sample represents <i>B. subtilis</i> , while the numbers that follow suit represent concentration of micellar solutions (e.g., P7B1250 contains $1250\text{ }\mu\text{g mL}^{-1}$ of P7-micelle added to <i>B. subtilis</i> ). .....	246
<b>Figure 3. 28:</b> TEM analyses of (A) P6-CUR, (B) P6-TBF, (C) P7-CUR, and (D) P7-TBF.....	247
<b>Figure 3. 29.</b> Drug release profiles of free CUR and TBF. All studies were conducted at $37\text{ }^{\circ}\text{C}$ in 1X PBS buffer (pH 7.4, +1% v/v Tween 80). Error bars represent a standard deviation of $n = 3$ . .....	248
<b>Figure 3. 30:</b> Drug release data fitted to zero-order model: (A) P6-CUR, (B) P7-CUR, (C) P6-TBF and (D) P7-CUR. ....	249
<b>Figure 3. 31:</b> Drug release data fitted to first-order model: (A) P6-CUR, (B) P7-CUR, (C) P6-TBF and (D) P7-CUR. ....	250

<b>Figure 3. 32:</b> Drug release data fitted to Korsmeyer-Peppas model: (A) P6-CUR, (B) P7-CUR, (C) P6-TBF and (D) P7-CUR. ....	251
<b>Figure 3. 33:</b> Drug release data fitted to Higuchi model: (A) P6-CUR, (B) P7-CUR, (C) P6-TBF and (D) P7-CUR. ....	252
<b>Figure 3. 34:</b> Growth curve analyses of <i>E. coli</i> in the presence of P7-CUR. Graph legends: P7C represents P7-CUR. Letter E following sample represents <i>E. coli</i> , while the numbers that follow suit represent concentration of micellar solutions (e.g., P7CE1250 contains 1250 $\mu\text{g mL}^{-1}$ of P7-CUR added to <i>E. coli</i> ). ....	253
<b>Figure 3. 35:</b> Growth curve analyses of <i>E. coli</i> in the presence of P7-TBF. Graph legends: P7T represents P7-TBF. Letter E following sample represents <i>E. coli</i> , while the numbers that follow suit represent concentration of micellar solutions (e.g., P7TE1250 contains 1250 $\mu\text{g mL}^{-1}$ of P7-TBF added to <i>E. coli</i> ). ....	253
<b>Figure 3. 36:</b> Growth curve analyses of <i>B. subtilis</i> in the presence of P7-CUR. Graph legends: P7C represents P7-CUR. Letter B following sample represents <i>B. subtilis</i> , while the numbers that follow suit represent concentration of micellar solutions (e.g., P7CB1250 contains 1250 $\mu\text{g mL}^{-1}$ of P7-CUR added to <i>B. subtilis</i> ). ....	254
<b>Figure 3. 37:</b> Growth curve analyses of <i>B. subtilis</i> in the presence of P7-TBF. Graph legends: P7T represents P7-TBF. Letter B following sample represents <i>B. subtilis</i> , while the numbers that follow suit represent concentration of micellar solutions (e.g., P7TB1250 contains 1250 $\mu\text{g mL}^{-1}$ of P7-TBF added to <i>B. subtilis</i> ). ....	254
<b>Figure 4. 1:</b> Optical images of P(AAm <sub>111</sub> -co-AN <sub>70</sub> ) dispersed in water showing turbidity transitions with temperature ( $c = 5.0 \text{ mg mL}^{-1}$ ). ....	268
<b>Figure 4. 2:</b> Transmittance studies with temperature of various samples at different concentrations. The first column represents P(AAm <sub>111</sub> -co-AN <sub>70</sub> ) with increasing concentrations, middle column represents P(AAm <sub>111</sub> -co-AN <sub>70</sub> )-b-PEG <sub>90</sub> with increasing concentrations, last column represents P(AAm <sub>111</sub> -co-AN <sub>70</sub> )-b-PEG <sub>90</sub> -b-PCL <sub>25</sub> with increasing concentrations. Red curves represent heating phase and blue curves represent cooling phase. ....	269
<b>Figure 4. 3:</b> DLS analyses of NPs derived from (A) P(AAm <sub>111</sub> -co-AN <sub>70</sub> )-b-PEG <sub>90</sub> (T6NPs) and (D) P(AAm <sub>111</sub> -co-AN <sub>70</sub> )-b-PEG <sub>90</sub> -b-PCL <sub>25</sub> (T7NPs). Studies were done across three cycles of heating-cooling, where data points shown represent the average particle size from 3 cycles. TEM image of T6NPs (B) before (20 °C) and (C) after heating (40 °C), and T7NPs (E) before (20 °C)	

and (F) after heating (40 °C). Samples were stained with 2% uranyl acetate solution prior to analysis..... 274

**Figure 4. 4:** (A) DLS distribution curves of T7NPs (black) and CUR-loaded T7NPs (CUR-NPs, orange), (B) DLS analyses of CUR-NPs with temperature, (C) TEM image of CUR-NPs before heating (20 °C), and (D) after heating (40 °C). Samples were stained with 2% uranyl acetate solution prior to analysis. .... 278

**Figure 4. 5:** UV-Vis spectra of CUR-loaded T7NP ( $c = 5.0 \text{ mg mL}^{-1}$ ) (A) heated from 20 to 60 °C, (B) subsequently cooled from 60 to 20 °C, and (C) heated again to 60 °C. .... 280

**Figure 4. 6:** Fluorescence spectrum of CUR-loaded T7NP with temperature ( $c = 5.0 \text{ mg mL}^{-1}$ ) (A) heated from 20 to 60 °C and (B) subsequently cooled from 60 to 20 °C..... 283

**Figure 4. 8:**  $^1\text{H}$  NMR spectrum of 4PBA..... 300

**Figure 4. 9:**  $^{13}\text{C}$  NMR spectrum of 4PBA..... 300

**Figure 4. 10:**  $^1\text{H}$  NMR spectrum of 4PB-PCL..... 301

**Figure 4. 11:**  $^{13}\text{C}$  NMR spectrum of 4PB-PCL..... 301

**Figure 4. 12:** MALDI-ToF MS spectrum of 4PB-PCL..... 302

**Figure 4. 13:** THF GPC traces of 4PB-PCL ( $D=1.20$ )..... 302

**Figure 4. 14:**  $^1\text{H}$  NMR spectrum of P(AAm<sub>111</sub>-*co*-AN<sub>70</sub>)..... 303

**Figure 4. 15:** FT-IR spectrum of P(AAm<sub>111</sub>-*co*-AN<sub>70</sub>)..... 303

**Figure 4. 16:**  $^1\text{H}$  NMR spectrum of P(AAm<sub>111</sub>-*co*-AN<sub>70</sub>)-*b*-PEG<sub>90</sub>..... 304

**Figure 4. 17:**  $^1\text{H}$  NMR spectrum of P(AAm<sub>111</sub>-*co*-AN<sub>70</sub>)-*b*-PEG<sub>90</sub>-*b*-PCL<sub>25</sub>..... 304

**Figure 4. 18:** TEM analyses of T7NPs (A) before and (B) after heating..... 305

**Figure 4. 19:** TEM analyses of CUR-NPs (A) before and (B) after heating..... 305

## List of Tables

---

<b>Table 1. 1:</b> Self-assembly methods and their pros and cons. ....	9
<b>Table 1. 2:</b> Varied strategies in the star polymer-based assemblies for drug delivery. ....	15
<b>Table 1. 3:</b> Examples of the <i>in vitro</i> and <i>in vivo</i> studies using star nanoformulations. ....	37
<b>Table 1. 4:</b> Gas-responsive polymer based nanoformulations in drug delivery.....	45
<b>Table 1. 5:</b> Stimuli-responsive miktoarm polymers for drug delivery.....	58
<b>Table 1. 6:</b> Recent advancements in UCST-based soft polymeric micelles for cargo delivery...	74
<b>Table 2. 1:</b> Properties of miktoarm polymers (MP1 and TA-MP2) and their associated self-assemblies. ....	136
<b>Table 2. 2:</b> Kinetic parameters of Cur-TA-MP2.....	147
<b>Table 2. 3:</b> pH values and CO <sub>2</sub> concentrations from Figure 2. 30. ....	183
<b>Table 3. 1:</b> Polymer and micelle characterization of P6 and P7. ....	205
<b>Table 3. 2:</b> Drug-loaded micelle characterization.....	210
<b>Table 3. 3:</b> Kinetic parameters of drug-loaded micelles. ....	215
<b>Table 4. 1:</b> Characteristics of samples 4PB-PCL, P(AAm <sub>111</sub> - <i>co</i> -AN <sub>70</sub> ), P(AAm <sub>111</sub> - <i>co</i> -AN <sub>70</sub> )- <i>b</i> -PEG <sub>90</sub> , P(AAm <sub>111</sub> - <i>co</i> -AN <sub>70</sub> )- <i>b</i> -PEG <sub>90</sub> - <i>b</i> -PCL <sub>25</sub> . ....	267
<b>Table 4. 2:</b> Cloud points of samples P(AAm <sub>111</sub> - <i>co</i> -AN <sub>70</sub> ), P(AAm <sub>111</sub> - <i>co</i> -AN <sub>70</sub> )- <i>b</i> -PEG <sub>90</sub> , P(AAm <sub>111</sub> - <i>co</i> -AN <sub>70</sub> )- <i>b</i> -PEG <sub>90</sub> - <i>b</i> -PCL <sub>25</sub> upon heating and cooling at different concentrations. Data points were extracted from Figure 4. 2 when 50% transmittance was reached.....	270

## List of Schemes

---

<b>Scheme 1:</b> Outline of the thesis.....	76
<b>Scheme 2. 1:</b> Schematic overview of the multi-responsive NP behavior achievable through a single functional group (bulky tertiary amine) incorporated into miktoarm copolymer precursor (PEG <sub>45</sub> ) <sub>2</sub> -(PCL <sub>32</sub> -NR <sub>2</sub> ), and biological evaluation of Cur-loaded micelles.....	126
<b>Scheme 2. 2:</b> Synthesis of MP1 and TA-MP2 polymers: (i) Sn(Oct) <sub>2</sub> , dry toluene, 115 °C, 24 h, 90%; (ii) CuBr, PMDETA, dry THF, rt, 48 h, 76%; (iii) bromoacetyl bromide, triethylamine, dry THF, rt, 24 h, yield= 75%; (iv) diisobutylamine, dry DMF, 85 °C, 24 h, 77%. For synthetic details of 1, 2, and 3 see Appendix A.....	135
<b>Scheme 2. 3:</b> Synthesis of MP1 and multi-responsive miktoarm polymer TA-MP2.....	167
<b>Scheme 3. 1:</b> Schematic overview of the dual-purpose polycationic NPs for targeting bacteria and drug delivery.....	197
<b>Scheme 3. 2:</b> Synthesis details utilizing a mix of arm- and core-first methods to obtain cationic amphiphilic copolymer P7.....	203
<b>Scheme 4. 1:</b> Schematic illustration of P(AAm- <i>co</i> -AN)- <i>b</i> -PEG- <i>b</i> -PCL-based self-assembly and its reversible transition in response to temperature.....	260
<b>Scheme 4. 2:</b> Synthesis of polymeric precursors for thermoresponsive polymer, P(AAm <sub>111</sub> - <i>co</i> -AN <sub>70</sub> )- <i>b</i> -PEG <sub>90</sub> - <i>b</i> -PCL <sub>25</sub> . ....	265
<b>Scheme 4. 3:</b> Schematic illustration of (A) micelle disassembly formed from P(AAm- <i>co</i> -AN)- <i>b</i> -PEG (T6NPs) and (B) retention of micellar structure formed from P(AAm- <i>co</i> -AN)- <i>b</i> -PEG- <i>b</i> -PCL (T7NPs). Green polymer represents P(AAm- <i>co</i> -AN), blue represents PEG, and pink polymer represents PCL.....	276

## List of Abbreviations

---

4PBA	(4-(prop-2-yn-1-yloxy)phenyl)methanol
4PB-PCL	(4-(prop-2-yn-1-yloxy)benzyl)-PCL
AAA	Aminoadipic acid
ABC	Accelerated blood clearance
ABP	4-acryloyloxybenzophenone
AD	( <i>N</i> -amidino)dodecyl acrylamide
AHMA	( <i>N</i> -amidino)hexyl methacrylamide
AMA	Allyl methacrylate
AMR	Antimicrobial resistance
AnMA	(Anthracene-9-carboxyl)ethyl methacrylate
APUEMA	2-(3-(2-aminophenyl)ureido)ethyl methacrylate hydrochloride
ATRP	Atom transfer radical polymerization
<i>A. Baumannii</i>	<i>Acinetobacter baumannii</i>
BA	<i>N</i> -benzylacrylamide
<i>B. cereus</i>	<i>Bacillus cereus</i>
<i>B. subtilis</i>	<i>Bacillus subtilis</i>
bis-MPA	2,2-bis(hydroxymethyl) propionic acid
Boc-GABA-OH	<i>N</i> -(tert-butoxycarbonyl)-4-aminobutyric acid
BZA	Benzoylacetone
CAA	(2'-acryloylamino-ethylene)-3 $\alpha$ ,7 $\alpha$ ,12 $\alpha$ -trihydroxy-5 $\beta$ -cholanoamide
CAC	Critical aggregation concentration
CDCl <sub>3</sub>	Deuterated chloroform
CDS	Per-6-( <i>tert</i> -butyldimethylsilyl)- $\beta$ -cyclodextrin
CHCl <sub>3</sub>	Chloroform
CI	Confidence intervals
CL	Caprolactone
CMA	Coumarin methacrylate
CMC	Critical micelle concentration
Coenzyme Q10	CoQ10

CPT	Camptothecin
CuAAC	Copper-catalyzed alkyne-azide cycloaddition
Cur/ CUR	Curcumin
<i>D</i>	Diameter
<i>D<sub>H</sub></i>	Hydrodynamic diameter
<i>Đ</i>	Polydispersity index
D <sub>2</sub> O	Deuterium oxide
DCC	Dicyclohexylcarbodiimide
DCM	Dichloromethane
DEAEMA	<i>N,N</i> -diethylaminoethyl methacrylate
DEEA	<i>N,N</i> -diethylaminoethyl acrylamide
DEX	Dextran
DL%	Drug loading
DLS	Dynamic light scattering
DMA	Dimethylacetamide
DMAA	<i>N,N</i> -dimethyl-acrylamide
DMAEMA	<i>N,N</i> -dimethylaminoethyl methacrylate
DMAP	4-dimethylaminopyridine
DMF	Dimethylformamide
DMNOBA	<i>N,N</i> -dimethyl- <i>N</i> -(2-nitrobenzyl)ethaneamine acrylamide
DMSO	Dimethyl sulfoxide
DMSO-d <sub>6</sub>	Deuterated dimethyl sulfoxide
DOX	Doxorubicin
DP	Degree of polymerization
DPBA	(3,5-bis(prop-2-yn-1-yloxy)phenyl)methanol
DTTP	dithioketal-linked ditocopheryl polyethylene glycol
DTX	Docetaxel
EDC	1-Ethyl-3-(3-dimethylaminopropyl)carbodiimide
EDTA	Ethylenediaminetetraacetic acid disodium salt dihydrate
EE%	Encapsulation efficiency
EGDMA	Ethyleneglycol dimethacrylate

EPR	Enhanced permeability and retention effect
ESI	Electrospray ionization
<i>E. aerogenes</i>	<i>Enterobacter aerogenes</i>
<i>E. coli</i>	<i>Escherichia coli</i>
FA	Folic acid
FBS	Fetal bovine serum
FTIR	Fourier-transform infrared spectroscopy
GA	Glycolamide
GPC	Gel permeation chromatography
HA	Hyaluronic acid
H <sub>2</sub> S	Hydrogen sulfide
HeLa	Henrietta Lacks
HLA-DR	Human leukocyte antigen – DR isotype
HPLC	High-performance liquid chromatography
HPMA	2-hydroxypropyl methacrylate
HSO <sub>3</sub> <sup>-</sup>	Bisulfite ions
HTPB	Hydroxyl-terminated polybutadiene
ICG	Indocyanine green
IFN- $\gamma$	Interferon $\gamma$
IL-1 $\beta$	Interleukin-1 $\beta$
<i>K. pneumonia</i>	<i>Klebsiella pneumonia</i>
LB	Lysogeny broth
LC	Loading capacity
LCST	Lower critical solution temperature
LF	Levofloxacin
LIPO-c/ Lipo-s	Doxorubicin-loaded liposomes
LL	Lower limit
LPS	Lipopolysaccharides
Lys	Lysine
$\lambda_{em}$	Emission wavelength
$\lambda_{ex}$	Excitation wavelength

M <sub>n</sub>	Number average molecular weight
M <sub>w</sub>	Weight average molecular weight
MA	Miktoarm
MALDI-ToF	Matrix-Assisted Laser Desorption/Ionization-Time Of Flight
MAPA	Multi-L-arginyl-poly-L-aspartate
MeO <sub>2</sub> MA	<i>N,N</i> -dimethylaminoethyl methacrylate
MePEG	Poly(ethylene glycol) methyl ether
Me <sub>6</sub> TREN	Tris(2- (dimethylamino)ethyl)amine
mPEG-N <sub>3</sub>	Azido-poly(ethylene glycol) monomethyl ether
mPEG-OTs	Tosylated poly(ethylene glycol) monomethyl ether
MC	Methyl cholate
MCF7	Michigan Cancer Foundation-7
MMA	Methyl methacrylate
MS	Mass spectrometry
MTT	3-(4,5-dimethylthiazol-2-yl)-2,5-diphenyltetrazolium bromide
MU	6-methyluracil
MW	Molecular weight
MWCO	Molecular weight cut-off
N <sub>3</sub> -Nap	<i>N</i> -(2-hydroxyethyl)-4-azide-1,8-naphthalimide
NAPMA	<i>N</i> -(2-aminophenyl)methacrylamide hydrochloride
NHS	<i>N</i> -Hydroxysuccinimide
NIM	Nimodipine
NIPAM	<i>N</i> -isopropylacrylamide
NMA-HTCC	<i>O</i> -acrylamidomethyl- <i>N</i> -[(2-hydroxy-3-trimethylammonium)propyl] chitosan chloride
NMR	Nuclear magnetic resonance
NO	Nitric oxide
NPs	Nanoparticles
OA	Oleic acid
OD	Optical density
PAA	Polyacrylic acid

PAAm	Polyacrylamide
PADS	Amidine-containing styrene polymer
PAGMA	Poly( <i>o</i> -azidomethylbenzoyl glycerol methacrylate)
PAOx	Poly(2-alkyl/aryl-2-oxazoline)
PAN	Polyacrylonitrile
PBMA	Poly[( <i>p</i> -dimethylamine)methylbenzyl methacrylate]
PBS	Phosphate buffer saline
PCCL	Poly(6-acetoxy- $\epsilon$ -caprolactone)
PCL	Polycaprolactone
PDMA	Poly( <i>N,N</i> -dimethylacrylamide)
PDMAEMA	Poly(2-(dimethylamino)ethyl methacrylate)
PDEAEMA	Poly(2-(diethylamino)ethyl methacrylate)
PEG	Poly(ethylene glycol)
pEGFP	Green fluorescence protein plasmid
PEGMA	Poly(ethylene glycol) methyl ether methacrylate
PEI	Poly(ethylene imine)
PEO	Poly(ethylene oxide)
PEOPA	Poly( <i>o</i> -phenylenediamine-L-glutamate)
PGlu	Poly(glutamic acid)
PGMA	Poly(glycerol methacrylate)
PHEMA	Poly(2-hydroxyethyl methacrylate)
PHPMA	Poly( <i>N</i> -(2-hydroxypropyl)methacrylamide)
PLA	Poly(lactic acid)
P(D)LA	Poly(d-lactide)
P(L)LA	Poly(l-lactide)
PLGA	Poly(lactide- <i>co</i> -glycolide)
PLL	Poly(L-lysine)
PLLSA	Poly(carboxylated-L-lysine)
PMA	Phorbol 12-myristate 13-acetate
PMAA	Poly(methacrylic acid)
PMDETA	<i>N,N,N',N'',N'''</i> -pentamethyldiethylenetriamine

PMEPPMA	Poly(4-(4-methoxyphenylazo)phenoxy methacrylate)
PMMA	Poly(methyl methacrylate)
PNAGA	poly( <i>N</i> -acryloylglycinamide)
PNBA	Poly(2-nireobenzyl acrylate)
PNIPAM	Poly( <i>N</i> -isopropylacrylamide)
PNVP	Poly( <i>N</i> -vinylpyrrolidone)
POEGMA	Polyoligo(ethylene glycol) methyl ether methacrylate
POSS-PDS	Pyridyldisulfanyl-functionalized polyhedral oligomeric silsesquioxane
PPS	Poly(propylene sulfide)
ppm	Parts per million
PS	Polystyrene
PSar	Polysarcosine
PSPB	Poly(sulfobetaine)
PtBA	Poly(tert-butylacrylate)
PTMC	Poly(trimethylene carbonate)
PTX	Paclitaxel
PUA	Poly(undecylenic acid)
PUPd	Palladacycle-connected polyurethane block
PVDF	Polyvinylidene fluoride
PVPOP	Poly(4-vinylphenyl 4-oxopentanoate)
Py	Pyrene
<i>P. aeruginosa</i>	<i>Pseudomonas aeruginosa</i>
<i>P. mirabilis</i>	<i>Proteus mirabilis</i>
$R_H$	Hydrodynamic radius
$R^2$	Correlation coefficients
RAFT	Reversible addition-fragmentation chain transfer
RBZ	Ranibizumab
RES	Reticuloendothelial system
RGD	Arginine-glycine-aspartic acid
RhB	Rhodamine B
ROP	Ring opening polymerization

ROS	Reactive Oxygen Species
RPM	Revolutions per minute
RPMI	Roswell Park Memorial Institute
SC-Dex	H <sub>2</sub> S-responsive cholesterol-modified dextran
SEM	Scanning electron microscope
SFRP	Stable free radical polymerization
SN-38	7-ethyl-10-hydroxycamptothecin
SP	Star polymer
SPION	Super-paramagnetic iron oxide nanoparticles
<i>S. aureus</i>	<i>Staphylococcus aureus</i>
<i>S. maltophilia</i>	<i>Stenotrophomonas maltophilia</i>
T <sub>c</sub>	Critical solution temperature
TBF	Terbinafine
TEM	Transmission electron microscope
TF-DEAE-AM	2,2,2-trifluoroethyl 3-( <i>N</i> -(2-(diethylamino)ethyl)acrylamido)propanoate
TFA	Trifluoroacetic acid
TFEMA	2,2,2-trifluoroethyl methacrylate
THF	Tetrahydrofuran
TMPTA	Trimethylolpropane trimethacrylate
TPEA	<i>N</i> -(2-acrylamidoethyl)-4-(1,2,2-triphenylvinyl)benzamide
TPGS	D- $\alpha$ -tocopheryl polyethylene glycol 1000 succinate
TPP <sup>+</sup>	Triphenylphosphonium cation
TPPBr	Triphenylphosphonium bromide
TPPP	Tetraphenylporphyrin
UCST	Upper critical solution temperature
UL	Upper limit
UV-Vis	Ultraviolet–visible
VCM	Vancomycin
VIm	Vinylimidazole
VS	Vinyl sulfone
WHO	World Health Organization

# Chapter 1: Introduction

This thesis contributes to the field of nanomedicine by utilizing techniques in polymer synthesis to engineer complex architectures and design soft nanoparticles with tailored properties for biomedical applications. By exploring polymer precursor composition in both branched and linear systems, it demonstrates how nanoparticle design can be optimized with specific functionalities, thereby enhancing their effectiveness in biomedical interventions.

The thesis begins with a comprehensive background section, laying the foundation for subsequent chapters by providing an extensive review of strategies for branched polymer modification and their versatility in self-assembled structures for various biomedical applications (Section 1.1). Branched polymers have emerged as a promising platform for designing soft nanoparticles due to their unique structural characteristics and tunable properties. The branched architectures provides a high degree of functional versatility, allowing for tunable control over size, shape, and functionality of the corresponding nanoparticles. These features are particularly interesting for biomedical applications to design nanoparticles that can be easily customized to meet specific requirements, which are demonstrated in Chapters 2 and 3. In Chapter 2, we demonstrate core modification techniques employed in nanoparticles to confer multiple responsivity to stimuli present at disease sites, such as CO<sub>2</sub>, pH, reactive oxygen species (ROS), and combinations thereof. To understand the unexplored potential of gas-responsive polymers, Section 1.2 sheds light on their advancements, limitations, and applicability in nanomedicine. Additionally, Section 1.3 provides an overview of the evolving landscape of miktoarm polymer-based stimuli-responsive systems in nanomedicine. This section aims to highlight the opportunities in advancing biomedical applications with these versatile macromolecules. Chapter 3 focuses on shell modifications aimed at achieving core-shell structures with cationic surfaces, thereby imparting intrinsic antibacterial properties to the nanoparticles. The presentation of antibacterial nanoparticles in Section 1.4 provides readers with an overview of the strategies employed and their potential applications in combating microbial pathogens.

In addition to miktoarm polymers, we demonstrate the use of triblock copolymers for *in situ* core/shell modifications to obtain stable nanoparticles with temperature-controlled morphological changes for drug delivery (Chapter 4). Specifically, this research explores the use of upper critical solution temperature (UCST) polymers, a relatively understudied area in the field of nanomedicine. To provide readers with an overview of the advancements in thermoresponsive polymers for drug delivery, Section 1.5 presents a discussion on the rationale behind utilizing thermoresponsive polymers and the current state of research using UCST polymers for drug delivery applications. Chapter 1 then concludes with an outline of the scope of thesis and contributions to original knowledge in Section 1.6. This section aims to emphasize the significance of this thesis in the field of nanomedicine by outlining its contributions. Overall, it offers strategies for the design and optimization of soft nanoparticles with tailored properties for more effective and targeted interventions.

### **1.1 Nanoengineering Branched Star Polymer-based Formulations: Scope, Strategies and Advances**

This section incorporates content adapted in part from published article, the citation of which is provided below and is reprinted with permission from Wiley-VCH GmbH.

Yong, H. W.; Kakkar, A. Nanoengineering Branched Star Polymer-Based Formulations: Scope, Strategies, and Advances. *Macromol. Biosci.* **2021**, *21*, 2100105.

#### *1.1.1. Abstract*

Soft nanoparticles continue to offer a promising platform for the encapsulation and controlled delivery of poorly water-soluble drugs and help enhance their bioavailability at targeted sites. Linear amphiphilic block copolymers are the most extensively investigated in formulating delivery vehicles. However, more recently, there has been increasing interest in utilizing branched macromolecules for nanomedicine, as these have been shown to lower critical micelle concentrations, form particles of smaller dimensions, facilitate the inclusion of varied compositions and function-based entities, as well as provide prolonged and sustained release of

cargo. In this review, it is aimed to discuss some of the key variables that are studied in tailoring branched architecture-based assemblies, and their influence on drug loading and delivery. By understanding structure–property relationships in these formulations, one can better design branched star polymers with suitable characteristics for efficient therapeutic interventions. The role played by polymer composition, chain architecture, crosslinking, stereocomplexation, compatibility between polymers and drugs, drug/polymer concentrations, and self-assembly methods in their performance as nanocarriers is highlighted.

### *1.1.2. Introduction*

Drug delivery technology is a broad field of research focusing on the development of novel materials to improve the efficacy of drugs administered into human body. There are a few reasons that signify the pressing need for such materials: (i) most active pharmaceutical agents are lipophilic, and thus sparingly soluble in an aqueous medium, which often results in their low dissolution rate, as well as poor bioavailability;<sup>1</sup> (ii) rapid clearance by the reticuloendothelial system (RES, e.g. liver and spleen), as soon as the body recognizes these as “foreign” substances; and (iii) lack of selectivity and non-specific interaction of pharmaceutical agents, which often lead to undesired side effects. In a quest to address this multi-faceted problem, a significant amount of effort has been devoted in developing drug delivery systems, including carbon nanotubes,<sup>2</sup> dendrimers,<sup>3,4</sup> polymeric micelles,<sup>5</sup> liposomes,<sup>6</sup> quantum dots,<sup>7,8</sup> superparamagnetic iron oxide nanoparticles (SPIONs),<sup>9</sup> gold nanoparticles and mesoporous silica nanoparticles,<sup>10</sup> to name a few. These nano-sized carriers are capable of housing poorly-water soluble drugs and retaining them in the blood circulation, subsequently enhancing their efficacy and bioavailability which is often critical for reducing dose frequency and increasing patient compliance.

Among the few nanocarriers mentioned above, amphiphilic block copolymers self-assembled into polymeric micelles, are one of the earliest reported soft nanoparticles. Since their discovery in the 1980s, these have paved the way in enhancing solubility of the lipophilic cargo by physical encapsulation, as well as delivery, using a passive mechanism through the widely invoked “enhanced permeation and retention effect”.<sup>11,12</sup> To augment their scope and specificity in drug release, a lot of emphasis has been placed on exploiting endo- and exogenous cues in designing

stimuli-responsive smart nanoformulations by introducing chemical entities sensitive specifically to pH, temperature, reactive oxygen species, glutathione, light etc.<sup>13</sup> In addition, the overall structure of polymer precursors has evolved from linear to branched, star-shaped, comb, brush, graft polymers, and hyperbranched structures including dendrimers. Such diversity in architecture has opened the door to more opportunities to identify limitations, and tailor nanoparticles with higher precision in drug delivery. The goal of this review is to evaluate how this diversity and progress in polymer science, have helped advance drug delivery, with the hope that branched architecture-based formulations will now be studied extensively in terms of their pharmacokinetic behavior, and progress into the realm of both *in vitro* and *in vivo* evaluations. We will highlight how an understanding of the basic parameters crucial to nanoformulation-based drug delivery can be modulated into the overall structure of the polymers, to design efficient drug delivery systems.

### *1.1.3. Emerging Potential of Branched Star Polymers as Nanocarriers*

Following the discovery of liposomes, amphiphilic linear block copolymers became, and remained a focus, in developing nanosized structures for drug delivery. Enormous progress has been made in developing synthetic methodologies, and obtaining an understanding of their self-assembly behavior, and most of what we know today stems from the study of the linear architectures. Detailed evaluations of their aqueous behavior have also given us predictability in morphologies of the resulting structures. It is now well understood that changes in hydrophilic/hydrophobic fractions in polymer compositions, play an important role in obtaining assemblies, ranging from star-like, crew-cut, and rod-shaped micelles, to polymersomes, and even lamellae structures.<sup>14</sup> Advances in synthesis have also contributed towards a library of functionalities that can be specially tailored to improve drug solubility, loading, release, and bioavailability, while keeping the dosage to a minimum. The properties of their ordered assemblies, as well as controlling factors, including polymer chemical composition and molecular weight, have also been investigated.<sup>15</sup> Branched architectures, on the other hand, have only recently started to attract attention, despite seeing first reports dating back to the 1960s.<sup>16, 17</sup> The progression in synthetic methods and characterization, have allowed polymer chemists to control and obtain more complex, multifunctional polymers with narrow molecular weight distributions, which are distinct from linear polymers. These include both symmetric and asymmetric stars, with either molecular or

chemical asymmetry, i.e., miktoarm polymers. Some typical star block copolymer architectures are depicted in Figure 1. 1. Synthesis of amphiphilic stars, which are the precursors to nanoassemblies, has been the focus of several reviews recently.<sup>18-22</sup> There has been tremendous effort devoted to developing methodologies to these well-defined homo- or heteroarm stars, which have employed the chlorosilanes method, pioneered by Hadjichristidis,<sup>23</sup> and core-first, arm-first, or grafting-on approaches. To have a better control over their molecular weights, free radical polymerization methods<sup>24-27</sup> including atom transfer radical polymerization (ATRP), reversible addition fragmentation chain transfer (RAFT), and stable free radical polymerization (SFRP), as well as ring-opening polymerization (ROP), have been utilized. In the stitching methodology (arms-first), which employs pre-synthesized polymeric arms covalently linked to the core, alkyne-azide “click”, and esterification reactions have been very popular.<sup>28-30</sup> Generally, a combination of core-first and arms-first methodologies have generated better outcomes in the synthesis of amphiphilic polymers for aqueous self-assembly.

More extensive investigations, both experimental and theoretical, have now begun to provide a better conception of this new and intriguing class of macromolecules.<sup>31-34</sup> One of the attractive features of branched macromolecules, as one would expect, is the variation in the number of arms from a central core, something unachievable with linear block copolymers. To obtain a similar composition as their linear counterparts, the molecular weight of each arm in a branched architecture is reduced and can be tailored with the number of core-linked polymers. With lower molecular weight polymeric arms, chain entanglement gets significantly reduced, and the overall structure becomes much more flexible and less viscous.<sup>35</sup> The mechanical and viscoelastic properties of star polymers are thus distinct from their linear analogs.<sup>36,37</sup> For some polymers that exhibit crystalline behavior at higher molecular weights, such as the much-favored polycaprolactone (PCL) that is biocompatible and biodegradable, keeping it short and in the amorphous state, is considered advantageous in enhancing hydrophobic interactions between the drug and the polymer. The unique core-shell structure formed from star block copolymers upon microphase separation also leads to spherical assemblies with smaller hydrodynamic diameters, compared to their linear analogs with similar molecular weights.<sup>38</sup>

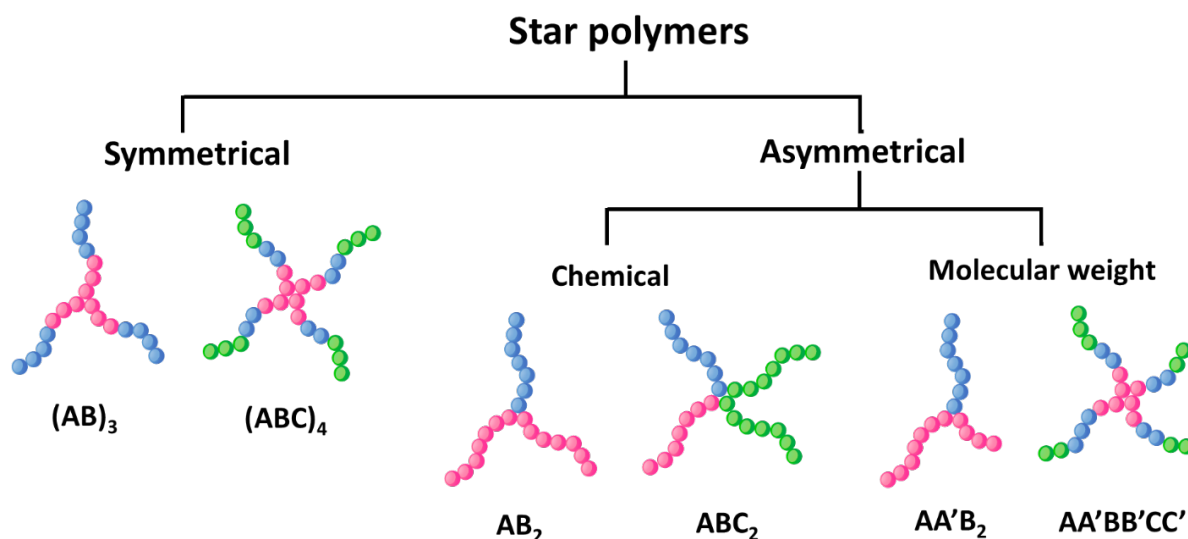


**Figure 1.1:** Symmetrical and asymmetrical star copolymers, where A, B/B' and C/C' are incompatible polymeric arms.

In addition to the aforementioned advantages, star polymers offer the possibility of incorporating a much higher number of functional groups. This has implications in a wide variety of applications, ranging from thermoplastic elastomers,<sup>39</sup> polyelectrolytes,<sup>40</sup> polyionic liquids,<sup>41</sup> hydrogels,<sup>42</sup> wearable electronics,<sup>43, 44</sup> and drug carriers.<sup>45, 46</sup> One can construct topologically complex architectures by controlling a number of factors, to alter their dimensions, morphologies, stability, and material properties, some of which will be touched upon in this review. Thus, star polymers constitute a relatively new addition to the family of macromolecules that are distinct, yet equally interesting as their linear analogues. In the context of drug delivery, the unique physicochemical properties of star polymers can bring advantages in improving the overall efficacy of pharmaceutical agents.<sup>47-49</sup> Considering that these are now starting to become ubiquitous polymeric architectures for biomedical applications, we aim to discuss some of the strategies in designing star copolymer-based self-assemblies for drug delivery. Some highlights of the structure of this review are provided in Figure 1. 2.

In this review, our aim is to concisely summarize key contributors that help tailor the efficacy of star-polymer-based nanoformulations in drug delivery, and how the branched architecture has been

modulated to better control each of these parameters. We will begin with a succinct discussion on various methods, including their pros and cons, to prepare self-assemblies of amphiphilic polymers in aqueous media, and formulation parameters of significance in drug delivery. It will be followed by i) a detailed discussion on star polymers-based assemblies; ii) how one could optimize these nanoparticles by articulating the star structure and its overall composition; iii) interesting variations that have been carried out in star polymers to enhance their effectiveness in drug delivery; and lastly iv) conclude with a brief outlook on prospects of star polymers in nanomedicine. Ultimately, the key takeaway is that nanoformulations containing active pharmaceutical agents need to have a balance of properties, which define their efficacy in carrier capacity, stability, as well as controlled and sustained drug release. Through an understanding of their direct or indirect structure-property relationships, one can aim to tailor the design of star polymer-based assemblies. In the family of star polymers, well-defined hyperbranched macromolecular cores, more commonly referred to as dendrimer-based star polymers, have also offered opportunities to expand the breadth of star polymers in biomedical applications.<sup>50-56</sup> Such highly branched architectures, pioneered by the group of Akira Hirao,<sup>57-59</sup> do not constitute the focus here, and have been extensively reviewed in the last few years.<sup>60-64</sup> Globular hyperbranched polymers, which are akin to dendrimers in relation to their three dimensional highly-branched configuration, but distinct in terms of their composition, have also been investigated for applications in drug delivery.<sup>65-68</sup> Various methodologies to synthesize such hyperbranched polymers were reviewed by Wang and Gao.<sup>69</sup> Amongst these, self-condensing vinyl polymerization, using controlled radical polymerization methods, has been widely applied for constructing a variety of hyperbranched polymers.<sup>70-72</sup> Considering the scope of the discussion here, the reader is directed to an elegant recent review by Cuneo and Gao on such hyperbranched star architectures.<sup>73</sup>

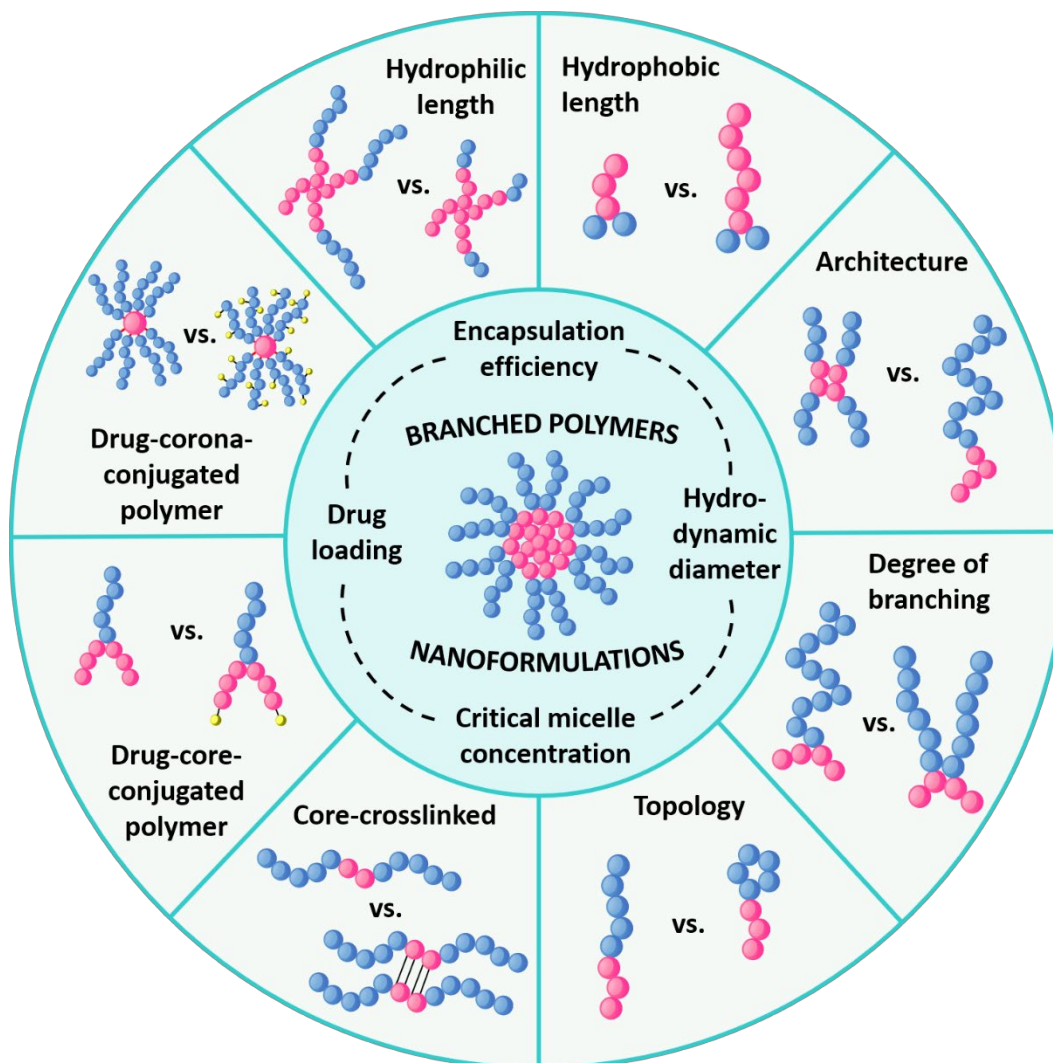


**Figure 1.2:** Key highlights of some of the parameters and variables of significance in designing star polymer-based nanoformulations.

#### 1.1.4. Polymer Self-assembly: Methods

There are a variety of methodologies that can induce self-assembly of amphiphilic copolymers and promote encapsulation of the desired therapeutic agents. Upon introduction of the polymer/drug solution into an aqueous medium, unimers start to spontaneously organize into more ordered structures, such as micelles, nanorods as well as polymersomes, depending on the composition of the copolymer. In general, the choice of the solvent depends on its miscibility with water, ability to solubilize both drug and the polymer, as well as its volatility/ ease of removal (i.e., low boiling

point). It is well known that the protocol adopted during self-assembly can significantly influence the overall properties of the resulting nanoparticles.<sup>74, 75</sup> A brief introduction to some of the commonly used self-assembly methods, together with an analysis of their advantages and disadvantages, are provided in Table 1. 1. A key requisite amongst these is the complete removal of the organic solvents, which is crucial as even a small amount could become toxic enough to kill cells.

**Table 1. 1:** Self-assembly methods and their pros and cons.

Method	Procedure	Advantages	Disadvantages	Ref
Direct dissolution	Dissolve both the polymer and drug directly into an aqueous solution.	Simple	<ul style="list-style-type: none"> <li>• More suitable for low molecular weight polymers and drugs, systems with short insoluble domains</li> <li>• Low encapsulation efficiency</li> <li>• May require additional external driving force (e.g. ultrasound)</li> </ul>	76-78
Dialysis	1. Dissolve the polymer and drug in a water-miscible organic solvent (e.g., tetrahydrofuran (THF), acetone, ethanol, dimethylformamide (DMF), dimethyl	<ul style="list-style-type: none"> <li>• Simple</li> <li>• Applicable to a wide range of polymers and drugs, which are lipophilic and immiscible with water).</li> </ul>	<ul style="list-style-type: none"> <li>• Complete removal of the organic solvent required.</li> <li>• Large amounts of water needed, difficult/impractical to scale up.</li> </ul>	79

	<p>sulfoxide (DMSO) or dimethylacetamide (DMA).</p> <p>2. Dialyze against deionized water. Self-assemblies are formed slowly as the organic solvent is removed by passive diffusion.</p>	<ul style="list-style-type: none"> <li>• Prevents formation of big aggregates</li> </ul>	<ul style="list-style-type: none"> <li>• Time-consuming</li> <li>• Can cause drug release, and result in lower encapsulation efficiencies.</li> <li>• Drug and polymer may also dialyze out over time.</li> </ul>	
Co-solvent evaporation/ Microphase separation	<p>1. Dissolve both the polymer and drug in a low boiling, nonselective and water-miscible organic solvent (e.g., THF or acetone).</p> <p>2. Add solution dropwise to water while stirring. nanoparticles are formed as the organic solvent slowly evaporates.</p> <p>3. Any excess drug can be removed by centrifugation at low RPMs.</p>	Prevents formation of big aggregates.	Complete removal of organic solvent is necessary.	77, 80
Solvent evaporation/ Thin-film hydration	1. Dissolve the polymer and drug in a water-miscible and low	High drug loading and encapsulation efficiency.	Organic solvent needs to be removed completely.	81

	<p>boiling organic solvent.</p> <p>2. Remove the organic solvent slowly under reduced pressure to obtain a thin film.</p> <p>3. Rehydrate the film while sonicating or stirring.</p>			
Oil-in-water/ solvent-in- water emulsion	<p>1. Dissolve the polymer and drug in a water-immiscible organic solvent (e.g., chloroform (CHCl<sub>3</sub>) or dichloromethane (DCM)).</p> <p>2. Add solution to water dropwise, followed by sonication or stirring to form an emulsion.</p>	<ul style="list-style-type: none"> <li>• Simple</li> <li>• Can be used for a wide range of polymers and drugs.</li> </ul>	<ul style="list-style-type: none"> <li>• Complete removal of the organic solvent is required.</li> <li>• Commonly used chlorinated solvents are carcinogens and toxic to the environment.</li> </ul>	82
Freeze-drying/ Lyophilization	<p>1. Dissolve the polymer and drug in a mixture of an organic solvent (e.g., tert-butanol, DMA) and water.</p> <p>2. Remove solvent at low temperatures and pressures. Micelles are formed upon freeze-drying.</p>	<ul style="list-style-type: none"> <li>• Stable assemblies.</li> <li>• Prevents degradation and leakage of loaded drug.</li> </ul>	<ul style="list-style-type: none"> <li>• Complete removal of the organic solvent is necessary.</li> <li>• Particles might aggregate during rehydration</li> </ul>	83, 84

	<p>3. Redisperse micelles in an aqueous medium. Any unencapsulated drug can be removed by centrifugation.</p>			
--	---	--	--	--

### 1.1.5. Key Parameters of Self-assemblies

#### Hydrodynamic Radius ( $R_H$ ) or Diameter ( $D_H$ )

Some of the common variables used to assess the clinical relevance of a polymer as a drug delivery vehicle include, but are not limited to, the hydrodynamic radius ( $R_H$ ) or diameter ( $D_H$ ), critical micelle concentration (CMC), drug loading capacity (DL%) and encapsulation efficiency (EE%). While the ideal dimensions of a nanocarrier vary depending on the mechanism and site of interest, these typically need to be larger than 10 nm to facilitate accumulation and ensure prolonged blood circulation. Too small, and they could get filtered out rapidly by kidney excretion, before delivering the drug to the intended site; too big (typically >200 nm), and these could be removed rapidly by the RES.<sup>85, 86</sup> In addition, larger nanoparticles diffuse slower in the bloodstream, and have a smaller surface area to volume ratio, which implies that drug release would be slower as it is further away from the surface. This, however, might not be a disadvantage, as polymeric micelles usually follow an uncontrolled “burst” release, before reaching a sustained release profile.

87

To ascertain the  $D_H$  of nanoparticles, dynamic light scattering (DLS) is typically used, by evaluating either number, area, volume, or intensity distributions. DLS relates the Brownian motion of particles to their sizes, through the Stokes-Einstein equation, and thus it is important to keep parameters such as temperature and viscosity of the medium constant throughout analysis.<sup>88</sup> However, since DLS cannot capture structural details, it is generally coupled with transmission electron microscopy (TEM) to visualize the nanoparticles. A disparity is often seen between values obtained from DLS and TEM, mainly due to the shrinking and drying of polymer formulations during sample preparation onto the TEM grids.<sup>89</sup> At times, there is also a discrepancy in samples prepared from deionized water and phosphate buffer solutions.<sup>90</sup> In addition, TEM is a number-

based observation, whereas DLS is generally based on intensity. Both methods are important in nanoparticle analyses, but DLS might be more relevant in drug delivery since it reflects the true dimensions of nanoparticles in a medium.

### Critical Aggregation Concentration

Critical aggregation concentration (CAC), or more commonly referred to as critical micelle concentration (CMC) for core-shell assemblies, is another key parameter in determining the viability of a polymer assembly in drug delivery. It gives an indication of the polymer concentration, needed to form micelles/polymersomes, and is often used to predict if the drug-loaded carriers will be retained or disassemble immediately upon administration. At lower concentrations, surfactants prefer to exist as unimers. With increasing concentrations, they tend to aggregate to shield the hydrophobic region from the aqueous medium, thereby reducing the free energy of the system. Micellar assemblies are segregated into distinct hydrophobic (core) and hydrophilic (shell) regions. Since drug-loaded nanocarriers are diluted extensively upon entry into blood circulation, self-assemblies with low CMCs ( $\mu\text{g mL}^{-1}$ ) are generally preferred to prevent any premature release of the drug. The latter can help prevent acute cytotoxicity to healthy cells, and rapid clearance.<sup>91</sup>

CMC can be experimentally determined through a number of direct and indirect techniques. Direct methods involve examining changes in physical properties as the micelles are formed. This can be achieved by using i) a tensiometer to measure increasing surface tension; or ii) conductometer to monitor an increase in conductivity, and its breaking point for ionic polymers;<sup>92</sup> or iii) DLS, to examine the increase in light scattering.<sup>93</sup> Indirect techniques rely on the use of a water-insoluble probe that exhibits different properties, as it partitions between the aqueous environment and the hydrophobic core of the micelle. This includes fluorimetry to measure fluorescent intensities of hydrophobic dyes such as pyrene,<sup>94</sup> coumarin-6<sup>95</sup> and Nile Red;<sup>96</sup> as well as UV-vis spectrophotometry to measure changes in absorption of conjugated probes like curcumin,<sup>97</sup> pyrene<sup>98</sup> and benzoylacetone (BZA).<sup>99</sup> A series of polymer concentrations is generally required to measure the changes, and each method has its own merits and limitations.<sup>100</sup> More recently,

titration<sup>101</sup> and Rayleigh interferometry<sup>102</sup> have also been reported for CMC determination, which can eliminate the need to prepare multiple polymer concentrations.

### Loading Capacity and Efficiency

Another important parameter of a nanocarrier in drug delivery is examining its efficacy to encapsulate drugs, and it is generally measured as drug loading capacity (DL%) or encapsulation efficiency (EE%). These are calculated using the following equations:

Drug loading capacity (weight %) (Equation 1)

$$= \frac{\text{Weight of drug in micelles}}{\text{Weight of drug + polymer used initially}} \times 100\%$$

Drug encapsulation efficiency (weight %) (Equation 2)

$$= \frac{\text{Weight of drug in micelles}}{\text{Weight of drug used initially}} \times 100\%$$

Both of these parameters can be calculated using UV-vis,<sup>103</sup> fluorescence,<sup>104</sup> or high-performance liquid chromatography (HPLC).<sup>105</sup> The measurements can be carried out either directly on the drug encapsulated in micelles, or indirectly using unencapsulated drugs in the aqueous medium. In both cases, a standard calibration curve is needed, in which the instrument signals can be translated into the amount of drug present. It can be easily obtained by preparing a series of drug solutions across a range of concentrations and plotting these against the measured property. Ideally, different concentrations should be prepared separately, and not from a common stock solution, to prevent any errors from propagating. It is also important to ensure that the absorption peaks of drug and solvent do not overlap. During loading, some of the drug might aggregate in water, which can be removed by centrifugation. The supernatant from centrifugation can then be separated with a suitably sized filter. Since any free drug is assumed to have been removed by centrifugation and filtration, the signal obtained from the instrument directly correlates to the amount of drug encapsulated in the nanocarrier.

### 1.1.6. Strategies to Design Branched Star Copolymers for Drug Delivery

In the following sections, we will discuss some of the strategies that have been examined in star polymers for the enhancement of drug encapsulation into their corresponding soft nanoparticles. Table 1. 2 below provides a summary of such star polymers with some of these parameters, the relevant properties of the polymers and soft nanoparticles, together with their efficacy in cargo loading.

**Table 1. 2:** Varied strategies in the star polymer-based assemblies for drug delivery.

Parameter	Variation	Polymer <sup>a</sup>	Cargo loaded	$D_H^b$	CMC <sup>c</sup>	DL% <sup>d</sup>	EE% <sup>e</sup>	Ref
Hydrophilic length	PEG <sub>2000</sub>	PCL <sub>2800</sub> -(PCL <sub>3100</sub> - <i>b</i> -PEG <sub>2000</sub> ) <sub>3</sub>	Doxorubicin	107	0.90	8.8	52.8	106
	PEG <sub>5000</sub>	PCL <sub>2800</sub> -(PCL <sub>3100</sub> - <i>b</i> -PEG <sub>5000</sub> ) <sub>3</sub>		72	3.45	9.1	54.6	
Hydrophobic length	PCL <sub>3000</sub>	(PEG <sub>775</sub> ) <sub>2</sub> -PCL <sub>3000</sub> <sup>f</sup>	Nimodipine	9	0.12	2.3	23	105
	PCL <sub>5800</sub>	(PEG <sub>775</sub> ) <sub>2</sub> -PCL <sub>5800</sub> <sup>f</sup>		10	0.07	3.0	30	
	PCL <sub>10000</sub>	(PEG <sub>775</sub> ) <sub>2</sub> -PCL <sub>10000</sub> <sup>f</sup>		50	0.17	3.2	32	
	PCL <sub>19000</sub>	(PEG <sub>775</sub> ) <sub>2</sub> -PCL <sub>19000</sub> <sup>f</sup>		28	0.04	7.0	70	
	PCL <sub>5800</sub>	PEG <sub>2000</sub> -PCL <sub>5800</sub> <sup>g</sup>		16	--	--	--	
	PCL <sub>6000</sub>	PEG <sub>775</sub> -PCL <sub>6000</sub> <sup>g</sup>		92	--	--	--	
Architecture	Linear	L-PCL <sub>4700</sub> - <i>b</i> -PDMAEMA <sub>15100</sub>	Doxorubicin	211	21.20	15.8	--	107
	Star	S-PCL <sub>4000</sub> - <i>b</i> -PDMAEMA <sub>15800</sub>		160	8.01	16.6	--	
Number of arms	3	(PCL <sub>2300</sub> ) <sub>2</sub> -POEGMA <sub>12300</sub>	Doxorubicin	73	18.19	4.4	34.3	89
	4	(PCL <sub>2300</sub> ) <sub>2</sub> -(POEGMA <sub>6000</sub> ) <sub>2</sub>		44	5.95	5.7	52.6	

	4	(PCL <sub>1600</sub> ) <sub>3</sub> - POEGMA <sub>11900</sub>		28	2.66	8.14	62.9	
	4	PCL <sub>5100</sub> - (POEGMA <sub>4000</sub> ) <sub>3</sub>		57	10.00	4.50	39.8	
Topology	Linear POEGMA	( <i>l</i> -POEGMA <sub>5400</sub> )- <i>b</i> -PCL <sub>3000</sub>	Doxorubicin	56	17.38	3.96	39.12	<sup>90</sup>
	Cyclic POEGMA	( <i>c</i> -POEGMA <sub>5400</sub> )- <i>b</i> -PCL <sub>2700</sub>		30	6.23	5.12	43.76	
Core crosslinked	UV- irradiation (min) 0	PMAA <sub>5700</sub> - <i>b</i> - HTPB <sub>2300</sub> - <i>b</i> - PMAA <sub>5700</sub>	Paclitaxel	90	53.56	6.6	33.6	<sup>108</sup>
	30			--	45.39	8.8	42.6	
	90			55	37.87	14.9	62.9	
Corona crosslinked	0%	PNIPAM <sub>15000</sub> - <i>b</i> - PLL <sub>6400</sub>	Prednisone acetate	128	--	--	--	<sup>109</sup>
	50%			132	--	2.1	18.6	
	100%			~140	--	2.5	21.4	
Stereocomplexation	P(L)LA only	PEG <sub>5000</sub> - P(L)LA <sub>2000</sub> - P(L)LA <sub>2000</sub>	Paclitaxel	28	19.10	--	--	<sup>110</sup>
	P(D)LA only	PEG <sub>5000</sub> - P(D)LA <sub>2000</sub> - P(D)LA <sub>2000</sub>		29	20.00	5.0- 7.9	--	
	P(L/D)LA	PEG <sub>5000</sub> - P(L)LA <sub>2000</sub> - P(D)LA <sub>2000</sub>		26	15.10	~10	--	
	P(L)LA mixed with P(D)LA	PEG <sub>5000</sub> - P(D)LA <sub>2000</sub> - P(DLA <sub>2000</sub> / PEG <sub>5000</sub> - P(L)LA <sub>2000</sub> - P(L)LA <sub>2000</sub>		32	10.00	11.6	--	

Drug-core compatibility	--	(PEG <sub>775</sub> ) <sub>2</sub> -PCL <sub>10000</sub>	Nimodipine	50.2	0.17	3.2	32	<sup>105</sup>
		(PEG <sub>750</sub> ) <sub>2</sub> -PCL <sub>10300</sub>	Curcumin	57.8	--	5.3	56	<sup>111</sup>
Drug- core- conjugated polymer	No conjugation	CDS(PCL <sub>710</sub> ) <sub>14</sub> (PEG <sub>1100</sub> ) <sub>7</sub>	Ibuprofen	17	2.95	3.5	11.7	<sup>112</sup>
		CDS(PCL <sub>710</sub> ) <sub>14</sub> (PEG <sub>2000</sub> ) <sub>7</sub>		11	6.53	2.3	7.7	
	Conjugated	CDS(PCL <sub>710</sub> ) <sub>14</sub> (PEG <sub>1100</sub> ) <sub>7</sub> -D		17	2.69	8.2	27.3	
		CDS(PCL <sub>710</sub> ) <sub>14</sub> (PEG <sub>2000</sub> ) <sub>7</sub> -D		12	6.46	6.1	20.3	
Drug-corona- conjugated polymer	No conjugation	SP-DTX-C	Docetaxel	114	--	13.7	62.7	<sup>113</sup>
	Conjugated	SP-DTX		57	36.50	20.1	55.7	
Drug: polymer concentration (wt%)	25	PEG <sub>2000</sub> -PCL <sub>3800</sub> -TPPBr	Coenzyme Q10	~55	--	~20	72-99	<sup>114</sup>
	50			~70		~50		
	75			~75		~70		
	100			~90		~90		
	125			~105		~120		
	150			~95		~140		
Choice of solvent	Acetone	PLGA <sub>4600</sub> -AAA(mPEG <sub>2000</sub> ) <sub>2</sub>	Ibuprofen	149	0.603	5.2	57.6	<sup>115</sup>
	DMSO			37	--	5.4	59.3	
	DMA			36	--	4.2	45.6	

<sup>a</sup> Subscript following polymer abbreviations denote  $M_n$  obtained using <sup>1</sup>H NMR. Subscript following parentheses (if any) denotes number of polymeric arms. Abbreviations used in order of appearance: PCL: polycaprolactone; PEG: polyethylene glycol; PDMAEMA: poly(2-dimethylamino)ethyl methacrylate; POEGMA: polyoligo(ethylene glycol)

methyl ether methacrylate; PMAA: poly(methacrylic acid); HTPB: hydroxyl-terminated polybutadiene; PLL= poly(L-lysine); P(L)LA: poly(L-lactide); P(D)LA: poly(D-lactide); CDS: per-6-(*tert*-butyldimethylsilyl)- $\beta$ -Cyclodextrin; SP: star polymer; DTX: docetaxel; TPPBr: triphenylphosphonium Bromide; PLGA: poly(lactide-co-glycolide); AAA: aminoadipic acid; <sup>b</sup> Hydrodynamic diameter obtained from DLS. <sup>c</sup> Critical micelle concentration. <sup>d</sup> Drug loading efficiency. <sup>e</sup> Drug encapsulation efficiency. <sup>f</sup> Miktoarm polymers. <sup>g</sup> Linear polymers.

### 1.1.6.1. Polymer Composition

Polymer composition is one of the most pivotal aspects in determining the efficacy of star copolymers for therapeutic interventions. One could alter it either through a chemical build-up of the polymer or its molecular weight. Extensive studies have been carried out on altering the hydrophilic: hydrophobic ratio of copolymers to optimize the drug solubilization/loading capability of micelles, besides tailoring self-assembly morphology, from spherical to worm-like micelles, and polymersomes. An important consideration is that the polymeric composition should generate a good balance between the hydrophobic microenvironment that surrounds the drug, and the hydrophilic layer that segregates and stabilizes the micelle between the incompatible core and the aqueous medium. Since making such adjustments would directly affect the carrier dimensions and CMC of polymeric micelles, it is very important to understand the implications of composition changes in tailoring drug delivery vehicles.

### Shell/Corona-forming Block and its Length

Poly(ethylene glycol) (PEG) (also known as poly(ethylene) oxide (PEO)) is the most commonly used polymer in forming the hydrophilic shell, for reasons including, (i) it is biocompatible and FDA-approved; (ii) has high solubility in water, independent of its molecular weight, temperature, or concentration; and (iii) presents antifouling, “stealth”-like properties, which are necessary for circulation, resisting protein adsorption and cell adhesion. These also prevent it from aggregating, making it go undetected by the body’s immune system, and subsequently increasing its circulation time in the bloodstream, and thus enhancing bioavailability. While being considered a gold standard in drug delivery, PEG poses several limitations that have motivated scientists to search for alternatives. These include its nonbiodegradability, potential immunogenicity, and highly toxic byproducts from its synthesis (class 1/ class 2b carcinogens).<sup>116, 117</sup> Changes in its pharmacokinetic

behavior have also been reported, which expedite renal clearance, as noted after injection of PEG-covered liposomes. This could be related to the antiPEG antibodies, leading to accelerated blood clearance (ABC) effect.<sup>118</sup>

Recently, polysarcosine (PSar) and poly(2-alkyl/aryl-2-oxazoline) (PAOx) have emerged as potential alternatives to PEG for biomedical applications. Despite being discovered several decades ago, both have only just started garnering interest for their biodegradability and “stealth”-like properties which are comparable to PEG. PSar is a highly hydrophilic polypeptoid based on the endogenous amino acid sarcosine, and its stealth-like properties largely stems from the absence of hydrogen bond donors which drastically reduces chances for protein adsorption.<sup>119, 120</sup> Several studies have shown higher biocompatibility, stability, and less immunogenic activity for PSar over PEG.<sup>121, 122</sup> On the other hand, PAOx provides great versatility in its chemical and physical properties by tuning the side chain of the monomer.<sup>123, 124</sup> Given the above-mentioned advantages of PSar and PAOx, these constitute excellent alternatives to PEG and PEGylation. Other hydrophilic polymers that have been studied include poly(L-lysine) (PLL),<sup>125</sup> poly(2-(dimethylamino)ethyl methacrylate) (PDMAEMA),<sup>126</sup> and poly(acrylamide) (PAAm) (Figure 1.3).<sup>127, 128</sup>

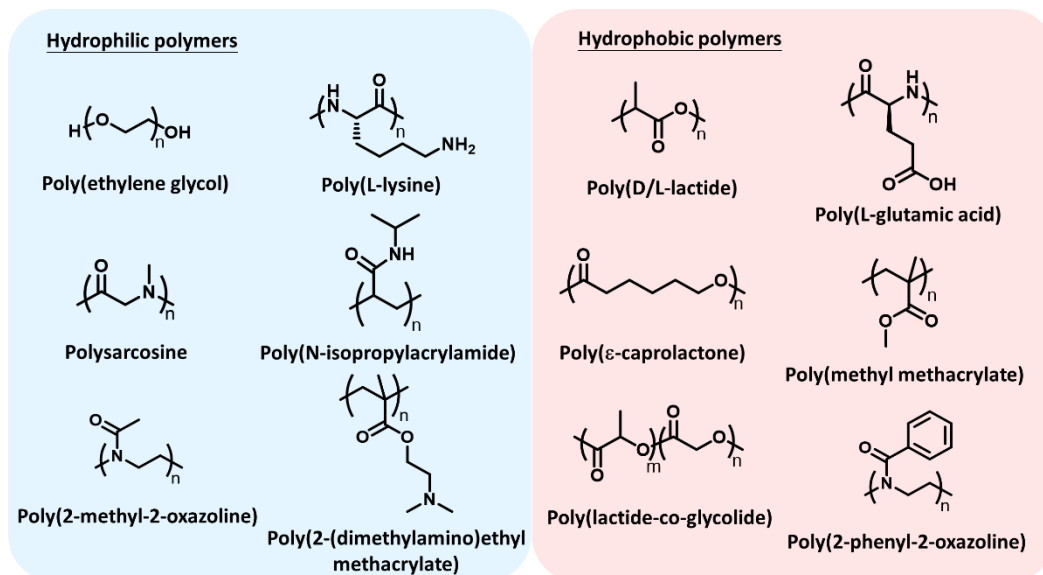


**Figure 1. 3:** Polymers commonly employed in nanocarriers for drug delivery.

In general, an increase in the hydrophilic content tends to give micelles with higher CMCs. In 2016, Zhu et al. reported on a study using  $A(AB)_3$  star polymers synthesized from an oligosaccharide core, ethyl- $\beta$ -D-glucoopyranoside, where  $A = PCL_{2800}$ ,  $A' = PCL_{3100}$  and  $B = PEG_{2000}$  or  $PEG_{5000}$  (numbers denote the molecular weight of the polymer).<sup>106</sup> Using Novozyme 435 as the catalyst, they managed to carry out selective ring-opening of  $\epsilon$ -caprolactone (CL) to obtain the asymmetric star copolymers. It was observed that with the increase in hydrophilic fraction from  $PEG_{2000}$  to  $PEG_{5000}$ , the hydrodynamic diameter decreased from 107 to 72 nm (Figure 1.4), while the CMC increased from 0.90 to  $3.45 \mu\text{g mL}^{-1}$  (Table 1. 2). This can be associated to the change in hydrophilic/hydrophobic ratio which affected the solvation/desolvation of PEG and PCL in the aqueous medium. It was noted that the  $PCL_{2800}-(PCL_{3100}-b-PEG_{5000})_3$  system was more likely to aggregate, probably due to its larger surface area and uniform shape, which favors aggregation. Doxorubicin (DOX) encapsulation efficiencies and loading capacities (EE% and DL%) did not change significantly with increasing hydrophilic ratio, since these may be more dependent on the interactions between the drug and the hydrophobic core.

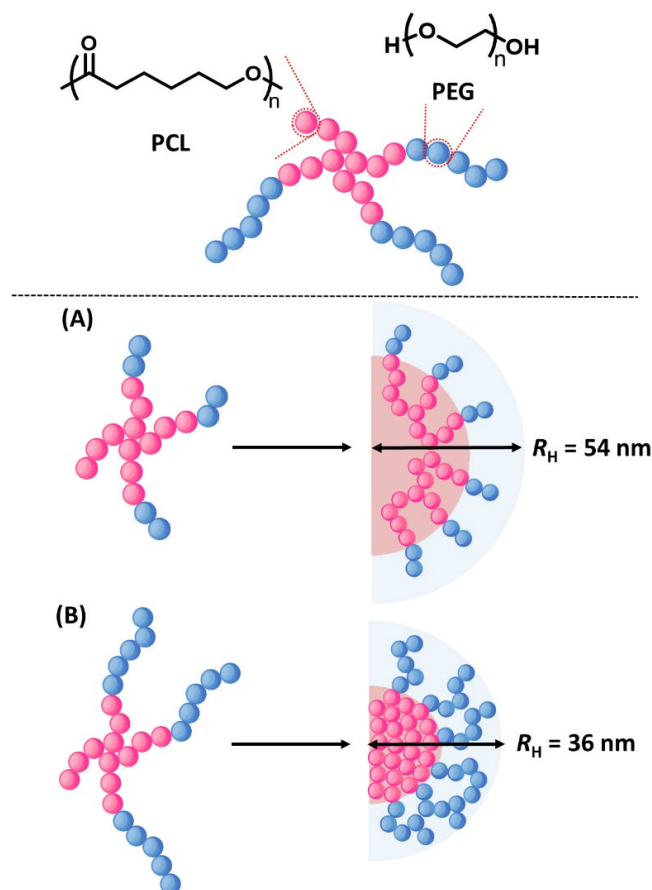


**Figure 1. 4:** Schematic illustration of hydrodynamic radii differences based on different hydrophilic lengths in star polymers; PCL = polycaprolactone and PEG = polyethylene glycol.

### Core-forming Block and its Length

The choice of the core-forming polymer has a more direct effect on the drug solubilization, loading capacity and release kinetics of the nanocarrier. As most drugs are physically encapsulated, it is imperative that the core-forming polymer is compatible with it. Polymers could be judiciously chosen to enhance hydrophobic,  $\pi$ - $\pi$ , and hydrogen bonding interactions with drug molecules. Increasing the length of the hydrophobic polymer has been shown to decrease CMC, as the micelles are more likely to aggregate and move away from the aqueous medium.<sup>129</sup> However, care should be taken to ensure a good balance between the hydrophilic and hydrophobic content to form a stable micellar structure. The downside of having larger hydrophobic domains is that the micelle

would typically have a bigger core, and thus a larger  $D_H$ . Other hydrophobic macromolecules that have been investigated as core-forming blocks in star copolymers include poly(D/L-lactide) (P(D/L)LA),<sup>130</sup> poly( $\epsilon$ -caprolactone) (PCL),<sup>131</sup> poly(lactide-*co*-glycolide) (PLGA),<sup>115</sup> poly(L-glutamic acid),<sup>132</sup> and poly(methyl methacrylate) (PMMA),<sup>133</sup> with PCL being one of the most popular choice in nanocarrier assisted drug delivery.<sup>134</sup> This FDA-approved polyester has been shown to degrade under physiologically-relevant conditions, through slow hydrolysis, into smaller monomeric or oligomeric lactic acids, such as caproic acid.<sup>135, 136</sup> These could potentially be metabolized and removed through renal clearance.<sup>137</sup> In general, the degradation rate is governed by a number of factors such as its crystallinity, overall nanoparticle composition and environmental conditions, which has been well-documented in a recent review on the degradation of PCL under varying physiological conditions.<sup>138</sup>

In 2010, a series of A<sub>2</sub>B-type micelles were reported, which had a (PEG<sub>775</sub>)<sub>2</sub>-PCL<sub>n</sub> composition, where the molecular weight of PCL varied from 3000, 5800, 10000 to 19000 ( $M_n = 5100-20000$ ).<sup>105</sup> The latter were self-assembled into micelles *via* the co-solvent evaporation method, and (PEG<sub>775</sub>)<sub>2</sub>-PCL<sub>19000</sub> was found to have the highest hydrodynamic radius. It was expected, as it has the longest PCL chain, which would result in a larger core. Micelles from (PEG<sub>775</sub>)<sub>2</sub>-PCL<sub>19000</sub> also had the lowest CMC, and the highest drug loading (7%) and encapsulation efficiencies (70%). The micelles barely increased in size upon nimodipine (NIM) encapsulation ( $R_H$  from 28 nm to 25 nm). More importantly, the solubility of NIM improved significantly from 3.86  $\mu\text{g mL}^{-1}$  when freely suspended, to  $\sim 700 \mu\text{g mL}^{-1}$  when encapsulated. Blank (PEG<sub>775</sub>)<sub>2</sub>-PCL<sub>5800</sub> and diblock linear copolymers, PEG<sub>2000</sub>-PCL<sub>5800</sub> and PEG<sub>775</sub>-PCL<sub>6000</sub> were also prepared, and it was noted that the branched miktoarm structure gave micelles of smaller sizes (Table 1. 2). This study and others have clearly shown that the properties of a micelle are very much governed by polymer composition.<sup>139</sup>

### 1.1.6.2. Polymer Architecture

#### Linear vs. Star Copolymers

As discussed earlier, the branched architecture offers interesting properties for improving the efficacy of polymeric nanocarriers as drug delivery vehicles. In addition to the miktoarm polymers

of AB<sub>2</sub> composition described above,<sup>105</sup> there are few other studies that have attempted to establish direct comparison of the efficacy of the linear and star polymer architectures. In 2014, Lo et al. synthesized and compared a 4-arm star copolymer (Star-PCL<sub>4000</sub>-*b*-PDMAEMA<sub>15800</sub>) with its linear analog (Linear-PCL<sub>4700</sub>-*b*-PDMAEMA<sub>15100</sub>) of a similar composition, to deliver green fluorescence protein plasmid (pEGFP) and DOX (Table 1. 2).<sup>107</sup> These amphiphilic copolymers that could deliver both gene and anticancer drugs, were synthesized from pentaerythritol by ROP of caprolactone (CL), and subsequent ATRP and 2-(dimethylamino)ethyl methacrylate (DMAEMA). Upon self-assembly in a pH 3.0 solution, the hydrodynamic diameters of the micelles were found to be approximately 160 and 211 nm, for the star and linear copolymers (Figure 1. 5). The CMC for the nanoparticles from the 4-arm branched copolymer (8.01 μg mL<sup>-1</sup>) was also lower than the linear analog (21.2 μg mL<sup>-1</sup>). Even after binding pEGFP to the micelles, the hydrodynamic diameter of the particles from star-PCL<sub>4000</sub>-*b*-PDMAEMA<sub>15800</sub> (~128 nm), was about half of that from linear-PCL<sub>4700</sub>-*b*-PDMAEMA<sub>15100</sub> (~283 nm). As the molecular weight was distributed among 4 arms in the star polymer, the cationic density was expected to be thinner, leading to smaller micelles. Although, both star and linear copolymers showed very similar DOX loading (DL% 16.6 and 15.8%), the star-shaped polymer had an overall slower drug release profile, increased cellular uptake, and was much more efficient at killing cancer cells.

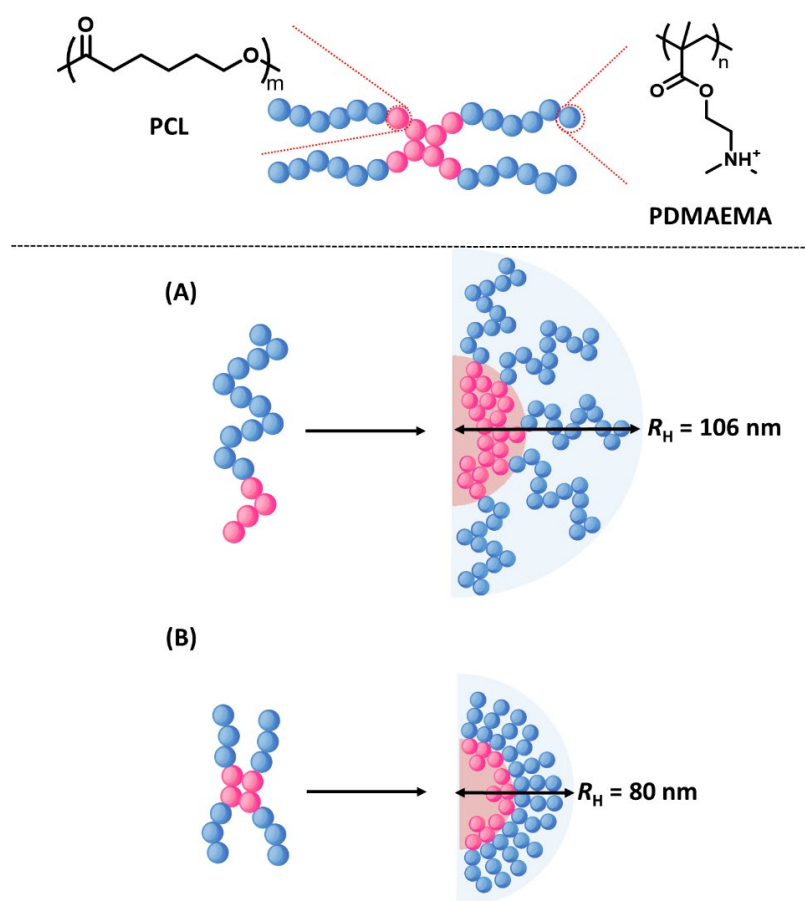


**Figure 1. 5:** Schematic illustration of hydrodynamic radii changes based on the packing of (A) linear, and (B) star PCL-*b*-PDMAEMA copolymers; PCL = polycaprolactone, and PDMAEMA = poly(2-(dimethylamino)ethyl methacrylate).

### Star Copolymers and the Degree of Branching

Another advantageous approach in lowering the CMCs is to adjust the degree of branching in amphiphilic star copolymers, as it affects the packing of unimers during self-assembly. For instance, Wang et al. studied 4 miktoarm polymers of the type  $A_2B$ ,  $A_2B_2$ ,  $A_3B$  and  $AB_3$  with similar compositions, where A= PCL and B= polyoligo(ethylene glycol) methyl ether methacrylate (POEGMA) (Table 1. 2).<sup>89</sup> Starting from either 1,1,1-tri(hydroxymethyl)ethane or pentaerythritol, they customized multifunctional initiators suitable for ROP of CL and ATRP of oligo(ethylene glycol) methyl ether methacrylate (OEGMA). From their findings, the 3-armed  $(PCL_{2300})_2$ -POEGMA<sub>12300</sub> had a larger hydrodynamic diameter (73 nm) and higher CMC ( $18.19 \mu\text{g mL}^{-1}$ ),

than the other 4-arm miktoarm polymers (28- 57 nm, 2.66-10.00  $\mu\text{g mL}^{-1}$ ). In addition, they compared the effect of the degree of branching of PCL moieties on the micelle stability. Not surprisingly, 4-armed (PCL<sub>1600</sub>)<sub>3</sub>-PEGMA<sub>11900</sub> had the smallest hydrodynamic diameter (28 nm) and CMC (2.66  $\mu\text{g mL}^{-1}$ ), most likely due to the higher degree of branching of the hydrophobic core, which led to a more compact, and therefore, smaller core (Figure 1. 6). The stability was further reflected in the dimensions of the micelle that was vastly similar despite being prepared in a salt-saturated PBS solution. Similarly, the same polymer also had the highest DL% (8.1%) and EE% (62.9%). Another study investigating the influence of various PLGA-PEG arms on the delivery of DOX had also been reported.<sup>104</sup>

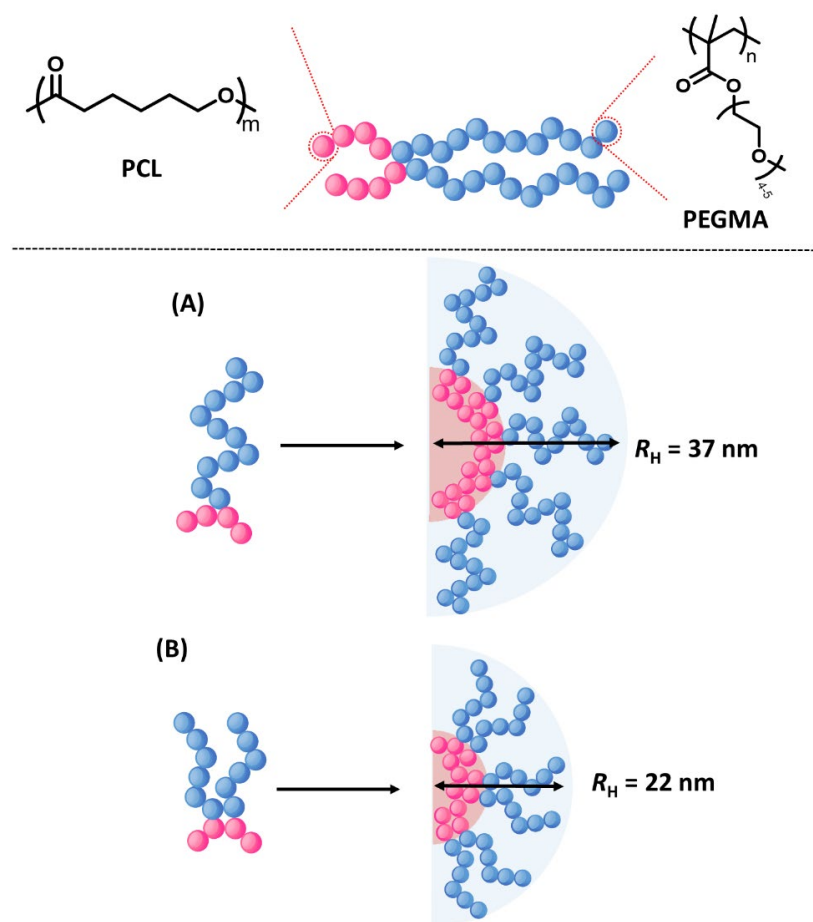


**Figure 1. 6:** Schematic illustration of hydrodynamic radii based on the packing of (A) 3-arm, and (B) 4-arm PCL-PEGMA star copolymers; PCL = polycaprolactone and PEGMA = poly(ethylene glycol) methyl ether methacrylate.

### Cyclic Topology

Besides changing the architecture of an entire polymer, one could also alter the topology of certain segments to confer more stability to the nanoparticles. As reported by Wang et al., the incorporation of POEGMA in a cyclic fashion, gave micelles of greater stability than its linear analogue.<sup>90</sup> Using the common dendrimer building block, 2,2-bis(hydroxymethyl) propionic acid (bis-MPA), as the starting material, they obtained a macroinitiator suitable for i) ATRP of OEGMA<sub>300</sub>; ii) copper-catalyzed alkyne-azide cycloaddition (CuAAC); iii) and ROP of CL to obtain a polymer with cyclic hydrophilic, and linear hydrophobic blocks. The CMC of the cyclic tadpole-like polymer (6.23  $\mu\text{g mL}^{-1}$ ) was found to be about one-third lower than the linear copolymer (17.38  $\mu\text{g mL}^{-1}$ ), most likely due to the bulky conformation and steric hindrance of cyclic OEG, which reduced the number of polymeric chains needed to achieve equilibrium (Figure 1. 7). Similarly, the cyclic tadpole-like polymer also showed a smaller hydrodynamic diameter, although the DL% and EE% did not differ significantly (Table 1. 2). However, the cyclic tadpole polymers exhibited slower release profiles of DOX and lower *in vitro* cytotoxicity.

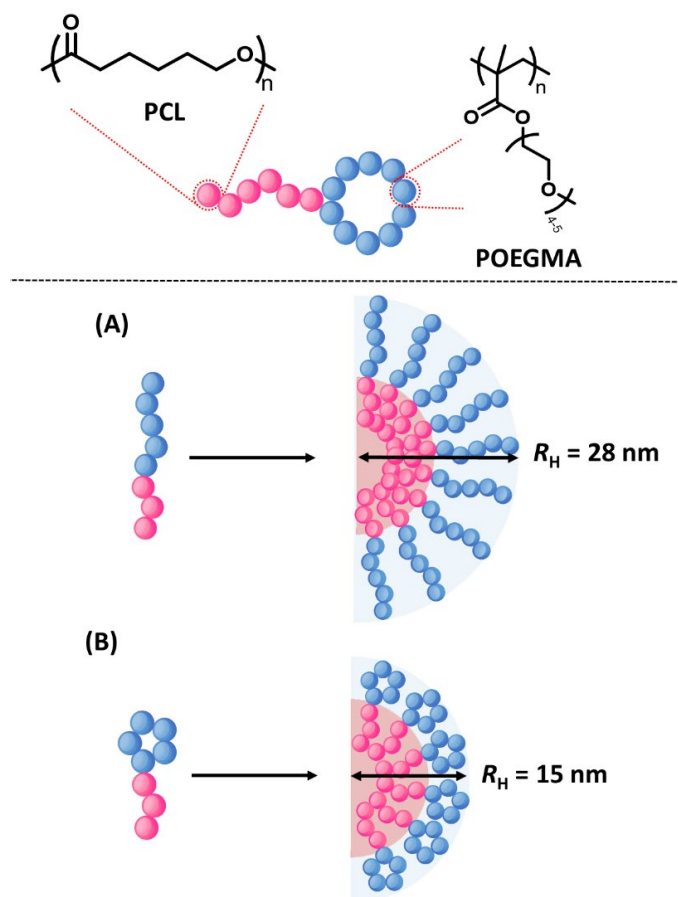


**Figure 1. 7:** Schematic illustration of hydrodynamic radii changes upon packing of (A) linear, and (B) star PCL-*b*-PDMAEMA copolymers; PCL = polycaprolactone and POEGMA = poly(oligo(ethylene glycol) methyl ether methacrylate).

#### 1.1.6.3. Core/ Shell-Cross-linked Micelles

An alternative approach to improving the stability of micelles, and prevent disassembly in the bloodstream, is to crosslink either the core or shell. In 2015, Xu et al. utilized the double bonds on hydroxyl-terminated polybutadiene (HTPB) as a cross-linker, to couple two PMAA<sub>66</sub>-*b*-HTPB-*b*-PMAA<sub>66</sub> chains to give a H-type 4-arm star block copolymer for loading of paclitaxel (PTX), where PMAA= poly(methacrylic acid).<sup>108</sup> By exposing the reaction solution to UV light at 365 nm, they examined the influence of irradiation time on the degree of cross-linking and the physicochemical properties of the self-assemblies. As the UV exposure time increased from 0 to 90 min, the degree of cross-linking increased, as much as 21%. This % cross-linking was sufficient

to improve micellar stability, and it was reflected in the CMC and hydrodynamic diameter (non-cross-linked:  $53.56 \mu\text{g mL}^{-1}$ , 89 nm; cross-linked:  $37.87 \mu\text{g mL}^{-1}$ , 55 nm, Figure 1. 8). The micelles prepared with increasing degrees of cross-linking had DL% and EE% twice of those without cross-linking. This enhancement can be attributed to the more closely packed unimers as they are linked, which places the chains close together with higher degrees of cross-linking (i.e., smaller dimensions). The cross-linking also led to slower drug release and less drug leakage in micelles. Another similar study with poly(N-(2-hydroxypropyl)methacrylamide) has also been reported.<sup>140</sup>

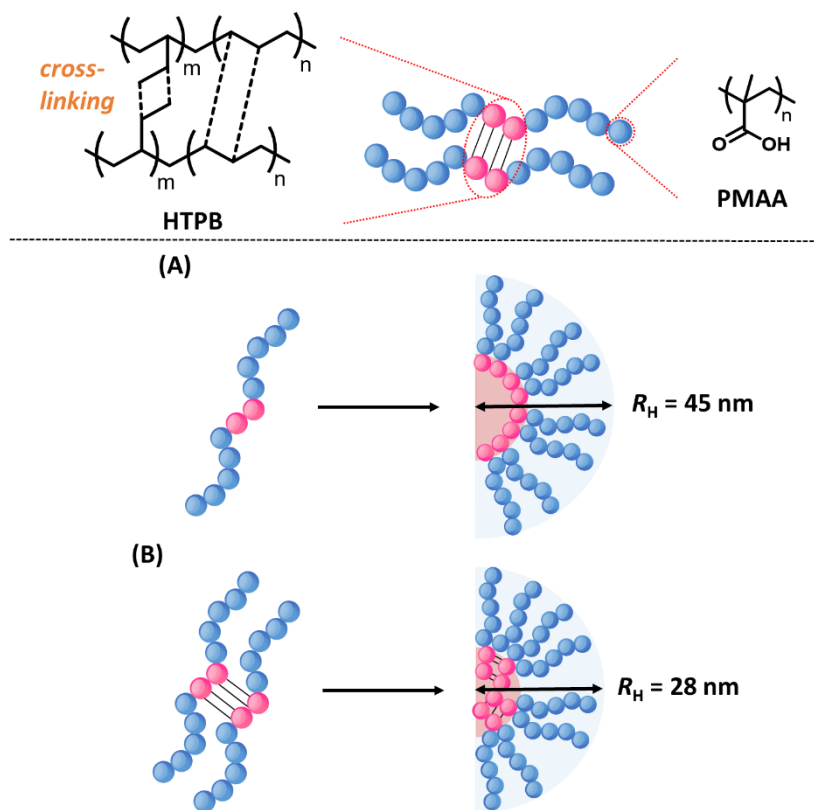


**Figure 1. 8:** Schematic illustration of hydrodynamic radii differences based on the packing of (A) non-crosslinked linear, and (B) cross-linked H-type star copolymers; HPTB = hydroxyl-terminated polybutadiene, and PMAA = poly(methacrylic acid).

Another study reported cross-linking the outer shell of a poly(N-isopropylacrylamide) (PNIPAM) and PLL-based dual responsive star system.<sup>109</sup> The PNIPAM<sub>15000</sub>-*b*-PLL<sub>6400</sub> copolymer was synthesized through a combination of ATRP of NIPAM, ROP of CL, and CuAAC to obtain a Y-

shape miktoarm copolymer. Using the amine groups on PLL and glutaraldehyde as the cross-linker, the group managed to obtain 100% or 50% cross-linking at 50 °C, with glutaraldehyde/amine ratios of 1:2 or 1:4, respectively. Without any cross-linking, the hydrodynamic radius of the copolymer was 128 nm at pH 12.0, with PLL forming the core and PNIPAM forming the shell. When the LCST behavior of PNIPAM was triggered during 50% cross-linking of PLL at 50 °C, the core-shell assemblies inverted to give a PNIPAM core and PLL as shell. The authors reported that the cross-linking also retained the core-shell structure, and even after cooling down to room temperature, the hydrodynamic radius did not change significantly (132-150 nm). This proved that the micelle did not go back to the original PLL-core and PNIPAM-shell assembly, although both polymers became hydrophilic simultaneously. The difference in hydrodynamic radii was even less significant for the 100% cross-linked micelles. The DL% and EE% of prednisone acetate were slightly better with the 100% cross-linked micelle (2.5% and 21.4% respectively), as compared to the 50% cross-linked micelle (2.1% and 18.6% respectively). The cumulative drug release was also slower with higher cross-linking. A possible explanation is that the permeability of the shell is altered with different degrees of cross-linking, which had an effect on its diffusion out of the micelle.

#### 1.1.6.4. Stereocomplexation and Mixed Micelles

While chemical cross-linking of either the core or shell can improve stability, some properties or functions of the polymer may be lost during the cross-linking process. Mixing micelles to form polymer stereocomplexes is an alternative strategy to enhance the encapsulation of drugs into nanocarriers. Polymer stereocomplexes rely on complementary, noncovalent interactions for enhanced kinetic stability and physicochemical behavior, compared to their parent analogs.<sup>141</sup> In the context of drug delivery, a great deal of research has been done on studying polylactides (P(D)LA and P(L)LA) and their stereocomplexes, as these are FDA-approved, biodegradable and can be produced from renewable resources such as corn starch. Due to strong interactions between P(L)LA and P(D)LA, these PLA stereocomplexes formed crystalline lattices that were more stable, stronger, and had a higher melting temperature than the homocrystallites. PLA stereocomplexes were also found to have enhanced barrier properties, which can lead to more controlled and prolonged drug release rates. The mechanical performance, which has an effect on tissue

penetration and distribution, can be further improved by using higher molecular weight polylactides, although homocrystallization of the enantiomers might supercede stereocomplex crystallization.<sup>142, 143</sup> In 2009, Nederberg et al. mixed enantiomeric P(L)LA and P(D)LA that were chemically bonded to PEG<sub>5000</sub> through bis-MPA.<sup>110</sup> They examined a few Y-shape PEG-(P(D/L-lactide)<sub>2</sub>) polymers such as PEG<sub>5000</sub>-P(L)LA<sub>2000</sub>-P(L)LA<sub>2000</sub>, PEG<sub>5000</sub>-P(D)LA<sub>2000</sub>-P(D)LA<sub>2000</sub>, PEG<sub>5000</sub>-P(L)LA<sub>2000</sub>-P(D)LA<sub>2000</sub> stereocomplex, and a mixture of PEG<sub>5000</sub>-P(D)LA<sub>2000</sub>-P(D)LA<sub>2000</sub>/ PEG<sub>5000</sub>-P(L)LA<sub>2000</sub>-P(L)LA<sub>2000</sub> stereocomplexes. The stereocomplexed micelles showed lower CMCs (10.0-15.1  $\mu\text{g mL}^{-1}$ ) and higher DL% (~10.0-11.6 wt%), compared to the parent polymers-based micelles, PEG<sub>5000</sub>-P(L)LA<sub>2000</sub>-P(L)LA<sub>2000</sub> (19.1  $\mu\text{g mL}^{-1}$ ) and PEG<sub>5000</sub>-P(D)LA<sub>2000</sub>-P(D)LA<sub>2000</sub> (20.0  $\mu\text{g mL}^{-1}$ , 7.9 wt%, Table 1. 2). Although this effect was not very evident with the blank micelles, it was much more prominent with the PTX-loaded micelles, where the nanoparticles were approximately 60 nm smaller and less dispersed than the parent polymer. The stereocomplexed micelles also displayed less initial burst, and slower release profiles of PTX over a span of 12 days. Other studies based on mixing polymer blends for tunable functions have also been reported.<sup>144, 145</sup>

#### 1.1.6.5. Compatibility between the Drug and Core-forming Block

The Flory-Huggins theory is commonly used in predicting the solubility of drug in a polymeric core, and can be determined with the following equation:<sup>146, 147</sup>

$$\chi_{sp} = (\delta_s - \delta_p)^2 (V_s/RT) \quad (\text{Equation 3})$$

where  $\chi_{sp}$  describes the interaction parameter between drug (s) and core-forming block (p).  $\delta_s$  is the Scatchard-Hildebrand solubility parameter of the drug;  $\delta_p$  is the Scatchard-Hildebrand solubility parameter of the polymer, and  $V_s$  is the molar volume of the drug. A lower positive value of  $\chi_{sp}$  infers that there is greater compatibility between the drug and the core. Similar kinds of computational approach might serve a better purpose in formulation design and facilitating drug-polymer pairing instead of relentlessly developing new formulations. For example, Sharma et al. estimated  $\chi_{sp}$  for nimodipine, Coenzyme Q10 and PCL, with values coming to 2.54 and 4.57 for nimodipine-PCL and CoQ10-PCL, respectively. Subsequently, this confirmed their findings on the superior loading of CoQ10 into their PEG-PCL based miktoarm polymer.

Apart from examining the interaction parameter, one could also exploit inherent interactions between cargo and polymer to enhance physical encapsulation of drug. In a comparative study using curcumin and NIM (Figure 1. 9, Table 1. 2), it was shown that in the assemblies from miktoarm polymer (PEG<sub>775</sub>)<sub>2</sub>-PCL<sub>10000</sub>, the core had more favorable interactions with curcumin.<sup>105, 111</sup> Aside from hydrophobic forces, it is possible for curcumin to form hydrogen bonds, and  $\pi$ - $\pi$  interactions with the polymer, which may contribute towards higher drug loading and encapsulation efficiencies. Similar studies comparing DOX and camptothecin compatibility in a few MAA-based homo- and heteroarm star/ miktoarm copolymers, as well as the effect of  $\pi$ - $\pi$  interactions on curcumin-loading into PEG-PCL star copolymers, have also been reported.<sup>148, 149</sup>

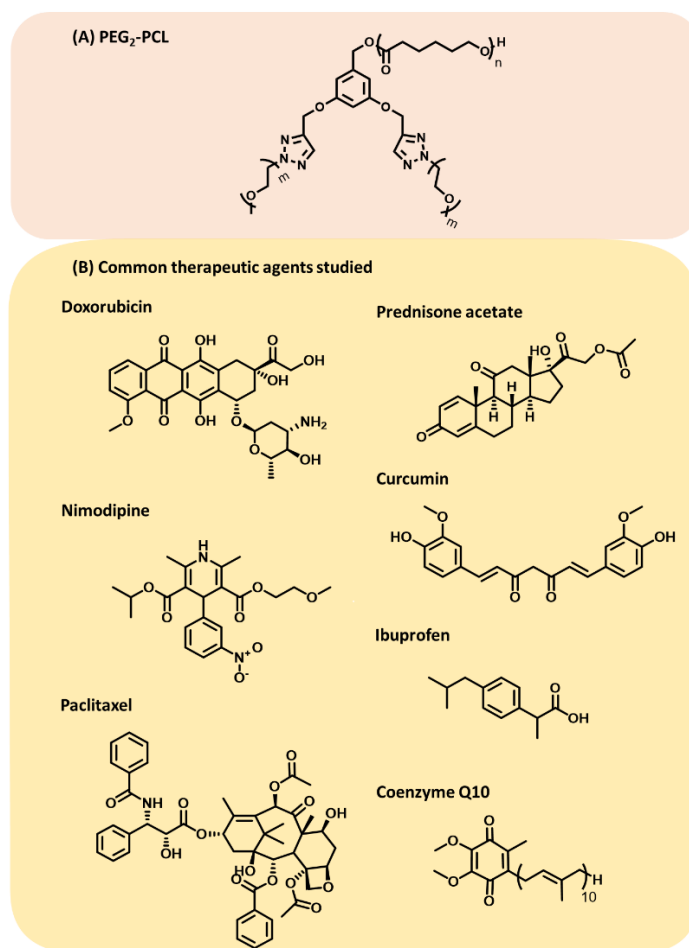


**Figure 1. 9:** Structure of PEG<sub>2</sub>-PCL miktoarm polymer that had been loaded with (B) nimodipine and (E) curcumin; PEG = poly(ethylene glycol) methyl ether and PCL = polycaprolactone, and structure of all the drugs that were summarized in Table 1. 2.

#### 1.1.6.6. Chemical Conjugation of the Drug to Polymer

Although the inherent drug-polymer interactions could be sufficiently strong, one could chemically conjugate the drug to enhance payload into the nanocarrier, as well as eliminate drug leakage and dose-dumping upon dilution. In 2010, Gou et al. compared ibuprofen-conjugated assemblies from star polymers, CDS(PCL<sub>710</sub>)<sub>14</sub>-(PEG<sub>1100</sub>)<sub>7</sub> and CDS(PCL<sub>710</sub>)<sub>14</sub>-(PEG<sub>1100</sub>)<sub>7</sub>-D, where CDS= per-6-(tert-butyldimethylsilyl)- $\beta$ -Cyclodextrin and D represents the drug-conjugated polymer.<sup>112</sup> Utilizing  $\beta$ -cyclodextrin and a combination of ROP and CuAAC reactions, they could attach ibuprofen on the PCL end, and self-assemble it into micelles by dialysis. It was reported that the ibuprofen-conjugated polymer showed significantly higher DL% and EE% (8.2% and 27.3%), as compared to the non-conjugated polymer (3.5% and 11.7%) (Figure 1. 10). They attributed these findings to the enhanced hydrophobic interactions between the conjugated hydrophobic drug and the core, as well as favorable interactions between conjugated and free ibuprofen. More importantly, the ibuprofen-conjugated polymers showed almost identical dimensions, CMC, and morphology, to the non-conjugated polymers. Similar observations were reported with the CDS(PCL<sub>710</sub>)<sub>14</sub>-(PEG<sub>2000</sub>)<sub>7</sub> and CDS(PCL<sub>710</sub>)<sub>14</sub>-(PEG<sub>2000</sub>)<sub>7</sub>-D miktoarm star copolymers (Table 1. 2). The hydrodynamic diameter, DL% and EE% also increased, while the CMC decreased with lower PEG fractions (i.e., more hydrophobic moieties). An earlier study by Gou et al. with an ibuprofen-conjugated (PCL<sub>3200</sub>)<sub>2</sub>-(PEG<sub>2000</sub>)<sub>2</sub>-D also showed the importance of employing both DLS and TEM for analysis, as loading of ibuprofen into the conjugated star polymer at a feed ratio of 3:10 wt% altered the morphology from spherical to wormlike due to increased hydrophobicity of the PCL core.<sup>150</sup> Another study involving conjugation of DOX on poly(glutamic acid)-core had also been reported in 2014.<sup>151</sup>

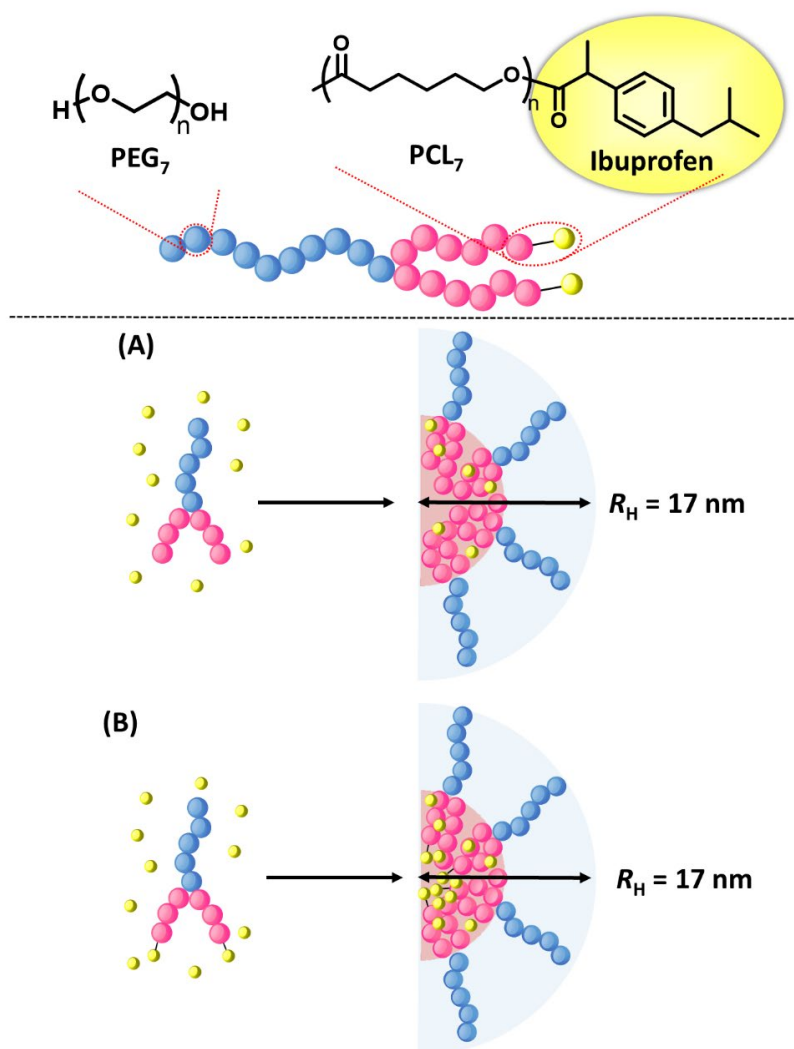


**Figure 1. 10:** Schematic illustration of changes in drug loading from (A) physical encapsulation, and (B) physical encapsulation, and chemical conjugation of ibuprofen at the core to PEG<sub>7</sub>-PCL<sub>14</sub>; PEG = poly(ethylene glycol) and PCL = polycaprolactone.

In another study, docetaxel (DTX) was conjugated to the corona of the micelles.<sup>113</sup> By coupling a pyridyldisulfanyl-functionalized polyhedral oligomeric silsesquioxane (POSS-PDS) with a thiol-terminated semitelechelic *N*-(2-hydroxypropyl) methacrylamide copolymer (P-SH), a dual pH and reduction-responsive polymer was obtained, which had suitable functional groups for the conjugation of DTX by hydrazone bonds. The authors compared the POSS-based star copolymers with DTX encapsulated at the core (SP-DTX-C), with another which had DTX chemically

conjugated in the corona, on top of having it encapsulated in the core (SP-DTX, Figure 1. 11). The combination of physical encapsulation and chemical conjugation enhanced several desirable properties of SP-DTX, giving smaller dimensions (57 nm vs. 114 nm), DL% (20.1% vs. 13.7%) and EE% (55.7% vs. 62.7%), relative to SP-DTX-C.

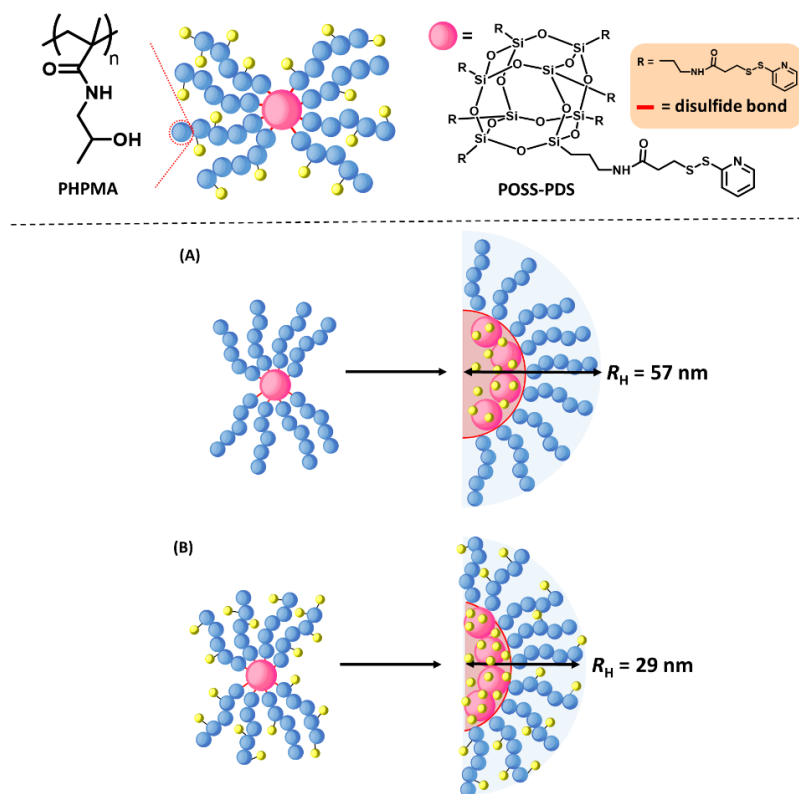


**Figure 1. 11:** Schematic illustration of changes in drug loading from (A) physical encapsulation (SP-DTX-C), and (B) physical encapsulation at the core and chemical conjugation at corona (SP-DTX) of DTX; PHPMA = poly(*N*-(2-hydroxypropyl) methacrylamide) and POSS-PDS = pyridyldisulfanyl-functionalized polyhedral oligomeric silsesquioxane.

#### 1.1.6.7. Polymer: Drug Feed Ratio

The polymer-to-drug feed ratio is another variable that is tunable by simply increasing the amount of drug during self-assembly. It is an important consideration in nanomedicine to maximize drug loading at the lowest possible polymer concentrations. It can be beneficial to patients, as it would require less frequent administration. Additionally, if the drug loading is very low (e.g., 20 wt%),

it infers that 80 wt% of the nanocarrier is the polymer itself, which the body would need to eliminate. This, in turn, puts extra stress on the patient, especially when the polymer is not biodegradable. It should be noted that higher drug loading does not necessarily result in faster release kinetics. As drugs naturally tend to get into a crystalline state upon increased concentrations, they are even more prone to crystallization as the system gets saturated.

The loading of drug into blank polymeric nanocarriers is often accompanied by an increase in hydrodynamic diameters, as the core expands to accommodate more cargo.<sup>110</sup> Therefore, an increase in DL% when the feed ratio increases, is also usually followed by an increase in its dimensions. In 2012, a few triphenylphosphonium cation (TPP<sup>+</sup>)-linked PEG-PCL miktoarm polymers were prepared through a combination of click and subsequent ROP reactions for the delivery of coenzyme Q10 (CoQ10) to mitochondria.<sup>114</sup> For one of the polymers PEG<sub>2000</sub>-PCL<sub>3800</sub>-TPPBr, there was a linear increase in CoQ10 loading into micelles, with respect to CoQ10/ polymer weight ratio (Table 1. 2). The encapsulation efficiencies were in the range of 72-99% , and the micellar size showed an enlarging trend within this range but was still sufficiently small at approximately 100 nm. Any further increase in drug concentration did not lead to more CoQ10 being loaded.

### 1.1.6.8. Choice of Solvent for Self-Assembly

The choice of the solvent, as described in the self-assembly methods section, has been shown to have a significant effect on the formulation morphology.<sup>152</sup> In 2019, a PLGA-PEG miktoarm star polymer was reported for the encapsulation of ibuprofen into their assemblies.<sup>115</sup> Before transferring the solutions into dialysis membranes, several solvents, including acetone, DMSO and DMA, were tested to dissolve the polymer and the drug. Interestingly, using acetone gave the largest mean particle diameter of 149 nm, while using DMSO and DMA led to much smaller dimensions, approximately 37 nm (Table 1. 2). In addition, the DL% and EE% with acetone (5.24% and 57.59%), and DMSO (5.39% and 59.26%), were better than DMA (4.15% and 45.59%). Hence, it was concluded that DMSO was the best solvent among the three to form PLGA-PEG-based self-assemblies with high loading capacities.

### 1.1.7. Biological Evaluations

One of the major objectives of the nanocarrier assisted drug delivery on a short term is to enhance the quality of life for the patients with effective therapeutic interventions, while finding better management and cure for high morbidity rate diseases, on a larger perspective. It desires a detailed biological (*in vitro*, as well as *in vivo*) evaluations of the nanoformulations, to determine important parameters including safety, distribution, specificity, accumulation, elimination, which would help carve a pathway to clinical translation.<sup>153-156</sup> A brief glimpse of the effort devoted in this direction is provided in Table 1. 3 below. It does not provide an exhaustive list of all the star polymers-based assemblies in drug delivery but includes some representative examples of the last few years. PEG-based star polymers have recently been reviewed for their contributions in designing nanoformulations for better therapeutic efficacy, and their translation into pre- and clinical trials.<sup>157</sup> An analysis of the literature, together with these examples, shows that much of the emphasis while evaluating star polymers in designing formulations has been on drug loading, release, and *in vitro* studies on different cell lines, generally related to cancerous tissues. There are some *in vivo* studies that have also followed, but remain small in number, in comparison. In addition, it is noted that there is a larger disparity in the macromolecular compositions in these, which makes developing structure-property relationships a bit difficult to discern. This is an area which needs to grow at a fast pace, considering the variety of star polymers that have been reported, with tailoring of the parameters noted in this review. It requires a collaborative effort between polymer chemists, pharmacologists, and physiologists. Such a dedicated approach needs to be brought into focus, as has been the case for linear diblock copolymers, which have attracted the attention of varied disciplines including chemical engineers.<sup>158-160</sup> The clinical translation process is quite complex, and the challenges can only be addressed with continued and elaborated studies of the varied star polymer formulations, both *in vitro* and *in vivo*. This will provide the required information related to the key physicochemical parameters, structure-efficacy relationship, and safety of the star polymers and their end products after degradation or metabolism.

**Table 1. 3:** Examples of the *in vitro* and *in vivo* studies using star nanoformulations.

<b>Star Polymer Composition<sup>a</sup></b>	<b>Cargo</b>	<b>Nano-formulation</b>	<b>Therapeutic Target</b>	<b>Biological Evaluation; cell lines/living organism</b>	<b>Ref</b>
(PEG <sub>775</sub> ) <sub>2</sub> -PCL <sub>5800</sub>	Nimodipine	Micelle	Neuroinflammation	<i>In vitro</i> : N9 cells	<sup>105</sup>
PCL <sub>3800</sub> -PEG <sub>2000</sub> -TPPBr	Coenzyme Q10	Micelle	Mitochondria	<i>In vitro</i> : N9 cells	<sup>114</sup>
(PEG <sub>750</sub> ) <sub>2</sub> -PCL <sub>4700-14200</sub>	Curcumin. Combination therapy with pifitrin, temozolomide	Micelle	Glioblastoma multiforme	<i>In vitro</i> : U251N cells	<sup>111</sup>
Star-PCL <sub>4000</sub> - <i>b</i> -PDMAEMA <sub>15800</sub>	Doxorubicin and pDNA co-delivery	Micelle	Chemotherapy and gene transfection	<i>In vitro</i> : CRL-5802, NCI-H358, MCF-7, 293T, and HEK 293T cells	<sup>107</sup>
VS-PEG-PTMC-MC-PTMC-PEG-VS	Doxorubicin	Micelle	ATCC 4T1 mouse breast cancer model	<i>In vitro</i> : MDA-MB-231 cells <i>In vivo</i> : female balb/c mice	<sup>161</sup>
POSS-PDS-(PHPMA <sub>32000</sub> ) <sub>8</sub>	Docetaxel	Micelle	Prostate xenograph tumor model	<i>In vitro</i> : PC3 cells. <i>In vivo</i> : Male nude mice	<sup>113</sup>
PCL-(PCL-PEG) <sub>3</sub>	Doxorubicin	Micelle	--	<i>In vitro</i> : HeLa cells	<sup>106</sup>

CD-PCL-SS- PEG(PNIPAM	Doxorubicin	Micelles	--	<i>In vitro</i> : HepG2 and LO2 cells	<sup>162</sup>
Star PEG <sub>5000</sub> - PPS <sub>180-370</sub>	BRAF inhibitor	Hydrogel	Wound healing, tissue repair	<i>In vivo</i> : Mice	<sup>163</sup>
CA-(PCL <sub>3100</sub> - <i>b</i> - PDEAEMA <sub>1100</sub> - <i>b</i> - PPEGMA <sub>2200</sub> ) <sub>3</sub>	Paclitaxel	Micelle	--	<i>In vitro</i> : NIH-3T3	<sup>164</sup>
Star-PEG <sub>1600</sub> - ICG-RGD-RBZ	Anti-vascular endothelial growth factor	Core-crosslinked stars	Age-related macular degeneration: Choroidal neovascularization	<i>In vitro</i> : ARPE-19, HUVECs cells. <i>In vivo</i> : Mice CNV models	<sup>165</sup>
Star based on PHPMA <sub>15000</sub> - 3000000	Doxorubicin	Star, cross-linked micelle	Orthotopic breast cancer model	<i>In vitro</i> : TNBC cell lines, MDA-MB-231 and MDA-MB-468. <i>In vivo</i> : Organ distribution in mice	<sup>166</sup>
PEG <sub>5000</sub> -Lys- (PCL <sub>13000</sub> ) <sub>2</sub>	Baicalein	--	Alzheimer's Disease	<i>In vivo</i> : Spatial memory and hippocampal expression	<sup>167</sup>
Star PCL <sub>2000</sub> - <i>g</i> - (PDMAEMA <sub>6700</sub> - <i>b</i> -PNIPAM <sub>1300</sub> ) <sub>6</sub>	Methotrexate	Micelle	Solid tumors	<i>In vitro</i> : MCF7 cells	<sup>168</sup>
OA-C=N-NH- (PEG <sub>5000</sub> ) <sub>2</sub> -VCM	Vancomycin	Micelle	--	<i>In vitro</i> : A549, MCF7 and HepG2 cells;	<sup>169</sup>

				<i>In vivo</i> : BALB/c mice	
(PEG <sub>2000</sub> ) <sub>2</sub> - PCL <sub>3600</sub>	Curcumin	Micelle	ROS/ GSH	<i>In vitro</i> : U251N cells	<sup>170</sup>
HA <sub>8000</sub> -sPLGA <sub>5500</sub>	Docetaxel	Cross-linked nanoparticles	CD44-overexpressing tumors	<i>In vitro</i> : A549 cells; <i>In vivo</i> : A549 tumor	<sup>171</sup>
$\beta$ -CD-(PNVP <sub>1600</sub> ) <sub>4</sub>	Doxorubicin	Micelle	Glioblastoma	<i>In vitro</i> : glioblastoma (C), and HEK 293 cells	<sup>172</sup>

<sup>a</sup>Abbreviations used in order of appearance: PEG: polyethylene glycol; PCL: polycaprolactone; TPPBr: triphenylphosphonium bromide; PDMAEMA: poly(2-dimethylamino)ethyl methacrylate; VS: vinyl sulfone; PTMC: poly(trimethylene carbonate); MC: methyl cholate; POSS-PDS: pyridyldisulfanyl-functionalized polyhedral oligomeric silsesquioxane; PHPMA: poly(N-(2-hydroxypropyl)methacrylamide);  $\beta$ -CD:  $\beta$ -cyclodextrin; PNIPAM: Poly(*N*-isopropylacrylamide); PPS: poly(propylene sulfide); PDEAEMA: poly(2-diethylamino)ethyl methacrylate; PEGMA: poly(ethylene glycol) methyl ether methacrylate; ICG: indocyanine green; RGD: arginine–glycine–aspartic acid; RBZ: ranibizumab; Lys: lysine; VCM: Vancomycin; HA: hyaluronic acid; PLGA: poly(lactide-co-glycolide); PNVP: poly(N-vinylpyrrolidone).

The efficacy of the soft nanoparticles depends heavily on their ability to reach target sites, by overcoming tremendous challenges to sustained blood circulation, nanobiointeractions, and cellular/intracellular uptake.<sup>173-177</sup> Several review articles have provided a detailed overview of the determining factors contributing to the biological fate of nanocarriers.<sup>178-181</sup> Upon introduction into the blood stream, the nanoparticles face elimination by RES. This is generally overcome by controlling opsonization, which depends on the physicochemical properties of nanoparticles. PEG, which is commonly used in drug delivery vehicles, as corona for example in amphiphilic star polymers based micelles (10-100 nm in size), is known to reduce such protein- nanoparticle interactions, and avoid nanocarrier removal by phagocytosis.<sup>182-184</sup> PEGylation is considered to be

the promising strategy in limiting (NOT completely restricting) RES based elimination, and enhancing blood retention and circulation. The nanoparticles subsequently follow either a passive (enhanced permeation retention) or active (using targeting moieties) pathways to arrive at the extracellular space. Accumulation at tumor sites depends on the stealth, stability, blood circulation/retention, targeting ability of the nanoparticles, among other factors such as leaky vasculature and angiogenesis.<sup>185, 186</sup> Nanoformulations using amphiphilic star polymers are helping address these, through modulating corona density of the nanoparticles, and the ease in introducing functional moieties for active transport and stimuli-responsive drug release. Cellular internalization of nanoparticles can take place through specific interactions with receptors, endocytosis, non-specific associations with the cell membrane, and uptake using pinocytosis.<sup>187</sup> There has been tremendous effort devoted to gain an understanding of the internalization pathways, and using it to direct nanoparticles into desired intracellular and sub-cellular locations.<sup>188</sup> The role of the entry pathway in trafficking nanoparticles into these desired sites, is not fully understood yet. Nanoengineering of efficient therapeutic interventions will come through a detailed evaluation of the uptake mechanisms, and their correlation with physicochemical characteristics of the nanoformulations.

### *1.1.8. Conclusions and Future Outlook*

Nanocarrier assisted drug delivery is a highly desired trait in combating high morbidity rate diseases, and yet a complex problem at multiple levels. Polymer therapeutics continue to offer a viable platform to address heterogeneity in diseases, biological mechanisms, delivery pathways, treatments, patient compliance etc.<sup>189</sup> Significant progress has been made in understanding nanocarrier-efficacy relationships, which can help guide the design of stable formulations, with improved bioavailability and safety of drugs. It has led to an evolution of the macromolecular precursors, through chemical innovation, from conventional linear block-copolymers to branched/star-shaped amphiphilic compositions. Star/branched polymers possess distinct topologies that lend them unique properties, which are of advantage in drug delivery. For example, branched architecture i) minimizes chain entanglements, leading to lower solution viscosities, which facilitates formulation administration; and ii) provides a strategical balance of key attributes including hydrodynamic volume, polymer chain end groups, flexibility etc., for enhanced blood

circulation and bioavailability.<sup>190, 191</sup> Their well-defined globular aqueous assemblies with denser hydrophilic shells show low critical micelle concentrations, high loading capacities, and controlled release of their cargo. In addition, functional chemical entities sensitive to a variety of endogenous cues could be easily introduced into the architecture, for better targeting and therapeutic outcome. These attractive features are contributing to an increasing interest in the scientific community in these macromolecules. An analysis of the literature shows that the field has undergone a major expansion from a small group to a growing list of researchers, as reflected in the number of publications in the last few years (Figure 1. 12).<sup>192</sup>

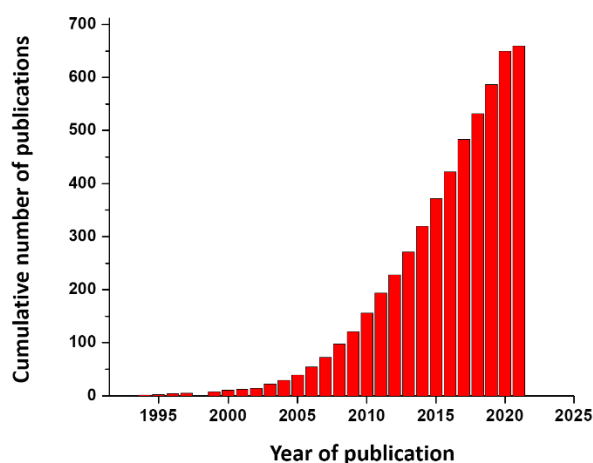


**Figure 1. 12:** Publications reporting studies on star polymers in drug delivery from 1992-2021.

As noted above, the use of star polymers is becoming more frequent in addressing key challenges in enhancing formulation stability, therapeutic index, surface functionalization, cell interactions, and targeted delivery. There is still much work to be done in establishing their efficacy, and comparative performance to linear block-copolymers. Several variables should be investigated in star polymers-based self-assembly in more detail, including the polymer-drug feed ratio, compatibility, choice of solvent, self-assembly method, and the ratio of solvent: water, during formulation preparation. The effect of pH and temperature on drug solubilization, that has been studied on Pluronic-based systems, can also be expanded on in star polymers-based assemblies, as it will be important to establish micelle stability at relevant pH and temperatures.<sup>193, 194</sup> Expanding

our understanding of these formulations will be a good approach to improve optimal dosing and patient compliance.

Leveraging on the many polymerization methods that have been developed, polymer chemists now have plenty of opportunities to design branched star polymers for targeted drug delivery, imaging, and even precision medicine. There have been attempts made at attaching ligands such as folate/folic acid (FA),<sup>195-197</sup> glycopolymers,<sup>198</sup> vitamin B12,<sup>199</sup> d- $\alpha$ -tocopheryl polyethylene glycol 1000 succinate (TPGS, also known as vitamin E TPGS),<sup>200</sup> onto the formulation shell-forming block to improve the binding affinity to specific cells. The insertion of these targeting moieties, typically through chemical conjugation by esterification, amidation or click conjugation, can assist in more efficient retention through ligand-receptor interactions which would usually rely only on passive targeting. The tricky thing about this approach is that the receptors should exclusively be found at targeted sites. On the contrary, stimuli-responsive polymers provide more straightforward approaches in achieving on-demand release as cancerous tissues would generally exhibit abnormal microenvironment conditions. It requires labile bonds such as hydrazones,<sup>169</sup> imine<sup>201</sup> and disulfide,<sup>162, 202</sup> or functional moieties that can be protonated/ deprotonated<sup>164</sup> or induce morphological changes reversibly to offer more spatiotemporal control over drug delivery. As such, star polymers provide tremendous opportunities in designing such smart self-assemblies, through synthetic manipulation of the composition of the branched polymeric structure. This can help facilitate accumulation and uptake at disease locations, through specific recognition and binding to receptors for enhanced bioavailability and therapeutic effect.

Direct comparison of the formulations from linear block copolymers with those from star compositions is one of the crucial aspects, which has not been well addressed. The lack of available data can be understood, due to the complexity in controlling all the properties (overall and individual polymeric arm molecular weights, hydrophilic fraction etc.), except for the linear or branched architecture. However, such analyses will add to the growing list of justifications for the need of branched structures in assembling effective therapeutic interventions.

Nanocarrier-assisted drug delivery will continue to stay forefront in addressing inadequacies that exist in taking sufficient amounts of potent pharmaceuticals to the site of action, manage high

morbidity rate diseases, increase patient compliance and quality of life. The role of polymer morphology in this quest is now well documented. This review has outlined the advances that have been made in optimizing branched star polymers-based formulations, through an understanding of varied parameters that influence their performance. We hope that the enthusiasm shown by the polymer community in recent years, in exploring the scope of star polymers in nanoengineering drug delivery, will continue to hold. There is sufficient evidence to move the investigations to more detailed *in vitro* studies, followed by successfully evaluating and establishing these claims *in vivo*, and subsequently bringing these to clinical trials. It can contribute significantly to removing the often-quoted weakness, “polymers have offered great potential in drug delivery for decades but have not performed well when it comes to bench-to-bedside translation”.

In Section 1.1, we provided a detailed analysis of branched star polymers in designing nanoparticles. Building upon this foundational understanding, the subsequent section explores polymeric nanoparticles engineered to respond to gas stimuli. These gas-responsive nanomaterials harness the dynamic interplay between polymers and environmental cues in designing drug delivery systems for precise therapeutic interventions.

## **1.2. The Unexplored Potential of Gas-responsive Polymers in Drug Delivery: Progress, Challenges and Outlook**

This section incorporates content adapted in part from published article, the citation of which is provided below and is reprinted with permission from Wiley-VCH GmbH.

Yong, H. W.; Kakkar, A. The Unexplored Potential of Gas-responsive Polymers in Drug Delivery: Progress, Challenges and Outlook. *Polym. Int.* **2022**, *71* (5), 514-520.

### *1.2.1 Abstract*

Targeted drug delivery based on polymeric nanoparticles has been a long-standing interest in nanomedicine for its beneficial traits including controlled and localized drug release. Gas-responsive polymers offer an advantageous platform and have been slowly gaining attention in

spatially locating and displaying unique interactions of specific responsive chemical entities in polymeric chains with endogenous gaseous stimuli. In this review, we highlight recent developments in polymeric nanoformulations with stimulant chemical entities for gasotransmitters such as NO, CO, H<sub>2</sub>S, SO<sub>2</sub>, O<sub>2</sub> and CO<sub>2</sub> in enhancing efficacy in therapeutic interventions. We underline some challenges and limitations of exploring these systems for clinical applications, and how we can further tap into the potential of these emerging materials.

### *1.2.2. Introduction*

Delivery of active pharmaceutical agents to disease sites using polymeric formulations continues to be a topical area of research to overcome limitations such as poor aqueous solubility, low bioavailability, and systemic toxicity.<sup>203</sup> Through a combined effort by chemists, pharmacologists and physiologists, a good understanding of key parameters in amphiphilic polymer-based nanoparticles design has emerged.<sup>189</sup> It is now becoming evident that directing drug-loaded soft nanoparticles to desired sites using endogenous cues is a gainful strategy in addressing challenges in managing high morbidity rate diseases. As such, stimuli-responsive polymers have gained intense limelight for a myriad of biomedical applications over the past few years.<sup>204-206</sup> Recent advances in the design of such environment-responsive polymers have demonstrated their potential in improving the efficacy of nanomedicine, by undergoing conformational or phase transitions that can be fine-tuned in relation to one or more internal cues such as pH, temperature, reactive oxygen species, glutathione etc.<sup>207</sup> The choice and incorporation of specific chemical entities responsive to selective stimuli into these polymers are of immense importance to achieve localized, targeted, and controlled release of therapeutic agents at disease sites, and thus increase drug efficacy and reduce unwanted side effects. Over the years, there has been immense progress made in designing polymeric precursors that can respond to a variety of gaseous stimulants. In this review, we will accentuate some of the latest reports on gas-responsive polymeric nanoparticles used for controlled and targeted release of their cargo.

#### *1.2.2.1. Gas-responsive Polymers*

Whilst many stimuli-responsive chemical entities have been incorporated into functional drug delivery systems, studies on gas-responsive polymers for biological applications have been

limited. The vast majority of polymeric nanoparticulate systems still rely on well-known endo/exogenous stimuli for regulated release of therapeutic cargo. Many gases, such as nitric oxide (NO), carbon monoxide (CO) and hydrogen sulfide (H<sub>2</sub>S) have been shown to be crucial intracellular signaling molecules in regulating bodily functions.<sup>208,209</sup> However, studies leveraging on these gaseous bio-activators are in their infancy stage, and there exist only nascent reports that have explored these gasotransmitters in detail. This feature article provides an overview of recently developed gas-responsive polymers for the controlled release of active pharmaceutical agents (Table 1. 4). Some of the limitations of such systems, as well as challenges in moving forward to translate these nanoformulations from bench-to-bedside, will also be highlighted. Our purpose is to familiarize the reader and provide an understanding as to how these gasotransmitters are becoming the next generation candidates in designing smart polymers for targeted drug delivery.

**Table 1. 4:** Gas-responsive polymer based nanoformulations in drug delivery.

<b>Gasotransmitter</b>	<b>Gas-responsive moiety</b>	<b>Polymer<sup>a</sup></b>	<b>Cargo</b>	<b>Formulation</b>	<b><i>In vitro/ in vivo</i> model</b>	<b>Ref</b>
NO	<i>o</i> -phenylenediamine	PEO <sub>45</sub> - <i>b</i> -PEOPA <sub>70</sub>	Rhodamine 6G	Nanorods	--	210
		HA-NO-LF	Levofloxacin	Micelles	RAW 264.7 cells/ Female Kunming mice	211
CO	Palladacycle dimer	PEG <sub>45</sub> -PUPd <sub>68</sub> -PEG <sub>45</sub>	Nile red	Micelles	--	212
	Pd-bridged	PDMAA <sub>0.97</sub> -PBMA <sub>0.03</sub>	Rhodamine B	Hydrogels	--	213
H <sub>2</sub> S	<i>o</i> -azidomethyl benzoate	PEO <sub>67</sub> - <i>b</i> -PAGMA <sub>25</sub>	Epinephrine	Vesicles	--	214

	N <sub>3</sub> -Nap	N <sub>3</sub> -Nap- PHEMA <sub>45</sub> - <i>b</i> - PMMA <sub>42</sub> -N <sub>3</sub>	Doxorubicin	Micelles	HeLa and 4T1 cells	215
	(2-azido- 1,3- phenylene)di methanol	SC-Dex	FITC-BSA	Hydrogel	--	216
SO <sub>2</sub>	Levulinate- protected phenol	PEG <sub>45</sub> - <i>b</i> - PVPOP <sub>14</sub>	SN-38/ R6G	Micelles	--	217
O <sub>2</sub> / CO <sub>2</sub>	TF-DEAE- AM	PEG <sub>45</sub> - <i>b</i> -poly(TF- DEAE-AM) <sub>20</sub>	Pyrene	Micelles	--	218
	TFEMA/ DMAEMA	PEG <sub>45</sub> - <i>b</i> - P(DMAEMA <sub>106</sub> - <i>co</i> -TFEMA <sub>53</sub> )- <i>b</i> - PMEPPMA <sub>56</sub>	Calcein	Vesicles	--	219
CO <sub>2</sub>	DEAEMA	PDMAA <sub>30</sub> - <i>b</i> - PDEAEMA <sub>400</sub>	Pyrene- 1,3,6,8- tetrasulfonic acid tetrasodium	Vesicles	--	220
		PEO <sub>45</sub> - <i>b</i> - P(DEAEMA <sub>100</sub> - <i>co</i> -CMA <sub>6</sub> )				
		P(AnMA <sub>3</sub> - <i>co</i> - MMA <sub>87</sub> )- <i>b</i> - PDEAEMA <sub>77</sub>	Curcumin			
	DMAEMA	PDMAEMA/TM PTMA	Naloxone	Hydrogel	--	222
		Lipo-C/ Lipo-S	Doxorubicin	Liposome	MCF-7S, MCF-7R cells	223

		P(MEO <sub>2</sub> MA <sub>180</sub> - <i>co</i> -DMAEMA <sub>38</sub> )- <i>b</i> -PEO <sub>455</sub> - <i>b</i> - P(MEO <sub>2</sub> MA <sub>180</sub> - <i>co</i> -DMAEMA <sub>38</sub> )	FITC-BSA	Hydrogel	--	224
		PDMAEMA <sub>80</sub> - <i>b</i> - PNBA <sub>21</sub>	Indomethaci n	Micelles	--	225
		PDMAEMA <sub>104</sub> - <i>b</i> - PS <sub>128</sub>	Indomethaci n	--	HeLa cells	226
		Py-PCL- <i>b</i> - P(NIPAM- <i>co</i> - DMAEMA)	Doxorubicin	Micelles	--	227
		PPEGMA <sub>9</sub> - P(HPMA <sub>200</sub> - <i>co</i> - DMAEMA <sub>80</sub> )	Bovine Serum Albumin	Vesicles	--	228
		PDMAEMA <sub>133</sub> - PEG <sub>500</sub> - PDMAEMA <sub>133</sub>	Rhodamine B	Vesicles	--	229
		PAAm <sub>70</sub> - PDMAEMA <sub>100</sub> - PAAm <sub>70</sub>	Rhodamine B	Vesicles	--	230
		PGMA <sub>43</sub> - P(HPMA <sub>350</sub> - <i>co</i> - DMAEMA <sub>50</sub> - <i>co</i> - AMA <sub>20</sub> )	Methylene blue	Vesicles	--	231
	DMAEMA/ PADS	PADS <sub>9</sub> - <i>b</i> - PDMAEMA <sub>17</sub>	Doxorubicin	Micelles/ Vesicles	--	232
	AD	PEO <sub>45</sub> - <i>b</i> -PAD <sub>61</sub>	Rhodamine B	Vesicles	--	233
		PEG <sub>45</sub> - <i>b</i> -PAD <sub>78</sub>	PEI-5/ PEI- 25	Polymersomes	--	234

	AHMA	Dex-g-PAHMA	Doxorubicin	Micelles	MCF-7 cells	235
	DEEA	P(DEEA-co-BA-co-DMNOBA-co-ABP)	Doxorubicin	Nanorod	--	236

<sup>a</sup> Subscript in polymer abbreviations denotes the degree of polymerization obtained using <sup>1</sup>H NMR. Abbreviations used are described here in alphabetical order: ABP: 4-acryloyloxy benzophenone; AD: (*N*-amidino)dodecyl acrylamide); AHMA: (*N*-amidino)hexyl methacrylamide; AMA: allyl methacrylate; AnMA: (anthracene-9-carboxyl) ethyl methacrylate; APUEMA: 2-(3-(2-aminophenyl) ureido)ethyl methacrylate hydrochloride; BA: *N*-benzylacrylamide; CMA: coumarin methacrylate; DEX: Dextran; DEAEMA: *N,N*-diethylamino ethyl methacrylate; DEEA: *N,N*-diethylaminoethyl acrylamide; DMAEMA: *N,N*-dimethylamino ethyl methacrylate; DMNOBA: *N,N*-dimethyl-*N*-(2-nitrobenzyl)-ethaneamine acrylamide; EGDMA: ethyleneglycol dimethacrylate; HA: hyaluronic acid; HPMA: 2-hydroxypropyl methacrylate; LF: levofloxacin; MEPPMA: 4-(4-methoxy-phenylazo)phenoxy methacrylate; MeO<sub>2</sub>MA: *N,N*-dimethylaminoethyl methacrylate; MMA: methyl methacrylate; N<sub>3</sub>-Nap: *N*-(2-hydroxyethyl)-4-azide-1,8-naphthalimide; NAPMA: *N*-(2-aminophenyl) methacrylamide hydrochloride; NIPAM: *N*-isopropylacrylamide; PADS: amidine-containing styrene polymer; PAGMA: poly(*o*-azidomethyl benzoyl glycerol methacrylate); PAAM: polyacrylamide; PBMA: poly(*p*-dimethylamine) methyl benzyl methacrylate); PCL: polycaprolactone; PDMAA: poly(*N,N*-dimethyl acrylamide); PEG: polyethylene glycol; PEI: poly(ethylene imine); PEO: polyethylene oxide; PEOPA: poly(*o*-phenylenediamineL-glutamate); PGMA: poly(glycerol methacrylate); PHEMA: poly(2-hydroxyethyl methacrylate); PLA: poly(lactic acid); PNBA: poly(2-nitrobenzyl acrylate); PS: polystyrene; PUPd: palladacycle-connected polyurethane block; PVPOP: poly(4-vinylphenyl 4-oxopentanoate); Py: pyrene; SC-Dex: H<sub>2</sub>S-responsive cholesterol-modified dextran; TF-DEAE: 2,2,2-trifluoroethyl 3-(2-(diethylamino)ethyl)amino)propanoate; TFEMA: 2,2,2-trifluoroethyl methacrylate; TMPTA: trimethylolpropane trimethacrylate; TPGS: D- $\alpha$ -tocopheryl polyethylene glycol 1000 succinate

#### 1.2.2.1.1. Nitric Oxide (NO)

Nitric oxide is a free radical species that is crucial in mediating several biological functions such as angiogenesis, apoptosis, vasodilation, and immune response.<sup>237</sup> Abnormally high levels of NO might lead to complications such as migraine and rheumatoid arthritis. One of the first reports on

NO-targeted polymeric systems was published in 2014 by Hu et al. on a dual NO- and thermo-responsive system,<sup>238</sup> followed by another that was NO- and CO<sub>2</sub>-responsive, in 2015.<sup>239</sup> They utilized *o*-phenylenediamine groups (Figure 1. 13) that converted into benzotriazole upon interaction with NO under extremely mild conditions to modify the overall self-assembly behavior of the polymeric nanoaggregates. Thereafter, polyethylene oxide (PEO) and hyaluronic acid (HA)-based NO-targeted polymers have also been prepared (Table 1. 4), both relying on *o*-phenylenediamine groups for disassembly of nanorods, as well as cleavage of levofloxacin-conjugated HA for targeted delivery of rhodamine 6G and levofloxacin respectively.<sup>210, 211</sup> These studies demonstrated immense potential and increasing interest in NO-responsive polymers, although they still pale very much in comparison to studies involving NO-releasing polymers, even when extended beyond the realm of drug delivery. The latter is much wider in scope, using responsive groups such as S-nitrosothiol<sup>240, 241</sup> and N-diazeniumdiolates<sup>242, 243</sup> incorporated into nanoparticles for antimicrobial/-biofilm activities in biomedical implants, NO-releasing hyperbranched polymers for antibacterial properties<sup>244-246</sup> and antibiofilm,<sup>247</sup> hybrid nanoparticles,<sup>248</sup> and others.<sup>249, 250</sup>

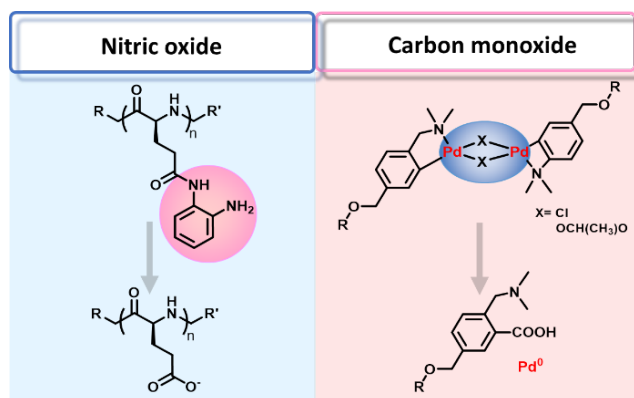


**Figure 1. 13:** *O*-phenylenediamine (NO-responsive) and Pd-bridged (CO-responsive) functionalities for gas-responsive polymers-based drug delivery systems.

#### 1.2.2.1.2. Carbon Monoxide (CO)

While mainly being labeled as an environmental pollutant and a “silent killer”, CO has also gained much attention in recent years as one of the three main gasotransmitters that are crucial in regulating physiological functions.<sup>250</sup> In contrast to NO, CO is not a free radical, and thus has

much longer biological half-life (minutes vs. seconds). Abnormalities in its metabolism have been linked to a series of complications such as blood pressure variations and vasodilation.<sup>251</sup> Along with its discovery as a biological regulator, the potential anti-inflammatory, cell-protective, anti-hypertensive activity and homeostatic action that CO exhibits, has rendered it a promising therapeutic agent that can be administered in many forms, including CO inhalation, CO-releasing molecules (CORMs) and organic CO-prodrugs.<sup>252-255</sup> Similar to CORMs that rely on inorganic metal complexes coordinated to CO, palladacycles (Figure 1. 13) have been popular in developing CO-triggered systems as fluorescent probes<sup>256, 257</sup> and surface enhanced Raman spectroscopy (SERS) nanosensors<sup>258</sup> for endogenous CO detection, and even more recently, for drug delivery (Table 1. 4).<sup>212</sup> In 2017, Xu et al. reported the first example of a CO-responsive palladacycle-containing ABA-type block copolymer for the enhanced delivery of Nile Red. The palladacycle linkage that was cleverly placed between two polyethylene glycol (PEG) blocks could be broken upon minimal CO exposure (30 nM/ 0.1 equivalent) to disrupt the overall stability of the self-assembled structure, as seen using NMR, dynamic light scattering and X-ray photoelectron spectroscopy. Such breakage facilitated the release of Nile Red, which could be modulated through varying levels of CO. The same group also reported a Pd-bridged CO-responsive hydrogel that exhibited self-healable properties.<sup>213</sup>

#### 1.2.2.1.3. Hydrogen Sulfide (H<sub>2</sub>S)

H<sub>2</sub>S is also one of the three main gasotransmitters (NO, CO and H<sub>2</sub>S) that is a key signaling molecule in regulating blood vessel dilation, cellular bioenergetics, and resisting inflammation.<sup>259</sup> As such, deficiency, and over-production of H<sub>2</sub>S has been associated with a number of complications and pathologies. At safe concentrations (<50 μM), the body can easily oxidize H<sub>2</sub>S to non-toxic byproducts. However, once tipped over this threshold, the gas can inhibit mitochondria functions and reduce cellular respiration, eventually causing cell death, and leading to complications such as angiocardopathy as well as neurodegeneration.<sup>260-262</sup> Since H<sub>2</sub>S acts as a good reducing agent, H<sub>2</sub>S-cleaveable *o*-azido-methylbenzoate (AzMB) groups (Figure 1. 14) have been utilized to induce disassembly of polymeric vesicles (Table 1. 4).<sup>214</sup> Poly(*o*-azidomethyl benzoyl glycerol methacrylate) (PAGMA) that initially formed the hydrophobic segment of the polymersome could be cleaved by H<sub>2</sub>S, yielding hydrophilic poly(glycerol methacrylate) (PGMA)

which disrupted the vesicle's stability to release epinephrine (EP) in a controlled manner with varying H<sub>2</sub>S concentrations. Another report drew inspiration from H<sub>2</sub>S-responsive fluorescence probes, using *N*-(2-hydroxyethyl)-4-azido-1,8-naphthalimide (N<sub>3</sub>-Nap) as a detectable and functional precursor, for the delivery of DOX.<sup>215</sup> In this system, the N<sub>3</sub>-Nap fluorophore was incorporated into poly(2-hydroxyethyl methacrylate)-*block*-poly(methyl methacrylate) (N<sub>3</sub>-Nap-PHEMA-*b*-PMMA-N<sub>3</sub>), providing charge reversibility on the self-assembled micelles, as H<sub>2</sub>S reduced N<sub>3</sub>-Nap to NH<sub>2</sub>-Nap.<sup>263</sup> This led to an improved cellular uptake of the DOX-loaded micelles through positive charge mediated targeting, as observed under confocal microscopy on HeLa and 4T1 cells. *In vivo* fluorescence imaging and biodistribution studies also showed better distribution of DOX at tumor sites with the H<sub>2</sub>S-responsive polymers. This study demonstrated how H<sub>2</sub>S that is readily available in multiple organs and tissues, could be fully utilized to enhance the delivery of therapeutic agents.

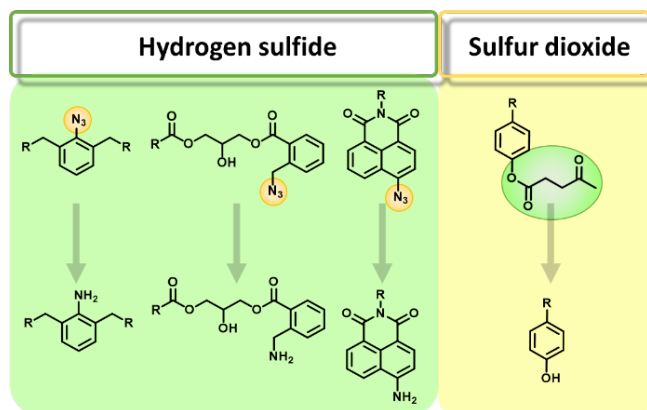


**Figure 1. 14:** Azido (H<sub>2</sub>S-responsive) and levulinate (SO<sub>2</sub>-responsive) functionalities gas-responsive polymers-based drug delivery systems.

#### 1.2.2.1.4. Sulfur Dioxide (SO<sub>2</sub>)

The most significant source of the colorless, foul-smelling SO<sub>2</sub> gas comes from industrial processes such as combustion of fossil fuels. It is also notorious for producing acid rain, which has a drastic effect on our health, surroundings, and ecosystem.<sup>264, 265</sup> In 2020, Li et al. designed the first SO<sub>2</sub>-responsive polymeric system composed of PEG and a newly designed polymer, poly(4-vinylphenyl 4-oxopentanoate) (PVPOP), that consisted of a levulinate-protected phenol which

could be hydrolyzed by readily formed sulfite ions ( $\text{SO}_3^{2-}$ ) under ambient conditions (Table 1. 4, Figure 1. 14).<sup>217</sup> The self-assembly of the linear diblock copolymer, PEG<sub>45</sub>-b-PVPOP<sub>14</sub> led to “large compound micelles” that could potentially be used to load both hydrophilic (rhodamine 6G) and hydrophobic (7-ethyl-10-hydroxycamptothecin, SN-38) drugs. It was demonstrated that the self-assembly characteristics and the release profile of SN-38 could be controlled by varying  $\text{SO}_3^{2-}$  concentrations and exposure time and was highly selective to  $\text{SO}_3^{2-}$  despite the presence of high levels of other bio-species.

#### 1.2.2.1.5. Oxygen ( $\text{O}_2$ )

Oxygen is another important gaseous molecule to tune the physiological functions in our body,<sup>266</sup> and is the only gas amongst gasotransmitters that does not have a bad rap. Similar to the other gaseous stimuli, research on  $\text{O}_2$ -responsive polymers is still in the early stages, with a few reports leveraging on the unique properties of branched architectures.<sup>267</sup> All  $\text{O}_2$ -responsive polymers recorded to date utilize aliphatic or aromatic-linked fluorine groups that adsorb  $\text{O}_2$  reversibly (Figure 1. 15), and which alters the hydrophilic/ hydrophobic balance of any aggregates.<sup>268-272</sup> This unique phenomenon has been attributed to the van der Waals interactions between  $\text{O}_2$  and C-F bonds, which might also suggest why the polymers can undergo multiple cycles of gas treatment under ambient conditions.<sup>273</sup> In 2018, Lin et al. reported a  $\text{CO}_2$ ,  $\text{O}_2$  and light-responsive vesicle formulation based on poly(ethylene glycol)methyl ether)-block-poly(N,N-dimethylamino ethyl methacrylate-co-2,2,2-trifluoro-ethyl methacrylate)-block-poly(4-(4-methoxyphenylazo)phenoxy methacrylate) (PEG<sub>45</sub>-b-P(DMAEMA<sub>106</sub>-co-TFEMA<sub>53</sub>)-b-PMEPPMA<sub>56</sub>) (Table 1. 4).<sup>219</sup> While the concept of  $\text{O}_2$  and  $\text{CO}_2$ -responsivity is not new, the change in self-assembly characteristics and release of calcein that was tunable with light, offers a different approach to potentially accommodate light as an exogeneous trigger to customize pharmacokinetics whenever needed.

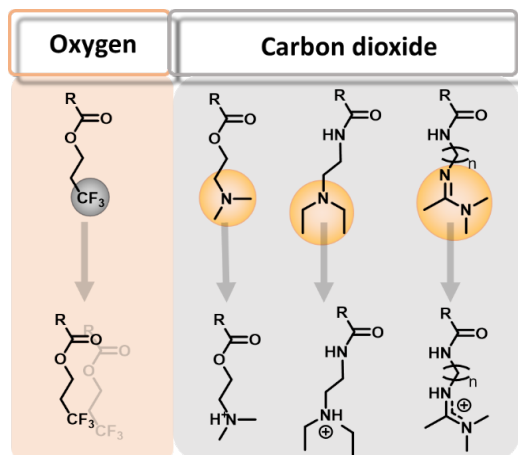


**Figure 1. 15:** Aliphatic fluorine ( $O_2$ -responsive) and tertiary amine/ amidine ( $CO_2$ -responsive) functionalities gas-responsive polymers-based drug delivery systems.

#### 1.2.2.1.6. Carbon Dioxide ( $CO_2$ )

$CO_2$  is probably the most familiar to us as a greenhouse gas. Atmospheric  $CO_2$  is now more than 50% higher than pre-industrial levels, setting global average temperatures and sea levels to a new high. As such,  $CO_2$ -responsive systems are becoming extremely popular and could be one of the solutions to reduce and repurpose  $CO_2$  into useful raw materials.<sup>274</sup> Some functionalities that have been proven to be responsive to  $CO_2$  include tertiary amines, amidines and guanidines that can be protonated/ deprotonated reversibly without any side products.<sup>275</sup> In the context of drug delivery,  $CO_2$ -responsive polymers seem to be attracting much more interest than the other gasotransmitters (Table 1. 4). Higher than usual  $CO_2$  levels in the body, otherwise known as hypercapnia, lead to respiratory acidosis caused by copious amounts of protons being produced. This lowering of pH may be beneficial for patients with acute lung injury, although the consequences far outweighs its benefits.<sup>276</sup> Exploiting the reversible and dynamic features of  $CO_2$ -responsive systems, Tian et al. recently explored (2-diethylamino)ethyl methacrylate (DEAEMA) to construct a dual  $CO_2$  and photo-responsive system that offered flexibility in its volume and wall thickness for delivery of curcumin (Figure 1. 16).<sup>221</sup> They observed significant changes in the morphology, as the self-assemblies were protonated to different degrees, giving a range of morphologies from micelles, worm-like micelles to small vesicles as the hydrophilic fractions of the nanoaggregates change. Subsequently, the combination of tertiary amine protonation by  $CO_2$  and dissociation of anthracene

photodimers by UV accelerated release of curcumin, which could potentially be utilized for better localization through external triggers. As one would expect, such a formulation is also responsive to low pH, with the drug release being accelerated at pH 5.0, as compared to pH 6.0 and pH 7.4.

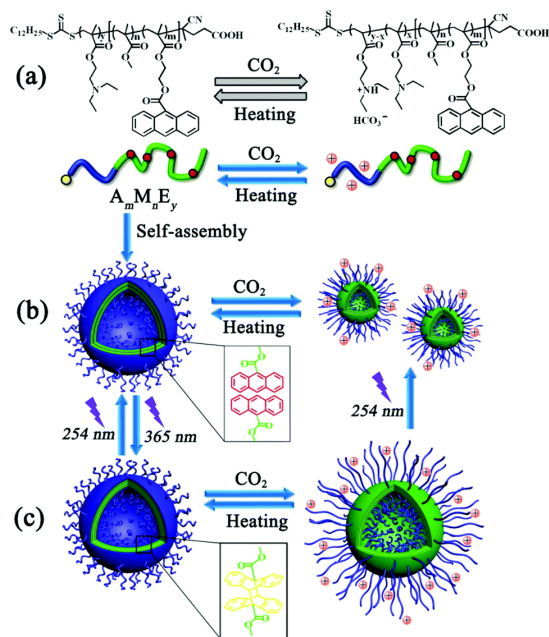


**Figure 1. 16:** Schematic representation of P(AnMA<sub>3</sub>-co-MMA<sub>87</sub>)-b-PDEAEMA<sub>77</sub> polymer with reversible polymersome-micelle morphologies controllable by CO<sub>2</sub> and UV light. Reproduced with permission from reference 221; Copyright 2019, Royal Society of Chemistry.

### 1.2.3. Challenges and Outlook with Gas-responsive Polymers

The high specificity and programmability of gas-responsive entities into polymeric soft nanoparticles, can enable controlled and sustained delivery of lipophilic drugs at targeted sites, and is emerging as a promising platform in nanomedicine. However, the design of such macromolecular assemblies to utilize gaseous endogenous chemical agents remains challenging. The key to widespread application of gas-responsive polymers in drug delivery lies not only in synthetic articulation of polymeric architectures, but also in developing a detailed understanding of the concentrations of gaseous agents at the desired sites, biological mechanisms through which they operate, and the physiological conditions at which such gases become beneficial. It is through such a structure-property relationship determination, one can start to design the polymeric systems

with desired spatial distribution of gas-responsive chemical entities and address key tenets including the levels of functional group sensitivity and the nanoparticle performance in stimuli-responsive drug delivery. Considering that many of these gasotransmitters exist as a tricky double-edged sword, more in-depth understanding of the essential role of the gas, and complications related to its dual beneficial and detrimental effects, should be studied. For example, NO, H<sub>2</sub>S and CO have been shown to exhibit both anti-cancer and carcinogenic properties.<sup>277</sup> Therefore, knowledge related to the sequential molecular and cellular consequences would help narrow the scope for polymer chemists to optimize these systems.

The quantification of these gases *in vivo* is a major hurdle that remains very difficult to overcome. Some of the gases, such as NO and CO, are very reactive and have short half-lives; others, such as CO<sub>2</sub> and SO<sub>2</sub>, react readily with water and dissociate into other derivatives. This makes detection and quantification challenging. It is not obvious as to how exactly we could measure the gas concentrations *in vivo* and ascertain how sensitive the nanoparticles should be to these triggers. Perhaps quantification of the gas derivatives is sufficient to infer the approximate concentrations. For instance, 60% of CO<sub>2</sub> in aqueous media is catalyzed by carbonic anhydrase to form carbonic acid, which readily dissociates into H<sup>+</sup> and HCO<sub>3</sub><sup>-</sup>. Only about 10% of CO<sub>2</sub> remains as CO<sub>2</sub> in the plasma, which will diffuse into the bloodstream to react with hemoglobin to form carboxyhemoglobin. Therefore, using HCO<sub>3</sub><sup>-</sup> might be more convenient to diagnose CO<sub>2</sub> levels indirectly. Although hypercapnia has been generally defined as CO<sub>2</sub> partial pressures of more than 45 mmHg, concentration of bicarbonate ions is also routinely used in arterial blood gas tests to evaluate hypercapnia in patients, as CO<sub>2</sub> is in equilibrium with carbonic acid.<sup>278</sup>

With a similar idea in mind, SO<sub>2</sub>-responsive polymers, (or rather SO<sub>3</sub><sup>2-</sup>-responsive) have been developed.<sup>217</sup> However, SO<sub>2</sub> is not the only source of endogenous SO<sub>3</sub><sup>2-</sup> or bisulfite (HSO<sub>3</sub><sup>-</sup>) ions, as metabolism of sulfur-containing amino acids such as cysteine regularly produces SO<sub>3</sub><sup>2-</sup>. The latter can also be oxidized to sulfate (SO<sub>4</sub><sup>2-</sup>) in the presence of sulfite oxidase that is widely distributed in the liver, heart, and kidney.<sup>279</sup> Therefore, one might argue that such measurements are not accurate representations of the SO<sub>2</sub> concentrations. NO detection also involves measurements such as the fluorescence or absorbance of both NO and its derived species.<sup>280, 281</sup> Regardless, this poses another interesting question: can we design functional moieties that respond

to the derived reactive species instead of the gas itself? This might expand the scope of such studies to include already-reported investigations intended for other functions, such as poly (3,4-ethylenedioxythiophene) (PEDOT) that has been used for NO<sub>3</sub><sup>-</sup> detection in soil.<sup>282</sup>

Although progress in synthetic polymer chemistry has contributed to the development of a library of macromolecules with desired special functions, many of them are not commercially available. In addition, the overall process often involves multistep synthetic procedures that might restrict their commercial potential, as these might not be cost or time-effective to scale up. Thus, simpler polymeric compositions, facile synthetic routes, or using commercially available monomers as seen with O<sub>2</sub> and CO<sub>2</sub>-responsive polymers, might be more practical approaches in translating these nanoformulations from bench-to bedside. Clear demonstration of the safety, biocompatibility, biodegradability, biodistribution and cytotoxicity is also necessary, before moving into clinical trials. Only very few *in vitro* and *in vivo* studies have been conducted to address the complexity of these systems (Table 1. 4), which is absolutely crucial to accelerate clinical translation.

### 1.2.4. Conclusions

Stimuli-responsive nanoformulations have offered tremendous opportunities to address key challenges in controlled and sustained release of active pharmaceutical agents and facilitate effective therapeutic interventions in high morbidity rate diseases. Utilizing gaseous triggers in the body is another such venue, which is starting to gain considerable attention from the scientific community. In this review, we attempted to briefly summarize the latest advances in the design of polymeric nanoparticles, which contain chemical entities reactive towards gaseous molecules, and act as endogenous cues for tailored release of drug molecules. To demonstrate the potential of such systems in nanomedicine, we introduced six commonly used gasotransmitters, NO, CO, H<sub>2</sub>S, SO<sub>2</sub>, O<sub>2</sub> and CO<sub>2</sub>, which are important in regulating physiological functions and have been utilized in triggering the release of drug molecules. We examined the versatility of such polymeric soft nanoparticles, in which chemical entities could be potentially activated by endo- or exogenous triggers in tailoring their pharmacokinetic profiles. Several examples noted above provide an overview of the activity in this area and suggest that much more still needs to be done to fully

explore and establish their potential in drug delivery. Amongst gas triggers, CO<sub>2</sub> has been extensively examined, due to the ease with which the polymeric precursors with desired functional chemical entities, could be synthetically articulated. There is still the need to adapt their aqueous assemblies to varied pH, relate these to quantitatively assessed internal CO<sub>2</sub> concentrations, and provide structure-function relationships. The evaluations of CO<sub>2</sub>-reactive soft nanoparticles do provide impetus for similar activity in developing nanoformulations for other such gas-triggered drug release systems. Despite the growing interest in gas-responsive polymers, the progress has been slow, which may be due to our lack of understanding of biological events at the gas-rich sites. It is expected that such evaluations will be forthcoming and will provide guidance to chemists in designing novel polymeric compositions. It is through such a convergent approach, one can envision highly efficient nanoformulations containing sufficient drug cargo, which is released on-call from gaseous triggers at disease sites. Once a detailed *in vitro* evaluation is followed by *in vivo* studies, it will expedite their bench-to-bed side translation.

### 1.3. Stimuli-responsive Polymeric Nanoparticles

Branched amphiphilic block copolymers continue to offer great potential in drug delivery. The versatility conferred by multiple branching segments in branched star polymers has led to the development of a diverse range of soft nanoparticles. Amongst these, asymmetric (miktoarm) polymers present an advantageous strategy for enhancing the scope of polymeric nanoparticles by adjusting the composition of their backbones. There is significant ease with which stimulus-responsive chemical functional units could be incorporated into branched architecture. Leveraging the distinctive attributes of these miktoarm polymers, including low CMCs, smaller sizes, and higher drug encapsulation efficiencies, makes these attractive precursors in designing efficient nanoformulations for drug delivery.<sup>283</sup>

Stimuli-responsive polymers, also known as smart polymers, are designed to respond to internal and external environmental cues.<sup>284</sup> This class of macromolecules has garnered significant attention due to its diverse biomedical applications. In controlled and triggered drug delivery systems, these polymers play a pivotal role in allowing targeted release of pharmaceutical agents in response to physiological environments.<sup>285</sup> These advances can help improve drug targeting,

minimize premature release, and maximize drug efficacy. Drug delivery systems typically exhibit responsiveness to a spectrum of stimuli, encompassing both endogenous stimuli such as pH, ROS, gases, and enzymes, as well as exogenous triggers such as temperature, light, magnetic, and ultrasound.<sup>286</sup> Their versatility and efficiencies have revolutionized drug delivery, offering potential for precise control over therapeutic release. Among the plethora of stimuli investigated, CO<sub>2</sub>, pH, and ROS stand out prominently due to their relevance in common health conditions such as cardiovascular diseases and aging.<sup>287</sup> While pH- and ROS-responsive drug delivery systems have received great attention, the focus has largely been on linear polymeric systems. In addition, the exploration of CO<sub>2</sub>-responsive systems has remained relatively underexplored, as described in Section 1.2. This notable disparity highlights the pressing need for further investigation and innovation, particularly within the realm of miktoarm polymers. Table 1. 5 summarizes stimuli-responsive miktoarm polymers that have been investigated for delivering a variety of pharmaceuticals. These formulations demonstrate diversity in composition for enabling targeted delivery to desired sites through the incorporation of various stimuli-responsive moieties. In Chapter 2, we explore several endogenous stimuli, namely CO<sub>2</sub>, pH, ROS, and combinations thereof, to unravel their potential for fine-tuning drug delivery systems. By meticulously dissecting their diverse properties, we aim to develop nanoparticles that hold promise for advancing nanomedicine.

**Table 1. 5:** Stimuli-responsive miktoarm polymers for drug delivery.

<b>Stimulus</b>	<b>Polymers<sup>a</sup></b>	<b>Cargo</b>	<b>Biological Evaluation: Cell lines/ living organism</b>	<b>Ref</b>
pH	(PCL <sub>24</sub> ) <sub>2</sub> (PDEAEMA <sub>16</sub> - <i>b</i> -PPEGMA <sub>19</sub> ) <sub>2</sub>	Doxorubicin	<i>In vitro</i> : HepG2 cells	288
	(PCL <sub>16</sub> ) <sub>3</sub> -(PDEAEMA <sub>14</sub> - <i>b</i> -PPEGMA <sub>10</sub> ) <sub>3</sub>	Doxorubicin	<i>In vitro</i> : HepG2 cells	139
	(PCL <sub>25</sub> ) <sub>3</sub> -(PDEAEMA <sub>15</sub> - <i>b</i> -PPEGMA <sub>12</sub> ) <sub>3</sub>			

	(PCL <sub>33</sub> ) <sub>3</sub> -(PDEAEMA <sub>12</sub> - <i>b</i> -PPEGMA <sub>10</sub> ) <sub>3</sub>			
	(PCL <sub>33</sub> ) <sub>3</sub> -(PDEAEMA <sub>21</sub> - <i>b</i> -PPEGMA <sub>11</sub> ) <sub>3</sub>			
	PEG <sub>114</sub> -(PGlu <sub>26</sub> ) <sub>2</sub> -DOX	Doxorubicin	<i>In vitro</i> : HeLa cells	151
	PEG <sub>114</sub> -(PGlu <sub>31</sub> ) <sub>2</sub> -DOX			
	mPEG <sub>45</sub> -PtBA <sub>40</sub> -PCL <sub>25</sub>	Naproxen	<i>In vitro</i> : HeLa cells	289
	mPEG <sub>45</sub> -PAA <sub>40</sub> -PCL <sub>25</sub>			
	mPEG <sub>45</sub> - <i>b</i> -P(MMA <sub>24</sub> - <i>co</i> -MAA <sub>25</sub> ) <sub>2</sub>	Methotrexate	--	290
	(PCL) <sub>2</sub> -P(MMA- <i>co</i> -MAA) <sub>6</sub>	Doxorubicin, Camptothecin	--	148
	OA-(PEG <sub>114</sub> ) <sub>2</sub>	Vancomycin	<i>In vitro</i> : A549, MCF7, HepG2 cells and <i>S. aureus</i> . <i>In vivo</i> : MRSA injected BALB/c mice	169
pH/ redox	PEG <sub>45</sub> - <i>a</i> -PCL <sub>44</sub> -SS-PDMAA <sub>150</sub>	Paclitaxel	<i>In vitro</i> : 4T1 cells.	291
pH/ redox/ NIR light (temperature)	PEG <sub>45</sub> - <i>a</i> -PCL <sub>44</sub> -SS-P(NIPAM <sub>78</sub> - <i>co</i> -DMAA <sub>57</sub> )	Paclitaxel, Cypate	<i>In vivo</i> : 4T1 injected female BALB/c mice	
Redox	(FA-PEG <sub>21</sub> ) <sub>1</sub> - <i>c</i> -(PEG <sub>21</sub> -CL <sub>13</sub> -SS-CPT) <sub>3</sub>	Camptothecin	<i>In vitro</i> : SKOV-3 cells	196
	(FA-PEG <sub>21</sub> ) <sub>2</sub> - <i>c</i> -(PEG <sub>21</sub> -CL <sub>20</sub> -SS-CPT) <sub>2</sub>			
	(FA-PEG <sub>21</sub> ) <sub>3</sub> - <i>c</i> -(PEG <sub>21</sub> -CL <sub>40</sub> -SS-CPT) <sub>1</sub>			

	(FA-PEG <sub>21</sub> ) <sub>1-c</sub> -(PEG <sub>21</sub> -CL <sub>20</sub> -SS-CPT) <sub>3</sub>			
	mPEG <sub>45</sub> -SS-(PMMA <sub>39</sub> ) <sub>2</sub>	Methotrexate	<i>In vitro</i> : HeLa cells	133
	mPEG-(SS-PLL) <sub>2</sub>	Plasmid DNA	<i>In vitro</i> : HeLa cells	292
	MA-PEG <sub>45</sub> - <i>b</i> -(PCL <sub>8</sub> ) <sub>2</sub>	Chlorin e6, Doxorubicin	<i>In vitro</i> : MDA-MB-231 cell	103
	DTTP	Doxorubicin	<i>In vitro</i> : HEK-293 and MCF-7 cells	293
	(PEO <sub>45</sub> ) <sub>2</sub> - <i>b</i> -PFMA <sub>15</sub>	Doxorubicin	<i>In vitro</i> : HEK-293, HeLa, and HT-29 cells	294
Temperature	PNIPAM <sub>130</sub> - <i>b</i> -(PLL <sub>44</sub> ) <sub>2</sub>	Prednisone acetate	--	109
	PNIPAM-(PUA) <sub>2</sub>	Prednisone acetate	--	295
	(PNIPAM) <sub>3</sub> -PMMA	Prednisone acetate	--	296
	(PPEGMA <sub>32</sub> - <i>b</i> -PMMA <sub>41</sub> )- <i>b</i> -(PMMA <sub>45</sub> - <i>b</i> -PNIPAM <sub>19</sub> ) <sub>2</sub>	Celecoxib	--	127
	PNIPAM <sub>56</sub> - <i>b</i> -(PCL <sub>182</sub> ) <sub>2</sub>	Doxorubicin	--	297

<sup>a</sup> Subscript following polymer abbreviations denotes the degree of polymerization, whereas subscript following parenthesis denotes degree of branching. Abbreviations used are described here in alphabetical order: CPT: camptothecin; DTTP: dithioketal-linked ditocopheryl polyethylene glycol; FA: folic acid; MA: miktoarm; OA: oleic acid; PAA: poly(acrylic acid); PLL= poly(L-lysine); PCL: poly( $\epsilon$ -caprolactone); PDEA: poly(2-(diethylamino)ethyl methacrylate); PDMAA: poly(*N,N*-dimethyl acrylamide); PEG: polyethylene glycol; PGlu: poly(glutamic acid); PMAA: poly(methacrylic acid); PMMA: poly (methyl methacrylate); PNIPAM: poly(*N*-isopropylacrylamide); PPEGMA: poly(poly(ethylene glycol) methyl ether methacrylate); *Pt*BA: poly(*tert*-butylacrylate); PUA: poly(undecylenic acid).

### 1.3.1. CO<sub>2</sub>-responsive Polymeric Nanoparticles

In recent years, there has been a surge of interest in CO<sub>2</sub>-responsive materials due to their abundance, non-toxicity, and biocompatibility.<sup>298</sup> In human body, CO<sub>2</sub> is primarily produced as a

byproduct of oxidative metabolism.<sup>299</sup> However, excessive levels of CO<sub>2</sub> in the body, a condition known as hypercapnia, induce respiratory acidosis by elevating the production of protons.<sup>276</sup> In the context of drug delivery, CO<sub>2</sub>-responsive polymers are intriguing due to their relevance across a spectrum of diseases, such as chronic obstructive pulmonary disease.<sup>300</sup> However, as detailed in Section 1.2, the availability of CO<sub>2</sub>-responsive polymers specifically tailored for drug delivery applications is limited, and branched systems with such responsiveness are even more scarce. Therefore, CO<sub>2</sub>-responsive systems that harness the reversible and dynamic properties of CO<sub>2</sub> hold promise for biomedical applications. One example of a CO<sub>2</sub>-responsive miktoarm star polymer was reported in 2017. Huo et al. synthesized a series of ABC (A = PEG, B = PS, C = poly(2-(*N,N*-diethylamino)ethyl methacrylate (PDEAEMA))-based nanoparticles with varying PDEAEMA molecular weights to study their CO<sub>2</sub>-induced morphology transition.<sup>301</sup> The gas responsiveness, attributed to the presence of PDEAEMA, increased with an increase in PDEAEMA molecular weight. This difference led to various morphology transitions upon introduction of CO<sub>2</sub>, facilitated by the protonation of PDEAEMA. With increasing PDEAEMA molecular weight from 9.3k to 25k, the morphology evolved from “*E. coli*-shaped” nanosheets to nanoribbons, and eventually to nanodiscs.

### 1.3.2. pH-responsive Polymeric Nanoparticles

The promising application of pH-responsive nanoparticles stems from variations in pH occurring across different physiological environments.<sup>302</sup> The stomach, for example, is highly acidic (pH 1.5-3.5), while lysosomal and intracellular endosomal environments are less acidic (pH 4.5-5.0 and pH 5.5-6.0, respectively), and the small intestine is weakly acidic (pH 5.5-6.8). In addition to exploiting pH variations within normal tissues, the disparities between these environments and tumor environments have also been utilized. Notably, extracellular tumor tissues typically exhibit pH values ranging from 6.5-7.0, contrasting the pH of 7.4 found in normal physiological environment.<sup>303</sup> Polymeric nanoparticles that leverage these diverse pH environments offer significant potential for drug delivery. For instance, Alizadeh et al. reported on a series of ABC (A = PEG, B = PCL, C = PAA) triblock star copolymers to form micelles for pH-dependent naproxen delivery.<sup>289</sup> PCL formed the hydrophobic core for naproxen encapsulation while mixed PEG/ PAA formed the hydrophilic corona. The pH sensitivity was conferred by the introduction

of PAA. They observed smaller micelle sizes at low pH due to the protonation of COOH groups of PAA, which led to hydrogen bonding complexation with PEG arms in the micellar corona. Between pH 6-10, the PEG/ PAA complexation was lost, due to repulsive forces between adjacent PAA arms that became ionized. The particles increased in size from 51 to 154 nm as the pH ranged from 2.2 to 10. The miktoarm polymers were used to encapsulate naproxen, which demonstrated pH-dependent release profiles. At pH 2.2, naproxen release profile was slower (35-50%) than at pH 7.4 (65-89%) due to a more compact micellar structure.

Lin et al. reported on a  $A_3(BC)_3$  (A = PCL, B = PDEAEMA, C = PPEGMA)- based miktoarm polymer for pH-dependent delivery of DOX.<sup>139</sup> In the self-assembly of this copolymer, PCL formed the hydrophobic core for DOX encapsulation, while PPEGMA formed the hydrophilic corona. pH sensitivity was obtained through the PDEAEMA polymer. Protonation of PDEAEMA at lower pH levels (pH < 8) led to a hydrophobic to hydrophilic transition, resulting in electrostatic repulsion between the PDEAEMA chains that promoted micellar swelling. Conversely, deprotonation of PDEAEMA at higher pH levels (pH > 8) led to a hydrophilic to hydrophobic transition, resulting in compact micellar structures. DOX release from the miktoarm polymer-based micelle demonstrated pH-dependent behavior. At pH 7.4, only 27-40% of DOX was released; at pH 6.5, 44-59% of DOX was released; at pH 5.0, 100% of DOX was released.

pH-responsive hydrazone functional groups have been used in linking constituents of an  $AB_2$  (A = oleic acid, B = PEG) miktoarm polymer for antibacterial drug delivery.<sup>169</sup> In this study, the hydrazone linker was synthesized by combining a hydrazide-functionalized G1 oleodendrimer with PEG-CHO. Upon aqueous self-assembly, the micelle served as a suitable nanocarrier for vancomycin. The pH responsivity was demonstrated at pH 6.0, when drug release reached 100% in 48 h. This effect was attributed to the cleavage of the hydrazone linker that resulted in micellar disassembly. In contrast, at pH 7.4, vancomycin release was 86% in 48 h.

In another study, miktoarm star polymers were prepared using D-(-)-salicin as a heterofunctional initiator, functionalized with six bromoester groups and two hydroxyl groups, for the ROP of caprolactone, and atom transfer radical polymerization (ATRP) of tert-butylmethacrylate (*t*BMA)/MMA, respectively.<sup>148</sup> The *t*-butyl groups were then removed to yield  $PCL_2-P(MMA-co-MAA)_6$

miktoarm polymers, which conferred pH sensitivity to the macromolecule. The polymers were utilized to encapsulate DOX and camptothecin. As expected, the drug-loaded nanoparticles exhibited pH-responsive behavior, where the release rates of both drugs were faster at pH 5.0 than at pH 7.4. This was attributed to the ionization of PMAA chains at pH 5.0 that led to micelle swelling, thereby accelerating drug release.

A similar example was reported by Huang et al., where they reported an AB<sub>2</sub> (A = PEG, B = P(MAA-co-MMA))-type miktoarm polymer for drug delivery.<sup>290</sup> The polymer synthesis involved linking a bromoisobutyrate initiator to a dihydroxybenzoic acid core, followed by coupling with mPEG-OH. The macroinitiator was then used for ATRP with MMA and *t*BMA, after which the *t*-butyl groups were removed through acidolysis to obtain the PEG-P(MAA-co-MMA)<sub>2</sub> miktoarm polymer. The pH responsive behavior of the micelles, conferred by the PMAA groups, was demonstrated by their release profile of methotrexate. At pH 1.2, a greater release of methotrexate was observed. 98% of methotrexate was released in 48 h, compared to 33% at pH 7.4. This pH-induced drug release suggests the potential of using miktoarm star polymers as effective drug delivery systems for targeted therapy.

### *1.3.3. ROS-responsive Polymeric Nanoparticles*

ROS, such as hydrogen peroxide (H<sub>2</sub>O<sub>2</sub>), superoxide anion (O<sub>2</sub><sup>•-</sup>), and hydroxy radicals (HO•), are highly reactive ions and free radicals formed through the partial reduction of oxygen within biological systems.<sup>304</sup> ROS are essential for various physiological functions, including hormone production, cell signaling regulation, and inflammation mediation.<sup>305</sup> However, when the equilibrium between ROS and antioxidant defense systems is disrupted, oxidative stress ensues.<sup>306</sup> In general, low levels of ROS regulate cell signaling pathway and support cell proliferation, whereas elevated levels of ROS cause damage to DNA, proteins, and lipids.<sup>307</sup> Importantly, oxidative stress induces numerous diseases, including cardiovascular disorders and neurodegenerative conditions.<sup>308, 309</sup> These abnormal biochemical changes at disease sites have sparked interest among researchers in leveraging the imbalance in ROS levels to develop ROS-responsive drug delivery systems. Through the incorporation of ROS-responsive functional

groups, various ROS-responsive drug delivery systems have been investigated.<sup>310-314</sup> These systems hold great potential for enhancing the efficacy and precision of drug delivery.

Considerable research has been dedicated to studying ROS-sensitive linkers, encompassing various functionalities such as thioethers, thioketals, selenium, diselenides, tellurium, and more.<sup>315-317</sup> However, majority of this work has focused on linear polymer systems; there has been relatively limited investigations into the potential of miktoarm star polymers in this area. One example incorporated a AB<sub>2</sub> (A= PEG, B= PCL)-based miktoarm star polymer responsive to <sup>1</sup>O<sub>2</sub>.<sup>103</sup> The copolymer was synthesized by ROP of caprolactone from a β-aminoacrylate containing PEG macroinitiator. The β-aminoacrylate group formed the basis for ROS-responsivity, as the polymer was sensitive to <sup>1</sup>O<sub>2</sub> that was generated by the photosensitizer, chlorin e6, upon exposure to red light laser irradiation. When chlorin e6 and DOX were loaded simultaneously into the nanoparticles, they observed DOX release of 26% in 24 h in the absence of irradiation. Under irradiation, β-aminoacrylate cleavage accelerated DOX release significantly to 68% in 24 h. Moreover, upon irradiation, the co-loaded nanoparticles demonstrated substantial uptake of DOX uptake into the cytoplasmic region of MDA-MB-231 cells.

An AB<sub>2</sub> (A= PEG, B= thioketal-linked tocopherol) miktoarm star polymer with a ROS-responsive linker was prepared, in which the hydrophilic PEG was linked to tocopherol via a thioketal linker.<sup>293</sup> The ROS-responsiveness of the amphiphile and its self-assemblies were verified by incubating with 100 μM of H<sub>2</sub>O<sub>2</sub> for 24 h to reduce the thioketal linkages. <sup>1</sup>H NMR analysis of the polymer revealed significantly diminished thioketal peaks and the emergence of new acetone peaks, indicating the formation of acetone as a by-product. DLS measurements also showed larger micelle diameters of 167 nm, compared to 15 nm in the absence of H<sub>2</sub>O<sub>2</sub>. This enlargement was attributed to the aggregation of cleaved polymeric arms. *In vitro* DOX release studies revealed that less than <26% of DOX was released over 24 h. Conversely, DOX delivery over the same timeframe was significantly higher at 53% when treated with 100 μM of H<sub>2</sub>O<sub>2</sub>.

As demonstrated above, various functional groups are employed to respond to distinct stimuli of interest. For instance, CO<sub>2</sub>-responsive materials typically rely on amine-based functional groups which undergo protonation or deprotonation in response to environmental changes to enhance

therapeutic efficacy, whereas pH-responsive materials rely on ionizable groups such as PMAA. On the other hand, ROS-responsive materials commonly rely on the presence of thioketal bonds, which undergo rapid cleavage to achieve stimulus responsivity. This requirement for a multitude of functional groups highlights the synthetic complexities involved in the fabrication of multistimuli-responsive polymers. Each functional group must be carefully selected before incorporation to ensure proper responsiveness to the intended stimuli. Furthermore, the incorporation of multiple functional groups introduces challenges associated with polymerization techniques, reaction conditions, etc., which can limit their efficient incorporation into polymers. Despite these challenges, the development of multistimuli responsive polymers holds great promise for enabling the design of nanoparticles that respond to complex physiological cues. Overcoming these challenges opens up exciting opportunities for developing advanced materials with tailored responsiveness for a wide range of biomedical applications.

### **1.4. Antibacterial Nanoparticles**

In addition to designing nanoparticles responsive to endogenous stimuli, there is interest in designing nanoparticles with enhanced interactions with microorganisms through surface modifications. This research area is explored in Chapter 3, where we introduce charged amine groups on the surface of nanoparticles to augment their interaction with bacteria. This approach allows for the integration of intrinsic antimicrobial properties alongside their application for drug delivery, ultimately aiming to achieve combination therapy.

The development of antimicrobials to combat bacteria, viruses, fungi, and parasites has significantly advanced healthcare and agricultural sectors worldwide. However, the imprudent use of antimicrobials in humans, animals, and plants has led to the emergence of antimicrobial-resistant pathogens, posing a threat to global health.<sup>318</sup> To address this issue, the World Health Organization has partnered with various stakeholders across multiple sectors to establish guidelines for the prudent use of medically important antimicrobials to mitigate antimicrobial resistance (AMR).<sup>319</sup> This multinational effort has undoubtedly highlighted the gravity of AMR and the need for innovative concepts to combat the issue promptly.

In general, bacteria are classified as either Gram-positive or Gram-negative based on their response to crystal violet. In response to this dye, Gram-positive bacteria show a purple hue, while Gram-negative bacteria appear colorless. This distinction stems from structural differences between their cell walls: Gram-positive bacteria have cell walls composed of teichoic acids and a thick peptidoglycan layer, whereas Gram-negative bacteria have cell walls constituting of lipopolysaccharides, phospholipids, and a thinner peptidoglycan layer (Figure 1. 17).<sup>320</sup> The thick peptidoglycan layer in Gram-positive bacteria retains the dye precipitate, imparting a purple hue; the thin peptidoglycan layer in Gram-negative bacteria is destroyed and is unable to retain the dye precipitate.<sup>321</sup> Therefore, Gram-negative bacteria are not stained.

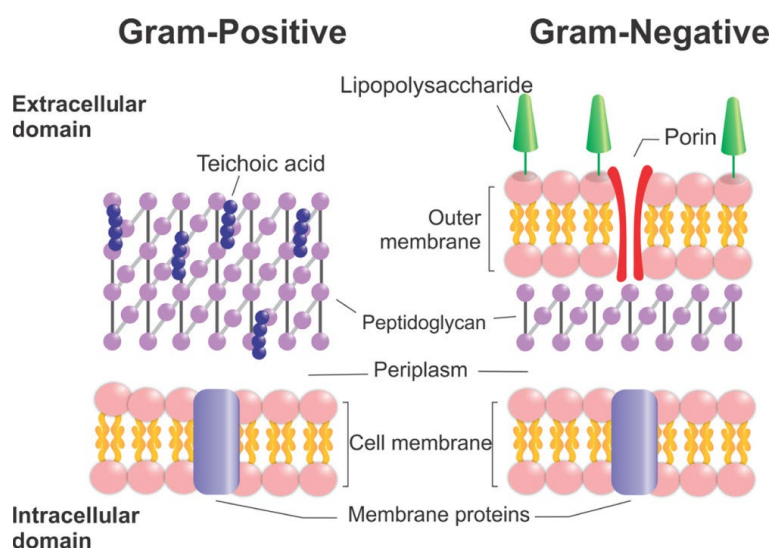


**Figure 1. 17:** Illustration of main components in Gram-positive and Gram-negative bacteria. Figure adapted from reference 320; Copyright 2020, American Chemical Society, used under Creative Commons CC-BY license.

Pathogens are said to develop resistance when they are less affected by conventional antibiotics. As a result, infections tend to aggravate, become increasingly challenging to cure, and persist longer, thereby increasing the risk of transmission to others.<sup>322</sup> Gram-negative bacteria are particularly resistant to many antibiotics that work on Gram-positive bacteria due to the presence of the additional outer membrane.<sup>323</sup> While the development of new antibiotics is one solution to

curb this issue, current progress in drug discovery has been limited and shows little improvement to keep pace with the growing prevalence of AMR.<sup>324</sup>

Cationic polymers which disrupt bacterial cell wall through electrostatic interactions hold significant potential for combating AMR. The negative charge on bacterial cell wall is usually the main target for eradicating bacteria. Both Gram-positive and Gram-negative bacteria have cytoplasmic membranes composed of anionic phospholipids such as cardiolipin, phosphatidylglycerol, and phosphatidylethanolamine, which vary in content.<sup>325</sup> Furthermore, under physiological conditions, Gram-positive bacteria tend to have a peptidoglycan layer that is anionic due to the presence of teichoic acids.<sup>326</sup> The lipopolysaccharide in Gram-negative bacteria also contributes to the negative charge of the bacterial cell wall. As a result, the net negative charge in the cell envelope promotes close interaction with cationic amphiphilic polymers through electrostatic attractions, which disrupts bacterial cell membranes.<sup>327</sup> This mechanism is different from that of antibiotics, which typically work by inhibiting DNA replication, RNA synthesis, or cell wall and protein synthesis.<sup>328,329</sup> Bacteria treated with antimicrobial polymers are also thought to be less prone to developing resistance, as the destruction occurs physically on the protective bacterial membrane.<sup>330</sup> Moreover, cationic polymers offer numerous advantages, including the ability to adjust morphology, charge density, cationic functionality, hydrophobic groups, biodegradability, all of which could potentially mitigate AMR. Some examples of cationic polymers that have exhibited good antibacterial properties include polyethyleneimines (PEI),<sup>331</sup> cationic polycarbonates,<sup>332, 333</sup> phosphonium polymers,<sup>334-336</sup> poly( $\alpha$ -amino acids),<sup>337, 338</sup> and cationic  $\beta$ -peptides,<sup>339</sup> among others.

Nanoparticles offer a promising approach for addressing challenges encountered in conventional antibiotic treatments.<sup>340</sup> Continual exploration and modification of nanoparticles have led to significant enhancements in antimicrobial outcomes while minimizing adverse effects on mammalian cells.<sup>341</sup> Within the realm of polymeric nanoparticles, various polymers have been used to fabricate nanoparticles to achieve such properties.<sup>342</sup> For instance, Choudhury et al. described a PEG-stabilized sulfur nanoparticle that inhibited various bacterial growth.<sup>343</sup> The authors harnessed the inherent toxicity of sulfur at high concentrations by utilizing sodium polysulfide and ammonium polysulfide to form nanoparticles, which were then stabilized by PEG<sub>9</sub>.

These PEGylated nanoparticles demonstrated potent inhibitory effects on bacterial growth with a minimum inhibitory concentration (MIC) as low as 9.41 mg L<sup>-1</sup> for *Acinetobacter baumannii* (*A. Baumannii*) and *Stenotrophomonas maltophilia* (*S. maltophilia*), and 18.82 mg L<sup>-1</sup> for *Escherichia coli* (*E. coli*), *Klebsiella pneumoniae* (*K. Pneumoniae*), and *Enterobacter aerogenes* (*E. aerogenes*). The nanoparticles exhibited bacterial inhibition at concentrations lower than the MIC of imipenem ( $\geq 32$  mg/L), a commonly used antibiotic. Importantly, the PEGylated nanoparticles displayed negligible cytotoxicity against HeLa cells even at 94 mg L<sup>-1</sup>, highlighting their potential as prospective antibacterial agents. Their findings suggest that these nanoparticles hold promise as future candidates for antibacterial agent development, offering a safer and potentially more effective alternative to traditional antibiotics.

Amphiphilic polymer-based nanoparticles are particularly useful for antimicrobial applications. These macromolecules consist of hydrophobic segments that provide a suitable environment for antibiotic encapsulation and hydrophilic segments that enable them to self-assemble into nanostructures with distinct properties. In a study by Chen et al., PEG-PCL copolymers were conjugated to vancomycin through pH-cleavable hydrazone bonds (Figure 1. 18).<sup>344</sup> The corresponding nanoparticles were used to encapsulate the antibiotic, ciprofloxacin, which resulted in nanoparticles of approximately 77 nm in diameter. Under acidic conditions (pH 6.0), the nanoparticles increased in size to 91 nm due to removal of hydrophilic vancomycin molecule through hydrazone cleavage. This alteration disrupted the hydrophobic/ hydrophilic balance, which led to the enlargement of the nanoparticles. When incubated with lipase at pH 6.0, PCL degradation also led to disturbed hydrophobic/ hydrophilic balance, which resulted in a collapse of the nanoparticle structure. The nanoparticles exhibited targeting capabilities against *Pseudomonas aeruginosa* (*P. aeruginosa*) attributed to the incorporation of vancomycin that binds to the outer membrane of the bacteria. When these nanoparticles encapsulated ciprofloxacin, differences in drug release were observed. Release studies showed a 9% increase at pH 6.0 compared to pH 7.4, which was further accelerated more than two-folds in the presence of lipase. MICs of ciprofloxacin-loaded nanoparticles tested against *P. aeruginosa* were determined to be 4  $\mu\text{g mL}^{-1}$ , demonstrating continuous inhibition due to the sustained drug release. SEM analyses revealed distorted and corrugated surfaces of *P. aeruginosa*. Importantly, the ciprofloxacin-loaded nanoparticles displayed negligible toxicity to mammalian cells. This study presents a novel

strategy to enhance bacterial interaction of nanoparticles by incorporating vancomycin and facilitating pH/ lipase-triggered antibiotic targeted release.

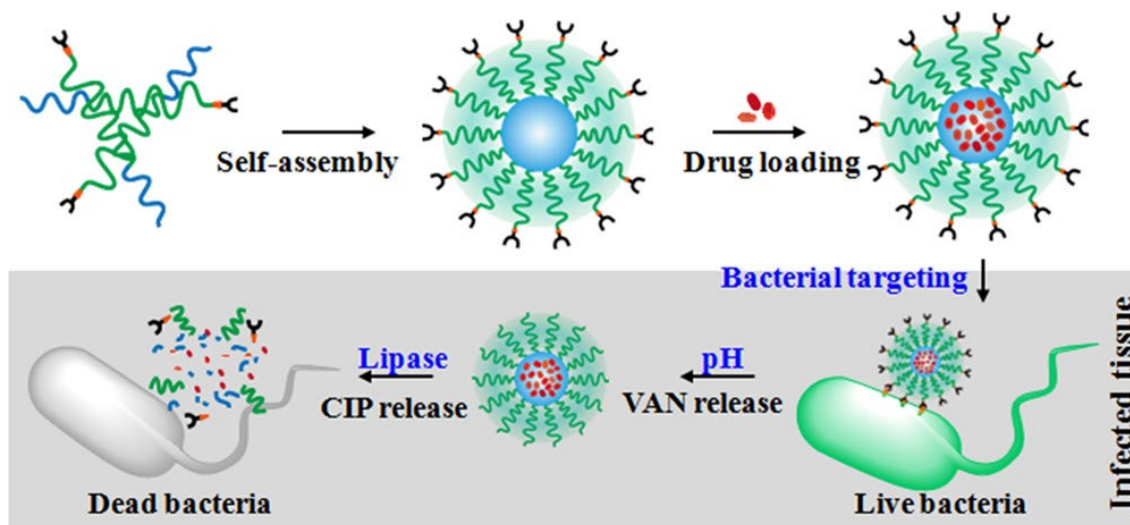


**Figure 1. 18:** Schematic representation of both vancomycin-mediated bacterial targeting and antibiotics release.<sup>344</sup> Reproduced with permission from Chen, M.; Xie, S.; Wei, J.; Song, X.; Ding, Z.; Li, X. Antibacterial Micelles with Vancomycin-Mediated Targeting and pH/Lipase-Triggered Release of Antibiotics. *ACS Appl. Mater. Interfaces* **2018**, *10* (43), 36814-36823. Copyright 2018, American Chemical Society.

Cationic amphiphilic polymers form a good basis for developing nanocarriers with dual functionality, combining antimicrobial properties and applications in drug delivery.<sup>345</sup> These polymers incorporate advantages of both cationic polymers and their self-assembly properties to achieve bifunctional therapy for combating antimicrobial infections. By forming nanostructures with charged hydrophilic shells and hydrophobic core, these polymers provide a suitable environment for drug encapsulation while exerting antimicrobial effects.<sup>346</sup> This unique design allows for the simultaneous delivery of therapeutic agents and antimicrobial action, making these nanoparticles highly promising candidates for combating infections. For example, Hisey et al. reported on PEO-PCL-based nanoparticles functionalized with phosphonium cations on the hydrophilic shell (Figure 1. 19).<sup>345</sup> The nanoparticles exhibited bactericidal activity against both *Staphylococcus aureus* (*S. aureus*) and *E. coli*, especially when compared to the corresponding

phosphonium small molecules or the non-functionalised nanoparticle. It was also shown that the intrinsically antibacterial nanoparticles possess the capability to encapsulate and release the antibiotic, tetracycline. Importantly, the nanoparticles exhibited no hemolysis of red blood cells, demonstrating its ability to selectively target bacterial cells.

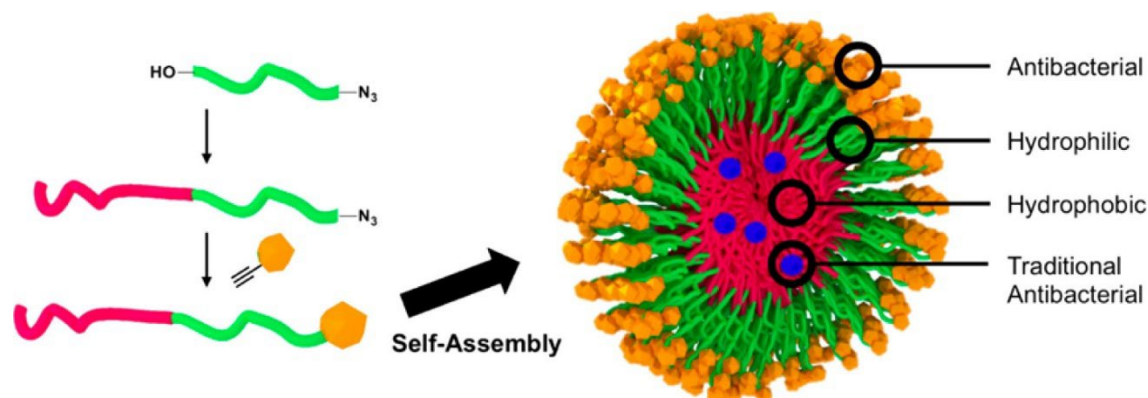


**Figure 1. 19:** Schematic illustrating a potential multimechanistic approach to treat bacterial infections using a phosphonium-functionalized micelle loaded with antibiotic.<sup>345</sup> Reproduced with permission from Hisey, B.; Ragona, P. J.; Gillies, E. R. Phosphonium-Functionalized Polymer Micelles with Intrinsic Antibacterial Activity. *Biomacromolecules* **2017**, *18* (3), 914-923 reference. Copyright 2017, American Chemical Society.

In a recent study, Guo et al. investigated a series of polycationic micelles containing lysine and octanoate/ myristate pendants.<sup>346</sup> These nanoparticles, encapsulated with Nile Red, displayed pH and enzyme-responsiveness, which accelerated release kinetics under acidic conditions (pH 5.5) and in the presence of lipase. Notably, the nanoparticles exhibited significant antibacterial activity against *Bacillus subtilis* (*B. subtilis*) and *E. coli*, as evident by various experiments including the broth microdilution method, SEM imaging, zone of inhibition studies and confocal microscopy experiments of live/ dead cell assay. They observed a remarkable decrease in bacterial growth, with MIC<sub>50</sub> values below 30  $\mu\text{g mL}^{-1}$ . Importantly, the nanoparticles displayed minimal toxicity against erythrocytes and human intestinal epithelial cells, highlighting the potential for safe and effective antimicrobial applications. Evidently, cationic micelles possess great potential in addressing challenges posed by microbial infections. Nevertheless, there remains a notable gap in

the field concerning miktoarm polymer-based antibacterial nanoparticles, which requires further exploration and innovation.

### **1.5. Thermoresponsive Polymeric Nanoparticles**

In addition to designing nanoparticles responsive to endogenous stimuli or engineered with enhanced interactions, there is growing interest in exploring temperature as a stimulus in drug delivery. The integration of stimuli-responsive polymers into temperature-sensitive nanoparticle formulations represents a sophisticated approach to achieve precise control over drug release. These systems capitalize on the inherent responsiveness of nanoparticles to changes in temperature, opening up new possibilities in the realm of drug delivery systems. The ability to fine-tune drug release profiles based on local temperature cues could open up a myriad of possibilities across various medical needs and revolutionize patient care. This innovation holds great potential for achieving personalized and targeted therapeutics, which is explored in Chapter 4.

Thermoresponsive polymers have generated strong interests for numerous applications due to their fast and efficient response to temperature variations. Among them, polymers exhibiting thermoresponsivity in water are of particular interest as they have great potential in biomedical applications such as therapeutic delivery,<sup>347, 348</sup> tissue engineering,<sup>349, 350</sup> wound healing,<sup>351</sup> etc.<sup>352-354</sup> Thermoresponsive polymers undergo phase transitions in response to thermal stimulus, experiencing changes in solubility with temperature. The point at which this phase transition is observed is defined as the critical solution temperature ( $T_C$ ). Depending on the nature of these changes, thermoresponsive polymers can be categorized into two distinct groups: those that exhibit upper critical solution temperature (UCST) behaviors, and those that possess a lower critical solution temperature (LCST, Figure 1. 20). Polymers with UCST properties are insoluble below  $T_C$ , but become increasingly soluble as temperature rises; LCST polymers exhibit the exact opposite behavior, being soluble below  $T_C$  and insoluble above it.

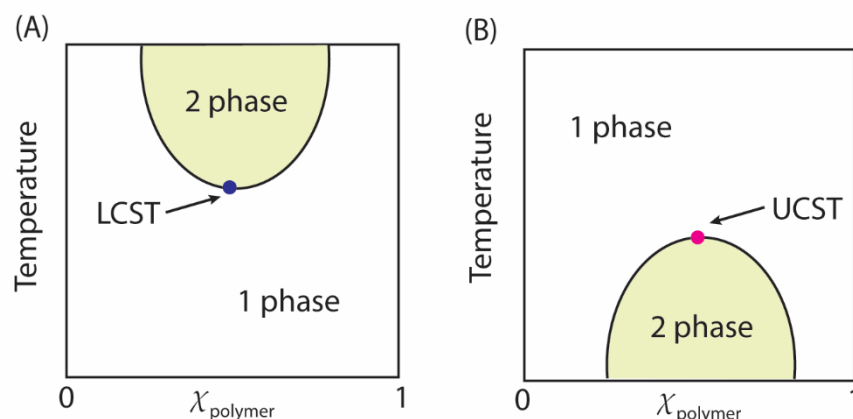


**Figure 1. 20:** Representative phase diagram for polymers exhibiting (A) LCST and (B) UCST behavior. Yellow shaded regions denote biphasic regions, whereas white areas represent one-phase regions.  $\chi_{\text{polymer}}$  indicates polymer fraction.

Thermodynamics form the basis for the phase separation of temperature-responsive polymers, as represented by the Gibbs free energy of mixing ( $\Delta G_{\text{mix}}$ ) in Equation 4; single-phase liquids are observed when  $\Delta G_{\text{mix}}$  is negative, whereas immiscible, phase-separated polymers are obtained when  $\Delta G_{\text{mix}}$  is greater than zero. Therefore, in the case of UCST polymers,  $\Delta G_{\text{mix}}$  tends to be positive at lower temperatures (i.e. two phases) and becomes negative with an increase in temperature (i.e. one phase). LCST polymers exhibit inversed properties:  $\Delta G_{\text{mix}}$  is negative at lower temperatures (i.e. miscible) and positive at higher temperatures (i.e. phase separated).

$$\Delta G_{\text{mix}} = \Delta H_{\text{mix}} - T\Delta S_{\text{mix}} \quad (\text{Equation 4})$$

Inter- and intramolecular interactions play a crucial role in governing  $\Delta G_{\text{mix}}$  and thereby affecting the transition properties of thermoresponsive polymers. For UCST polymers in water, strong polymer-polymer interactions, typically built upon hydrogen bonding (non-ionic) or Coulombic interactions (ionic), allow the macromolecule to achieve a globule-to-coil transition. Below the UCST, strong inter- and intramolecular hydrogen bonding/ Coulombic interactions induces phase separation of the polymers. As these supramolecular interactions weaken with temperature ( $\Delta H_{\text{mix}}$

>0), the polymer becomes soluble in water to give a single, miscible phase. Therefore, the solvation/ desolvation of UCST polymers is also regarded as an enthalpy-driven process. On the contrary, LCST behaviors are entropy-driven. Strong intermolecular interactions between LCST polymers and water tend to dominate at lower temperatures ( $\Delta H_{\text{mix}} < 0$ ) but gradually weaken with heating. The water cages surrounding the repeating units are disrupted and replaced by hydrophobic interactions that induce polymer aggregation. The gain in enthalpy due to hydrogen bond/ Coulombic interaction breaking makes  $\Delta H_{\text{mix}}$  less negative, allowing  $T\Delta S_{\text{mix}}$  to dominate, resulting in demixing of the system. Consequently, these polymers undergo a coil-to-globule transition above their LCSTs.

Previous studies have largely focused on LCST polymers as their thermoresponsivity is more achievable under relevant conditions (0-100 °C), with the most notable example being poly(*N*-isopropyl acrylamide) (PNIPAM) having a LCST of 32 °C.<sup>355-359</sup> In contrast, UCST polymers, have traditionally exhibited phase transitions beyond these relevant conditions or have relied on the presence of organic solvents to demonstrate thermoresponsivity, limiting their biomedical applications.<sup>360, 361</sup> However, extensive research efforts have unveiled a deeper understanding of UCST behavior, leading to the development of UCST polymers that are more readily achievable and tailorable for various applications.<sup>362-365</sup> Poly (*N*-acryloyl glycinamide) (PNAGA) is one of the first non-ionic UCST polymers reported to have transition temperatures within relevant conditions in water. The strong hydrogen bonds between the carbonyl and amine groups facilitate transition from immiscible phases to single-phase, miscible liquids. This characteristic has been utilized across a wide range of applications.<sup>366, 367</sup> In 2016, Hui et al. reported on a PNAGA-based UCST polymer with a phase transition temperature of 47 °C.<sup>368</sup> In their study, the polymer-based drug delivery system showed responsive DOX release upon heat generation by photothermal agents when exposed to near-infrared laser, which was diminished in the absence of laser irradiation. Through the strategic incorporation of PNAGA to control the hydrophobic-to-hydrophilic transition, their system facilitated rapid localized heating and enabled spatiotemporal control over the release of DOX exclusively to cancer cells. In addition to PNAGA-based copolymers, polyacrylamide (PAAm)-based copolymers have garnered attention for their UCST properties. AAm is commonly copolymerized with hydrophobic comonomers such as acrylonitrile (AN) to obtain P(AAm-*co*-AN), thereby achieving UCST behavior in aqueous solutions. In 2017,

Lin et al. reported on a P(AAm-co-AN)-based triblock copolymer for CO<sub>2</sub>-and temperature-controlled Nile Red release.<sup>369</sup> The copolymer, denoted as PEG-*b*-P(AAm-co-AN)-*b*-PDEAEMA, exhibited reversible UCST behaviors that could be regulated by the concentration of CO<sub>2</sub> introduced: higher CO<sub>2</sub> concentrations resulted in lower UCST. The copolymer also self-assembled into vesicles in aqueous solutions. However, upon CO<sub>2</sub> purging, the nanoparticles transitioned from vesicles to micelles, which disassembled when temperatures were raised above the UCST. Through the strategic incorporation of P(AAm-co-AN) and PDEAEMA, their system enabled the controlled release of Nile Red regulated by both CO<sub>2</sub> and temperature. Both PNAGA- and PAAm-based polymers have UCST properties driven by hydrogen bonding. Zwitterionic polymers, like polysulfobetaines, can also exhibit UCST behavior in water driven by strong coulombic interactions. However, zwitterionic polymers are encumbered by their sensitivity to salts.<sup>370</sup> As salts act to screen the charges present on zwitterionic polymers, they significantly impact the inter- and intramolecular interactions, consequently influencing the UCST behavior of the polymer. These fluctuations in thermoresponsivity in the presence of salts pose challenges in maintaining consistent behavior, limiting their suitability for biomedical applications. Nevertheless, there has been a surge in interest and exploration of UCST polymers, particularly non-ionic systems, highlighting their enormous potential as innovative materials.<sup>363, 371-375</sup> Table 1. 6 presents an overview of the latest developments in UCST-based soft polymeric micelles, which have been investigated for their potential in drug delivery applications.

**Table 1. 6:** Recent advancements in UCST-based soft polymeric micelles for cargo delivery.

Polymers <sup>a</sup>	Cargo	Biological Evaluation; cell lines/living organism	Ref
P(NAGA-co-BA)	Doxorubicin	<i>In vitro</i> : HeLa cells	368
PEG- <i>g</i> -P(AAm-co-AN)	Doxorubicin	<i>In vitro</i> : BEL-7402 and LO 2 cells; <i>In vivo</i> : BEL-7402 cells injected female BALB/c mice	376
(PEG <sub>45</sub> - <i>b</i> -P(AAm <sub>223</sub> -co-AN <sub>103</sub> )- <i>b</i> -PDEAEMA <sub>83</sub> )	Nile red	--	369

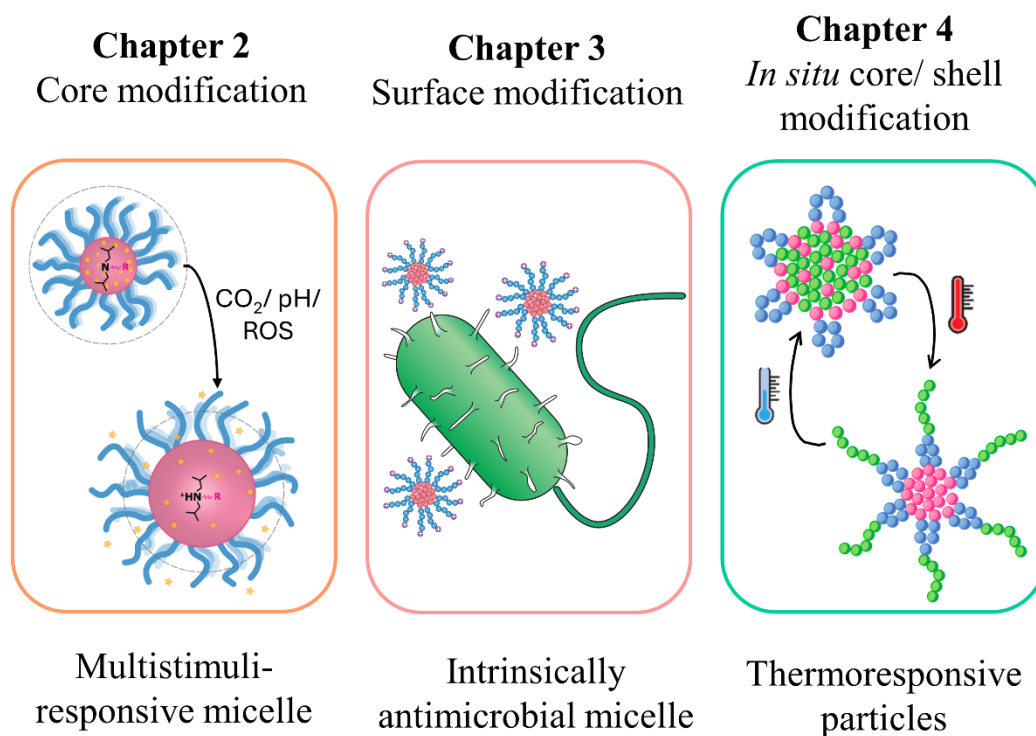
PEG- <i>b</i> -P(NAGA- <i>co</i> -AN)	Doxorubicin, IR780	<i>In vitro</i> : MCF-7 and MCF-7/DOX cells	377
iMAPA-PEG	Doxorubicin	--	378
P(HEMA <sub>205</sub> - <i>g</i> -DOX <sub>25</sub> - <i>co</i> -DMAA <sub>243</sub> )- <i>b</i> -P(AAm <sub>187</sub> - <i>co</i> -AN <sub>103</sub> )	Doxorubicin, camptothecin	<i>In vitro</i> : 4T1 cells; <i>In vivo</i> : 4T1 cells injected female BALB/c mice	379
mPEG- <i>b</i> -P(AAm- <i>co</i> -AN- <i>co</i> -VIm)	Doxorubicin, IR780	<i>In vitro</i> : Erythrocytes and 4T1 cells <i>In vivo</i> : 4T1 cells injected female BALB/c mice	380
P(AAm- <i>co</i> -AN)- <i>b</i> -POEGMA	Doxorubicin	<i>In vitro</i> : OVCAR-3 cells	381
P(AAm- <i>co</i> -AN- <i>co</i> -TPPP)- <i>b</i> -POEGMA	IR780	<i>In vitro</i> : A549 cells <i>In vivo</i> : A459 cells injected female BALB/c mice	382
PEG <sub>114</sub> - <i>b</i> -P(AAm <sub>580</sub> - <i>co</i> -AN <sub>165</sub> )	Cabazitaxel, IR780	<i>In vitro</i> : 4T1 cells <i>In vivo</i> : 4T1 cells injected female BALB/c mice	383
P(HPMA-GA) <sub>50</sub>	BSA, Nile Red	<i>In vitro</i> : DC2.4 cell line <i>In vivo</i> : C57BL/6 10 week old mice	365
PLLSA <sub>31</sub> - <i>g</i> -PSPB <sub>125</sub>	Lysozyme	<i>In vitro</i> : L929 cells	384
PLLSA <sub>31</sub> - <i>g</i> -PSPB <sub>181</sub>			
PCCL <sub>40</sub> - <i>g</i> -MU <sub>25</sub>	5-Fluorouracil	<i>In vitro</i> : L929 cell	385
P(AAm- <i>co</i> -TPEA- <i>co</i> -CAA)	Doxorubicin	<i>In vitro</i> : NIH-3T3 and HeLa cells	386

<sup>a</sup> Subscript in polymer abbreviations denotes the degree of polymerization. Abbreviations used are described here in alphabetical order: iMAPA: insoluble component of multi-L-arginyl-poly-L-aspartate; P(AAm-*co*-AN): poly(acrylamide-*co*-acrylonitrile); P(AAm-*co*-TPEA-*co*-CAA): poly(acrylamide-*co*-(*N*-(2-acrylamidoethyl)-4-(1,2,2-triphenylvinyl)benzamide)-*co*-((2'-acryloylamino-ethylene)-3 $\alpha$ ,7 $\alpha$ ,12 $\alpha$ -trihydroxy-5 $\beta$ -cholanoamide)); PCCL-*g*-MU: poly(6-acetoxy- $\epsilon$ -caprolactone)-*graft*-(6-methyluracil); PDEAEMA: poly(*N,N*-diethylamino ethyl methacrylate); PEG: poly(ethylene glycol); P(HEMA<sub>205</sub>-*g*-DOX-*co*-DMAA<sub>243</sub>): poly((2-hydroxyethyl methacrylate)-*graft*-doxorubicin- (*N,N*-dimethyl-acrylamide));

P(HPMA-GA): poly(*N*-(2-hydroxypropyl)methacrylamide)-glycolamide); PLLSA-*graft*-PSPB: poly(carboxylated-L-lysine)-*graft*-poly(sulfobetaine); P(NAGA-*co*-BA): poly(*N*-acryloylglycinamide-*co*-butyl acrylate); P(NAGA-*co*-AN): poly(*N*-acryloylglycinamide-*co*-acrylonitrile); POEGMA: poly(oligo(ethylene glycol) methyl ether methacrylate); TPPP: tetraphenylporphyrin; VIm: vinylimidazole.

## 1.6. Scope of Thesis and Contribution to Original Knowledge

This thesis showcases nanoparticles with architectures that can be easily tailored for biomedical applications (Scheme 1). By focusing on nanoparticles responsive to various endogenous stimuli, such as CO<sub>2</sub>, pH, ROS, temperature, and enhanced interaction with bacteria, it contributes to the design of smart drug delivery systems with customizable functionalities for specific biomedical purposes. Whether it is imparting multi-stimuli responsivity, intrinsic antimicrobial properties, or temperature-controlled reversible morphological transitions, these nanoparticles demonstrate versatility and flexibility, and hold great potential in addressing a range of therapeutic challenges. The specific contributions to original knowledge are detailed below.



**Scheme 1:** Outline of the thesis.

Traditional approaches to designing multistimuli-responsive nanoparticles often involve incorporating multiple functional groups into polymeric precursors, leading to synthetic complexities and limited responsivity to physiological environments. Nanoparticles that could leverage several endogenous stimuli simultaneously with a single functional group can offer a powerful tool in nanomedicine. Chapter 2 investigates the use of a single functional group, namely tertiary amines, incorporated into the core of our nanoparticles, to obtain nanocarriers that are responsive to multiple stimuli. This work offers a streamlined and efficient synthetic strategy, thereby overcoming the challenges associated with synthetic complexity, a novel contribution absent in current literature. The use of tertiary amines as multifunctional responsive groups enables nanoparticles to respond to various endogenous stimuli, including CO<sub>2</sub>, pH, ROS, as well as the combined effect of CO<sub>2</sub> and ROS. Additionally, the curcumin-loaded nanoparticles have been shown to mitigate drug toxicity while maintaining its therapeutic efficacy. This innovative approach contributes to the development of more efficient and versatile nanocarriers suitable for therapeutic applications.

While amines incorporated in the core offer multi-stimuli responsive nanoparticles, charged amines are known to confer antimicrobial properties. By incorporating these amines onto the nanoparticle shell, Chapter 3 capitalizes on the well-known antimicrobial properties of cationic compounds. The resulting nanosized micelles exhibit intrinsic antimicrobial activities, offering a promising strategy for combating microbial infections without the need for additional antimicrobial agents. We demonstrate the use of miktoarm star polymers to yield antimicrobial micelles, diverging from the predominance of linear systems. Miktoarm polymers are advantageous due to their branching architecture, leading to nanoparticles with higher charge density for enhanced antimicrobial activities. The core-shell structure obtained facilitates encapsulation of therapeutic agents, offering a bifunctional therapeutic approach, serving as both a bacteria inhibitor and a drug carrier to combat AMR through combination therapy. Such an approach has not been widely explored and is, to our knowledge, the first to be demonstrated through miktoarm polymers. This application of miktoarm polymers expands the scope of their potential biomedical applications and highlights their versatility as a platform for the design of multifunctional nanoparticles with enhanced therapeutic properties.

Chapter 4 contributes to the field of nanomedicine by introducing a novel approach to temperature-responsive nanoparticle design using UCST polymers. We investigate the use of temperature to facilitate transitions in nanoparticle morphologies, thereby enhancing the design of smart nanoparticles suitable for biomedical applications. While LCST polymers are extensively used to obtain temperature-responsive polymers for biomedical applications, UCST polymers are seldom explored. By capitalizing the UCST properties of P(AAm-co-AN), in addition to biocompatible PEG and PCL, this work focuses on the use of UCST polymers for achieving temperature-dependent transitions in nanoparticle morphologies. The designed polymer facilitates stable, reversible transformations between in response to temperature changes. These temperature-induced morphological transitions offer a versatile platform for tailoring drug delivery applications, and highlights the importance of structural design in regulating temperature-responsive nanomaterials.

## 1.7. References

1. Choi, Y. K.; Poudel, B. K.; Marasini, N.; Yang, K. Y.; Kim, J. W.; Kim, J. O.; Choi, H.-G.; Yong, C. S. Enhanced Solubility and Oral Bioavailability of Itraconazole by Combining Membrane Emulsification and Spray Drying Technique. *Int. J. Pharm.* **2012**, *434* (1), 264-271.
2. Saleemi, M. A.; Kong, Y. L.; Yong, P. V. C.; Wong, E. H. An Overview of Recent Development in Therapeutic Drug Carrier System Using Carbon Nanotubes. *J. Drug Deliv. Sci. Technol.* **2020**, *59*, 101855.
3. Soliman, G. M.; Sharma, A.; Maysinger, D.; Kakkar, A. Dendrimers and Miktoarm Polymers Based Multivalent Nanocarriers for Efficient and Targeted Drug Delivery. *Chem. Commun.* **2011**, *47* (34), 9572-9587.
4. Caminade, A.-M.; Turrin, C.-O. Dendrimers for Drug Delivery. *J. Mater. Chem. B* **2014**, *2* (26), 4055-4066.
5. Cabral, H.; Miyata, K.; Osada, K.; Kataoka, K. Block Copolymer Micelles in Nanomedicine Applications. *Chem. Rev.* **2018**, *118* (14), 6844-6892.

6. Sercombe, L.; Veerati, T.; Moheimani, F.; Wu, S. Y.; Sood, A. K.; Hua, S. Advances and Challenges of Liposome Assisted Drug Delivery. *Front. Pharmacol.* **2015**, *6*, 286.
7. Probst, C. E.; Zrazhevskiy, P.; Bagalkot, V.; Gao, X. Quantum Dots as a Platform for Nanoparticle Drug Delivery Vehicle Design. *Adv. Drug Del. Rev.* **2013**, *65* (5), 703-718.
8. Molaei, M. J. Carbon Quantum Dots and Their Biomedical and Therapeutic Applications: A Review. *RSC Adv.* **2019**, *9* (12), 6460-6481.
9. Palanisamy, S.; Wang, Y.-M. Superparamagnetic Iron Oxide Nanoparticulate System: Synthesis, Targeting, Drug Delivery and Therapy in Cancer. *Dalton Trans.* **2019**, *48* (26), 9490-9515.
10. Argyo, C.; Weiss, V.; Bräuchle, C.; Bein, T. Multifunctional Mesoporous Silica Nanoparticles as a Universal Platform for Drug Delivery. *Chem. Mater.* **2014**, *26* (1), 435-451.
11. Hassan, S.; Prakash, G.; Bal Ozturk, A.; Saghazadeh, S.; Farhan Sohail, M.; Seo, J.; Remzi Dokmeci, M.; Zhang, Y. S.; Khademhosseini, A. Evolution and Clinical Translation of Drug Delivery Nanomaterials. *Nano Today* **2017**, *15*, 91-106.
12. Maeda, H.; Tsukigawa, K.; Fang, J. A Retrospective 30 years after Discovery of the Enhanced Permeability and Retention Effect of Solid Tumors: Next-Generation Chemotherapeutics and Photodynamic Therapy—Problems, Solutions, and Prospects. *Microcirculation* **2016**, *23* (3), 173-182.
13. Dai, Y.; Chen, X.; Zhang, X. Recent Advances in Stimuli-Responsive Polymeric Micelles via Click Chemistry. *Polym. Chem.* **2019**, *10* (1), 34-44.
14. Mai, Y.; Eisenberg, A. Self-Assembly of Block Copolymers. *Chem. Soc. Rev.* **2012**, *41* (18), 5969-5985.
15. Kulthe, S. S.; Choudhari, Y. M.; Inamdar, N. N.; Mourya, V. Polymeric Micelles: Authoritative Aspects for Drug Delivery. *Des. Monomers Polym.* **2012**, *15* (5), 465-521.

16. Morton, M.; Helminiak, T. E.; Gadkary, S. D.; Bueche, F. Preparation and Properties of Monodisperse Branched Polystyrene. *J. Polym. Sci.* **1962**, *57* (165), 471-482.
17. Zelinski, R. P.; Wofford, C. F. Synthesis of Trichain and Tetrachain Radial Polybutadienes. *J. Polym. Sci., Part A: Gen. Pap.* **1965**, *3* (1), 93-103.
18. Guo, X.; Choi, B.; Feng, A.; Thang, S. H. Polymer Synthesis with More Than One Form of Living Polymerization Method. *Macromol. Rapid Commun.* **2018**, *39* (20), 1800479.
19. Michalski, A.; Brzezinski, M.; Lapienis, G.; Biela, T. Star-Shaped and Branched Polylactides: Synthesis, Characterization, and Properties. *Prog. Polym. Sci.* **2019**, *89*, 159-212.
20. Zhao, Y. Facile Synthesis and Topological Transformation of Multicomponent Miktoarm Star Copolymers. *Macromol. Rapid Commun.* **2019**, *40* (6), 1800571.
21. Gao, Y.; Zhou, D.; Lyu, J.; A, S.; Xu, Q.; Newland, B.; Matyjaszewski, K.; Tai, H.; Wang, W. Complex Polymer Architectures through Free-Radical Polymerization of Multivinyl Monomers. *Nat. Rev. Chem.* **2020**, *4* (4), 194-212.
22. Oliveira, A. S. R.; Mendonça, P. V.; Simões, S.; Serra, A. C.; Coelho, J. F. J. Amphiphilic Well-Defined Degradable Star Block Copolymers by Combination of Ring-Opening Polymerization and Atom Transfer Radical Polymerization: Synthesis and Application as Drug Delivery Carriers. *J. Polym. Sci.* **2021**, *59* (3), 211-229.
23. Hadjichristidis, N. Synthesis of Miktoarm Star ( $\mu$ -Star) Polymers. *J. Polym. Sci., Part A: Polym. Chem.* **1999**, *37* (7), 857-871.
24. Kadam, P. G.; Mhaske, S. Synthesis of Star-Shaped Polymers. *Des. Monomers Polym.* **2011**, *14* (6), 515-540.
25. Matyjaszewski, K. Advanced Materials by Atom Transfer Radical Polymerization. *Adv. Mater.* **2018**, *30* (23), 1706441.

26. Xu, F.-J. Versatile Types of Hydroxyl-Rich Polycationic Systems via O-Heterocyclic Ring-Opening Reactions: From Strategic Design to Nucleic Acid Delivery Applications. *Prog. Polym. Sci.* **2018**, *78*, 56-91.
27. Sims, M. B. Controlled Radical Copolymerization of Multivinyl Crosslinkers: A Robust Route to Functional Branched Macromolecules. *Polym. Int.* **2021**, *70* (1), 14-23.
28. Fan, X.; Win, K. Y.; Hu, Z.; Loh, X. J.; Li, Z. Precise Synthesis of PS-PLA Janus Star-Like Copolymer. *Macromol. Rapid Commun.* **2019**, *40* (5), 1800217.
29. Harn, Y.-W.; He, Y.; Wang, Z.; Chen, Y.; Liang, S.; Li, Z.; Li, Q.; Zhu, L.; Lin, Z. Synthesis of Amphiphilic and Double Hydrophilic Star-Like Block Copolymers and the Dual pH-Responsiveness of Unimolecular Micelle. *Macromolecules* **2020**, *53* (19), 8286-8295.
30. Doganci, M. D.; Caner, D.; Doganci, E.; Ozkoc, G. Effects of Hetero-Armed Star-Shaped PCL-PLA Polymers with Poss Core on Thermal, Mechanical, and Morphological Properties of PLA. *J. Appl. Polym. Sci.* **2021**, *138* (29), 50712.
31. Nabid, M. R.; Tabatabaei Rezaei, S. J.; Sedghi, R.; Niknejad, H.; Entezami, A. A.; Oskooie, H. A.; Heravi, M. M. Self-Assembled Micelles of Well-Defined Pentaerythritol-Centered Amphiphilic A<sub>4</sub>B<sub>8</sub> Star-Block Copolymers Based on PCL and PEG for Hydrophobic Drug Delivery. *Polymer* **2011**, *52* (13), 2799-2809.
32. Kinsey, T.; Mapesa, E. U.; Wang, W.; Hong, K.; Mays, J.; Kilbey, S. M.; Sangoro, J. Impact of Molecular Architecture on Dynamics of Mikroarm Star Copolymers. *Macromolecules* **2018**, *51* (14), 5401-5408.
33. Holler, S.; Moreno, A. J.; Zamponi, M.; Bačová, P.; Willner, L.; Iatrou, H.; Falus, P.; Richter, D. The Role of the Functionality in the Branch Point Motion in Symmetric Star Polymers: A Combined Study by Simulations and Neutron Spin Echo Spectroscopy. *Macromolecules* **2018**, *51* (1), 242-253.

34. Liu, L.; den Otter, W. K.; Briels, W. J. Coarse-Grained Simulations of Three-Armed Star Polymer Melts and Comparison with Linear Chains. *J. Phys. Chem. B* **2018**, *122* (44), 10210-10218.
35. Gury, L.; Gauthier, M.; Cloitre, M.; Vlassopoulos, D. Colloidal Jamming in Multiarm Star Polymer Melts. *Macromolecules* **2019**, *52* (12), 4617-4623.
36. Kida, T.; Tanaka, R.; Nitta, K.-h.; Shiono, T. Effect of the Number of Arms on the Mechanical Properties of a Star-Shaped Cyclic Olefin Copolymer. *Polym. Chem.* **2019**, *10* (41), 5578-5583.
37. von Tiedemann, P.; Yan, J.; Barent, R. D.; Spontak, R. J.; Floudas, G.; Frey, H.; Register, R. A. Tapered Multiblock Star Copolymers: Synthesis, Selective Hydrogenation, and Properties. *Macromolecules* **2020**, *53* (11), 4422-4434.
38. Ren, J. M.; McKenzie, T. G.; Fu, Q.; Wong, E. H. H.; Xu, J.; An, Z.; Shanmugam, S.; Davis, T. P.; Boyer, C.; Qiao, G. G. Star Polymers. *Chem. Rev.* **2016**, *116* (12), 6743-6836.
39. Burns, A. B.; Register, R. A. Mechanical Properties of Star Block Polymer Thermoplastic Elastomers with Glassy and Crystalline End Blocks. *Macromolecules* **2016**, *49* (24), 9521-9530.
40. Lee, D.; Jung, H. Y.; Park, M. J. Solid-State Polymer Electrolytes Based on AB<sub>3</sub>-Type Miktoarm Star Copolymers. *ACS Mater. Lett.* **2018**, *7* (8), 1046-1050.
41. Xu, W.; Ledin, P. A.; Shevchenko, V. V.; Tsukruk, V. V. Architecture, Assembly, and Emerging Applications of Branched Functional Polyelectrolytes and Poly(Ionic Liquid)s. *ACS Appl. Mater. Interfaces* **2015**, *7* (23), 12570-12596.
42. Ida, S.; Toda, S.; Oyama, M.; Takeshita, H.; Kanaoka, S. Multiarm Star-Crosslinked Hydrogel: Polymer Network with Thermoresponsive Free-End Chains Densely Connected to Crosslinking Points. *Macromol. Rapid Commun.* **2020**, *42* (8), 2000558.

43. Hung, C.-C.; Nakahira, S.; Chiu, Y.-C.; Isono, T.; Wu, H.-C.; Watanabe, K.; Chiang, Y.-C.; Takashima, S.; Borsali, R.; Tung, S.-H.; et al. Control over Molecular Architectures of Carbohydrate-Based Block Copolymers for Stretchable Electrical Memory Devices. *Macromolecules* **2018**, *51* (13), 4966-4975.
44. Hwang, H.; Park, S. Y.; Kim, J. K.; Kim, Y. M.; Moon, H. C. Star-Shaped Block Copolymers: Effective Polymer Gelators of High-Performance Gel Electrolytes for Electrochemical Devices. *ACS Appl. Mater. Interfaces* **2019**, *11* (4), 4399-4407.
45. Yang, D.-P.; Oo, M. N. N. L.; Deen, G. R.; Li, Z.; Loh, X. J. Nano-Star-Shaped Polymers for Drug Delivery Applications. *Macromol. Rapid Commun.* **2017**, *38* (21), 1700410.
46. Holm, R.; Douverne, M.; Weber, B.; Bauer, T.; Best, A.; Ahlers, P.; Koynov, K.; Besenius, P.; Barz, M. Impact of Branching on the Solution Behavior and Serum Stability of Starlike Block Copolymers. *Biomacromolecules* **2019**, *20* (1), 375-388.
47. Pispas, S.; Hadjichristidis, N.; Potemkin, I.; Khokhlov, A. Effect of Architecture on the Micellization Properties of Block Copolymers: A<sub>2</sub>B Miktoarm Stars vs AB Diblocks. *Macromolecules* **2000**, *33* (5), 1741-1746.
48. Xu, J.; Ge, Z.; Zhu, Z.; Luo, S.; Liu, H.; Liu, S. Synthesis and Micellization Properties of Double Hydrophilic A<sub>2</sub>BA<sub>2</sub> and A<sub>4</sub>BA<sub>4</sub> Non-Linear Block Copolymers. *Macromolecules* **2006**, *39* (23), 8178-8185.
49. Wu, W.; Wang, W.; Li, J. Star Polymers: Advances in Biomedical Applications. *Prog. Polym. Sci.* **2015**, *46*, 55-85.
50. Tungala, K.; Adhikary, P.; Azmeera, V.; Kumar, K.; Ramesh, K.; Krishnamoorthi, S. Dendrimer Like Star Polymer Based on  $\beta$ -Cyclodextrin with ABC Type Miktoarms. *RSC Adv.* **2016**, *6* (47), 41594-41607.
51. Amirova, A.; Rodchenko, S.; Milenin, S.; Tatarinova, E.; Kurlykin, M.; Tenkovtsev, A.; Filippov, A. Influence of a Hydrophobic Core on Thermoresponsive Behavior of Dendrimer-

- Based Star-Shaped Poly(2-isopropyl-2-oxazoline) in Aqueous Solutions. *J. Polym. Res.* **2017**, *24* (8), 124.
52. Etrych, T.; Daumová, L.; Pokorná, E.; Tušková, D.; Lidický, O.; Kolářová, V.; Pankrác, J.; Šefc, L.; Chytil, P.; Klener, P. Effective Doxorubicin-Based Nano-Therapeutics for Simultaneous Malignant Lymphoma Treatment and Lymphoma Growth Imaging. *J. Controlled Release* **2018**, *289*, 44-55.
53. Kosakowska, K. A.; Casey, B. K.; Kurtz, S. L.; Lawson, L. B.; Grayson, S. M. Evaluation of Amphiphilic Star/Linear–Dendritic Polymer Reverse Micelles for Transdermal Drug Delivery: Directing Carrier Properties by Tailoring Core Versus Peripheral Branching. *Biomacromolecules* **2018**, *19* (8), 3163-3176.
54. Francica, J. R.; Laga, R.; Lynn, G. M.; Mužíková, G.; Androvič, L.; Aussedat, B.; Walkowicz, W. E.; Padhan, K.; Ramirez-Valdez, R. A.; Parks, R.; et al. Star Nanoparticles Delivering HIV-1 Peptide Minimal Immunogens Elicit Near-Native Envelope Antibody Responses in Nonhuman Primates. *PLoS Biol.* **2019**, *17* (6), e3000328.
55. England, R. M.; Moss, J. I.; Gunnarsson, A.; Parker, J. S.; Ashford, M. B. Synthesis and Characterization of Dendrimer-Based Polysarcosine Star Polymers: Well-Defined, Versatile Platforms Designed for Drug-Delivery Applications. *Biomacromolecules* **2020**, *21* (8), 3332-3341.
56. Kostka, L.; Kotrchová, L.; Šubr, V.; Libánská, A.; Ferreira, C. A.; Malátová, I.; Lee, H. J.; Barnhart, T. E.; Engle, J. W.; Cai, W.; et al. HPMa-Based Star Polymer Biomaterials with Tuneable Structure and Biodegradability Tailored for Advanced Drug Delivery to Solid Tumours. *Biomaterials* **2020**, *235*, 119728.
57. Akira, H.; Ishizone, T. Dendrimer-Like Star Branched Polymers. In *Encyclopedia of Polymeric Nanomaterials*, Kobayashi, S., Müllen, K. Eds.; Springer Berlin Heidelberg, 2015; pp 525-534.

58. Wong, J. C.; Xiang, L.; Ngoi, K. H.; Chia, C. H.; Jin, K. S.; Hirao, A.; Ree, M. Seventeen-Armed Star Polystyrenes in Various Molecular Weights: Structural Details and Chain Characteristics. *Polymers* **2020**, *12* (9), 1894.
59. Lin, Y.; Sakaguchi, T.; Hashimoto, T. Extremely High Gas Permeability of Naphthyl Group-Containing Diarylacetylene Copolymers. *Polymer* **2021**, *212*, 123305.
60. Hirao, A.; Hayashi, M.; Loykulnant, S.; Sugiyama, K.; Ryu, S. W.; Haraguchi, N.; Matsuo, A.; Higashihara, T. Precise Syntheses of Chain-Multi-Functionalized Polymers, Star-Branched Polymers, Star-Linear Block Polymers, Densely Branched Polymers, and Dendritic Branched Polymers Based on Iterative Approach Using Functionalized 1,1-Diphenylethylene Derivatives. *Prog. Polym. Sci.* **2005**, *30* (2), 111-182.
61. Taton, D.; Feng, X.; Gnanou, Y. Dendrimer-Like Polymers: A New Class of Structurally Precise Dendrimers with Macromolecular Generations. *New J. Chem.* **2007**, *31* (7), 1097-1110.
62. Hutchings, L. R. Dendrimacs and Hypermacs – Emerging as More Than Just Model Branched Polymers. *Soft Matter* **2008**, *4* (11), 2150-2159.
63. Higashihara, T.; Sugiyama, K.; Yoo, H.-S.; Hayashi, M.; Hirao, A. Combining Living Anionic Polymerization with Branching Reactions in an Iterative Fashion to Design Branched Polymers. *Macromol. Rapid Commun.* **2010**, *31* (12), 1031-1059.
64. Hirao, A.; Yoo, H.-S. Dendrimer-Like Star-Branched Polymers: Novel Structurally Well-Defined Hyperbranched Polymers. *Polym. J.* **2011**, *43* (1), 2-17.
65. Caminade, A.-M.; Yan, D.; Smith, D. K. Dendrimers and Hyperbranched Polymers. *Chem. Soc. Rev.* **2015**, *44* (12), 3870-3873.
66. Pedziwiatr-Werbicka, E.; Milowska, K.; Dzmirutuk, V.; Ionov, M.; Shcharbin, D.; Bryszewska, M. Dendrimers and Hyperbranched Structures for Biomedical Applications. *Eur. Polym. J.* **2019**, *119*, 61-73.

67. Jafari, M.; Abolmaali, S. S.; Najafi, H.; Tamaddon, A. M. Hyperbranched Polyglycerol Nanostructures for Anti-Biofouling, Multifunctional Drug Delivery, Bioimaging and Theranostic Applications. *Int. J. Pharm.* **2020**, *576*, 118959.
68. Kavand, A.; Anton, N.; Vandamme, T.; Serra, C. A.; Chan-Seng, D. Synthesis and Functionalization of Hyperbranched Polymers for Targeted Drug Delivery. *J. Controlled Release* **2020**, *321*, 285-311.
69. Wang, X.; Gao, H. Recent Progress on Hyperbranched Polymers Synthesized via Radical-Based Self-Condensing Vinyl Polymerization. *Polymers* **2017**, *9* (6), 188.
70. Wang, X.; Graff, R. W.; Shi, Y.; Gao, H. One-Pot Synthesis of Hyperstar Polymers via Sequential ATRP of Inimers and Functional Monomers in Aqueous Dispersed Media. *Polym. Chem.* **2015**, *6* (37), 6739-6745.
71. Alfurhood, J. A.; Bachler, P. R.; Sumerlin, B. S. Hyperbranched Polymers via RAFT Self-Condensing Vinyl Polymerization. *Polym. Chem.* **2016**, *7* (20), 3361-3369.
72. Sudo, Y.; Kawai, R.; Nabae, Y.; Hayakawa, T.; Kakimoto, M.-a. Self-Condensing Vinyl Polymerization of a Switchable Chain Transfer Monomer for Facile Synthesis of Star-Shaped Block Copolymers. *Appl. Surf. Sci.* **2019**, *474*, 187-193.
73. Cuneo, T.; Gao, H. Recent Advances on Synthesis and Biomaterials Applications of Hyperbranched Polymers. *Wiley Interdiscip. Rev.: Nanomed. Nanobiotechnol.* **2020**, *12* (6), e1640.
74. Miller, T.; van Colen, G.; Sander, B.; Golas, M. M.; Uezguen, S.; Weigandt, M.; Goepferich, A. Drug Loading of Polymeric Micelles. *Pharm. Res.* **2013**, *30* (2), 584-595.
75. Ding, X.; Han, N.; Wang, J.; Sun, Y.; Ruan, G. Effects of Organic Solvents on the Structures of Micellar Nanocrystals. *RSC Adv.* **2017**, *7* (26), 16131-16138.

76. Khanna, K.; Varshney, S.; Kakkar, A. Designing Miktoarm Polymers Using a Combination of “Click” Reactions in Sequence with Ring-Opening Polymerization. *Macromolecules* **2010**, *43* (13), 5688-5698.
77. Karayianni, M.; Pispas, S. Self-Assembly of Amphiphilic Block Copolymers in Selective Solvents. In *Fluorescence Studies of Polymer Containing Systems*, Procházka, K. Ed.; Springer International Publishing, 2016; pp 27-63.
78. Honda, S.; Yamamoto, T.; Tezuka, Y. Tuneable Enhancement of the Salt and Thermal Stability of Polymeric Micelles by Cyclized Amphiphiles. *Nat. Commun.* **2013**, *4* (1), 1574.
79. Rezaei, S. J. T.; Nabid, M. R.; Niknejad, H.; Entezami, A. A. Folate-Decorated Thermoresponsive Micelles Based on Star-Shaped Amphiphilic Block Copolymers for Efficient Intracellular Release of Anticancer Drugs. *Int. J. Pharm.* **2012**, *437* (1), 70-79.
80. Moquin, A.; Sharma, A.; Cui, Y.; Lau, A.; Maysinger, D.; Kakkar, A. Asymmetric AB<sub>3</sub> Miktoarm Star Polymers: Synthesis, Self-Assembly, and Study of Micelle Stability Using AF<sub>4</sub> for Efficient Drug Delivery. *Macromol. Biosci.* **2015**, *15* (12), 1744-1754.
81. Ai, X.; Zhong, L.; Niu, H.; He, Z. Thin-Film Hydration Preparation Method and Stability Test of DOX-Loaded Disulfide-Linked Polyethylene Glycol 5000-Lysine-Di-Tocopherol Succinate Nanomicelles. *Asian J. Pharm. Sci.* **2014**, *9* (5), 244-250.
82. Zhang, X.; Xiao, Y.; Lang, M. Synthesis and Degradation Behavior of Miktoarm Poly( $\epsilon$ -Caprolactone)<sub>2</sub>-*b*-Poly(L-Lactone)<sub>2</sub> Microspheres. *Polym. J.* **2013**, *45* (4), 420-426.
83. Yang, W.; Yu, C.; Wu, C.; Yao, S. Q.; Wu, S. Cell-Penetrating Poly(disulfide)-Based Star Polymers for Simultaneous Intracellular Delivery of miRNAs and Small Molecule Drugs. *Polym. Chem.* **2017**, *8* (27), 4043-4051.
84. Abdelwahed, W.; Degobert, G.; Stainmesse, S.; Fessi, H. Freeze-Drying of Nanoparticles: Formulation, Process and Storage Considerations. *Adv. Drug Del. Rev.* **2006**, *58* (15), 1688-1713.

85. Rizvi, S. A. A.; Saleh, A. M. Applications of Nanoparticle Systems in Drug Delivery Technology. *Saudi Pharm. J.* **2018**, *26* (1), 64-70.
86. Ohya, Y. Polymeric Micelles Stabilized by Electrostatic Interactions for Drug Delivery. In *Tailored Polymer Architectures for Pharmaceutical and Biomedical Applications*, Acs Symposium Series, Vol. 1135; American Chemical Society, 2013; pp 87-101.
87. Soleymani Abyaneh, H.; Vakili, M. R.; Zhang, F.; Choi, P.; Lavasanifar, A. Rational Design of Block Copolymer Micelles to Control Burst Drug Release at a Nanoscale Dimension. *Acta Biomater.* **2015**, *24*, 127-139.
88. Stetefeld, J.; McKenna, S. A.; Patel, T. R. Dynamic Light Scattering: A Practical Guide and Applications in Biomedical Sciences. *Biophys. Rev.* **2016**, *8* (4), 409-427.
89. Wang, M.; Zhang, X.; Peng, H.; Zhang, M.; Zhang, X.; Liu, Z.; Ma, L.; Wei, H. Optimization of Amphiphilic Miktoarm Star Copolymers for Anticancer Drug Delivery. *ACS Biomater. Sci. Eng.* **2018**, *4* (8), 2903-2910.
90. Wang, Y.; Wu, Z.; Ma, Z.; Tu, X.; Zhao, S.; Wang, B.; Ma, L.; Wei, H. Promotion of Micelle Stability via a Cyclic Hydrophilic Moiety. *Polym. Chem.* **2018**, *9* (19), 2569-2573.
91. Lu, Y.; Yue, Z.; Xie, J.; Wang, W.; Zhu, H.; Zhang, E.; Cao, Z. Micelles with Ultralow Critical Micelle Concentration as Carriers for Drug Delivery. *Nat. Biomed. Eng.* **2018**, *2* (5), 318-325.
92. Chakraborty, T.; Chakraborty, I.; Ghosh, S. The Methods of Determination of Critical Micellar Concentrations of the Amphiphilic Systems in Aqueous Medium. *Arabian J. Chem.* **2011**, *4* (3), 265-270.
93. Topel, Ö.; Çakır, B. A.; Budama, L.; Hoda, N. Determination of Critical Micelle Concentration of Polybutadiene-*block*-Poly(ethyleneoxide) Diblock Copolymer by Fluorescence Spectroscopy and Dynamic Light Scattering. *J. Mol. Liq.* **2013**, *177*, 40-43.

94. Wang, M.; Long, J.; Zhang, S.; Liu, F.; Zhang, X.; Zhang, X.; Sun, L.; Ma, L.; Yu, C.; Wei, H. Folate-Targeted Anticancer Drug Delivery via a Combination Strategy of a Micelle Complex and Reducible Conjugation. *ACS Biomater. Sci. Eng.* **2020**, *6* (3), 1565-1572.
95. Fluksman, A.; Benny, O. A Robust Method for Critical Micelle Concentration Determination Using Coumarin-6 as a Fluorescent Probe. *Anal. Methods* **2019**, *11* (30), 3810-3818.
96. Blasco, E.; Schmidt, B. V. K. J.; Barner-Kowollik, C.; Piñol, M.; Oriol, L. Dual Thermo- and Photo-Responsive Micelles Based on Miktoarm Star Polymers. *Polym. Chem.* **2013**, *4* (16), 4506-4514.
97. Mondal, S.; Ghosh, S. Role of Curcumin on the Determination of the Critical Micellar Concentration by Absorbance, Fluorescence and Fluorescence Anisotropy Techniques. *J. Photochem. Photobiol. B: Biol.* **2012**, *115*, 9-15.
98. Basu Ray, G.; Chakraborty, I.; Moulik, S. P. Pyrene Absorption Can Be a Convenient Method for Probing Critical Micellar Concentration (CMC) and Indexing Micellar Polarity. *J. Colloid Interface Sci.* **2006**, *294* (1), 248-254.
99. Bagheri, A.; Jafari-Chashmi, P. Study of Aggregation Behavior between N-Lauryl Sarcosine Sodium and Dodecyltrimethylammonium Bromide in Aqueous Solution, Using Conductometric and Spectrophotometric Techniques. *J. Mol. Liq.* **2019**, *282*, 466-473.
100. Scholz, N.; Behnke, T.; Resch-Genger, U. Determination of the Critical Micelle Concentration of Neutral and Ionic Surfactants with Fluorometry, Conductometry, and Surface Tension—a Method Comparison. *J. Fluoresc.* **2018**, *28* (1), 465-476.
101. Wu, S.; Liang, F.; Hu, D.; Li, H.; Yang, W.; Zhu, Q. Determining the Critical Micelle Concentration of Surfactants by a Simple and Fast Titration Method. *Anal. Chem.* **2020**, *92* (6), 4259-4265.

102. Cruz Barrios, E.; Annunziata, O. Determination of Critical Micelle Concentration from the Diffusion-Driven Dilution of Micellar Aqueous Mixtures. *Langmuir* **2021**, *37* (8), 2855-2862.
103. Saravanakumar, G.; Park, H.; Kim, J.; Park, D.; Pramanick, S.; Kim, D. H.; Kim, W. J. Miktoarm Amphiphilic Block Copolymer with Singlet Oxygen-Labile Stereospecific  $\beta$ -Aminoacrylate Junction: Synthesis, Self-Assembly, and Photodynamically Triggered Drug Release. *Biomacromolecules* **2018**, *19* (6), 2202-2213.
104. Ma, G.; Zhang, C.; Zhang, L.; Sun, H.; Song, C.; Wang, C.; Kong, D. Doxorubicin-Loaded Micelles Based on Multiarm Star-Shaped PLGA-PEG Block Copolymers: Influence of Arm Numbers on Drug Delivery. *J. Mater. Sci.: Mater. Med.* **2015**, *27* (1), 17.
105. Soliman, G. M.; Sharma, R.; Choi, A. O.; Varshney, S. K.; Winnik, F. M.; Kakkar, A. K.; Maysinger, D. Tailoring the Efficacy of Nimodipine Drug Delivery Using Nanocarriers Based on A<sub>2</sub>B Miktoarm Star Polymers. *Biomaterials* **2010**, *31* (32), 8382-8392.
106. Zhu, M.-m.; Song, F.; Nie, W.-c.; Wang, X.-l.; Wang, Y.-z. A Facile Chemoenzymatic Synthesis of Amphiphilic Miktoarm Star Copolymers from a Sugar Core and Their Potential for Anticancer Drug Delivery. *Polymer* **2016**, *93*, 159-166.
107. Lo, Y.-L.; Chen, G.-J.; Feng, T.-H.; Li, M.-H.; Wang, L.-F. Synthesis and Characterization of S-PCL-PDMAEMA for Co-Delivery of pDNA and DOX. *RSC Adv.* **2014**, *4* (22), 11089-11098.
108. Xu, J.-W.; Xu, F.; Luo, Y.-L. Core Crosslinked H-Type Poly(methacrylic acid)-*block*-Hydroxyl Terminated Polybutadiene-*block*-Poly(methacrylic acid) Four-Armed Star Block Copolymer Micelles for Intercellular Drug Release. *J. Bioact. Compat. Polym.* **2015**, *30* (4), 349-365.
109. Li, L.-Y.; He, W.-D.; Li, J.; Zhang, B.-Y.; Pan, T.-T.; Sun, X.-L.; Ding, Z.-L. Shell-Cross-Linked Micelles from PNIPAM-*b*-(PLL)<sub>2</sub> Y-Shaped Miktoarm Star Copolymer as Drug Carriers. *Biomacromolecules* **2010**, *11* (7), 1882-1890.

110. Nederberg, F.; Appel, E.; Tan, J. P. K.; Kim, S. H.; Fukushima, K.; Sly, J.; Miller, R. D.; Waymouth, R. M.; Yang, Y. Y.; Hedrick, J. L. Simple Approach to Stabilized Micelles Employing Miktoarm Terpolymers and Stereocomplexes with Application in Paclitaxel Delivery. *Biomacromolecules* **2009**, *10* (6), 1460-1468.
111. Soliman, G. M.; Sharma, A.; Cui, Y.; Sharma, R.; Kakkar, A.; Maysinger, D. Miktoarm Star Micelles Containing Curcumin Reduce Cell Viability of Sensitized Glioblastoma. *J. Nanomed. Biother. Discovery* **2014**, *4* (2), 1000124.
112. Gou, P.-F.; Zhu, W.-P.; Shen, Z.-Q. Synthesis, Self-Assembly, and Drug-Loading Capacity of Well-Defined Cyclodextrin-Centered Drug-Conjugated Amphiphilic A<sub>14</sub>B<sub>7</sub> Miktoarm Star Copolymers Based on Poly( $\epsilon$ -caprolactone) and Poly(ethylene glycol). *Biomacromolecules* **2010**, *11* (4), 934-943.
113. Yang, Q.; Li, L.; Sun, W.; Zhou, Z.; Huang, Y. Dual Stimuli-Responsive Hybrid Polymeric Nanoparticles Self-Assembled from POSS-Based Starlike Copolymer-Drug Conjugates for Efficient Intracellular Delivery of Hydrophobic Drugs. *ACS Appl. Mater. Interfaces* **2016**, *8* (21), 13251-13261.
114. Sharma, A.; Soliman, G. M.; Al-Hajaj, N.; Sharma, R.; Maysinger, D.; Kakkar, A. Design and Evaluation of Multifunctional Nanocarriers for Selective Delivery of Coenzyme Q10 to Mitochondria. *Biomacromolecules* **2012**, *13* (1), 239-252.
115. Chong, Y. K.; Zainol, I.; Ng, C. H.; Ooi, I. H. Miktoarm Star Polymers Nanocarrier: Synthesis, Characterisation, and In-Vitro Drug Release Study. *J. Polym. Res.* **2019**, *26* (3), 79.
116. Knop, K.; Hoogenboom, R.; Fischer, D.; Schubert, U. S. Poly(ethylene glycol) in Drug Delivery: Pros and Cons as Well as Potential Alternatives. *Angew. Chem. Int. Ed.* **2010**, *49* (36), 6288-6308.

117. Heyes, C. D.; Groll, J.; Möller, M.; Nienhaus, G. U. Synthesis, Patterning and Applications of Star-Shaped Poly(ethylene glycol) Biofunctionalized Surfaces. *Mol. BioSyst.* **2007**, *3* (6), 419-430.
118. Su, Y.; Liu, M.; Xiong, Y.; Ding, J.; Liu, X.; Song, Y.; Deng, Y. Effects of Stability of PEGylated Micelles on the Accelerated Blood Clearance Phenomenon. *Drug Delivery Transl. Res.* **2019**, *9* (1), 66-75.
119. Birke, A.; Ling, J.; Barz, M. Polysarcosine-Containing Copolymers: Synthesis, Characterization, Self-Assembly, and Applications. *Prog. Polym. Sci.* **2018**, *81*, 163-208.
120. Hu, Y.; Hou, Y.; Wang, H.; Lu, H. Polysarcosine as an Alternative to PEG for Therapeutic Protein Conjugation. *Bioconj. Chem.* **2018**, *29* (7), 2232-2238.
121. Weber, B.; Birke, A.; Fischer, K.; Schmidt, M.; Barz, M. Solution Properties of Polysarcosine: From Absolute and Relative Molar Mass Determinations to Complement Activation. *Macromolecules* **2018**, *51* (7), 2653-2661.
122. Bleher, S.; Buck, J.; Muhl, C.; Sieber, S.; Barnert, S.; Witzigmann, D.; Huwyler, J.; Barz, M.; Süss, R. Poly(sarcosine) Surface Modification Imparts Stealth-Like Properties to Liposomes. *Small* **2019**, *15* (50), 1904716.
123. Hoogenboom, R. Poly(2-oxazoline)s: A Polymer Class with Numerous Potential Applications. *Angew. Chem. Int. Ed.* **2009**, *48* (43), 7978-7994.
124. Viegas, T. X.; Bentley, M. D.; Harris, J. M.; Fang, Z.; Yoon, K.; Dizman, B.; Weimer, R.; Mero, A.; Pasut, G.; Veronese, F. M. Polyoxazoline: Chemistry, Properties, and Applications in Drug Delivery. *Bioconj. Chem.* **2011**, *22* (5), 976-986.
125. Liu, T.; Zhang, Y.-f.; Liu, S.-y. Drug and Plasmid DNA Co-Delivery Nanocarriers Based on ABC-type Polypeptide Hybrid Miktoarm Star Copolymers. *Chin. J. Polym. Sci.* **2013**, *31* (6), 924-937.

126. Qian, X.; Long, L.; Shi, Z.; Liu, C.; Qiu, M.; Sheng, J.; Pu, P.; Yuan, X.; Ren, Y.; Kang, C. Star-Branched Amphiphilic PLA-*b*-PDMAEMA Copolymers for Co-Delivery of miR-21 Inhibitor and Doxorubicin to Treat Glioma. *Biomaterials* **2014**, *35* (7), 2322-2335.
127. Zhu, J.; Liu, Y.; Xiao, L.; Zhou, P. Temperature-Sensitive (BA)(AC)<sub>2</sub> Miktoarm Star Diblock Copolymer Based on PMMA, PPEGMA, and PNIPAm. *Macromol. Chem. Phys.* **2016**, *217* (6), 773-782.
128. Huo, H.; Ma, X.; Dong, Y.; Qu, F. Light/Temperature Dual-Responsive ABC Miktoarm Star Terpolymer Micelles for Controlled Release. *Eur. Polym. J.* **2017**, *87*, 331-343.
129. Shalaby, K. S.; Soliman, M. E.; Bonacucina, G.; Cespi, M.; Palmieri, G. F.; Sasmour, O. A.; El Shamy, A. A.; Illum, L.; Casettari, L. Nanoparticles Based on Linear and Star-Shaped Poly(ethylene glycol)-Poly( $\epsilon$ -caprolactone) Copolymers for the Delivery of Antitubulin Drug. *Pharm. Res.* **2016**, *33* (8), 2010-2024.
130. Liu, Q.; Cai, C.; Dong, C.-M. Poly(L-lactide)-*b*-Poly(ethylene oxide) Copolymers with Different Arms: Hydrophilicity, Biodegradable Nanoparticles, *In Vitro* Degradation, and Drug-Release Behavior. *J. Biomed. Mater. Res., Part A* **2009**, *88A* (4), 990-999.
131. Soliman, G. M.; Redon, R.; Sharma, A.; Mejía, D.; Maysinger, D.; Kakkar, A. Miktoarm Star Polymer Based Multifunctional Traceable Nanocarriers for Efficient Delivery of Poorly Water Soluble Pharmacological Agents. *Macromol. Biosci.* **2014**, *14* (9), 1312-1324.
132. Yang, L.; Hu, X.; Wang, W.; Liu, S.; Sun, T.; Huang, Y.; Jing, X.; Xie, Z. Y-Shaped Block Copolymer (Methoxy-Poly(ethylene glycol))<sub>2</sub>-*b*-Poly(L-glutamic acid): Preparation, Self-Assembly, and Use as Drug Carriers. *RSC Adv.* **2014**, *4* (78), 41588-41596.
133. Zhou, Q.-H.; Lin, J.; Li, L.-D.; Shang, L. Biodegradable Micelles Self-Assembled from Miktoarm Star Block Copolymers for MTX Delivery. *Colloid. Polym. Sci.* **2015**, *293* (8), 2291-2300.

134. Washington, K. E.; Kularatne, R. N.; Karmegam, V.; Biewer, M. C.; Stefan, M. C. Recent Advances in Aliphatic Polyesters for Drug Delivery Applications. *Wiley Interdiscip. Rev.: Nanomed. Nanobiotechnol.* **2017**, *9* (4), e1446.
135. Díaz, E.; Sandonis, I.; Valle, M. B. *In Vitro* Degradation of Poly(caprolactone)/nHA Composites. *J. Nanomater.* **2014**, *2014*, 802435.
136. Zhang, F.; King, M. W. Biodegradable Polymers as the Pivotal Player in the Design of Tissue Engineering Scaffolds. *Adv. Healthcare Mater.* **2020**, *9* (13), 1901358.
137. Sun, H.; Mei, L.; Song, C.; Cui, X.; Wang, P. The *In Vivo* Degradation, Absorption and Excretion of PCL-Based Implant. *Biomaterials* **2006**, *27* (9), 1735-1740.
138. Bartnikowski, M.; Dargaville, T. R.; Ivanovski, S.; Hutmacher, D. W. Degradation Mechanisms of Polycaprolactone in the Context of Chemistry, Geometry and Environment. *Prog. Polym. Sci.* **2019**, *96*, 1-20.
139. Lin, W.; Nie, S.; Zhong, Q.; Yang, Y.; Cai, C.; Wang, J.; Zhang, L. Amphiphilic Miktoarm Star Copolymer (PCL)<sub>3</sub>-(PDEAEMA-*b*-PPEGMA)<sub>3</sub> as pH-Sensitive Micelles in the Delivery of Anticancer Drug. *J. Mater. Chem. B* **2014**, *2* (25), 4008-4020.
140. Tucker, B. S.; Getchell, S. G.; Hill, M. R.; Sumerlin, B. S. Facile Synthesis of Drug-Conjugated PHPMA Core-Crosslinked Star Polymers. *Polym. Chem.* **2015**, *6* (23), 4258-4263.
141. Slager, J.; Domb, A. J. Biopolymer Stereocomplexes. *Adv. Drug Del. Rev.* **2003**, *55* (4), 549-583.
142. Tsuji, H. Poly(lactic acid) Stereocomplexes: A Decade of Progress. *Adv. Drug Del. Rev.* **2016**, *107*, 97-135.
143. Hui, Y.; Yi, X.; Hou, F.; Wibowo, D.; Zhang, F.; Zhao, D.; Gao, H.; Zhao, C.-X. Role of Nanoparticle Mechanical Properties in Cancer Drug Delivery. *ACS Nano* **2019**, *13* (7), 7410-7424.

144. Huang, X.; Xiao, Y.; Lang, M. Self-Assembly of pH-sensitive Mixed Micelles Based on Linear and Star Copolymers for Drug Delivery. *J. Colloid Interface Sci.* **2011**, *364* (1), 92-99.
145. Cajot, S.; Van Butsele, K.; Paillard, A.; Passirani, C.; Garcion, E.; Benoit, J. P.; Varshney, S. K.; Jérôme, C. Smart Nanocarriers for pH-triggered Targeting and Release of Hydrophobic Drugs. *Acta Biomater.* **2012**, *8* (12), 4215-4223.
146. Patel, S.; Lavasanifar, A.; Choi, P. Application of Molecular Dynamics Simulation to Predict the Compatability between Water-Insoluble Drugs and Self-Associating Poly(ethylene oxide)-*b*-Poly( $\epsilon$ -caprolactone) Block Copolymers. *Biomacromolecules* **2008**, *9* (11), 3014-3023.
147. Danquah, M.; Fujiwara, T.; Mahato, R. I. Self-Assembling Methoxypoly(ethylene glycol)-*b*-Poly(carbonate-*co*-L-lactide) Block Copolymers for Drug Delivery. *Biomaterials* **2010**, *31* (8), 2358-2370.
148. Mielańczyk, A.; Odrobińska, J.; Grządka, S.; Mielańczyk, Ł.; Neugebauer, D. Miktoarm Star Copolymers from D(-)-Salicin Core Aggregated into Dandelion-Like Structures as Anticancer Drug Delivery Systems: Synthesis, Self-Assembly and Drug Release. *Int. J. Pharm.* **2016**, *515* (1), 515-526.
149. Buwalda, S.; Al Samad, A.; El Jundi, A.; Bethry, A.; Bakkour, Y.; Coudane, J.; Nottelet, B. Stabilization of Poly(ethylene glycol)-Poly( $\epsilon$ -caprolactone) Star Block Copolymer Micelles via Aromatic Groups for Improved Drug Delivery Properties. *J. Colloid Interface Sci.* **2018**, *514*, 468-478.
150. Gou, P.-F.; Zhu, W.-P.; Xu, N.; Shen, Z.-Q. Synthesis, Self-Assembly and Drug-Loading Capacity of Well-Defined Drug-Conjugated Amphiphilic A<sub>2</sub>B<sub>2</sub> Type Miktoarm Star Copolymers Based on Poly( $\epsilon$ -caprolactone) and Poly(ethylene glycol). *J. Polym. Sci., Part A: Polym. Chem.* **2009**, *47* (24), 6962-6976.

151. Sui, B.; Xu, H.; Jin, J.; Gou, J.; Liu, J.; Tang, X.; Zhang, Y.; Xu, J.; Zhang, H.; Jin, X. Self-Assembled Micelles Composed of Doxorubicin Conjugated Y-Shaped PEG-Poly(glutamic Acid)<sub>2</sub> Copolymers via Hydrazone Linkers. *Molecules* **2014**, *19* (8), 11915-11932.
152. Bagheri, M.; Bresseleers, J.; Varela-Moreira, A.; Sandre, O.; Meeuwissen, S. A.; Schiffelers, R. M.; Metselaar, J. M.; van Nostrum, C. F.; van Hest, J. C. M.; Hennink, W. E. Effect of Formulation and Processing Parameters on the Size of mPEG-*b*-P(HPMA-Bz) Polymeric Micelles. *Langmuir* **2018**, *34* (50), 15495-15506.
153. Kopeček, J.; Yang, J. Polymer Nanomedicines. *Adv. Drug Del. Rev.* **2020**, *156*, 40-64.
154. Ashford, M. B.; England, R. M.; Akhtar, N. Highway to Success—Developing Advanced Polymer Therapeutics. *Adv. Ther.* **2021**, *4* (5), 2000285.
155. Hwang, D.; Ramsey, J. D.; Kabanov, A. V. Polymeric Micelles for the Delivery of Poorly Soluble Drugs: From Nanoformulation to Clinical Approval. *Adv. Drug Del. Rev.* **2020**, *156*, 80-118.
156. van den Berg, A. I. S.; Yun, C.-O.; Schiffelers, R. M.; Hennink, W. E. Polymeric Delivery Systems for Nucleic Acid Therapeutics: Approaching the Clinic. *J. Controlled Release* **2021**, *331*, 121-141.
157. Zhao, X.; Si, J.; Huang, D.; Li, K.; Xin, Y.; Sui, M. Application of Star Poly(ethylene glycol) Derivatives in Drug Delivery and Controlled Release. *J. Controlled Release* **2020**, *323*, 565-577.
158. Kakkar, A.; Traverso, G.; Farokhzad, O.; Weissleder, R.; Langer, R. Evolution of Macromolecular Complexity in Drug Delivery Systems. *Nat. Rev. Chem.* **2017**, *1*, 0063.
159. Liu, Y.; Wang, J.; Xiong, Q.; Hornburg, D.; Tao, W.; Farokhzad, O. C. Nano–Bio Interactions in Cancer: From Therapeutics Delivery to Early Detection. *Acc. Chem. Res.* **2021**, *54* (2), 291-301.

160. Sadeghi, I.; Byrne, J.; Shakur, R.; Langer, R. Engineered Drug Delivery Devices to Address Global Health Challenges. *J. Controlled Release* **2021**, *331*, 503-514.
161. Yang, C.; Liu, S. Q.; Venkataraman, S.; Gao, S. J.; Ke, X.; Chia, X. T.; Hedrick, J. L.; Yang, Y. Y. Structure-Directing Star-Shaped Block Copolymers: Supramolecular Vesicles for the Delivery of Anticancer Drugs. *J. Controlled Release* **2015**, *208*, 93-105.
162. Fan, X.; Wang, X.; Cao, M.; Wang, C.; Hu, Z.; Wu, Y.-L.; Li, Z.; Loh, X. J. “Y”-Shape Armed Amphiphilic Star-Like Copolymers: Design, Synthesis and Dual-Responsive Unimolecular Micelle Formation for Controlled Drug Delivery. *Polym. Chem.* **2017**, *8* (36), 5611-5620.
163. Zhu, S.; Li, S.; Escuin-Ordinas, H.; Dimatteo, R.; Xi, W.; Ribas, A.; Segura, T. Accelerated Wound Healing by Injectable Star Poly(ethylene glycol)-*b*-Poly(propylene sulfide) Scaffolds Loaded with Poorly Water-Soluble Drugs. *J. Controlled Release* **2018**, *282*, 156-165.
164. Feng, J.; Wen, W.; Jia, Y.-G.; Liu, S.; Guo, J. pH-Responsive Micelles Assembled by Three-Armed Degradable Block Copolymers with a Cholic Acid Core for Drug Controlled-Release. *Polymers* **2019**, *11* (3), 511.
165. Cai, W.; Chen, Q.; Shen, T.; Yang, Q.; Hu, W.; Zhao, P.; Yu, J. Intravenous Anti-VEGF Agents with RGD Peptide-Targeted Core Cross-Linked Star (CCS) Polymers Modified with Indocyanine Green for Imaging and Treatment of Laser-Induced Choroidal Neovascularization. *Biomater. Sci.* **2020**, *8* (16), 4481-4491.
166. Pearce, A. K.; Anane-Adjei, A. B.; Cavanagh, R. J.; Monteiro, P. F.; Bennett, T. M.; Taresco, V.; Clarke, P. A.; Ritchie, A. A.; Alexander, M. R.; Grabowska, A. M.; et al. Effects of Polymer 3D Architecture, Size, and Chemistry on Biological Transport and Drug Delivery *In Vitro* and in Orthotopic Triple Negative Breast Cancer Models. *Adv. Healthcare Mater.* **2020**, *9* (22), 2000892.

167. Aghajanzadeh, M.; Andalib, S.; Danafar, H.; Rostamizadeh, K.; Sharafi, A. The Effect of Baicalein-Loaded Y-Shaped Miktoarm Copolymer on Spatial Memory and Hippocampal Expression of DHCR24, SELADIN and SIRT6 Genes in Rat Model of Alzheimer. *Int. J. Pharm.* **2020**, *586*, 119546.
168. Motamedi, S.; Massoumi, B.; Jaymand, M.; Hamishehkar, H. A Dual Stimuli-Responsive Star-Shaped Nanocarrier as *De Novo* Drug Delivery System for Chemotherapy of Solid Tumors. *J. Polym. Res.* **2020**, *27* (9), 272.
169. Sonawane, S. J.; Kalhapure, R. S.; Jadhav, M.; Rambharose, S.; Mocktar, C.; Govender, T. AB<sub>2</sub>-Type Amphiphilic Block Copolymer Containing a pH-Cleavable Hydrazone Linkage for Targeted Antibiotic Delivery. *Int. J. Pharm.* **2020**, *575*, 118948.
170. Lotocki, V.; Yazdani, H.; Zhang, Q.; Gran, E. R.; Nyrko, A.; Maysinger, D.; Kakkar, A. Miktoarm Star Polymers with Environment-Selective ROS/GSH Responsive Locations: From Modular Synthesis to Tuned Drug Release through Micellar Partial Corona Shedding and/or Core Disassembly. *Macromol. Biosci.* **2021**, *21* (2), 2000305.
171. Wang, X.; Cheng, R.; Zhong, Z. Facile Fabrication of Robust, Hyaluronic Acid-Surfaced and Disulfide-Crosslinked PLGA Nanoparticles for Tumor-Targeted and Reduction-Triggered Release of Docetaxel. *Acta Biomater.* **2021**, *125*, 280-289.
172. Ramesh, K.; Balavigneswaran, C. K.; Siboro, S. A. P.; Muthuvijayan, V.; Lim, K. T. Synthesis of Cyclodextrin-Derived Star Poly(*N*-vinylpyrrolidone)/Poly(lactic-*co*-glycolide) Supramolecular Micelles via Host-Guest Interaction for Delivery of Doxorubicin. *Polymer* **2021**, *214*, 123243.
173. Dawidczyk, C. M.; Kim, C.; Park, J. H.; Russell, L. M.; Lee, K. H.; Pomper, M. G.; Searson, P. C. State-of-the-Art in Design Rules for Drug Delivery Platforms: Lessons Learned from FDA-Approved Nanomedicines. *J. Controlled Release* **2014**, *187*, 133-144.
174. Blanco, E.; Shen, H.; Ferrari, M. Principles of Nanoparticle Design for Overcoming Biological Barriers to Drug Delivery. *Nat. Biotechnol.* **2015**, *33* (9), 941-951.

175. Chen, Q.; Liu, G.; Liu, S.; Su, H.; Wang, Y.; Li, J.; Luo, C. Remodeling the Tumor Microenvironment with Emerging Nanotherapeutics. *Trends Pharmacol. Sci.* **2018**, *39* (1), 59-74.
176. Behzadi, S.; Serpooshan, V.; Tao, W.; Hamaly, M. A.; Alkawareek, M. Y.; Dreaden, E. C.; Brown, D.; Alkilany, A. M.; Farokhzad, O. C.; Mahmoudi, M. Cellular Uptake of Nanoparticles: Journey inside the Cell. *Chem. Soc. Rev.* **2017**, *46* (14), 4218-4244.
177. Zhang, Z.; Zhang, D.; Qiu, B.; Cao, W.; Liu, Y.; Liu, Q.; Li, X. Icebreaker-Inspired Janus Nanomotors to Combat Barriers in the Delivery of Chemotherapeutic Agents. *Nanoscale* **2021**, *13* (13), 6545-6557.
178. Li, Y.; Wang, J.; Wientjes, M. G.; Au, J. L. S. Delivery of Nanomedicines to Extracellular and Intracellular Compartments of a Solid Tumor. *Adv. Drug Del. Rev.* **2012**, *64* (1), 29-39.
179. Au, J. L. S.; Yeung, B. Z.; Wientjes, M. G.; Lu, Z.; Wientjes, M. G. Delivery of Cancer Therapeutics to Extracellular and Intracellular Targets: Determinants, Barriers, Challenges and Opportunities. *Adv. Drug Del. Rev.* **2016**, *97*, 280-301.
180. Muntimadugu, E.; Kommineni, N.; Khan, W. Exploring the Potential of Nanotherapeutics in Targeting Tumor Microenvironment for Cancer Therapy. *Pharmacol. Res.* **2017**, *126*, 109-122.
181. Sabourian, P.; Yazdani, G.; Ashraf, S. S.; Frounchi, M.; Mashayekhan, S.; Kiani, S.; Kakkar, A. Effect of Physico-Chemical Properties of Nanoparticles on Their Intracellular Uptake. *Int. J. Mol. Sci.* **2020**, *21* (21), 8019.
182. Gustafson, H. H.; Holt-Casper, D.; Grainger, D. W.; Ghandehari, H. Nanoparticle Uptake: The Phagocyte Problem. *Nano Today* **2015**, *10* (4), 487-510.
183. Tang, Y.; Wang, X.; Li, J.; Nie, Y.; Liao, G.; Yu, Y.; Li, C. Overcoming the Reticuloendothelial System Barrier to Drug Delivery with a “Don’t-Eat-Us” Strategy. *ACS Nano* **2019**, *13* (11), 13015-13026.

184. Poon, W.; Zhang, Y.-N.; Ouyang, B.; Kingston, B. R.; Wu, J. L. Y.; Wilhelm, S.; Chan, W. C. W. Elimination Pathways of Nanoparticles. *ACS Nano* **2019**, *13* (5), 5785-5798.
185. Stylianopoulos, T.; Jain, R. K. Design Considerations for Nanotherapeutics in Oncology. *Nanomed. Nanotechnol. Biol. Med.* **2015**, *11* (8), 1893-1907.
186. Zhang, C.; Yan, L.; Wang, X.; Zhu, S.; Chen, C.; Gu, Z.; Zhao, Y. Progress, Challenges, and Future of Nanomedicine. *Nano Today* **2020**, *35*, 101008.
187. Li, J.; Mao, H.; Kawazoe, N.; Chen, G. Insight into the Interactions between Nanoparticles and Cells. *Biomater. Sci.* **2017**, *5* (2), 173-189.
188. Rennick, J. J.; Johnston, A. P. R.; Parton, R. G. Key Principles and Methods for Studying the Endocytosis of Biological and Nanoparticle Therapeutics. *Nat. Nanotechnol.* **2021**, *16* (3), 266-276.
189. Mitchell, M. J.; Billingsley, M. M.; Haley, R. M.; Wechsler, M. E.; Peppas, N. A.; Langer, R. Engineering Precision Nanoparticles for Drug Delivery. *Nat. Rev. Drug Discov.* **2021**, *20* (2), 101-124.
190. Khor, S. Y.; Hu, J.; McLeod, V. M.; Quinn, J. F.; Williamson, M.; Porter, C. J. H.; Whittaker, M. R.; Kaminskis, L. M.; Davis, T. P. Molecular Weight (Hydrodynamic Volume) Dictates the Systemic Pharmacokinetics and Tumour Disposition of PolyPEG Star Polymers. *Nanomed. Nanotechnol. Biol. Med.* **2015**, *11* (8), 2099-2108.
191. Berteau, C.; Filipe-Santos, O.; Wang, T.; Rojas, H. E.; Granger, C.; Schwarzenbach, F. Evaluation of the Impact of Viscosity, Injection Volume, and Injection Flow Rate on Subcutaneous Injection Tolerance. *Med Devices (Auckl)* **2015**, *8*, 473-484.
192. *Star Polymer Drug Delivery.* Scopus, [https://www.scopus.com/results/results.uri?src=s&st1=&st2=&sot=b&sdt=b&origin=searchbasic&rr=&sl=43&s=TITLE-ABS-KEY%20\(Star%20polymers%20drug%20delivery\)](https://www.scopus.com/results/results.uri?src=s&st1=&st2=&sot=b&sdt=b&origin=searchbasic&rr=&sl=43&s=TITLE-ABS-KEY%20(Star%20polymers%20drug%20delivery)) (accessed Feb 27, 2021).

193. Basak, R.; Bandyopadhyay, R. Encapsulation of Hydrophobic Drugs in Pluronic F127 Micelles: Effects of Drug Hydrophobicity, Solution Temperature, and pH. *Langmuir* **2013**, *29* (13), 4350-4356.
194. Singla, P.; Singh, O.; Sharma, S.; Betlem, K.; Aswal, V. K.; Peeters, M.; Mahajan, R. K. Temperature-Dependent Solubilization of the Hydrophobic Antiepileptic Drug Lamotrigine in Different Pluronic Micelles—a Spectroscopic, Heat Transfer Method, Small-Angle Neutron Scattering, Dynamic Light Scattering, and *In Vitro* Release Study. *ACS Omega* **2019**, *4* (6), 11251-11262.
195. Sulistio, A.; Lowenthal, J.; Blencowe, A.; Bongiovanni, M. N.; Ong, L.; Gras, S. L.; Zhang, X.; Qiao, G. G. Folic Acid Conjugated Amino Acid-based Star Polymers for Active Targeting of Cancer Cells. *Biomacromolecules* **2011**, *12* (10), 3469-3477.
196. Zhang, Y.; Chen, M.; Luo, X.; Zhang, H.; Liu, C.; Li, H.; Li, X. Tuning Multiple Arms for Camptothecin and Folate Conjugations on Star-Shaped Copolymers to Enhance Glutathione-Mediated Intracellular Drug Delivery. *Polym. Chem.* **2015**, *6* (12), 2192-2203.
197. Saeedi, S.; Murjan, S.; Nabid, M. R. Redox and pH Dual Sensitive Folate-Modified Star-Like Amphiphilic Copolymer Based on Castor Oil for Controlled Doxorubicin Delivery. *J. Drug Deliv. Sci. Technol.* **2021**, *62*, 102391.
198. Wang, X.; Liu, L.; Luo, Y.; Shi, H.; Li, J.; Zhao, H. Comb-Shaped Glycopolymer/Peptide Bioconjugates by Combination of RAFT Polymerization and Thiol-ene “Click” Chemistry. *Macromol. Biosci.* **2012**, *12* (11), 1575-1582.
199. Nieto-Orellana, A.; Li, H.; Rosiere, R.; Wauthoz, N.; Williams, H.; Monteiro, C. J.; Bosquillon, C.; Childerhouse, N.; Keegan, G.; Coghlan, D.; et al. Targeted PEG-Poly(glutamic acid) Complexes for Inhalation Protein Delivery to the Lung. *J. Controlled Release* **2019**, *316*, 250-262.

200. Wang, K.; Guo, L.; Xiong, W.; Sun, L.; Zheng, Y. Nanoparticles of Star-Like Copolymer Mannitol-Functionalized Poly(lactide)-Vitamin E TPGS for Delivery of Paclitaxel to Prostate Cancer Cells. *J. Biomater. Appl.* **2014**, *29* (3), 329-340.
201. Liu, J.; Duong, H.; Whittaker, M. R.; Davis, T. P.; Boyer, C. Synthesis of Functional Core, Star Polymers via RAFT Polymerization for Drug Delivery Applications. *Macromol. Rapid Commun.* **2012**, *33* (9), 760-766.
202. Ai, X.; Sun, J.; Zhong, L.; Wu, C.; Niu, H.; Xu, T.; Lian, H.; Han, X.; Ren, G.; Ding, W.; et al. Star-Shape Redox-Responsive PEG-Sheddable Copolymer of Disulfide-Linked Polyethylene Glycol-Lysine-di-Tocopherol Succinate for Tumor-Triggering Intracellular Doxorubicin Rapid Release: Head-to-Head Comparison. *Macromol. Biosci.* **2014**, *14* (10), 1415-1428.
203. Kaur, J.; Mishra, V.; Singh, S. K.; Gulati, M.; Kapoor, B.; Chellappan, D. K.; Gupta, G.; Dureja, H.; Anand, K.; Dua, K.; et al. Harnessing Amphiphilic Polymeric Micelles for Diagnostic and Therapeutic Applications: Breakthroughs and Bottlenecks. *J. Controlled Release* **2021**, *334*, 64-95.
204. Cook, A. B.; Decuzzi, P. Harnessing Endogenous Stimuli for Responsive Materials in Theranostics. *ACS Nano* **2021**, *15* (2), 2068-2098.
205. Hsu, P.-H.; Almutairi, A. Recent Progress of Redox-Responsive Polymeric Nanomaterials for Controlled Release. *J. Mater. Chem. B* **2021**, *9* (9), 2179-2188.
206. Hershberger, K. K.; Gauger, A. J.; Bronstein, L. M. Utilizing Stimuli Responsive Linkages to Engineer and Enhance Polymer Nanoparticle-Based Drug Delivery Platforms. *ACS Appl. Bio Mat.* **2021**, *4* (6), 4720-4736.
207. Wang, S.; Liu, Q.; Li, L.; Urban, M. W. Recent Advances in Stimuli-Responsive Commodity Polymers. *Macromol. Rapid Commun.* **2021**, *42* (18), 2100054.
208. Wang, R. Gasotransmitters: Growing Pains and Joys. *Trends Biochem. Sci.* **2014**, *39* (5), 227-232.

209. Fagone, P.; Mazzon, E.; Bramanti, P.; Bendtzen, K.; Nicoletti, F. Gasotransmitters and the Immune System: Mode of Action and Novel Therapeutic Targets. *Eur. J. Pharmacol.* **2018**, *834*, 92-102.
210. Liu, R.; Xu, M.; Yan, Q. Nitric Oxide-Biosignal-Responsive Polypeptide Nanofilaments. *ACS Mater. Lett.* **2020**, *9* (3), 323-327.
211. Lu, C.; Xiao, Y.; Liu, Y.; Sun, F.; Qiu, Y.; Mu, H.; Duan, J. Hyaluronic Acid-Based Levofloxacin Nanomicelles for Nitric Oxide-triggered Drug Delivery to Treat Bacterial Infections. *Carbohydr. Polym.* **2020**, *229*, 115479.
212. Xu, M.; Liu, L.; Hu, J.; Zhao, Y.; Yan, Q. CO-Signaling Molecule-Responsive Nanoparticles Formed from Palladium-Containing Block Copolymers. *ACS Mater. Lett.* **2017**, *6* (4), 458-462.
213. Xu, M.; Hao, X.; Hu, Z.; Yan, Q. Palladium-Bridged Polymers as CO-Biosignal-Responsive Self-Healing Hydrogels. *Polym. Chem.* **2020**, *11* (4), 779-783.
214. Yan, Q.; Sang, W. H<sub>2</sub>S Gasotransmitter-Responsive Polymer Vesicles. *Chem. Sci.* **2016**, *7* (3), 2100-2105.
215. Zhang, H.; Kong, X.; Tang, Y.; Lin, W. Hydrogen Sulfide Triggered Charge-Reversal Micelles for Cancer-Targeted Drug Delivery and Imaging. *ACS Appl. Mater. Interfaces* **2016**, *8* (25), 16227-16239.
216. Hsu, P.-H.; Kawasaki, R.; Yamana, K.; Isozaki, H.; Kawamura, S.; Ikeda, A.; Almutairi, A. Hydrogen Sulfide-Responsive Self-Assembled Nanogel. *ACS Appl. Polym. Mater.* **2020**, *2* (9), 3756-3760.
217. Li, R.; Huang, X.; Lu, G.; Feng, C. Sulfur Dioxide Signaling Molecule-Responsive Polymeric Nanoparticles. *Biomater. Sci.* **2020**, *8* (8), 2300-2307.

218. Jiang, X.; Chun, F.; Lu, G.; Xiaoyu, H. Oxygen and Carbon Dioxide Dual Gas-Responsive Homopolymers and Diblock Copolymers Synthesized via Raft Polymerization. *Polym. Chem.* **2017**, *8* (7), 1163-1176.
219. Lin, S.; Shang, J.; Zhang, X.; Theato, P. “Breathing” CO<sub>2</sub>-, O<sub>2</sub>-, and Light-Responsive Vesicles from a Triblock Copolymer for Rate-Tunable Controlled Release. *Macromol. Rapid Commun.* **2018**, *39* (1), 1700313.
220. Yan, B.; Han, D.; Boissière, O.; Ayotte, P.; Zhao, Y. Manipulation of Block Copolymer Vesicles Using CO<sub>2</sub>: Dissociation or “Breathing”. *Soft Matter* **2013**, *9* (6), 2011-2016.
221. biTian, J.; Huang, B.; Xiao, C.; Vana, P. Intelligent CO<sub>2</sub>- and Photo-Dual-Responsive Polymer Vesicles with Tunable Wall Thickness. *Polym. Chem.* **2019**, *10* (13), 1610-1618.
222. Satav, S. S.; Bhat, S.; Thayumanavan, S. Feedback Regulated Drug Delivery Vehicles: Carbon Dioxide Responsive Cationic Hydrogels for Antidote Release. *Biomacromolecules* **2010**, *11* (7), 1735-1740.
223. Liu, J.; Ma, H.; Wei, T.; Liang, X.-J. CO<sub>2</sub> Gas Induced Drug Release from pH-sensitive Liposome to Circumvent Doxorubicin Resistant Cells. *Chem. Commun.* **2012**, *48* (40), 4869-4871.
224. Han, D.; Boissiere, O.; Kumar, S.; Tong, X.; Tremblay, L.; Zhao, Y. Two-Way CO<sub>2</sub>-Switchable Triblock Copolymer Hydrogels. *Macromolecules* **2012**, *45* (18), 7440-7445.
225. Wang, X.; Jiang, G.; Li, X.; Tang, B.; Wei, Z.; Mai, C. Synthesis of Multi-Responsive Polymeric Nanocarriers for Controlled Release of Bioactive Agents. *Polym. Chem.* **2013**, *4* (17), 4574-4577.
226. Wang, X.; Jiang, G.; Wei, Z.; Li, X.; Tang, B. Preparation and Drug Release Property of CO<sub>2</sub> Stimulus-Sensitive Poly(*N*, *N*-dimethylaminoethyl methacrylate)-*b*-Polystyrene Nanoparticles. *Eur. Polym. J.* **2013**, *49* (10), 3165-3170.

227. Yuan, W.; Shen, J.; Zou, H. Amphiphilic Block Copolymer Terminated with Pyrene Group: From Switchable CO<sub>2</sub>-Temperature Dual Responses to Tunable Fluorescence. *RSC Adv.* **2015**, *5* (17), 13145-13152.
228. Tan, J.; Zhang, X.; Liu, D.; Bai, Y.; Huang, C.; Li, X.; Zhang, L. Facile Preparation of CO<sub>2</sub>-responsive Polymer Nano-Objects via Aqueous Photoinitiated Polymerization-Induced Self-Assembly (Photo-PISA). *Macromol. Rapid Commun.* **2017**, *38* (13), 1600508.
229. Duan, W.; Jing, X.; Tan, J.; Tao, M.; Wang, L.; Lu, H. CO<sub>2</sub>-Switchable Vesicles-Network Structure Transition and Drug Release Property. *J. Dispersion Sci. Technol.* **2018**, *39* (9), 1309-1315.
230. Jing, X.-W.; Huang, Z.-Y.; Lu, H.-S.; Wang, B.-G. CO<sub>2</sub>-Sensitive Amphiphilic Triblock Copolymer Self-Assembly Morphology Transition and Accelerating Drug Release from Polymeric Vesicle. *Chin. J. Polym. Sci.* **2018**, *36* (1), 18-24.
231. Yu, L.; Zhang, Y.; Dai, X.; Xu, Q.; Zhang, L.; Tan, J. Open-Air Preparation of Cross-Linked CO<sub>2</sub>-Responsive Polymer Vesicles by Enzyme-Assisted Photoinitiated Polymerization-Induced Self-Assembly. *Chem. Commun.* **2019**, *55* (79), 11920-11923.
232. Zou, H.; Yuan, W. CO<sub>2</sub>- and Thermo-Responsive Vesicles: From Expansion–Contraction Transformation to Vesicles-Micelles Transition. *Polym. Chem.* **2015**, *6* (13), 2457-2465.
233. Yan, Q.; Zhou, R.; Fu, C.; Zhang, H.; Yin, Y.; Yuan, J. CO<sub>2</sub>-Responsive Polymeric Vesicles That Breathe. *Angew. Chem. Int. Ed.* **2011**, *50* (21), 4923-4927.
234. Yan, Q.; Wang, J.; Yin, Y.; Yuan, J. Breathing Polymersomes: CO<sub>2</sub>-Tuning Membrane Permeability for Size-Selective Release, Separation, and Reaction. *Angew. Chem. Int. Ed.* **2013**, *52* (19), 5070-5073.
235. Che, N.; Yang, S.; Kang, H.; Liu, R.; Li, Z.; Liu, Z.; Li, P.; Qu, X.; Huang, Y. Synthesis and Properties of CO<sub>2</sub>-Switchable Dex-g-PAHMA Copolymers. *Polym. Chem.* **2014**, *5* (24), 7109-7120.

236. Lin, S.; Huang, X.; Guo, R.; Chen, S.; Lan, J.; Theato, P. UV-Triggered CO<sub>2</sub>-Responsive Behavior of Nanofibers and Their Controlled Drug Release Properties. *J. Polym. Sci., Part A: Polym. Chem.* **2019**, *57* (14), 1580-1586.
237. Mintz, J.; Vedenko, A.; Rosete, O.; Shah, K.; Goldstein, G.; Hare, J. M.; Ramasamy, R.; Arora, H. Current Advances of Nitric Oxide in Cancer and Anticancer Therapeutics. *Vaccines* **2021**, *9* (2), 94.
238. Hu, J.; Whittaker, M. R.; Duong, H.; Li, Y.; Boyer, C.; Davis, T. P. Biomimetic Polymers Responsive to a Biological Signaling Molecule: Nitric Oxide Triggered Reversible Self-Assembly of Single Macromolecular Chains into Nanoparticles. *Angew. Chem. Int. Ed.* **2014**, *53* (30), 7779-7784.
239. Hu, J.; Whittaker, M. R.; Li, Y.; Quinn, J. F.; Davis, T. P. The Use of Endogenous Gaseous Molecules (NO and CO<sub>2</sub>) to Regulate the Self-Assembly of a Dual-Responsive Triblock Copolymer. *Polym. Chem.* **2015**, *6* (13), 2407-2415.
240. Zhou, Y.; Tan, J.; Wu, J.; Zhang, Q.; Andre, J.; Xi, C.; Chen, Z.; Meyerhoff, M. E. Nitric Oxide Releasing Poly(vinylidene fluoride-co-hexafluoropropylene) Films Using a Fluorinated Nitric Oxide Donor to Greatly Decrease Chemical Leaching. *Acta Biomater.* **2019**, *90*, 112-121.
241. Lutzke, A.; Tapia, J. B.; Neufeld, M. J.; Reynolds, M. M. Sustained Nitric Oxide Release from a Tertiary S-Nitrosothiol-Based Polyphosphazene Coating. *ACS Appl. Mater. Interfaces* **2017**, *9* (3), 2104-2113.
242. Fleming, G.; Aveyard, J.; Fothergill, J. L.; McBride, F.; Raval, R.; D'Sa, R. A. Nitric Oxide Releasing Polymeric Coatings for the Prevention of Biofilm Formation. *Polymers* **2017**, *9* (11), 601.
243. Zhang, Y.; Tang, K.; Chen, B.; Zhou, S.; Li, N.; Liu, C.; Yang, J.; Lin, R.; Zhang, T.; He, W. A Polyethylenimine-Based Diazoniumdiolate Nitric Oxide Donor Accelerates Wound Healing. *Biomater. Sci.* **2019**, *7* (4), 1607-1616.

244. Yang, L.; Teles, F.; Gong, W.; Dua, S. A.; Martin, L.; Schoenfisch, M. H. Antibacterial Action of Nitric Oxide-Releasing Hyperbranched Polymers against *Ex Vivo* Dental Biofilms. *Dent. Mater.* **2020**, *36* (5), 635-644.
245. Yang, L.; Schoenfisch, M. H. Nitric Oxide-releasing Hyperbranched Polyaminoglycosides for Antibacterial Therapy. *ACS Appl. Bio Mat.* **2018**, *1* (4), 1066-1073.
246. Yang, L.; Jing, L.; Jiao, Y.; Wang, L.; Marchesan, J. T.; Offenbacher, S.; Schoenfisch, M. H. *In Vivo* Antibacterial Efficacy of Nitric Oxide-Releasing Hyperbranched Polymers against *Porphyromonas Gingivalis*. *Mol. Pharm.* **2019**, *16* (9), 4017-4023.
247. Worley, B. V.; Schilly, K. M.; Schoenfisch, M. H. Anti-Biofilm Efficacy of Dual-Action Nitric Oxide-Releasing Alkyl Chain Modified Poly(amidoamine) Dendrimers. *Mol. Pharm.* **2015**, *12* (5), 1573-1583.
248. Fraix, A.; Conte, C.; Gazzano, E.; Riganti, C.; Quaglia, F.; Sortino, S. Overcoming Doxorubicin Resistance with Lipid-Polymer Hybrid Nanoparticles Photoreleasing Nitric Oxide. *Mol. Pharm.* **2020**, *17* (6), 2135-2144.
249. Quinn, J. F.; Whittaker, M. R.; Davis, T. P. Delivering Nitric Oxide with Nanoparticles. *J. Controlled Release* **2015**, *205*, 190-205.
250. Yang, C.; Jeong, S.; Ku, S.; Lee, K.; Park, M. H. Use of Gasotransmitters for the Controlled Release of Polymer-Based Nitric Oxide Carriers in Medical Applications. *J. Controlled Release* **2018**, *279*, 157-170.
251. Motterlini, R.; Otterbein, L. E. The Therapeutic Potential of Carbon Monoxide. *Nat. Rev. Drug Discov.* **2010**, *9* (9), 728-743.
252. Ji, X.; Wang, B. Strategies toward Organic Carbon Monoxide Prodrugs. *Acc. Chem. Res.* **2018**, *51* (6), 1377-1385.

253. Yan, H.; Du, J.; Zhu, S.; Nie, G.; Zhang, H.; Gu, Z.; Zhao, Y. Emerging Delivery Strategies of Carbon Monoxide for Therapeutic Applications: From CO Gas to CO Releasing Nanomaterials. *Small* **2019**, *15* (49), 1904382.
254. Zhou, Y.; Yu, W.; Cao, J.; Gao, H. Harnessing Carbon Monoxide-Releasing Platforms for Cancer Therapy. *Biomaterials* **2020**, *255*, 120193.
255. Siracusa, R.; Schaufler, A.; Calabrese, V.; Fuller, P. M.; Otterbein, L. E. Carbon Monoxide: From Poison to Clinical Trials. *Trends Pharmacol. Sci.* **2021**, *42* (5), 329-339.
256. Liu, K.; Kong, X.; Ma, Y.; Lin, W. Preparation of a Nile Red–Pd-Based Fluorescent CO Probe and Its Imaging Applications *In Vitro* and *In Vivo*. *Nature Protocols* **2018**, *13* (5), 1020-1033.
257. Morstein, J.; Höfler, D.; Ueno, K.; Jurss, J. W.; Walvoord, R. R.; Bruemmer, K. J.; Rezgui, S. P.; Brewer, T. F.; Saitoe, M.; Michel, B. W.; et al. Ligand-Directed Approach to Activity-Based Sensing: Developing Palladacycle Fluorescent Probes That Enable Endogenous Carbon Monoxide Detection. *J. Am. Chem. Soc.* **2020**, *142* (37), 15917-15930.
258. Cao, Y.; Li, D.-W.; Zhao, L.-J.; Liu, X.-Y.; Cao, X.-M.; Long, Y.-T. Highly Selective Detection of Carbon Monoxide in Living Cells by Palladacycle Carbonylation-Based Surface Enhanced Raman Spectroscopy Nanosensors. *Anal. Chem.* **2015**, *87* (19), 9696-9701.
259. Szabo, C.; Coletta, C.; Chao, C.; Módis, K.; Szczesny, B.; Papapetropoulos, A.; Hellmich, M. R. Tumor-Derived Hydrogen Sulfide, Produced by Cystathionine- $\beta$ -Synthase, Stimulates Bioenergetics, Cell Proliferation, and Angiogenesis in Colon Cancer. *Proc. Natl. Acad. Sci.* **2013**, *110* (30), 12474-12479.
260. Li, L.; Rose, P.; Moore, P. K. Hydrogen Sulfide and Cell Signaling. *Annu. Rev. Pharmacol. Toxicol.* **2011**, *51* (1), 169-187.
261. Benchoam, D.; Cuevasanta, E.; Möller, M. N.; Alvarez, B. Hydrogen Sulfide and Persulfides Oxidation by Biologically Relevant Oxidizing Species. *Antioxidants* **2019**, *8* (2), 48.

262. Paul, B. D.; Snyder, S. H.; Kashfi, K. Effects of Hydrogen Sulfide on Mitochondrial Function and Cellular Bioenergetics. *Redox Biology* **2021**, *38*, 101772.
263. Henthorn, H. A.; Pluth, M. D. Mechanistic Insights into the H<sub>2</sub>S-Mediated Reduction of Aryl Azides Commonly Used in H<sub>2</sub>S Detection. *J. Am. Chem. Soc.* **2015**, *137* (48), 15330-15336.
264. Perera, F. Pollution from Fossil-Fuel Combustion Is the Leading Environmental Threat to Global Pediatric Health and Equity: Solutions Exist. *Int. J. Env. Res. Public Health* **2018**, *15* (1), 16.
265. Lin, C.-K.; Lin, R.-T.; Chen, P.-C.; Wang, P.; De Marcellis-Warin, N.; Zigler, C.; Christiani, D. C. A Global Perspective on Sulfur Oxide Controls in Coal-Fired Power Plants and Cardiovascular Disease. *Sci. Rep.* **2018**, *8* (1), 2611.
266. Yeo, E.-J. Hypoxia and Aging. *Exp. Mol. Med.* **2019**, *51* (6), 1-15.
267. Zhao, X.; Wu, W.; Zhang, J.; Dai, W.; Zhao, Y. Thermoresponse and Self-Assembly of an ABC Star Quarterpolymer with O<sub>2</sub> and Redox Dual-Responsive Y Junctions. *Polym. Chem.* **2018**, *9* (9), 1095-1108.
268. Zhang, Q.; Zhu, S. Oxygen–Nitrogen Switchable Copolymers of 2,2,2-Trifluoroethyl Methacrylate and *N,N*-Dimethylaminoethyl Methacrylate. *Macromol. Rapid Commun.* **2014**, *35* (19), 1692-1696.
269. Zhang, Q.; Zhu, S. Oxygen and Carbon Dioxide Dual Responsive Nanoaggregates of Fluoro- and Amino-Containing Copolymer. *ACS Mater. Lett.* **2014**, *3* (8), 743-746.
270. Lei, L.; Zhang, Q.; Shi, S.; Zhu, S. Oxygen and Carbon Dioxide Dual Gas-Responsive and Switchable Microgels Prepared from Emulsion Copolymerization of Fluoro- and Amino-Containing Monomers. *Langmuir* **2015**, *31* (7), 2196-2201.
271. Lei, L.; Zhang, Q.; Shi, S.; Zhu, S. Oxygen-Switchable Thermo-Responsive Random Copolymers. *Polym. Chem.* **2016**, *7* (34), 5456-5462.

272. Lei, L.; Zhang, Q.; Shi, S.; Zhu, S. Oxygen and Carbon Dioxide Dual Gas-Switchable Thermoresponsive Homopolymers. *ACS Mater. Lett.* **2016**, *5* (7), 828-832.
273. Choi, J. Y.; Kim, J. Y.; Moon, H. J.; Park, M. H.; Jeong, B. CO<sub>2</sub>- and O<sub>2</sub>-Sensitive Fluorophenyl End-Capped Poly(ethylene glycol). *Macromol. Rapid Commun.* **2014**, *35* (1), 66-70.
274. Cunningham, M. F.; Jessop, P. G. Carbon Dioxide-Switchable Polymers: Where Are the Future Opportunities? *Macromolecules* **2019**, *52* (18), 6801-6816.
275. Darabi, A.; Jessop, P. G.; Cunningham, M. F. CO<sub>2</sub>-Responsive Polymeric Materials: Synthesis, Self-Assembly, and Functional Applications. *Chem. Soc. Rev.* **2016**, *45* (15), 4391-4436.
276. Shigemura, M.; Lecuona, E.; Sznajder, J. I. Effects of Hypercapnia on the Lung. *J Physiol.* **2017**, *595* (8), 2431-2437.
277. Szabo, C. Gasotransmitters in Cancer: From Pathophysiology to Experimental Therapy. *Nat. Rev. Drug Discov.* **2016**, *15* (3), 185-203.
278. Sood, P.; Paul, G.; Puri, S. Interpretation of Arterial Blood Gas. *Indian J. Crit. Care Med.* **2010**, *14* (2), 57-64.
279. Stipanuk, M. H. Metabolism of Sulfur-Containing Amino Acids: How the Body Copes with Excess Methionine, Cysteine, and Sulfide. *J. Nutr.* **2020**, *150*, 2494S-2505S.
280. Iverson, N. M.; Hofferber, E. M.; Stapleton, J. A. Nitric Oxide Sensors for Biological Applications. *Chemosensors* **2018**, *6* (1), 8.
281. Möller, M. N.; Rios, N.; Trujillo, M.; Radi, R.; Denicola, A.; Alvarez, B. Detection and Quantification of Nitric Oxide-Derived Oxidants in Biological Systems. *J. Biol. Chem.* **2019**, *294* (40), 14776-14802.

282. Rudd, S.; Dalton, M.; Buss, P.; Treijs, A.; Portmann, M.; Ktoris, N.; Evans, D. Selective Uptake and Sensing of Nitrate in Poly(3,4-ethylenedioxythiophene). *Sci. Rep.* **2017**, *7* (1), 16581.
283. Lotocki, V.; Kakkar, A. Miktoarm Star Polymers: Branched Architectures in Drug Delivery. *Pharmaceutics* **2020**, *12* (9), 827.
284. Wei, M.; Gao, Y.; Li, X.; Serpe, M. J. Stimuli-Responsive Polymers and Their Applications. *Polym. Chem.* **2017**, *8* (1), 127-143.
285. Ulbrich, K.; Holá, K.; Šubr, V.; Bakandritsos, A.; Tuček, J.; Zbořil, R. Targeted Drug Delivery with Polymers and Magnetic Nanoparticles: Covalent and Noncovalent Approaches, Release Control, and Clinical Studies. *Chem. Rev.* **2016**, *116* (9), 5338-5431.
286. Indermun, S.; Govender, M.; Kumar, P.; Choonara, Y. E.; Pillay, V. Stimuli-Responsive Polymers as Smart Drug Delivery Systems: Classifications Based on Carrier Type and Triggered-Release Mechanism. In *Stimuli Responsive Polymeric Nanocarriers for Drug Delivery Applications, Volume 1*, Makhlouf, A. S. H., Abu-Thabit, N. Y. Eds.; Woodhead Publishing, 2018; pp 43-58.
287. Yang, B.; Chen, Y.; Shi, J. Reactive Oxygen Species (ROS)-Based Nanomedicine. *Chem. Rev.* **2019**, *119* (8), 4881-4985.
288. Lin, W.; Nie, S.; Xiong, D.; Guo, X.; Wang, J.; Zhang, L. pH-Responsive Micelles Based on (PCL)<sub>2</sub>(PDEA-*b*-PPEGMA)<sub>2</sub> Miktoarm Polymer: Controlled Synthesis, Characterization, and Application as Anticancer Drug Carrier. *Nanoscale Res. Lett.* **2014**, *9* (1), 243.
289. Alizadeh, R.; Ghaemy, M. pH-Responsive ABC Type Miktoarm Star Terpolymers: Synthesis via Combination of Click Reaction and SET-LRP, Characterization, Self-Assembly, and Controlled Drug Release. *Polymer* **2015**, *66*, 179-191.

290. Huang, L.-m.; Li, L.-d.; Shang, L.; Zhou, Q.-h.; Lin, J. Preparation of pH-Sensitive Micelles from Miktoarm Star Block Copolymers by ATRP and Their Application as Drug Nanocarriers. *React. Funct. Polym.* **2016**, *107*, 28-34.
291. An, X.; Zhu, A.; Luo, H.; Ke, H.; Chen, H.; Zhao, Y. Rational Design of Multi-Stimuli-Responsive Nanoparticles for Precise Cancer Therapy. *ACS Nano* **2016**, *10* (6), 5947-5958.
292. Kim, Y.; Uthaman, S.; Nurunnabi, M.; Mallick, S.; Oh, K. S.; Kang, S.-W.; Cho, S.; Kang, H. C.; Lee, Y.-k.; Huh, K. M. Synthesis and Characterization of Bioreducible Cationic Biarm Polymer for Efficient Gene Delivery. *Int. J. Biol. Macromol.* **2018**, *110*, 366-374.
293. Kim, H.-C.; Kim, E.; Lee, S. G.; Lee, S. J.; Jeong, S. W.; Lee, Y. J.; Kwon, M. K.; Choi, S.-K.; Hwang, J. S.; Choi, E. Reactive Oxygen Species-Responsive Miktoarm Amphiphile for Triggered Intracellular Release of Anti-Cancer Therapeutics. *Polymers* **2021**, *13* (24), 4418.
294. Kumar, P.; Kim, S.-H.; Yadav, S.; Jo, S.-H.; Yoo, S., II; Park, S.-H.; Lim, K. T. Redox-Responsive Core-Cross-Linked Micelles of Miktoarm Poly(ethylene oxide)-*b*-Poly(furfuryl methacrylate) for Anticancer Drug Delivery. *ACS Appl. Mater. Interfaces* **2023**, *15* (10), 12719-12734.
295. Li, Y.-Y.; Zhang, X.-Z.; Cheng, H.; Kim, G.-C.; Cheng, S.-X.; Zhuo, R.-X. Novel Stimuli-Responsive Micelle Self-Assembled from Y-Shaped P(UA-Y-NIPAAm) Copolymer for Drug Delivery. *Biomacromolecules* **2006**, *7* (11), 2956-2960.
296. Wei, H.; Zhang, X.; Cheng, C.; Cheng, S.-X.; Zhuo, R.-X. Self-Assembled, Thermosensitive Micelles of a Star Block Copolymer Based on PMMA and PNIPAAm for Controlled Drug Delivery. *Biomaterials* **2007**, *28* (1), 99-107.
297. Farnaz, F.; Massoumi, B.; Banaei, A.; Jaymand, M. A Thermal-Responsive Y-Shaped Miktoarm Amphiphilic Block Copolymer Composed of Poly( $\epsilon$ -caprolactone) and Poly(*N*-isopropylacrylamide) as a Nano-Micellar Carrier for Anti-Cancer Drugs. *Polym. Sci., Ser. B* **2020**, *62* (5), 540-549.

298. Liu, H.; Lin, S.; Feng, Y.; Theato, P. CO<sub>2</sub>-Responsive Polymer Materials. *Polym. Chem.* **2017**, *8* (1), 12-23.
299. Cummins, E. P.; Selfridge, A. C.; Sporn, P. H.; Sznajder, J. I.; Taylor, C. T. Carbon Dioxide-Sensing in Organisms and Its Implications for Human Disease. *Cell. Mol. Life Sci.* **2014**, *71* (5), 831-845.
300. Herren, T.; Achermann, E.; Hegi, T.; Reber, A.; Stäubli, M. Carbon Dioxide Narcosis Due to Inappropriate Oxygen Delivery: A Case Report. *J. Med. Case Rep.* **2017**, *11* (1), 204.
301. Huo, M.; Du, H.; Zeng, M.; Pan, L.; Fang, T.; Xie, X.; Wei, Y.; Yuan, J. CO<sub>2</sub>-Stimulated Morphology Transition of ABC Miktoarm Star Terpolymer Assemblies. *Polym. Chem.* **2017**, *8* (18), 2833-2840.
302. Zhu, Y.-J.; Chen, F. pH-Responsive Drug-Delivery Systems. *Chem. - Asian J.* **2015**, *10* (2), 284-305.
303. Oh, K. T.; Oh, Y. T.; Oh, N.-M.; Kim, K.; Lee, D. H.; Lee, E. S. A Smart Flower-Like Polymeric Micelle for pH-Triggered Anticancer Drug Release. *Int. J. Pharm.* **2009**, *375* (1), 163-169.
304. Ray, P. D.; Huang, B.-W.; Tsuji, Y. Reactive Oxygen Species (ROS) Homeostasis and Redox Regulation in Cellular Signaling. *Cell. Signal.* **2012**, *24* (5), 981-990.
305. Sies, H.; Jones, D. P. Reactive Oxygen Species (ROS) as Pleiotropic Physiological Signalling Agents. *Nat. Rev. Mol. Cell Biol.* **2020**, *21* (7), 363-383.
306. Lennicke, C.; Cochemé, H. M. Redox Metabolism: ROS as Specific Molecular Regulators of Cell Signaling and Function. *Mol. Cell* **2021**, *81* (18), 3691-3707.
307. Niedzielska, E.; Smaga, I.; Gawlik, M.; Moniczewski, A.; Stankowicz, P.; Pera, J.; Filip, M. Oxidative Stress in Neurodegenerative Diseases. *Mol. Neurobiol.* **2016**, *53* (6), 4094-4125.

308. Houldsworth, A. Role of Oxidative Stress in Neurodegenerative Disorders: A Review of Reactive Oxygen Species and Prevention by Antioxidants. *Brain Commun.* **2024**, *6* (1), fcad356.
309. Rauf, A.; Khalil, A. A.; Awadallah, S.; Khan, S. A.; Abu-Izneid, T.; Kamran, M.; Hemeg, H. A.; Mubarak, M. S.; Khalid, A.; Wilairatana, P. Reactive Oxygen Species in Biological Systems: Pathways, Associated Diseases, and Potential Inhibitors—a Review. *Food Sci. Nutr.* **2024**, *12* (2), 675-693.
310. Sun, C.; Liang, Y.; Hao, N.; Xu, L.; Cheng, F.; Su, T.; Cao, J.; Gao, W.; Pu, Y.; He, B. A ROS-responsive Polymeric Micelle with a  $\pi$ -Conjugated Thioketal Moiety for Enhanced Drug Loading and Efficient Drug Delivery. *Org. Biomol. Chem.* **2017**, *15* (43), 9176-9185.
311. Wang, J.; Li, D.; Tao, W.; Lu, Y.; Yang, X.; Wang, J. Synthesis of an Oxidation-Sensitive Polyphosphoester Bearing Thioether Group for Triggered Drug Release. *Biomacromolecules* **2019**, *20* (4), 1740-1747.
312. Wang, G.; Huang, P.; Qi, M.; Li, C.; Fan, W.; Zhou, Y.; Zhang, R.; Huang, W.; Yan, D. Facile Synthesis of a H<sub>2</sub>O<sub>2</sub>-Responsive Alternating Copolymer Bearing Thioether Side Groups for Drug Delivery and Controlled Release. *ACS Omega* **2019**, *4* (17), 17600-17606.
313. Sun, C.; Tan, Y.; Xu, H. From Selenite to Diselenide-Containing Drug Delivery Systems. *ACS Mater. Lett.* **2020**, *2* (9), 1173-1177.
314. Mathew, J.; Ru, H.; Le, T.-N.; Pham, H.-P.; Kumar, P.; Lee, C.-K.; Shunmugam, R.; Rao, N. V. ROS-responsive Camptothecin-Linked Thioketal Drug Delivery System Based on Ring-Closing Polymerization. *Eur. Polym. J.* **2024**, *202*, 112646.
315. Tao, W.; He, Z. ROS-Responsive Drug Delivery Systems for Biomedical Applications. *Asian J. Pharm. Sci.* **2018**, *13* (2), 101-112.
316. Ye, H.; Zhou, Y.; Liu, X.; Chen, Y.; Duan, S.; Zhu, R.; Liu, Y.; Yin, L. Recent Advances on Reactive Oxygen Species-Responsive Delivery and Diagnosis System. *Biomacromolecules* **2019**, *20* (7), 2441-2463.

317. Gao, F.; Xiong, Z. Reactive Oxygen Species Responsive Polymers for Drug Delivery Systems. *Front. Chem.* **2021**, *11*, 1115603.
318. Blair, J. M. A.; Webber, M. A.; Baylay, A. J.; Ogbolu, D. O.; Piddock, L. J. V. Molecular Mechanisms of Antibiotic Resistance. *Nat. Rev. Microbiol.* **2015**, *13* (1), 42-51.
319. *WHO List of Medically Important Antimicrobials*; World Health Organization, 2024. <https://www.who.int/news/item/08-02-2024-who-medically-important-antimicrobial-list-2024>.
320. Cremin, K.; Jones, B. A.; Teahan, J.; Meloni, G. N.; Perry, D.; Zerfass, C.; Asally, M.; Soyer, O. S.; Unwin, P. R. Scanning Ion Conductance Microscopy Reveals Differences in the Ionic Environments of Gram-Positive and Negative Bacteria. *Anal. Chem.* **2020**, *92* (24), 16024-16032.
321. Wilhelm, M. J.; Sheffield, J. B.; Sharifian Gh, M.; Wu, Y.; Spahr, C.; Gonella, G.; Xu, B.; Dai, H.-L. Gram's Stain Does Not Cross the Bacterial Cytoplasmic Membrane. *ACS Chem. Biol.* **2015**, *10* (7), 1711-1717.
322. Uddin, T. M.; Chakraborty, A. J.; Khusro, A.; Zidan, B. M. R. M.; Mitra, S.; Emran, T. B.; Dhama, K.; Ripon, M. K. H.; Gajdács, M.; Sahibzada, M. U. K.; et al. Antibiotic Resistance in Microbes: History, Mechanisms, Therapeutic Strategies and Future Prospects. *J. Infect. Public Health* **2021**, *14* (12), 1750-1766.
323. Saxena, D.; Maitra, R.; Bormon, R.; Czekanska, M.; Meiers, J.; Titz, A.; Verma, S.; Chopra, S. Tackling the Outer Membrane: Facilitating Compound Entry into Gram-Negative Bacterial Pathogens. *npj Antimicrob. Resist.* **2023**, *1* (1), 17.
324. Lewis, K. Platforms for Antibiotic Discovery. *Nat. Rev. Drug Discov.* **2013**, *12* (5), 371-387.
325. Si, Z.; Zheng, W.; Prananty, D.; Li, J.; Koh, C. H.; Kang, E.-T.; Pethe, K.; Chan-Park, M. B. Polymers as Advanced Antibacterial and Antibiofilm Agents for Direct and Combination Therapies. *Chem. Sci.* **2022**, *13* (2), 345-364.

326. Gross, M.; Cramton, S. E.; Götz, F.; Peschel, A. Key Role of Teichoic Acid Net Charge in *Staphylococcus aureus* Colonization of Artificial Surfaces. *Infect. Immun.* **2001**, *69* (5), 3423-3426.
327. Hoque, J.; Akkapeddi, P.; Yadav, V.; Manjunath, G. B.; Uppu, D. S. S. M.; Konai, M. M.; Yarlagadda, V.; Sanyal, K.; Haldar, J. Broad Spectrum Antibacterial and Antifungal Polymeric Paint Materials: Synthesis, Structure–Activity Relationship, and Membrane-Active Mode of Action. *ACS Appl. Mater. Interfaces* **2015**, *7* (3), 1804-1815.
328. Kohanski, M. A.; Dwyer, D. J.; Collins, J. J. How Antibiotics Kill Bacteria: From Targets to Networks. *Nat. Rev. Microbiol.* **2010**, *8* (6), 423-435.
329. Halawa, E. M.; Fadel, M.; Al-Rabia, M. W.; Behairy, A.; Nouh, N. A.; Abdo, M.; Olga, R.; Fericean, L.; Atwa, A. M.; El-Nablaway, M.; et al. Antibiotic Action and Resistance: Updated Review of Mechanisms, Spread, Influencing Factors, and Alternative Approaches for Combating Resistance. *Front. Pharmacol.* **2024**, *14*, 1305294.
330. Shi, J.; Chen, C.; Wang, D.; Wang, Z.; Liu, Y. The Antimicrobial Peptide LI14 Combats Multidrug-Resistant Bacterial Infections. *Commun. Biol.* **2022**, *5* (1), 926.
331. Liu, M.; Li, J.; Li, B. Mannose-Modified Polyethylenimine: A Specific and Effective Antibacterial Agent against *Escherichia Coli*. *Langmuir* **2018**, *34* (4), 1574-1580.
332. Chin, W.; Zhong, G.; Pu, Q.; Yang, C.; Lou, W.; De Sessions, P. F.; Periaswamy, B.; Lee, A.; Liang, Z. C.; Ding, X.; et al. A Macromolecular Approach to Eradicate Multidrug Resistant Bacterial Infections While Mitigating Drug Resistance Onset. *Nat. Commun.* **2018**, *9* (1), 917.
333. Parkin, H. C.; Street, S. T. G.; Gowen, B.; Da-Silva-Correa, L. H.; Hof, R.; Buckley, H. L.; Manners, I. Mechanism of Action and Design of Potent Antibacterial Block Copolymer Nanoparticles. *J. Am. Chem. Soc.* **2024**, *146* (8), 5128-5141.
334. Cuthbert, T. J.; Hisey, B.; Harrison, T. D.; Trant, J. F.; Gillies, E. R.; Ragogna, P. J. Surprising Antibacterial Activity and Selectivity of Hydrophilic Polyphosphoniums

- Featuring Sugar and Hydroxy Substituents. *Angew. Chem. Int. Ed.* **2018**, *57* (39), 12707-12710.
335. Kудay, H.; Süer, N. C.; Bayır, A.; Aksu, B.; Hatipoğlu, A.; Güncü, M. M.; Acaroğlu Degitz, İ.; Gallei, M.; Eren, T. Design of Aromatic Ring-Based Polyphosphonium Salts Synthesized via ROMP and the Investigation into Their Antibacterial and Hemolytic Activities. *ACS Appl. Polym. Mater.* **2021**, *3* (12), 6524-6538.
336. Sun, X.; Cao, P.; Bai, X.; He, Y.; Song, P.; Wang, R. Poly(phosphonium)-functionalized Double-Armed  $\beta$ -CD Antimicrobial Material via RAFT. *Macromolecules* **2023**, *56* (23), 9498-9508.
337. Hou, Z.; Shankar, Y. V.; Liu, Y.; Ding, F.; Subramanion, J. L.; Ravikumar, V.; Zamudio-Vázquez, R.; Keogh, D.; Lim, H.; Tay, M. Y. F.; et al. Nanoparticles of Short Cationic Peptidopolysaccharide Self-Assembled by Hydrogen Bonding with Antibacterial Effect against Multidrug-Resistant Bacteria. *ACS Appl. Mater. Interfaces* **2017**, *9* (44), 38288-38303.
338. Shen, W.; He, P.; Xiao, C.; Chen, X. From Antimicrobial Peptides to Antimicrobial Poly( $\alpha$ -amino acid)s. *Adv. Healthcare Mater.* **2018**, *7* (20), 1800354.
339. Liu, L.; Courtney, K. C.; Huth, S. W.; Rank, L. A.; Weisblum, B.; Chapman, E. R.; Gellman, S. H. Beyond Amphiphilic Balance: Changing Subunit Stereochemistry Alters the Pore-Forming Activity of Nylon-3 Polymers. *J. Am. Chem. Soc.* **2021**, *143* (8), 3219-3230.
340. Gao, W.; Chen, Y.; Zhang, Y.; Zhang, Q.; Zhang, L. Nanoparticle-based Local Antimicrobial Drug Delivery. *Adv. Drug Del. Rev.* **2018**, *127*, 46-57.
341. Yeh, Y.-C.; Huang, T.-H.; Yang, S.-C.; Chen, C.-C.; Fang, J.-Y. Nano-based Drug Delivery or Targeting to Eradicate Bacteria for Infection Mitigation: A Review of Recent Advances. *Front. Chem.* **2020**, *8*, 286.
342. Mondal, S. K.; Chakraborty, S.; Manna, S.; Mandal, S. M. Antimicrobial Nanoparticles: Current Landscape and Future Challenges. *RSC Pharm.* **2024**, *1*, 388-402.

343. Roy Choudhury, S.; Ghosh, M.; Mandal, A.; Chakravorty, D.; Pal, M.; Pradhan, S.; Goswami, A. Surface-Modified Sulfur Nanoparticles: An Effective Antifungal Agent against *Aspergillus niger* and *Fusarium oxysporum*. *Appl. Microbiol. Biotechnol.* **2011**, *90* (2), 733-743.
344. Chen, M.; Xie, S.; Wei, J.; Song, X.; Ding, Z.; Li, X. Antibacterial Micelles with Vancomycin-Mediated Targeting and pH/Lipase-Triggered Release of Antibiotics. *ACS Appl. Mater. Interfaces* **2018**, *10* (43), 36814-36823.
345. Hisey, B.; Ragogna, P. J.; Gillies, E. R. Phosphonium-Functionalized Polymer Micelles with Intrinsic Antibacterial Activity. *Biomacromolecules* **2017**, *18* (3), 914-923.
346. Ghosh, D.; Yadav, S.; Bag, S.; Mallick, A. I.; De, P. Antibacterial Activity of Hydrophobicity Modulated Cationic Polymers with Enzyme and pH-Responsiveness. *J. Mater. Chem. B* **2024**, *12* (11), 2894-2904.
347. Fan, X.; Cheng, H.; Wang, X.; Ye, E.; Loh, X. J.; Wu, Y.-L.; Li, Z. Thermoresponsive Supramolecular Chemotherapy by “V”-Shaped Armed  $\beta$ -Cyclodextrin Star Polymer to Overcome Drug Resistance. *Adv. Healthcare Mater.* **2018**, *7* (7), 1701143.
348. Sharma, R.; Ungar, D.; Dyson, E.; Rimmer, S.; Chechik, V. Functional Magnetic Nanoparticles for Protein Delivery Applications: Understanding Protein–Nanoparticle Interactions. *Nanoscale* **2024**, *16* (5), 2466-2477.
349. Doberenz, F.; Zeng, K.; Willems, C.; Zhang, K.; Groth, T. Thermoresponsive Polymers and Their Biomedical Application in Tissue Engineering – a Review. *J. Mater. Chem. B* **2020**, *8* (4), 607-628.
350. Nakamura, M.; Nishimura, S.-n.; Higashi, N.; Koga, T. Thermo-Responsive Injectable Hydrogels from Linear and Star-Shaped Block Copolymers Composed of Amino Acid-Derived Vinyl Polymer and Poly(ethylene glycol) for Biomedical Applications. *Mater. Adv.* **2024**, *5* (2), 665-674.

351. Mairal, A.; Mehrotra, S.; Kumar, A.; Maiwal, R.; Marsal, J.; Kumar, A. Hyaluronic Acid-Conjugated Thermoresponsive Polymer-Based Bioformulation Enhanced Wound Healing and Gut Barrier Repair of a TNBS-Induced Colitis Injury *Ex Vivo* Model in a Dynamic Perfusion Device. *ACS Appl. Mater. Interfaces* **2024**, *16* (5), 5382-5400.
352. Vanparijs, N.; Nuhn, L.; De Geest, B. G. Transiently Thermoresponsive Polymers and Their Applications in Biomedicine. *Chem. Soc. Rev.* **2017**, *46* (4), 1193-1239.
353. Xu, X.; Bizmark, N.; Christie, K. S. S.; Datta, S. S.; Ren, Z. J.; Priestley, R. D. Thermoresponsive Polymers for Water Treatment and Collection. *Macromolecules* **2022**, *55* (6), 1894-1909.
354. Zeqiri, E.; da Silva, M. A.; Aspinall, S. R.; Hoffman, E.; Hutter, V.; Cook, M. T. Thermoreversible Gels for the Encapsulation of Macrophages: Evaluation of Polymer Type on Rheology and Cytocompatibility. *RSC Appl. Polym.* **2024**, *2* (1), 32-46.
355. Luo, G.-F.; Chen, W.-H.; Zhang, X.-Z. 100th Anniversary of Macromolecular Science Viewpoint: Poly(*N*-isopropylacrylamide)-based Thermally Responsive Micelles. *ACS Mater. Lett.* **2020**, *9* (6), 872-881.
356. Narumi, A.; Sato, S.-i.; Shen, X.; Kakuchi, T. Precision Synthesis for Well-Defined Linear and/or Architecturally Controlled Thermoresponsive Poly(*N*-substituted acrylamide)s. *Polym. Chem.* **2022**, *13* (10), 1293-1319.
357. Goyal, R.; Sahu, S.; Mitra, S.; Niranjana, R.; Priyadarshini, R.; Yadav, R.; Lochab, B. Nanocellulose-Reinforced 4D Printed Hydrogels: Thermoresponsive Shape Morphing and Drug Release. *ACS Appl. Polym. Mater.* **2024**, *6* (2), 1348-1361.
358. Yang, L.; Ren, P.; Wei, D.; Liang, M.; Xu, L.; Tao, Y.; Jiao, G.; Zhang, T.; Zhang, Q. Temperature-Controlled Screening of Catechol Groups in Poly(*N*-isopropylacrylamide-*co*-dopamine methacrylamide) for Cell Detachment. *ACS Appl. Polym. Mater.* **2024**, *6* (4), 2061-2075.

359. Zhang, X.; Ding, H.; Li, Z.; Bai, Y.; Zhang, L. A “Mesh Scaffold” That Regulates the Mechanical Properties and Restricts the Phase Transition-Induced Volume Change of the PNIPAM-Based Hydrogel for Wearable Sensors. *Mater. Horiz.* **2024**, *11* (3), 835-846.
360. Longenecker, R.; Mu, T.; Hanna, M.; Burke, N. A. D.; Stöver, H. D. H. Thermally Responsive 2-Hydroxyethyl Methacrylate Polymers: Soluble–Insoluble and Soluble–Insoluble–Soluble Transitions. *Macromolecules* **2011**, *44* (22), 8962-8971.
361. Roth, P. J.; Jochum, F. D.; Theato, P. UCST-Type Behavior of Poly[oligo(ethylene glycol) methyl ether methacrylate] (POEGMA) in Aliphatic Alcohols: Solvent, Co-Solvent, Molecular Weight, and End Group Dependences. *Soft Matter* **2011**, *7* (6), 2484-2492.
362. Niskanen, J.; Tenhu, H. How to Manipulate the Upper Critical Solution Temperature (UCST)? *Polym. Chem.* **2017**, *8* (1), 220-232.
363. Seuring, J.; Agarwal, S. First Example of a Universal and Cost-Effective Approach: Polymers with Tunable Upper Critical Solution Temperature in Water and Electrolyte Solution. *Macromolecules* **2012**, *45* (9), 3910-3918.
364. Zhao, C.; Dolmans, L.; Zhu, X. X. Thermoresponsive Behavior of Poly(acrylic acid-co-acrylonitrile) with a UCST. *Macromolecules* **2019**, *52* (12), 4441-4446.
365. Zhang, Z.; Li, H.; Kasmi, S.; Van Herck, S.; Deswarte, K.; Lambrecht, B. N.; Hoogenboom, R.; Nuhn, L.; De Geest, B. G. A Synthetic, Transiently Thermoresponsive Homopolymer with UCST Behaviour within a Physiologically Relevant Window. *Angew. Chem. Int. Ed.* **2019**, *58* (23), 7866-7872.
366. Seuring, J.; Bayer, F. M.; Huber, K.; Agarwal, S. Upper Critical Solution Temperature of Poly(*N*-acryloyl glycinamide) in Water: A Concealed Property. *Macromolecules* **2012**, *45* (1), 374-384.
367. Xu, Z.; Liu, W. Poly(*N*-acryloyl glycinamide): A Fascinating Polymer That Exhibits a Range of Properties from UCST to High-Strength Hydrogels. *Chem. Commun.* **2018**, *54* (75), 10540-10553.

368. Hui, L.; Qin, S.; Yang, L. Upper Critical Solution Temperature Polymer, Photothermal Agent, and Erythrocyte Membrane Coating: An Unexplored Recipe for Making Drug Carriers with Spatiotemporally Controlled Cargo Release. *ACS Biomater. Sci. Eng.* **2016**, *2* (12), 2127-2132.
369. Lin, S.; Shang, J.; Theato, P. CO<sub>2</sub>-Triggered UCST Transition of Amphiphilic Triblock Copolymers and Their Self-Assemblies. *Polym. Chem.* **2017**, *8* (17), 2619-2629.
370. Vishnevetskaya, N. S.; Hildebrand, V.; Niebuur, B.-J.; Grillo, I.; Filippov, S. K.; Laschewsky, A.; Müller-Buschbaum, P.; Papadakis, C. M. Aggregation Behavior of Doubly Thermoresponsive Polysulfobetaine-*b*-Poly(*N*-isopropylacrylamide) Diblock Copolymers. *Macromolecules* **2016**, *49* (17), 6655-6668.
371. Aoki, T.; Nakamura, K.; Sanui, K.; Kikuchi, A.; Okano, T.; Sakurai, Y.; Ogata, N. Adenosine-Induced Changes of the Phase Transition of Poly(6-(acryloyloxymethyl)uracil) Aqueous Solution. *Polym. J.* **1999**, *31* (11), 1185-1188.
372. Shimada, N.; Ino, H.; Maie, K.; Nakayama, M.; Kano, A.; Maruyama, A. Ureido-Derivatized Polymers Based on Both Poly(allylurea) and Poly(L-citrulline) Exhibit UCST-Type Phase Transition Behavior under Physiologically Relevant Conditions. *Biomacromolecules* **2011**, *12* (10), 3418-3422.
373. Meiswinkel, G.; Ritter, H. A New Type of Thermoresponsive Copolymer with UCST-Type Transitions in Water: Poly(*N*-vinylimidazole-*co*-1-vinyl-2-(hydroxymethyl)imidazole). *Macromol. Rapid Commun.* **2013**, *34* (12), 1026-1031.
374. Di, Y.; Ma, X.; Li, C.; Liu, H.; Fan, X.; Wang, M.; Deng, H.; Jiang, T.; Yin, Z.; Deng, K. A New Thermosensitive Poly(*N*-propionyl-aspartic acid/ethylene glycol) with No Cytotoxicity and Tunable UCST. *Macromol. Chem. Phys.* **2014**, *215* (4), 365-371.
375. Zhang, H.; Tong, X.; Zhao, Y. Diverse Thermoresponsive Behaviors of Uncharged UCST Block Copolymer Micelles in Physiological Medium. *Langmuir* **2014**, *30* (38), 11433-11441.

376. Li, W.-S.; Wang, X.-J.; Zhang, S.; Hu, J.-B.; Du, Y.-L.; Kang, X.-Q.; Xu, X.-L.; Ying, X.-Y.; You, J.; Du, Y.-Z. Mild Microwave Activated, Chemo-Thermal Combinational Tumor Therapy Based on a Targeted, Thermal-Sensitive and Magnetic Micelle. *Biomaterials* **2017**, *131*, 36-46.
377. Deng, Y.; Käfer, F.; Chen, T.; Jin, Q.; Ji, J.; Agarwal, S. Let There Be Light: Polymeric Micelles with Upper Critical Solution Temperature as Light-Triggered Heat Nanogenerators for Combating Drug-Resistant Cancer. *Small* **2018**, *14* (37), 1802420.
378. Tseng, W.-C.; Fang, T.-Y.; Lin, Y.-C.; Huang, S.-J.; Huang, Y.-H. Reversible Self-Assembly Nanovesicle of UCST Response Prepared with Multi-L-Arginyl-Poly-L-Aspartate Conjugated with Polyethylene Glycol. *Biomacromolecules* **2018**, *19* (12), 4585-4592.
379. Yang, J.; Zhai, S.; Qin, H.; Yan, H.; Xing, D.; Hu, X. NIR-Controlled Morphology Transformation and Pulsatile Drug Delivery Based on Multifunctional Phototheranostic Nanoparticles for Photoacoustic Imaging-Guided Photothermal-Chemotherapy. *Biomaterials* **2018**, *176*, 1-12.
380. Yang, Z.; Cheng, R.; Zhao, C.; Sun, N.; Luo, H.; Chen, Y.; Liu, Z.; Li, X.; Liu, J.; Tian, Z. Thermo- and pH-Dual Responsive Polymeric Micelles with Upper Critical Solution Temperature Behavior for Photoacoustic Imaging-Guided Synergistic Chemo-Photothermal Therapy against Subcutaneous and Metastatic Breast Tumors. *Theranostics* **2018**, *8* (15), 4097-4115.
381. Bordat, A.; Soliman, N.; Ben Chraït, I.; Manerlax, K.; Yagoubi, N.; Boissenot, T.; Nicolas, J.; Tsapis, N. The Crucial Role of Macromolecular Engineering, Drug Encapsulation and Dilution on the Thermoresponsiveness of UCST Diblock Copolymer Nanoparticles Used for Hyperthermia. *Eur. J. Pharm. Biopharm.* **2019**, *142*, 281-290.
382. Jiang, D.; Chen, C.; Xue, Y.; Cao, H.; Wang, C.; Yang, G.; Gao, Y.; Wang, P.; Zhang, W. NIR-Triggered “Off/on” Photodynamic Therapy through a Upper Critical Solution Temperature Block Copolymer. *ACS Appl. Mater. Interfaces* **2019**, *11* (40), 37121-37129.

383. Tian, J.; Huang, B.; Li, H.; Cao, H.; Zhang, W. NIR-Activated Polymeric Nanoplatform with Upper Critical Solution Temperature for Image-Guided Synergistic Photothermal Therapy and Chemotherapy. *Biomacromolecules* **2019**, *20* (6), 2338-2349.
384. Zhao, D.; Rajan, R.; Matsumura, K. Dual Thermo- and pH-Responsive Behavior of Double Zwitterionic Graft Copolymers for Suppression of Protein Aggregation and Protein Release. *ACS Appl. Mater. Interfaces* **2019**, *11* (43), 39459-39469.
385. Zhu, S.; Wen, L.; Xiao, Y.; Lang, M. Poly( $\epsilon$ -Caprolactone) with pH and UCST Responsiveness as a 5-Fluorouracil Carrier. *Polym. Chem.* **2020**, *11* (32), 5173-5180.
386. Jia, Y.-G.; Chen, K.-F.; Gao, M.; Liu, S.; Wang, J.; Chen, X.; Wang, L.; Chen, Y.; Song, W.; Zhang, H.; et al. Visualizing Phase Transition of Upper Critical Solution Temperature (UCST) Polymers with AIE. *Sci. China: Chem.* **2021**, *64* (3), 403-407.

# Chapter 2: Single Functional Group Platform for Multi-Stimuli Responsivities: Tertiary Amine for CO<sub>2</sub>/pH/ROS-Triggered Cargo Release in Nanocarriers

## 2.1. Opening Remarks

Stimuli-responsive polymers offer a promising platform for the design of nanoformulations capable of controlled and sustained release of active pharmaceutical agents, addressing crucial requirements in drug delivery systems. These characteristics were extensively evaluated in Chapter 1. However, despite significant advancements, there is still an unmet need for simplifying the synthetic design of responsive nanoparticles (NPs), particularly by utilizing a versatile chemical entity capable of responding to multiple targets simultaneously. In Chapter 2, we aim to address this gap by demonstrating the feasibility of utilizing a single, multifunctional tertiary amine to achieve NPs responsive to CO<sub>2</sub>, pH, ROS, and CO<sub>2</sub> + ROS. The tertiary amine, integrated in the NP core, endows the NPs with multi-stimuli responsiveness, facilitating precise drug release in response to various environmental cues. Moreover, we show the performance of the drug-loaded NPs *in vitro*, evaluating their efficacy and therapeutic outcomes. Overall, the findings presented in this chapter offer an innovative approach to obtain multistimuli-responsive NPs as effective drug delivery systems.

This chapter is adapted from a published article, which is reprinted with permission from the American Chemical Society. The citation is as follows:

Yong, H. W.; Ferron, M.; Mecteau, M.; Mihalache-Avram, T.; Lévesque, S.; Rhéaume, É.; Tardif, J.- C.; Kakkar, A. Single Functional Group Platform for Multistimuli Responsivities: Tertiary Amine for CO<sub>2</sub>/pH/ROS-Triggered Cargo Release in Nanocarriers. *Biomacromolecules* **2023**, *24*, 4064–4077.

## 2.2. Abstract

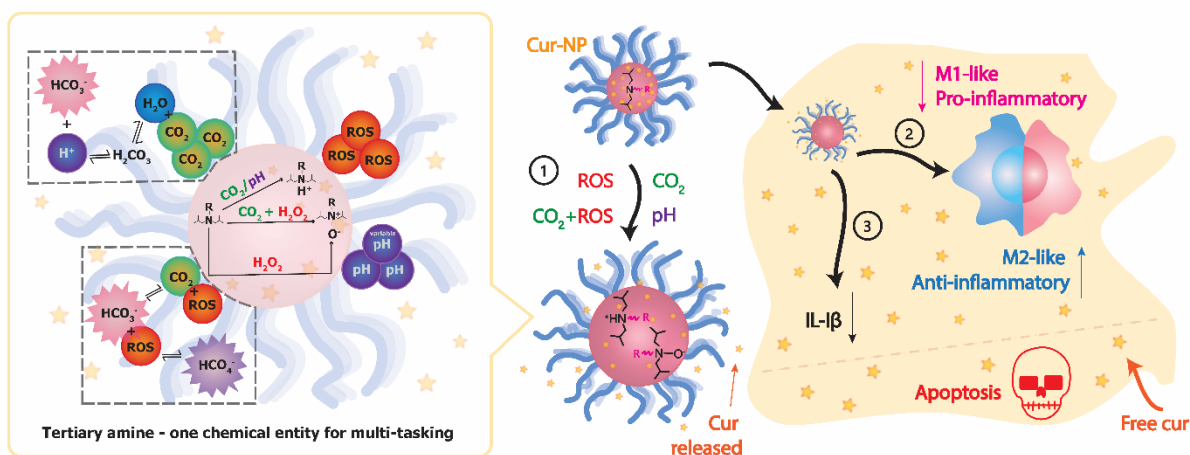
Design of multi-stimuli responsive soft NP often presents synthetic complexities and limited breadth in exploiting changes surrounding physiological environments. Nanocarriers that could collectively take advantage of several endogenous stimuli can offer a powerful tool in nanomedicine. Herein, we have capitalized on the chemical versatility of a single tertiary amine to construct miktoarm polymers based nanocarriers that respond to dissolved CO<sub>2</sub>, varied pH, reactive oxygen species (ROS), and ROS+CO<sub>2</sub>. Curcumin (Cur), an anti-inflammatory phytopharmaceutic, was loaded into micelles, and we validated the sensitivity of the tertiary amine in tuning Cur release. An *in vitro* evaluation indicated that Cur encapsulation strongly suppressed its toxicity at high concentrations; significantly inhibited nigericin-induced secretion of interleukin-1 $\beta$  by THP-1 macrophages; and the proportion of M2/M1 (anti-inflammatory/pro-inflammatory macrophages) was higher for Cur-loaded NPs than free Cur. Our approach highlights the potential of a simple-by-design strategy in expanding the scope of polymeric NPs in drug delivery.

## 2.3. Introduction

Polymeric NPs have advanced a viable approach in delivering poorly water-soluble drugs, reducing undesired toxicity, and facilitating clinical translation.<sup>1-4</sup> To enhance the efficacy of drug delivery nanotechnologies, significant emphasis has been placed on exploiting pathological alterations at disease locations including low pH, elevated reactive oxygen species (ROS) concentrations, higher temperatures etc., by incorporating selective chemical entities into their macromolecular precursors to achieve targeted delivery.<sup>5-11</sup> Such nanocarriers typically respond well to specific endogenous cues to enhance drug release.<sup>12, 13</sup> Due to insufficient biological understanding and complex double-edged behavior of biologically active gases, studies on gas-responsive polymers for drug delivery are progressing at a relatively slow pace.<sup>14-19</sup> As a regulator of blood pH, CO<sub>2</sub> exists mainly in 3 different forms in the body; the hydrated state (HCO<sub>3</sub><sup>-</sup>), bound to hemoglobin (carbamate), and as dissolved CO<sub>2</sub>.<sup>20</sup> At disease sites, especially tumor, the build-up of CO<sub>2</sub> (hypercapnia) tends to be associated with acidosis and hypoxia, which can confer chemoresistance in lung cancer cells, as well as aggravate pancreatic cancer.<sup>21, 22</sup> On top of that, the overproduction of reactive oxygen species (ROS), such as hydrogen peroxide (H<sub>2</sub>O<sub>2</sub>), superoxide (O<sub>2</sub><sup>•-</sup>), hydroxy radicals (•OH), and singlet oxygen (<sup>1</sup>O<sub>2</sub>) can cause dysfunctions that can be observed in pathologies

such as cardiovascular and neurodegenerative diseases, diabetes, and aging.<sup>23-27</sup> As such, changes in  $\text{CO}_2$ , pH and ROS concentrations constitute important markers in the microenvironments at disease sites. The interrelationships of these molecules and their implications are of great relevance to the progression, aggressiveness, and prevention of diseases. For example, it has been demonstrated that i) increased  $\text{CO}_2$  concentrations can intensify reactive oxygen species toxicity and  $\text{H}_2\text{O}_2$  induced mutagenesis; and ii) increased  $\text{HCO}_3^-/\text{CO}_2$  levels can enhance  $\text{H}_2\text{O}_2$ -mediated hyperoxidation.<sup>28, 29</sup>

Responsive behavior to soft NPs is generally conferred by introducing various chemical functional groups into the polymeric architecture.<sup>30-33</sup> It often adds to complexities in polymer synthesis, cost, scale-up etc., as well as limits their efficacy in exploiting the full potential of the biological cues.<sup>34, 35</sup> We questioned if a single chemical entity that could respond to diverse signals prevalent in the physiological environment ( $\text{CO}_2$ , pH and  $\text{H}_2\text{O}_2$ ) could offer a highly efficient formulation design strategy, and significantly enhance the scope of NPs in drug delivery. In this work, we demonstrate the utility of an extremely hydrophobic tertiary amine in configuring multistimuli-responsive NPs (Scheme 2. 1).



**Scheme 2. 1:** Schematic overview of the multi-responsive NP behavior achievable through a single functional group (bulky tertiary amine) incorporated into miktoarm copolymer precursor  $(\text{PEG}_{45})_2$ - $(\text{PCL}_{32}\text{-NR}_2)$ , and biological evaluation of Cur-loaded micelles.

Our choice for the tertiary amine as the sole stimuli-sensitive center for controlled release of therapeutic molecules such as Cur, was guided by its rich and versatile chemistry: ionizable groups such as tertiary amines respond very well to changes in pH;<sup>36</sup> and tertiary amines also undergo oxidation to N-oxides,<sup>37</sup> which can be catalyzed in the presence of CO<sub>2</sub>.<sup>38</sup> The latter is a multistep process and proceeds through formation of peroxymonocarbonate (HCO<sub>4</sub><sup>-</sup>), which accelerates the oxidation of tertiary amines into N-oxides. The protonation/oxidation of these chemical entities in local biological environments can induce an imbalance in hydrophobic/hydrophilic ratio and help tailor cargo release from micellar hydrophobic cores of nanoformulations.

Incorporating tertiary amines in each repeat unit of the hydrophobic polymer chain in the amphiphilic polymeric precursors to formulations, has been the mainstay in designing CO<sub>2</sub>-/pH-responsive drug delivery systems. Such nanocarriers have been successfully employed in accelerating low pH-triggered drug release from nanocarriers.<sup>39</sup> In our design strategy, with only one tertiary amine at the terminal end of the hydrophobic chain, we aimed to tune and obtain sustained drug release in response to any of the three stimuli or combinations thereof. Single tertiary amine covalently attached in this manner is expected to become a part of and contribute towards the overall core hydrophobicity upon aqueous self-assembly. Therefore, subtle changes brought on in acidic or oxidizing media will perturb the core environment, enforcing modifications in the chain packing. This will result in NP swelling and create a less favorable core environment for any lipophilic drug. These subtle disruptions will expedite cargo release.

Stimuli-responsive amphiphilic branched AB<sub>2</sub> architecture reported here, contained a biodegradable polycaprolactone (PCL, A) arm terminated with diisobutylamine (forming the tertiary amine), and two biocompatible polyethylene glycol (PEG, B) chains. Polymer composition is an important variable in enhancing the efficacy of nanoformulations in therapeutic interventions. Amphiphilic linear block copolymers have been extensively investigated in developing colloidal suspensions for drug delivery. Asymmetric branched polymers offer a platform to vary the arrangement of their hydrophobic/hydrophilic components in space. For example, keeping a similar composition to that of a linear AB copolymer, the molecular weights of the individual B arms are lowered in AB<sub>n</sub>-type arrangements, leading to reduced chain entanglement. Therefore, core-shell formulations from the aqueous self-assemblies of miktoarm stars possess highly beneficial traits

including small dimensions, low critical micelle concentrations (CMCs), denser corona, enhanced stability, high encapsulation efficiencies etc.<sup>40-42</sup> In addition, due to the ease of introducing different polymeric arms, many studies have focused on personalizing miktoarm copolymers with desired functions for better outcomes in intended applications.<sup>43-46</sup> In the current study, we utilized the branched architecture to design a stimuli-responsive miktoarm polymer with a tertiary amine group that became an intricate part of the micelle hydrophobic core, offering tuned responsiveness to various stimuli (CO<sub>2</sub>, pH, ROS, and ROS+CO<sub>2</sub>) and resulting in controlled release of Cur.

Cur, a flavonoid polyphenol found in the rhizome of turmeric, has been extensively investigated for its beneficial pleiotropic therapeutic effects, especially through antioxidant and anti-inflammatory mechanisms of action. It is known to target several signaling pathways and regulate biological activities of the cell.<sup>47</sup> However, its clinical efficacy is severely limited by its poor bioavailability, which is mainly due to its extremely low solubility in water (~0.6 µg/mL) and limited stability.<sup>48</sup> Cur is widely used in food recipes in Asia, and even with high safe dosages of approximately 12 g/day, its poor bioavailability of less than 1% limits its concentration in circulation.<sup>49</sup> Several strategies to overcome these limitations and enhance the pharmacological virtue of Cur have been explored over the years.<sup>50</sup> With our stimuli-responsive miktoarm-based assemblies, we demonstrate that encapsulation of this anti-inflammatory drug into nanoformulations (i) strongly suppresses its toxicity; ii) significantly inhibits nigericin-induced secretion of interleukin-1 $\beta$ , a powerful pro-inflammatory cytokine, by THP-1 macrophages; and iii) increase the proportion of M2/M1 (anti-inflammatory/pro-inflammatory macrophages ensuing polarization) compared to free Cur at high concentrations. Our studies suggested much lower toxicity and better sustained efficacy of Cur-polymeric formulations in pathologies where the anti-inflammatory properties of this phytopharmaceutic are needed.

## 2.4. Experimental Section

### Materials

Bromoacetyl bromide ( $\geq 98\%$ , Sigma-Aldrich),  $\epsilon$ -caprolactone monomer (99%, ACROS Organics), copper (I) bromide (CuBr, 98%, Sigma-Aldrich), 18-crown-6 (99%, Sigma-Aldrich), curcumin (Cur,  $\geq 65\%$ , Sigma-Aldrich), 3,5-dihydroxybenzyl alcohol (99%, Sigma-Aldrich), diisobutylamine (99%, Sigma-Aldrich), ethylenediaminetetraacetic acid disodium salt dihydrate

(EDTA) (99.0-101.0%, Sigma-Aldrich), magnesium sulfate anhydrous ( $\text{MgSO}_4$ , Fisher Chemical), *N,N,N',N'',N''*-pentamethyldiethylenetriamine (PMDETA) (99%, Sigma-Aldrich), potassium carbonate ( $\text{K}_2\text{CO}_3$ ,  $\geq 99.0\%$ , ACP Chemicals), poly(ethylene glycol) methyl ether (MePEG<sub>2000</sub>-OTs, 2000 g/mol, TCI Chemicals), propargyl bromide (~80% in toluene, Sigma-Aldrich), pyrene (98%, Sigma-Aldrich), sodium bicarbonate ( $\text{NaHCO}_3$ , 99.7-100.3%, Fisher Chemical), sodium hydroxide ( $\text{NaOH}$ ,  $\geq 97\%$ , ACP chemicals), sodium azide ( $\text{NaN}_3$ ,  $\geq 99.5\%$ , Sigma-Aldrich), *p*-toluenesulfonyl chloride ( $\geq 98\%$ , Sigma-Aldrich), triethylamine (ACP chemicals), and tin(II) 2-ethylhexanoate ( $\text{Sn}(\text{Oct})_2$ , 92.5-100.0%, Sigma-Aldrich) were used as received. 13 mm PVDF filters (0.22  $\mu\text{m}$ , non-sterile) were purchased from SyringeFilter.com.

### Synthesis of (MePEG<sub>2000</sub>)<sub>2</sub>-PCL<sub>3600</sub> (MP1)

Synthesis of hydrophobic PCL arm (2) and hydrophilic PEG arm (3) can be found in Appendix A. To a stirred solution of 2 (0.200 g, 0.100 mmol, 1 eq) in dry THF, 3 (0.235 g, 0.061 mmol, 2 eq) and CuBr (0.018 g, 0.125 mmol, 2.5 eq) were added under nitrogen with magnetic stirring. A separate solution of PMDETA (0.022 g, 0.127 mmol, 2.5 eq) in dry THF was subsequently added and the mixture was allowed to react at room temperature for 48 h. The solution was then concentrated and dialysed once with EDTA and twice with deionized water for 24 h each. The solution was then concentrated and precipitated in cold diethyl ether. The product was collected with vacuum filtration and dried in the desiccator (0.3 g, 76% yield).  $^1\text{H}$  NMR ( $\text{CDCl}_3$ , 500 MHz):  $\delta$  (ppm) 1.34- 1.40 (m, 68H, (-OC-CH<sub>2</sub>-CH<sub>2</sub>-CH<sub>2</sub>-CH<sub>2</sub>-CH<sub>2</sub>-O)<sub>33</sub>), 1.60- 1.67 (m, 133H, (-OC-CH<sub>2</sub>-CH<sub>2</sub>-CH<sub>2</sub>-CH<sub>2</sub>-CH<sub>2</sub>-O)<sub>33</sub>), 2.29 (t, 66H, (-OC-CH<sub>2</sub>-CH<sub>2</sub>-CH<sub>2</sub>-CH<sub>2</sub>-CH<sub>2</sub>-O)<sub>33</sub>), 3.37 (s, 6H, -OCH<sub>3</sub>), 3.63 (s, 358H, CH<sub>2</sub>-CH<sub>2</sub>-O), 4.05 (t, 65H, (-OC-CH<sub>2</sub>-CH<sub>2</sub>-CH<sub>2</sub>-CH<sub>2</sub>-CH<sub>2</sub>-O)<sub>33</sub>).  $^{13}\text{C}$  { $^1\text{H}$ } NMR ( $\text{CDCl}_3$ , 125 MHz):  $\delta$  (ppm) 24.7, 25.7, 28.5, 34.2, 64.3, 174.

### Synthesis of MABr

To a solution of MP1 (7900 g/mol, 0.310 g, 0.039 mmol, 1 eq) in dry THF (30 mL), triethylamine (0.019 mL, 0.188 mmol, 5 eq) was added and cooled in an ice bath. Bromoacetyl bromide (0.317 mL, 1.571 mmol, 40 eq) was dissolved in dry THF (20 mL) and added slowly by dropwise addition. The solution was allowed to raise to room temperature and react for 24 h under nitrogen gas with magnetic stirring. The crude product was filtered by vacuum filtration and the filtrate was dried under reduced pressure, dissolved in DCM, and washed with  $\text{NaHCO}_3$  and deionized water thrice.

The organic solution was collected and dried with  $\text{MgSO}_4$ , concentrated, and precipitated by dropwise addition into ice cold diethyl ether (1:10= DCM: diethyl ether). The product was then centrifuged at 3000 rpm for 10 minutes and the precipitate was collected and dried in a desiccator (0.2 g, 75% yield).  $^1\text{H}$  NMR ( $\text{CDCl}_3$ , 500 MHz):  $\delta$  (ppm) 1.37- 1.40 (m, 69H, (-OC- $\text{CH}_2$ - $\text{CH}_2$ - $\text{CH}_2$ - $\text{CH}_2$ - $\text{CH}_2$ -O) $_{33}$ ), 1.61- 1.67 (m, 139H, (-OC- $\text{CH}_2$ - $\text{CH}_2$ - $\text{CH}_2$ - $\text{CH}_2$ - $\text{CH}_2$ -O) $_{33}$ ), 2.30 (t, 67H, (-OC- $\text{CH}_2$ - $\text{CH}_2$ - $\text{CH}_2$ - $\text{CH}_2$ - $\text{CH}_2$ -O) $_{33}$ ), 3.37 (s, 3H, -OCH $_3$ ), 3.45- 3.70 (m, 347H,  $\text{CH}_2$ - $\text{CH}_2$ -O), 3.82 (s, 2H, CH $_2$ -Br), 4.05 (t, 67H, (-OC- $\text{CH}_2$ - $\text{CH}_2$ - $\text{CH}_2$ - $\text{CH}_2$ - $\text{CH}_2$ -O) $_{33}$ ).  $^{13}\text{C}$   $\{^1\text{H}\}$  NMR ( $\text{CDCl}_3$ , 125 MHz):  $\delta$  (ppm) 24.7, 25.6, 28.5, 34.2, 59.2, 64.3, 70.7, 173.4.

### Synthesis of TA-MP2

To a solution of MABr (3600 g/mol, 0.232 g, 0.029 mmol, 1 eq) in dry DMF (30 mL), diisobutylamine (0.019 mL, 0.147 mmol, 5 eq) was added under nitrogen. The reaction mixture was heated to 85 °C under nitrogen for 24 h. The solution was allowed to cool and precipitated by dropwise addition into ice cold diethyl ether (1:10= DCM: diethyl ether). The product was then centrifuged at 3000 rpm for 10 minutes and the precipitate was collected and dried in a desiccator (0.2 g, 77% yield).  $^1\text{H}$  NMR ( $\text{CDCl}_3$ , 500 MHz):  $\delta$  (ppm) 0.86 (d, 12H, N- $\text{CH}_2\text{CH}(\text{CH}_3)_2$ ), 1.34- 1.40 (m, 71H, (-OC- $\text{CH}_2$ - $\text{CH}_2$ - $\text{CH}_2$ - $\text{CH}_2$ - $\text{CH}_2$ -O) $_{33}$  and N- $\text{CH}_2\text{CH}(\text{CH}_3)_2$ ), 1.60- 1.67 (m, 141H, (-OC- $\text{CH}_2$ - $\text{CH}_2$ - $\text{CH}_2$ - $\text{CH}_2$ - $\text{CH}_2$ -O) $_{33}$  and N- $\text{CH}_2\text{CH}(\text{CH}_3)_2$ ), 2.29 (t, 68H, (-OC- $\text{CH}_2$ - $\text{CH}_2$ - $\text{CH}_2$ - $\text{CH}_2$ - $\text{CH}_2$ -O) $_{33}$ ), 3.28 (s, 2H, CH $_2$ ), 3.37 (s, 6H, -OCH $_3$ ), 3.63 (m, 361H,  $\text{CH}_2$ - $\text{CH}_2$ -O), 4.05 (t, 69H, (-OC- $\text{CH}_2$ - $\text{CH}_2$ - $\text{CH}_2$ - $\text{CH}_2$ - $\text{CH}_2$ -O) $_{33}$ ).  $^{13}\text{C}$   $\{^1\text{H}\}$  NMR ( $\text{CDCl}_3$ , 125 MHz):  $\delta$  (ppm) 20.7, 24.7, 25.6, 26.9, 28.5, 34.2, 59.2, 63.5, 64.3, 60.6, 72.1, 173.7.

### Preparation of blank and Cur-loaded polymeric micelles

In brief, MP1 or TA-MP2 (5.0 mg) was dissolved in HPLC grade acetone (2 mL). In a separate vial, Cur (0.5 mg) was dissolved in HPLC grade acetone (1 mL). The two solutions were mixed and dropped into Milli-Q water (2 mL) at a rate of 1 drop  $\text{s}^{-1}$  while stirring. The mixture was left exposed overnight in the dark (typically 21 h) with continuous stirring while the acetone evaporated. The solution was centrifuged at 1000 rpm for 10 min and passed through a 13 mm PVDF filter (0.22  $\mu\text{m}$ , non-sterile). Milli-Q water was added to get a 2 mL solution (if needed) to obtain a final micellar concentration of 2.5 mg  $\text{mL}^{-1}$ . The blank micelles were prepared using the same protocol but without Cur. The solutions were used immediately after preparation.

### CMC determination

In a typical preparation, series of polymer concentrations dissolved in HPLC grade acetone were prepared (0.000122 - 1.0 mg ml<sup>-1</sup>). A 6 μM pyrene solution dissolved in HPLC grade acetone was also prepared. Each polymer and pyrene solution were dropped simultaneously into 1 mL of Milli-Q water at a rate of 1 drop s<sup>-1</sup> while stirring. The mixture was left exposed overnight in the dark with continuous stirring while the acetone evaporated. Milli-Q water was added to the mixture to get a 1 mL solution (if needed). The samples were detected using a Varian Cary Eclipse fluorescence spectrometer from Agilent to obtain the peak intensity ratios at 333 nm and 338 nm. A plot of  $\lambda_{338}/\lambda_{333}$  intensity against polymer concentration was used to determine the CMC by determining the concentration at which the intensity ratios increased.

### Size changes with CO<sub>2</sub> bubbling

In a typical preparation, a blank micellar sample was prepared as mentioned previously. The solution was then bubbled with CO<sub>2</sub> at a rate of 1 bubble per 3 s for a desired duration. The solution was then analysed with DLS and TEM.

### Protonation/oxidation with CO<sub>2</sub>/ CO<sub>2</sub>+ H<sub>2</sub>O<sub>2</sub>

In a typical preparation, CO<sub>2</sub> was bubbled into a 0.45 mL solution of D<sub>2</sub>O through a needle at a rate of 1 bubble per 3 s for 0.5 h. The solution was allowed to equilibrate before adding 15 mg of the polymer and then equilibrated again for 0.5 h before analysing it with <sup>1</sup>H NMR.

For the CO<sub>2</sub>-accelerated oxidation of the tertiary amine, 11.2 μL of 30% H<sub>2</sub>O<sub>2</sub> were added into 0.45 mL D<sub>2</sub>O. The solution was bubbled with CO<sub>2</sub> at a rate of 1 bubble per 3 s for 0.5 h and then allowed to sit to equilibrate before adding 15 mg of polymer. The solution was equilibrated again for 0.5 h before analyses.

### Drug loading and release

The drug-loaded micellar solution (2 mL) was prepared as described previously. The solution was transferred to a Spectra/Por® 3 dialysis membrane (standard RC, 3.5 kDa MWCO) and dialyzed against 140 mL of phosphate buffer saline (PBS, 0.01 M, pH 7.4) containing 1% v/v Tween 80. 20 μL aliquots of the solution were collected from the dialysis membrane at desired intervals. The

aliquots were diluted 100 folds with methanol to dissolve the Cur for analysis. An Agilent Cary 50Bio UV-Vis spectrometer was used to measure the absorption intensities of Cur at 425 nm at room temperature. The measurements were referred to with a standard Cur curve to obtain the mass of Cur at each interval. Drug loading (DL%) and encapsulation efficiencies (EL%) were calculated with the following equations:

$$DL\% = \frac{\text{Mass of drug encapsulated}}{\text{Mass of drug and polymer added}} \times 100\%$$

$$EE\% = \frac{\text{Mass of drug encapsulated}}{\text{Mass of drug added}} \times 100\%$$

### Cell culture

Human monocytic THP-1 cells (ATCC, #TIB-202) were cultivated in RPMI 1640 culture medium (Wisent, #350-000-CL) supplemented with 10% of heat inactivated fetal bovine serum (FBS, Wisent, #090150) and 1% penicillin/streptomycin (Wisent #450-201-EL) at 37 °C under 5% CO<sub>2</sub>. Cells were seeded at 750 000 cells/mL in 96-well plates (200 µl/well) for MTT assay or 6-well plates (2 mL/well) culture plates for flow cytometry and IL-1β secretion analyses. The monocytic cells were differentiated into macrophages by exposure to 100 ng/mL of phorbol 12-myristate 13-acetate (PMA, Sigma, #P1585) for 72 h. After differentiation, cells were stimulated with Cur or Cur-loaded TA-MP2 micelles (Cur-TA-MP2) at 10, 30, 50 or 100 µM for 1 h or 24 h. Except for MTT assays, cells were harvested with trypsin-EDTA, and the reaction was stopped with PBS with 10% FBS.

### Cell viability and apoptosis

After 1 or 24 h of stimulation, cells were incubated with thiazolyl blue tetrazolium bromide (MTT, Millipore Sigma, # M2128) for 2 h at 37°C and 5% CO<sub>2</sub> in the dark. The medium was removed, and mitochondrial metabolic activity was measured by dissolving the formazan formed inside the cells in 100 µL of dimethyl sulfoxide (DMSO). The absorbance was read at 575 nm and cell viability was expressed in % of control cells, without treatment.

Apoptosis was evaluated by flow cytometry. Cells were suspended in Annexin buffer (BD Pharmingen, #556454) and incubated with Annexin V-FITC probe (BD Pharmingen, #556420)

and propidium iodide dye (BD Pharmingen, #556463) for 15 min. Flow cytometry analysis was performed on at least 30,000 cells per condition. Results were expressed in % of total cells.

### Quantification of interleukin-1 $\beta$ secretion by western blotting

Cells were pre-treated with Cur or Cur-TA-MP2 at 50  $\mu$ M or an equivalent volume of medium (control). After 24 h, media were replaced and supplemented with nigericin at 10  $\mu$ M for 30 min or an equivalent volume of medium (control nigericin). At the end of the protocol, media were collected for immunoblotting analyses. Immunoblotting was performed using 45  $\mu$ L of conditioned media and electrophoresed using 12% TGX Stain-Free (Bio-Rad) gels. Samples were transferred into a PVDF membrane overnight at 10 V. Membrane was blocked with 5% non-fat dry milk in TBST and then incubated with IL-1 $\beta$  antibody (dilution 1/1000, Cell Signalling, #83186) overnight at 4°C, washed in TBST and incubated with an anti-rabbit antibody (dilution 1/10000, ThermoScientific, #32460). Membrane was incubated using chemiluminescence substrate (Western Lighting Ultra, Perkin Elmer, NEL1120001EA) to reveal IL-1 $\beta$  signal. Stain-Free technology allowed quantification of total protein in acrylamide gel for normalization. Finally, results were expressed in % of nigericin cells without treatment.

### Flow cytometry

To assess the differentiation of macrophages into inflammatory (M1) or anti-inflammatory (M2) profile, cells were co-stimulated with 1  $\mu$ g/mL lipopolysaccharides (LPS) from *Escherichia coli* O111:B4 (Sigma # L2630) and 20 ng/mL human interferon  $\gamma$  (IFN- $\gamma$ , Sigma # SRP3058) for 24 h.<sup>51</sup> A co-treatment with Cur or Cur-TA-MP2 was administered. Staining with 7-AAD (Biolegend, #420404) for viability and with anti-HLA-DR antibody (BD, #563696) was performed for 30 min. Cells were fixed with BD Fix/Perm (BD, #51-2090) for 20 min at 4°C. After 2 washes, cells were incubated with an anti-CD68 antibody (Invitrogen, #51-0689-42) for 30 min at 4 °C. Flow cytometry analysis of cell surface expression of HLA-DR and CD68 was performed on 30,000 cells per condition. Results were expressed in % of viable cells.

### Statistical analyses

Cell viability and M1/M2 differentiation comparisons of combinations of molecules and concentrations were evaluated using mixed-effects models with the intercept as random effect to consider correlation within replicates.

For IL-1 $\beta$  secretion from cells exposed to nigericin, Cur or Cur-TA-MP2 treatment comparisons at a concentration of 50  $\mu$ M were performed using mixed-effects models with only the intercept as random effect to consider correlation within replicates. In addition, mean and 95% confidence intervals (95%CI) of control cells without nigericin and without treatment, Cur 50  $\mu$ M added to cells exposed to nigericin and Cur-TA-MP2 50  $\mu$ M added to cells exposed to nigericin were compared to control cells only exposed to nigericin (assigned to a value of 1).

For apoptosis evaluation, Cur or Cur-TA-MP2 treatment comparisons at a concentration of 50  $\mu$ M were performed using mixed-effects models with only the intercept as random effect to consider correlation within replicates.

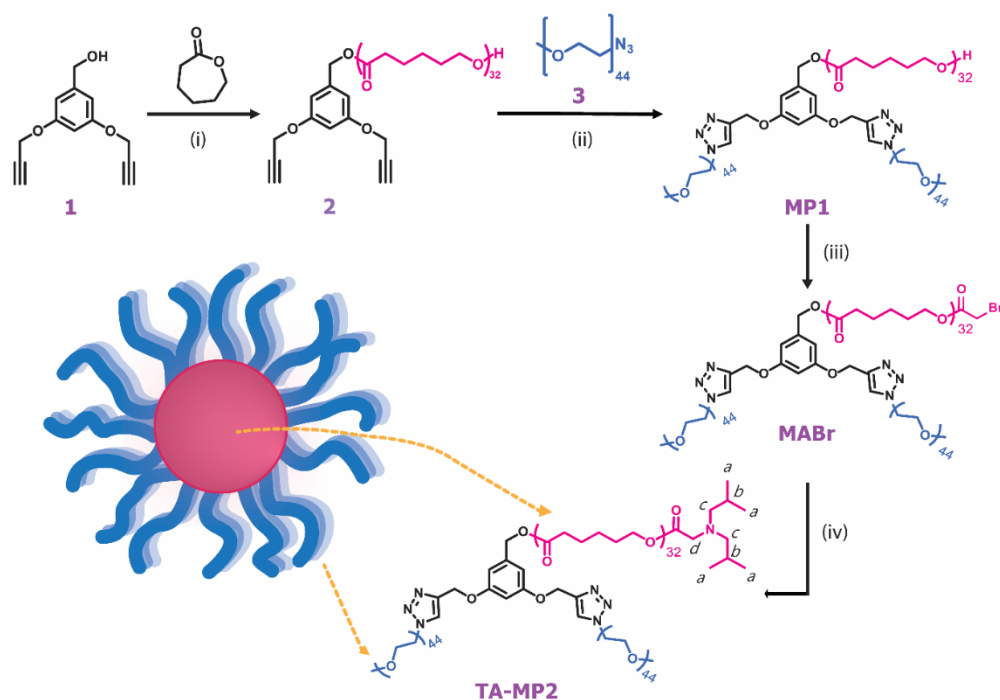
Models were done for pretreatment durations of 1 h and 24 h. Furthermore, adjusted means and their 95%CI from these models were presented. In all cases, basic assumptions were checked prior to analysis. P values < 0.05 were considered statistically significant. Analyses were performed with SAS® release 9.4 (SAS Institute Inc., Cary, NC, USA).

## 2.5. Results and Discussion

### Synthesis of miktoarm polymers

The AB<sub>2</sub> miktoarm star polymers without/with a tertiary amine at the terminus of the hydrophobic arm A, were prepared by combination of arm-first and core-first methods (Scheme 2. 2, MP1, TA-MP2). The synthetic methodology adopted to construct the branched architectures employed efficient ring opening polymerization and copper catalyzed alkyne-azide cycloaddition (click) reaction. Overall goal in the synthetic articulation was to simplify the construction of such architectures, accompanied by detailed characterization at each step of the build-up towards the desired miktoarm polymers. Hydrophilic PEG has been a long-standing choice in formulations due to its ability to impart stealth behavior, extend blood circulation, reduce clearance by the body's mononuclear phagocytic system and lower toxicity.<sup>52-54</sup> By reducing serum protein adsorption,

biocompatible PEG is able to provide steric stabilization and act as a protective barrier to mitigate the effects of protein-NP interaction.<sup>55-57</sup> With reduced colloidal destabilization, NPs generally have prolonged circulation half-lives and offer better avenues as drug delivery vehicles. Biodegradable polyester, PCL, is FDA approved, and has been widely utilized in drug delivery and tissue engineering applications.<sup>58-60</sup> Polymer linked diisobutylamine was selected as the multi-stimuli sensitive center. Diisobutylamine has a predicted pKa of 10.91, and we estimated its pKa upon covalent linking to the polymer, by comparison to its closest analog, N-methyl diisobutylamine. The latter has a predicted pKa of 9.59. Hydrophobicity of the linked tertiary amine together with high predicted pKa are expected to help promote protonation under varied conditions (dissolved CO<sub>2</sub>/pH).



**Scheme 2. 2:** Synthesis of MP1 and TA-MP2 polymers: (i) Sn(Oct)<sub>2</sub>, dry toluene, 115 °C, 24 h, 90%; (ii) CuBr, PMDETA, dry THF, rt, 48 h, 76%; (iii) bromoacetyl bromide, triethylamine, dry THF, rt, 24 h, yield= 75%; (iv) diisobutylamine, dry DMF, 85 °C, 24 h, 77%. For synthetic details of 1, 2, and 3 see Appendix A.

The synthesis began with functionalization of commercially available 3,5-dihydroxybenzyl alcohol with two alkyne groups using propargyl bromide. The resulting dipropargyl-benzyl alcohol (1) was used as an initiator for the ring-opening polymerization (ROP) of  $\epsilon$ -caprolactone, leading to PCL-linked core (2). Azido-PEG<sub>2000</sub>-monomethyl ether (3) was subsequently prepared according to a previously reported procedure.<sup>61</sup> Compound 2 was then conjugated with 3 using the copper-catalyzed azide-alkyne cycloaddition click reaction, yielding a (PEG<sub>2000</sub>)<sub>2</sub>-PCL<sub>3600</sub> miktoarm block copolymer (MP1). The terminal OH on MP1 was subsequently reacted with bromoacetyl bromide, followed by diisobutylamine to obtain the desired multi-stimuli-responsive miktoarm polymer TA-MP2. The build-up of the branched architectures was established by a combination of <sup>1</sup>H and <sup>13</sup>C NMR, MALDI-TOF, ESI, and GPC (Table 2. 1, Figure 2. 6-2.22). Elemental analysis through electron spray ionization was used to further verify the presence of the terminal amine group, and complete absence of Br and its isotopes. The GPC chromatograms of both MP1 and TA-MP2 also showed single peaks with narrow dispersity of 1.20 (Figure 2. 22), confirming the successful synthesis of both polymers and absence of homopolymers 2 and 3.

**Table 2. 1:** Properties of miktoarm polymers (MP1 and TA-MP2) and their associated self-assemblies.

Polymer	Molar mass <sup>a</sup>	$\mathcal{D}^b$	CMC [ $\mu\text{g mL}^{-1}$ ] <sup>c</sup>	Blank micelles				Cur-loaded micelles (no CO <sub>2</sub> )			
				No CO <sub>2</sub>		CO <sub>2</sub>		DL%	EE%	$D_H$ [nm] <sup>d</sup>	D [nm] <sup>e</sup>
				$D_H$ [nm] <sup>d</sup>	D [nm] <sup>e</sup>	$D_H$ [nm] <sup>d</sup>	D [nm] <sup>e</sup>				
MP1	7900	1.20	3.43	62 ± 6	48	66 ± 9	45	6.6 ± 0.5	72.8 ± 5.2	57 ± 7	50
TA-MP2	8000	1.20	3.25	57 ± 5	40	93 ± 21	52	7.4 ± 0.6	81.8 ± 6.4	56 ± 5	40

<sup>a</sup> Estimated from a combination of <sup>1</sup>H NMR and MALDI-TOF. <sup>b</sup> Dispersity from GPC. <sup>c</sup> CMC obtained through fluorescence measurements. <sup>d</sup> Hydrodynamic diameter ( $D_H$ ) obtained by DLS. <sup>e</sup> Diameter (D) obtained by TEM. All error bars represent a standard deviation of n=3.

### Aqueous self-assembly of MP1 and TA-MP2

Polymeric NPs from amphiphilic polymers have been prepared using a variety of methods, and each offers its own merits and limitations. Co-solvent evaporation method is simple, effective, and widely used for encapsulation of small hydrophobic drugs.<sup>62</sup> We adopted it to induce aqueous self-assembly of MP1 and TA-MP2, which were expected to form micelles as the hydrophilic-to-total mass ratios were 50% or above.<sup>63-65</sup> Dynamic light scattering analyses revealed that MP1-based NPs (thereafter known as MP1-micelles) were slightly larger than those from TA-MP2 (thereafter known as TA-MP2-micelles), with mean hydrodynamic diameters ( $D_H$ ) of 62 nm and 57 nm, respectively (Table 2. 1, Figure 2. 23). Transmission electron microscopy (TEM) analyses showed spherical micelles, with similar trend in size, with larger diameter for MP1-micelles (48 nm) than TA-MP2-micelles (40 nm, Figure 2. 24). The sizes obtained from TEM were smaller in general than those from DLS, most likely due to dehydration of the micellar solution during TEM sample preparation. However, DLS provides a better estimation of the changes in hydrodynamic diameters of NPs. Nevertheless,  $D_H$  and size evaluations using TEM clearly suggested that these NPs have dimensions ideally suited for applications in biology. Smaller sizes for the assemblies from AB<sub>2</sub> polymer with a hydrophobic tertiary amine at the terminus of polycaprolactone (arm A) than the one without it, suggested tighter packing at the core in these systems. Next, CMCs of MP1 and TA-MP2 were evaluated using pyrene, a classic fluorophore in such studies.<sup>66-68</sup> Upon introduction into bloodstream, NPs undergo extensive dilution, and low CMC is desired for formulation stability. The ratio of fluorescent intensities at 338 nm and 333 nm were calculated and the intersection at which a spike in intensity was seen was determined as the CMC (Figure 2. 25). The CMC of MP1 at 3.43  $\mu\text{g mL}^{-1}$  was found to be slightly higher than TA-MP2 (3.25  $\mu\text{g mL}^{-1}$ ). Nevertheless, both CMCs were quite low, thus implying that such assemblies are stable and are expected to stay intact upon extensive dilution during circulation.

### Evaluation of stimuli-responsive behavior of TA-MP2 using NMR and DLS

We examined the responsivity of TA-MP2 towards dissolved CO<sub>2</sub> and CO<sub>2</sub> + H<sub>2</sub>O<sub>2</sub> using <sup>1</sup>H NMR in D<sub>2</sub>O. 0.45 mL of D<sub>2</sub>O was treated with respective stimulus for 0.5 h before adding TA-MP2 to it, and then the mixture was allowed to equilibrate for another 0.5 h. We chose this small 1 h window to note changes taking place on the tertiary amine. Under these conditions, we expected protonation or oxidation of the tertiary amine to begin, which could be observed through a

downward shift of the protons on the amine. In D<sub>2</sub>O, both PCL and tertiary amine showed broad, convoluted peaks (Figure 2. 26), which can be attributed to the non-selective and insoluble behavior of both segments in aqueous media. As expected, the change in polarity on the nitrogen atom of the tertiary amine due to CO<sub>2</sub> bubbling was reflected with a downward chemical shift of CH<sub>3</sub> marked *a* (Scheme 2. 2) from 0.88 to 0.99 ppm; and *b* CH (from 1.65 to 2.12 ppm); *c* CH<sub>2</sub> from around 2.30 (which overlapped with PCL protons in the original spectrum of TA-MP2) to 3.30 ppm; and *d* CH<sub>2</sub> from ~3.40 (overlapped with PEG-OCH<sub>3</sub> protons) to 4.20 ppm.<sup>69</sup> In both CO<sub>2</sub> and CO<sub>2</sub> + H<sub>2</sub>O<sub>2</sub> spectra, almost identical chemical shifts were observed.

We subsequently determined responsivities of MP1-micelles and TA-MP2-micelles upon CO<sub>2</sub> bubbling using DLS. CO<sub>2</sub> was bubbled into micellar solutions for 0.5 h at the same rate of 3 bubbles per second as mentioned above. Under these conditions, we expected the tertiary amine to get positively charged (quaternized), and our goal was to examine if the latter induces changes within the micellar core, which may be reflected with an enlargement in size. As expected, MP1-micelles showed no change in the hydrodynamic diameter, whereas TA-MP2-micelles swelled to about 63% larger than its original size. A similar trend with increase in size upon CO<sub>2</sub> bubbling was observed using TEM (Figure 2. 27).

### Cur-loading into NPs

Cur, a flavonoid polyphenol, was chosen as a model drug for encapsulation due to its excellent antioxidant and anti-inflammatory properties.<sup>70, 71</sup> The low bioavailability and rapid elimination of Cur are common reasons for its limited administration, therefore drug delivery technologies such as micellar formulations become paramount in increasing its efficacy. DL% and EE% for Cur loaded into MP1-micelles (Cur-MP1) and TA-MP2 micelles (Cur-TA-MP2) are summarized in Table 2. 1 (Figure 2. 28-29). It is interesting to note that Cur-TA-MP2 showed an overall higher DL% and EE% compared to Cur-MP1, which may suggest a stronger drug-polymer interaction due to additional hydrophobicity in the core environment of Cur-TA-MP2. Cur-TA-MP2 had EE% of >80%, which was significantly higher than the Cur-loaded micelles from a linear triblock copolymer, poly[2-(dimethylamino)ethyl methacrylate-*b*-lauryl methacrylate-*b*-(oligo ethylene glycol)methacrylate] of about 12%.<sup>72</sup>

### Cur release studies

Release of Cur from both MP1- and TA-MP2-micelles was examined using the dialysis method. Although both Cur-MP1 and Cur-TA-MP2 showed slow and sustained release at room temperature over 72 h, there were noticeable differences between these NPs (Figure 2. 1). Cur-MP1 showed almost 35% Cur release in the first 4 h but it was only 10-12% in Cur-TA-MP2, which in general displayed much slower and sustained release than Cur-MP1. This may once again suggest better overall packing and interactions of the drug with the core containing tertiary amine, leading to slow diffusion of the drug from a well-packed hydrophobic shell in TA-MP2-micelles.

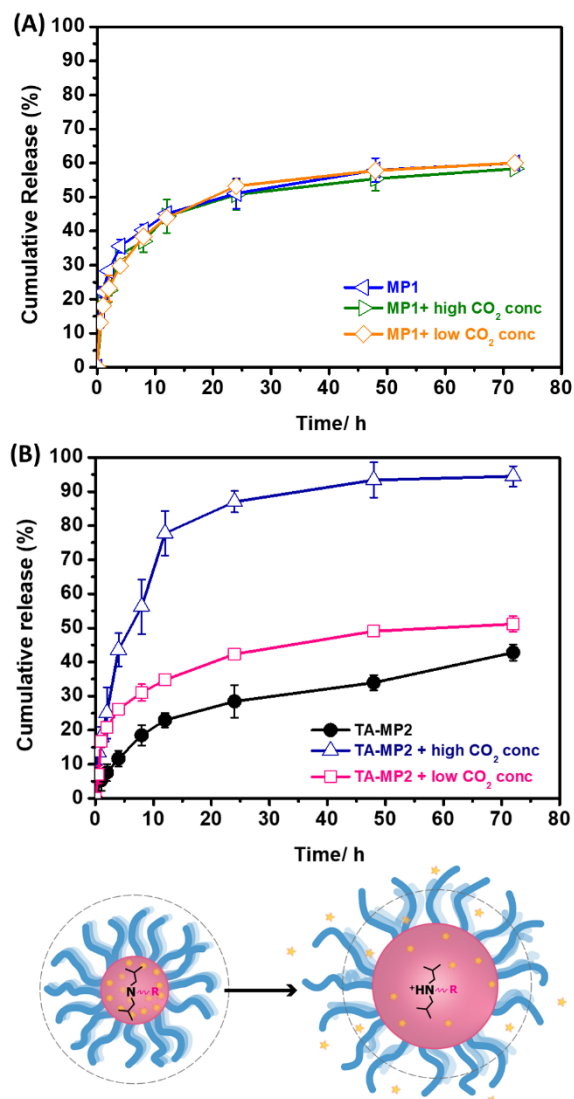


**Figure 2. 1:** Cur-release from (A) Cur-MP1 and (B) Cur-TA-MP2 in the absence and presence of CO<sub>2</sub>. All studies were conducted in 0.01 M PBS buffer with 1% v/v Tween 80 at pH 7.4. Error bars represent a standard deviation of n=3.

### Dissolved CO<sub>2</sub>-induced Cur release

Leveraging on the fact that majority of CO<sub>2</sub> exists as HCO<sub>3</sub><sup>-</sup> in the body, we were intrigued to examine CO<sub>2</sub> bubbling-induced pH variations in Milli-Q water and PBS buffer. NPs were prepared in water and the solution was placed in a dialysis tubing for drug release studies, where PBS buffer constitutes the outside medium. CO<sub>2</sub> was bubbled into Milli-Q water (without any NPs) and PBS

solution (0.01 M, pH 7.4, +1% v/v Tween-80) separately, at a rate of 3 bubbles per second and changes in pH over a period of 72 h were recorded (Figure 2. 30, Table 2. 3). Dissolution of CO<sub>2</sub> in an aqueous medium established an equilibrium with carbonic acid. The initial pH of Milli-Q water was slightly acidic at 6.11, possibly owing to some atmospheric CO<sub>2</sub> that dissolves naturally in it. Upon CO<sub>2</sub> bubbling at a constant rate, the pH dropped to 4.84 over 0.5 h, coming very close to the pH of 10 mM H<sub>2</sub>CO<sub>3</sub>. In PBS, the original pH at 7.40 gradually dropped to only 6.53 after 12 h. Further CO<sub>2</sub> bubbling did not bring any reduction in the pH. Interestingly, with the addition of 200 mM H<sub>2</sub>O<sub>2</sub> to PBS buffer, the initial pH at 7.4 decreased only slightly to 7.36, and upon continued bubbling of CO<sub>2</sub> it dropped to 6.98 in 2h and plateaued at 6.79 in 8 h.

The CO<sub>2</sub>-induced changes in Cur release profiles of the formulations were then examined with two different strategies: i) bubbling CO<sub>2</sub> directly into the dialysis tubing (with expected higher CO<sub>2</sub> concentrations with pH dropping to 4.84 in just 0.5 h, as described above); ii) in the external PBS buffer (with lower CO<sub>2</sub> concentrations with change in pH from 7.4 to 6.53 in 12 h). At higher CO<sub>2</sub> concentrations, we observed no changes in the release profile for Cur-MP1 (Figure 2. 1A), while Cur-TA-MP2 with the tertiary amine at the core showed a highly accelerated release of Cur (Figure 2. 1B). In the first 4 h we noticed a 45% Cur release, which continued to increase to 55% in 8 h, and 75% in 12 h. Thereafter, Cur followed a sustained release with most of the drug released in 72 h. This is consistent with changes in the hydrophobic core of the micelles by protonation of tertiary amine in the highly acidic environment created by dissolved CO<sub>2</sub>. The quaternized amine creates a hydrophilic/hydrophobic imbalance in the core where the drug is encapsulated, which eventually expedites Cur expulsion from the hydrophobic interior. We compared cargo release upon CO<sub>2</sub> bubbling from the only example of polymeric NPs containing tertiary amines in the polymer backbone repeat units that we could find in the literature. Rhodamine B (RhB) was loaded into polymeric vesicles from a linear triblock co-polymer, polyacrylamide-*b*-poly(2-(dimethylamino)ethyl methacrylate)-*b*-polyacrylamide (PAAm<sub>70</sub>-*b*-PDMAEMA<sub>100</sub>-*b*-PAAm<sub>70</sub>). Upon CO<sub>2</sub> bubbling into the formulation solution, an accelerated cargo release was observed with 40% of RhB released in 30 min.<sup>64</sup> Cur release profiles of NPs from Cur-MP1 and stimuli-responsive Cur-TA-MP2 were subsequently examined by bubbling CO<sub>2</sub> into the PBS medium (lower CO<sub>2</sub> concentrations as described above). Under these conditions, Cur-TA-MP2 had approximately 15% increase in Cur release over 48 h. For the non-responsive Cur-MP1, an almost

identical release pattern to CO<sub>2</sub>-free conditions was observed. These experiments highlight the control such a system offers through tuned CO<sub>2</sub> concentrations, sensitivity to varied amounts of CO<sub>2</sub>, and its potential to deliver Cur with a desired dose under hypercapnia conditions.

It was expected that Cur release from stimuli-responsive formulation will follow the mechanism of amine protonation, followed by swelling. We examined the changes different CO<sub>2</sub> concentrations bring to the overall morphology and stability of Cur-loaded micelles using DLS and TEM (Figure 2. 2 and Figure 2. 31-32). Under high CO<sub>2</sub> concentration conditions, hydrodynamic diameters of Cur-TA-MP2 increased from 57 nm to 134 nm in 6.5 h, and to 188 nm in 12 h. A similar increase in hydrodynamic diameters from the original 20-200 nm to >680 nm has been reported in vesicles from the linear triblock co-polymer, PAAm<sub>70</sub>-*b*-PDMAEMA<sub>100</sub>-*b*-PAAm<sub>70</sub> used for RhB loading.<sup>73</sup> Our results were also supported by TEM, in which a size increase over 6.5 h was observed. At longer time intervals (12 h) TEM micrographs showed the formation of large aggregates, which suggested micelle disassembly. This may be triggered by the slightly positively charged core that makes it more susceptible to aqueous solvation, thereby inducing a shift to the outer polar phase and affecting the stability of the micelles. Nevertheless, we could still observe a large population of micelles after 12 h (Figure 2. 2D), which may be due to the bulk of the core that consists of hydrophobic PCL that impedes such hydration. Collectively, both DLS and TEM showed expansion of micelles upon protonation, and eventual slow disassembly under these conditions. Such controlled release and micelle transformations could help tune desired drug dosage release from NPs in a timely manner.

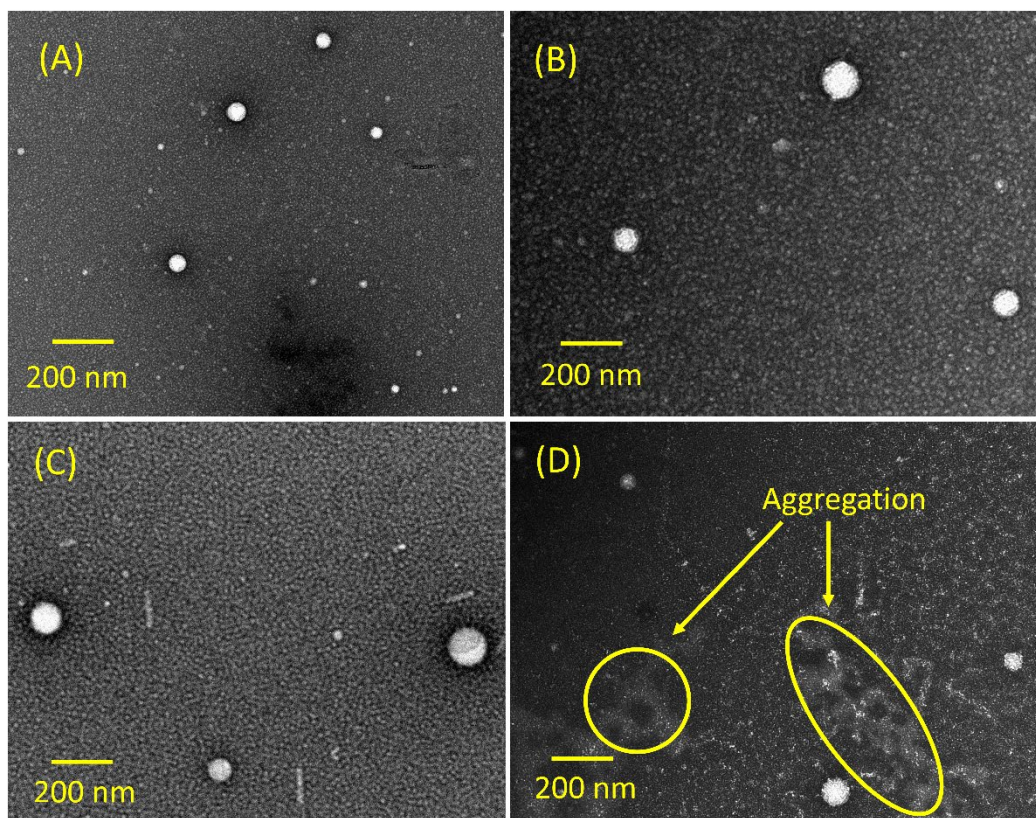


**Figure 2. 2:** TEM of Cur-TA-MP2 showing small increments in size after continuous CO<sub>2</sub> bubbling: (A) CO<sub>2</sub> 0 h, D= 40 nm; (B) CO<sub>2</sub> 0.5 h, D= 53 nm; (C) CO<sub>2</sub> 6.5 h, D= 68 nm; (D) CO<sub>2</sub> 12 h, aggregation.

### pH-responsive Cur release

Cur release from Cur-TA-MP2 was then examined under different biological environments: pH: 7.4, normal physiological; 6.5, tumor extracellular; and 5.5-4.0 tumor lysosomes.<sup>74-76</sup> To attain the desired pH, we used PBS and sodium acetate solutions to ensure that the buffering capacity was within the desired range. As seen in Figure 2. 3A, Cur-TA-MP2 exhibited pH-dependent release, with small increments as the pH decreased. At pH 7.4, nearly 43% of Cur was released within 72 h; 48% at pH 6.5; 54% at pH 5.5, and 60% at pH 4.0. These results are consistent with slow diffusion of protons from the outside medium into the dialysis tubing and then into the micellar core, followed by protonation of the tertiary amine. The latter leads to micelle core destabilization due to electrostatic repulsion, promoting accelerated Cur release. It is important to highlight the

comparative analysis of the responsive NPs reported here, to the commonly developed pH-responsive systems which generally contain amine functional group in each repeat unit of the polymer precursors. In such systems, an increase of 40% in drug release is reported with decreasing pH.<sup>53</sup>

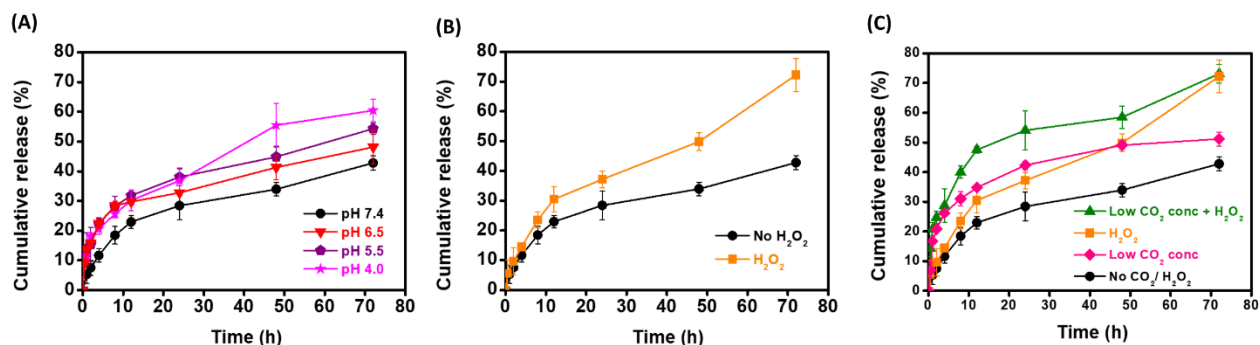


**Figure 2. 3:** Cur-release profiles from Cur-TA-MP2 (A) at room temperature under different pH: pH 7.4 (in 0.01 M PBS), pH 6.5 (in 0.01 M PBS), pH 5.5 (in 0.01 M PBS), and pH 4.0 (in 0.01 M sodium acetate buffer); (B) in the absence and presence of H<sub>2</sub>O<sub>2</sub>; (C) with the combination of CO<sub>2</sub> + H<sub>2</sub>O<sub>2</sub> + tertiary amine. All studies were conducted in buffers with 1% v/v Tween 80. Error bars represent a standard deviation of n=3.

In a recent study, dual-pH responsive polymeric micelles from poly(2-diisopropylamino)ethyl methacrylate-*b*-poly(4-formylphenyl methacrylate-co-polyethylene glycol monomethyl ether methacrylate) were investigated for doxorubicin (DOX) release.<sup>77</sup> DOX release at pH 7.4 increased from 20% after 30 h to >50% at pH 6.5. This system had tertiary amine units in each repeat unit of the pH responsive block (poly(2-diisopropylamino)ethyl methacrylate, and an additional pH-sensitive imine bond which gets cleaved at low pH. These will contribute to an additional increase in DOX release at low pH. TA-MP2 in comparison has a single amine per polymer chain, and our system is designed to remain intact by swelling to adjust any disparity in hydrophobic/hydrophilic ratios and provide slow and sustained release over time. To ascertain this and determine any morphological changes, DLS and TEM analyses were carried out (Figure 2. 33-34). At 12 h, we observed a gradual increase in hydrodynamic diameter from 57 nm to 87 nm as the pH dropped

from 7.4 to 4.0. TEM showed intact micellar structures that were also expanding slowly in acidic media, confirming pH-responsive stability of the micelles.

### ROS-responsive Cur release

Sensitivity of the micelle core-based tertiary amine to ROS and its influence on drug release was then examined with 200 mM H<sub>2</sub>O<sub>2</sub>, a widely used concentration for such studies (Figure 2. 3B).<sup>78</sup> <sup>79</sup> With H<sub>2</sub>O<sub>2</sub>, tertiary amines are known to form amine N-oxides, which are widely employed as stoichiometric oxidants as well as stabilizers in topical pharmaceuticals.<sup>80, 81</sup> As expected, we observed an increase in Cur release from Cur-TA-MP2 upon incubation with H<sub>2</sub>O<sub>2</sub>, which accelerated to ~72% after 72 h, compared to 40% without any stimulus. As noted earlier, the addition of H<sub>2</sub>O<sub>2</sub> to buffer solution did not bring any noticeable change in pH. It clearly suggests that the increase in Cur release noted above is consistent with slow oxidation of tertiary amine under non-catalytic conditions. TEM evaluation of the changes in morphology/stability of micelles in response to ROS was impeded by the instability of TEM grids. It caused etching of the grid surface upon exposure to H<sub>2</sub>O<sub>2</sub>, a strong oxidizing agent (Figure 2. 35). We thus followed such changes with DLS instead (Figure 2. 36) and observed a 30% increase in size from 57 nm at 0 h to 84 nm after 12 h. This suggests that the micelle formulation is stable and undergoes expected expansion upon exposure to ROS.

### CO<sub>2</sub>/ROS (H<sub>2</sub>O<sub>2</sub>)-combined Cur release

Dissolved CO<sub>2</sub> is known to catalyze oxidation of tertiary amines with H<sub>2</sub>O<sub>2</sub>, which should influence Cur release with the combination of CO<sub>2</sub> and ROS (H<sub>2</sub>O<sub>2</sub>) environments. Considering the abundance of ROS and HCO<sub>3</sub><sup>-</sup> in tumor microenvironments, a nanocarrier that responds to such a mixture present at disease sites to deliver suitable therapeutic agents is especially interesting. In addition, CO<sub>2</sub> accelerated oxidation of tertiary amines by H<sub>2</sub>O<sub>2</sub> leading to the formation of N-oxides avoids the formation of N-nitrosamines that are known carcinogens.<sup>82</sup>

To the best of our knowledge, this is the only system reported to utilize this unique pathway in designing smart polymeric formulations. As reported above, efficiency of Cur release was enhanced under both low and high CO<sub>2</sub> concentrations, as well as with the addition of H<sub>2</sub>O<sub>2</sub>. With the CO<sub>2</sub> + H<sub>2</sub>O<sub>2</sub> pairing, we expected increased Cur release from the catalytic oxidation of tertiary

amine. However, under high CO<sub>2</sub> concentrations, Cur release was found to be too rapid, which makes partitioning its effect of stimuli-pairing from CO<sub>2</sub> alone a difficult task. To avoid rapid release under high CO<sub>2</sub> concentrations, we examined catalytic oxidation of amine by H<sub>2</sub>O<sub>2</sub> under low CO<sub>2</sub> concentrations. As expected, it led to an increase in Cur release with CO<sub>2</sub>/ H<sub>2</sub>O<sub>2</sub> combined stimuli. For example, upon comparing Cur release at 12 h interval and beginning with 20% Cur release with no stimulus, it increased to 30% with CO<sub>2</sub>, 35% with H<sub>2</sub>O<sub>2</sub>, and 50% with combined CO<sub>2</sub>/ H<sub>2</sub>O<sub>2</sub> (Figure 2. 3C).

### Dissolution kinetics

Drug kinetic models provide an understanding of several critical properties in pharmaceutical formulations.<sup>83</sup> Important details such as drug diffusion coefficient and release behavior can be predicted to help in formulation optimization.<sup>84</sup> We evaluated several well-known mathematical models of zero order, first order, Higuchi, and Korsmeyer-Peppas to understand the mechanism of drug transport out of our systems. By comparing the correlation coefficients ( $R^2$ ) for different models, we determined that our system fits the Higuchi model the best with the highest  $R^2$  for Cur-TA-MP2 under all conditions (Table 2. 2, Figure 2. 37-40). This indicates that Cur release follows the Higuchi pattern driven by Fickian diffusion.

**Table 2. 2:** Kinetic parameters of Cur-TA-MP2.

Model	Parameter	Cur-TA-MP2							
		No stimuli (pH 7.4)	High CO <sub>2</sub> conc	Low CO <sub>2</sub> conc	pH 6.5	pH 5.5	pH 4.0	H <sub>2</sub> O <sub>2</sub>	Low CO <sub>2</sub> +H <sub>2</sub> O <sub>2</sub>
Zero-order	<b>k<sub>0</sub></b> (mg h <sup>-1</sup> )	0.551	1.173	0.579	0.526	0.609	0.743	0.926	0.794
	<b>R<sup>2</sup></b>	0.832	0.637	0.678	0.748	0.793	0.872	0.918	0.743
First-order	<b>k<sub>1</sub></b> (h <sup>-1</sup> ) x 10 <sup>-3</sup>	38.2	32.2	27.2	26.3	27.6	29.5	44.2	27.9
	<b>R<sup>2</sup></b>	0.466	0.314	0.304	0.352	0.345	0.420	0.500	0.299
Korsmeyer -Peppas	<b>k<sub>K-P</sub></b> (h <sup>-n</sup> )	2.787	10.757	7.932	7.596	7.989	7.471	2.976	10.442
	<b>n</b>	0.727	0.617	0.516	0.478	0.487	0.521	0.818	0.503
	<b>R<sup>2</sup></b>	0.844	0.580	0.554	0.538	0.538	0.586	0.862	0.492
Higuchi	<b>k<sub>H</sub></b> (mg <sup>1/3</sup> h <sup>-1/2</sup> )	5.295	14.306	7.537	6.562	7.210	7.818	7.936	9.860
	<b>R<sup>2</sup></b>	0.986	0.937	0.934	0.946	0.961	0.984	0.990	0.947
<b>Best fit</b>	Higuchi								

### Biological evaluation

Cell viability assessment of PMA-differentiated human THP-1 macrophages after exposure to free Cur and to Cur-TA-MP2 was performed using an MTT assay that quantifies mitochondrial activity

by colorimetry. The results of different conditions were normalized to control cells without treatment. 1 h-exposure to both caused no significant alteration of cell viability ( $p=0.068$ , Figure 2. 4A). A longer 24 h stimulation using a low concentration (10  $\mu\text{M}$ ) of free Cur or Cur-TA-MP2 did not modify the adjusted mean cell viability (95% confidence intervals (95%CI) are reported for adjusted means using the format 95%CI[LL; UL] where LL is the lower limit of the confidence interval and UL is the upper limit): 1.05 95%CI(0.93; 1.16) ( $p=0.96$ ) and 1.08 95%CI(0.96; 1.21) ( $p=0.56$ ), respectively, compared to control cells (1.05 95%CI(0.93; 1.16)). Cur at 50  $\mu\text{M}$  and 100  $\mu\text{M}$ , however, significantly reduced cell viability to 0.42 95%CI(0.31; 0.53) ( $p<0.0001$ ) and 0.01 95%CI(-0.13; 0.15) ( $p<0.0001$ ). At this exposure duration, encapsulation of Cur within TA-MP2-micelles protected cells against cell death when compared to using the highest concentrations of Cur ( $p<0.0001$  at 50  $\mu\text{M}$  and  $p<0.0001$  at 100  $\mu\text{M}$  of Cur and Cur-TA-MP2) (Figure 2. 4B). It has been shown that in THP-1 monocytic cells, a 24 h-stimulation at 30, 40 and 50  $\mu\text{M}$  of Cur caused apoptosis in a concentration-dependent manner.<sup>85</sup>

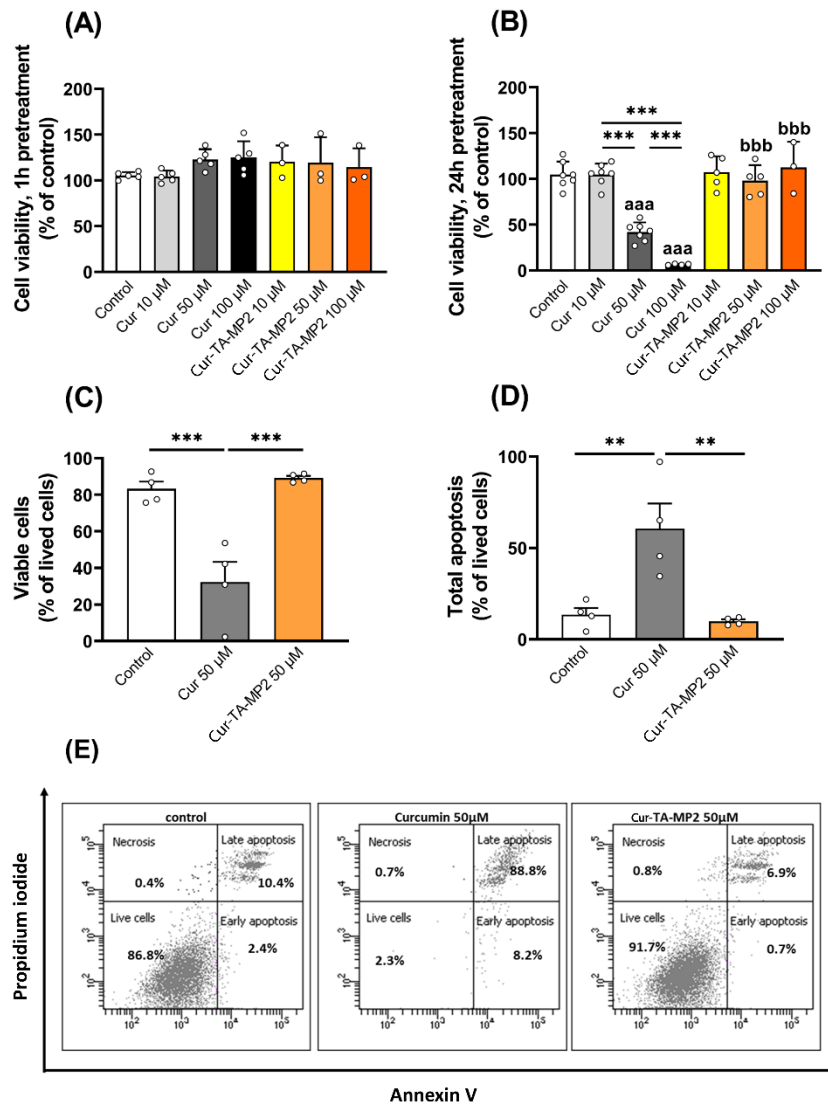


**Figure 2. 4:** Upper panels A and B: MTT assessment of cell viability of THP-1 human macrophages following (A) 1 h or (B) 24 h exposure of Cur or Cur-TA-MP2 at 10, 50 or 100  $\mu$ M. Lower panels C-E: Flow cytometry assessment using propidium iodide and Annexin V labeling of (C) viable cells and (D) apoptotic cell percentages of the THP-1 human macrophages following 24 h exposure of Cur or Cur-TA-MP2 at 50  $\mu$ M. (E) Dot plot graphs of flow cytometry. Results are expressed as mean  $\pm$  SEM of 3 to 9 biological replicates. aaa: comparison with control, bbb: comparison with the same concentration of Cur when  $p < 0.001$ , \*\*\*:  $p < 0.001$ .

To assess the anti-inflammatory activity of Cur, we used nigericin as an activator of the inflammasome. Nigericin is well-known to activate the inflammasome signaling pathway and stimulate inflammatory responses in cells, especially macrophages.<sup>86</sup> A specific response to nigericin is the increased secretion of the pro-inflammatory cytokine interleukin-1 $\beta$  (IL-1 $\beta$ ). IL-1 $\beta$  secretion was quantified by immunoblotting. The results were normalized using total protein “in gel” quantification of each sample and expressed as a ratio of the nigericin-treated cells. As expected, 30-minutes exposure with 10  $\mu$ M nigericin significantly increased IL-1 $\beta$  secretion in the media compared to unexposed control cells ( $p < 0.05$ , Figure 2. 5A-C). Relative to control cells exposed to nigericin, after a short 1 h-pretreatment of Cur 50  $\mu$ M, IL-1 $\beta$  secretion was markedly decreased (0.09 95%CI(0.00; 0.18)) whereas the equivalent concentration of Cur-TA-MP2 did not cause a noteworthy reduction (0.81 95%CI(0.46; 1.17), which clearly depicts a significant difference between free Cur and its nanoformulation in TA-MP2-micelles ( $p = 0.02$ ). After a longer 24 h-pretreatment, both Cur and Cur-TA-MP2 reduced IL-1 $\beta$  secretion (0.04 95%CI(-0.02; 0.09) and 0.15 95%CI(-0.11; 0.42), respectively, relative to control cells exposed to nigericin alone, and these two forms of Cur were no longer different from each other ( $p = 0.25$ ).

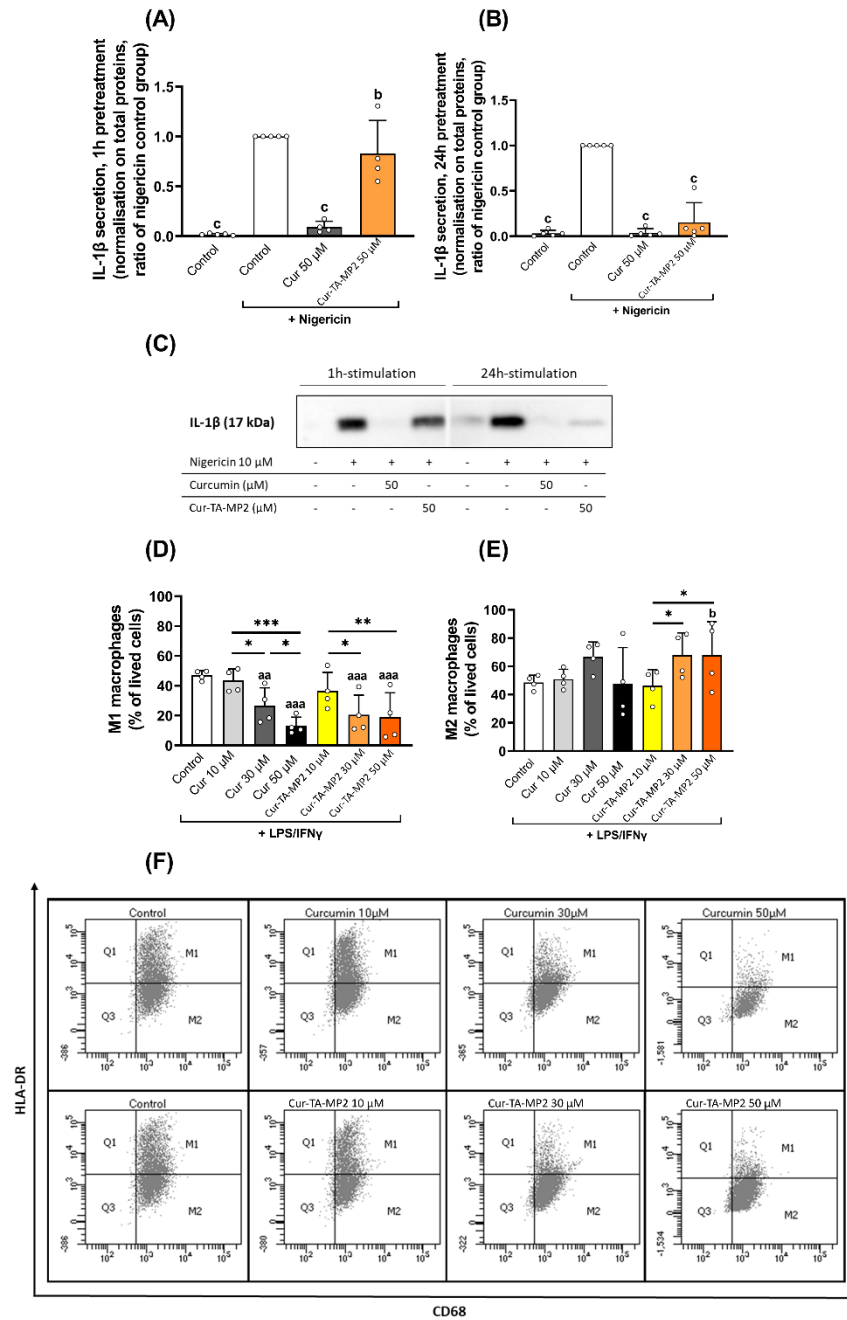


**Figure 2. 5:** Upper panels A-C: Anti-inflammatory activity of Cur assessed by quantification of interleukin-1 $\beta$  (IL-1 $\beta$ ) secretion using Q western blotting analysis after (A) 1 h or (B) 24 h exposure of THP-1 cells to Cur and Cur-TA-MP2 at 50  $\mu$ M and inflammasome activation using nigericin (Figure 2. 41). THP-1 cells were treated with Cur or Cur-TA-MP2 for 1 h or 24 h before nigericin 10  $\mu$ M exposure for 30 minutes. (C) Nigericin induced THP-1's secretion of IL-1 $\beta$  in culture media.

Lower panels D-F: (D) Anti-inflammatory activity of Cur and Cur-TA-MP2 assessed by polarization of THP-1 macrophages into CD68<sup>+</sup>HLA-DR<sup>+</sup> (M1 phenotype) or (E) CD68<sup>+</sup>HLA-DR<sup>-</sup> (M2-like phenotype) cells using flow cytometry analysis as represented by dot plots (F). To induce M1 polarization, THP-1 cells were co-treated with LPS-IFN $\gamma$  and Cur or Cur-TA-MP2 at 10, 30 or 50  $\mu$ M for a 24 h exposure. Results are expressed as mean  $\pm$  SEM of 4 to 5 biological replicates. a: comparison with control, b: comparison with the same concentration of Cur when  $p < 0.05$ , c: comparison with nigericin-exposed control when  $p < 0.05$ . \*\*\*:  $p < 0.001$ , aa:  $p < 0.01$ , aaa:  $p < 0.001$ .

PMA-differentiated THP-1 macrophages can be polarized as M1-, pro-inflammatory, or M2-, anti-inflammatory, macrophages. We studied the impact of a 24 h treatment with Cur and Cur-TA-MP2 on THP-1 macrophage polarization. THP-1 macrophages were exposed to the M1 inducers LPS and interferon (IFN)- $\gamma$  in presence of different concentrations of Cur, Cur-TA-MP2 or in control condition. At the end of the treatment, macrophage polarization was evaluated by flow cytometry according to the protocol of Zhou et al. using fluorescent labeling of CD68 and HLA-DR to quantify the cell surface expression of these proteins (Figure 2. 5D-F).<sup>51</sup> CD68 is a macrophage marker whereas HLA-DR is used here as a marker of macrophage activation. Cur treatments at 30 and 50  $\mu$ M resulted in a significant decrease of HLA-DR<sup>+</sup>CD68<sup>+</sup> M1 phenotype proportion ( $p = 0.003$  and  $p < 0.001$ , respectively compared to control, Figure 2. 5D) without significant modification of HLA-DR<sup>-</sup>CD68<sup>+</sup> M2-like phenotype ( $p = 0.072$  and  $p = 0.912$ , Figure 2. 5E). Cur-TA-MP2 treatments at 30 and 50  $\mu$ M also resulted in a decrease of M1 macrophage phenotype proportion ( $p < 0.001$  and  $p < 0.001$ , respectively compared to control, Figure 2. 5D) and a tendency to increased M2 phenotype ( $p = 0.058$  and  $p = 0.057$ , respectively compared to control, Figure 2. 5E). Moreover, at 50  $\mu$ M, Cur-TA-MP2 produced a higher increase of M2-like phenotype compared to Cur ( $p = 0.046$ , Figure 2. 5E). These results are in accordance with Zhou et al., and indicate an improved anti-inflammatory effect of Cur-TA-MP2 compared to free Cur. The improvement of the anti-inflammatory phenotype observed at 50  $\mu$ M of Cur-TA-MP2 could result from the lower toxicity of this Cur formulation compared to free Cur on M2-like cells after 24h treatment.<sup>87</sup>

## 2.6. Conclusions

We have developed a strategy to simplify the design of stimuli-responsive formulations, which utilize a single chemical entity to interact with varied endogenous markers for sustained delivery of small-molecule therapeutics. Such NPs have low CMCs, excellent stability, high loading of Cur, and tuned release in response to multiple stimuli prevalent at several disease sites, namely dissolved CO<sub>2</sub>, varied pH, ROS, and the combination of CO<sub>2</sub>/ROS. Depending on the microenvironment, Cur release could be accelerated to up to 80% within 12 h, which offers a broad spectrum to its applicability. We demonstrated lower toxicity and sustained anti-inflammatory efficacy of nano-formulated Cur in macrophage cell models. This work highlights i) the potential of a single chemical entity (tertiary amine) in facilitating the design of smart nanoformulations which offers a platform for further elaboration; and ii) remarkable ability of the Cur-loaded NPs to slowly release Cur and preserve its efficacy while abolishing its toxicity at high concentrations. Such formulations could provide a new avenue to improve preclinical and clinical issues associated with Cur.

## 2.7. References

1. Hwang, D.; Ramsey, J. D.; Kabanov, A. V. Polymeric Micelles for the Delivery of Poorly Soluble Drugs: From Nanoformulation to Clinical Approval. *Adv. Drug Del. Rev.* **2020**, *156*, 80-118.
2. Kakkar, A.; Traverso, G.; Farokhzad, O.; Weissleder, R.; Langer, R. Evolution of Macromolecular Complexity in Drug Delivery Systems. *Nat. Rev. Chem.* **2017**, *1*, 0063.
3. Wong, X. Y.; Sena-Torralba, A.; Álvarez-Diduk, R.; Muthoosamy, K.; Merkoçi, A. Nanomaterials for Nanotheranostics: Tuning Their Properties According to Disease Needs. *ACS Nano* **2020**, *14* (3), 2585-2627.
4. Osorno, L. L.; Brandley, A. N.; Maldonado, D. E.; Yiantsos, A.; Mosley, R. J.; Byrne, M. E. Review of Contemporary Self-Assembled Systems for the Controlled Delivery of Therapeutics in Medicine. *Nanomaterials* **2021**, *11* (2), 278.

5. Renoux, B.; Raes, F.; Legigan, T.; Péraudeau, E.; Eddhif, B.; Poinot, P.; Tranoy-Opalinski, I.; Alsarraf, J.; Koniev, O.; Kolodych, S.; et al. Targeting the Tumour Microenvironment with an Enzyme-Responsive Drug Delivery System for the Efficient Therapy of Breast and Pancreatic Cancers. *Chem. Sci.* **2017**, *8* (5), 3427-3433.
6. Le, N. T. T.; Nguyen, T. N. Q.; Cao, V. D.; Hoang, D. T.; Ngo, V. C.; Hoang Thi, T. T. Recent Progress and Advances of Multi-Stimuli-Responsive Dendrimers in Drug Delivery for Cancer Treatment. *Pharmaceutics* **2019**, *11* (11), 591.
7. Liu, Y.; Chen, F.; Zhang, K.; Wang, Q.; Chen, Y.; Luo, X. pH-Responsive Reversibly Cross-Linked Micelles by Phenol–Yne Click via Curcumin as a Drug Delivery System in Cancer Chemotherapy. *J. Mater. Chem. B* **2019**, *7* (24), 3884-3893.
8. Cook, A. B.; Decuzzi, P. Harnessing Endogenous Stimuli for Responsive Materials in Theranostics. *ACS Nano* **2021**, *15* (2), 2068-2098.
9. Dong, X.; Brahma, R. K.; Fang, C.; Yao, S. Q. Stimulus-Responsive Self-Assembled Prodrugs in Cancer Therapy. *Chem. Sci.* **2022**, *13* (15), 4239-4269.
10. Baghbanbashi, M.; Kakkar, A. Polymersomes: Soft Nanoparticles from Miktoarm Stars for Applications in Drug Delivery. *Mol. Pharm.* **2022**, *19* (6), 1687-1703.
11. Song, Y.; Ding, Y.; Dong, C.-M. Stimuli-Responsive Polypeptide Nanoassemblies: Recent Progress and Applications in Cancer Nanomedicine. *Wiley Interdiscip. Rev.: Nanomed. Nanobiotechnol.* **2022**, *14* (2), e1742.
12. Mitchell, M. J.; Billingsley, M. M.; Haley, R. M.; Wechsler, M. E.; Peppas, N. A.; Langer, R. Engineering Precision Nanoparticles for Drug Delivery. *Nat. Rev. Drug Discov.* **2021**, *20* (2), 101-124.
13. Ding, Y.; Wang, C.; Ma, Y.; Zhu, L.; Lu, B.; Wang, Y.; Wang, J.; Chen, T.; Dong, C.-M.; Yao, Y. pH/ROS Dual-Responsive Supramolecular Polypeptide Prodrug Nanomedicine Based on Host-Guest Recognition for Cancer Therapy. *Acta Biomater.* **2022**, *143*, 381-391.

14. Kajimura, M.; Nakanishi, T.; Takenouchi, T.; Morikawa, T.; Hishiki, T.; Yukutake, Y.; Suematsu, M. Gas Biology: Tiny Molecules Controlling Metabolic Systems. *Respir. Physiol. Neurobiol.* **2012**, *184* (2), 139-148.
15. Farrugia, G.; Szurszewski, J. H. Carbon Monoxide, Hydrogen Sulfide, and Nitric Oxide as Signaling Molecules in the Gastrointestinal Tract. *Gastroenterology* **2014**, *147* (2), 303-313.
16. Zhang, Q.; Zhu, S. Oxygen and Carbon Dioxide Dual Responsive Nanoaggregates of Fluoro- and Amino-Containing Copolymer. *ACS Mater. Lett.* **2014**, *3* (8), 743-746.
17. Fagone, P.; Mazzon, E.; Bramanti, P.; Bendtzen, K.; Nicoletti, F. Gasotransmitters and the Immune System: Mode of Action and Novel Therapeutic Targets. *Eur. J. Pharmacol.* **2018**, *834*, 92-102.
18. Pałasz, A.; Menezes, I. C.; Worthington, J. J. The Role of Brain Gaseous Neurotransmitters in Anxiety. *Pharmacol. Rep.* **2021**, *73* (2), 357-371.
19. Yong, H. W.; Kakkar, A. The Unexplored Potential of Gas-Responsive Polymers in Drug Delivery: Progress, Challenges and Outlook. *Polym. Int.* **2022**, *71* (5), 514-520.
20. Geers, C.; Gros, G. Carbon Dioxide Transport and Carbonic Anhydrase in Blood and Muscle. *Physiol. Rev.* **2000**, *80* (2), 681-715.
21. Kikuchi, R.; Iwai, Y.; Tsuji, T.; Watanabe, Y.; Koyama, N.; Yamaguchi, K.; Nakamura, H.; Aoshiba, K. Hypercapnic Tumor Microenvironment Confers Chemoresistance to Lung Cancer Cells by Reprogramming Mitochondrial Metabolism *In Vitro*. *Free Radical Biol. Med.* **2019**, *134*, 200-214.
22. Nevler, A.; Brown, S. Z.; Nauheim, D.; Portocarrero, C.; Rodeck, U.; Bassig, J.; Schultz, C. W.; McCarthy, G. A.; Lavu, H.; Yeo, T. P.; et al. Effect of Hypercapnia, an Element of Obstructive Respiratory Disorder, on Pancreatic Cancer Chemoresistance and Progression. *J. Am. Coll. Surg.* **2020**, *230* (4), 659-667.

23. Asmat, U.; Abad, K.; Ismail, K. Diabetes Mellitus and Oxidative Stress—a Concise Review. *Saudi Pharm. J.* **2016**, *24* (5), 547-553.
24. Kudryavtseva, A. V.; Krasnov, G. S.; Dmitriev, A. A.; Alekseev, B. Y.; Kardymon, O. L.; Sadritdinova, A. F.; Fedorova, M. S.; Pokrovsky, A. V.; Melnikova, N. V.; Kaprin, A. D.; et al. Mitochondrial Dysfunction and Oxidative Stress in Aging and Cancer. *Oncotarget* **2016**, *7*, 44879-44905.
25. van der Vliet, A.; Janssen-Heininger, Y. M. W.; Anathy, V. Oxidative Stress in Chronic Lung Disease: From Mitochondrial Dysfunction to Dysregulated Redox Signaling. *Mol. Aspects Med.* **2018**, *63*, 59-69.
26. Senoner, T.; Dichtl, W. Oxidative Stress in Cardiovascular Diseases: Still a Therapeutic Target? *Nutrients* **2019**, *11* (9), 2090.
27. Singh, A.; Kukreti, R.; Saso, L.; Kukreti, S. Oxidative Stress: A Key Modulator in Neurodegenerative Diseases. *Molecules* **2019**, *24* (8), 1583.
28. Ezraty, B.; Chabalier, M.; Ducret, A.; Maisonneuve, E.; Dukan, S. CO<sub>2</sub> Exacerbates Oxygen Toxicity. *EMBO reports* **2011**, *12* (4), 321-326.
29. Collin, F. Chemical Basis of Reactive Oxygen Species Reactivity and Involvement in Neurodegenerative Diseases. *Int. J. Mol. Sci.* **2019**, *20* (10), 2407.
30. Chen, W.; Du, J. Ultrasound and pH Dually Responsive Polymer Vesicles for Anticancer Drug Delivery. *Sci. Rep.* **2013**, *3* (1), 2162.
31. Yuan, W.; Shen, J.; Zou, H. Amphiphilic Block Copolymer Terminated with Pyrene Group: From Switchable CO<sub>2</sub>-Temperature Dual Responses to Tunable Fluorescence. *RSC Adv.* **2015**, *5* (17), 13145-13152.
32. Jiang, X.; Chun, F.; Lu, G.; Xiaoyu, H. Oxygen and Carbon Dioxide Dual Gas-Responsive Homopolymers and Diblock Copolymers Synthesized via RAFT Polymerization. *Polym. Chem.* **2017**, *8* (7), 1163-1176.

33. John, J. V.; Uthaman, S.; Augustine, R.; Chen, H.; Park, I.-K.; Kim, I. pH/Redox Dual Stimuli-Responsive Sheddable Nanodaisies for Efficient Intracellular Tumour-Triggered Drug Delivery. *J. Mater. Chem. B* **2017**, *5* (25), 5027-5036.
34. Cao, Z.-Q.; Wang, G.-J. Multi-Stimuli-Responsive Polymer Materials: Particles, Films, and Bulk Gels. *Chem. Rec.* **2016**, *16* (3), 1398-1435.
35. Fu, X.; Hosta-Rigau, L.; Chandrawati, R.; Cui, J. Multi-Stimuli-Responsive Polymer Particles, Films, and Hydrogels for Drug Delivery. *Chem* **2018**, *4* (9), 2084-2107.
36. Dai, X.; Bai, Y.; Zhang, Y.; Ma, Z.; Li, J.; Sun, H.; Zhang, X. Protonation–Activity Relationship of Bioinspired Ionizable Glycomimetics for the Growth Inhibition of Bacteria. *ACS Appl. Bio Mat.* **2020**, *3* (6), 3868-3879.
37. Macherey, A.-C.; Dansette, P. M. Chemical Mechanisms of Toxicity: Basic Knowledge for Designing Safer Drugs. In *The Practice of Medicinal Chemistry (Second Edition)*, Wermuth, C. G. Ed.; Academic Press, 2003; pp 545-560.
38. Balagam, B.; Richardson, D. E. The Mechanism of Carbon Dioxide Catalysis in the Hydrogen Peroxide N-Oxidation of Amines. *Inorg. Chem.* **2008**, *47* (3), 1173-1178.
39. Li, B.; Shan, M.; Di, X.; Gong, C.; Zhang, L.; Wang, Y.; Wu, G. A Dual pH- and Reduction-Responsive Anticancer Drug Delivery System Based on PEG–SS–Poly(Amino Acid) Block Copolymer. *RSC Adv.* **2017**, *7* (48), 30242-30249.
40. Wang, M.; Zhang, X.; Peng, H.; Zhang, M.; Zhang, X.; Liu, Z.; Ma, L.; Wei, H. Optimization of Amphiphilic Miktoarm Star Copolymers for Anticancer Drug Delivery. *ACS Biomater. Sci. Eng.* **2018**, *4* (8), 2903-2910.
41. Cook, A. B.; Perrier, S. Branched and Dendritic Polymer Architectures: Functional Nanomaterials for Therapeutic Delivery. *Adv. Funct. Mater.* **2020**, *30* (2), 1901001.
42. Yong, H. W.; Kakkar, A. Nanoengineering Branched Star Polymer-Based Formulations: Scope, Strategies, and Advances. *Macromol. Biosci.* **2021**, *21* (8), 2100105.

43. Gaitzsch, J.; Chudasama, V.; Morecroft, E.; Messenger, L.; Battaglia, G. Synthesis of an Amphiphilic Miktoarm Star Terpolymer for Self-Assembly into Patchy Polymersomes. *ACS Mater. Lett.* **2016**, *5* (3), 351-354.
44. Saravanakumar, G.; Park, H.; Kim, J.; Park, D.; Pramanick, S.; Kim, D. H.; Kim, W. J. Miktoarm Amphiphilic Block Copolymer with Singlet Oxygen-Labile Stereospecific  $\beta$ -Aminoacrylate Junction: Synthesis, Self-Assembly, and Photodynamically Triggered Drug Release. *Biomacromolecules* **2018**, *19* (6), 2202-2213.
45. Kumar, P.; Kim, S.-H.; Yadav, S.; Jo, S.-H.; Yoo, S., II; Park, S.-H.; Lim, K. T. Redox-Responsive Core-Cross-Linked Micelles of Miktoarm Poly(ethylene oxide)-*b*-Poly(furfuryl methacrylate) for Anticancer Drug Delivery. *ACS Appl. Mater. Interfaces* **2023**, *15* (10), 12719-12734.
46. Zhang, Y.; Xu, C.; Zhang, D.; Chen, X. Proteinosomes via Self-Assembly of Thermoresponsive Miktoarm Polymer Protein Bioconjugates. *Biomacromolecules* **2023**, *24* (5), 1994-2002.
47. Farghadani, R.; Naidu, R. Curcumin: Modulator of Key Molecular Signaling Pathways in Hormone-Independent Breast Cancer. *Cancers* **2021**, *13* (14), 3427.
48. Kunnumakkara, A. B.; Hegde, M.; Parama, D.; Girisa, S.; Kumar, A.; Daimary, U. D.; Garodia, P.; Yeniseti, S. C.; Oommen, O. V.; Aggarwal, B. B. Role of Turmeric and Curcumin in Prevention and Treatment of Chronic Diseases: Lessons Learned from Clinical Trials. *ACS Pharmacol. Transl. Sci.* **2023**, *6* (4), 447-518.
49. Suresh, K.; Nangia, A. Curcumin: Pharmaceutical Solids as a Platform to Improve Solubility and Bioavailability. *CrystEngComm* **2018**, *20* (24), 3277-3296.
50. Li, L.; Zhang, X.; Pi, C.; Yang, H.; Zheng, X.; Zhao, L.; Wei, Y. Review of Curcumin Physicochemical Targeting Delivery System. *Int. J. Nanomedicine* **2020**, *15*, 9799-9821.

51. Zhou, Y.; Zhang, T.; Wang, X.; Wei, X.; Chen, Y.; Guo, L.; Zhang, J.; Wang, C. Curcumin Modulates Macrophage Polarization through the Inhibition of the Toll-Like Receptor 4 Expression and Its Signaling Pathways. *Cell. Physiol. Biochem.* **2015**, *36* (2), 631-641.
52. Knop, K.; Hoogenboom, R.; Fischer, D.; Schubert, U. S. Poly(ethylene glycol) in Drug Delivery: Pros and Cons as Well as Potential Alternatives. *Angew. Chem. Int. Ed.* **2010**, *49* (36), 6288-6308.
53. Gulati, N. M.; Stewart, P. L.; Steinmetz, N. F. Bioinspired Shielding Strategies for Nanoparticle Drug Delivery Applications. *Mol. Pharm.* **2018**, *15* (8), 2900-2909.
54. Shi, L.; Zhang, J.; Zhao, M.; Tang, S.; Cheng, X.; Zhang, W.; Li, W.; Liu, X.; Peng, H.; Wang, Q. Effects of Polyethylene Glycol on the Surface of Nanoparticles for Targeted Drug Delivery. *Nanoscale* **2021**, *13* (24), 10748-10764.
55. Lu, J.; Owen, S. C.; Shoichet, M. S. Stability of Self-Assembled Polymeric Micelles in Serum. *Macromolecules* **2011**, *44* (15), 6002-6008.
56. Lazzari, S.; Moscatelli, D.; Codari, F.; Salmona, M.; Morbidelli, M.; Diomedede, L. Colloidal Stability of Polymeric Nanoparticles in Biological Fluids. *J. Nanopart. Res.* **2012**, *14* (6), 920.
57. Moore, T. L.; Rodriguez-Lorenzo, L.; Hirsch, V.; Balog, S.; Urban, D.; Jud, C.; Rothen-Rutishauser, B.; Lattuada, M.; Petri-Fink, A. Nanoparticle Colloidal Stability in Cell Culture Media and Impact on Cellular Interactions. *Chem. Soc. Rev.* **2015**, *44* (17), 6287-6305.
58. Malikmammadov, E.; Tanir, T. E.; Kiziltay, A.; Hasirci, V.; Hasirci, N. PCL and PCL-Based Materials in Biomedical Applications. *J. Biomater. Sci., Polym. Ed.* **2018**, *29* (7-9), 863-893.
59. Thijssen, Q.; Cornelis, K.; Alkaissy, R.; Locs, J.; Damme, L. V.; Schaubroeck, D.; Willaert, R.; Snelling, S.; Mouthuy, P.-A.; Van Vlierberghe, S. Tough Photo-Cross-Linked PCL-Hydroxyapatite Composites for Bone Tissue Engineering. *Biomacromolecules* **2022**, *23*, 1366-1375.

60. Yang, Y.; Wu, H.; Fu, Q.; Xie, X.; Song, Y.; Xu, M.; Li, J. 3D-Printed Polycaprolactone-Chitosan Based Drug Delivery Implants for Personalized Administration. *Mater. Des.* **2022**, *214*, 110394.
61. Lotocki, V.; Yazdani, H.; Zhang, Q.; Gran, E. R.; Nyrko, A.; Maysinger, D.; Kakkar, A. Miktoarm Star Polymers with Environment-Selective ROS/GSH Responsive Locations: From Modular Synthesis to Tuned Drug Release through Micellar Partial Corona Shedding and/or Core Disassembly. *Macromol. Biosci.* **2021**, *21* (2), 2000305.
62. Lavasanifar, A.; Samuel, J.; Kwon, G. S. Micelles Self-Assembled from Poly(ethylene oxide)-*block*-Poly(N-hexyl stearate L-aspartamide) by a Solvent Evaporation Method: Effect on the Solubilization and Haemolytic Activity of Amphotericin B. *J. Controlled Release* **2001**, *77* (1), 155-160.
63. Discher, D. E.; Ahmed, F. Polymersomes. *Annu. Rev. Biomed. Eng.* **2006**, *8* (1), 323-341.
64. Schuetz, P.; Greenall, M. J.; Bent, J.; Furzeland, S.; Atkins, D.; Butler, M. F.; McLeish, T. C. B.; Buzza, D. M. A. Controlling the Micellar Morphology of Binary PEO-PCL Block Copolymers in Water-THF through Controlled Blending. *Soft Matter* **2011**, *7* (2), 749-759.
65. Liu, G.-Y.; Chen, C.-J.; Ji, J. Biocompatible and Biodegradable Polymersomes as Delivery Vehicles in Biomedical Applications. *Soft Matter* **2012**, *8* (34), 8811-8821.
66. Xia, Y.; Ding, S.; Liu, Y.; Qi, Z. Facile Synthesis and Self-Assembly of Amphiphilic Polyether-Octafunctionalized Polyhedral Oligomeric Silsesquioxane via Thiol-Ene Click Reaction. *Polymers* **2017**, *9* (7), 251.
67. Xie, Y.; Li, J.; Li, Z.; Sun, T.; Wang, Y.; Qu, G. The Adsorption and Aggregation Properties of Dendritic Cationic Tetrameric Surfactants. *RSC Adv.* **2018**, *8* (63), 36015-36024.
68. Wang, M.; Long, J.; Zhang, S.; Liu, F.; Zhang, X.; Zhang, X.; Sun, L.; Ma, L.; Yu, C.; Wei, H. Folate-Targeted Anticancer Drug Delivery via a Combination Strategy of a Micelle Complex and Reducible Conjugation. *ACS Biomater. Sci. Eng.* **2020**, *6* (3), 1565-1572.

69. Pepin, S.; Blanchet, P.; Landry, V. Performances of White Pine and White Spruce Treated with Organic Fungicides Using an Aqueous Buffered Amine Oxide Preservation System. *BioResources* **2018**, *14* (1), 25.
70. Naksuriya, O.; Okonogi, S.; Schiffelers, R. M.; Hennink, W. E. Curcumin Nanoformulations: A Review of Pharmaceutical Properties and Preclinical Studies and Clinical Data Related to Cancer Treatment. *Biomaterials* **2014**, *35* (10), 3365-3383.
71. Hewlings, S. J.; Kalman, D. S. Curcumin: A Review of Its Effects on Human Health. *Foods* **2017**, *6* (10), 92.
72. Skandalis, A.; Selianitis, D.; Sory, D. R.; Rankin, S. M.; Jones, J. R.; Pispas, S. Poly(2-(dimethylamino) ethyl methacrylate)-*b*-poly(lauryl methacrylate)-*b*-poly(oligo ethylene glycol methacrylate) Triblock Terpolymer Micelles as Drug Delivery Carriers for Curcumin. *J. Appl. Polym. Sci.* **2022**, *139*, e52899.
73. Jing, X.-W.; Huang, Z.-Y.; Lu, H.-S.; Wang, B.-G. CO<sub>2</sub>-Sensitive Amphiphilic Triblock Copolymer Self-Assembly Morphology Transition and Accelerating Drug Release from Polymeric Vesicle. *Chin. J. Polym. Sci.* **2018**, *36* (1), 18-24.
74. Gao, W.; Chan, J. M.; Farokhzad, O. C. pH-Responsive Nanoparticles for Drug Delivery. *Mol. Pharm.* **2010**, *7* (6), 1913-1920.
75. Mo, R.; Gu, Z. Tumor Microenvironment and Intracellular Signal-Activated Nanomaterials for Anticancer Drug Delivery. *Mater. Today* **2016**, *19* (5), 274-283.
76. Deirram, N.; Zhang, C.; Kermaniyan, S. S.; Johnston, A. P. R.; Such, G. K. pH-Responsive Polymer Nanoparticles for Drug Delivery. *Macromol. Rapid Commun.* **2019**, *40* (10), 1800917.
77. Mao, J.; Li, Y.; Wu, T.; Yuan, C.; Zeng, B.; Xu, Y.; Dai, L. A Simple Dual-pH Responsive Prodrug-Based Polymeric Micelles for Drug Delivery. *ACS Appl. Mater. Interfaces* **2016**, *8* (27), 17109-17117.

78. Zhang, T.; Chen, X.; Xiao, C.; Zhuang, X.; Chen, X. Synthesis of a Phenylboronic Ester-Linked PEG-Lipid Conjugate for ROS-responsive Drug Delivery. *Polym. Chem.* **2017**, *8* (40), 6209-6216.
79. Zhang, Y.-M.; Xia, M.; Ao, R.; Gao, L.-X.; Tang, Y.; Huang, J.-H.; Luo, Y.-F.; Chen, Z.-Z.; Wang, B.-C.; Huang, Z. Smart Design of Mitochondria-Targeted and ROS-Responsive CPI-613 Delivery Nanoplatfrom for Bioenergetic Pancreatic Cancer Therapy. *Nanomaterials* **2021**, *11* (11), 2875.
80. G. Godfrey, A.; Ganem, B. Ready Oxidation of Halides to Aldehydes Using Trimethylamine N-Oxide in Dimethylsulfoxide. *Tetrahedron Lett.* **1990**, *31* (34), 4825-4826.
81. Benson, H.; Kita-Tokarczyk, K.; Leinweber, D.; Neuhoff, H.; Kratz, A.; Romanski, S. Cosmetic Compositions Comprising Estolide Esters and Uses for Hair Treatment. US US10,238,591, Mar 26, 2019.
82. Baumeister, T.; Zikeli, S.; Kitzler, H.; Aigner, P.; Wieczorek, P. P.; Röder, T. Continuous Flow Synthesis of Amine Oxides by Oxidation of Tertiary Amines. *React. Chem. Eng.* **2019**, *4* (7), 1270-1276.
83. Mathematical Models of Drug Release. In *Strategies to Modify the Drug Release from Pharmaceutical Systems*, Bruschi, M. L. Ed.; Woodhead Publishing, 2015; pp 63-86.
84. Paarakh, M. P.; Jose, P. A.; Setty, C. M.; Peterchristoper, G. V. Release Kinetics – Concepts and Applications. *IJPRT* **2018**, *8* (1), 12-20.
85. Yang, C.-W.; Chang, C.-L.; Lee, H.-C.; Chi, C.-W.; Pan, J.-P.; Yang, W.-C. Curcumin Induces the Apoptosis of Human Monocytic Leukemia THP-1 Cells Via the Activation of JNK/ERK Pathways. *BMC Complementary Altern. Med.* **2012**, *12* (1), 22.
86. Cheneval, D.; Ramage, P.; Kastelic, T.; Szelestenyi, T.; Niggli, H.; Hemmig, R.; Bachmann, M.; MacKenzie, A. Increased Mature Interleukin-1 $\beta$  (IL-1 $\beta$ ) Secretion from THP-1 Cells Induced by Nigericin Is a Result of Activation of P45 IL-1 $\beta$ -Converting Enzyme Processing. *J. Biol. Chem.* **1998**, *273* (28), 17846-17851.

87. Ahsan, H.; Hadi, S. M. Strand Scission in DNA Induced by Curcumin in the Presence of Cu(II). *Cancer Lett.* **1998**, *124* (1), 23-30.

## 2.8 Appendix A: Supporting Information for Chapter 2

### Characterization

#### Nuclear Magnetic Resonance (NMR)

All NMR spectra were recorded either on a Bruker AVIIIHD 500 MHz or Varian VNMRS 500 MHz spectrometer at ambient temperature. The residual undeuterated solvent in chloroform-d and deuterium oxide was used as the internal standard and were calibrated at 7.26 ppm ( $^1\text{H}$  NMR) and 77.16 ppm ( $^{13}\text{C}$  NMR), and 4.79 ppm ( $^1\text{H}$  NMR), respectively.

#### Matrix-assisted Laser Desorption Ionization- Time of Flight (MALDI-ToF)

Mass spectra were acquired in linear positive ion mode using a Bruker MALDI Autoflex III TOF mass spectrometer controlled by Flex Analysis.

#### Attenuated Total Reflectance- Fourier-transform Infrared Spectrometer (ATR-FTIR)

An ATR-FTIR spectrometer equipped with a single bounce diamond crystal and a LiTaO<sub>3</sub> detector was used to confirm the structure of MePEG<sub>2000</sub>-N<sub>3</sub>. Measurements were conducted with dry polymer samples at room temperature from 400 to 4000 cm<sup>-1</sup>.

#### Gel Permeation Chromatography (GPC)

The number-average molecular weight ( $M_n$ ) and polydispersity index ( $D$ ) were determined using GPC with THF as an eluent. Measurements were performed on a Waters Breeze system equipped with 3 Waters Styragel HR columns (HR1 with a molar mass range of 100-5000 g mol<sup>-1</sup>, HR2 with a molar mass range of 500-20000 g mol<sup>-1</sup>, HR4 with a molar mass range of 5000-600000 g mol<sup>-1</sup>) and a guard column. The flow rate was 0.3 mL min<sup>-1</sup> (40 °C) while the standards used were polymethyl methacrylate (PMMA) standards (PSS Polymer Standards Service GmbH, molar masses ranging from 682 to 1520000 g mol<sup>-1</sup>). Sample detection and quantification were conducted with a differential refractive index detector (RI 2414).

### Dynamic Light Scattering (DLS)

The hydrodynamic diameters and distribution of blank and drug-loaded micelles were measured by DLS using a Brookhaven Instrument NanoBrook Omni equipped with a 40 mW diode laser operating at 640 nm at room temperature.

### Transmission Electron Microscopy (TEM)

The morphologies of blank and drug-loaded micelles were examined with a FEI Tecnai 12 BioTwin 120 kV microscope equipped with an AMT XR80 CCD Camera System located at the Facility for Electron Microscopy Research (FEMR) at McGill University. The solutions were stained with 2% uranyl acetate prior to analysis.

### Fluorescence

The fluorescence spectra were measured using a Varian Cary Eclipse fluorescence spectrometer at room temperature.

### pH measurements

pH measurements were carried out at room temperature using the Fisherbrand™ 13-636-AE150 accumet AE150 pH meter equipped with a Fisherbrand™ accumet™ AE series single junction gel pH electrode.

### Ultraviolet-visible spectroscopy (UV-Vis)

The Cur standard curve and drug release studies were recorded on an Agilent UV-Vis spectrophotometer Cary50 operating with a Xenon lamp at room temperature. All measurements were done in triplicates.

### Application of drug release kinetic models on release data

*Zero-order model:* The drug release was represented by the equation:

$$C_t = C_0 + k_0t$$

where  $C_t$  = amount of drug released at time  $t$ ,  $C_0$  = initial concentration of drug at time  $t=0$ ,  $k_0$  = zero-order rate constant. Here, a %cumulative drug release vs. time graph was plotted to obtain  $k_0$  (slope of graph) and the correlation coefficient ( $R^2$ ) value.

*First-order model:* The drug release was represented by the equation:

$$\log C = \log C_0 - k_1 \frac{t}{2.303}$$

where C= % drug remaining at time t, C<sub>0</sub>= initial concentration of the drug, k<sub>1</sub>= first order rate constant, expressed in h<sup>-1</sup>. Here, a log %cumulative drug release vs. time graph was plotted to obtain R<sup>2</sup>, while K<sub>1</sub> = slope of the graph \* 2.303.

*Higuchi model:* The drug release was represented by the equation:

$$\frac{M_t}{M_\infty} = k_H t^{\frac{1}{2}}$$

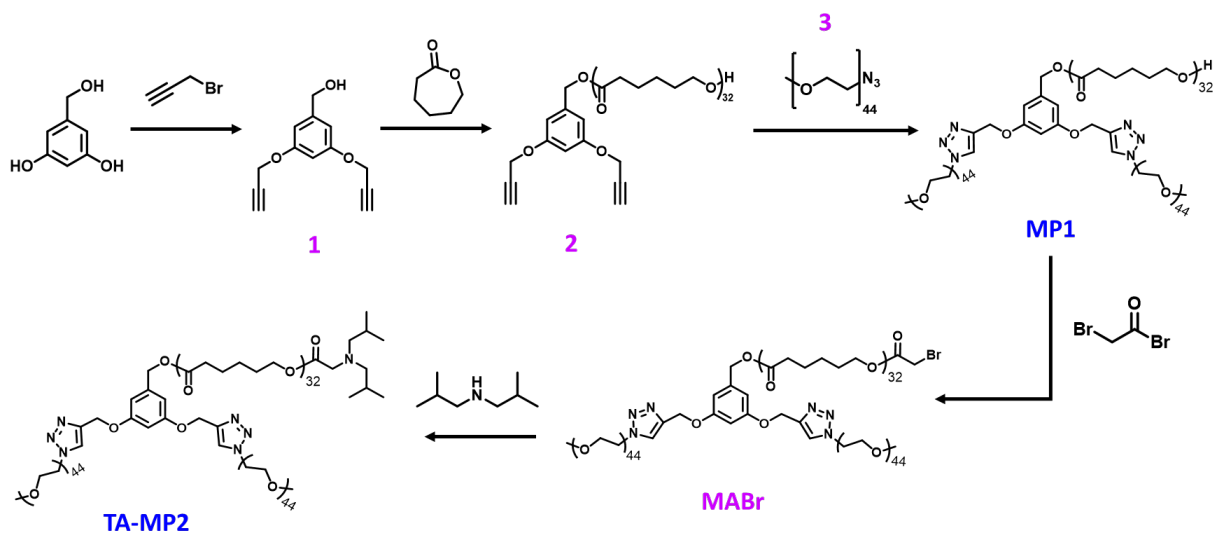
where M<sub>t</sub>/M<sub>∞</sub>= fraction of drug released at time t, M<sub>t</sub>= amount of drug released at time t, M<sub>∞</sub>= amount of drug released after time ∞, k<sub>H</sub>= Higuchi release kinetic constant. Here, a %cumulative drug release vs. square root of time graph was plotted to obtain k<sub>H</sub> (slope of graph) and R<sup>2</sup>.

*Korsmeyer-Peppas model:* The drug release was represented by the equation:

$$\frac{M_t}{M_\infty} = k_{K-P} t^n$$

where M<sub>t</sub>/M<sub>∞</sub>= fraction of drug released at time t, M<sub>t</sub>= amount of drug released in time t, M<sub>∞</sub>= amount of drug released after time ∞, k<sub>K-P</sub>= the Korsmeyer release rate constant, n is the diffusional exponent. Here, a log %cumulative drug release vs. log time graph was plotted to obtain n (slope of graph) and R<sup>2</sup>, while k<sub>K-P</sub> was obtained by inverse log (graph intersection).

## Synthesis



**Scheme 2. 3:** Synthesis of MP1 and multi-responsive miktoarm polymer TA-MP2.

### Synthesis of 3,5- bis(prop-2-ynyloxy)benzyl methanol (1)

To a stirred solution of propargyl bromide (3.18 mL, 35.69 mmol, 2.5 eq) and 3,5-dihydroxybenzyl alcohol (2.00 g, 14.27 mmol, 1 eq) in acetone (50 mL),  $K_2CO_3$  (2.56 g, 18.52 mmol, 1.3 eq) and 18-crown-6 (0.15 g, 0.57 mmol, 0.04 eq) were added and the reaction mixture was refluxed at 65 °C under nitrogen for 24 h with magnetic stirring. After cooling down to room temperature, any residue from the reaction mixture was removed by vacuum filtration. The filtrate was then evaporated to dryness under reduced pressure and partitioned between water and dichloromethane (DCM). The aqueous layer was extracted with DCM three times and the combined organic extracts were dried with anhydrous  $Na_2SO_4$  and then dried under reduced pressure. The crude product was purified by column chromatography using 1:1 hexane and ethyl acetate. After evaporation of solvents, the product was recovered as an off-white solid (2.7 g, 87% yield).  $^1H$  NMR ( $CDCl_3$ , 500 MHz):  $\delta$  (ppm) 1.93 (br s, 1H, -OH), 2.53 (t, 2H, -OCCCH), 4.63 (s, 2H, - $CH_2OH$ ), 4.67 (d, 4H, - $OCH_2$ ), 6.53 (t, 1H, Ar H), 6.62 (s, 2H, Ar H).  $^{13}C\{^1H\}$  NMR ( $CDCl_3$ , 125 MHz):  $\delta$  (ppm) 56.1, 65.2, 75.8, 78.5, 101.6, 106.3, 143.7, 158.9.

Synthesis of 3,5- bis(prop-2-ynyloxy)benzyl polycaprolactone (2)

1 (0.1 g, 0.46 mmol, 1 eq) was dissolved in dry toluene and heated to 100 °C under nitrogen with magnetic stirring.  $\epsilon$ -caprolactone (1.8 mL, 67 mmol, 35 eq) was subsequently added to the mixture and heated to 110 °C. Tin(II) 2-ethyl hexanoate (0.015 mL, 0.67 mmol, 0.1 eq) was then added and the reaction mixture was refluxed at 115 °C for 24 h. After cooling down to room temperature, the solvent was removed under reduced pressure. The crude product was purified by dissolving in minimal DCM and precipitated in ice cold methanol. The product was collected under vacuum filtration and dried in a dessicator (1.8 g, 90% yield).  $^1\text{H}$  NMR ( $\text{CDCl}_3$ , 500 MHz):  $\delta$  (ppm) 1.34- 1.40 (m, 67H, (-OC-CH<sub>2</sub>-CH<sub>2</sub>-CH<sub>2</sub>-CH<sub>2</sub>-CH<sub>2</sub>-O)<sub>33</sub>), 1.60- 1.67 (m, 140H, (-OC-CH<sub>2</sub>-CH<sub>2</sub>-CH<sub>2</sub>-CH<sub>2</sub>-CH<sub>2</sub>-O)<sub>33</sub>), 2.31 (t, 66H, (-OC-CH<sub>2</sub>-CH<sub>2</sub>-CH<sub>2</sub>-CH<sub>2</sub>-CH<sub>2</sub>-O)<sub>33</sub>), 2.52 (t, 2H, -C $\equiv$ CH), 4.04 (t, 67H, (-OC-CH<sub>2</sub>-CH<sub>2</sub>-CH<sub>2</sub>-CH<sub>2</sub>-CH<sub>2</sub>-O)<sub>33</sub>), 4.66 (d, 4H, CH<sub>2</sub>-C $\equiv$ C), 5.04 (s, 2H, CH<sub>2</sub>-OH), 6.56 (t, 1H, Ar-H), 6.59 (d, 2H, Ar-H).  $^{13}\text{C}$  { $^1\text{H}$ } NMR ( $\text{CDCl}_3$ , 125 MHz):  $\delta$  (ppm) 24.7, 25.7, 28.5, 34.2, 56.1, 62.8, 64.2, 65.9, 75.9, 78.4, 101.9, 107.6, 158.9, 173.7. MS: MALDI-TOF  $M_n$  = 3635.30;  $M_w$  = 3743.79; PDI = 1.03; DP = 32.

Synthesis of tosyl PEG<sub>2000</sub> monomethyl ether (MePEG<sub>2000</sub>-OTs)

MePEG<sub>2000</sub> monomethyl ether (3 g, 1.5 mmol, 1 eq) was added to a 3-neck flask and dissolved in THF under nitrogen. Subsequently, a solution of NaOH (0.18 g, 4.5 mmol, 3 eq) dissolved in 0.5 mL H<sub>2</sub>O was added. A separate solution of *p*-toluenesulfonyl chloride (0.858 g, 4.5 mmol, 3 eq) in THF was added slowly dropwise to the reaction mixture. After letting it stir overnight, the solvent was removed from the flask under reduced pressure, and the product was extracted with DCM thrice from water. The organic extracts were combined and dried with MgSO<sub>4</sub>. The solution was then filtered, concentrated, and then precipitated into ice cold diethyl ether under vigorous stirring. The pure precipitated product was obtained by filtration as a white solid (2.6 g, 79% yield).  $^1\text{H}$  NMR ( $\text{CDCl}_3$ , 500 MHz):  $\delta$  (ppm) 2.43 (s, 3H, CH<sub>3</sub>), 3.36 (s, 3H, OCH<sub>3</sub>), 3.63 (m, 182H, PEG), 4.14 (t, 2H, CH<sub>2</sub>-OTs), 7.33 (d, 2H, H-Ar), 7.78 (d, 2H, H-Ar).  $^{13}\text{C}$  { $^1\text{H}$ } NMR ( $\text{CDCl}_3$ , 125 MHz):  $\delta$  (ppm) 21.8, 59.2, 70.7, 127.2, 128.1, 129.9, 130.4.

Synthesis of azido PEG<sub>2000</sub> monomethyl ether (3)

MePEG<sub>2000</sub>-OTs (2.4 g, 1.14 mmol, 1 eq), NaN<sub>3</sub> (0.592 g, 9.11 mmol, 8 eq) and anhydrous ethanol were added to a 3-neck flask under nitrogen. The reaction mixture was heated to 90 °C and stirred for 24 h. The ethanol was then removed under reduced pressure and the mixture was extracted 4 times with DCM from water before drying with MgSO<sub>4</sub>. The product was then concentrated in DCM and precipitated by dropwise addition to ice cold diethyl ether. After filtration and drying under reduced pressure, a white solid product was obtained (2.1 g, 94% yield). <sup>1</sup>H NMR (CDCl<sub>3</sub>, 500 MHz): δ (ppm) 3.37 (s, 3H, OCH<sub>3</sub>), 3.49 (t, 2H, CH<sub>2</sub>-O), 3.63 (m, 181H, PEG). <sup>13</sup>C{<sup>1</sup>H} NMR (CDCl<sub>3</sub>, 125 MHz): δ (ppm) 50.8, 59.1, 61.8, 70.6, 72.0, 72.6.

## Supplementary Figures

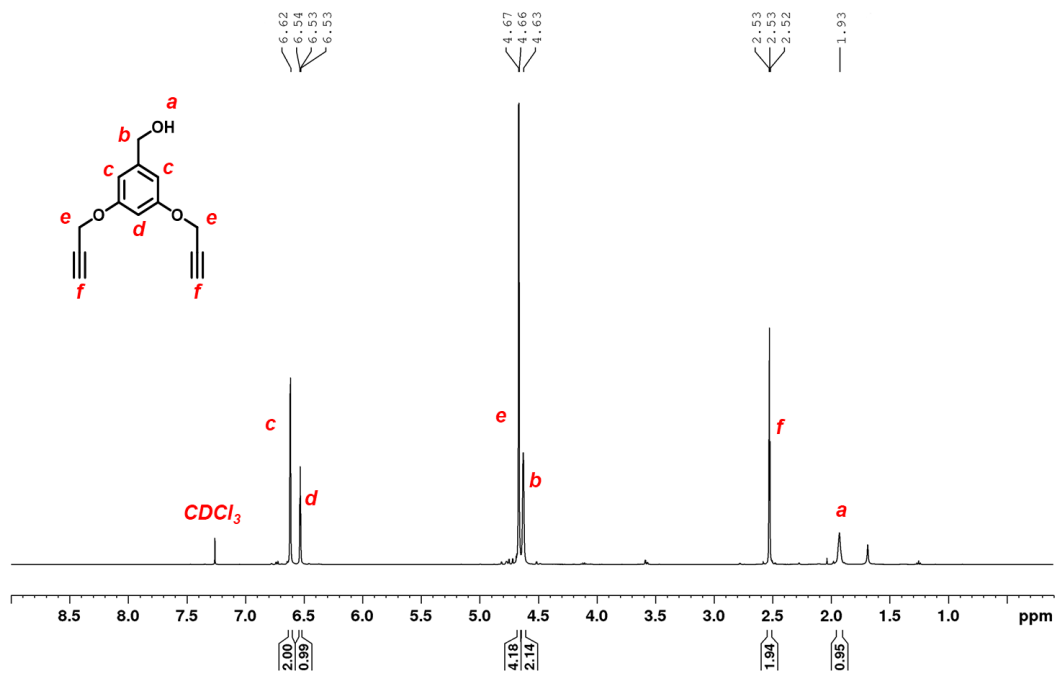


Figure 2. 6:  $^1\text{H}$  NMR spectrum of 3,5-bis(prop-2-ynoxy)benzyl methanol (1).

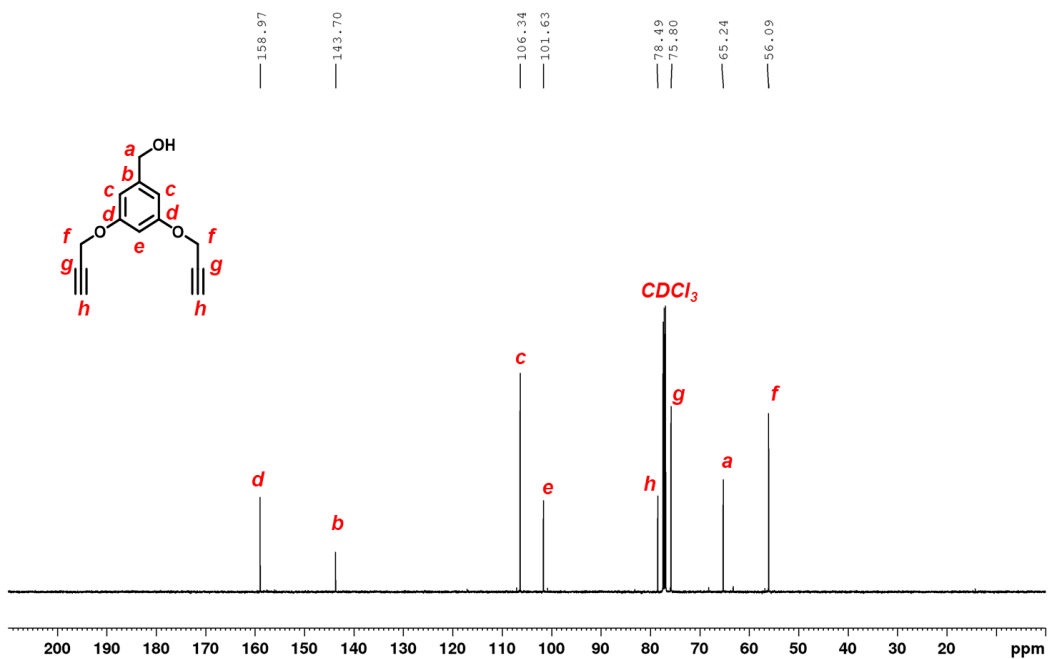


Figure 2. 7:  $^{13}\text{C}$  NMR spectrum of 1.

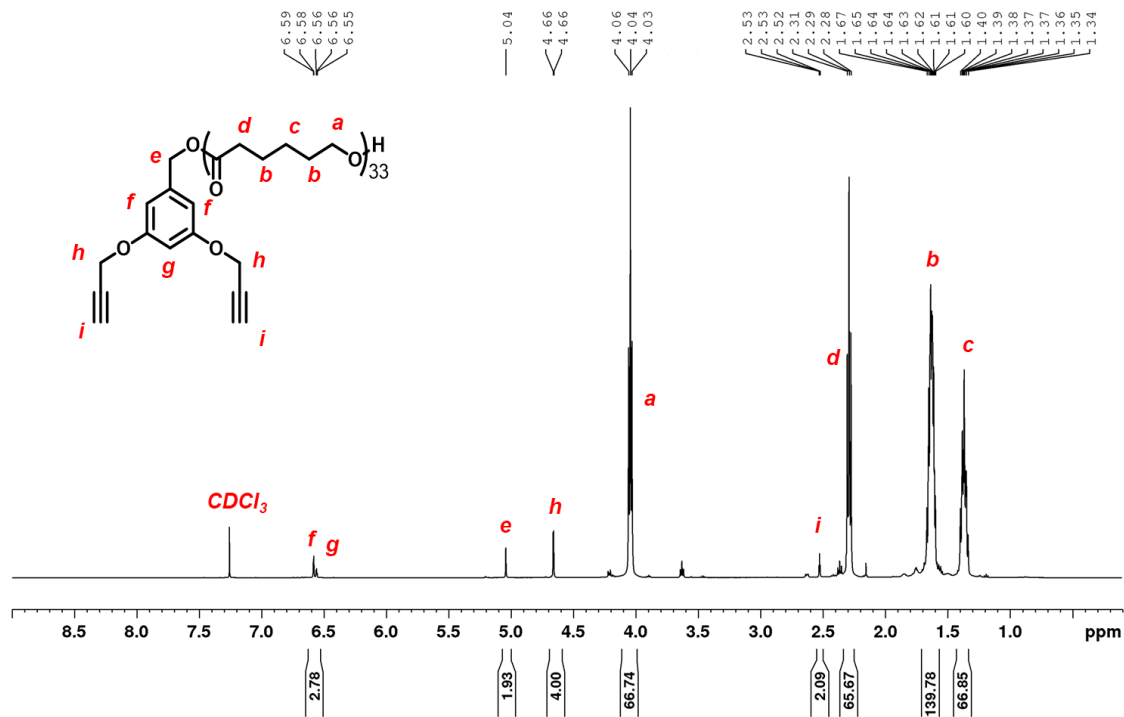


Figure 2. 8:  $^1\text{H}$  NMR spectrum of 3,5- bis(prop-2-ynoxy)benzyl polycaprolactone (2).

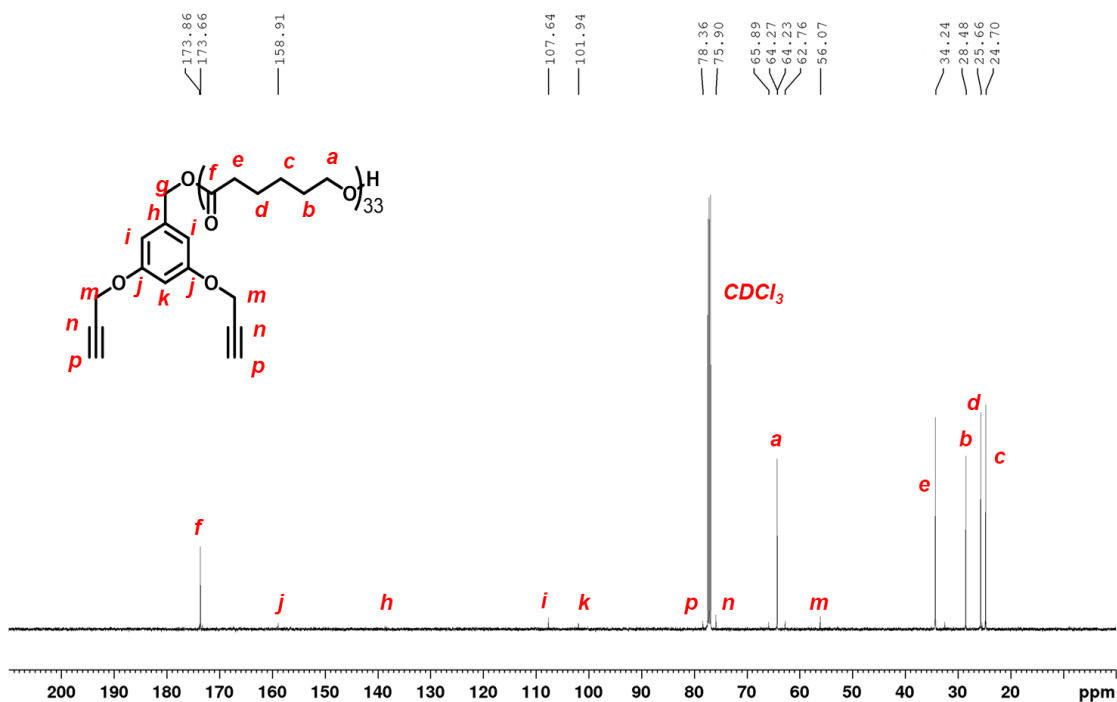


Figure 2. 9:  $^{13}\text{C}$  NMR spectrum of 2.



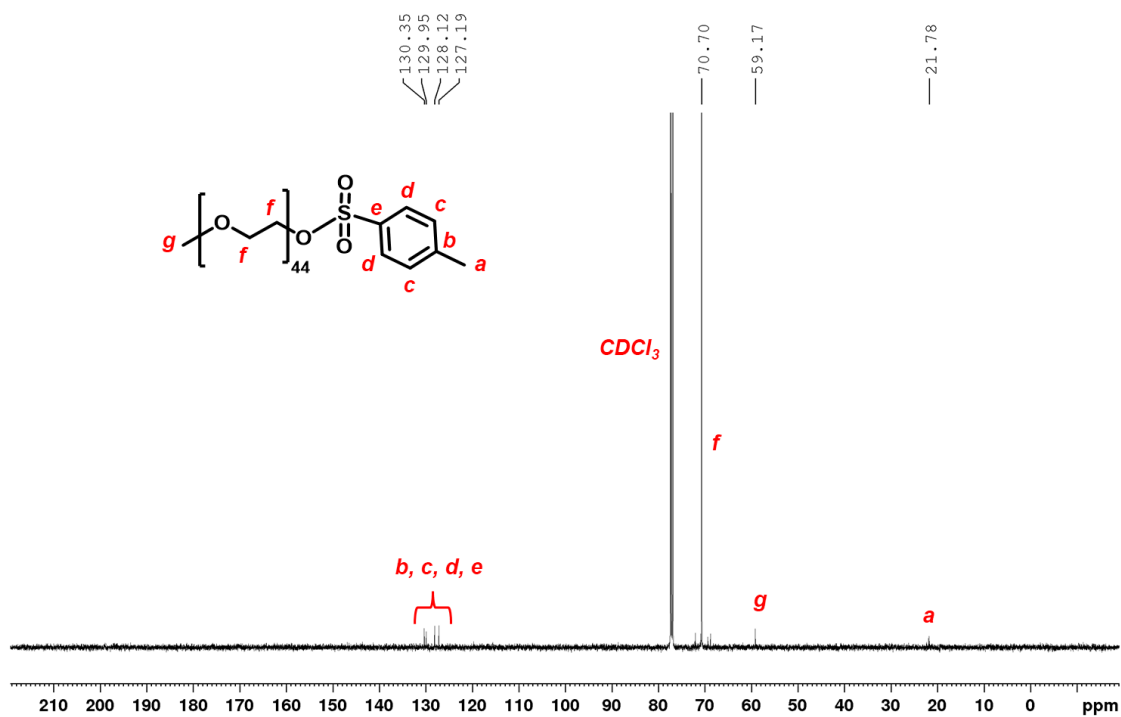


Figure 2. 12:  $^{13}\text{C}$  NMR spectrum of MePEG<sub>2000</sub>-OTs.

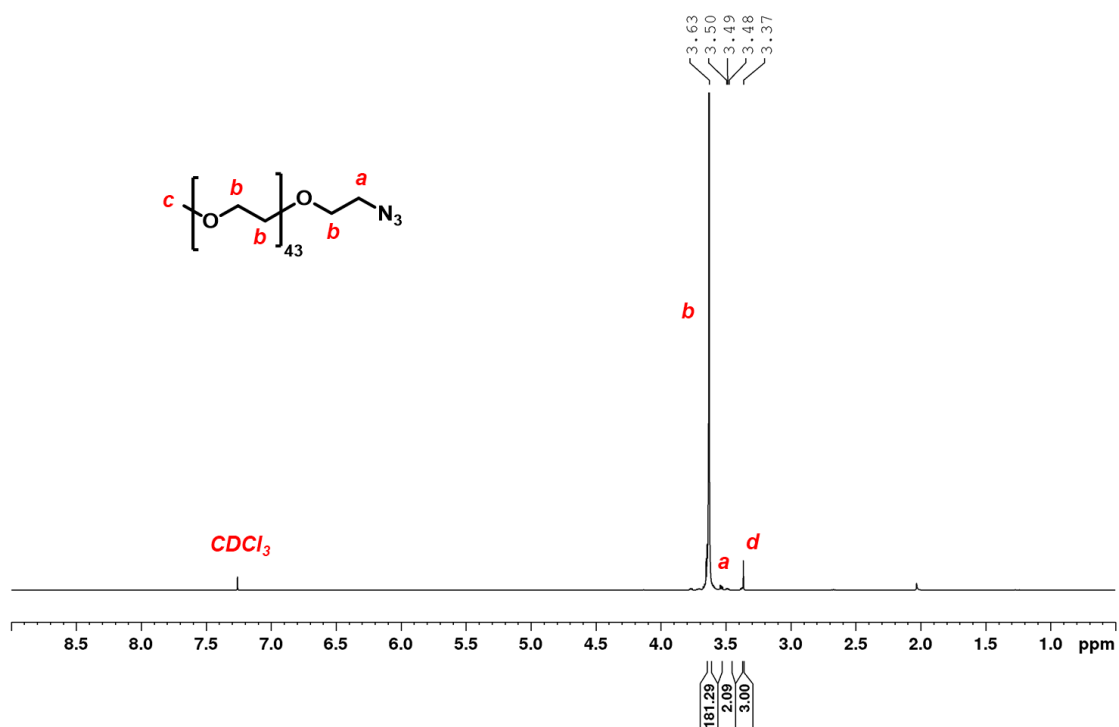


Figure 2. 13:  $^1\text{H}$  NMR spectrum of azido PEG<sub>2000</sub> monomethyl ether (3).

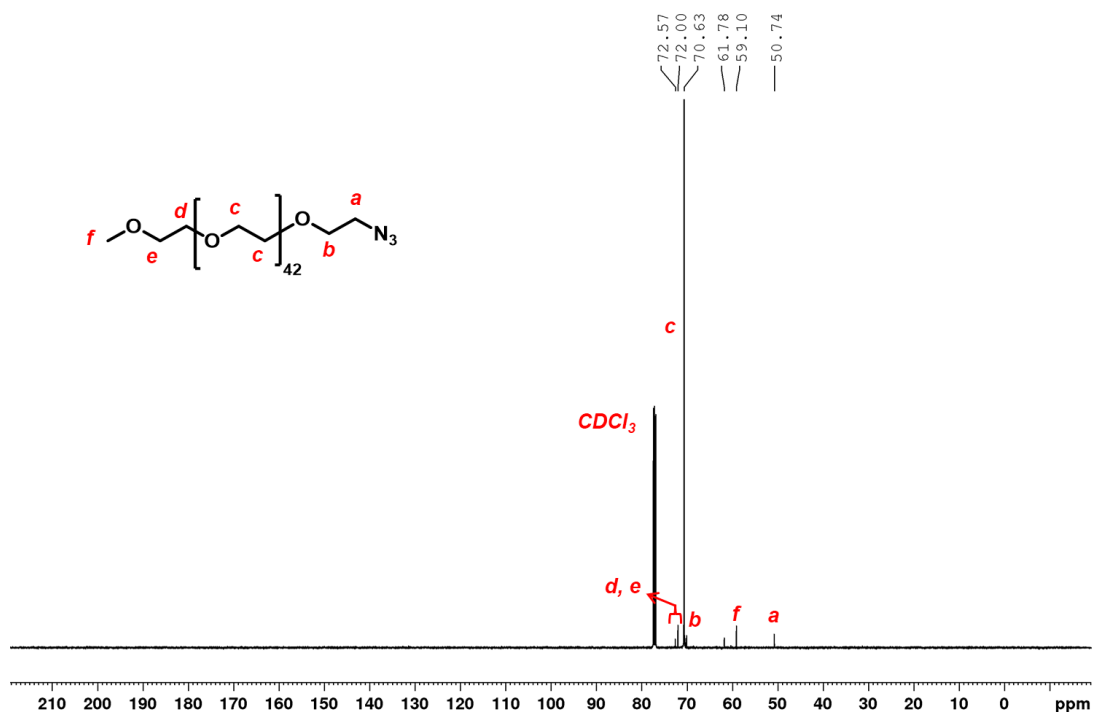


Figure 2. 14:  $^{13}\text{C}$  NMR spectrum of 3.

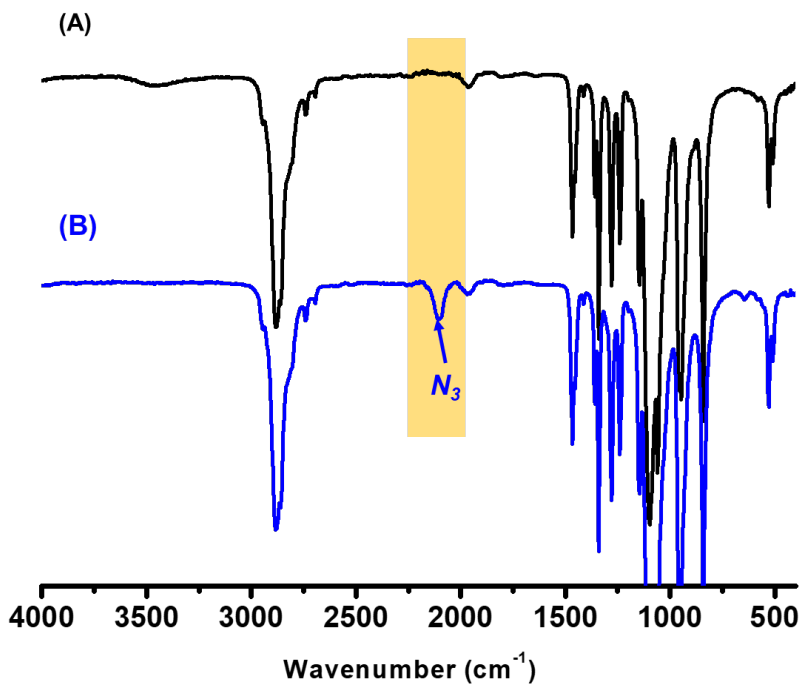


Figure 2. 15: FTIR spectrum of (A) MePEG<sub>2000</sub> monomethyl ether and (B) 3. The presence of the azide in 3 was confirmed by the appearance of a peak at 2120  $\text{cm}^{-1}$ .

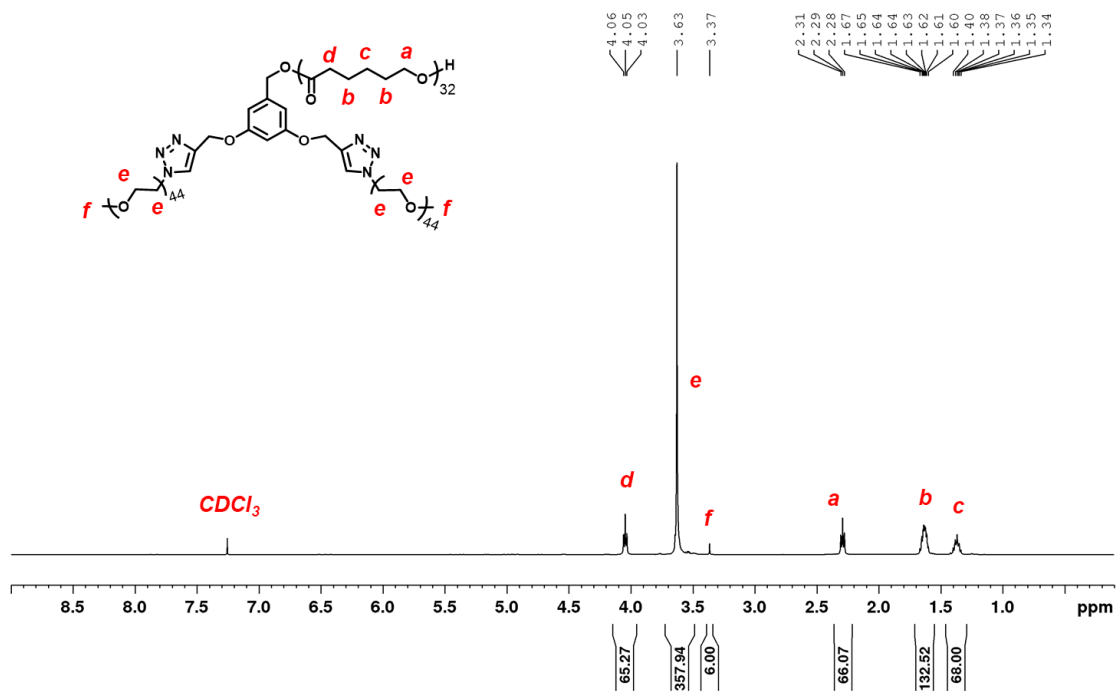


Figure 2. 16: <sup>1</sup>H NMR spectrum of (MePEG<sub>2000</sub>)<sub>2</sub>-PCL<sub>3600</sub> (MP1).

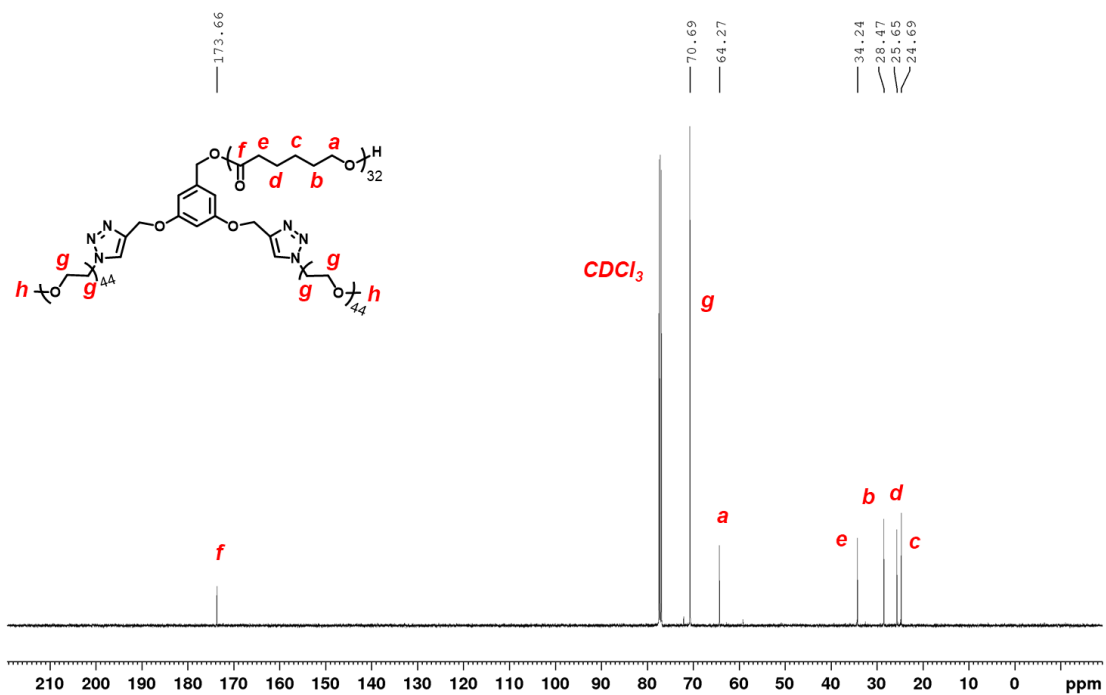
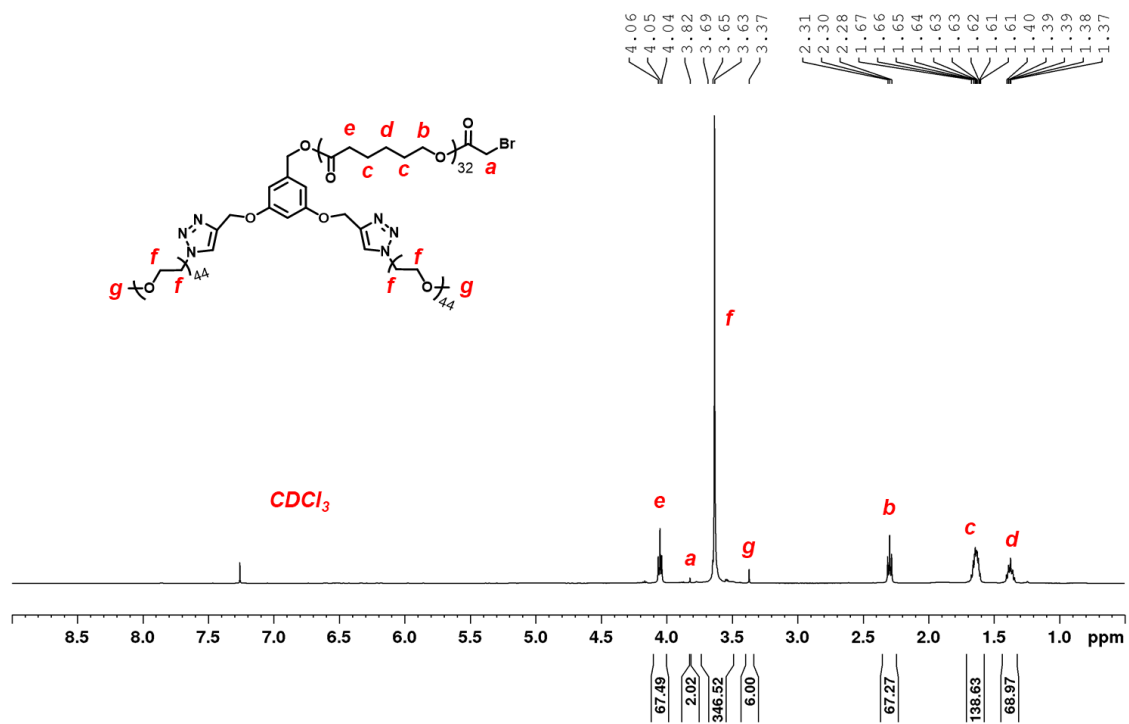
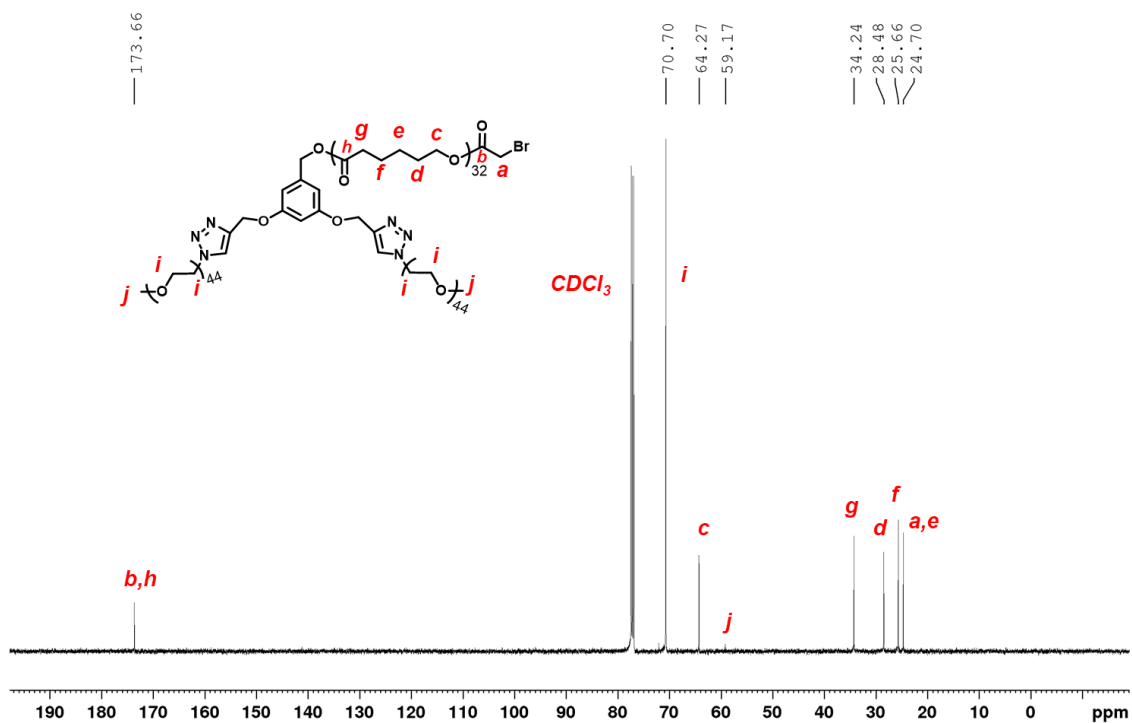
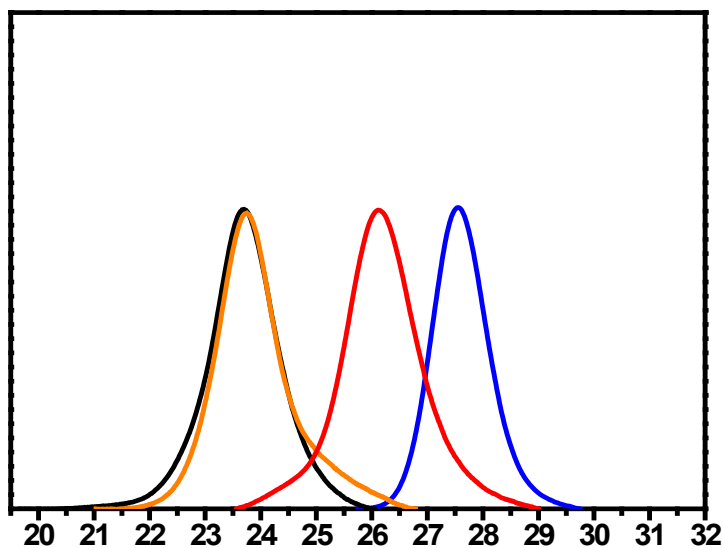


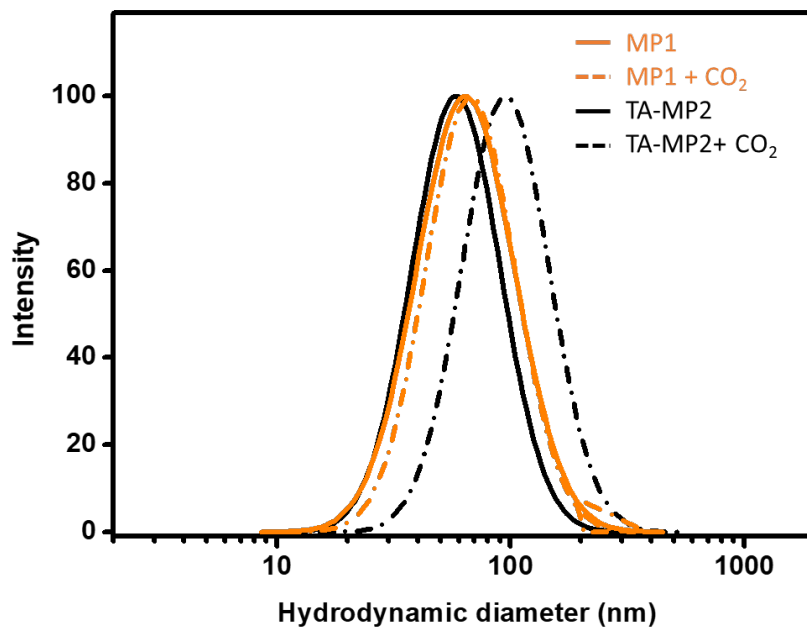
Figure 2. 17: <sup>13</sup>C NMR spectrum of MP1.

Figure 2. 18:  $^1\text{H}$  NMR spectrum of MABr.Figure 2. 19:  $^{13}\text{C}$  NMR spectrum of MABr.





**Figure 2. 22:** GPC traces of 3 (blue  $D=1.06$ ), 2 (red,  $D=1.15$ ), MP1 (orange,  $D=1.20$ ), and TA-MP2 (black,  $D=1.19$ ).



**Figure 2. 23:** Size changes of MP1-micelles and TA-MP2-micelles upon bubbling CO<sub>2</sub>.

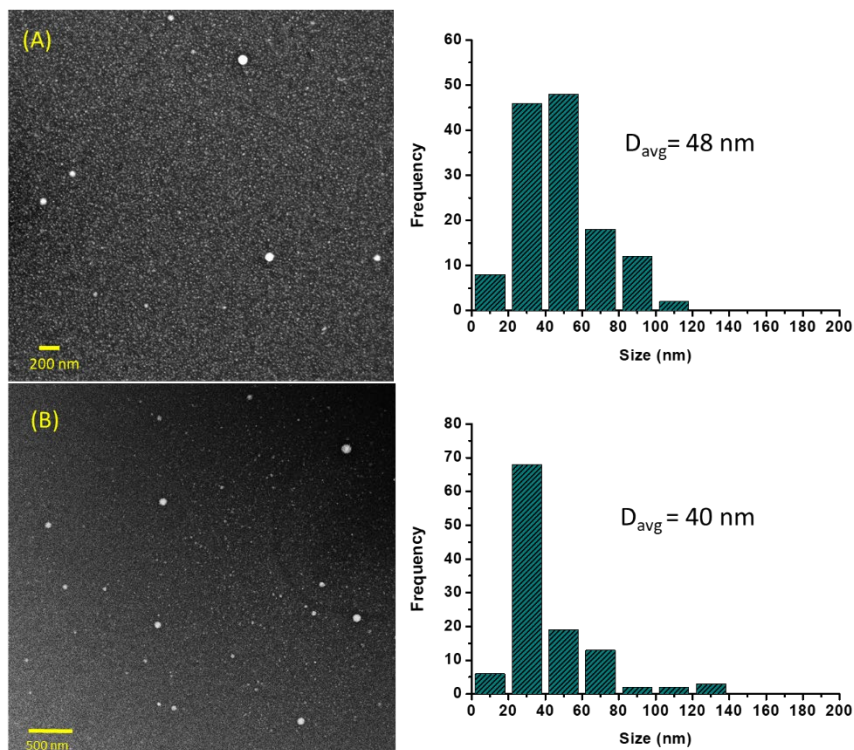


Figure 2. 24: TEM images and analyses of (A) MP1-micelles and (B) TA-MP2-micelles.

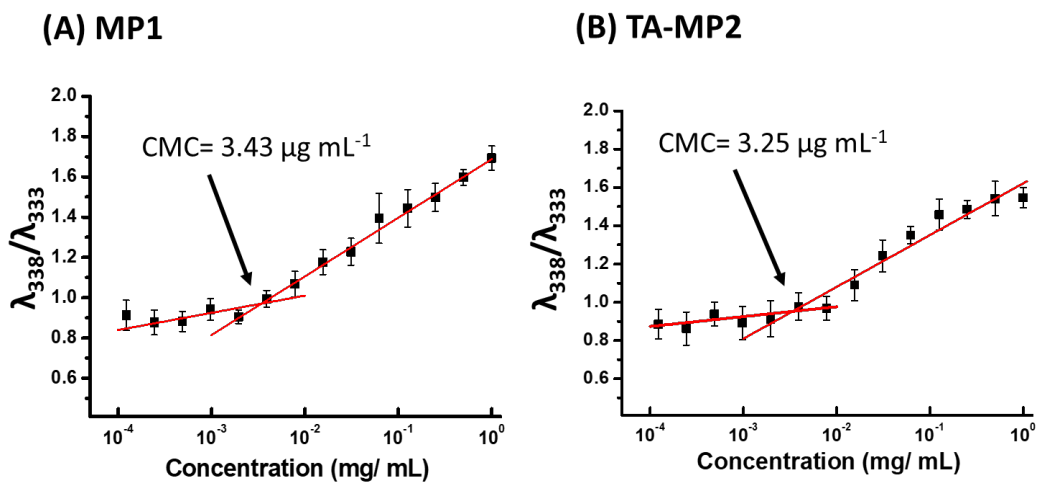
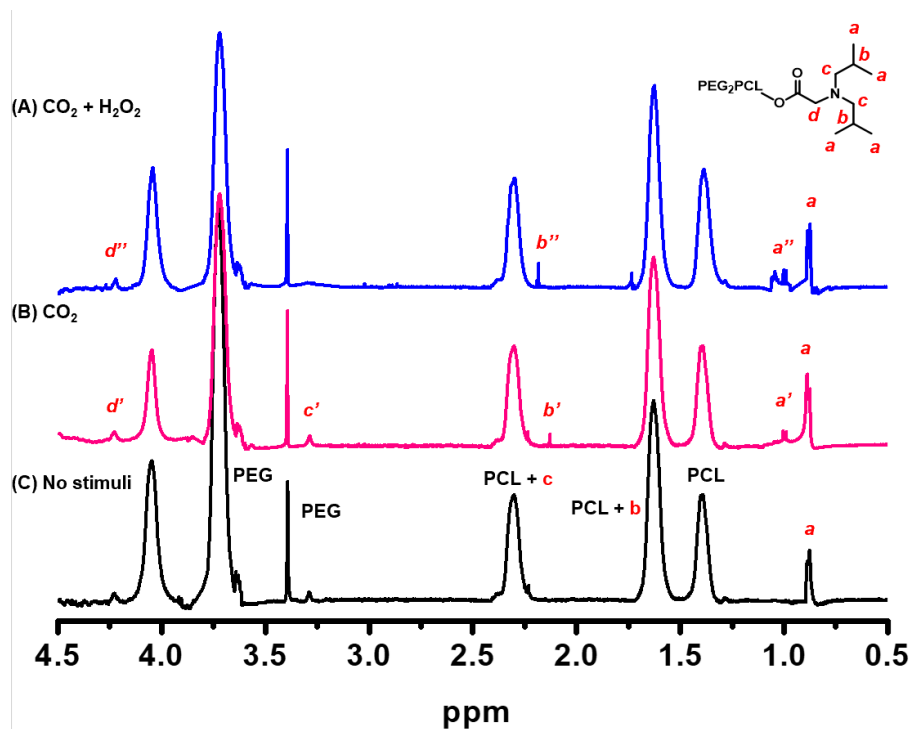
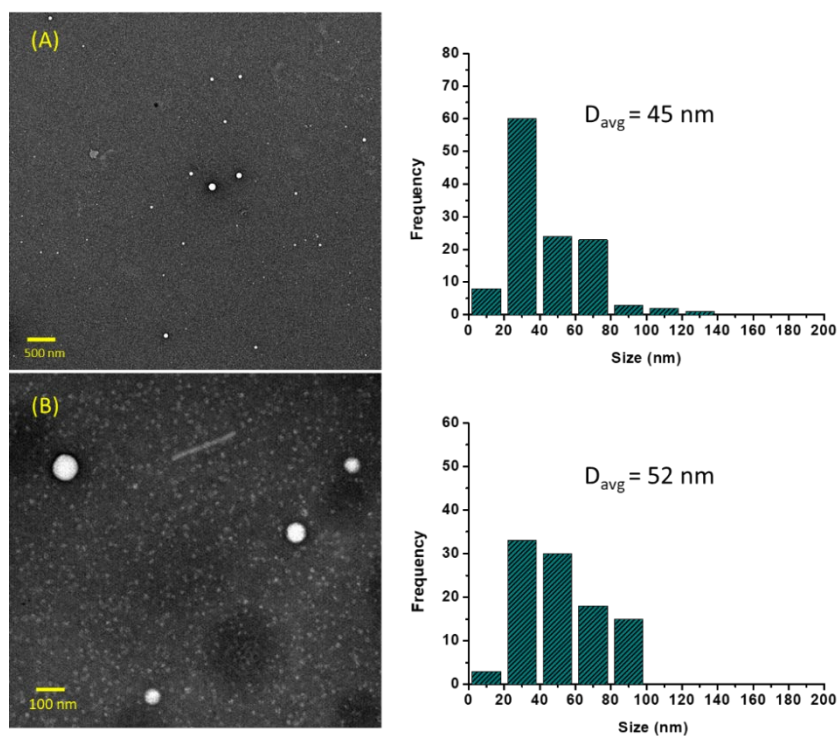


Figure 2. 25: CMC determination of (A) MP1 and (B) TA-MP2. (Pyrene ( $6 \mu\text{M}$ ) was used as the fluorescent probe. Error bars represent a standard deviation of  $n=3$ .



**Figure 2. 26:**  $^1\text{H}$  NMR analysis of TA-MP2 with (A)  $\text{CO}_2 + \text{H}_2\text{O}_2$ , (B)  $\text{CO}_2$ , and (C) no stimulus.



**Figure 2. 27:** TEM images and analyses of (A) MP1-micelles and (B) TA-MP2-micelles after  $\text{CO}_2$  bubbling for 0.5 h.

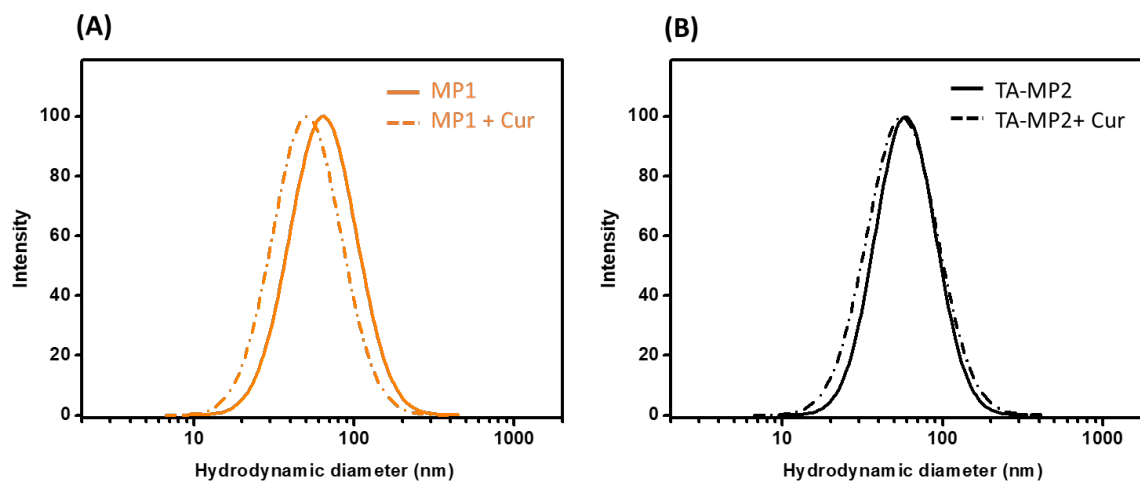


**Figure 2. 28:** Size distribution upon Cur loading into (A) MP1-micelles and (B) TA-MP2-micelles.

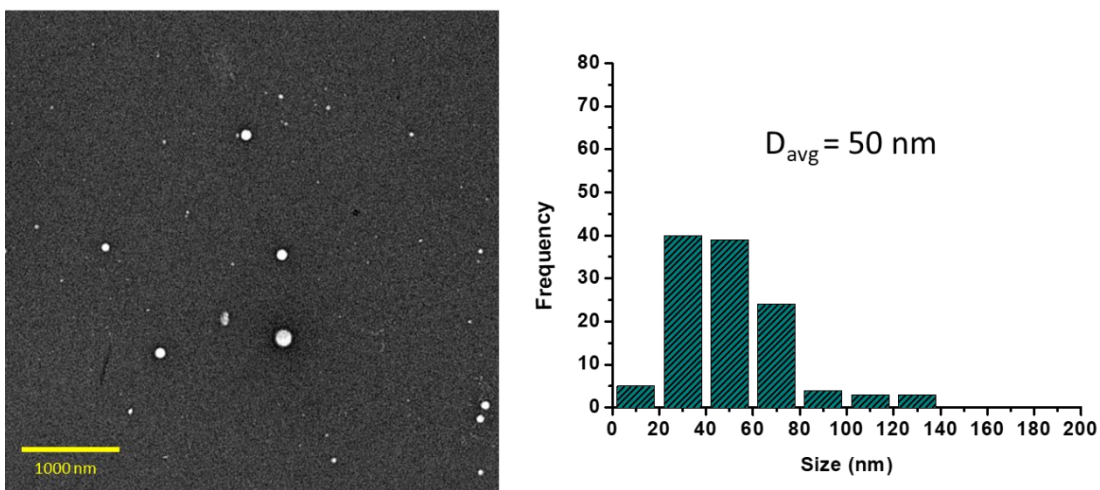


**Figure 2. 29:** TEM image and analysis of Cur-MP1.

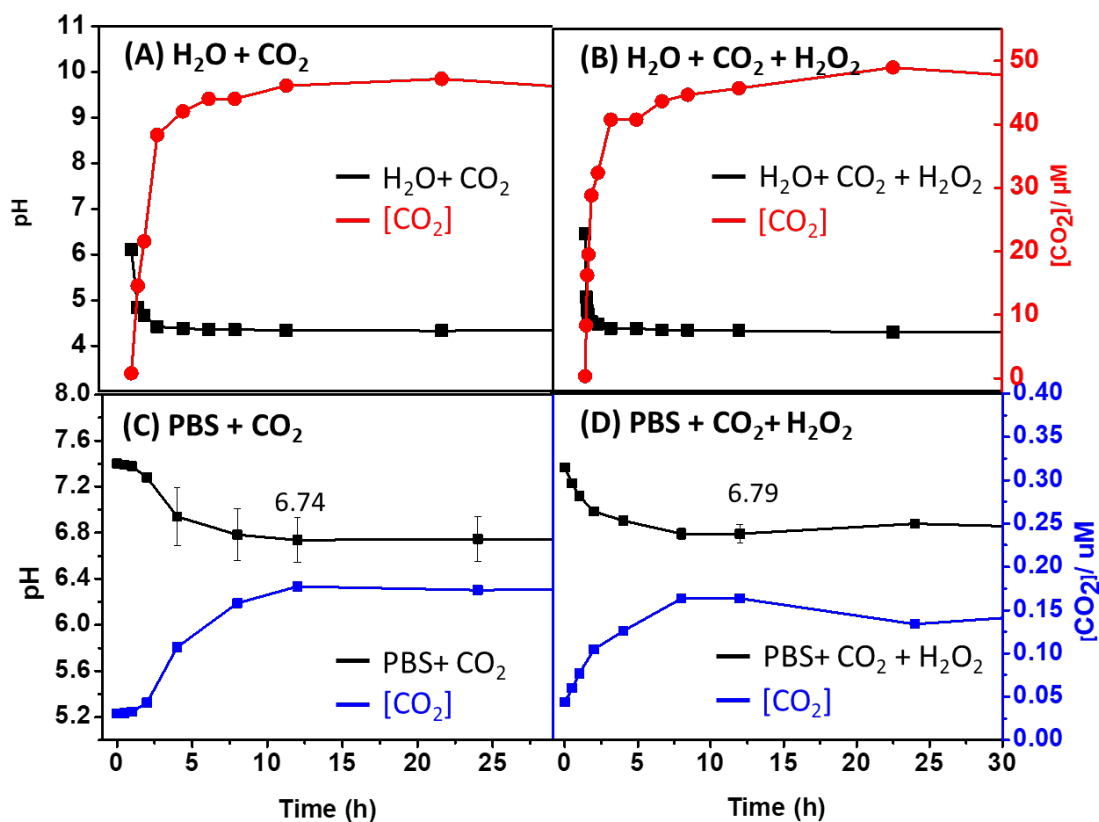


**Figure 2. 30:** pH (black) and CO<sub>2</sub> concentrations (red/blue) measurements of: (A) Milli-Q water + CO<sub>2</sub>; (B) Milli-Q water + CO<sub>2</sub> + H<sub>2</sub>O<sub>2</sub>; (C) PBS + CO<sub>2</sub>; and (D) PBS + CO<sub>2</sub> + H<sub>2</sub>O<sub>2</sub>. Values of pH and CO<sub>2</sub> concentrations are listed in Table S1. Error bars represent a standard deviation of n=3

**Table 2. 3:** pH values and CO<sub>2</sub> concentrations from Figure 2. 30.

Time (h)	Milli-Q water+ CO <sub>2</sub>		Milli-Q water + CO <sub>2</sub> + H <sub>2</sub> O <sub>2</sub>		PBS + CO <sub>2</sub>		PBS + CO <sub>2</sub> + H <sub>2</sub> O <sub>2</sub>	
	pH	[CO <sub>2</sub> ]/ μM	pH	[CO <sub>2</sub> ]/ μM	pH	[CO <sub>2</sub> ]/ μM	pH	[CO <sub>2</sub> ]/ μM
0	6.11	0.8	6.48	0.3	7.4	0.03981	7.36	0.04365
0.5	4.84	14.5	4.54	28.8	7.39	0.04074	7.22	0.0598
1	4.67	21.4	4.49	32.4	7.38	0.04201	7.11	0.07703
2	4.42	38.0	4.39	40.7	6.98	0.05248	6.98	0.10471
4	4.38	41.7	4.39	40.7	7.3	0.11482	6.9	0.12589
8	4.36	43.7	4.35	44.7	6.56	0.16469	6.79	0.16343
12	4.36	45.7	4.34	45.7	6.53	0.18337	6.78	0.16343
24	4.33	46.8	4.31	48.9	6.52	0.1792	6.87	0.13386
48	4.36	43.7	4.34	45.7	6.52	0.18337	6.79	0.16218
72	4.25	56.2	4.42	38.0	6.66	0.21878	6.84	0.14454

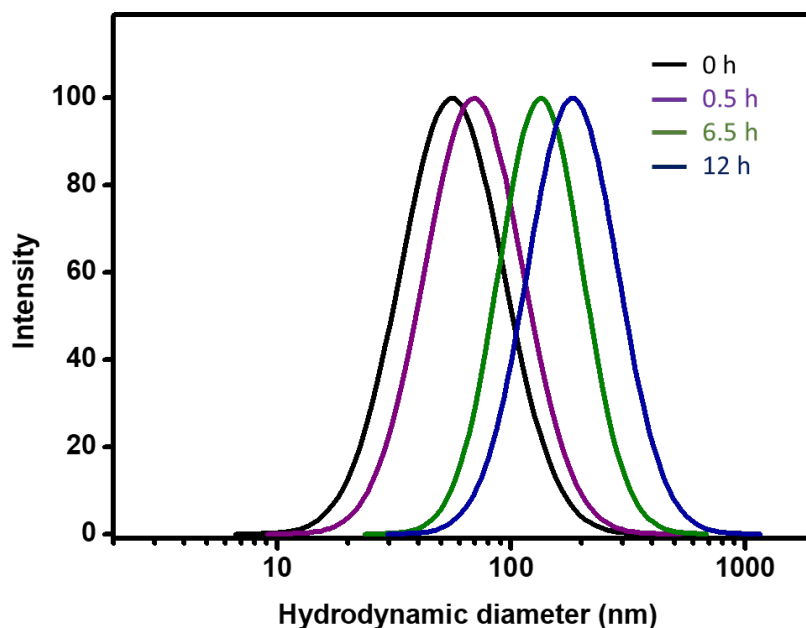


**Figure 2. 31:** DLS analysis of Cur-TA-MP2 upon treatment with CO<sub>2</sub> over time: 0 h (no CO<sub>2</sub>, black, 57 nm), 0.5 h (purple, 71 nm), 6.5 h (green, 134 nm), and 12 h (blue, 188 nm).

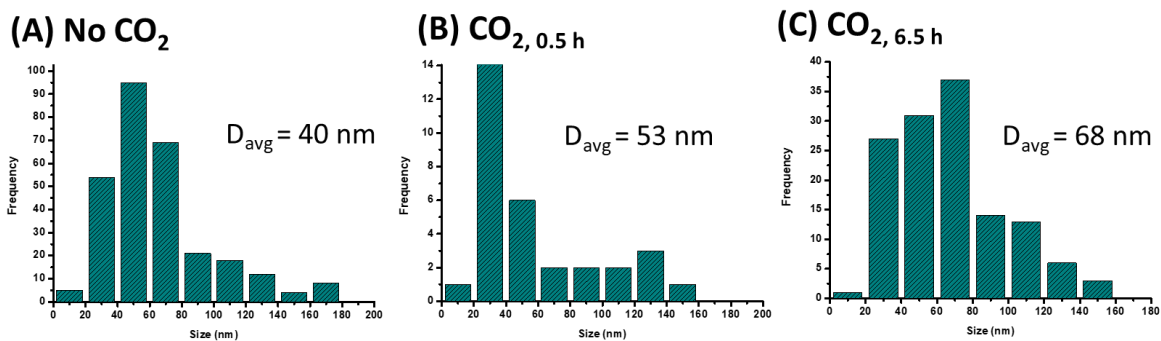


**Figure 2. 32:** TEM analysis of Cur-TA-MP2 with CO<sub>2</sub> over time: (A) 0 h (no CO<sub>2</sub>), (B) 0.5 h, (C) 6.5 h, and (D) 12 h.

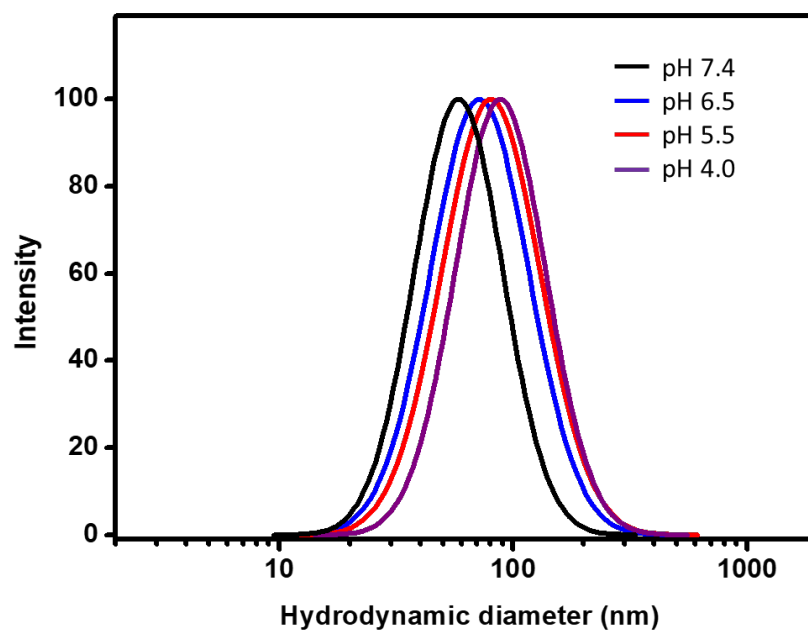


**Figure 2. 33:** DLS study of Cur-TA-MP2 after 12 h in varied pH media: pH 7.4 (black, 57 nm), pH 6.5 (blue, 72 nm), pH 5.5 (red, 79 nm), and pH 4.0 (purple, 87 nm).

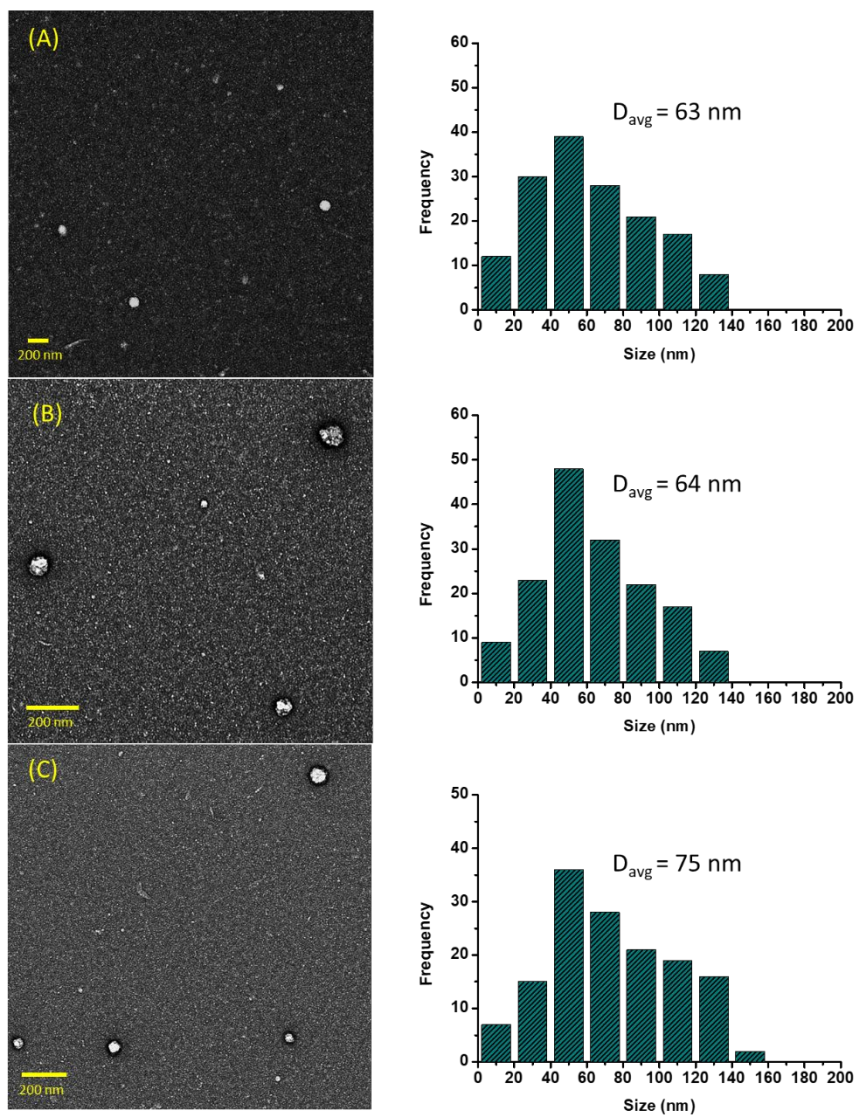


**Figure 2. 34:** TEM of Cur-TA-MP2 solution after 12 h in varied pH media: (A) pH 6.5; (B) pH 5.5; and (C) pH 4.0.

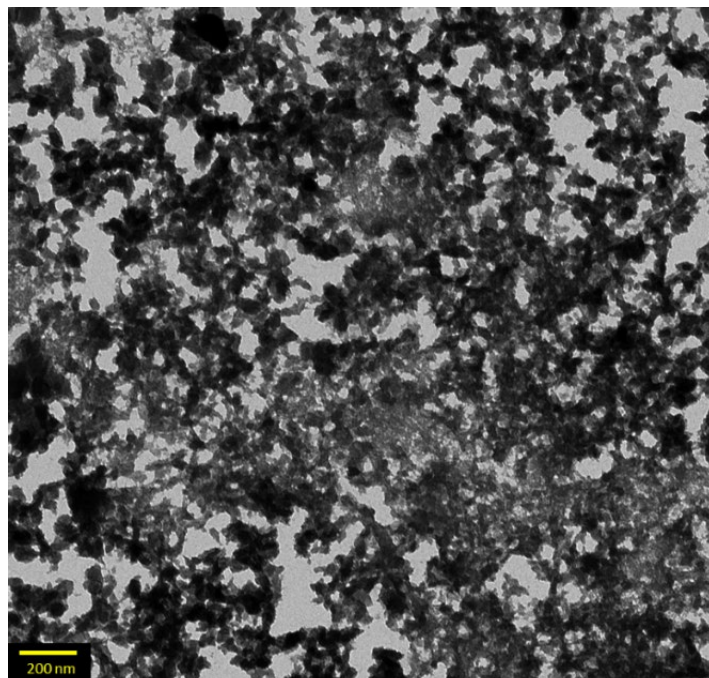


**Figure 2. 35:** TEM grid upon depositing Cur-TA-MP2 solution containing H<sub>2</sub>O<sub>2</sub>.

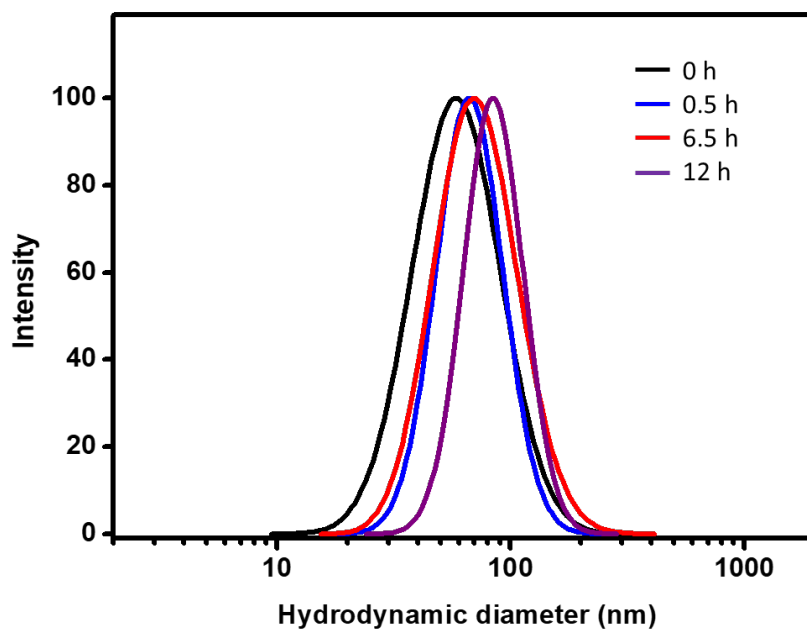


**Figure 2. 36:** DLS of Cur-TA-MP2 in 200 mM H<sub>2</sub>O<sub>2</sub> solution at various time intervals: 0 h (black, 57 nm), 0.5 h (blue, 67 nm), 6.5 h (red, 69 nm), and 12 h (purple, 84 nm).

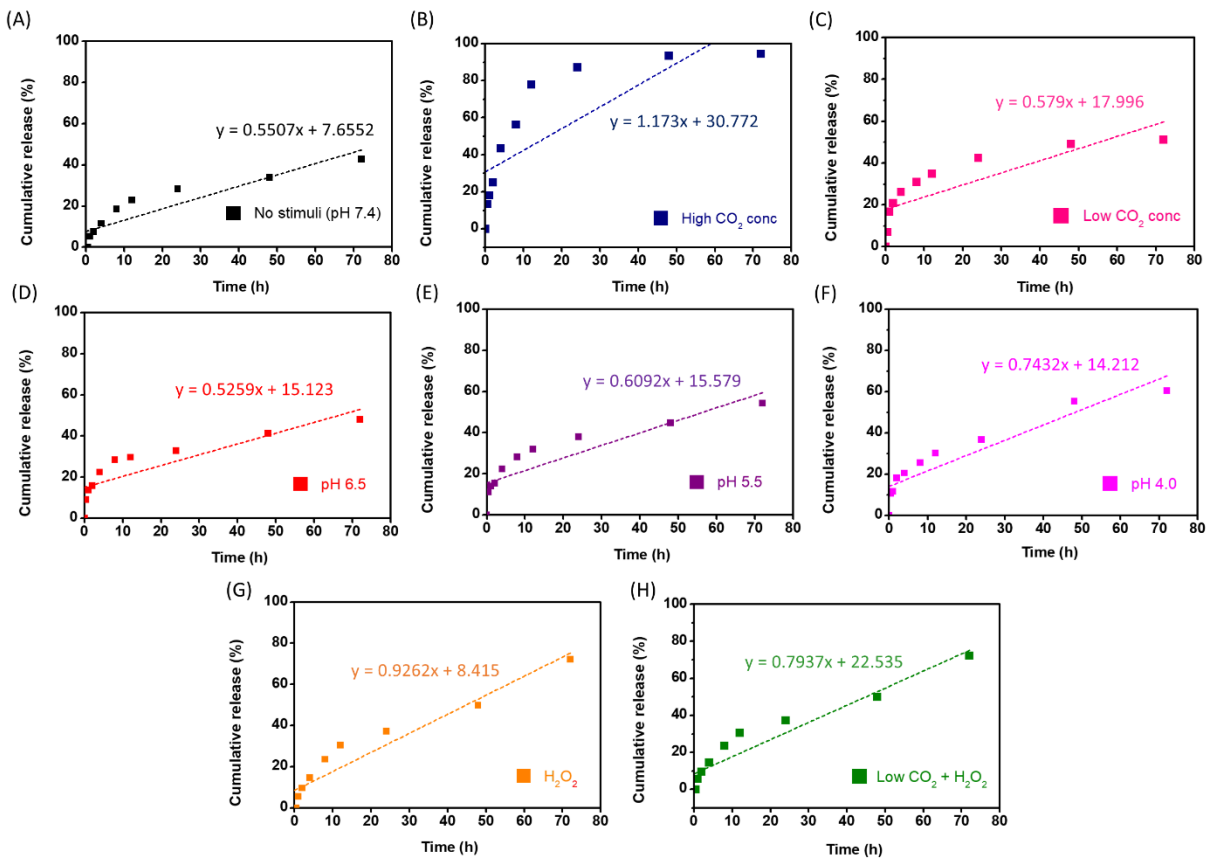


**Figure 2. 37:** Drug release data of Cur-TA-MP2 fitted to zero-order model. (A) No stimuli (pH 7.4), (B) high CO<sub>2</sub> conc, (C) low CO<sub>2</sub>, (D) pH 6.5, (E) pH 5.5, (F) pH 4.0, (G) H<sub>2</sub>O<sub>2</sub>, (F) low CO<sub>2</sub>+ H<sub>2</sub>O<sub>2</sub>.

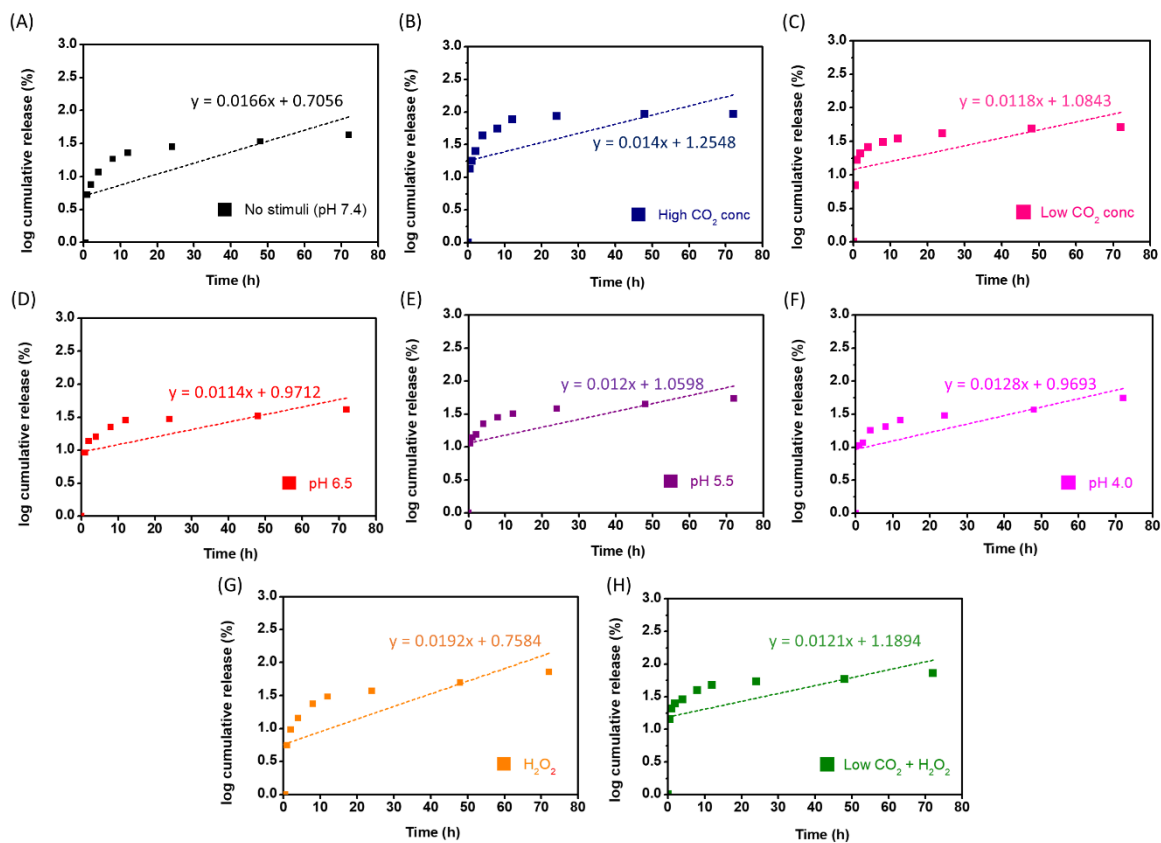


**Figure 2. 38:** Drug release data fitted to first-order model. (A) No stimuli (pH 7.4), (B) high CO<sub>2</sub> conc, (C) low CO<sub>2</sub>, (D) pH 6.5, (E) pH 5.5, (F) pH 4.0, (G) H<sub>2</sub>O<sub>2</sub>, (F) low CO<sub>2</sub>+ H<sub>2</sub>O<sub>2</sub>.

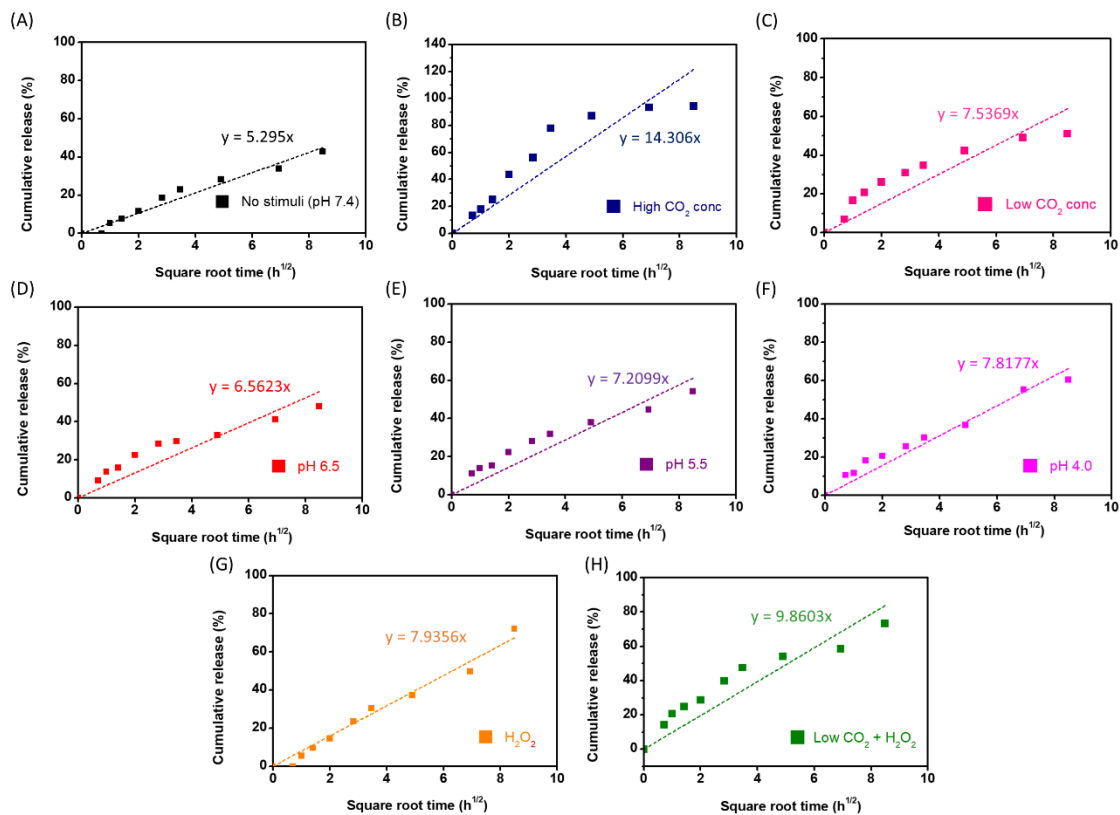


**Figure 2. 39:** Drug release data fitted to Higuchi model. (A) No stimuli (pH 7.4), (B) high  $CO_2$  conc, (C) low  $CO_2$ , (D) pH 6.5, (E) pH 5.5, (F) pH 4.0, (G)  $H_2O_2$ , (F) low  $CO_2 + H_2O_2$ .

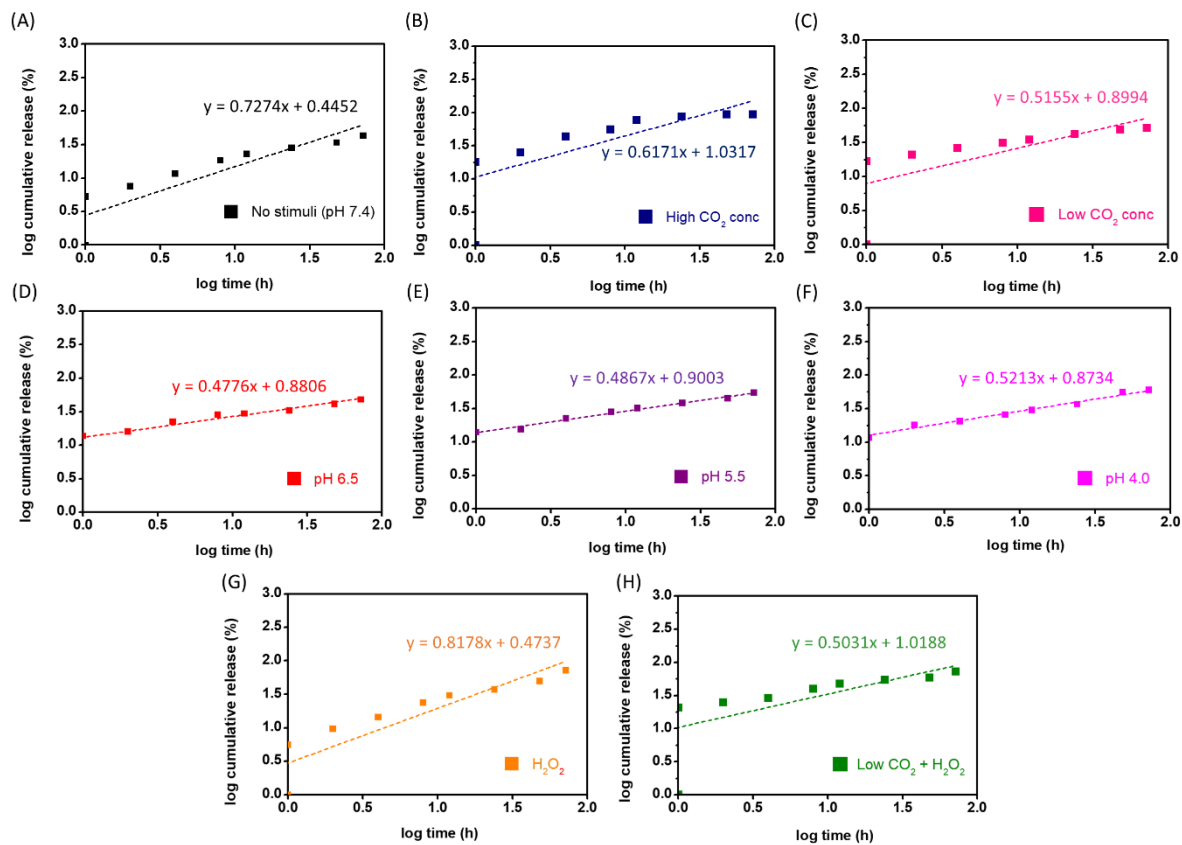


**Figure 2. 40:** Drug release data fitted to Korsmeyer-Peppas model. (A) No stimuli (pH 7.4), (B) high CO<sub>2</sub> conc, (C) low CO<sub>2</sub>, (D) pH 6.5, (E) pH 5.5, (F) pH 4.0, (G) H<sub>2</sub>O<sub>2</sub>, (H) low CO<sub>2</sub>+ H<sub>2</sub>O<sub>2</sub>.

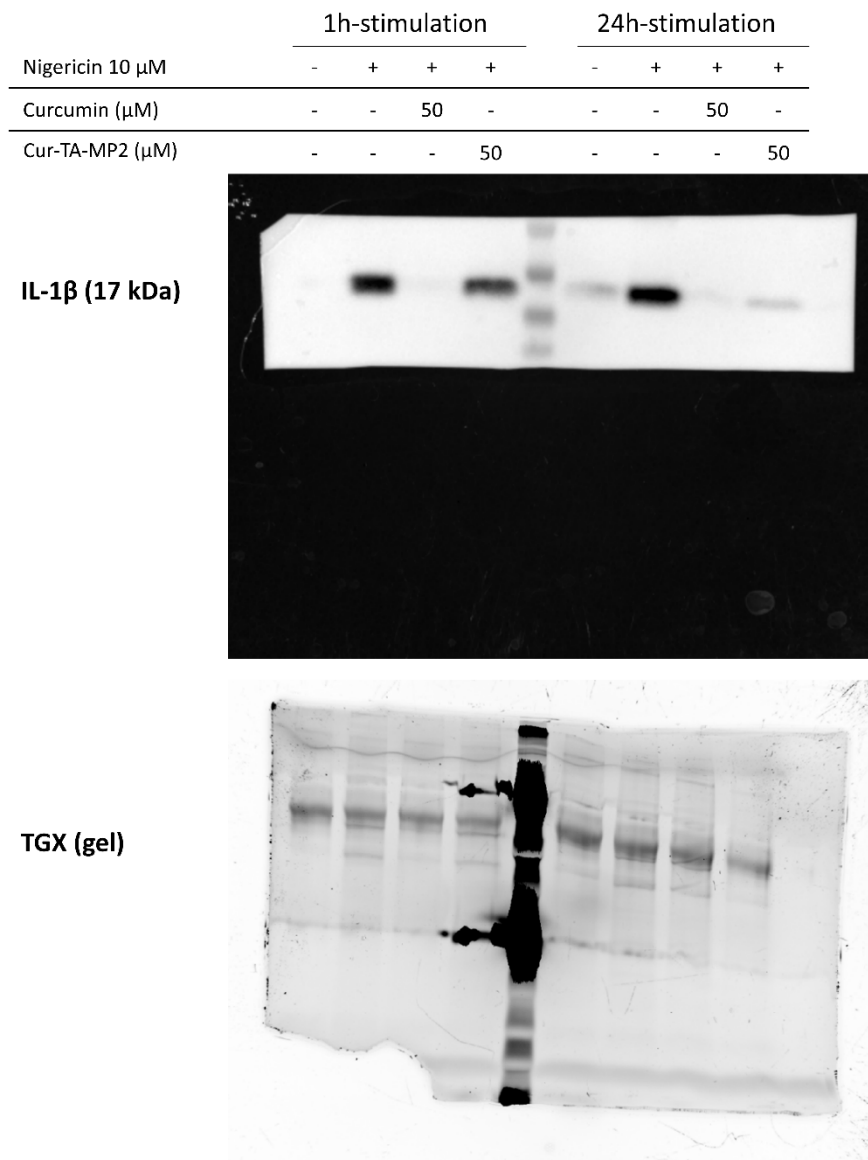


**Figure 2. 41:** Raw images for Western blot data.

# Chapter 3: Soft Nanoparticles as Antimicrobial Agents and Carriers of Microbiocides for Enhanced Inhibition Activity

## 3.1. Opening remarks

We demonstrated the utility of our core modification methodology to simplify the development of multi-stimuli responsive polymeric nanoparticles (NPs) for controlled and environment selective drug delivery in Chapter 2. Given the ongoing threat of bacterial infections to global health, there is an urgent need to develop alternative platforms for bactericidal agents. To address this critical issue, we considered a macromolecular platform that utilizes surface modification and strategically integrating charged amine entities onto the hydrophilic shell of soft NPs, into which active small molecule antibacterial agents could be physically encapsulated. Our design strategy confers NPs with intrinsic antimicrobial properties, while preserving their ability to deliver potent antibacterial cargo. We demonstrate the efficacy of these NPs against known bacterial strains, and their potential in combination therapy: intrinsic bactericidal efficacy, as well as delivery of antibacterial agents.

This chapter is adapted from a manuscript that has been accepted for publication in the *Journal of Materials Chemistry B*.

Yong, H. W.; Ojagh, S. M. A.; Théberge-Julien, G.; Castellanos, L. S. R.; van de Ven, T.; Rhéaume, É.; Tardif, J.-C.; Kakkar, A. Soft Nanoparticles as Antimicrobial Agents and Carriers of Microbiocides for Enhanced Inhibition Activity. *J. Mat. Chem. B* **2024**, DOI: 10.1039/D4TB01200C.

### 3.2. Abstract

Antibiotic resistance continues to pose significant health challenges. Considering severe limitations in the discovery and supply of new antibiotics, there is unmet need in designing alternative and more effective strategies in addressing this global issue. Polymeric NPs with cationic shell surface offer a highly promising approach in coupling their inherent bactericidal action with sustained delivery of small lipophilic microbiocides. We have utilized this platform in assembling multi-tasking soft core-shell NPs from star polymers with the desired asymmetric arms composition. These stable NPs with low critical micelle concentration (CMC) are imparted intrinsic antimicrobial potency due to high positive charge density in the corona, as well as loading of active biocidal agents (curcumin and terbinafine) for potential dual and adjuvant inhibition. The strategic combination allows for both immediate (direct contact) and extended (drug delivery) bacterial activity for better therapeutic efficacy. Micellar NPs with and without therapeutic cargo were highly efficient against both *Escherichia coli* (*E. coli*) and *Bacillus subtilis* (*B. subtilis*), representative Gram-negative and Gram-positive bacteria, respectively. Interestingly, we observed bacteria- and concentration-dependent effects, in which higher concentration of charged NPs were more effective against *E. coli*, whereas *B. subtilis* were inhibited only at lower concentration. This work highlights a valuable platform to work towards combination therapy through NPs with charged coronas and delivery of potent therapeutics to overcome antimicrobial resistance.

### 3.3. Introduction

Bacterial infection is a surging health concern affecting millions of people worldwide. It can lead to life-threatening conditions including sepsis, bacteraemia, tuberculosis, and endocarditis if left untreated.<sup>1,2</sup> Patients who are immunocompromised for a variety of reasons such as cancer, organ transplant, or HIV, are especially vulnerable to bacterial infections.<sup>3-5</sup> Antibiotics have traditionally played a crucial role; however, the emergence of drug-resistant pathogens is alarming and severely threatens our ability to intervene. The latest World Health Organization (WHO) global priority pathogens list has highlighted the need for new antibiotics to address this urgency, which further stresses the gravity and research efforts necessary to curb this problem.<sup>6</sup>

Current therapeutic agents used to combat bacterial infections can be classified as either bacteriostatic or bactericidal.<sup>7</sup> The former work by interfering with bacterial protein synthesis to inhibit growth, while the latter involve inhibition of bacterial cell wall synthesis or disruption of cell wall structure to induce nutrient loss, which eventually leads to cell death.<sup>8</sup> Some bacteriostatic agents include sulphonamides like sulfamethoxazole or macrolides such as clarithromycin,<sup>9, 10</sup> whereas fluoroquinolones namely ciprofloxacin or glycopeptides including vancomycin possess bactericidal activity.<sup>11</sup> With the increasing instances of drug-resistance strains, and deficiency in discovery and supply of new antibiotics, there is pressing need to develop alternative strategies in designing effective microbial agents.

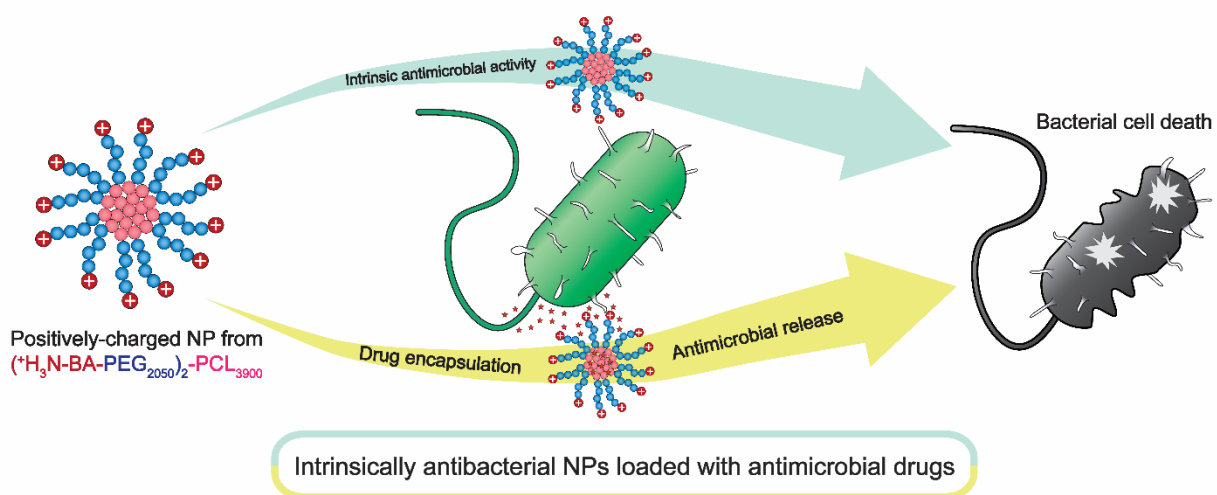
Cationic polymers which can disrupt bacterial cell wall have been explored for their activity in preventing cell growth.<sup>12-22</sup> These materials disrupt the negatively-charged bacterial cell wall through electrostatic interactions with the polymeric cationic moieties. This interaction impairs cell wall integrity, leading to leakage of cytoplasmic contents and eventual cell lysis.<sup>23</sup> For example, polyethyleneimine (PEI) and integrated PEI-based hybrid polymers have been extensively explored for antibacterial activity.<sup>24-28</sup> Recently, branched PEI-crosslinked cellulose (BC-PEI) was used to prepare antibacterial face masks,<sup>29</sup> which were effective in inhibiting *Staphylococcus aureus* (*S. aureus*) and *Pseudomonas aeruginosa* (*P. aeruginosa*) growth. To work around high toxicity of such polymers towards mammalian cells,<sup>30, 31</sup> mannose-modified PEIs were prepared which showed low cytotoxicity against HeLa cells but excellent effectiveness against *E. coli*.<sup>32</sup> Several studies on PEI-grafted polyurethane ureteral stent surfaces have also shown to reduce growth of *Klebsiella pneumonia* (*K. pneumonia*), *Proteus mirabilis* (*P. mirabilis*), and *E. coli* without significant cytotoxicity against L929 cells.<sup>33, 34</sup>

To enhance our efficacy in addressing escalating antibiotic resistance, we were intrigued to engineer soft NPs with cationic shell surface, which could also efficiently encapsulate biocidal agents. These nanoscale alternatives offer opportunities in disrupting cell growth through multiple actions, including electrostatic interactions with the cell membrane; entering cells and interfere with their components; and sustained delivery of active bactericides (Scheme 3. 1). Towards this goal, we report herein an AB<sub>2</sub> miktoarm (*mikto*, Greek meaning different; A = polycaprolactone (PCL), B = polyethylene glycol (PEG) with terminal end amine functionality) polymer-based

micelles with positively-charged PEG shell and a hydrophobic PCL core. Branched star polymers offer opportunities in designing NPs of small sizes, low CMCs, high encapsulation efficiencies, and rendering balanced high charged density to hydrophilic shell surfaces.<sup>35, 36</sup> Such a multifunctional approach presents an efficient platform to address current challenges of bacterial infections using combination therapy.

Nanoscale micellar formulations were evaluated for their ability to inhibit microbial growth of *E. coli* and *B. subtilis*. We explored the potential to combine intrinsic-antimicrobial activity of NPs with physically encapsulated drugs for additive effects. Curcumin (CUR) and terbinafine (TBF) were selected as the antimicrobial agents for this study. CUR is a naturally occurring polyphenol extracted from the rhizome of *Curcuma longa*.<sup>37</sup> It has been widely shown to possess anti-inflammatory, antioxidant, anticancer properties, as well as antibacterial efficacy on several persistent Gram-negative and Gram-positive bacteria, including *P. aeruginosa*, *S. aureus*, *B. subtilis*, *Bacillus cereus* (*B. cereus*), and *E. coli*.<sup>38-42</sup> However, poor pharmacokinetics of CUR, including poor aqueous solubility and stability have restricted its versatile usage.<sup>43</sup>

TBF is a lipophilic allylamine that has a wide spectrum fungicidal activity.<sup>44</sup> As one of the drugs listed under the WHO's model list of essential medicines, the potency of TBF and its efficiency over several other antifungals have been demonstrated in clinical studies.<sup>45</sup> Nevertheless, low penetration rates and poor aqueous solubility of TBF limit its application, and require the need for repeated treatments.<sup>46</sup> In addition, there has been an increase in clinical failures as certain pathogenic fungi develop resistance to TBF,<sup>47</sup> which governs the need for a solution to overcome this hurdle. Although TBF is a well-known antifungal agent, some studies have shown potency against bacterial strains such as *S. aureus*.<sup>48</sup> We examined if TBF alone and loaded into NPs was effective as antibacterial agents for *E. coli* and *B. subtilis*. Our studies present a multifaceted approach in designing alternative antibacterials agents, and we demonstrate that NPs i) inhibit growth of both *E. coli* and *B. subtilis*, and ii) can be further utilized as drug nanocarriers to achieve sustained inhibition of bacteria.



**Scheme 3. 1:** Schematic overview of the dual-purpose polycationic NPs for targeting bacteria and drug delivery.

### 3.4. Experimental Section

#### Reagents

Poly(ethylene glycol) (2050 g/ mol, Sigma Aldrich), silver nitrate ( $AgNO_3$ ,  $\geq 99.0\%$ , Sigma-Aldrich), sodium hydroxide ( $NaOH$ ,  $\geq 97\%$ , ACP chemicals), sodium azide ( $NaN_3$ ,  $\geq 99.5\%$ , Sigma-Aldrich), *N*-(*tert*-Butoxycarbonyl)-4-aminobutyric Acid (Boc-GABA-OH,  $\geq 98\%$ , TCI America), *N,N'*-dicyclohexylcarbodiimide (DCC, 99%, Sigma-Aldrich), 4-(dimethylamino)pyridine (DMAP, ReagentPlus®,  $\geq 99\%$ , Sigma-Aldrich), propargyl bromide ( $\sim 80\%$  in toluene, Sigma-Aldrich), 3,5-dihydroxybenzyl alcohol (99%, Sigma-Aldrich), potassium carbonate ( $K_2CO_3$ ,  $\geq 99.0\%$ , Sigma-Aldrich), 18-crown-6 (99%, Sigma-Aldrich), tin(II) 2-ethylhexanoate ( $Sn(Oct)_2$ , 92.5-100.0%, Sigma-Aldrich), copper (I) bromide ( $CuBr$ , 98%, Sigma-Aldrich), *N,N,N',N'',N''*-pentamethyldiethylenetriamine (PMDETA, 99%, Sigma-Aldrich), ethylenediaminetetraacetic acid disodium salt dihydrate (EDTA, 99.0-101.0%, Sigma-Aldrich), trifluoroacetic acid (TFA, ReagentPlus®, 99%, Sigma-Aldrich), curcumin (CUR,  $>95\%$ , Oakwood Products), terbinafine HCl (TBF) were used as received. *p*-toluenesulfonyl chloride ( $\geq 98\%$ , Sigma-Aldrich) was recrystallized from petroleum ether before use.  $\epsilon$ -caprolactone monomer (99%, ACROS Organics) was distilled over  $CaH_2$  before use. 13 mm PVDF filters (0.22  $\mu m$ , non-sterile) were purchased from SyringeFilter.com.

Synthesis of (Boc-GABA-PEG<sub>2000</sub>)<sub>2</sub>-PCL<sub>3900</sub> (P6)

Synthetic details for the hydrophilic PEG (P3) arm and hydrophobic PCL core (P5) can be found in Appendix B. P5 (0.186 g, 0.0439 mmol, 1 eq), P3 (0.200 g, 0.0894 mmol, 2 eq), CuBr (0.0162 g, 0.113 mmol, 2.5 eq) were dissolved in dry toluene under nitrogen with magnetic stirring. A solution of PMDETA (0.0194 g, 0.112 mmol, 2.5 eq) in dry toluene was then added, and the solution was allowed to react at room temperature for 48 h. The mixture was then concentrated and dialysed once with EDTA and twice with deionized water for 24 h each. The solution was then concentrated and precipitated in cold diethyl ether. The product was collected with vacuum filtration and dried in the desiccator. Yield: 87% (0.32 g). <sup>1</sup>H NMR (500 MHz, CDCl<sub>3</sub>): δ (ppm) 1.34- 1.41 (m, 71H, (-OCCH<sub>2</sub>CH<sub>2</sub>CH<sub>2</sub>CH<sub>2</sub>CH<sub>2</sub>O)<sub>35</sub>), 1.43 (s, 18H, -C(CH<sub>3</sub>)<sub>3</sub>), 1.60- 1.67 (m, 157H, (-OCCH<sub>2</sub>CH<sub>2</sub>CH<sub>2</sub>CH<sub>2</sub>CH<sub>2</sub>O)<sub>35</sub>), 1.81 (m, 4H, -NHCH<sub>2</sub>CH<sub>2</sub>CH<sub>2</sub>CO), 2.29 (t, 69H, (-OCCH<sub>2</sub>CH<sub>2</sub>CH<sub>2</sub>CH<sub>2</sub>CH<sub>2</sub>O)<sub>35</sub>), 2.38 (t, 4H, -NHCH<sub>2</sub>CH<sub>2</sub>CH<sub>2</sub>CO), 3.15 (t, 4H, -NHCH<sub>2</sub>CH<sub>2</sub>CH<sub>2</sub>CO), 3.49 (t, 4H, -OCCH<sub>2</sub>CH<sub>2</sub>(CH<sub>2</sub>CH<sub>2</sub>O)<sub>46</sub>), 3.63 (s, 370H, -(CH<sub>2</sub>CH<sub>2</sub>O)<sub>46</sub>), 3.88 (t, 4H, -OCCH<sub>2</sub>CH<sub>2</sub>(CH<sub>2</sub>CH<sub>2</sub>O)<sub>46</sub>), 4.05 (t, 67H, (-OCCH<sub>2</sub>CH<sub>2</sub>CH<sub>2</sub>CH<sub>2</sub>CH<sub>2</sub>O)<sub>33</sub>), 4.22 (t, 4H, -(CH<sub>2</sub>CH<sub>2</sub>O)<sub>46</sub>CH<sub>2</sub>CH<sub>2</sub>OOC), 4.58 (t, 4H, -(CH<sub>2</sub>CH<sub>2</sub>O)<sub>46</sub>CH<sub>2</sub>CH<sub>2</sub>OOC), 5.03 (s, 2H, -ArCH<sub>2</sub>O), 5.16 (s, 4H, -ArOCH<sub>2</sub>), 6.59 (s, 3H, -ArH), 7.83 (s, 2H, triazole). <sup>13</sup>C NMR (125 MHz, CDCl<sub>3</sub>): δ (ppm) 24.7, 25.7, 28.5, 34.2, 63.7, 64.3, 69.2, 70.7, 173.7.

Synthesis of (<sup>+</sup>H<sub>3</sub>N-BA-PEG<sub>2000</sub>)<sub>2</sub>-PCL<sub>3900</sub> (P7)

P6 (0.136 g, 0.017 mmol, 1 eq) was dissolved in DCM (0.5 mL) with magnetic stirring. Trifluoroacetic acid (0.5 mL) was added into the solution and allowed to react for 5 min. The solutions were then removed under vacuum and washed extensively with methanol. The product was then precipitated in cold diethyl ether, collected, and dried in the desiccator. Yield: 80% (0.11 g). <sup>1</sup>H NMR (500 MHz, CDCl<sub>3</sub>): δ (ppm) 1.34- 1.41 (m, 70H, (-OCCH<sub>2</sub>CH<sub>2</sub>CH<sub>2</sub>CH<sub>2</sub>CH<sub>2</sub>O)<sub>35</sub>), 1.60- 1.67 (m, 147H, (-OCCH<sub>2</sub>CH<sub>2</sub>CH<sub>2</sub>CH<sub>2</sub>CH<sub>2</sub>O)<sub>35</sub>), 1.81 (m, 4H, -CH<sub>2</sub>CH<sub>2</sub>CH<sub>2</sub>NH<sub>3</sub><sup>+</sup>), 2.29 (t, 72H, (-OCCH<sub>2</sub>CH<sub>2</sub>CH<sub>2</sub>CH<sub>2</sub>CH<sub>2</sub>O)<sub>35</sub>), 2.38 (t, 4H, -CH<sub>2</sub>CH<sub>2</sub>CH<sub>2</sub>NH<sub>3</sub><sup>+</sup>), 3.06 (t, 4H, -CH<sub>2</sub>CH<sub>2</sub>CH<sub>2</sub>NH<sub>3</sub><sup>+</sup>), 3.49 (t, 4H, -OCCH<sub>2</sub>CH<sub>2</sub>(CH<sub>2</sub>CH<sub>2</sub>O)<sub>45</sub>), 3.63 (s, 364H, -(CH<sub>2</sub>CH<sub>2</sub>O)<sub>45</sub>), 3.88 (t, 4H, -OCCH<sub>2</sub>CH<sub>2</sub>(CH<sub>2</sub>CH<sub>2</sub>O)<sub>45</sub>), 4.05 (t, 67H, (-OCCH<sub>2</sub>CH<sub>2</sub>CH<sub>2</sub>CH<sub>2</sub>CH<sub>2</sub>O)<sub>33</sub>), 4.27 (t, 4H, -(CH<sub>2</sub>CH<sub>2</sub>O)<sub>45</sub>CH<sub>2</sub>CH<sub>2</sub>OOC), 4.55 (t, 4H, -(CH<sub>2</sub>CH<sub>2</sub>O)<sub>45</sub>CH<sub>2</sub>CH<sub>2</sub>OOC), 5.03 (s, 2H, -ArCH<sub>2</sub>O),

5.16 (s, 4H, -ArOCH<sub>2</sub>), 6.59 (s, 3H, -ArH), 7.83 (s, 2H, triazole). <sup>13</sup>C NMR (125 MHz, CDCl<sub>3</sub>): δ (ppm) 24.7, 25.7, 28.5, 34.3, 64.3, 70.7, 173.7.

#### Preparation of blank and drug-loaded polymeric micelles

To prepare blank NPs, the desired polymer (P6 or P7, 5 mg) was dissolved in 2 mL of HPLC-grade acetone in a vial. The polymer solution was then dropped into Milli-Q water (2 mL) at a rate of 1 drop s<sup>-1</sup> while stirring. The acetone was allowed to evaporate overnight in the dark with continuous stirring. The solution was then passed through a 0.22 μm PVDF filter. Milli-Q water was added (if needed) to obtain a final volume of 2 mL.

To prepare the CUR-loaded NPs, the desired polymer (P6 or P7, 5 mg) was dissolved in 2 mL of HPLC-grade acetone in a vial. In another vial, CUR (0.5 mg) was dissolved in HPLC-grade acetone (1 mL). The CUR solution was then mixed with the polymer solution and dropped into Milli-Q water (2 mL) at a rate of 1 drop s<sup>-1</sup> while stirring. The acetone was allowed to evaporate overnight in the dark with continuous stirring. The solution was then centrifuged for 10 min at 1000 rpm and passed through a 0.22 μm PVDF filter. Milli-Q water was added (if needed) to obtain a final volume of 2 mL. TBF-loaded NPs were also prepared using the same protocol but with HPLC-grade DCM instead of acetone.

#### CMC Determination

A series of polymer concentrations ranging from 0.000122 mg ml<sup>-1</sup> to 1.0 mg ml<sup>-1</sup> in HPLC-grade acetone were prepared. A 6 μM pyrene in HPLC-grade acetone solution was also prepared separately. Each polymer and pyrene solution were dropped concurrently into Milli-Q water (1 mL) at a rate of 1 drop s<sup>-1</sup> while stirring. The acetone was allowed to evaporate overnight in the dark with continuous stirring. Milli-Q water was added to obtain a final volume of 1 mL. The fluorescence spectra were recorded, and the CMC was examined by using a plot of λ<sub>338</sub>/ λ<sub>333</sub> intensity against polymer concentration to determine the concentration at which the intensity ratios increased.

Drug Loading and Release

The drug-loaded NP solution was transferred to a Spectra/Por 3 dialysis membrane (standard RC, 3.5 kDa MWCO). The solution was dialyzed against 140 mL of phosphate-buffered saline (PBS, 0.01 M, pH 7.4) containing 1% v/v Tween 80 at 37 °C. At desired intervals, 20 µL aliquots were collected from the dialysis membrane and diluted 100 folds with methanol (for CUR) or DMSO (for TBF) for analysis. The absorption intensities (425 nm for CUR and 285 nm for TBF) were measured at room temperature. The results were referred to a standard drug curve to obtain the mass of drug remaining at each interval. Drug loading (DL %) and encapsulation efficiencies (EE %) were then calculated using the following equations:

$$DL\% = \frac{\text{Mass of drug encapsulated}}{\text{Mass of drug and polymer added}} \times 100\%$$

$$EE\% = \frac{\text{Mass of drug encapsulated}}{\text{Mass of drug added}} \times 100\%$$

Drug Release Kinetic Studies

The drug release kinetic studies were examined by applying model equations as follows:

*Zero-order model:*  $C_t = C_0 + k_0t$

where  $C_t$  = amount of drug released at time  $t$ ,  $C_0$  = initial concentration of drug at time  $t=0$ ,  $k_0$  = zero-order rate constant. A graph of %cumulative drug release vs. time was plotted to obtain the slope of graph ( $k_0$ ) and correlation coefficient value ( $R^2$ ).

*First-order model:*  $\log C = \log C_0 - k_1 \frac{t}{2.303}$

where  $C$  = % drug remaining at time  $t$ ,  $C_0$  = initial concentration of the drug,  $k_1$  = first order rate constant, expressed in  $h^{-1}$ . A graph of log %cumulative drug release vs. time was plotted to obtain  $R^2$ , whereas  $k_1$  = slope of the graph \* 2.303.

*Higuchi model:*  $\frac{M_t}{M_\infty} = k_H t^{\frac{1}{2}}$

where  $M_t/M_\infty$  = fraction of drug released at time  $t$ ,  $M_t$  = amount of drug released at time  $t$ ,  $M_\infty$  = amount of drug released after time  $\infty$ ,  $k_H$  = Higuchi release kinetic constant. A graph

of %cumulative drug release vs. square root of time was plotted to obtain the slope of the graph ( $k_H$ ) and  $R^2$ .

*Korsmeyer-Peppas model:* 
$$\frac{M_t}{M_\infty} = k_{K-P} t^n$$

where  $M_t/M_\infty$ = fraction of drug released at time t,  $M_t$ = amount of drug released in time t,  $M_\infty$ = amount of drug released after time  $\infty$ ,  $k_{K-P}$ = Korsmeyer release rate constant,  $n$ = diffusional exponent. A graph of log %cumulative drug release vs. log time was plotted to obtain slope of the graph ( $n$ ) and  $R^2$ , while  $k_{K-P}$  was obtained from the inverse log (intersection point). Cumulative release data up to 60% was utilized.

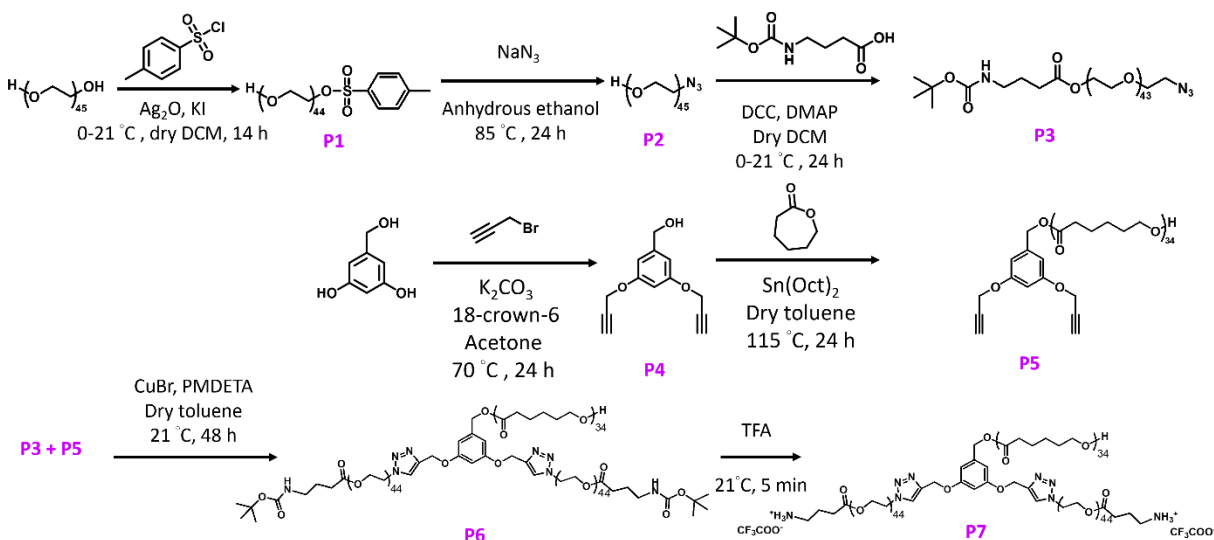
### Assessing the Antimicrobial Activity

To determine the antimicrobial efficiency of P6- and P7-micelles on *E. coli* ATCC 25922 and *B. subtilis* ATCC 6633, two-fold serial dilutions were conducted. The bacterial cultures were diluted with LB broth to achieve an optical density of 0.05 at 600 nm ( $OD_{600}$ ). In parallel, blank P6- and P7-micelles were prepared according to the procedure mentioned previously. The stock micellar solution was then diluted with Milli-Q water to obtain six different concentrations ranging from 78-2500  $\mu\text{g mL}^{-1}$ . Next, 160  $\mu\text{L}$  of bacterial suspension was then added to the wells of a 96-well microplate followed by 40  $\mu\text{L}$  of micellar solutions. The positive control was a bacteria suspension treated with PBS and the negative control was a mixture of LB broth and PBS that did not contain any bacteria. The  $OD_{600}$  of each well was assessed every hour up to 24 h at 37 °C using a SynergyH4 multimode plate reader (BioTek, USA). Three replicates were performed for each concentration. The  $OD_{600}$  obtained at each interval was subtracted with the OD of LB media. Thereafter, a graph of corrected OD over time was plotted to observe the change in bacterial growth over 24 h. The effectiveness of P6-CUR, P7-CUR, P6-TBF, and P7-TBF on both *E. coli* and *B. subtilis* were also analysed with the same protocol but with drug-loaded micelles. To examine the inhibition of CUR and TBF on both bacteria strains, a similar procedure was applied but the drugs were dissolved in 0.75% DMSO due to their poor aqueous solubility. The drug concentrations prepared ranged from 25-300  $\mu\text{g mL}^{-1}$ .

### 3.5. Results and Discussion

#### Synthesis and characterization of cationic miktoarm polymers

Cationic star polymers containing PEG and PCL were synthesized as shown in Scheme 3. 2. PEG offers several unique properties that make it suitable for biomedical applications, including excellent biocompatibility, low toxicity and stealth that minimizes protein adsorption for prolonged circulation half-life.<sup>49</sup> PCL is a hydrophobic polyester that confers biodegradability and biocompatibility to NPs.<sup>50</sup> The branched polymer was prepared via a combination of arm-first and core-first methods. First, an asymmetric functionalization of PEG<sub>2050</sub> via the Ag<sub>2</sub>O-mediated monotosylation was carried out to obtain  $\alpha$ -tosyl- $\omega$ -hydroxyl PEG<sub>2050</sub> (P1). Monotosylation is essential in achieving a positively charged micelle as the free -OH group is then used for esterification with Boc-GABA-OH. The <sup>1</sup>H NMR spectrum of the heterobifunctional polymer contained characteristic tosyl peaks (Figure 3. 7). Tosyl group was then displaced using NaN<sub>3</sub> to yield  $\alpha$ -azido- $\omega$ -hydroxyl PEG<sub>2050</sub> (P2). Introduction of azide group to PEG would allow us to attach the hydrophilic arm onto the hydrophobic core through robust click chemistry. <sup>1</sup>H NMR spectrum of P2 showed the disappearance of distinct peaks for the tosyl group seen in P1, while the remaining OH group shifted slightly upfield (Figure 3. 9). The presence of the azide group was further confirmed by the band at 2102 cm<sup>-1</sup> in the IR spectrum (Figure 3. 21). Subsequently, a Steglich esterification was conducted to link P2 to commercially available Boc-GABA-OH. <sup>1</sup>H NMR spectrum showed peaks distinct for Boc groups and the adjacent amide group (Figure 3. 11); while the IR spectrum showed retention of the azide peak at 2102 cm<sup>-1</sup>, confirming successful heterofunctionalization of PEG. The dipropargylated core without (P4) and with PCL (P5) were synthesized according to a previously published procedure.<sup>51</sup> The degree of polymerization (DP) was calculated by comparing the integral of the benzyl protons between 6.57-6.60 ppm to that of the methylene protons in PCL at 4.06 ppm (Figure 3. 13), and the hydrophobic arm was determined to have a DP of 34, with a number-average molecular weight of 4100 Da.



**Scheme 3. 2:** Synthesis details utilizing a mix of arm- and core-first methods to obtain cationic amphiphilic copolymer P7.

We subsequently carried out copper-catalysed azide-alkyne cycloaddition to obtain the miktoarm polymer P6.  $^1\text{H}$  NMR spectrum of P6 showed successful addition of characteristic peaks from PEG and Boc onto P5 (Figure 3. 16), while GPC traces confirmed the synthesis without any residual hydrophilic or hydrophobic arms (Figure 3. 20). Lastly, Boc groups in P6 were removed by addition of trifluoroacetic acid to confer hydrophilicity and positive charge to the miktoarm polymer P7. Complete deprotection of P6 was confirmed by  $^1\text{H}$  NMR that showed absence of Boc groups, confirming successful formation of P7 copolymer (Figure 3. 18).

### Preparation and characterization of micelles

The size and CMC of NPs are important parameters that can significantly influence their performance in biological applications.<sup>52</sup> In the NP assemblies, PCL is expected to aggregate to form the particle core and be shielded from the aqueous medium by the hydrophilic PEG. A hydrodynamic diameter of 20-200 nm has been consistently highlighted to be the ideal window in minimizing nonspecific uptake by the reticuloendothelial system while maximizing delivery through the enhanced permeation and retention effect.<sup>53</sup> NPs from  $\text{AB}_2$  polymers (P6 and P7) were prepared with continuous stirring to facilitate solvent/ polymer dispersion and solvent evaporation. Both P6 and P7 self-assembled into spherical NPs, subsequently known as P6-micelles and P7-

micelles, which were analysed using DLS and TEM (Figure 3. 1, Table 3. 1, Figure 3. 22). DLS showed monomodal size distribution of particles for both, in which hydrodynamic diameters were approximately 44 and 92 nm, respectively. Since both polymers possess hydrophobic PCL with similar molecular weight and composition, difference in size suggests that it is related to the hydrophilic shell which is charged at the termini in P7-micelles, compared to the one without (P6-micelles). The added electrostatic surface repulsion in P7-micelles led to enlargement and increase in micelle size. Such an expansion has also been observed in other lysine/ polyphosphoester/ primary amine systems.<sup>54-56</sup> TEM analyses showed uniform micelles with average size smaller than those determined using DLS, approximately 42 nm for P6-micelles and 87 nm for P7-micelles. Zeta ( $\zeta$ )-potential values suggest that P7-micelles have a positive charge of about 15 mV, while P6-micelles were slightly negative.

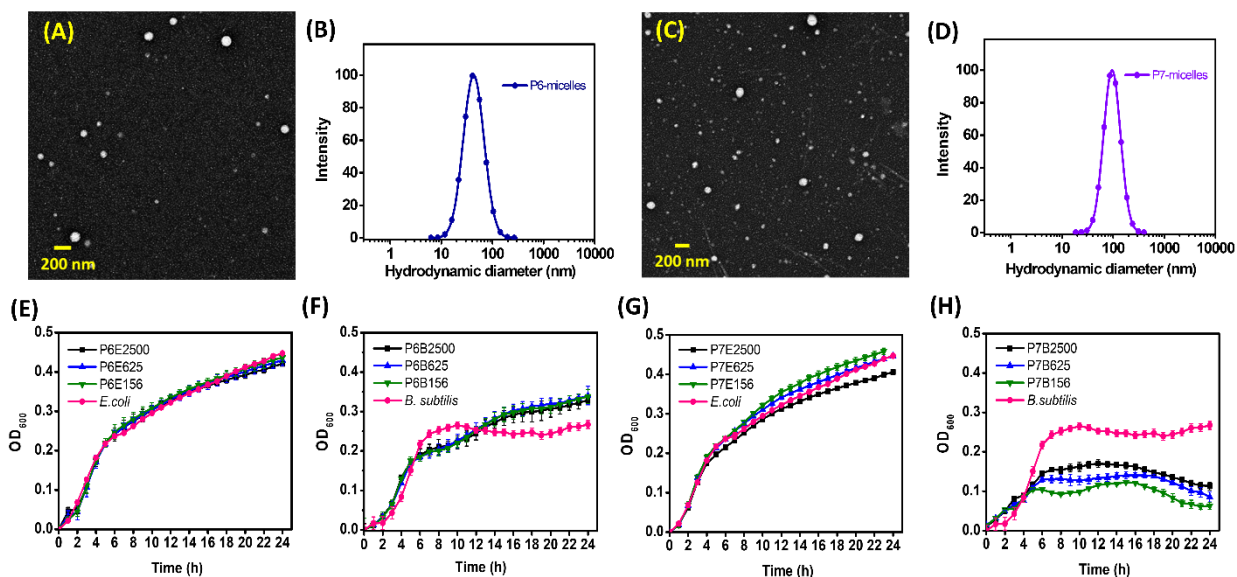


**Figure 3. 1:** (A) TEM image and (B) DLS analyses of P6-micelles, (C) TEM image and (D) DLS analyses of P7-micelles. Growth curves of (E) *E. coli* and (F) *B. subtilis* incubated with P6-micelles, growth curves of (G) *E. coli* and (H) *B. subtilis* treated with P7-micelles. Graph legends: P6 represents P6-micelles whereas P7 represents P7-micelles. Letter following sample represents bacterial strains, while the numbers that follow suit represent concentration of micellar solutions (e.g., P6E2500 contains 2500  $\mu\text{g mL}^{-1}$  of P6-micelle added to *E. coli*, P7B2500 contains 2500  $\mu\text{g}$

mL<sup>-1</sup> of P6-micelle added to *B. subtilis*). For additional concentrations tested, see Appendix B (Figure 3. 24-27).

**Table 3. 1:** Polymer and micelle characterization of P6 and P7.

Sample	$M_{n,NMR}^a$ (Da)	$\mathcal{D}^b$	Blank-micelles		CMC ( $\mu\text{g mL}^{-1}$ ) <sup>d</sup>
			$D_H$ (nm) <sup>c</sup>	$\zeta$ (mV) <sup>c</sup>	
P6	8200	1.38	44 ± 8	-5.69 ± 2.07	4.66
P7	8000	1.54	92 ± 10	15.66 ± 3.07	7.75

<sup>a</sup>Number-average molecular weight of polymers estimated from <sup>1</sup>H NMR. <sup>b</sup>Dispersity of polymers obtained from THF GPC. <sup>c</sup>Hydrodynamic diameter ( $D_H$ ) and zeta potential ( $\zeta$ ) obtained by DLS. <sup>d</sup>CMC determined by pyrene fluorescence studies.

CMC reflects the stability of a nanocarrier when introduced into blood circulation. Low CMC is advantageous to ensure retention of micellar structure and drug solubility in biological media even under extensive dilutions.<sup>57</sup> To evaluate the CMC of our system, we encapsulated the fluorescence probe, pyrene, into our polymers as detailed previously (Figure 3. 23). The transition from unimers to well-defined polymeric micelles created different microenvironments for the partition of pyrene that can be easily detected by fluorescence. CMC of P6 was determined to be 4.66  $\mu\text{g mL}^{-1}$ , whereas that for P7 was 7.75  $\mu\text{g mL}^{-1}$ , approximately 1.7-fold higher than P6. This increase is consistent with the increase in size observed in DLS.

#### Evaluation of antibacterial properties of P6- and P7-micelles

The positively-charged shell on NPs facilitates their adhesion to the negatively-charged bacteria surface through electrostatic interactions.<sup>58</sup> Gram-negative bacteria exhibit a negative charge due to the presence of a lipopolysaccharide layer on the outer leaflet of their membrane, while the negative charge on Gram-positive bacteria stems from the teichoic acid embedded within the peptidoglycan layer.<sup>59</sup> Despite Gram-negative bacteria having a thinner peptidoglycan layer, the

additional outer membrane serves as an additional diffusion barrier, rendering them more resistant against antibiotic treatments.<sup>60</sup>

Gram-positive *B. subtilis* and Gram-negative *E. coli* were chosen to investigate the antibacterial activity of our NPs. *E. coli* are renowned as prevalent bacteria in wound infections and hold clinical significance. Meanwhile, the inclusion of *B. subtilis* stemmed from its genetic affinity with diverse pathogens, notably *B. cereus*, a bacterium commonly associated with wound infections.<sup>61</sup> We performed 96-well plate method to evaluate effects of blank P6- and P7-micelles on bacterial growth. Optical density measurements at 600 nm were taken hourly over a 24 h period. In all cases, constant or minimal/ decreasing optical densities over time indicated limited bacterial growth or no bacterial growth. Conversely, an increase in optical density suggested enhanced bacterial growth. Given the positive charge of P7-micelles, which enables interaction with the negatively-charged bacterial cell membrane, we anticipated these NPs to possess intrinsic antibacterial properties. Consequently, minimal inhibitory effect from P6-micelles that lack specific interactions with the bacterial cell membrane is expected. The growth curves for both bacterial strains are summarised in Figure 3. 1E-1H, and additional concentrations tested are presented in Figure 3. 24-27. As shown in Figure 3. 1E-F and as expected, P6-micelles demonstrate no inhibitory effect on the growth of *E. coli* and *B. subtilis*, even at concentrations up to 2500  $\mu\text{g mL}^{-1}$ , aligning with our hypothesis regarding their lack of specific bacterial cell membrane interactions.

Subsequently, we examined the inhibitory efficacy of P7-micelles on *E. coli* and *B. subtilis* bacteria, which was found to be both bacteria- and NP concentration-dependent. Notably, while *E. coli* inhibition was only evident at higher concentration of P7-micelles (2500  $\mu\text{g mL}^{-1}$ , Figure 3. 1G), inhibition of *B. subtilis* was pronounced even at lower concentrations (156  $\mu\text{g mL}^{-1}$ , Figure 3. 1H). These results are in agreement with previous reports on cationic polymers, which have shown greater effectiveness against Gram-positive bacteria.<sup>62</sup> The growth rates of *B. subtilis* also displayed several distinct logarithmic, stationary, and death phases. In the absence of P7-micelles, *B. subtilis* followed a logarithmic phase between 0-7 h, and a relatively stationary phase until 24 h. Treatment with P7-micelles altered this growth curve, with variations depending on NP concentration. At lower concentrations of 156  $\mu\text{g mL}^{-1}$ , *B. subtilis* exhibited a logarithmic phase

between 0-5 h, stationary phase between up to 10 h, and a steady increase in cell density until 15 h, before entering the death phase. Conversely, concentrations of 625 and 2500  $\mu\text{g mL}^{-1}$  demonstrated a very similar but more stable stationary phase before entering death phase at about 14 h, indicating that higher concentrations are more efficient in consistently inhibiting bacterial growth compared to lower concentrations. These results clearly suggest that P7-micelles exhibit intrinsic antimicrobial activity, with the inhibitory activity dependent on NP concentration. The concentration-dependent biocidal activity has also been shown earlier for cationic polymers. For example, Lim and Hudson examined antimicrobial activity of *S. aureus* (Gram-positive bacteria) relative to the concentration of *O*-acrylamidomethyl-*N*-[(2-hydroxy-3-trimethylammonium)propyl]chitosan chloride (NMA-HTCC).<sup>63</sup> Their study revealed that cationic chitosan effectively inhibited *E. coli* and *S. aureus* growth, with the peak antimicrobial activity observed at the lowest tested concentration of 10 ppm. The inverse relationship observed, wherein higher concentrations of chitosan (200 ppm) exhibited diminished antimicrobial activity, was attributed to the coating of bacterial cell membranes which prevents leakage of intracellular components. Nevertheless, our research highlights the efficacy of cationic P7-micelles against various bacterial strains, demonstrating its versatility in addressing diverse microbial threats.

#### SEM analyses of bacteria

The inhibition of bacterial growth by cationic NPs is typically through electrostatic attractions with the negatively-charged bacterial membrane.<sup>64</sup> Morphological changes of *E. coli* and *B. subtilis* in response to NP solutions were analysed using SEM (Figure 3. 2). The bacterial cells incubated without any NP treatment were used as blank controls. Figure 3. 2A shows intact and rod-shaped *E. coli*, with lengths ranging from 1.5-3.0  $\mu\text{m}$ . Following incubation with P6-micelles for 24 h, the bacterial cells remained intact and were approximately 2.0  $\mu\text{m}$  long (Figure 3. 2C). In contrast, treatment with P7-micelles induced deformations in *E. coli*, resulting in hollow and ruptured structures (Figure 3. 2E). These observations are indicative of *E. coli* inhibition upon treatment with P7-micelles, which may induce cell leakage by disrupting the bacterial membrane. Chakraborti et al. have reported analogous disintegration of *E. coli* structures, achieved through treatment with PEI-functionalized ZnO.<sup>65</sup> This treatment disrupted bacterial membrane, leading to leakage of cellular proteins.

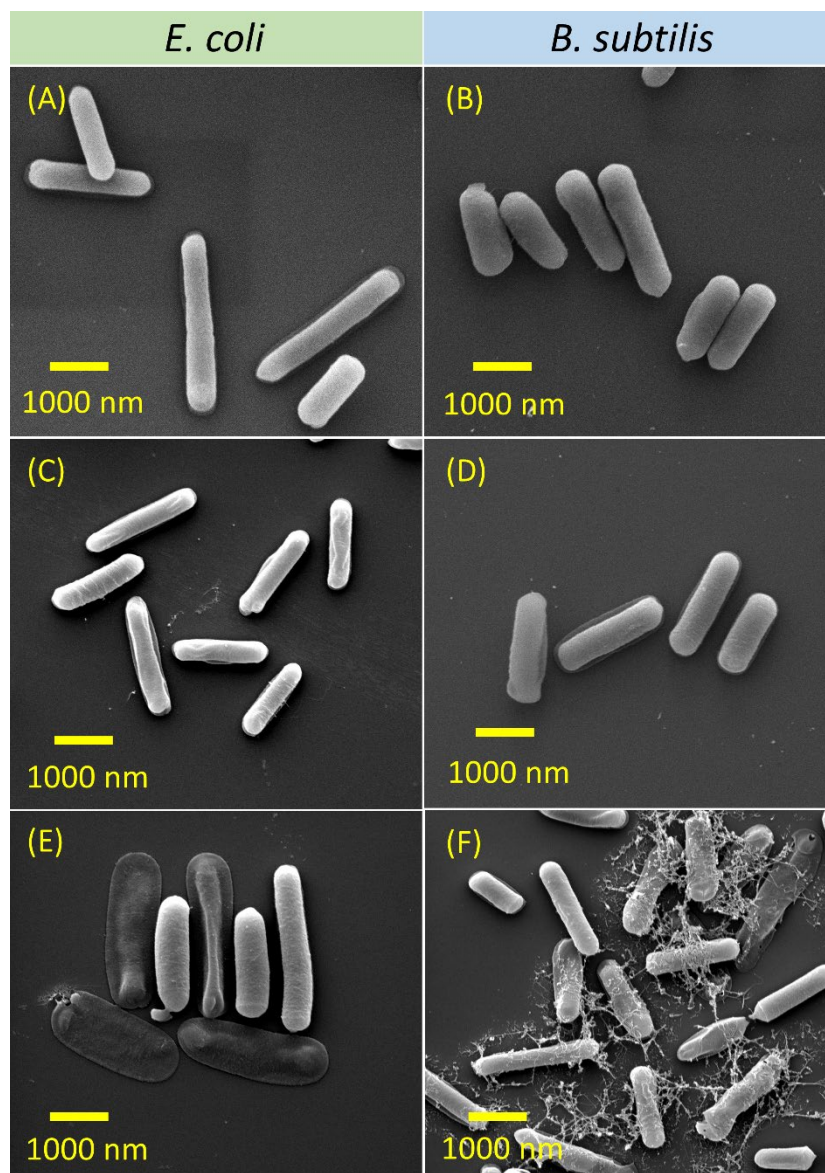


**Figure 3. 2:** SEM images of untreated (A) *E. coli* and (B) *B. subtilis*, *E. coli* incubated with (C) P6-micelles, (E) P7-micelles, and *B. subtilis* with (D) P6-micelles, (F) P7-micelles. Bacteria were incubated with P6-/P7-micelles ( $2500 \mu\text{g mL}^{-1}$ ) for 24 h prior to fixing.

In studies with *B. subtilis*, we observed slightly shorter rod shapes of 1.0-2.5  $\mu\text{m}$  (Figure 3. 2B). Due to neutral hydrophilic shell, P6-micelles displayed no effect on *B. subtilis* inhibition as the bacteria still appeared long and were approximately 1.5-2.5  $\mu\text{m}$  (Figure 3. 2D). However, when *B. subtilis* was incubated with P7-micelles, several distorted, ruptured, and irregular bacteria were observed (Figure 3. 2F). These results suggest cell membrane rupture, leading to leakage of

cytoplasmic contents, resulting in cell death. Such observations have also been reported by Tanganini et al., who utilized SEM to visualize the damage induced by self-assembled lignin NPs on *B. subtilis*, and similar deformed structures in bacterial cell morphology were noted, demonstrating the potential of NPs as antimicrobial agents.<sup>66</sup>

### Drug loading into P6- and P7-micelles

The deformations observed in both *E. coli* and *B. Subtilis* highlighted the potential of P7-micelles as promising alternatives to antibiotics. Additionally, their core-shell structure provides additional advantages beyond their intrinsic antimicrobial properties. This design enables encapsulation and controlled delivery of antibiotics, potentially offering additive or synergistic effects to enhance the overall antimicrobial efficacy of NPs. This feature presents a multifaceted approach in combatting microbial infections. To ascertain these advantages, CUR and TBF were first loaded into micelles from P6 and P7 at a polymer:drug ratio of 10:1. Drug loading capacity (DL%) and encapsulation efficiency (EE%) of CUR-loaded NPs were determined to be i) 6.6% and 72.4% for P6-micelles (P6-CUR); and 3.4% and 36.9% for P7-micelles (P7-CUR, Table 3. 2). We noted that the loading in P6-CUR was almost twice as much compared to P7-CUR. This disparity in CUR encapsulation may be due to a drop in pH when P7 was introduced into water during self-assembly (pH 4.3), which created an acidic environment that further suppressed aqueous solubility of CUR and subsequently reduced its encapsulation.<sup>67</sup> In contrast, the pH of P6 in water was 6.8, which helped prevent crystallization of CUR. NP sizes of P6 and P7-based micelles were examined by DLS and TEM (Figure 3. 3, Figure 3. 28). In general, hydrophobic drugs such as CUR may provide additional driving force for self-assembly to give denser and smaller micelles, which was observed in both P6-CUR (45 nm) and P7-CUR (54 nm) compared to their blank counterparts.<sup>68</sup>  $\zeta$ -potential experiments revealed values of 3.4 mV (P6-CUR) and 7.14 mV (P7-CUR). Due to the dehydration process, TEM revealed marginally smaller sizes than DLS, 44 nm (P6-CUR) and 52 nm (P7-CUR).

**Table 3. 2:** Drug-loaded micelle characterization.

<b>Samples</b>	<b>P6-CUR</b>	<b>P7-CUR</b>	<b>P6-TBF</b>	<b>P7-TBF</b>
<b>DL%<sup>a</sup></b>	6.6 ± 0.1	3.4 ± 0.6	6.6 ± 0.8	8.7 ± 0.6
<b>EE%<sup>a</sup></b>	72.4 ± 1.3	36.9 ± 6.7	72.7 ± 8.8	95.7 ± 6.1
<b><i>D<sub>H</sub></i> (nm)<sup>b</sup></b>	45 ± 13	54 ± 7	134 ± 10	115 ± 11
<b>ζ (mV)<sup>b</sup></b>	3.4 ± 0.6	7.14 ± 0.73	4.17 ± 1.55	16.04 ± 10.04

<sup>a</sup>Drug loading (DL%) and encapsulation efficiencies (EE%) obtained by UV-Vis. <sup>b</sup>Hydrodynamic diameter (*D<sub>H</sub>*) and zeta potential (ζ) obtained by DLS.

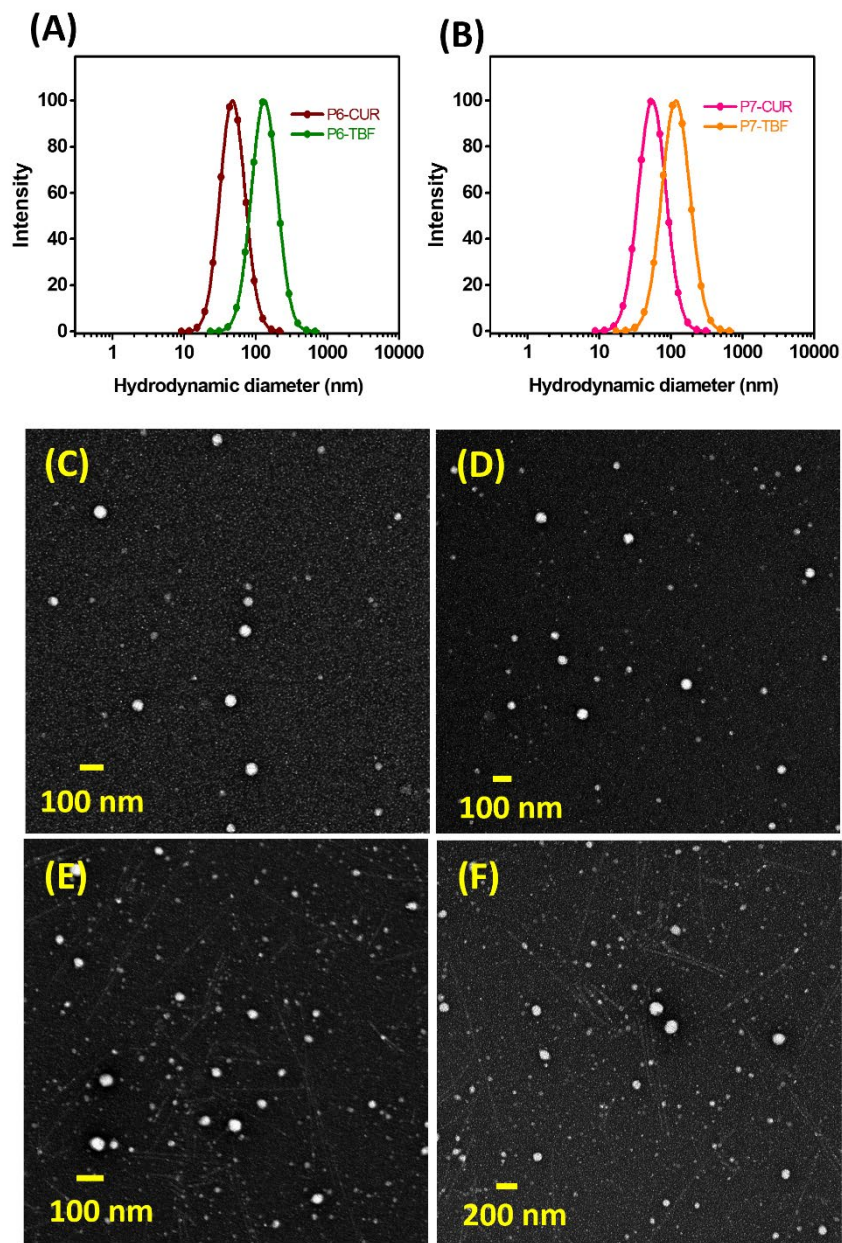


**Figure 3. 3:** DLS analyses of (A) P6-CUR and P6-TBF, and (B) P7-CUR and P7-TBF. TEM images of (C) P6-CUR, (D) P6-TBF, (E) P7-CUR, and (F) P7-TBF.

DL and EE for TBF-encapsulated self-assemblies were found to be i) 6.6% and 72.7% for P6-micelles (P6-TBF) and ii) 8.7% and 95.7% for P7-micelles (P7-TBF), suggesting better encapsulation of TBF than CUR for P7. This is, to our knowledge, the first study examining TBF

loading into miktoarm polymer based micellar assemblies. DLS showed particle sizes of 134 nm for P6-TBF and 115 nm for P7-TBF, and  $\zeta$ -potential values were determined to be 4.17 mV (P6-TBF) and 16.04 mV (P7-TBF). TEM revealed smaller particle sizes of 70 nm and 74 nm for P6-TBF and P7-TBF, respectively, due to dehydration effects during sample preparation.

### Drug release studies from P6- and P7-micelles

Drug release from nanoformulations was evaluated under simulated physiological conditions (0.01 M PBS, pH 7.4, 37 °C). We noted that the introduction of positively-charged corona did not impede drug release significantly. As depicted in Figure 3. 4A, CUR release over time was marginally faster from P7-micelles. The most significant differences were observed in the early hours of drug release (0-8 h), where CUR release was higher from P6-CUR than cationic P7-CUR NPs; beyond 8 h, the cumulative differences periodically diminished. For instance, within the first hour, the release from P6-CUR was 27%, whereas it was slightly slower at 19% for P7-CUR. At 2 h, the release was at 38% for P6-CUR and 29% for P7-CUR; 4 h, 45% for P6-CUR and 37% with P7-CUR; at 8 h, 51% for P6-CUR and 51% for P7-CUR. These differences were, however, quite miniscule, and suggest that the cationic shell did not cause any significant delay in CUR release. In subsequent time period, CUR release from P7-CUR was found to be slightly faster than P6-CUR: 24 h: 59% for P6-CUR, and 66% for P7-CUR; 48 h: 75% for P6-CUR and 74% for P7-CUR; and finally 72 h: 80% for P6-CUR and 83% for P7-CUR.

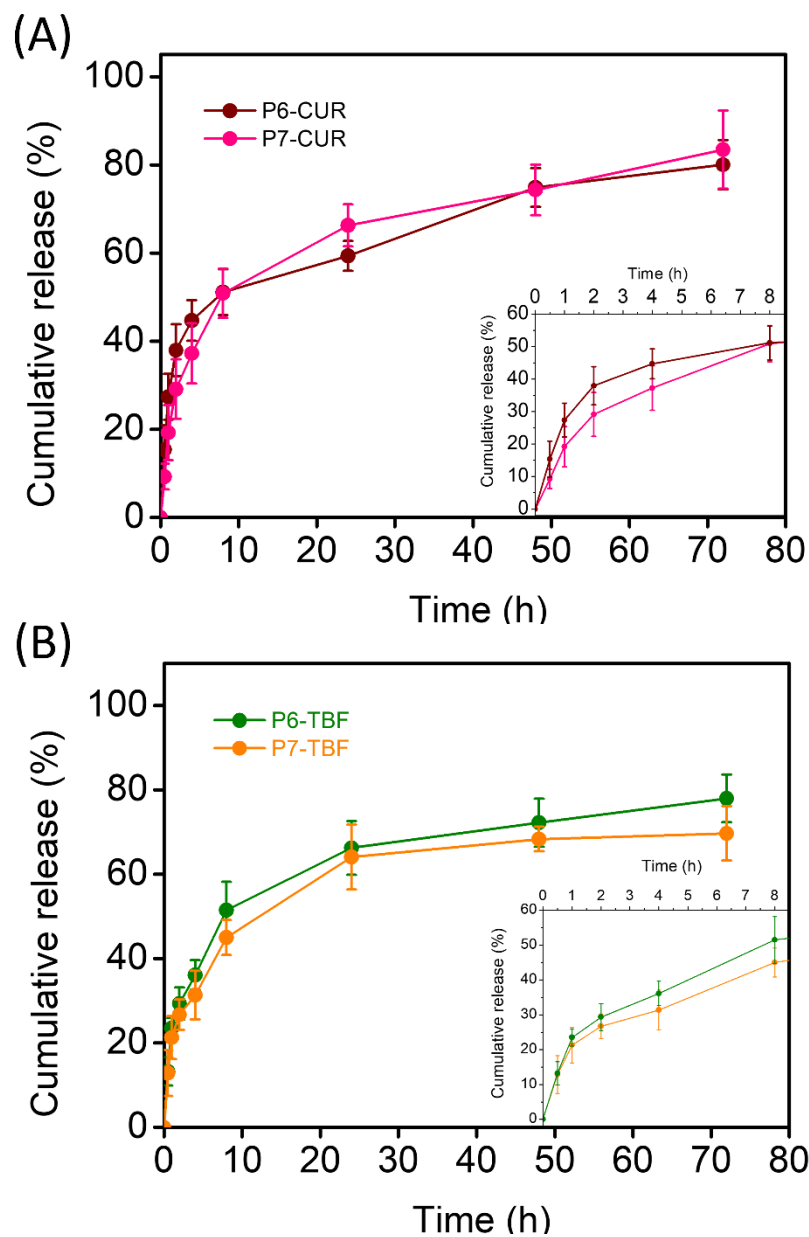


**Figure 3. 4:** (A) CUR release from P6-CUR and P7-CUR, (B) TBF release from P6-TBF and P7-TBF. All studies were conducted at 37 °C in 1X PBS buffer (pH 7.4, +1% v/v Tween 80). Error bars represent a standard deviation of  $n = 3$ .

For TBF-loaded micelles, P6-TBF exhibited slightly faster release rates than P7-TBF over the observed time period (Figure 3. 4B). The disparity in release rates between the two systems generally increased in the first 8 h. For example, 1 h: TBF release was 23 % for P6-TBF and 21% for P7-TBF; 2 h, 29% for P6-TBF and 27% for P7-TBF, indicating a trend of slightly faster release

of P6-TBF. This trend continued with 36% release for P6-TBF and 31% for P7-TBF at 4 h, 52% for P6-TBF and 64% for P7-TBF at 8 h. From 8 h, minimal differences were noted between P6-TBF and P7-TBF. Specifically, at 24 h, the release was 66% for P6-TBF and 64% for P7-TBF; at 48 h, 72% for P6-TBF and 68% for P7-TBF; and finally at 72 h, 78% for P6-TBF and 70% for P7-TBF. These results further highlight that the positively-charged shell in P7-micelles did not interfere with the release of varied drugs with different pharmacokinetics. It also suggests that the multifunctional P7-micelles are promising candidates not only for their intrinsic antimicrobial properties but also as effective antibiotic delivery vehicles, showcasing their versatility and potential in combating microbial infections.

#### Drug release kinetic studies

To investigate the mechanism of drug release, we assessed the release curves to several standard mathematical models. These models offer insights into whether drug release is primarily diffusion-based or dissolution-driven, which can facilitate the formulation of pharmaceuticals and predict drug bioavailability in the body.<sup>69,70</sup> We evaluated the zero order, first order, Higuchi, and Korsmeyer-Peppas models by comparing the correlation coefficients ( $R^2$ ) (Table 3. 3, Figure 3. 30-33). For CUR release from P6-micelles, the Higuchi model demonstrated the best fit, yielding an  $R^2$  and a  $k_H$  value of 0.914 and 12.075, respectively. This result suggests that drug release was governed by Fickian diffusion. P7-CUR also exhibited the best fit with the Higuchi model; however, corresponding results from the Korsmeyer-Peppas model yielded comparatively good  $R^2$  values of 0.950 compared to 0.951. This evaluation is indicative that drug release was controlled by more than one process (i.e., anomalous transport), which was further confirmed as the  $n$  value was 0.586. In general, spherical particles are said to follow anomalous transport when  $0.43 < n < 0.85$ .<sup>71</sup> The Korsmeyer-Peppas model was also the most suited to describe delivery of TBF from both P6- and P7-micelles, with the highest  $R^2$  values of 0.957 and 0.964, respectively. TBF release from P6-micelles was driven by non-Fickian diffusion ( $n = 0.454$ ), whereas TBF delivery from P7-micelles was diffusion controlled ( $n \leq 0.43$ ).

**Table 3. 3:** Kinetic parameters of drug-loaded micelles.

Model	Parameter	P6-CUR	P7-CUR	P6-TBF	P7-TBF
<b>Zero order</b>	$k_0$ (mg h <sup>-1</sup> )	0.903	0.987	0.907	0.825
	$R^2$	0.654	0.744	0.714	0.699
<b>First order</b>	$k_1$ (h <sup>-1</sup> ) x 10 <sup>-3</sup>	27.6	31.6	29.5	28.8
	$R^2$	0.268	0.339	0.313	0.312
<b>Korsmeyer- Peppas</b>	$k_{K-P}$ (h <sup>-n</sup> )	24.362	16.669	19.738	18.919
	n	0.417	0.586	0.454	0.418
	$R^2$	0.909	0.950	0.957	0.964
<b>Higuchi</b>	$k_H$ (mg <sup>1/3</sup> h <sup>-1/2</sup> )	12.075	11.491	11.116	10.264
	$R^2$	0.914	0.951	0.939	0.935

#### Evaluation of antibacterial properties of CUR and TBF loaded P7-micelles

We were intrigued in exploring potential antibacterial properties of our intrinsically active NPs which were loaded with small molecule antimicrobial agents, and focused our investigation on P7-CUR and P7-TBF for this purpose. CUR is known for its ability to inhibit bacterial growth by interfering with membrane proteins and disrupting cellular processes.<sup>41, 72</sup> It has been shown that CUR can easily permeate bacterial membranes, rendering bacteria more susceptible to antibiotics. *E. coli* inhibition studies with free CUR are presented in Figure 3. 5A. CUR exhibited concentration-dependent antimicrobial activity against *E. coli*: concentrations of CUR at 200-300 µg mL<sup>-1</sup> were found to be much more potent in inhibiting *E. coli* growth, while lower concentrations of 50-150 µg mL<sup>-1</sup> displayed reduced efficacy.

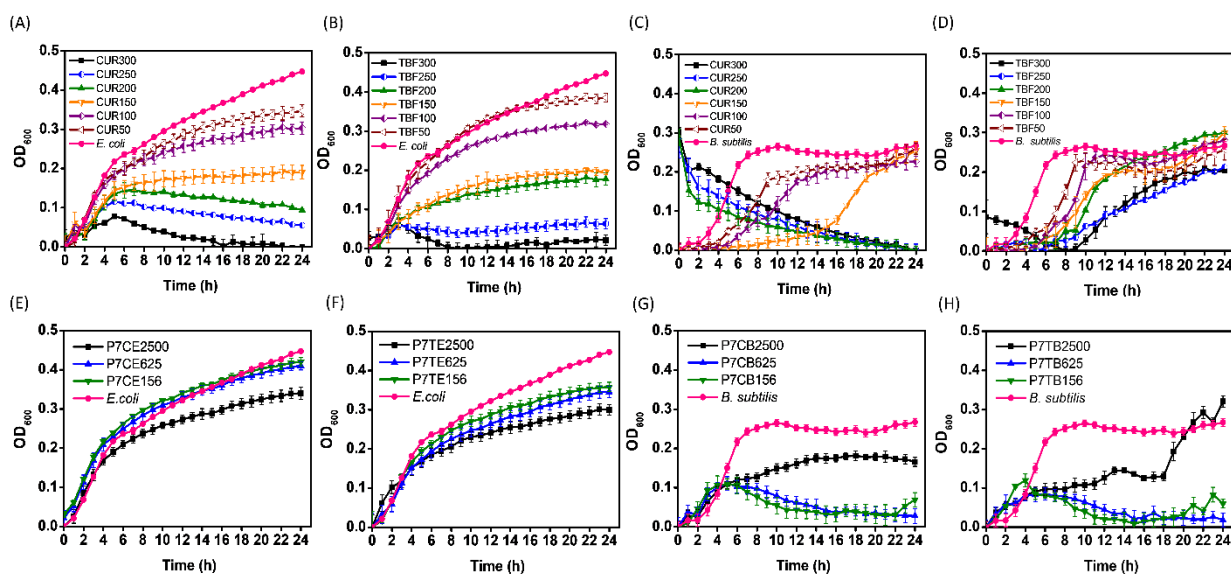


**Figure 3. 5:** Growth curves of *E. coli* treated with (A) CUR and (B) TBF, *B. subtilis* treated with (C) CUR and (D) TBF, *E. coli* treated with (E) P7-CUR and (F) P7-TBF, and *B. subtilis* treated with (G) P7-CUR and (H) P7-TBF. Graph legends: P7C represents P7-CUR whereas P7T represents P7-TBF. Letter following sample represents bacterial strains, while the numbers that follow suit represent concentration of micellar solutions (e.g., P7CE2500 contains  $2500 \mu\text{g mL}^{-1}$  of P7-CUR added to *E. coli*, P7TB2500 contains  $2500 \mu\text{g mL}^{-1}$  of P7-TBF added to *B. subtilis*). For additional concentrations tested, see Appendix B (Figure 3. 34-37).

As noted above, empty P7-micelles showed intrinsic antibacterial activity against *E. coli* only at higher concentrations ( $2500 \mu\text{g mL}^{-1}$ , Figure 3. 1G). Inhibition of *E. coli* with P7-CUR nanoformulations became prominent after 16 h at concentrations as low as  $156\text{-}625 \mu\text{g mL}^{-1}$  (Figure 3. 5E), which contained only  $5.7$  to  $23.0 \mu\text{g mL}^{-1}$  of CUR. When P7-CUR concentrations were increased to  $1250$  to  $2500 \mu\text{g mL}^{-1}$  (containing  $46.1$  to  $92.2 \mu\text{g mL}^{-1}$  of encapsulated CUR), *E. coli* growth was inhibited as early as 3 h. These results clearly suggest that i) P7-CUR shows much better efficacy against *E. coli* than empty P7-micelles, which show intrinsic antibacterial activity only at concentrations of  $2500 \mu\text{g mL}^{-1}$  or higher; and ii) CUR encapsulated in P7-micelles is effective in the onset of *E. coli* growth inhibition with concentrations of encapsulated CUR lower or comparable to free CUR. The onset of inhibition with P7-CUR is related to gradual diffusion and delivery of CUR from P7-CUR. These findings highlight advantages offered by P7-micelles

as a nanocarrier: intrinsic biocidal activity, coupled with delivery of a potent lipophilic antibacterial agent. By leveraging on these properties, P7-CUR collectively provides better efficacy in impeding *E. coli* growth, and offers a promising approach for combating bacterial infections.

Subsequently, we analysed growth curves of *E. coli* upon treatment with TBF and P7-TBF. The reported mode of action of TBF involves inhibition of squalene epoxidase that is responsible for converting squalene to squalene epoxide, a key precursor in ergosterol biosynthesis.<sup>73, 74</sup> As ergosterol synthesis is impeded, integrity of the cell membrane is compromised and subsequently weakened. In addition, intracellular accumulation of squalene results in rapid cell death, as it is toxic to fungal cells.<sup>75</sup> TBF showed concentration-dependent antimicrobial activity against *E. coli* (Figure 3. 5B), with concentrations of TBF at 250-300  $\mu\text{g mL}^{-1}$  proving to be more efficient in inhibiting *E. coli* growth than lower concentrations (50-200  $\mu\text{g mL}^{-1}$ ).

The inhibition of *E. coli* with P7-TBF was also found to be concentration dependent (Figure 3. 5F), with an onset of inhibition at 4 h, which increased with an increase in concentration of 156-2500  $\mu\text{g mL}^{-1}$  of P7-TBF. The time-related inhibitory effect was particularly pronounced at the highest concentration of 2500  $\mu\text{g mL}^{-1}$ , which contained 240  $\mu\text{g mL}^{-1}$  of TBF. Comparatively, at P7-TBF concentrations of 156-625  $\mu\text{g mL}^{-1}$  (containing 15-60  $\mu\text{g mL}^{-1}$  of TBF), lower amounts led to lesser TBF-induced activity. As noted above for CUR, the inhibitory effect of P7-TBF on *E. coli* growth is relatively higher than empty P7-micelles (without encapsulated TBF); and the onset of inhibition from encapsulated TBF in P7-TBF is related to its time-dependent release. These results demonstrate once again potential dual action applications of these nanoformulations: direct intrinsic bactericidal activity and timely release of antimicrobial agents.

As for *E. coli*, CUR showed concentration-dependent inhibitory activity against *B. subtilis* (Figure 3. 5C). Concentrations of CUR at 200-300  $\mu\text{g mL}^{-1}$  were found to effectively arrest *B. subtilis* growth, whereas CUR at lower concentrations (50-150  $\mu\text{g mL}^{-1}$ ) only slowed down bacterial growth. At 50  $\mu\text{g mL}^{-1}$  of CUR, *B. subtilis* exhibited a logarithmic growth phase between 0-9 h, followed by a relatively stationary phase persisting until 24 h. With an increase in concentration to 100  $\mu\text{g mL}^{-1}$ , the logarithmic phase extended to 14 h before transitioning into the stationary

phase; at  $150 \mu\text{g mL}^{-1}$ , the logarithmic phase was further prolonged to 24 h, with no discernible stationary phase observed.

Inhibition by P7-CUR against *B. subtilis* was also concentration-dependent (Figure 3. 5G). With P7-CUR concentrations in the range of  $156\text{-}625 \mu\text{g mL}^{-1}$ , which contained  $5.7\text{-}23.0 \mu\text{g mL}^{-1}$  of CUR, *B. subtilis* exhibited exponential growth in the first 4 h before entering the death phase. This earlier onset of the death phase clearly suggests that P7-CUR is more effective at inhibiting *B. subtilis* growth than P7-micelles, in which cells entered death phase only at 16 h. It was also evident that CUR encapsulated in P7-micelles effectively inhibited *B. subtilis* growth at concentrations lower than free CUR (Figure 3.5 C and G). Additionally, at lower P7-CUR concentrations, nanoformulations were found to be more efficient at inhibiting *B. subtilis* growth than *E. coli*. This disparity in efficacy may be attributed to structural differences in the bacterial cell membrane, as reported by Ngwabebhoh et al.<sup>76</sup> As noted for empty P7-micelles, higher concentration of P7-CUR ( $2500 \mu\text{g mL}^{-1}$ , containing  $92 \mu\text{g mL}^{-1}$  of CUR) was not as effective in inhibiting growth of *B. subtilis*. This suggests that at higher concentrations, NPs likely coat the external bacterial surface, which prevented cell leakage and reduced its potency.<sup>63</sup> It leads to additive effects of P7-CUR being observed only at lower concentrations. Our findings suggest that the combined efficacy of P7-micelles and CUR against *B. subtilis* can be optimally realized at lower concentrations of drug loaded antibacterial formulation (P7-CUR).

In a similar study with TBF and P7-TBF on *B. subtilis*, it was noted that free TBF efficacy was also concentration dependent (Figure 3. 5D). Between  $50\text{-}100 \mu\text{g mL}^{-1}$ , *B. subtilis* showed a logarithmic growth phase between 0-9 h, followed by a relatively stationary phase persisting until 24 h. Upon increasing the concentration to  $150\text{-}250 \mu\text{g mL}^{-1}$ , the logarithmic phase extended to 24 h, resulting in no discernible stationary phase; at  $300 \mu\text{g mL}^{-1}$ , TBF effectively impeded *B. subtilis* growth from the onset until 8 h, beyond which it entered the logarithmic phase.

In contrast, lower concentrations of P7-TBF were more efficient against *B. subtilis* (Figure 3. 5H). With P7-TBF concentrations of  $156\text{-}625 \mu\text{g mL}^{-1}$  (containing  $15\text{-}60 \mu\text{g mL}^{-1}$  of TBF), the bacteria experienced a logarithmic growth in the first 4 h. Subsequently, optical density at 600 nm gradually decreased, indicating a reduction in the population of *B. subtilis* in the presence of P7-TBF. In

comparison to empty P7-micelles, for which cells entered death phase at 16 h, the earlier onset of the death phase suggests that P7-TBF is more effective at inhibiting *B. subtilis* growth, and at encapsulated TBF concentrations lower than free TBF (Figure 3.5 D and H). However, at 2500  $\mu\text{g mL}^{-1}$  (containing 240  $\mu\text{g mL}^{-1}$  of encapsulated TBF), the effectiveness of P7-TBF in inhibiting *B. subtilis* growth diminished when compared to blank P7-micelles. Similar to P7-CUR, it is possible that higher concentrations of nanoformulations formed a protective coating on the external bacterial surface, subsequently preventing leakage of cell contents and reducing its efficacy. Therefore, additive effects of P7-micelles and TBF were observed only at lower concentrations. Nevertheless, inhibition seen at lower concentrations highlights the potential of encapsulating TBF into intrinsically antimicrobial P7-micelles to impede *B. subtilis* growth, providing promising avenues for utilizing P7-micelles as dual-action formulations to inhibit bacterial growth and deliver therapeutic agents.

### SEM analyses of bacteria

SEM was used to gain visual insights into the morphology of both *E. coli* and *B. subtilis* after exposure to CUR, TBF, P7-CUR, and P7-TBF (Figure 3. 6). Upon exposure to CUR, *E. coli* retained their rod-like shapes, measuring approximately 2-3  $\mu\text{m}$  in length (Figure 3. 6A). However, closer inspection of the images revealed much rougher surfaces compared to untreated *E. coli*, which are indicative of the disruptive effects of CUR on membrane integrity. Similarly, treatment with P7-CUR also resulted in wrinkly surfaces (Figure 3. 6B), affirming the inhibitory efficacy of P7-CUR against *E. coli* growth.

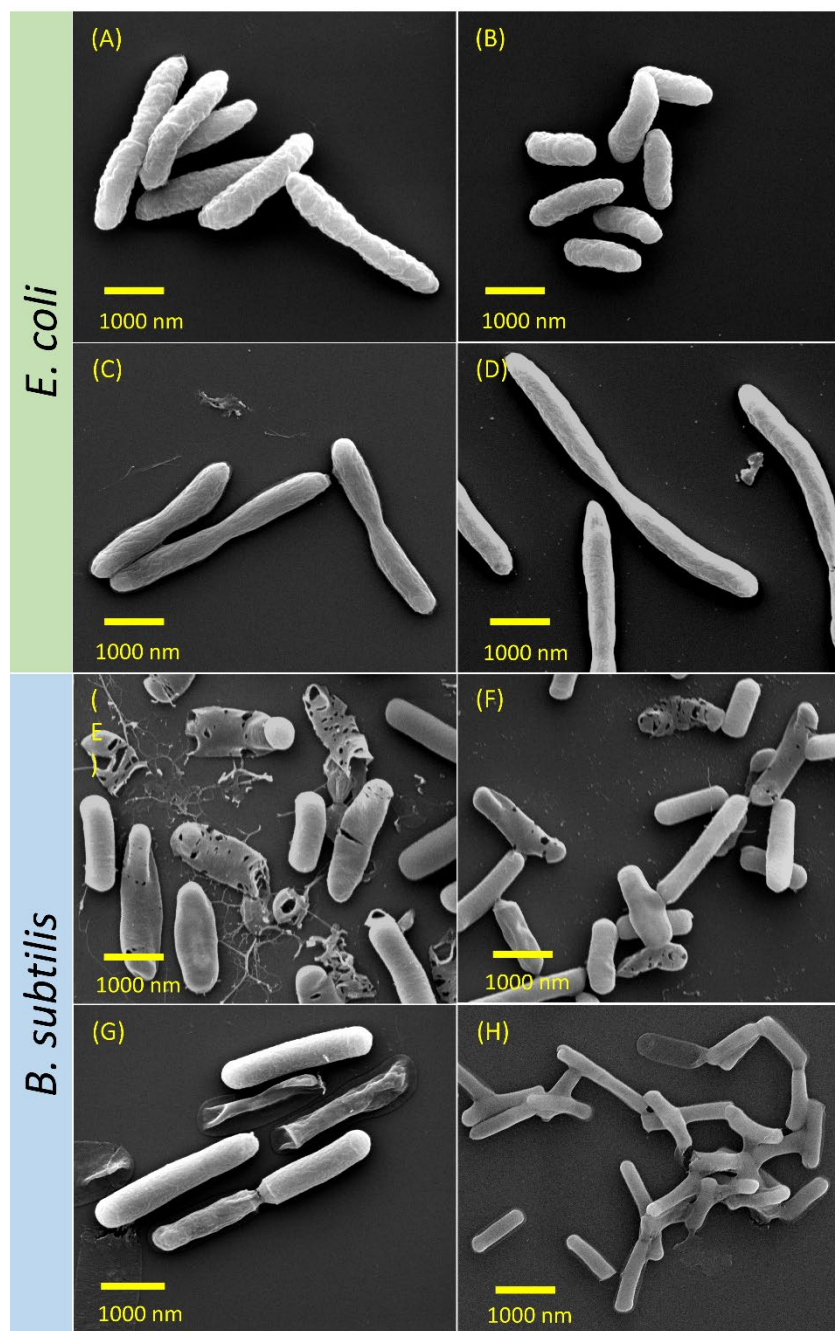


**Figure 3. 6:** SEM images of *E. coli* incubated with (A) CUR, (B) P7-CUR, (C) TBF, (D) P7-TBF and *B. subtilis* incubated with (E) CUR, (F) P7-CUR, (G) TBF, (H) P7-TBF. Bacteria were incubated with samples ( $2500 \mu\text{g mL}^{-1}$ ) for 24 h prior to fixing.

In *E. coli* incubated with TBF (Figure 3. 6C), the most noticeable difference compared to untreated *E. coli* were the elongated structures, with lengths ranging from 3-7  $\mu\text{m}$ . Notably, a slight pinch was also seen in the middle of the bacterial cells, similar to those reported by Rivas-Marin et al. in *Gemmata obscuriglobus*.<sup>77</sup> These abnormalities suggest that TBF likely slowed down the division and growth of *E. coli* cells. Non-uniform surfaces were also observed which suggested membrane damage. *E. coli* exposed to P7-TBF resulted in similar non-uniform structures that were approximately 3-8  $\mu\text{m}$  (Figure 3. 6D). These observations suggest effective inhibition of *E. coli* growth induced by P7-TBF, complementing results obtained from the growth curve measurements.

The morphology of *B. subtilis* incubated with varied formulations were subsequently evaluated. Treatment with CUR resulted in deformed, perforated structures, accompanied by debris likely originating from dead bacteria (Figure 3. 6E). These observations suggest weakened bacterial cell membrane, and a more pronounced effect of CUR on *B. subtilis* compared to *E. coli*. The absence of an outer membrane in *B. subtilis* may allow less obstructed diffusion of CUR, which could lead to an improvement in bacterial inhibition. Similarly, when *B. subtilis* was incubated with P7-CUR, analogous misshaped, punctured structures were observed, clearly suggesting effectiveness of P7-CUR in impeding *B. subtilis* growth (Figure 3. 6F). The observed morphological deformations collectively provide evidence for the disruptive impact of P7-TBF on *B. subtilis*, further emphasizing its potential in addressing microbial infections.

Morphology of *B. subtilis* exposed to TBF is shown in Figure 3. 6G, and it shows several interesting observations such as wrinkled surfaces, shrunken bacteria contents, and ruptured bacteria. These results suggest damage to the bacterial membrane upon TBF exposure. Moreover, when *B. subtilis* was treated with P7-TBF (Figure 3. 6H), the bacterial membrane appeared significantly damaged as no distinct boundaries could be observed. In addition, we observed several ruptured structures, all of which suggested effectiveness of P7-TBF to inhibit *B. subtilis* growth. These collectively highlight the potent antimicrobial activity of P7-TBF to disrupt bacterial membrane and impede bacterial growth effectively. In 2017, Mukherjee et al. synthesized a leucine-based poly(2-hydroxyethyl methacrylate) for treatment *B. subtilis*.<sup>78</sup> They noted fusion of *B. subtilis* cell membrane upon polymer treatment, which caused surface collapse in the bacterial

cells. Ding et al. also reported a quinine-based quarternized polymer that induced adhesion of individual *B. subtilis* cells, revealing the potent effect of their polymer on bacterial cells.<sup>79</sup>

### 3.6. Conclusions

Cationic NPs offer a promising multifunctional platform in the ongoing battle against antimicrobial resistance. We have capitalized on the dual functionality of such NPs, which not only inhibit bacterial growth through their cationic shell but also serve as vehicles for the targeted delivery of antimicrobial agents. A pivotal aspect of our strategy involves the synthesis of miktoarm polymers with cationic amine moieties (P7), achieved through a meticulous combination of arm- and core-first methods. The polymer self-assembles into well-defined micelles with a positively-charged hydrophilic shell, thus imparting intrinsic antimicrobial properties to the NPs. Cationic P7-micelles are particularly effective against the Gram-positive bacterium, *B. subtilis*, which could be attributed to favourable interactions between the positively-charged amines of P7-micelles and the oppositely charged bacteria membrane. However, P7-micelles are less effective against the Gram-negative bacterium, *E. coli*, possibly due to additional lipopolysaccharide layer that impedes penetration. Nanoformulations reported in this study extend beyond their intrinsic antimicrobial properties, as they also serve as proficient nanocarriers to deliver antimicrobial agents such as CUR and TBF. P7-CUR and P7-TBF exhibit inhibitory activity against *E. coli* at higher concentrations, whereas their effectiveness against *B. subtilis* is optimized at lower concentrations. This versatility highlights the potential of P7-micelles as a multifaceted approach to combat microbial infections. By leveraging their intrinsic antimicrobial properties and adeptness as efficient nanocarriers for antimicrobial agents, cationic NPs offer an advantageous avenue in the quest to address antimicrobial resistance.

### 3.7. References

1. Murray, C. J. L.; Ikuta, K. S.; Sharara, F.; Swetschinski, L.; Robles Aguilar, G.; Gray, A.; Han, C.; Bisignano, C.; Rao, P.; Wool, E.; et al. Global Burden of Bacterial Antimicrobial Resistance in 2019: A Systematic Analysis. *The Lancet* **2022**, 399 (10325), 629-655.

2. Yusuf, K.; Sampath, V.; Umar, S. Bacterial Infections and Cancer: Exploring This Association and Its Implications for Cancer Patients. *Int. J. Mol. Sci.* **2023**, *24* (4), 3110.
3. Huang, L.; Crothers, K. HIV-Associated Opportunistic Pneumonias. *Respirology* **2009**, *14* (4), 474-485.
4. Van de Louw, A.; Mirouse, A.; Peyrony, O.; Lemiale, V.; Azoulay, E. Bacterial Pneumonias in Immunocompromised Patients. *Semin. Respir. Crit. Care Med.* **2019**, *40* (04), 498-507.
5. Franquet, T.; Domingo, P. Pulmonary Infections in People Living with HIV. *Radiol. Clin. North Am.* **2022**, *60* (3), 507-520.
6. WHO fungal priority pathogens list to guide research, development and public health action. Geneva: World Health Organization; 2022. Licence: CC BY-NC-SA 3.0 IGO.
7. Orrell-Trigg, R.; Awad, M.; Gangadoo, S.; Cheeseman, S.; Shaw, Z. L.; Truong, V. K.; Cozzolino, D.; Chapman, J. Rapid Screening of Bacteriostatic and Bactericidal Antimicrobial Agents against *Escherichia Coli* by Combining Machine Learning (Artificial Intelligence) and UV-Vis Spectroscopy. *Analyst* **2024**, *149* (5), 1597-1608.
8. Kohanski, M. A.; Dwyer, D. J.; Collins, J. J. How Antibiotics Kill Bacteria: From Targets to Networks. *Nat. Rev. Microbiol.* **2010**, *8* (6), 423-435.
9. Loree, J.; Lappin, S. L. *Bacteriostatic Antibiotics*. StatPearls Publishing, 2023. <https://www.ncbi.nlm.nih.gov/books/NBK547678/> (accessed Oct 15, 2023).
10. Patel, P.; Wermuth, H. R.; Calhoun, C.; Hall, G. A. *Antibiotics*. StatPearls Publishing, 2023. <https://www.ncbi.nlm.nih.gov/books/NBK535443/> (accessed Oct 15, 2023).
11. Tits, J.; Cammue, B. P. A.; Thevissen, K. Combination Therapy to Treat Fungal Biofilm-Based Infections. *Int. J. Mol. Sci.* **2020**, *21* (22), 8873.
12. You, K.; Gao, B.; Wang, M.; Wang, X.; Okoro, K. C.; Rakhimbekzoda, A.; Feng, Y. Versatile Polymer-Based Strategies for Antibacterial Drug Delivery Systems and Antibacterial Coatings. *J. Mater. Chem. B* **2022**, *10* (7), 1005-1018.

13. Yu, L.; Lin, C.; Zheng, Z.; Li, Z.; Wang, X. Self-Assembly of pH-Responsive Biodegradable Mixed Micelles Based on Anionic and Cationic Polycarbonates for Doxorubicin Delivery. *Colloids Surf., B* **2016**, *145*, 392-400.
14. Nimmagadda, A.; Liu, X.; Teng, P.; Su, M.; Li, Y.; Qiao, Q.; Khadka, N. K.; Sun, X.; Pan, J.; Xu, H.; et al. Polycarbonates with Potent and Selective Antimicrobial Activity toward Gram-Positive Bacteria. *Biomacromolecules* **2017**, *18* (1), 87-95.
15. Chin, W.; Zhong, G.; Pu, Q.; Yang, C.; Lou, W.; De Sessions, P. F.; Periaswamy, B.; Lee, A.; Liang, Z. C.; Ding, X.; et al. A Macromolecular Approach to Eradicate Multidrug Resistant Bacterial Infections While Mitigating Drug Resistance Onset. *Nat. Commun.* **2018**, *9* (1), 917.
16. Parkin, H. C.; Street, S. T. G.; Gowen, B.; Da-Silva-Correa, L. H.; Hof, R.; Buckley, H. L.; Manners, I. Mechanism of Action and Design of Potent Antibacterial Block Copolymer Nanoparticles. *J. Am. Chem. Soc.* **2024**, *146* (8), 5128-5141.
17. Cuthbert, T. J.; Hisey, B.; Harrison, T. D.; Trant, J. F.; Gillies, E. R.; Ragogna, P. J. Surprising Antibacterial Activity and Selectivity of Hydrophilic Polyphosphoniums Featuring Sugar and Hydroxy Substituents. *Angew. Chem. Int. Ed.* **2018**, *57* (39), 12707-12710.
18. Kunday, H.; Süer, N. C.; Bayır, A.; Aksu, B.; Hatipoğlu, A.; Güncü, M. M.; Acaroğlu Degitz, İ.; Gallei, M.; Eren, T. Design of Aromatic Ring-Based Polyphosphonium Salts Synthesized via ROMP and the Investigation into Their Antibacterial and Hemolytic Activities. *ACS Appl. Polym. Mater.* **2021**, *3* (12), 6524-6538.
19. Sun, X.; Cao, P.; Bai, X.; He, Y.; Song, P.; Wang, R. Poly(phosphonium)-Functionalized Double-Armed  $\beta$ -CD Antimicrobial Material via RAFT. *Macromolecules* **2023**, *56* (23), 9498-9508.
20. Hou, Z.; Shankar, Y. V.; Liu, Y.; Ding, F.; Subramanion, J. L.; Ravikumar, V.; Zamudio-Vázquez, R.; Keogh, D.; Lim, H.; Tay, M. Y. F.; et al. Nanoparticles of Short Cationic

- Peptidopolysaccharide Self-Assembled by Hydrogen Bonding with Antibacterial Effect against Multidrug-Resistant Bacteria. *ACS Appl. Mater. Interfaces* **2017**, *9* (44), 38288-38303.
21. Shen, W.; He, P.; Xiao, C.; Chen, X. From Antimicrobial Peptides to Antimicrobial Poly( $\alpha$ -amino acid)s. *Adv. Healthcare Mater.* **2018**, *7* (20), 1800354.
  22. Liu, L.; Courtney, K. C.; Huth, S. W.; Rank, L. A.; Weisblum, B.; Chapman, E. R.; Gellman, S. H. Beyond Amphiphilic Balance: Changing Subunit Stereochemistry Alters the Pore-Forming Activity of Nylon-3 Polymers. *J. Am. Chem. Soc.* **2021**, *143* (8), 3219-3230.
  23. Pasquier, N.; Keul, H.; Heine, E.; Moeller, M.; Angelov, B.; Linser, S.; Willumeit, R. Amphiphilic Branched Polymers as Antimicrobial Agents. *Macromol. Biosci.* **2008**, *8* (10), 903-915.
  24. Jiang, C.; Chen, J.; Li, Z.; Wang, Z.; Zhang, W.; Liu, J. Recent Advances in the Development of Polyethylenimine-Based Gene Vectors for Safe and Efficient Gene Delivery. *Expert Opin. Drug Deliv.* **2019**, *16* (4), 363-376.
  25. Mazrad, Z. A. I.; Choi, C. A.; Kwon, Y. M.; In, I.; Lee, K. D.; Park, S. Y. Design of Surface-Coatable NIR-Responsive Fluorescent Nanoparticles with PEI Passivation for Bacterial Detection and Killing. *ACS Appl. Mater. Interfaces* **2017**, *9* (38), 33317-33326.
  26. Virgen-Ortíz, J. J.; dos Santos, J. C. S.; Berenguer-Murcia, Á.; Barbosa, O.; Rodrigues, R. C.; Fernandez-Lafuente, R. Polyethylenimine: A Very Useful Ionic Polymer in the Design of Immobilized Enzyme Biocatalysts. *J. Mater. Chem. B* **2017**, *5* (36), 7461-7490.
  27. Fan, Z.; Po, K. H. L.; Wong, K. K.; Chen, S.; Lau, S. P. Polyethylenimine-Modified Graphene Oxide as a Novel Antibacterial Agent and Its Synergistic Effect with Daptomycin for Methicillin-Resistant Staphylococcus Aureus. *ACS Appl. Nano Mater.* **2018**, *1* (4), 1811-1818.
  28. Liu, W.; Pei, W.; Moradi, M.; Zhao, D.; Li, Z.; Zhang, M.; Xu, D.; Wang, F. Polyethyleneimine Functionalized Mesoporous Magnetic Nanoparticles with Enhanced

- Antibacterial and Antibiofilm Activity in an Alternating Magnetic Field. *ACS Appl. Mater. Interfaces* **2022**, *14* (16), 18794-18805.
29. Heli, B.; Younes, G. R.; Arguindeguy, K.; Ajji, A. Synthesis and Characterization of Antimicrobial Bacterial Cellulose Crosslinked with Branched Polyethylenimine. *Carbohydr. Polym. Technol. Appl.* **2024**, *7*, 100457.
  30. Fattahi, N.; Gorgannezhad, L.; Masoule, S. F.; Babanejad, N.; Ramazani, A.; Raoufi, M.; Sharifikolouei, E.; Foroumadi, A.; Khoobi, M. PEI-Based Functional Materials: Fabrication Techniques, Properties, and Biomedical Applications. *Adv. Colloid Interface Sci.* **2024**, *325*, 103119.
  31. Keshavarz, V.; Kazemi, M.; Khalvati, B.; Zare, F.; Dehshahri, A.; Sadeghpour, H. Surface Decoration of Low Molecular Weight Polyethylenimine (LMW PEI) by Phthalated Dextrin for Improved Delivery of Interleukin-12 Plasmid. *Biotechnol. Prog.* **2024**, e3443.
  32. Liu, M.; Li, J.; Li, B. Mannose-Modified Polyethylenimine: A Specific and Effective Antibacterial Agent against Escherichia Coli. *Langmuir* **2018**, *34* (4), 1574-1580.
  33. Gultekinoglu, M.; Kurum, B.; Karahan, S.; Kart, D.; Sagiroglu, M.; Ertaş, N.; Haluk Ozen, A.; Ulubayram, K. Polyethyleneimine Brushes Effectively Inhibit Encrustation on Polyurethane Ureteral Stents Both in Dynamic Bioreactor and *In Vivo*. *Mater. Sci. Eng., C* **2017**, *71*, 1166-1174.
  34. Gultekinoglu, M.; Tunc Sarisozen, Y.; Erdogan, C.; Sagiroglu, M.; Aksoy, E. A.; Oh, Y. J.; Hinterdorfer, P.; Ulubayram, K. Designing of Dynamic Polyethyleneimine (PEI) Brushes on Polyurethane (PU) Ureteral Stents to Prevent Infections. *Acta Biomater.* **2015**, *21*, 44-54.
  35. Lotocki, V.; Yazdani, H.; Zhang, Q.; Gran, E. R.; Nyrko, A.; Maysinger, D.; Kakkar, A. Miktoarm Star Polymers with Environment-Selective ROS/GSH Responsive Locations: From Modular Synthesis to Tuned Drug Release through Micellar Partial Corona Shedding and/or Core Disassembly. *Macromol. Biosci.* **2021**, *21* (2), 2000305.

36. Zhu, Z.; Jeong, G.; Kim, S.-J.; Gadwal, I.; Choe, Y.; Bang, J.; Oh, M.-K.; Khan, A.; Rao, J. Balancing Antimicrobial Performance with Hemocompatibility in Amphiphilic Homopolymers. *J. Polym. Sci., Part A: Polym. Chem.* **2018**, *56* (21), 2391-2396.
37. Manasa, P. S. L.; Kamble, A. D.; Chilakamarthi, U. Various Extraction Techniques of Curcumin—a Comprehensive Review. *ACS Omega* **2023**, *8* (38), 34868-34878.
38. Rudrappa, T.; Bais, H. P. Curcumin, a Known Phenolic from *Curcuma Longa*, Attenuates the Virulence of *Pseudomonas Aeruginosa* PAO1 in Whole Plant and Animal Pathogenicity Models. *J. Agric. Food. Chem.* **2008**, *56* (6), 1955-1962.
39. Dogra, N.; Choudhary, R.; Kohli, P.; Haddock, J. D.; Makwana, S.; Horev, B.; Vinokur, Y.; Droby, S.; Rodov, V. Polydiacetylene Nanovesicles as Carriers of Natural Phenylpropanoids for Creating Antimicrobial Food-Contact Surfaces. *J. Agric. Food. Chem.* **2015**, *63* (9), 2557-2565.
40. Gunes, H.; Gulen, D.; Mutlu, R.; Gumus, A.; Tas, T.; Topkaya, A. E. Antibacterial Effects of Curcumin: An *In Vitro* Minimum Inhibitory Concentration Study. *Toxicol. Ind. Health* **2016**, *32* (2), 246-250.
41. Zheng, D.; Huang, C.; Huang, H.; Zhao, Y.; Khan, M. R. U.; Zhao, H.; Huang, L. Antibacterial Mechanism of Curcumin: A Review. *Chem. Biodivers.* **2020**, *17* (8), e2000171.
42. Hettiarachchi, S. S.; Perera, Y.; Dunuweera, S. P.; Dunuweera, A. N.; Rajapakse, S.; Rajapakse, R. M. G. Comparison of Antibacterial Activity of Nanocurcumin with Bulk Curcumin. *ACS Omega* **2022**, *7* (50), 46494-46500.
43. Jagannathan, R.; Abraham, P. M.; Poddar, P. Temperature-Dependent Spectroscopic Evidences of Curcumin in Aqueous Medium: A Mechanistic Study of Its Solubility and Stability. *J. Phys. Chem. B* **2012**, *116* (50), 14533-14540.
44. Garcia-Effron, G.; Gomez-Lopez, A.; Mellado, E.; Monzon, A.; Rodriguez-Tudela, J. L.; Cuenca-Estrella, M. *In Vitro* Activity of Terbinafine against Medically Important Non-

- Dermatophyte Species of Filamentous Fungi. *J. Antimicrob. Chemother.* **2004**, *53* (6), 1086-1089.
45. Web Annex A. World Health Organization Model List of Essential Medicines – 23rd List, 2023. In: The selection and use of essential medicines 2023: Executive summary of the report of the 24th WHO Expert Committee on the Selection and Use of Essential Medicines, 24 – 28 April 2023. Geneva: World Health Organization; 2023 (WHO/MHP/HPS/EML/2023.02). Licence: CC BY-NC-SA 3.0 IGO.
  46. AbdelSamie, S. M.; Kamel, A. O.; Sasmour, O. A.; Ibrahim, S. M. Terbinafine Hydrochloride Nanovesicular Gel: *In Vitro* Characterization, *Ex Vivo* Permeation and Clinical Investigation. *Eur. J. Pharm. Sci.* **2016**, *88*, 91-100.
  47. Łagowski, D.; Gnat, S.; Nowakiewicz, A.; Osińska, M.; Dyla, M. Intrinsic Resistance to Terbinafine among Human and Animal Isolates of Trichophyton Mentagrophytes Related to Amino Acid Substitution in the Squalene Epoxidase. *Infection* **2020**, *48* (6), 889-897.
  48. Arjmand, G.; Haeri, M. R. Antibacterial Effect of Some Eukaryotic Sterol Biosynthesis Inhibitors. *Adv. Biomed. Res.* **2022**, *11* (1), 90.
  49. Friedl, J. D.; Nele, V.; De Rosa, G.; Bernkop-Schnürch, A. Bioinert, Stealth or Interactive: How Surface Chemistry of Nanocarriers Determines Their Fate *In Vivo*. *Adv. Funct. Mater.* **2021**, *31* (34), 2103347.
  50. Pawar, R.; Pathan, A.; Nagaraj, S.; Kapare, H.; Giram, P.; Wavhale, R. Polycaprolactone and Its Derivatives for Drug Delivery. *Polym. Adv. Technol.* **2023**, *34* (10), 3296-3316.
  51. Yong, H. W.; Ferron, M.; Mecteau, M.; Mihalache-Avram, T.; Lévesque, S.; Rhéaume, É.; Tardif, J.-C.; Kakkar, A. Single Functional Group Platform for Multistimuli Responsivities: Tertiary Amine for CO<sub>2</sub>/pH/ROS-Triggered Cargo Release in Nanocarriers. *Biomacromolecules* **2023**, *24* (9), 4064–4077.
  52. Yong, H. W.; Kakkar, A. Nanoengineering Branched Star Polymer-Based Formulations: Scope, Strategies, and Advances. *Macromol. Biosci.* **2021**, *21* (8), 2100105.

53. Rizvi, S. A. A.; Saleh, A. M. Applications of Nanoparticle Systems in Drug Delivery Technology. *Saudi Pharm. J.* **2018**, *26* (1), 64-70.
54. Deng, C.; Chen, X.; Yu, H.; Sun, J.; Lu, T.; Jing, X. A Biodegradable Triblock Copolymer Poly(ethylene glycol)-*b*-poly(L-lactide)-*b*-poly(L-lysine): Synthesis, Self-Assembly, and RGD Peptide Modification. *Polymer* **2007**, *48* (1), 139-149.
55. Zhang, S.; Zou, J.; Zhang, F.; Elsabahy, M.; Felder, S. E.; Zhu, J.; Pochan, D. J.; Wooley, K. L. Rapid and Versatile Construction of Diverse and Functional Nanostructures Derived from a Polyphosphoester-Based Biomimetic Block Copolymer System. *J. Am. Chem. Soc.* **2012**, *134* (44), 18467-18474.
56. Scarano, W.; de Souza, P.; Stenzel, M. H. Dual-Drug Delivery of Curcumin and Platinum Drugs in Polymeric Micelles Enhances the Synergistic Effects: A Double Act for the Treatment of Multidrug-Resistant Cancer. *Biomater. Sci.* **2015**, *3* (1), 163-174.
57. Su, H.; Wang, F.; Ran, W.; Zhang, W.; Dai, W.; Wang, H.; Anderson, C. F.; Wang, Z.; Zheng, C.; Zhang, P.; et al. The Role of Critical Micellization Concentration in Efficacy and Toxicity of Supramolecular Polymers. *Proc. Natl. Acad. Sci.* **2020**, *117* (9), 4518-4526.
58. Haktaniyan, M.; Bradley, M. Polymers Showing Intrinsic Antimicrobial Activity. *Chem. Soc. Rev.* **2022**, *51* (20), 8584-8611.
59. Silhavy, T. J.; Kahne, D.; Walker, S. The Bacterial Cell Envelope. *Cold Spring Harbor Perspect. Biol.* **2010**, *2* (5), a000414.
60. Breijyeh, Z.; Jubeh, B.; Karaman, R. Resistance of Gram-Negative Bacteria to Current Antibacterial Agents and Approaches to Resolve It. *Molecules* **2020**, *25* (6), 1340.
61. Tavakolian, M.; Okshevsky, M.; van de Ven, T. G. M.; Tufenkji, N. Developing Antibacterial Nanocrystalline Cellulose Using Natural Antibacterial Agents. *ACS Appl. Mater. Interfaces* **2018**, *10* (40), 33827-33838.

62. Westman, E.-H.; Ek, M.; Enarsson, L.-E.; Wågberg, L. Assessment of Antibacterial Properties of Polyvinylamine (PVAm) with Different Charge Densities and Hydrophobic Modifications. *Biomacromolecules* **2009**, *10* (6), 1478-1483.
63. Lim, S.-H.; Hudson, S. M. Synthesis and Antimicrobial Activity of a Water-Soluble Chitosan Derivative with a Fiber-Reactive Group. *Carbohydr. Res.* **2004**, *339* (2), 313-319.
64. Divya, K.; Vijayan, S.; George, T. K.; Jisha, M. S. Antimicrobial Properties of Chitosan Nanoparticles: Mode of Action and Factors Affecting Activity. *Fibers Polym.* **2017**, *18* (2), 221-230.
65. Chakraborti, S.; Mandal, A. K.; Sarwar, S.; Singh, P.; Chakraborty, R.; Chakrabarti, P. Bactericidal Effect of Polyethyleneimine Capped ZnO Nanoparticles on Multiple Antibiotic Resistant Bacteria Harboring Genes of High-Pathogenicity Island. *Colloids Surf., B* **2014**, *121*, 44-53.
66. Tanganini, I. C.; Camargos, C. H. M.; Jackson, J. C.; Rezende, C. A.; Ceccato-Antonini, S. R.; Faria, A. F. Self-Assembled Lignin Nanoparticles Produced from Elephant Grass Leaves Enable Selective Inactivation of Gram-Positive Microorganisms. *RSC Sustainability* **2024**, *2* (2), 459-474.
67. Kharat, M.; Du, Z.; Zhang, G.; McClements, D. J. Physical and Chemical Stability of Curcumin in Aqueous Solutions and Emulsions: Impact of pH, Temperature, and Molecular Environment. *J. Agric. Food. Chem.* **2017**, *65* (8), 1525-1532.
68. Basak, R.; Bandyopadhyay, R. Encapsulation of Hydrophobic Drugs in Pluronic F127 Micelles: Effects of Drug Hydrophobicity, Solution Temperature, and Ph. *Langmuir* **2013**, *29* (13), 4350-4356.
69. Mathematical Models of Drug Release. In *Strategies to Modify the Drug Release from Pharmaceutical Systems*, Bruschi, M. L. Ed.; Woodhead Publishing, 2015; pp 63-86.
70. Paarakh, M. P.; Jose, P. A.; Setty, C. M.; Peterchristoper, G. V. Release Kinetics – Concepts and Applications. *IJPRT* **2018**, *8* (1), 12-20.

71. Hsiao, M.-H.; Lin, K.-H.; Liu, D.-M. Improved Ph-Responsive Amphiphilic Carboxymethyl-Hexanoyl Chitosan–Poly(acrylic acid) Macromolecules for Biomedical Applications. *Soft Matter* **2013**, *9* (8), 2458-2466.
72. Tyagi, P.; Singh, M.; Kumari, H.; Kumari, A.; Mukhopadhyay, K. Bactericidal Activity of Curcumin I Is Associated with Damaging of Bacterial Membrane. *PLOS ONE* **2015**, *10* (3), e0121313.
73. Nowosielski, M.; Hoffmann, M.; Wyrwicz, L. S.; Stepniak, P.; Plewczynski, D. M.; Lazniewski, M.; Ginalski, K.; Rychlewski, L. Detailed Mechanism of Squalene Epoxidase Inhibition by Terbinafine. *J. Chem. Inf. Model.* **2011**, *51* (2), 455-462.
74. Ryder, N. S. Terbinafine: Mode of Action and Properties of the Squalene Epoxidase Inhibition. *Br. J. Dermatol.* **1992**, *126* (s39), 2-7.
75. Gupta, A. K.; Elewski, B.; Joseph, W. S.; Lipner, S. R.; Daniel, C. R.; Tosti, A.; Guenin, E.; Ghannoum, M. Treatment of Onychomycosis in an Era of Antifungal Resistance: Role for Antifungal Stewardship and Topical Antifungal Agents. *Mycoses* **2024**, *67* (1), e13683.
76. Asabuwa Ngwabebhoh, F.; Ilkar Erdagi, S.; Yildiz, U. Pickering Emulsions Stabilized Nanocellulosic-Based Nanoparticles for Coumarin and Curcumin Nanoencapsulations: *In Vitro* Release, Anticancer and Antimicrobial Activities. *Carbohydr. Polym.* **2018**, *201*, 317-328.
77. Rivas-Marin, E.; Stettner, S.; Gottshall, E. Y.; Santana-Molina, C.; Helling, M.; Basile, F.; Ward, N. L.; Devos, D. P. Essentiality of Sterol Synthesis Genes in the Planctomycete Bacterium Gemmata Obscuriglobus. *Nat. Commun.* **2019**, *10* (1), 2916.
78. Mukherjee, I.; Ghosh, A.; Bhadury, P.; De, P. Side-Chain Amino Acid-Based Cationic Antibacterial Polymers: Investigating the Morphological Switching of a Polymer-Treated Bacterial Cell. *ACS Omega* **2017**, *2* (4), 1633-1644.

79. Ding, H.-H.; Zhao, M.-H.; Zhai, L.; Zhen, J.-B.; Sun, L.-Y.; Chigan, J.-Z.; Chen, C.; Li, J.-Q.; Gao, H.; Yang, K.-W. A Quinine-Based Quaternized Polymer: A Potent Scaffold with Bactericidal Properties without Resistance. *Polym. Chem.* **2021**, *12* (16), 2397-2403.

### 3.8 Appendix B: Supporting Information for Chapter 3

#### Characterization

A Bruker AVIIIHD 500 MHz spectrometer was used to record all NMR spectra at ambient temperature. The spectra were calibrated at 7.26 ppm ( $^1\text{H}$  NMR)/ 77.16 ppm ( $^{13}\text{C}$  NMR) respectively in relation to the residual undeuterated solvent in chloroform-d. A Bruker MALDI Autoflex III TOF mass spectrometer controlled by Flex Analysis was used to acquire the mass spectra in linear positive ion mode. The presence of the azide group in PEG<sub>2050</sub>-N<sub>3</sub> was confirmed using an Attenuated total reflectance- Fourier-transform infrared spectrometer (ATR-FTIR) spectrometer equipped with a single bounce diamond crystal and a LiTaO<sub>3</sub> detector. All measurements were conducted at room temperature from 400 to 4000 cm<sup>-1</sup>. The number-average molecular weight ( $M_n$ ) and polydispersity index ( $D$ ) were determined using GPC with THF as an eluent. Measurements were performed on a Waters Breeze system equipped with 3 Waters Styragel HR columns (HR1 with a molar mass range of 100-5000 g mol<sup>-1</sup>, HR2 with a molar mass range of 500-20000 g mol<sup>-1</sup>, HR4 with a molar mass range of 5000-600000 g mol<sup>-1</sup>) and a guard column. The flow rate was 0.3 mL min<sup>-1</sup> (40 °C) while the standards used were polymethyl methacrylate (PMMA) standards (PSS Polymer Standards Service GmbH, molar masses ranging from 682 to 1520000 g mol<sup>-1</sup>). Sample detection and quantification were conducted with a differential refractive index detector (RI 2414). A Brookhaven Instrument NanoBrook Omni equipped with a 40-mW diode laser operating at 640 nm was used to obtain the hydrodynamic diameters, polydispersity index and zeta potential of micelles at room temperature. A Varian Cary Eclipse fluorescence spectrometer was used to measure the change in fluorescence intensities of pyrene at room temperature. A FEI Tecnai 12 BioTwin 120 kV transmission electron microscope (TEM) equipped with an AMT XR80 CCD Camera System located at the Facility for Electron Microscopy Research (FEMR) at McGill University was used to examine the morphologies of micelles. All solutions were stained with 2% uranyl acetate and left to dry overnight prior to analysis. The CUR and TBF standard curves, as well as the release studies were examined on a Varian Cary50 Ultraviolet-visible (UV-Vis) spectrophotometer equipped with a Xenon lamp at ambient temperature. A FEI Quanta 450 Environmental Scanning Electron Microscope (SEM) located at the FEMR was used to image the bacteria in the absence/ presence of micellar solutions.

In general, the bacteria solutions were centrifuged at 14,000 rpm for 5 mins and the supernatant was replaced with 0.5 mL of 2.5% glutaraldehyde in PBS (0.1 M, pH 7.4). After dispersing the bacteria in the fixative at 4 °C for 1 day, the bacteria were washed with 0.5 mL PBS twice before embedding on a poly(L-lysine) coated 12 mm glass slide. The samples were then dehydrated by immersing in increasing ethanol concentrations of 30%, 50%, 70%, 80%, 90%, 95% for 10 min each, and twice at 100% for an additional 10 min each. The solution was then dried in a Leica Microsystems EM CPD300 Critical Point Dryer before coating with platinum (5 nm) using a Leica Microsystems EM ACE600 High-Resolution Sputter Coater at room temperature.

### Synthesis

#### Synthesis of $\alpha$ -tosyl- $\omega$ -hydroxyl PEG<sub>2050</sub> (P1)

Fresh Ag<sub>2</sub>O was first prepared by adding a 9 mL aqueous solution of NaOH (0.120 g, 3.00 mmol) at 85 °C to a separate 2 mL aqueous solution of AgNO<sub>3</sub> (0.700 g, 4.12 mmol) at 85 °C. The brown solid formed was collected and washed extensively with hot water and methanol before drying overnight under reduced pressure. PEG<sub>2050</sub> (2.50 g, 1.22 mmol, 1 eq), Ag<sub>2</sub>O (0.433 g, 1.87 mmol, 1.5 eq), KI (0.042 g, 0.25 mmol, 0.2 eq) and dry DCM were added into a 3-neck flask under nitrogen and cooled in an ice bath. In another flask, *p*-toluenesulfonyl chloride (0.250 g, 1.31 mmol, 1.05 eq) was dissolved in dry DCM before adding dropwise into the PEG<sub>2050</sub> solution via an addition funnel. The reaction was stirred continuously under a nitrogen atmosphere and allowed to proceed at room temperature for 14 h. The final reaction mixture was then centrifuged at 3000 RPM for 10 min. The supernatant was concentrated and dropped in excess cold diethyl ether to precipitate the product. The product was filtered and dried under reduced pressure to yield a white powder. Yield: 92% (2.46 g). <sup>1</sup>H NMR (500 MHz, CDCl<sub>3</sub>):  $\delta$  (ppm) 2.43 (s, 3H, -CH<sub>3</sub>), 2.74 (br s, 1H, OH), 3.62 (m, 180H, -(CH<sub>2</sub>CH<sub>2</sub>O)<sub>44</sub>), 3.70 (t, 2H, -CH<sub>2</sub>CH<sub>2</sub>OH), 4.14 (t, 2H, CH<sub>2</sub>OTs), 7.32 (d, 2H, -ArH), 7.77 (d, 2H, -ArH). <sup>13</sup>C{<sup>1</sup>H} NMR (125 MHz, CDCl<sub>3</sub>):  $\delta_c$  (ppm) 21.8, 61.8, 68.8, 69.4, 70.4, 70.7, 70.9, 72.7, 128.1, 129.9, 133.2, 144.9.

#### Synthesis of $\alpha$ -azide- $\omega$ -hydroxyl PEG<sub>2050</sub> (P2)

P1 (2.500 g, 1.11 mmol, 1 eq), NaN<sub>3</sub> (0.616 g, 9.48 mmol, 8 eq) and anhydrous ethanol were added to a round bottom flask under a nitrogen atmosphere. The reaction mixture was then refluxed at

85 °C with continuous stirring for 24 h. All the solvent was removed, and the crude product was dissolved in DCM. The solution was then washed 2 times with brine and another 2 times with water before drying with MgSO<sub>4</sub>. After removing the drying agent, the product was concentrated using a rotary evaporator and precipitated by dropwise addition to ice cold diethyl ether. The precipitate was then filtered before drying under reduced pressure to obtain a white solid product. Yield: 95% (2.2 g). <sup>1</sup>H NMR (500 MHz, CDCl<sub>3</sub>): δ (ppm) 2.69 (s, 1H, -OH), 3.38 (t, 2H, -CH<sub>2</sub>CH<sub>2</sub>N<sub>3</sub>), 3.64 (s, 180H, -(CH<sub>2</sub>CH<sub>2</sub>O)<sub>43</sub>), 3.71 (t, 2H, -CH<sub>2</sub>CH<sub>2</sub>N<sub>3</sub>), 3.77 (t, 2H, -CH<sub>2</sub>CH<sub>2</sub>OH). <sup>13</sup>C {<sup>1</sup>H} NMR (125 MHz, CDCl<sub>3</sub>): δ (ppm) 50.8, 61.9, 70.2, 70n.5, 70.7, 72.7.

#### Synthesis of Boc-NH-PEG<sub>2050</sub>-N<sub>3</sub> (P3)

P2 (2 g, 0.956 mmol, 1 eq), *N*-(*tert*-Butoxycarbonyl)-4-aminobutyric acid (Boc-GABA-OH, 0.308 g, 1.43 mmol, 1.5 eq), DMAP (0.247 g, 1.91 mmol, 2 eq) and dry DCM were added into a round bottom flask under nitrogen. The flask was chilled to 0 °C. A separate solution of DCC (0.833 g, 3.82 mmol, 4 eq) in dry DCM was then added dropwise slowly into the flask under nitrogen. The reaction mixture was left to react for 24 h. Afterwards, dry DCM was removed completely, and the crude product was dissolved in acetone (10 mL). Any precipitate was then removed by vacuum filtration and the solution was concentrated and precipitated by dropwise addition to ice cold diethyl ether. The product was filtered before drying under reduced pressure to obtain a white solid product. Yield: 75% (1.60 g). <sup>1</sup>H NMR (500 MHz, CDCl<sub>3</sub>): δ (ppm) 1.42 (s, 9H, -C(CH<sub>3</sub>)<sub>3</sub>), 1.81 (m, 2H, -NHCH<sub>2</sub>CH<sub>2</sub>CH<sub>2</sub>CO), 2.38 (t, 2H, -NHCH<sub>2</sub>CH<sub>2</sub>CH<sub>2</sub>CO), 3.15 (t, 2H, -NHCH<sub>2</sub>CH<sub>2</sub>CH<sub>2</sub>CO), 3.38 (t, 2H, -OCH<sub>2</sub>CH<sub>2</sub>N<sub>3</sub>), 3.49 (t, 2H, -OCH<sub>2</sub>CH<sub>2</sub>N<sub>3</sub>), 3.63 (m, 180H, -(CH<sub>2</sub>CH<sub>2</sub>O)<sub>43</sub>), 3.77 (t, 2H, -OCCH<sub>2</sub>CH<sub>2</sub>(CH<sub>2</sub>CH<sub>2</sub>O)<sub>43</sub>), 4.22 (t, 2H, -OCCH<sub>2</sub>CH<sub>2</sub>(CH<sub>2</sub>CH<sub>2</sub>O)<sub>43</sub>), 4.72 (br s, 1 H, NH). <sup>13</sup>C {<sup>1</sup>H} NMR (125 MHz, CDCl<sub>3</sub>): δ (ppm) 28.5, 31.6, 50.8, 63.7, 69.2, 70.2, 70.8, 79.3, 156.1, 173.5.

#### Synthesis of 3,5- bis(prop-2-ynyloxy)benzyl polycaprolactone (P5)

P4 was synthesized as reported in Chapter 2. To a flask containing P4 (0.1 g, 0.463 mmol, 1 eq), dry toluene was added and heated to 100 °C under nitrogen with magnetic stirring. ε-caprolactone (1.8 mL, 16.2 mmol, 35 eq) was then added and the flask was further heated

to 110 °C. Next, tin(II) 2-ethyl hexanoate (0.015 mL, 0.469 mmol, 0.1 eq) was added and the reaction mixture was refluxed at 115 °C for 24 h. Toluene was first evaporated off under reduced pressure and the crude product was dissolved in minimal DCM followed by precipitation in ice cold methanol. The product was collected and dried in a desiccator. Yield= 83% (1.95 g).  $^1\text{H}$  NMR (500 MHz,  $\text{CDCl}_3$ ):  $\delta$  (ppm) 1.35- 1.41 (m, 70H, (-OCCH<sub>2</sub>CH<sub>2</sub>CH<sub>2</sub>CH<sub>2</sub>CH<sub>2</sub>O)<sub>33</sub>), 1.61- 1.68 (m, 136H, (-OCCH<sub>2</sub>CH<sub>2</sub>CH<sub>2</sub>CH<sub>2</sub>CH<sub>2</sub>O)<sub>33</sub>), 2.30 (t, 66H, (-OCCH<sub>2</sub>CH<sub>2</sub>CH<sub>2</sub>CH<sub>2</sub>CH<sub>2</sub>O)<sub>33</sub>), 2.54 (t, 2H, -C $\equiv$ CH), 4.06 (t, 68H, (-OCCH<sub>2</sub>CH<sub>2</sub>CH<sub>2</sub>CH<sub>2</sub>CH<sub>2</sub>O)<sub>33</sub>), 4.68 (d, 4H, -CH<sub>2</sub>C $\equiv$ C), 5.06 (s, 2H, -ArCH<sub>2</sub>O), 6.57 (t, 1H, -ArH), 6.60 (d, 2H, -ArH).  $^{13}\text{C}\{^1\text{H}\}$  NMR (125 MHz,  $\text{CDCl}_3$ ):  $\delta$  (ppm) 24.7, 25.7, 28.5, 34.4, 56.1, 62.8, 64.3, 65.9, 75.9, 78.4, 101.9, 107.6, 158.9, 173.7. MS: MALDI-ToF  $M_n = 3411.83$ ;  $M_w = 3478.16$ ; PDI = 1.02; DP = 30.

### Supplementary Figures

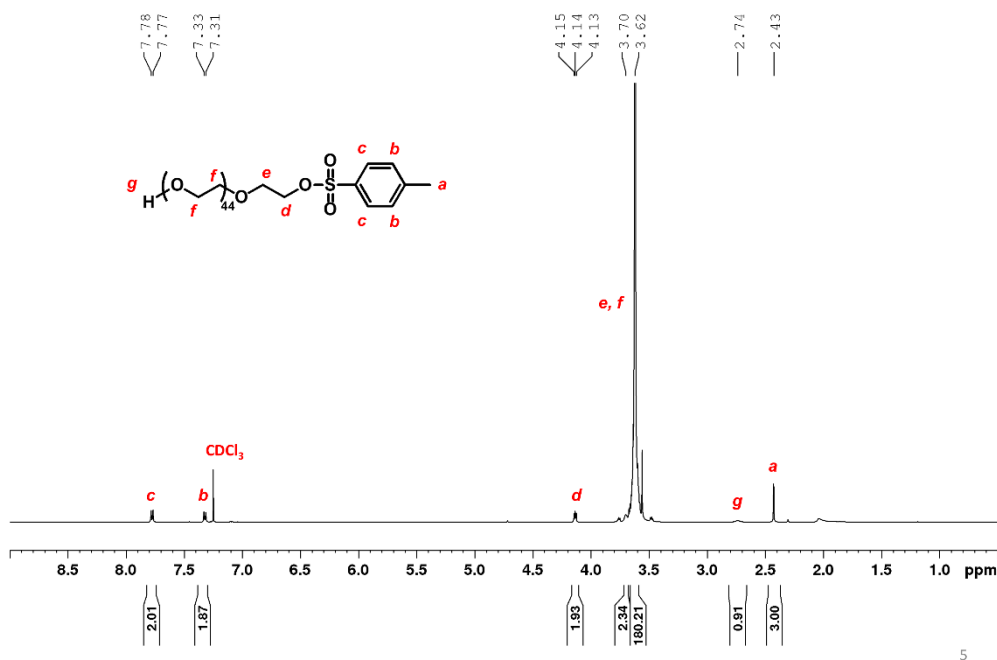


Figure 3. 7:  $^1\text{H}$  NMR spectrum of P1.

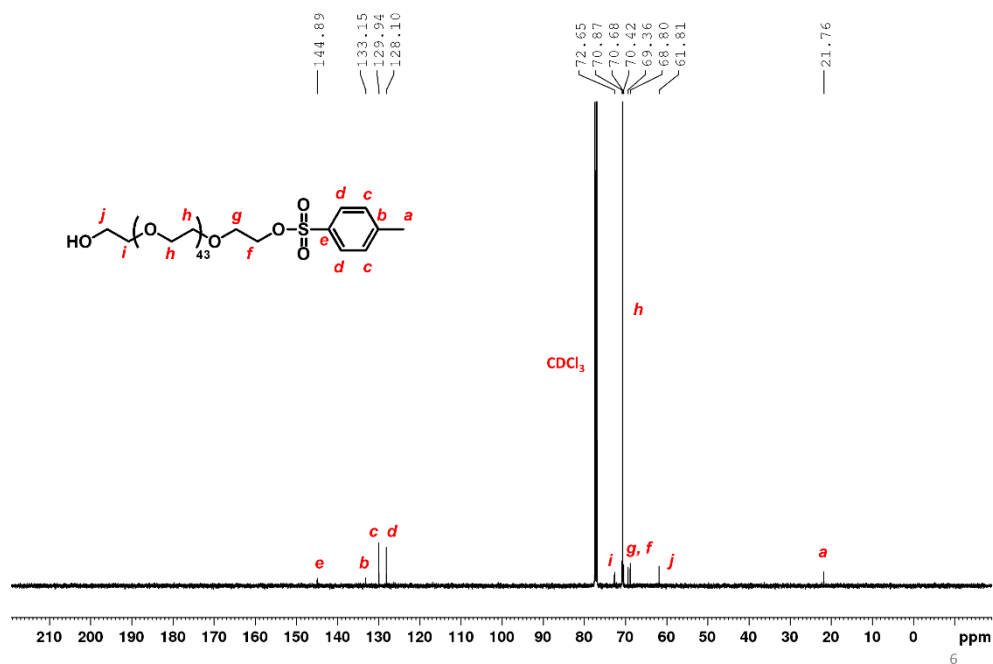


Figure 3. 8:  $^{13}\text{C}$  NMR spectrum of P1.

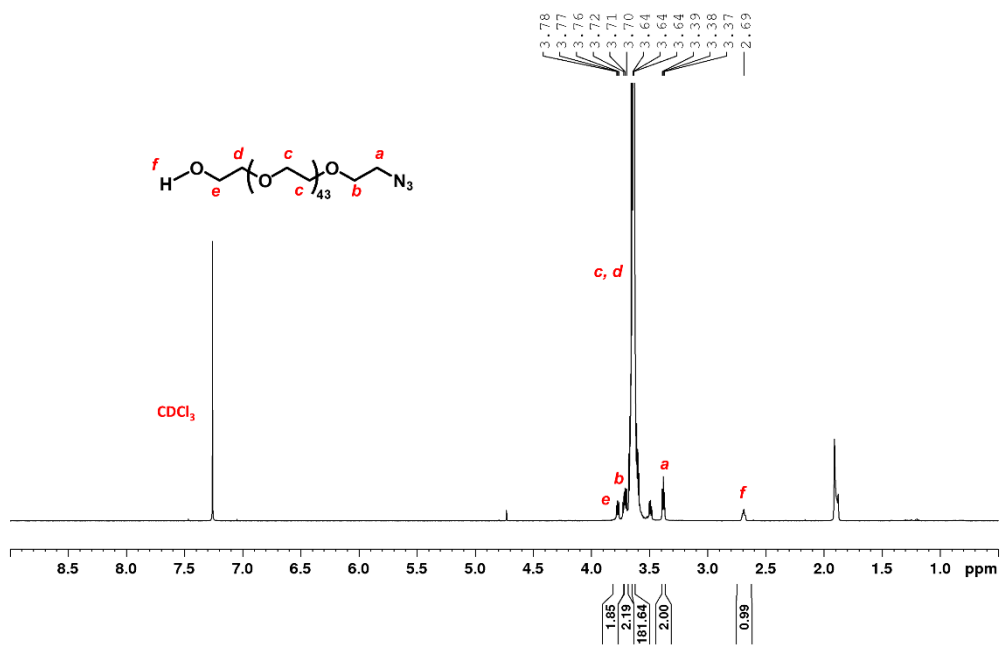
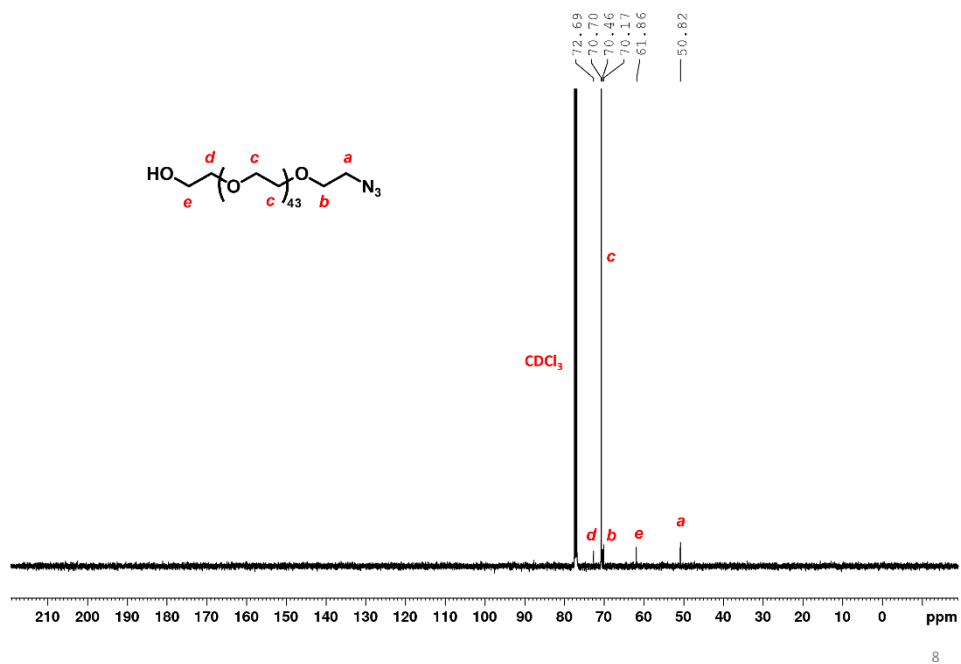
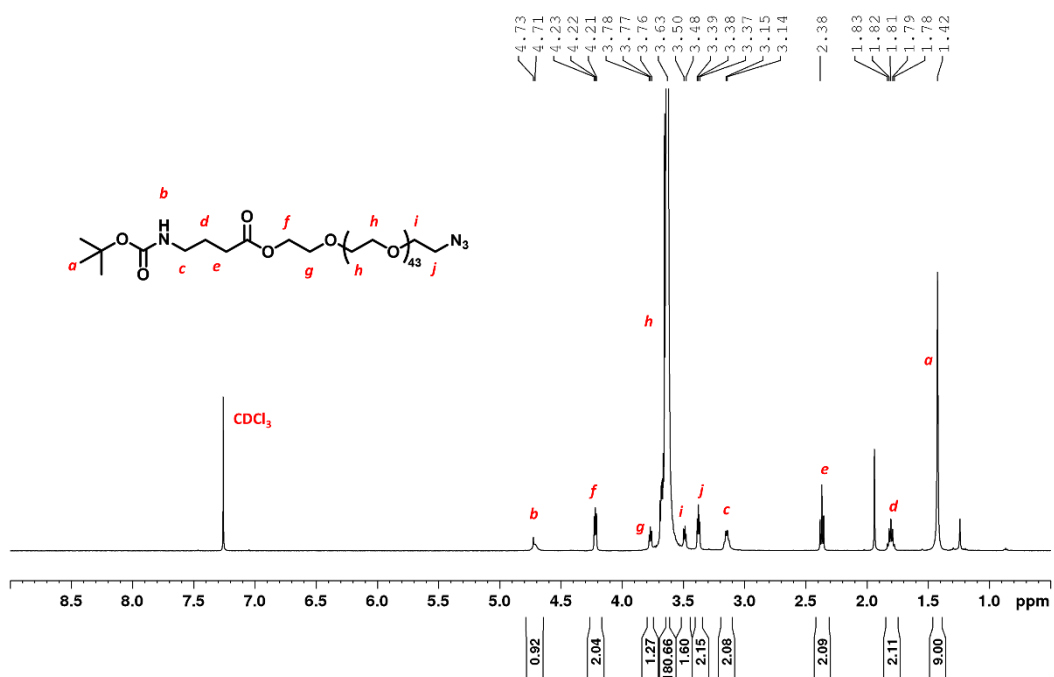
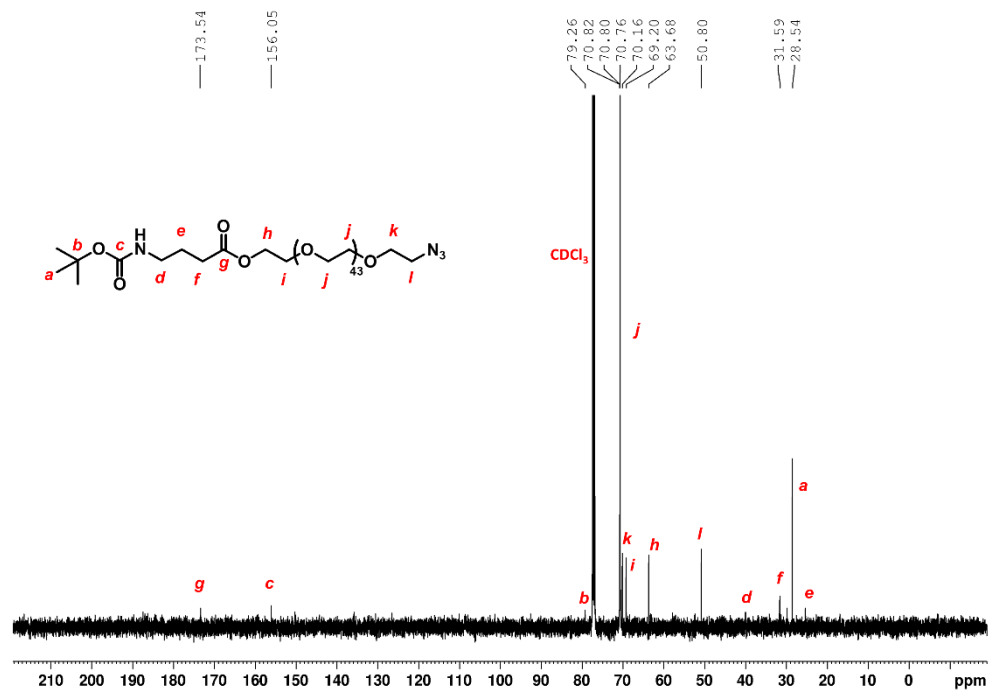
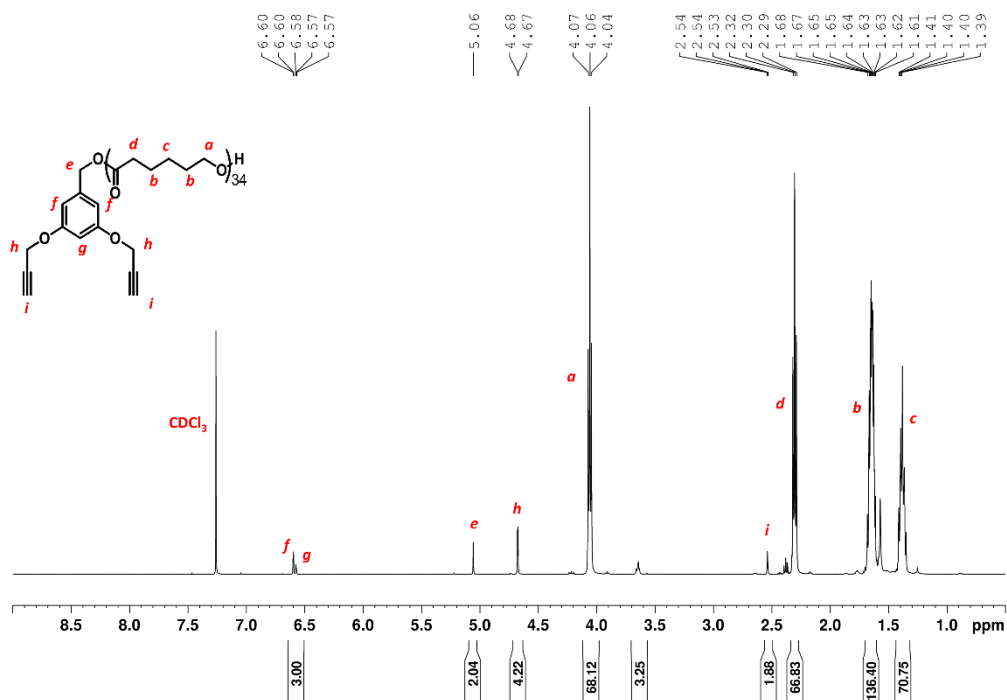


Figure 3. 9:  $^1\text{H}$  NMR spectrum of P2.

Figure 3. 10:  $^{13}\text{C}$  NMR spectrum of P2.Figure 3. 11:  $^1\text{H}$  NMR spectrum of P3.

Figure 3. 12:  $^{13}\text{C}$  NMR spectrum of P3.Figure 3. 13:  $^1\text{H}$  NMR spectrum of P5.

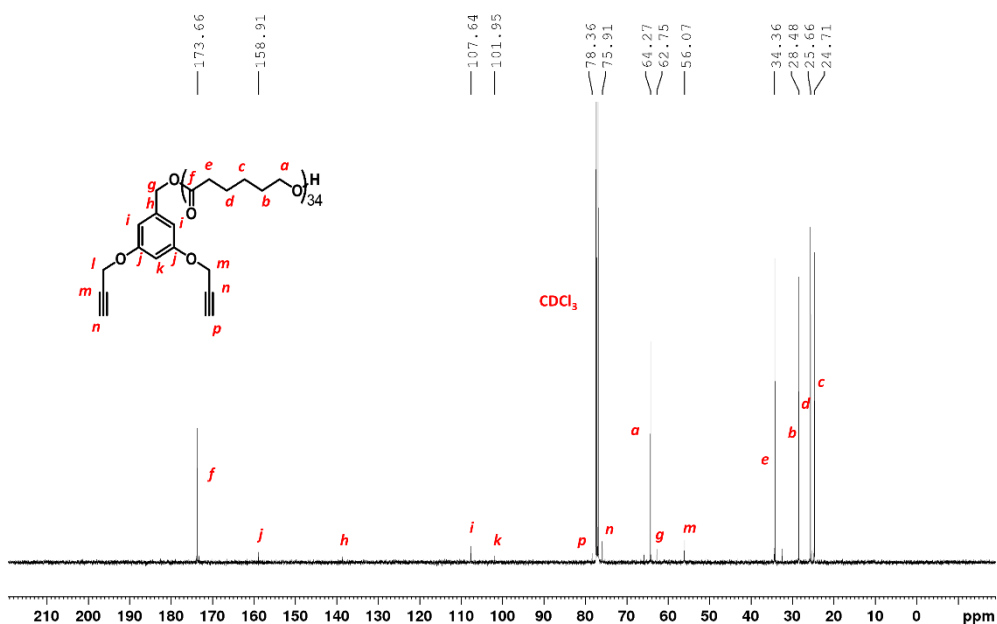


Figure 3. 14:  $^{13}\text{C}$  NMR spectrum of P5.

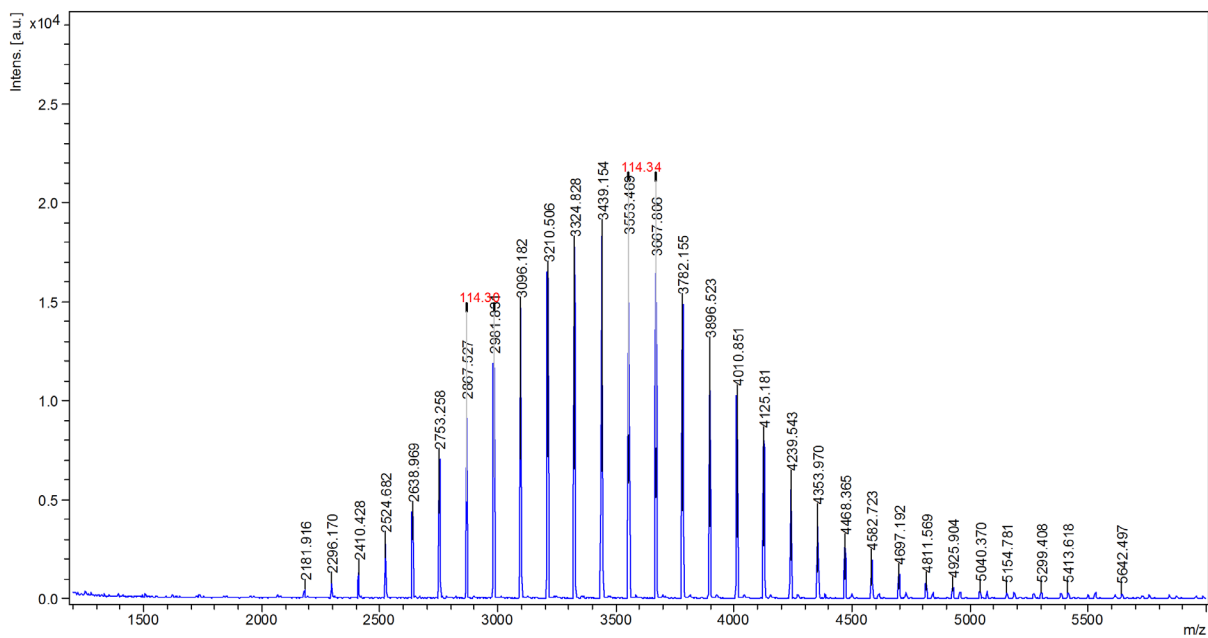
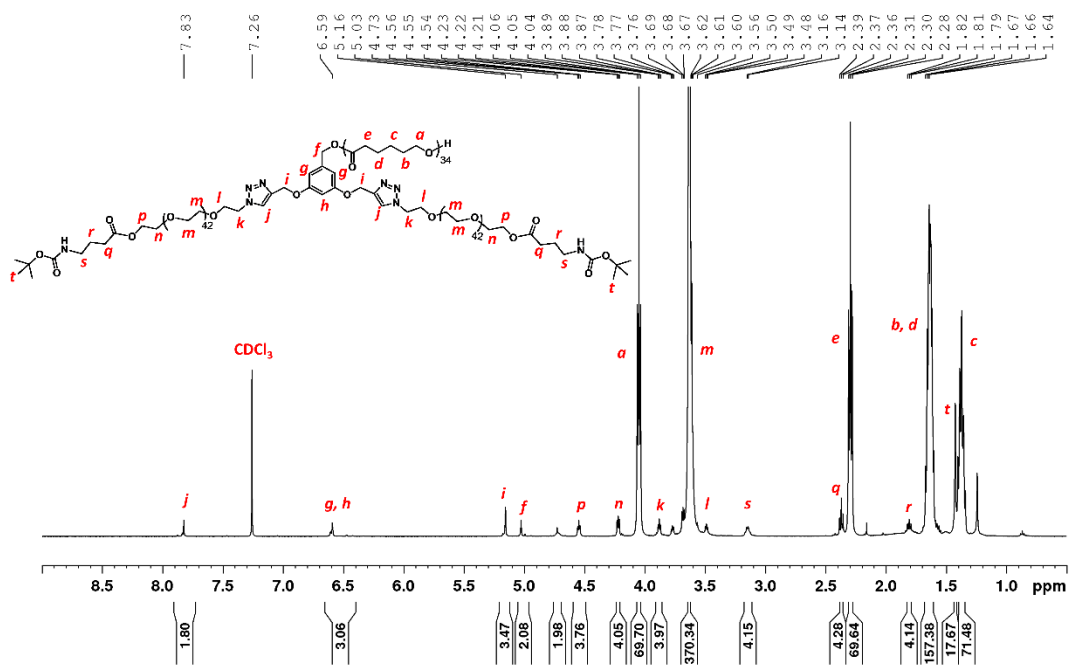
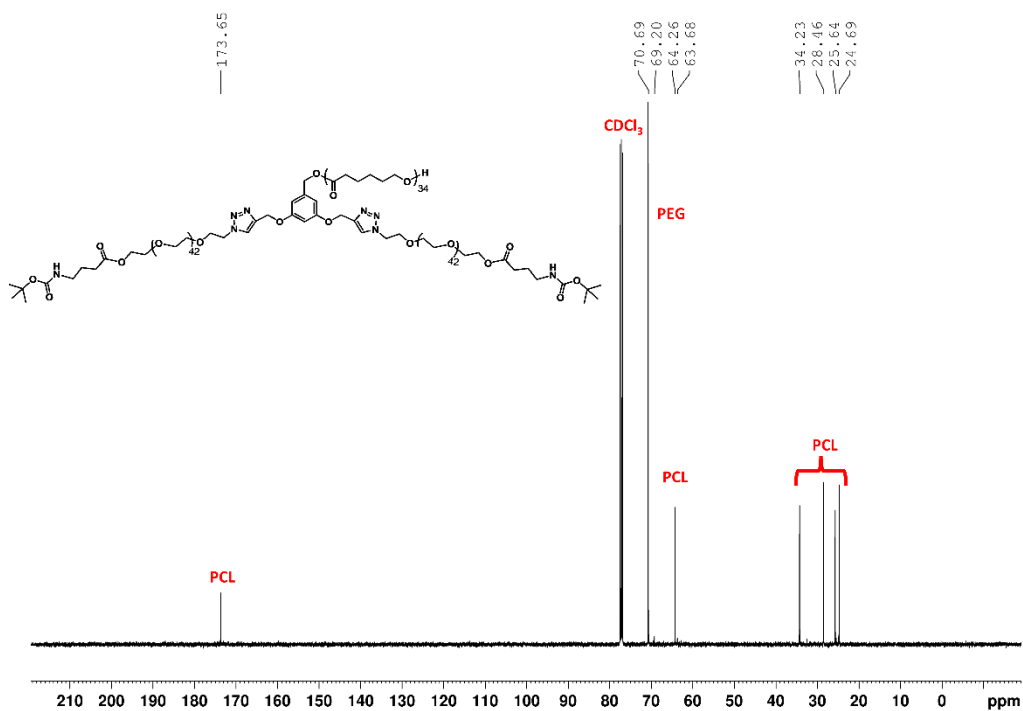


Figure 3. 15: MALDI-ToF spectrum of P5.

Figure 3. 16:  $^1\text{H}$  NMR spectrum of P6.Figure 3. 17:  $^{13}\text{C}$  NMR spectrum of P6.

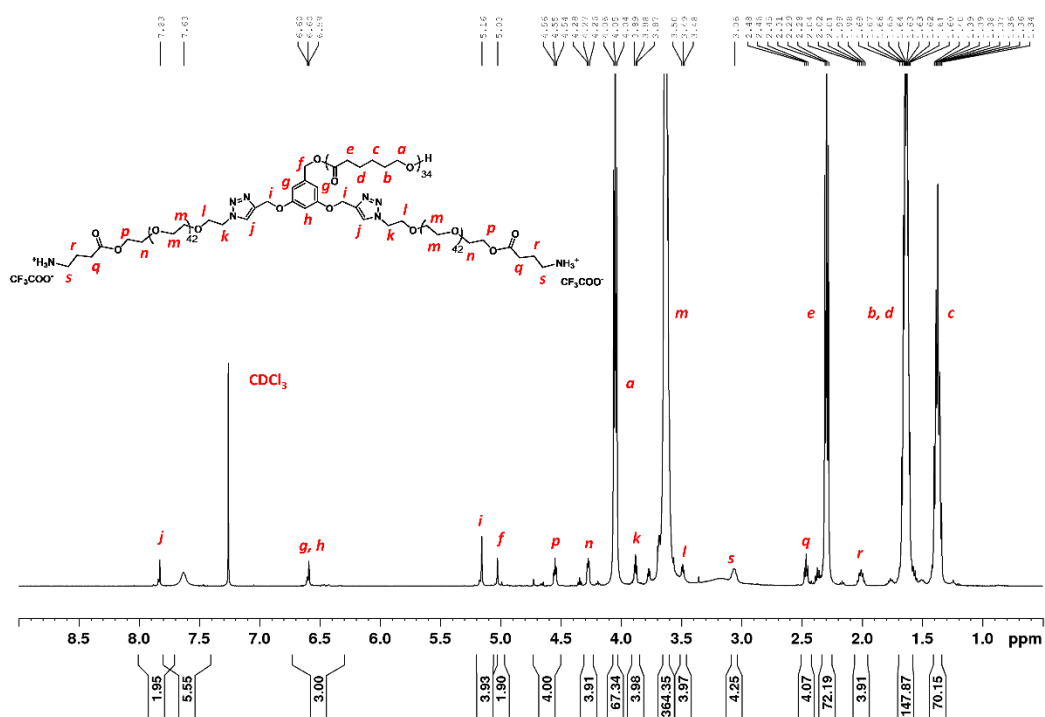


Figure 3. 18:  $^1\text{H}$  NMR spectrum of P7.

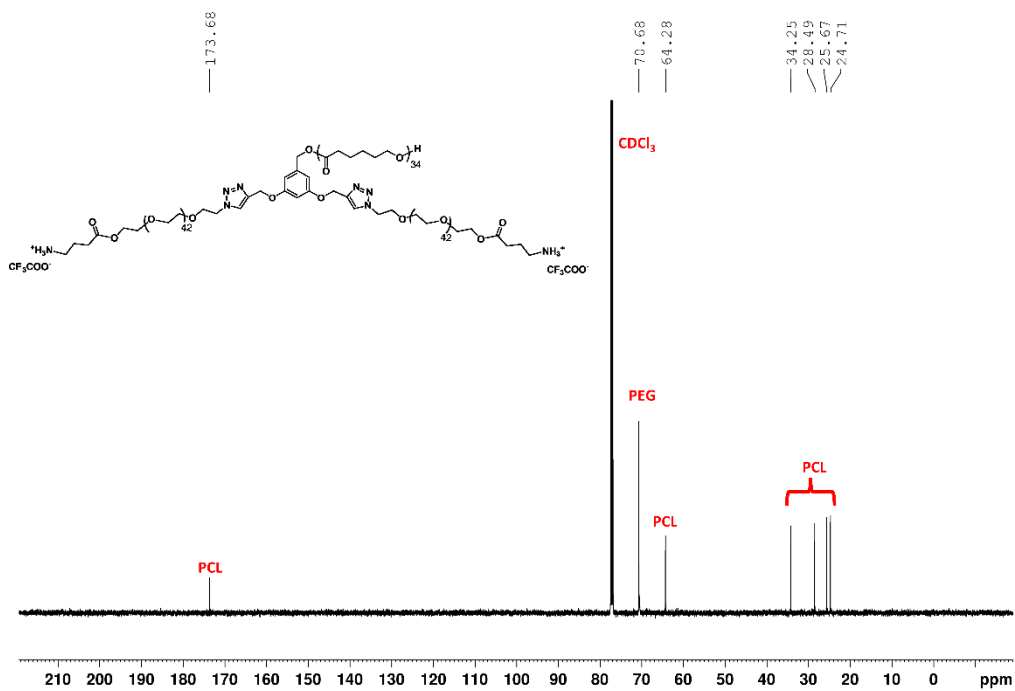
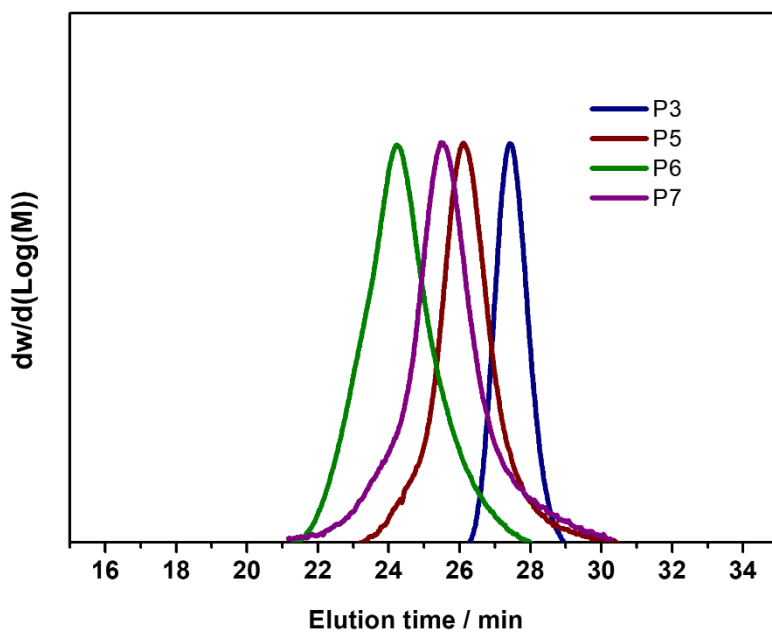
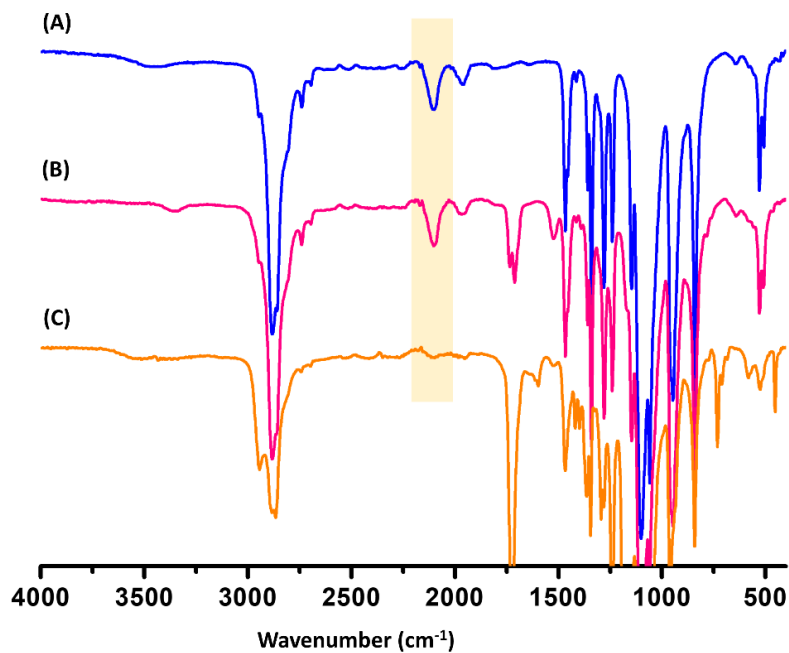


Figure 3. 19:  $^{13}\text{C}$  NMR spectrum of P7.



**Figure 3. 20:** GPC traces of P3 (blue  $D=1.11$ ), P5 (brown,  $D=1.26$ ), P6 (green,  $D=1.38$ ), and P7 (purple,  $D=1.54$ ).



**Figure 3. 21:** FTIR spectrum of (A) P2, (B) P3 and (C) P6. The presence of the azide in P2 and P3 was confirmed by the appearance of a peak at 2120 cm<sup>-1</sup>.

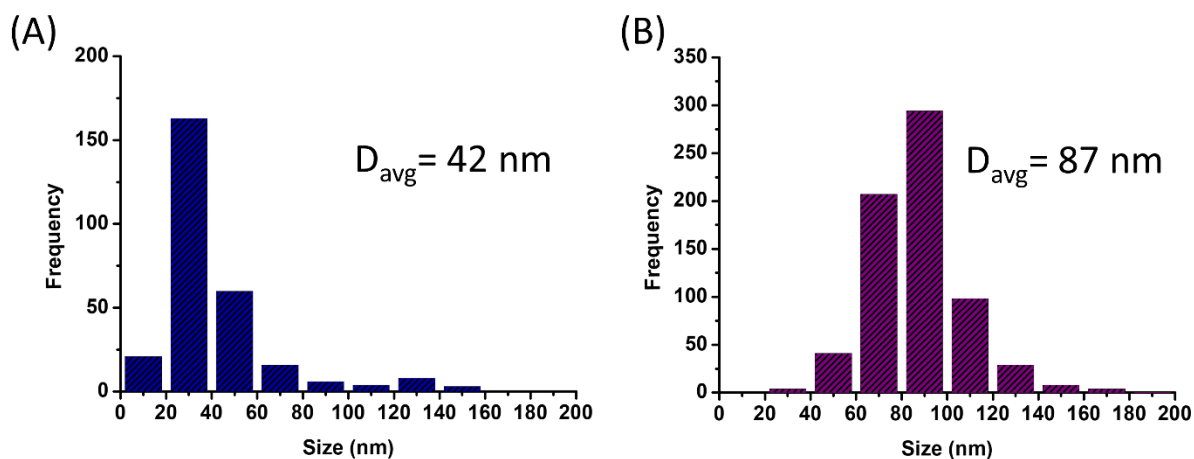


**Figure 3. 22:** TEM analyses of (A) P6-micelles and (B) P7-micelles.

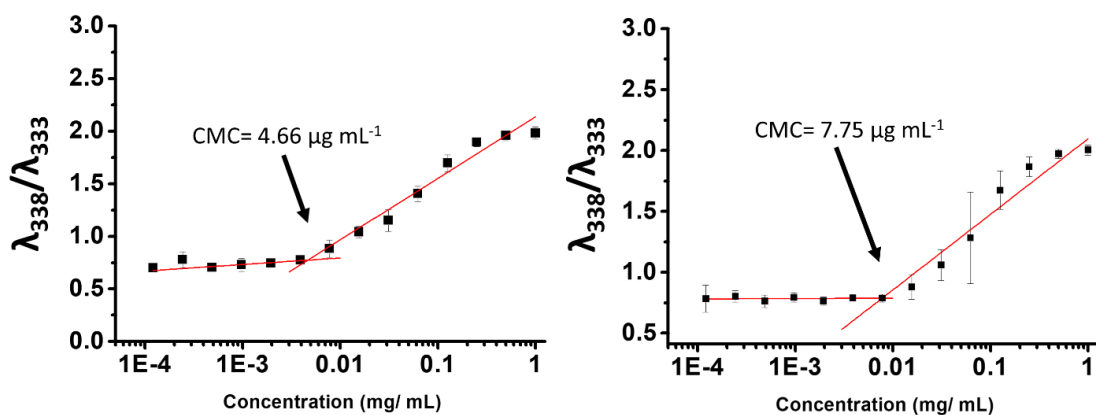


**Figure 3. 23:** The CMC of (A) P6-micelles and (B) P7-micelles derived from the plot of fluorescence intensity of pyrene at 338 nm and 333 nm against polymer concentration.

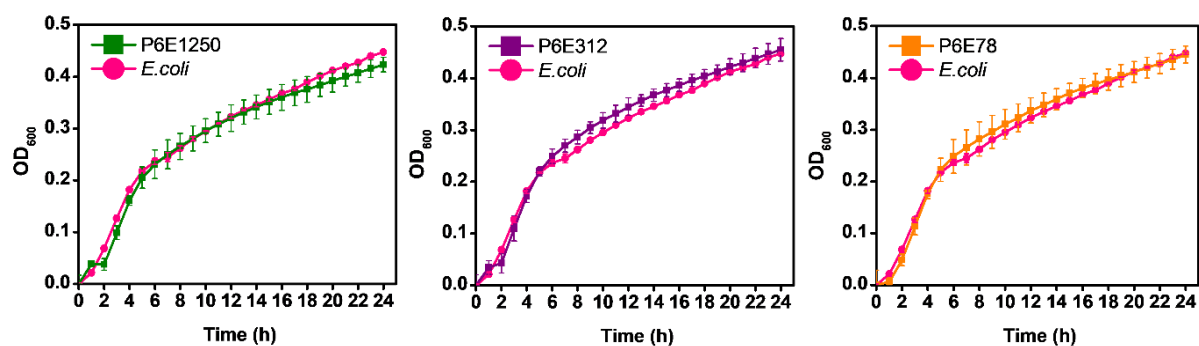


**Figure 3. 24:** Growth curve analyses of *E. coli* in the presence of P6-micelles. Graph legends: P6 represents P6-micelles. Letter E following sample represents *E. coli*, while the numbers that follow suit represent concentration of micellar solutions (e.g., P6E1250 contains 1250  $\mu\text{g mL}^{-1}$  of P6-micelle added to *E. coli*).

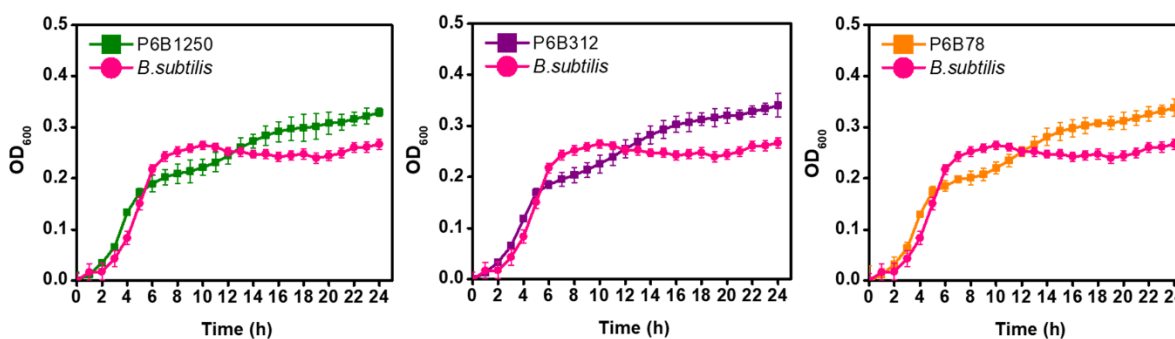


**Figure 3. 25:** Growth curve analyses of *B. subtilis* in the presence of P6-micelles. Graph legends: P6 represents P6-micelles. Letter B following sample represents *B. subtilis*, while the numbers that follow suit represent concentration of micellar solutions (e.g., P6B1250 contains 1250  $\mu\text{g mL}^{-1}$  of P6-micelle added to *B. subtilis*).

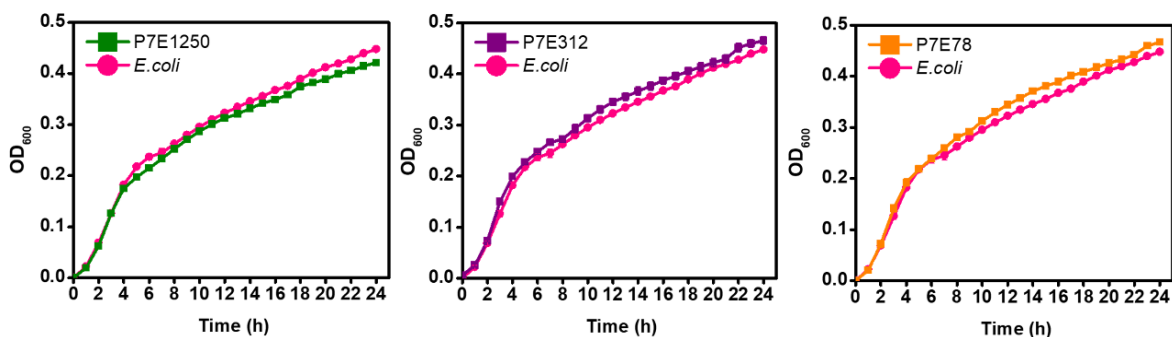


**Figure 3. 26:** Growth curve analyses of *E. coli* in the presence of P7-micelles. Graph legends: P6 represents P7-micelles. Letter E following sample represents *E. coli*, while the numbers that follow suit represent concentration of micellar solutions (e.g., P7E1250 contains 1250  $\mu\text{g mL}^{-1}$  of P7-micelle added to *E. coli*).

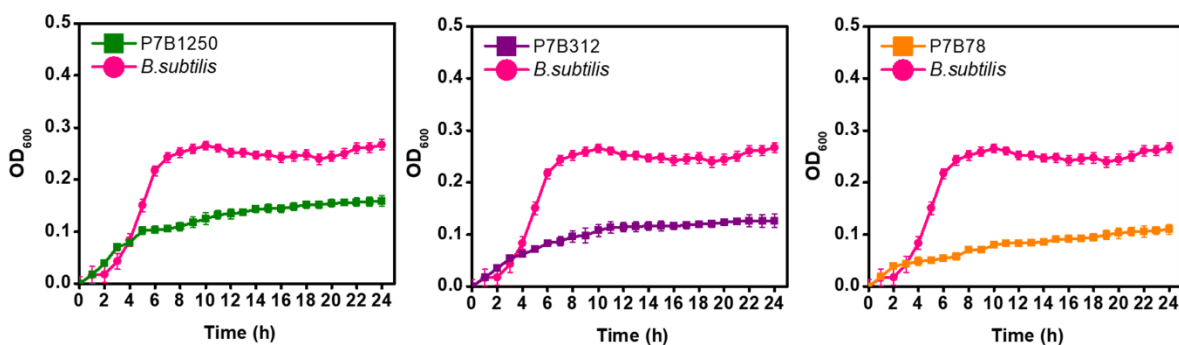


**Figure 3. 27:** Growth curve analyses of *B. subtilis* in the presence of P7-micelles. Graph legends: P7 represents P7-micelles. Letter B following sample represents *B. subtilis*, while the numbers that follow suit represent concentration of micellar solutions (e.g., P7B1250 contains 1250  $\mu\text{g mL}^{-1}$  of P7-micelle added to *B. subtilis*).

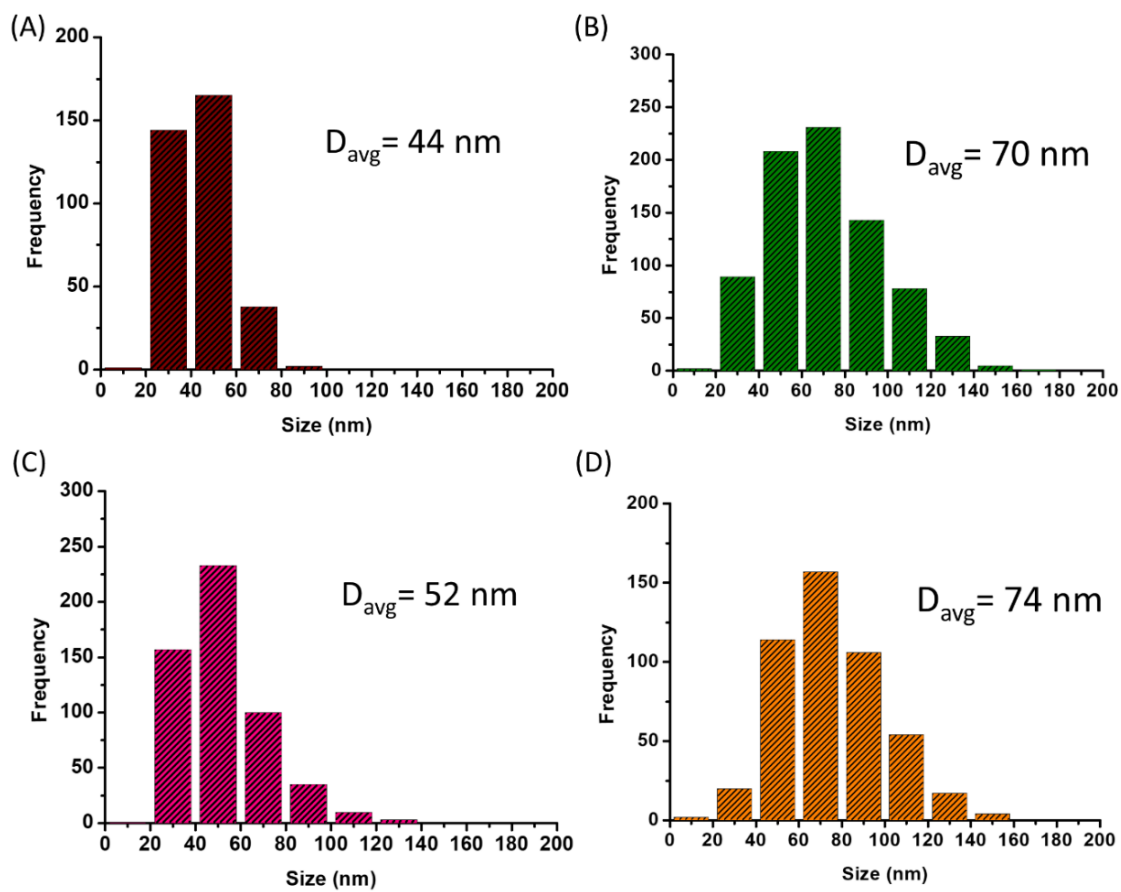


**Figure 3. 28:** TEM analyses of (A) P6-CUR, (B) P6-TBF, (C) P7-CUR, and (D) P7-TBF.

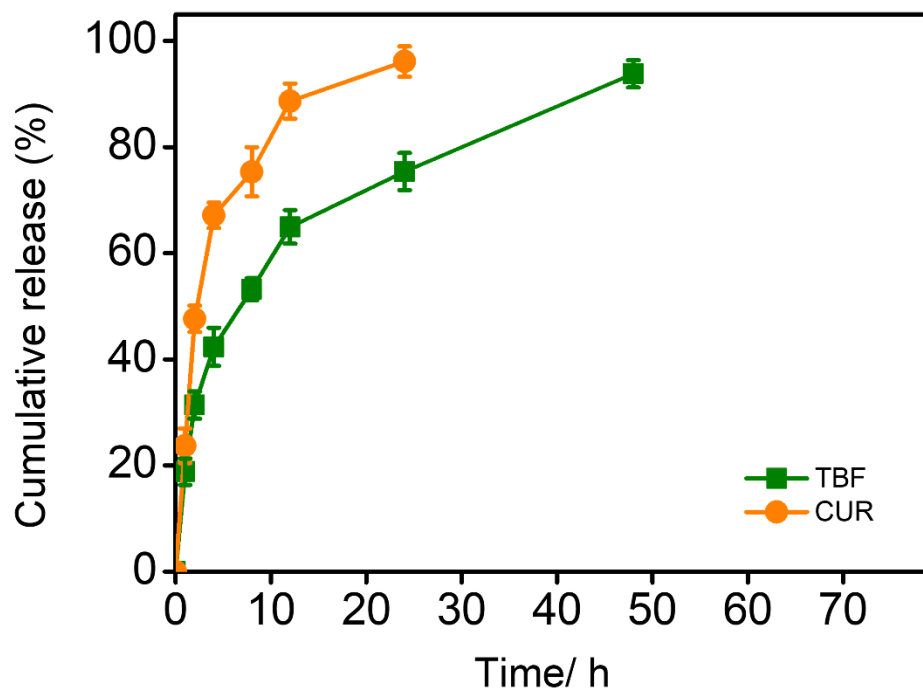


**Figure 3. 29.** Drug release profiles of free CUR and TBF. All studies were conducted at 37 °C in 1X PBS buffer (pH 7.4, +1% v/v Tween 80). Error bars represent a standard deviation of n = 3.

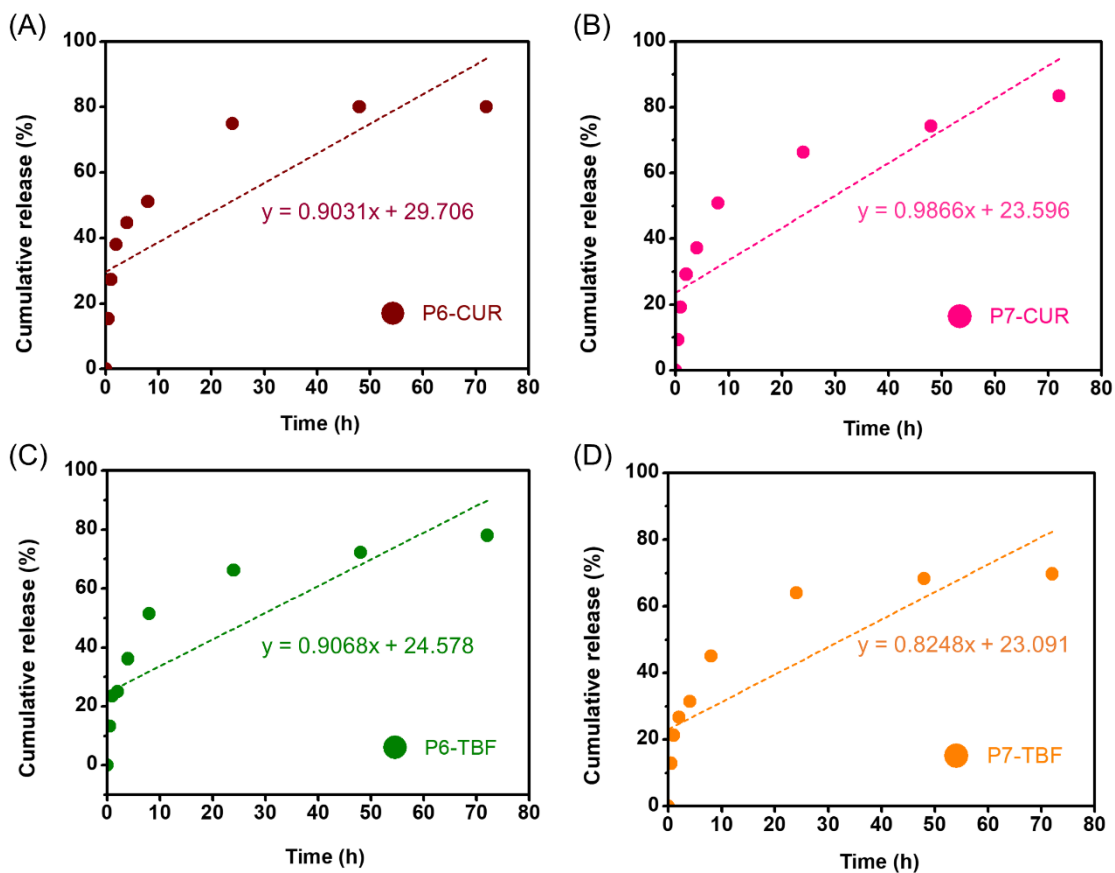


**Figure 3. 30:** Drug release data fitted to zero-order model: (A) P6-CUR, (B) P7-CUR, (C) P6-TBF and (D) P7-TBF.

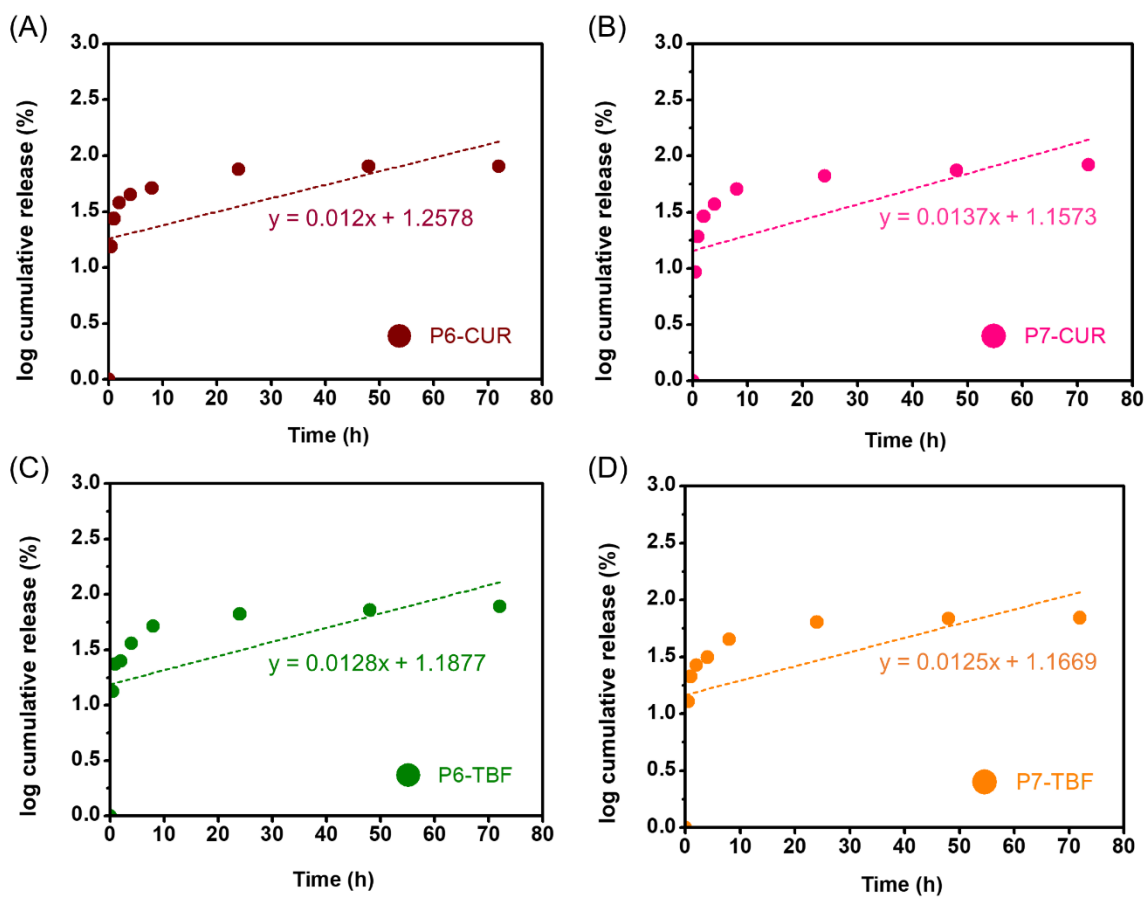


**Figure 3. 31:** Drug release data fitted to first-order model: (A) P6-CUR, (B) P7-CUR, (C) P6-TBF and (D) P7-CUR.

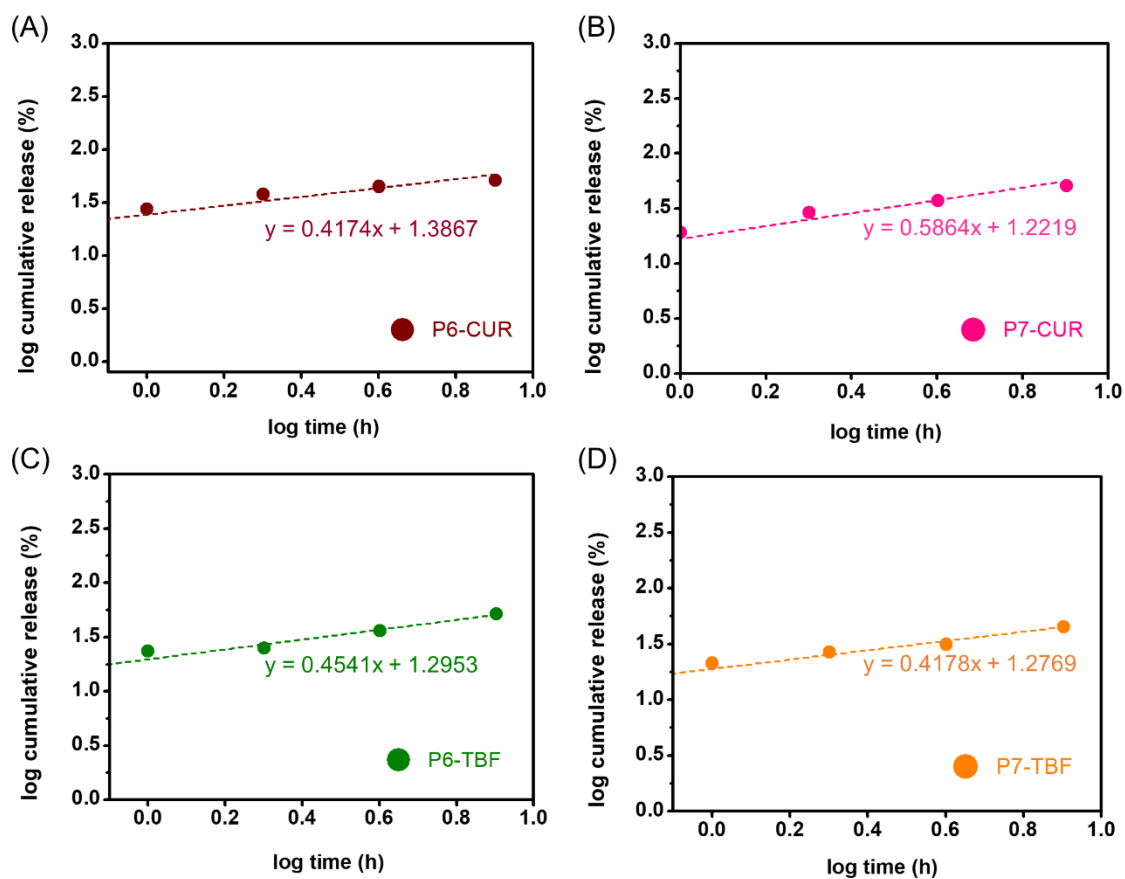


**Figure 3. 32:** Drug release data fitted to Korsmeyer-Peppas model: (A) P6-CUR, (B) P7-CUR, (C) P6-TBF and (D) P7-CUR.

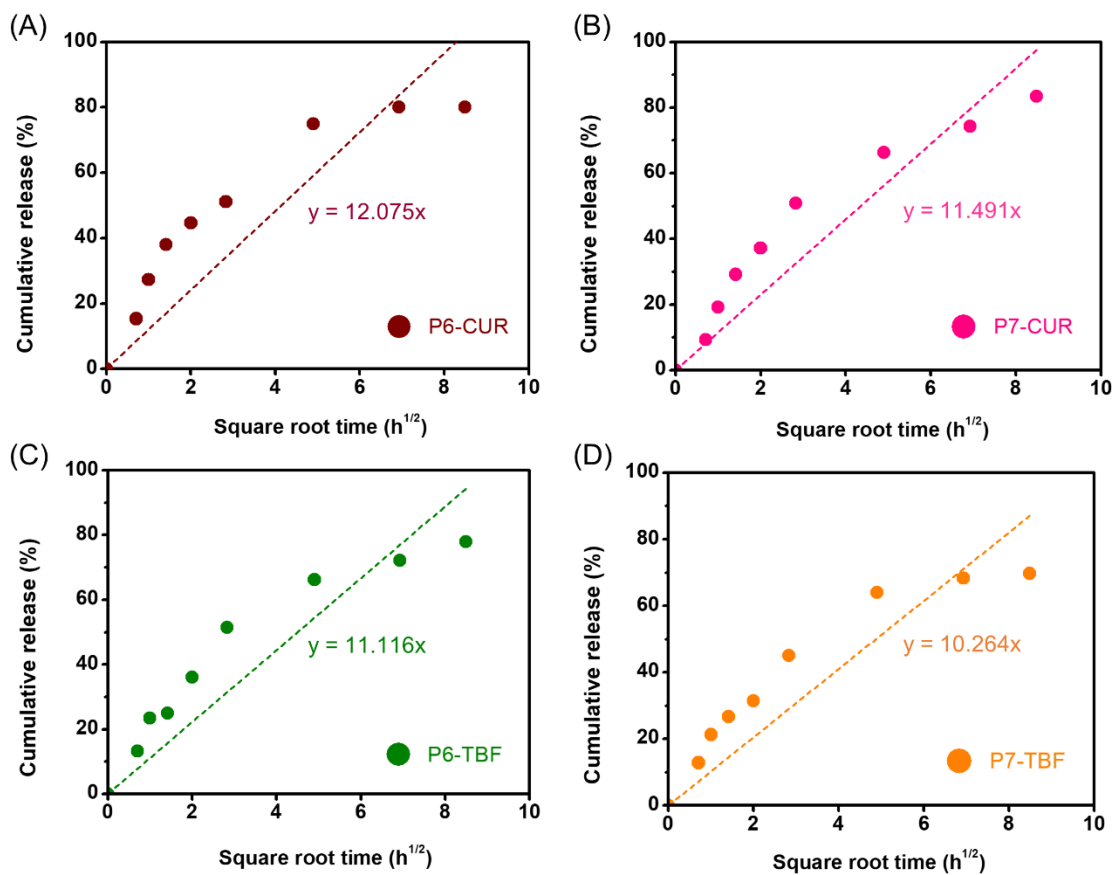


**Figure 3. 33:** Drug release data fitted to Higuchi model: (A) P6-CUR, (B) P7-CUR, (C) P6-TBF and (D) P7-CUR.

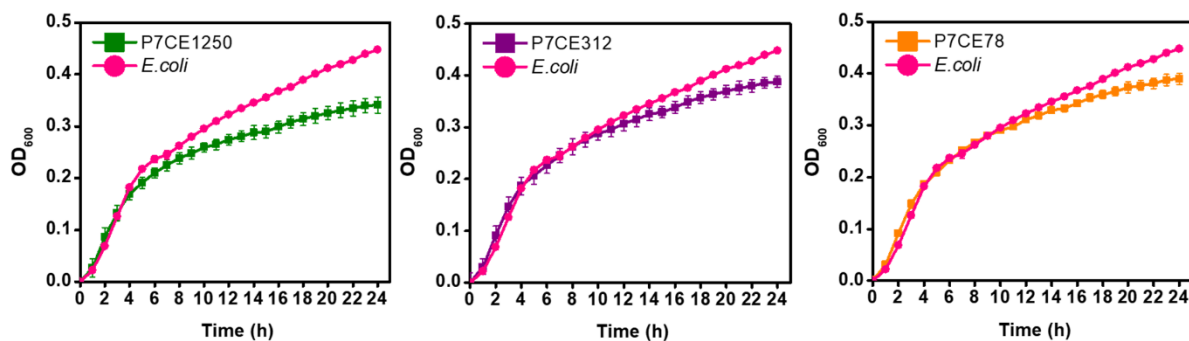


**Figure 3. 34:** Growth curve analyses of *E. coli* in the presence of P7-CUR. Graph legends: P7C represents P7-CUR. Letter E following sample represents *E. coli*, while the numbers that follow suit represent concentration of micellar solutions (e.g., P7CE1250 contains 1250  $\mu\text{g mL}^{-1}$  of P7-CUR added to *E. coli*).

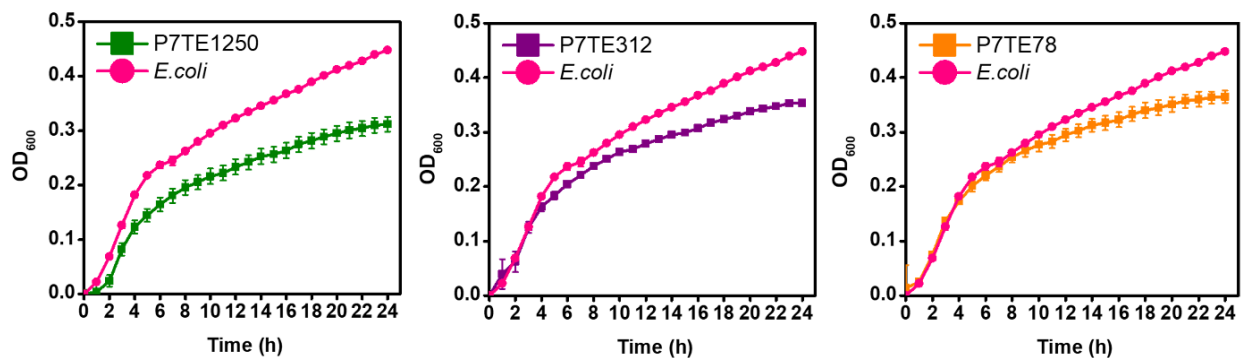


**Figure 3. 35:** Growth curve analyses of *E. coli* in the presence of P7-TBF. Graph legends: P7T represents P7-TBF. Letter E following sample represents *E. coli*, while the numbers that follow suit represent concentration of micellar solutions (e.g., P7TE1250 contains 1250  $\mu\text{g mL}^{-1}$  of P7-TBF added to *E. coli*).

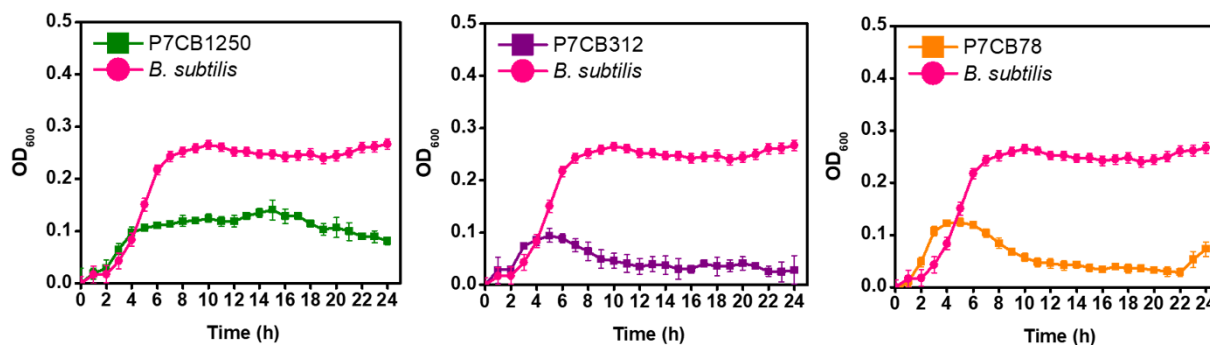


**Figure 3. 36:** Growth curve analyses of *B. subtilis* in the presence of P7-CUR. Graph legends: P7C represents P7-CUR. Letter B following sample represents *B. subtilis*, while the numbers that follow suit represent concentration of micellar solutions (e.g., P7CB1250 contains 1250  $\mu\text{g mL}^{-1}$  of P7-CUR added to *B. subtilis*).

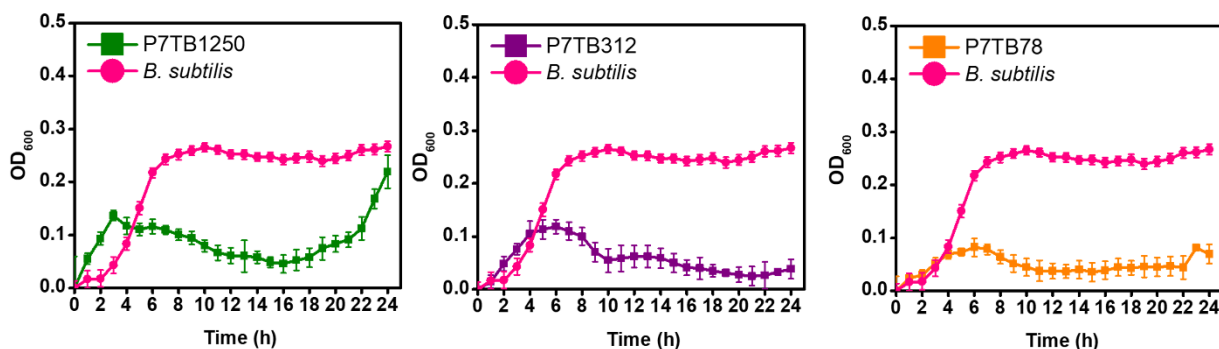


**Figure 3. 37:** Growth curve analyses of *B. subtilis* in the presence of P7-TBF. Graph legends: P7T represents P7-TBF. Letter B following sample represents *B. subtilis*, while the numbers that follow suit represent concentration of micellar solutions (e.g., P7TB1250 contains 1250  $\mu\text{g mL}^{-1}$  of P7-TBF added to *B. subtilis*).

# Chapter 4: Soft Nanoparticles with Induced Reversible Morphological Transitions through Upper Critical Solution Temperature for Controlled Drug Release

## 4.1. Opening Remarks

In Chapters 2 and 3 we explored post-polymerization modification methods to design NPs with varied core and shell structures, and demonstrated that such structures provide a versatile platform for applications in stimuli-directed controlled drug delivery, and co-adjuvant antibacterial applications. In Chapter 4, we explore polymer precursor design strategies for stable *in situ* nanoparticle (NP) morphology transformations. It is based on a model ABC (A = poly(acrylamide-*co*-acrylonitrile) (P(AAm-*co*-AN)), B = polyethylene glycol (PEG), C = polycaprolactone (PCL)) triblock copolymer, in which functions of each polymeric segment are pre-determined. This design strategy yields NPs exhibiting upper critical solution temperature (UCST)-behavior, which was utilized in facilitating temperature-controlled reversible morphological transitions. We subsequently demonstrate that such dynamic transitions can be leveraged in drug delivery for controlled and sustained cargo release rates, offering a versatile tool in the design and optimization of next-generation drug delivery systems.

This chapter is forming the basis of a manuscript being prepared for submission.

Yong, H. W.; Kakkar, A. Soft Nanoparticles with Induced Reversible Morphological Transitions through Upper Critical Solution Temperature for Controlled Drug Release, **2024**, *Manuscript in preparation*.

## 4.2. Abstract

Well-defined polymeric nanoparticles (NPs) continue to play a pivotal role in the advancement of nanomedicine. Soft NPs have employed diverse functional groups that facilitate drug release in response to various stimuli within microenvironments. In general, nanocarriers often collapse or lose their distinctive structural integrity due to modifications induced by the environmental stimuli. Consequentially, the controlled release of pharmaceutical cargo poses serious challenges, impeding their progression towards clinical translation. To overcome these issues, we report the design and exploration of an ABC (A = poly(acrylamide-*co*-acrylonitrile) (P(AAm-*co*-AN)), B = poly(ethylene glycol) (PEG), C = polycaprolactone (PCL)) triblock copolymer that upon self-assembly, undergo stable, reversible and controlled temperature-induced morphological transformations. Owing to the upper critical solution temperature (UCST) properties conferred by poly(AAm-*co*-AN), NPs undergo morphology transitions above the cloud point of 39 °C (concentration = 5.0 mg mL<sup>-1</sup>). The latter can be reversed below the cloud point through incorporation of non-thermoresponsive PEG and PCL chains that ensures stable NP morphologies under varied conditions. A detailed evaluation of these NP structural characteristics using turbidity, dynamic light scattering and transmission electron microscopy measurements was utilized to explore the potential of dynamic interplay of NP morphologies in developing a temperature-controlled delivery platform using curcumin (CUR) as a model drug. By harnessing temperature as a trigger for structural transformations, CUR release can be easily controlled without disassembly of NPs.

## 4.3. Introduction

Stimuli-responsive polymers represent an emerging class of innovative materials that exhibit changes in their physical and chemical properties in response to varied environments.<sup>1</sup> The key in designing these polymers lies in integrating chemical functional groups that could respond to common stimuli including pH, temperature, redox states, light, and specific enzymes.<sup>2</sup> The advances in designing stimuli-responsive polymers have led to nanomaterials with diverse applications such as biosensors,<sup>3,4</sup> bioimaging,<sup>5,6</sup> drug delivery,<sup>7,8</sup> and self-cleaning membranes.

<sup>9</sup> Thermoresponsive polymers have been widely studied for a myriad of applications due to their fast and efficient response to temperature variations.<sup>10-12</sup> Amongst these, polymers exhibiting temperature responsivity in an aqueous medium are of particular interest as they have great potential in biomedical applications.<sup>13-17</sup> Such polymers undergo phase transitions which impart controlled solubility behavior in response to temperature.<sup>18</sup> The point at which this phase transition is observed is defined as the critical solution temperature ( $T_c$ ). These polymers can be separated into two distinct groups: those that exhibit an i) upper critical solution temperature (UCST), and ii) a lower critical solution temperature (LCST).<sup>19</sup> Polymers with UCST properties are insoluble below  $T_c$ , but their solubility gradually increases with increasing temperature; while LCST polymers exhibit the exact opposite behavior: soluble below  $T_c$  and insoluble above it. These reversible transitions make these polymers highly attractive for designing temperature sensitive smart materials.<sup>20-22</sup>

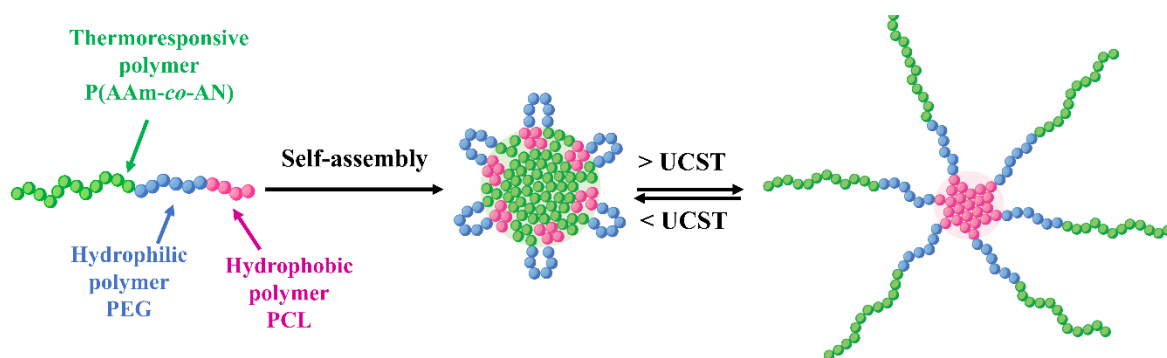
LCST polymers have been widely investigated as their thermoresponsivity is more achievable under physiologically relevant conditions. A prominent example of this is poly(*N*-isopropyl acrylamide) (PNIPAM).<sup>23-28</sup> In contrast, UCST polymers have been relatively sparsely studied, and much less for biological applications.<sup>29-32</sup> UCST properties are typically driven by either hydrogen bonds or coulombic interactions.<sup>33</sup> For hydrogen bonded systems, strong polymer-polymer interactions, such as those formed between the carbonyl and amine groups in poly(*N*-acryloylglycinamide) (PNAGA), facilitate the transition from insoluble to soluble with temperature. This trait has been utilized in inducing photothermal properties and enables spatiotemporal control over doxorubicin release.<sup>34, 35</sup> Coulombic interactions have also been observed to promote UCST behavior, exemplified by polybetaines.<sup>36-38</sup> For instance, Sponchioni et al. reported on a poly(sulfobetaine-*co*-sulfobetaine)-*block*-poly(caprolactone-2-hydroxyethyl methacrylate) that has tunable UCST values, nanoparticle (NP) size, and biodegradation rate.<sup>39</sup> With a wide range of adjustability, they synthesized polymers with UCST under physiological conditions ( $30 < T < 45$  °C) and examined their drug delivery potential using pyrene as a probe, demonstrating the possibility of controlled release by changing the phase state of the NPs *in situ*. However, most ionic UCST polymers have limited biomedical applications due to their sensitivity

to electrolytes, which affects their phase transition behavior.<sup>40, 41</sup> Hence, there has been greater emphasis on non-ionic UCST polymers, such as PNAGA or poly(acrylamide-*co*-acrylonitrile) (P(AAm-*co*-AN)), due to their broader applicability in biomedical settings.<sup>42</sup>

Soft NP drug delivery systems are typically composed of diblock amphiphilic copolymers, such as AB (linear) or AB<sub>n</sub> (branched), where A represents the hydrophobic segment and B represents the hydrophilic segment.<sup>43-45</sup> Typically, these NPs adopt a star-like hydrophobic core/hydrophilic shell micelle morphology.<sup>46</sup> The hydrophobic core facilitates encapsulation of poorly water-soluble drugs, making them promising candidates for drug delivery applications. When an additional hydrophobic block is added to form linear ABA or even ABC-type copolymers, triblock copolymers can assume different conformations, wherein the central B blocks loop to adopt a flower-like structure, contrasting the extended state seen in star-like micelles.<sup>47-49</sup> In this configuration, both A and C polymers contribute to the core.<sup>50</sup> Flower-like micelles share similar characteristics with conventional star-like micelles such as small size and low critical micelle concentration. Additionally, flower-like micelles typically yield NPs that are compact and dense, which enhance their stability under physiological conditions, mitigate premature drug release and ensure targeted drug delivery at intended sites of action.<sup>51, 52</sup> Flower-like micelles can also be engineered to undergo responsive behavior for controlled and triggered drug release.<sup>53-56</sup> However, most flower-like micelles contain stimuli-responsive hydrophobic blocks that undergo cleavage upon stimulus activation, triggering disassembly.<sup>57, 58</sup> This mechanism limits controlled drug release from the system once dissolved. NPs that maintain stability upon stimuli trigger have significant potential in providing multiple dose dependent-release events while ensuring controlled release at intended sites.

Herein, we report a UCST-responsive ABC (A = P(AAm-*co*-AN), B = polyethylene glycol (PEG), C = polycaprolactone (PCL)) triblock copolymer, the first demonstration of its self-assembly into stable NPs that undergo reversible transitions with temperature; and an evaluation of its potential in controlled drug release. We adopted poly(AAm-*co*-AN) as the polymer segment for UCST behavior, that is expected to induce transition from flower- to star-like morphology in soft NPs.

This choice was motivated by its non-ionic thermoresponsive and easily tunable phase behavior.<sup>59</sup> Hydrophilic PEG and hydrophobic PCL were used as components of amphiphilic co-polymer composition. In our design strategy, we incorporated PEG between the P(AAm-co-AN) and PCL blocks, with PEG confined to a loop conformation within the hydrophilic shell surrounding the hydrophobic core composed of poly(AAm-co-AN) and PCL (Scheme 4. 1). This conformation would likely yield flower-like micelles with a stable interface between the core and aqueous environment below UCST. As temperature rises beyond the cloud point, changes in poly(AAm-co-AN) solubility, would induce stable reorganization with PEG and poly(AAm-co-AN) as the hydrophilic shell, and PCL remaining in the core. This would enable retention of the stable self-assembly structure even beyond the phase transition temperature. Conversely, as the temperature decreases, poly(AAm-co-AN) will undergo phase separation, leading to the reinforcement of the hydrophobic core in conjunction with PCL, and possibly restoring the initial morphology. These reversible morphological changes enable fabrication of self-assemblies undergoing *in situ* transformations, which are leveraged to examine their potential in designing dose-specific drug delivery nanocarriers. In the initial structure, the larger core size formed from P(AAm-co-AN) and PCL will promote enhanced encapsulation and retention of water-insoluble drugs. Consequently, during the transition at higher temperatures, drug release is anticipated due to changes in hydrophobic core composition. Conversely, as the self-assembly reverts to its initial structure, drug release is expected to be attenuated. In comparison to traditional systems that undergo complete disassembly under stimuli, the carefully designed reversible morphological changes can offer precise temporal and spatial control over drug delivery. This approach holds great promise for achieving efficient drug delivery and minimize off-target effects for efficient therapeutic outcomes. We used curcumin (CUR), a naturally occurring polyphenol extracted from a turmeric plant, as the model drug to evaluate the drug delivery capability of our system.<sup>60</sup> It has been shown that CUR possesses antioxidant, anti-inflammatory, antibacterial, and anticancer properties.<sup>61</sup> Nevertheless, its poor aqueous solubility and stability have hindered its applications.<sup>62</sup> Additionally, owing to the unique molecular structure and photophysical properties, CUR is also widely employed as a probe to monitor the environmental changes in self-assembly structures,<sup>63</sup><sup>64</sup> and we also utilized it to investigate the morphological transitions in our studies.



**Scheme 4. 1:** Schematic illustration of P(AAm-*co*-AN)-*b*-PEG-*b*-PCL-based self-assembly and its reversible transition in response to temperature.

#### 4.4. Experimental Section

##### Materials

4-hydroxybenzyl alcohol (99%, Sigma-Aldrich), propargyl bromide (~80% in toluene, Sigma-Aldrich), potassium carbonate ( $K_2CO_3$ ,  $\geq 99.0\%$ , Sigma-Aldrich), 18-crown-6 (99%, Sigma-Aldrich), tin(II) 2-ethylhexanoate ( $Sn(Oct)_2$ , 92.5-100.0%, Sigma-Aldrich), 4-cyano-4-[(dodecylsulfanylthiocarbonyl)sulfanyl]pentanoic acid (CDTPA, 97%, Sigma-Aldrich), acrylamide (AAM,  $\geq 99\%$ , Sigma-Aldrich), 4,4'-azobis(4-cyanovaleric acid) (V-501,  $\geq 98.0\%$ , Sigma-Aldrich), sodium carbonate ( $Na_2CO_3$ ,  $\geq 99.5\%$ , Sigma-Aldrich), polyethylene glycol (4000 g/mol, Sigma-Aldrich), silver nitrate ( $AgNO_3$ ,  $\geq 99\%$ , Sigma-Aldrich), sodium hydroxide (NaOH,  $\geq 97.0\%$ , ACP Chemicals), potassium iodide (KI, American Chemicals Ltd), sodium azide ( $NaN_3$ ,  $\geq 99.5\%$ , Sigma-Aldrich), 1-ethyl-3-(3-dimethylaminopropyl)carbodiimide (EDC,  $\geq 97.0\%$ , Sigma-Aldrich), *N*-hydroxysuccinimide (NHS, 98%, Sigma-Aldrich), cupric sulfate pentahydrate ( $CuSO_4 \cdot 5H_2O$ , Fisher Chemical), (+)-sodium L-ascorbate (NaAsc,  $\geq 98\%$ , Sigma-Aldrich), ethylenediaminetetraacetic acid disodium salt dihydrate (EDTA) (99.0-101.0%, Sigma-Aldrich), curcumin (CUR, 95%, Oakwood Chemical) were used as received. *p*-toluenesulfonyl chloride ( $\geq 98\%$ , Sigma-Aldrich) was recrystallized from petroleum ether before use.  $\epsilon$ -caprolactone

monomer (99%, ACROS Organics) was distilled over  $\text{CaH}_2$  before use. Acrylonitrile (AN,  $\geq 99\%$ , Sigma-Aldrich) was passed through aluminum oxide (activated, basic, Brockmann I, 150 mesh, 58 Å, Sigma-Aldrich) before use.

### Synthesis

#### Synthesis of (4-(prop-2-yn-1-yloxy)phenyl)methanol (4PBA)

To a stirred solution of propargyl bromide (0.540 mL, 6.04 mmol, 1.5 eq) and 4-hydroxybenzyl alcohol (0.5 g, 3.93 mmol, 1 eq) in acetone (22 mL),  $\text{K}_2\text{CO}_3$  (0.724 g, 5.24 mmol, 1.3 eq) and 18-crown-6 (0.043 g, 0.163 mmol, 0.04 eq) were added and the reaction mixture was refluxed at 65 °C under nitrogen for 24 h with magnetic stirring. After cooling to room temperature, any residue from the reaction mixture was removed by vacuum filtration. The filtrate was then evaporated to dryness under reduced pressure and partitioned between water and dichloromethane (DCM). The aqueous layer was extracted with dichloromethane (3 x 50 mL) and the combined organic extracts were dried with anhydrous  $\text{MgSO}_4$  and subsequently solvent was removed under reduced pressure. The crude product was purified by column chromatography using 1:1 hexane/ethyl acetate mixture. After evaporation of solvents, the product was recovered as a brown oil. Yield: 87% (2.69 g).  $^1\text{H}$  NMR (500 MHz,  $\text{CDCl}_3$ ):  $\delta$  (ppm) 2.07 (br s, 1H, -OH), 2.53 (t, 2H,  $-\text{C}\equiv\text{CH}$ ), 4.58 (s, 2H,  $-\text{CH}_2\text{OH}$ ), 4.67 (d, 2H,  $-\text{OCH}_2$ ), 7.27 (d, 2H, Ar-H), 7.29 (d, 2H, Ar-H).  $^{13}\text{C}$  { $^1\text{H}$ } NMR ( $\text{CDCl}_3$ , 125 MHz):  $\delta$  (ppm) 55.9, 64.9, 75.7, 78.6, 115.0, 128.7, 134.2, 157.1.

#### Synthesis of 4-(prop-2-ynyloxy)benzyl polycaprolactone (4PB-PCL)

4PBA (0.15 g, 0.926 mmol, 1 eq) was dissolved in dry toluene (24 mL) and heated to 100 °C under nitrogen with magnetic stirring.  $\epsilon$ -caprolactone (2.88 mL, 25.9 mmol, 28 eq) was subsequently added to the mixture and heated to 110 °C. Tin(II) 2-ethyl hexanoate (0.03 mL, 0.09 mmol, 0.1 eq) was then added and the reaction mixture was refluxed at 115 °C for 24 h. After cooling to room temperature, the solvent was removed under reduced pressure. The crude product was purified by dissolving in minimal DCM and precipitated in ice cold methanol. The product was collected under vacuum filtration and dried in a desiccator. Yield= 88% (1.8 g).  $^1\text{H}$  NMR (500 MHz,  $\text{CDCl}_3$ ):  $\delta$

(ppm) 1.36- 1.43 (m, 54H, (-OC-CH<sub>2</sub>-CH<sub>2</sub>-CH<sub>2</sub>-CH<sub>2</sub>-CH<sub>2</sub>-O)<sub>25</sub>), 1.61- 1.66 (m, 108H, (-OC-CH<sub>2</sub>-CH<sub>2</sub>-CH<sub>2</sub>-CH<sub>2</sub>-CH<sub>2</sub>-O)<sub>25</sub>), 2.30 (t, 53H, (-OC-CH<sub>2</sub>-CH<sub>2</sub>-CH<sub>2</sub>-CH<sub>2</sub>-CH<sub>2</sub>-O)<sub>25</sub>), 2.52 (t, 2H, -C≡CH), 4.05 (t, 51H, (-OC-CH<sub>2</sub>-CH<sub>2</sub>-CH<sub>2</sub>-CH<sub>2</sub>-CH<sub>2</sub>-O)<sub>25</sub>), 4.69 (d, 2H, CH<sub>2</sub>-C≡C), 5.04 (s, 2H, CH<sub>2</sub>-OH), 6.95 (d, 2H, Ar-H), 7.29 (d, 2H, Ar-H). <sup>13</sup>C {<sup>1</sup>H} NMR (CDCl<sub>3</sub>, 125 MHz): δ (ppm) 24.7, 25.7, 28.5, 34.3, 55.9, 64.3, 65.9, 75.8, 115.1, 129.25, 130.10, 173.7.

#### Synthesis of poly(acrylamide-co-acrylonitrile) (P(AAm-co-AN))

CDTPA (0.05 g, 0.124 mmol, 1 eq), AAm (1.07 g, 15.1 mmol, 122 eq), V-501 (0.009 g, 0.032 mmol, 0.26 eq), and Na<sub>2</sub>CO<sub>3</sub> (0.005 g, 0.047 mmol, 0.38 eq) were added into a Schlenk tube with a magnetic stir bar. Milli-Q water (10 mL) was added into the Schlenk tube, and the solution was degassed by vigorous purging with nitrogen. In a separate flask, excess AN was degassed with vigorous nitrogen purging. The AN (0.513 g, 9.67 mmol, 78 eq) was then transferred under airtight conditions into the Schlenk flask. The mixture was then placed into a pre-heated oil bath at 65 °C and allowed to react for 24 h. The crude product was precipitated by dropwise addition into excess ice-cold methanol three times. The precipitate was then collected and dried under vacuum. Yield= 72% (1.18 g). <sup>1</sup>H-NMR (500 MHz, DMSO-d<sub>6</sub>): 0.85 ppm (t, 3H, -(CH<sub>2</sub>)<sub>11</sub>CH<sub>3</sub>), 1.24 ppm (s, 17H, -S-CH<sub>2</sub>-CH<sub>2</sub>-(CH<sub>2</sub>)<sub>9</sub>-), 1.25-1.95 ppm (m, 2H, -CH<sub>2</sub>- in the backbone), 1.96-3.00 ppm (m, 1H, -CH- in the backbone), 6.60-7.90 ppm (m, 2H, NH<sub>2</sub>CO-).

#### Synthesis of poly(acrylamide-co-acrylonitrile)-*block*-poly[(ethylene glycol)] (P(AAm-co-AN)-*b*-PEG)

HO-PEG<sub>90</sub>-N<sub>3</sub> was synthesized according to the procedure outlined in Chapter 3. The synthesis of P(AAm-co-AN)-*b*-PEG was conducted by referencing a previous procedure, with minor modifications.<sup>65</sup> In brief, P(AAm-co-AN) (0.300 g, 0.024 mmol, 1.1 eq), EDC (0.011 g, 0.071 mmol, 3.2 eq), and Milli-Q water (20 mL) were added to a 3-neck flask under nitrogen gas. In a separate round bottom flask, HO-PEG<sub>90</sub>-N<sub>3</sub> (0.1 g, 0.022 mmol, 1 eq), NHS (0.009 g, 0.747 mmol, 3.4 eq), and Milli-Q water (10 mL) were added. The latter PEG solution was added into the EDC-containing 3-neck flask, and the reaction was allowed to react at 25 °C for 48 h. The solution was concentrated and precipitated three times in methanol. The product was then collected and dried

under vacuum. A yellow product was obtained. Yield= 84% (0.35 g).  $^1\text{H-NMR}$  (500 MHz, DMSO- $d_6$ ): 0.85 ppm (t, 3H,  $-(\text{CH}_2)_{11}\text{CH}_3$ ), 1.24 ppm (s, 19H,  $-\text{S}-\text{CH}_2-\text{CH}_2-(\text{CH}_2)_9-$ ), 1.25–2.20 ppm (m, 2H,  $-\text{CH}_2-$  in the backbone), 2.08–3.00 ppm (m, 1H,  $-\text{CH}-$  in the backbone), 3.51 ppm (s, 369H,  $-(\text{CH}_2-\text{CH}_2)_{90}-$ ), 6.60–7.90 ppm (m, 2H,  $\text{NH}_2\text{CO}-$ ).

Synthesis of poly(acrylamide-co-acrylonitrile)-block-poly[(ethylene glycol)]-block-polycaprolactone (P(AAm-co-AN)-b-PEG-b-PCL)

4PB-PCL (0.027 g, 0.009 mmol, 1.5 eq), P(AAm-co-AN)-b-PEG (0.100 g, 0.006 mmol, 1 eq),  $\text{CuSO}_4 \cdot 5\text{H}_2\text{O}$  (0.003 g, 0.012 mmol, 2 eq), and NaASc (0.005 g, 0.025 mmol, 4.2 eq) were added to a 3-neck flask under nitrogen gas. Milli-Q water (50 mL) was added, and the reaction was allowed to react at 45 °C for 48 h. The solution was concentrated and then washed with methanol, followed by acetone, and then THF, three times each. The product was further dialyzed with EDTA and Milli-Q water, then collected and dried under reduced pressure to obtain a yellow solid. Yield= 51% (0.06 g).  $^1\text{H-NMR}$  (500 MHz, DMSO- $d_6$ ): 1.20-1.30 ppm (m, PCL H,  $-\text{OC}-\text{CH}_2-\text{CH}_2-\text{CH}_2-\text{CH}_2-\text{CH}_2-\text{O}$ ), 1.30–2.05 ppm (m, 2H,  $-\text{CH}_2-$  in the backbone), 1.40-1.54 ppm (m, PCL H,  $-\text{OC}-\text{CH}_2-\text{CH}_2-\text{CH}_2-\text{CH}_2-\text{CH}_2-\text{O}$ ), 2.08–3.00 ppm (m, 1H,  $-\text{CH}-$  in the backbone), 2.23 ppm (t, PCL H,  $-\text{OC}-\text{CH}_2-\text{CH}_2-\text{CH}_2-\text{CH}_2-\text{CH}_2-\text{O}$ ), 3.48 ppm (s, 354H,  $-(\text{CH}_2-\text{CH}_2)_{90}-$ ), 3.89-3.94 ppm (t, 37 H,  $-\text{OC}-\text{CH}_2-\text{CH}_2-\text{CH}_2-\text{CH}_2-\text{CH}_2-\text{O}$ ), 6.60–7.90 ppm (m, 2H,  $\text{NH}_2\text{CO}-$ ).

Preparation of blank and drug-loaded NPs

The self-assemblies were prepared via the cosolvent evaporation method. The polymers P(AAm-co-AN)-b-PEG or P(AAm-co-AN)-b-PEG-b-PCL (5 mg) were dissolved in a 1:1 acetone: water mixture (1 mL). The solution was stirred, and the acetone was allowed to evaporate overnight. The aqueous solution was then passed through a 0.22  $\mu\text{m}$  PVDF filter and used immediately for analysis. CUR-encapsulated micelles were prepared with the same procedure but with drug (0.5 mg) dissolved in acetone together with the polymer, before introduction to an aqueous medium. The amount of CUR encapsulated into NPs was measured by studying the UV-Vis absorption at

426 nm and comparing it to a standard calibration curve. The drug loading (DL%) and encapsulation efficiency (EE%) were then calculated as follows:

$$\text{DL\%} = \frac{\text{Mass of drug encapsulated}}{\text{Mass of drug and polymer added}} \times 100\%$$
$$\text{EE\%} = \frac{\text{Mass of drug encapsulated}}{\text{Mass of drug added}} \times 100\%$$

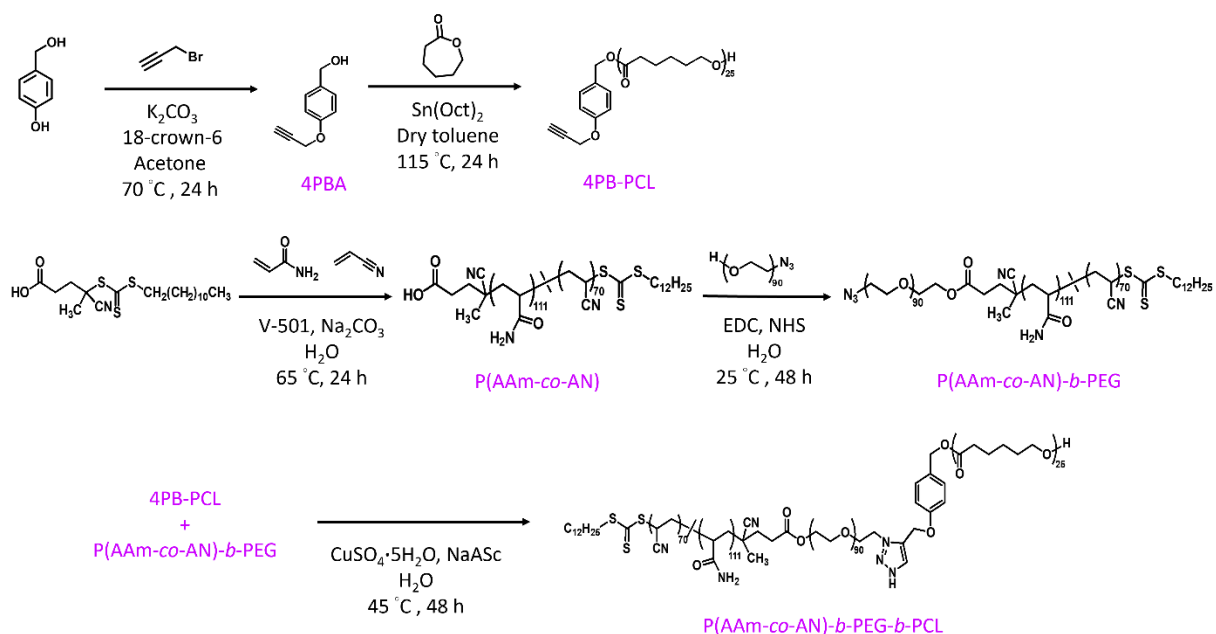
#### Drug Loading and Release

Drug release studies were conducted by transferring the drug-loaded micellar solution to a Spectra/Por 3 dialysis membrane (standard RC, 3.5 kDa MWCO). The solution was dialyzed against 140 mL of phosphate-buffered saline (PBS, 0.01 M, pH 7.4) containing 1% v/v Tween 80 at specified temperatures (25 °C / 37 °C / 25-37 °C). At desired intervals, 20 µL aliquots were collected from the dialysis bag and diluted 100 folds with methanol for analysis. The absorption intensities at 426 nm were measured at room temperature. The results were referred to a standard drug curve to obtain the mass of drug remaining at each interval.

### **4.5. Results & Discussion**

#### Synthesis and characterization of polymers

The methodology to synthesize ABC copolymer is detailed in Scheme 4. 2. For example, 4-hydroxybenzoic acid was propargylated according to a previously reported procedure to introduce an alkyne moiety (4PBA, Figure 4. 8- 4.9).<sup>66</sup> 4PBA was subsequently used as an initiator for the ring-opening polymerization (ROP) of ε-caprolactone to obtain 4PB-PCL. The degree of polymerization (DP) was calculated by comparing the integral of the benzyl protons between 6.95-6.96 ppm to that of the methylene protons in PCL at 4.05 ppm (Figure 4. 10- 4.13). Thus, the hydrophobic arm has a DP of 25 and a number-average molecular weight ( $M_n$ ) of 3000 Da (Table 4. 1).



**Scheme 4. 2:** Synthesis of polymeric precursors for thermoresponsive polymer, P(AAm<sub>111</sub>-co-AN<sub>70</sub>)-b-PEG<sub>90</sub>-b-PCL<sub>25</sub>.

Polymers with UCST behavior were prepared via reversible-addition-fragmentation chain transfer (RAFT) polymerization to obtain P(AAm-co-AN). The use of trithiocarbonate, CDTPA, as a RAFT agent ensures hydrolytic stability while having high transfer constants to facilitate polymerization of both “more activated” monomers, AAm and AN.<sup>67</sup> The cloud point of P(AAm-co-AN) is known to vary depending on the copolymer composition and concentration.<sup>68</sup> The ratio of AAm to AN is frequently adjusted to tailor the cloud point by controlling the monomer feed ratios during synthesis.<sup>69</sup> A higher AN content or copolymer concentration typically results in elevated phase transition temperatures due to increased polymer-polymer interactions. However, predicting the exact cloud point has proven to be challenging: for example, Seuring and Agarwal first reported the UCST behavior of P(AAm-co-AN) in water, noting a phase transition temperature of approximately 57 °C with 16.9 mol% AN content (concentration,  $c = 1 \text{ wt}\%$ ).<sup>69</sup> Chen et al. found a UCST of 55 °C with 67.5 % AN content ( $c = 1 \text{ mg mL}^{-1}$ );<sup>70</sup> Du et al. reported a UCST of 33 °C with 18.8 mol% AN ( $c = 1 \text{ mg mL}^{-1}$ ).<sup>71</sup> Additionally, Otsuka et al. observed

UCSTs of 6.5 °C and 56 °C when AN contents were 15.0 % and 31.8%, respectively ( $c = 1$  w/v%).<sup>71</sup> The significant variations in cloud points, even with similar AN contents, may stem from differences in polymerization techniques and reagents employed.<sup>68, 72</sup> Nevertheless, several P(AAm-*co*-AN) systems that have been reported with phase transition behaviors suitable for biomedical applications ( $< 45$  °C) had AN content between 7.5-30%.<sup>42, 73, 74</sup> Therefore, we developed the copolymer close to this limit (7.5-30%) for a preliminary investigation, anticipating that the cloud points would decrease as the AN content decreases when P(AAm<sub>111</sub>-*co*-AN<sub>70</sub>) is attached to PEG<sub>90</sub> and PCL<sub>25</sub>.

P(AAm-*co*-AN) was characterized using <sup>1</sup>H NMR and FT-IR. The <sup>1</sup>H NMR displayed methylene protons in the backbone at approximately 1.25-3.00 ppm. The characteristic peak for the amine protons from AAm was broad at about 6.60-7.90 ppm (Figure 4. 14). 111 units of AAm and 70 units of AN were estimated from <sup>1</sup>H NMR by integrating resonances at 0.85 ppm from the end CH<sub>3</sub> group of the RAFT agent, 1.32-3.01 ppm from the polymer backbone, and 6.60-7.90 ppm from AAm. This corresponds to a number-average molecular weight of 12200 Da and an AAm:AN molar ratio of 69: 31. Additionally, FT-IR was used to verify the presence of characteristic peaks in AAm and AN (Figure 4. 15). The distinct bands of -CN (from AN) and C=O (from AAm) were observed at 2245 cm<sup>-1</sup> and 1662 cm<sup>-1</sup>, respectively. Limited solubility of the polymer restricted its characterization using routine techniques such as gel permeation chromatography. Subsequently, P(AAm<sub>111</sub>-*co*-AN<sub>70</sub>)-*b*-PEG<sub>90</sub> was synthesized by attaching heterofunctionalized HO-PEG<sub>90</sub>-N<sub>3</sub> to P(AAm<sub>111</sub>-*co*-AN<sub>70</sub>). <sup>1</sup>H NMR spectrum of P(AAm<sub>111</sub>-*co*-AN<sub>70</sub>)-*b*-PEG<sub>90</sub> showed characteristic PEG peaks at 3.51 ppm (Figure 4. 16). Finally, the products were clicked via a copper-catalyzed azide-alkyne cycloaddition to obtain P(AAm<sub>111</sub>-*co*-AN<sub>70</sub>)-*b*-PEG<sub>90</sub>-PCL<sub>25</sub>. The distinct peaks for PCL were seen in the <sup>1</sup>H NMR (Figure 4. 17).

**Table 4. 1:** Characteristics of samples 4PB-PCL, P(AAm<sub>111</sub>-*co*-AN<sub>70</sub>), P(AAm<sub>111</sub>-*co*-AN<sub>70</sub>)-*b*-PEG<sub>90</sub>, P(AAm<sub>111</sub>-*co*-AN<sub>70</sub>)-*b*-PEG<sub>90</sub>-*b*-PCL<sub>25</sub>.

Polymer	$M_n$ (g/ mol) <sup>a</sup>	AN content by mass (%)	Hydrophobic content by mass (%)
4PB-PCL	3000	--	100%
P(AAm <sub>111</sub> - <i>co</i> -AN <sub>70</sub> )	12200	31	31
P(AAm <sub>111</sub> - <i>co</i> -AN <sub>70</sub> )- <i>b</i> -PEG <sub>90</sub>	16000	23	23
P(AAm <sub>111</sub> - <i>co</i> -AN <sub>70</sub> )- <i>b</i> -PEG <sub>90</sub> - <i>b</i> -PCL <sub>25</sub>	19000	20	35

<sup>a</sup> Estimated from <sup>1</sup>H NMR.

#### Thermal responsivity of copolymers in water

To investigate the phase transition behavior of the copolymers in water, we initially investigated their transmittance in response to temperature. P(AAm<sub>111</sub>-*co*-AN<sub>70</sub>), comprising 69 mol% of AAm and 31 mol% of AN exhibited UCST behavior, as detailed below. The cloud points of P(AAm<sub>111</sub>-*co*-AN<sub>70</sub>) solutions at various concentrations were studied, which were defined as the point at which 50% transmittance was reached. P(AAm<sub>111</sub>-*co*-AN<sub>70</sub>) was placed in water and sonicated to allow dispersion. In general, the aqueous solution of P(AAm<sub>111</sub>-*co*-AN<sub>70</sub>) showed turbid to transparent change upon heating, and subsequently return to an opaque suspension upon cooling (Figure 4. 1). The visual transitions observed were reflected in the transmission changes, which increased with a rise in temperature and decreased when cooled. This transition was in accordance with the expected UCST-type behavior. Additionally, we noted decreased transmittance with increasing P(AAm<sub>111</sub>-*co*-AN<sub>70</sub>) concentrations (Figure 4. 2). In a 0.625 mg mL<sup>-1</sup> aqueous solution of P(AAm<sub>111</sub>-*co*-AN<sub>70</sub>), the relative transmittance was high (25%). With a further increase in concentration (up to 20.0 mg mL<sup>-1</sup>), transmittance decreased to approximately 2-10% due to incorporation of more water-insoluble P(AAm<sub>111</sub>-*co*-AN<sub>70</sub>) in solution. Moreover, we noted intriguing patterns in the cloud points with temperature (Table 4. 2). At a concentration of 0.625 mg mL<sup>-1</sup>, the cloud point was measured at 28 °C. As the concentration increased to 1.25 mg mL<sup>-1</sup>

<sup>1</sup>, the cloud point rose by 5 °C, then by 2 °C from 1.25 to 2.5 mg mL<sup>-1</sup>, and by 1 °C from 2.5 to 5 mg mL<sup>-1</sup>. Subsequently, it decreased by 2 °C from 5.0 to 10.0 mg mL<sup>-1</sup> and by 1 °C from 10.0 to 20.0 mg mL<sup>-1</sup>. These observations suggest an influence of polymer concentration, and consequently, hydrogen bonding, on polymer phase separation. Similar concentration-dependent transitions have been reported by Hou and Wu.<sup>75</sup> In their studies, they observed that the cloud point of P(AAm-co-AN) decreased by 5 °C when the concentration decreased by a factor of 10. This decrease was accompanied by broadening of the transition at lower concentrations, demonstrating the concentration-dependency of P(AAm-co-AN)-based systems. Nevertheless, the reversible thermoresponsive nature of P(AAm<sub>111</sub>-co-AN<sub>70</sub>) with 31 mol% of AN, and its cloud points close to physiological relevance suggest that our design strategy is suitable for UCST-based NPs for biomedical applications.

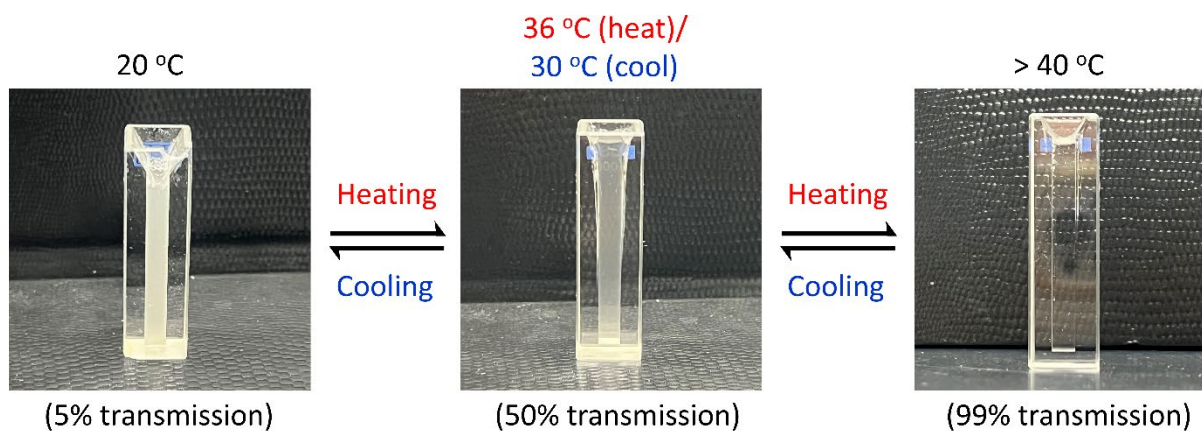


**Figure 4. 1:** Optical images of P(AAm<sub>111</sub>-co-AN<sub>70</sub>) dispersed in water showing turbidity transitions with temperature ( $c = 5.0 \text{ mg mL}^{-1}$ ).

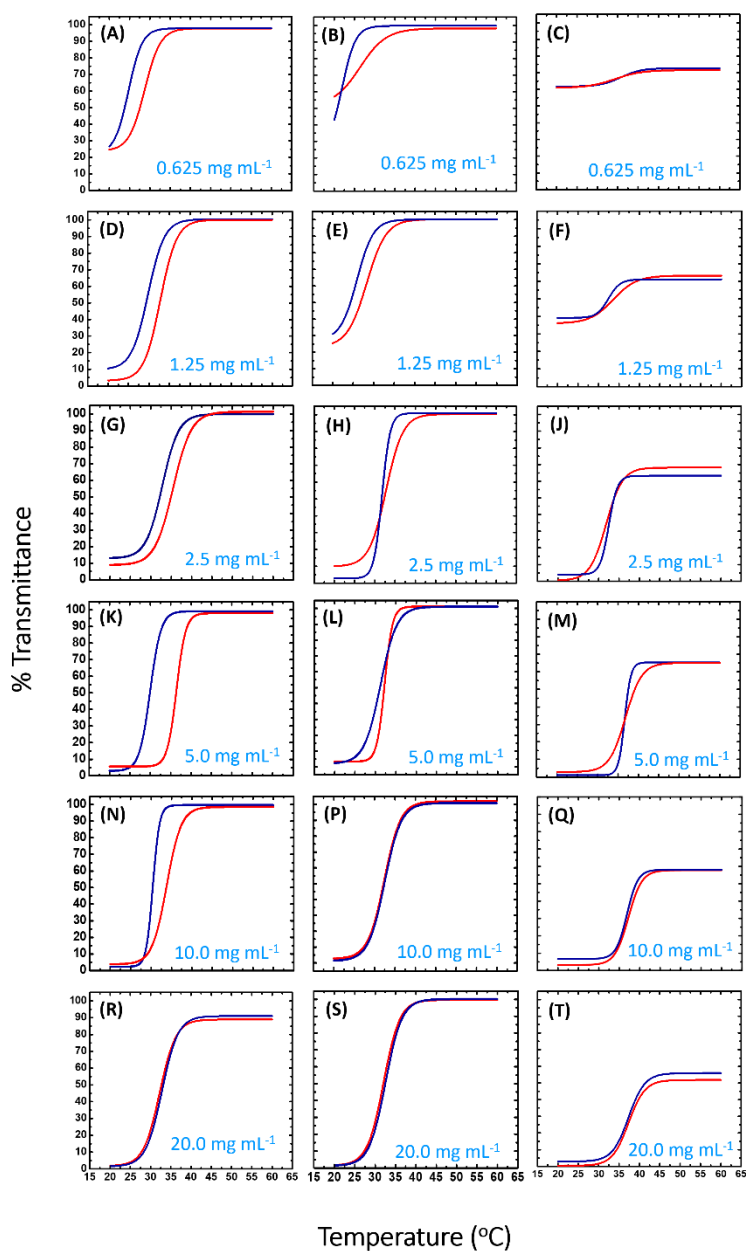


**Figure 4. 2:** Transmittance studies with temperature of various samples at different concentrations. The first column represents P(AAm<sub>111</sub>-co-AN<sub>70</sub>) with increasing concentrations, middle column represents P(AAm<sub>111</sub>-co-AN<sub>70</sub>)-b-PEG<sub>90</sub> with increasing concentrations, last column represents P(AAm<sub>111</sub>-co-AN<sub>70</sub>)-b-PEG<sub>90</sub>-b-PCL<sub>25</sub> with increasing concentrations. Red curves represent heating phase and blue curves represent cooling phase.

**Table 4. 2:** Cloud points of samples P(AAm<sub>111</sub>-*co*-AN<sub>70</sub>), P(AAm<sub>111</sub>-*co*-AN<sub>70</sub>)-*b*-PEG<sub>90</sub> , P(AAm<sub>111</sub>-*co*-AN<sub>70</sub>)-*b*-PEG<sub>90</sub>-*b*-PCL<sub>25</sub> upon heating and cooling at different concentrations. Data points were extracted from Figure 4. 2 when 50% transmittance was reached.

Concentration (mg mL <sup>-1</sup> )	Cloud point (°C)					
	P(AAm <sub>111</sub> - <i>co</i> -AN <sub>70</sub> )		P(AAm <sub>111</sub> - <i>co</i> -AN <sub>70</sub> )- <i>b</i> -PEG <sub>90</sub>		P(AAm <sub>111</sub> - <i>co</i> -AN <sub>70</sub> )- <i>b</i> -PEG <sub>90</sub> - <i>b</i> -PCL <sub>25</sub>	
	Heat	Cool	Heat	Cool	Heat	Cool
<b>0.625</b>	28	21	--	21	--	--
<b>1.25</b>	33	29	27	27	34	32
<b>2.5</b>	35	30	33	32	34	34
<b>5.0</b>	36	30	32	33	39	37
<b>10.0</b>	34	30	32	32	40	39
<b>20.0</b>	33	33	32	32	44	42

Subsequently, we investigated the UCST behavior of P(AAm<sub>111</sub>-*co*-AN<sub>70</sub>) conjugated to hydrophilic PEG<sub>90</sub> (P(AAm<sub>111</sub>-*co*-AN<sub>70</sub>)-*b*-PEG<sub>90</sub>) at the same concentrations. PEG was chosen to constitute the corona in the flower-like micelle due to its biocompatibility and ease of functionalization.<sup>76</sup> The integration of PEG has been shown to reduce interactions between P(AAm-*co*-AN) segments, leading to lower transition temperatures, such as those reported by Huang et al.<sup>77</sup> They reported a 5.1 °C decrease in cloud point after attaching PEG<sub>45</sub> (*c* = 1.0 mg mL<sup>-1</sup>). In our studies, the incorporation of PEG<sub>90</sub> reduced the AN content from 31% to 23%. The incorporation of PEG<sub>90</sub> also enhanced solubility as the hydrophobic content also decreased from 31% to 23%, as observed in the higher transmittance at 0.625 and 1.25 mg mL<sup>-1</sup>, in comparison to P(AAm<sub>111</sub>-*co*-AN<sub>70</sub>).

Nevertheless, P(AAm<sub>111</sub>-*co*-AN<sub>70</sub>)-*b*-PEG<sub>90</sub> solutions showed several similarities to P(AAm<sub>111</sub>-*co*-AN<sub>70</sub>), such as turning from insoluble to soluble with temperature increments and reverting to insoluble when temperature decreased. P(AAm<sub>111</sub>-*co*-AN<sub>70</sub>)-*b*-PEG<sub>90</sub> solutions also displayed

increased turbidity and elevated cloud points at higher polymer concentrations. For instance, at a concentration of  $0.625 \text{ mg mL}^{-1}$ , P(AAm<sub>111</sub>-*co*-AN<sub>70</sub>)-*b*-PEG<sub>90</sub> exhibited a high transmittance of 57%, rendering it without a measurable cloud point. Upon increasing the concentration to  $1.25 \text{ mg mL}^{-1}$ , the cloud point was observed at  $27 \text{ }^\circ\text{C}$ . Subsequently, the cloud points remained consistent, ranging approximately between  $31\text{-}32 \text{ }^\circ\text{C}$  when concentration varied from  $2.5\text{-}20.0 \text{ mg mL}^{-1}$ . These transitions are characteristic of UCST-type polymers, demonstrating concentration-dependent transition behavior. Furthermore, we observed only a small hysteresis of  $1\text{-}3 \text{ }^\circ\text{C}$  across all concentrations tested, suggesting good reversibility in the phase transition. The reversible UCST properties demonstrated by P(AAm<sub>111</sub>-*co*-AN<sub>70</sub>)-*b*-PEG<sub>90</sub> within physiological conditions provide a platform for the development of UCST-based NPs.

The phase transition of P(AAm<sub>111</sub>-*co*-AN<sub>70</sub>)-*b*-PEG<sub>90</sub> conjugated to hydrophobic PCL<sub>25</sub> (P(AAm<sub>111</sub>-*co*-AN<sub>70</sub>)-*b*-PEG<sub>90</sub>-*b*-PCL<sub>25</sub>) was subsequently examined. PCL was chosen as the hydrophobic block due to its non-thermoresponsive behavior, ensuring the retention of NP morphology. Upon attachment of PCL<sub>25</sub>, the AN content decreased further to 20% while the hydrophobic content increased to 35%. P(AAm<sub>111</sub>-*co*-AN<sub>70</sub>)-*b*-PEG<sub>90</sub> solutions exhibited UCST-type behavior, as evidenced by the increase in transmittance upon heating, and subsequent decrease in transmittance upon cooling. The cloud points of P(AAm<sub>111</sub>-*co*-AN<sub>70</sub>)-*b*-PEG<sub>90</sub>-*b*-PCL<sub>25</sub> also exhibited concentration-dependent behavior, and an increase of up to  $10 \text{ }^\circ\text{C}$  was observed as the concentration rose from  $1.25$  to  $20.0 \text{ mg mL}^{-1}$ . Between  $1.25\text{-}2.5 \text{ mg mL}^{-1}$ , the cloud points were identical at  $34 \text{ }^\circ\text{C}$ , then increased by  $5 \text{ }^\circ\text{C}$  at  $5.0 \text{ mg mL}^{-1}$ , followed by a rise of  $1 \text{ }^\circ\text{C}$  at  $10.0 \text{ mg mL}^{-1}$ , and finally by  $4 \text{ }^\circ\text{C}$  at  $20.0 \text{ mg mL}^{-1}$ . Notably, P(AAm<sub>111</sub>-*co*-AN<sub>70</sub>)-*b*-PEG<sub>90</sub>-*b*-PCL<sub>25</sub> did not fully solubilize, reaching peak transmission values of  $50\text{-}73\%$  at  $60 \text{ }^\circ\text{C}$ . For a  $0.625 \text{ mg mL}^{-1}$  aqueous solution of P(AAm<sub>111</sub>-*co*-AN<sub>70</sub>)-*b*-PEG<sub>90</sub>-PCL<sub>25</sub>, the maximum transmission was  $73\%$ . With an increase in concentration, the highest achievable transmittance decreased, with the lowest being  $50\%$  when  $c = 20.0 \text{ mg mL}^{-1}$ . Previous analyses from P(AAm<sub>111</sub>-*co*-AN<sub>70</sub>)-*b*-PEG<sub>90</sub> suggested that it has been solubilized, but in P(AAm<sub>111</sub>-*co*-AN<sub>70</sub>)-*b*-PEG<sub>90</sub>-*b*-PCL<sub>25</sub>, PCL may have prevented further solvation of the copolymer in water. This intriguing phenomenon is

advantageous in designing polymeric NPs that possibly do not disassemble completely with temperature, even beyond the cloud points.

#### Analyses of blank self-assemblies and temperature-directed morphological transitions

Polymers P(AAm<sub>111</sub>-*co*-AN<sub>70</sub>)-*b*-PEG<sub>90</sub> and P(AAm<sub>111</sub>-*co*-AN<sub>70</sub>)-*b*-PEG<sub>90</sub>-*b*-PCL<sub>25</sub> were subsequently utilized to prepare NPs separately for the evaluation of their self-assemblies. These two polymers were chosen to examine the significance of PCL in maintaining stable NP morphologies. In a typical cosolvent evaporation method used to induce self-assembly in amphiphilic block copolymers, the entire polymer is dissolved in volatile organic solvents, such as acetone, before being added into the aqueous medium. Acetone is then allowed to evaporate slowly over time, leading to the formation of NPs. However, due to limited solubility of both P(AAm<sub>111</sub>-*co*-AN<sub>70</sub>)-*b*-PEG<sub>90</sub> and P(AAm<sub>111</sub>-*co*-AN<sub>70</sub>)-*b*-PEG<sub>90</sub>-*b*-PCL<sub>25</sub>, we noted that a 1:1 ratio of acetone to water was necessary to completely solubilize the copolymers for self-assembly. This may be due to a difference in solubility of the individual polymers: acetone dissolves PEG and PCL, while water dissolves PAAm and PEG. Furthermore, a mixture of acetone-water improves the solubility of PAN.<sup>78</sup> Therefore, employing a mixture of solvents is necessary to ensure that all components are solubilized adequately, facilitating the self-assembly process for NP formation. As we envisioned the use of these systems for drug delivery, we narrowed the concentration to a value that would exhibit phase transition close to physiological temperature (37 °C). Therefore, P(AAm<sub>111</sub>-*co*-AN<sub>70</sub>)-*b*-PEG<sub>90</sub>-*b*-PCL<sub>25</sub> at  $c = 5.0 \text{ mg mL}^{-1}$  was selected for self-assembly as the cloud points are closest to human body temperature. Dynamic light scattering (DLS) and transmission electron microscopy (TEM) were used to evaluate the NP sizes and visualize their morphologies. The self-assemblies of P(AAm<sub>111</sub>-*co*-AN<sub>70</sub>)-*b*-PEG<sub>90</sub> (T6NPs) in water were first evaluated. As depicted in Figure 4. 3A, the size of the micelles generally decreased with increasing temperatures. T6NPs were found to be 142 nm at 20 °C. As the solution approached the cloud point (32 °C), the NPs drastically shrank below 20 nm. This small particle size stayed consistent between 35-60 °C. DLS analyses suggested formation of smaller particles beyond the cloud point, which was possibly due to the solvation of P(AAm<sub>111</sub>-*co*-AN<sub>70</sub>)-*b*-PEG<sub>90</sub>, as demonstrated in the transmittance studies. This observation aligns with findings reported by Li et

al.<sup>79</sup> In their studies, they found that sizes of the micelles from P(AAm-*co*-AN)-*g*-PEG decreased as the temperature increased from 4 to 43 °C. When the temperature exceeded beyond 43 °C, micelles disassembled. A clear interpretation of micellar morphology was supplemented by TEM. Figure 4. 3B-3C depict TEM of solutions of T6NPs before and after heating, respectively. The aliquot after heating was collected during the third heating cycle at 40 °C, which was frozen promptly in liquid nitrogen upon collection. During TEM sample preparation, the solution was gently warmed by hand and drop-casted onto the grid immediately upon thawing. Initially, T6NPs showed spherical micelles, with sizes of approximately 100 nm. However, post-heating, it is evident that much smaller particles are formed, with several clusters of aggregation. Compared to spherical structures seen prior to heating, different morphologies observed after heating suggest that T6NPs are not stable with temperature, rendering this system unsuitable for designing NPs with stable and reversible morphological transitions.

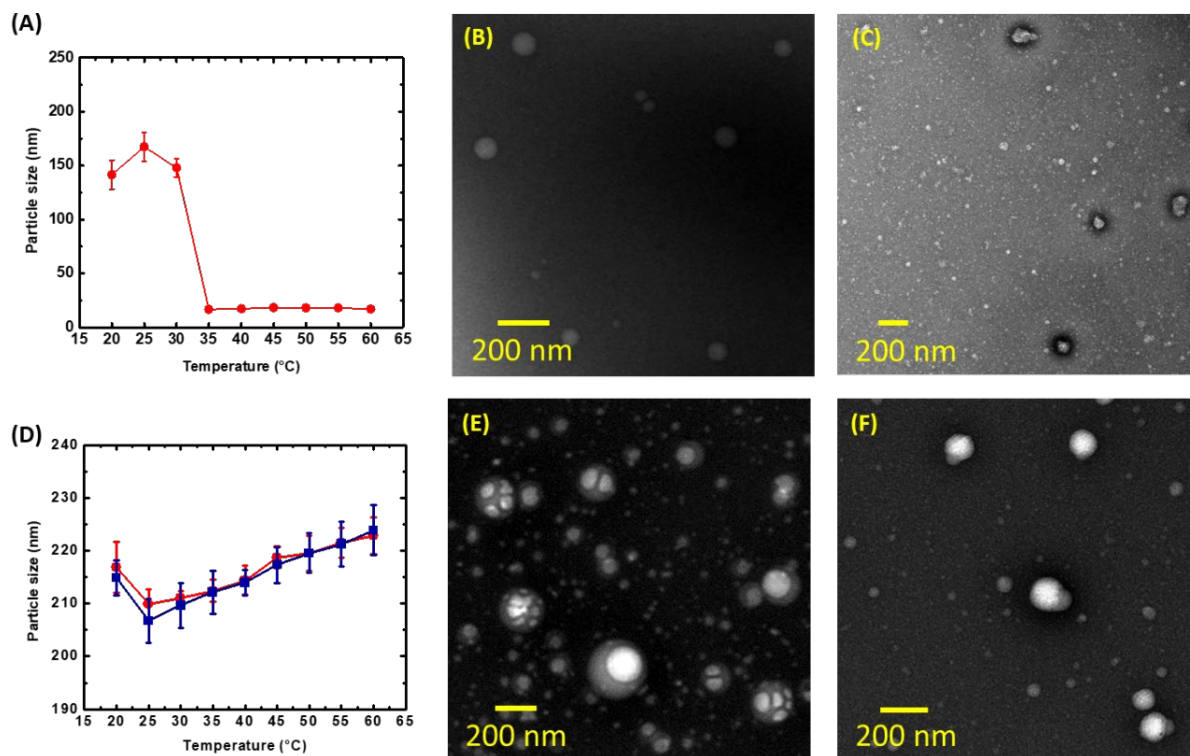
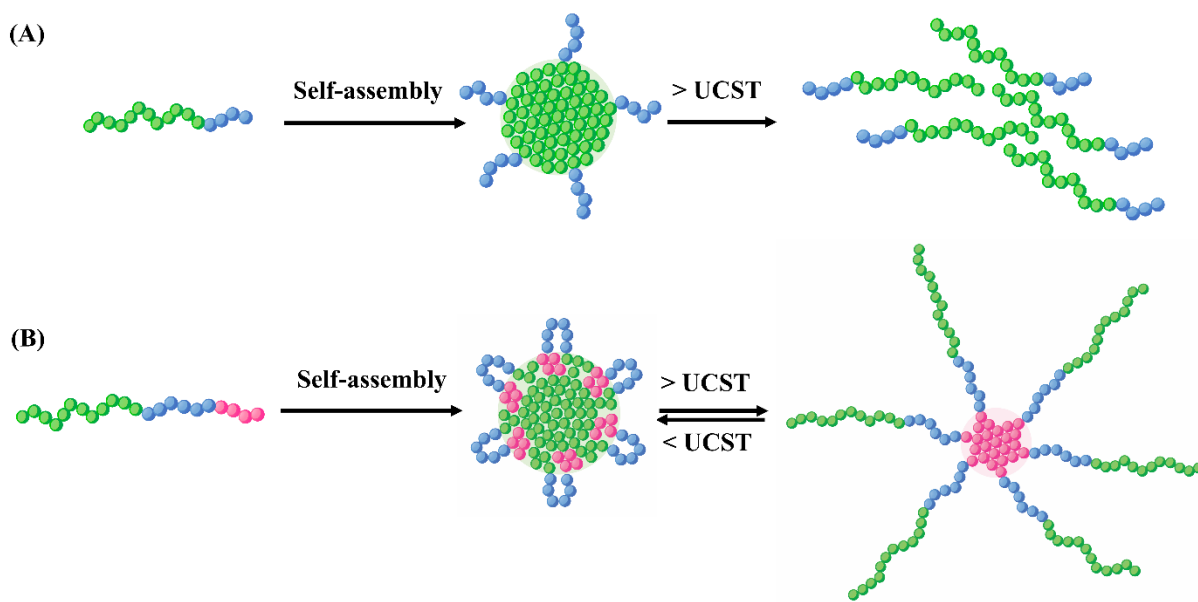


**Figure 4. 3:** DLS analyses of NPs derived from (A) P(AAm<sub>111</sub>-*co*-AN<sub>70</sub>)-*b*-PEG<sub>90</sub> (T6NPs) and (D) P(AAm<sub>111</sub>-*co*-AN<sub>70</sub>)-*b*-PEG<sub>90</sub>-*b*-PCL<sub>25</sub> (T7NPs). Studies were done across three cycles of heating-cooling, where data points shown represent the average particle size from 3 cycles. TEM image of T6NPs (B) before (20 °C) and (C) after heating (40 °C), and T7NPs (E) before (20 °C) and (F) after heating (40 °C). Samples were stained with 2% uranyl acetate solution prior to analysis.

Subsequently, we analyzed self-assemblies formed from P(AAm<sub>111</sub>-*co*-AN<sub>70</sub>)-*b*-PEG<sub>90</sub>-*b*-PCL<sub>25</sub> (T7NPs) with temperature. The same procedure utilized to self-assemble P(AAm<sub>111</sub>-*co*-AN<sub>70</sub>)-*b*-PEG<sub>90</sub> was applied. Overall, T7NPs exhibited a small increase in size from 20 °C to 60 °C, with the most significant change occurring between 20-25 °C (Figure 4. 3D). At 20 °C, the hydrodynamic diameter was measured at 216 nm, slightly decreasing to 209 nm at 25 °C. As temperature rises, the enhanced solubility of P(AAm-*co*-AN) may trigger reorganization of

T7NPs, as P(AAm-*co*-AN) transitions from the hydrophobic core to the hydrophilic shell. This may result in smaller hydrophobic cores due to the reduced P(AAm-*co*-AN) content, as well as P(AAm-*co*-AN) and PEG arms that are not yet fully extended. Thereafter, T7NPs gradually expanded with increasing temperatures to 223 nm at 60 °C. These changes in size likely stem from increase in solubility of P(AAm<sub>111</sub>-*co*-AN<sub>70</sub>)-*b*-PEG<sub>90</sub>-*b*-PCL<sub>25</sub>, inducing a reorganization of the NP structure to form a core solely consisting of PCL, alongside a more hydrophilic shell composed of extended PEG and P(AAm-*co*-AN) chains (Scheme 4. 3). This reorganization was reflected in DLS measurements as an increase in particle size, consistent with the potential flower-to-star-like transformation. In the flower-like structure, PEG chains are confined and restricted, creating a more compact hydrophilic shell which forms smaller NPs; in the star-like structure, PEG chains are extended and are more flexible, forming larger NPs. Similar observations were also reported by Wu et al., who reported larger micellar sizes formed from PCL<sub>3.4k</sub>-PEG<sub>4k</sub> (star-like) as compared to PCL<sub>1.5k</sub>-PEG<sub>4k</sub>-PCL<sub>1.5k</sub> (flower-like).<sup>80</sup> DLS analyses of the hydrodynamic diameter upon cooling demonstrated the reversibility of this system, with the size changes closely mirroring the temperature increase, albeit in reverse. The decrease in temperature likely induces phase separation of P(AAm-*co*-AN) to redistribute into the core with PCL, while PEG forms the hydrophilic shell once again, maintaining stable NPs throughout temperature variations.



**Scheme 4. 3:** Schematic illustration of (A) micelle disassembly formed from P(AAm-*co*-AN)-*b*-PEG (T6NPs) and (B) retention of micellar structure formed from P(AAm-*co*-AN)-*b*-PEG-*b*-PCL (T7NPs). Green polymer represents P(AAm-*co*-AN), blue represents PEG, and pink polymer represents PCL.

Given the limitations of DLS in ascertaining morphological changes, we analyzed our samples by TEM. The collection and preparation of TEM samples closely follow the procedures outlined for T6NPs, as described previously. Figure 4. 3E-3F illustrate representative TEM images of T7NPs before and after heating. Prior to heating, the diameters of the dried NPs were approximately 205 nm (Figure 4. 18). The smaller diameter, compared with those obtained by DLS, is due to absence of solvent swelling due to water removal during TEM sample preparation. Interestingly, distinct domains within the core were observed, as evidenced by the delineated white cores surrounded by grey domains. This observation suggests immiscibility between the core forming blocks, P(AAm-*co*-AN) and PCL, that led to microphase separation within the hydrophobic core. Similar microphase separation has been reported by Liu and Feng, who observed it in fluorocarbon-terminated Pluronic F127-based multicompartiment micelles.<sup>81</sup> Using TEM, they observed two separated phases within one micellar core, suggesting the incompatibility between the core

forming blocks, propylene oxide, and the fluorocarbon segments. Interestingly, upon heating to 40 °C, the phase separation became less apparent, resulting in more uniform core-shell structures. This observation is consistent with the expected reorganization of the NP as P(AAm-co-AN) becomes soluble, resulting in its extension to the corona. Through DLS and TEM analyses of T7NPs, it is evident that the self-assemblies are stable with temperature. The incorporation of non-thermoresponsive PCL stabilizes the overall structure across multiple heating-cooling cycles by preventing complete solubilization of the copolymer. In contrast, the absence of PCL leads to disassembled micelles, as demonstrated with T6NPs. These results showcase the stable, unique morphological transitions attainable with T7NPs, highlighting their significant potential in nanomedicine.

#### Analysis of CUR-loaded NP morphology changes through DLS and TEM

A potential application of T7NPs is the controlled release of cargo. As shown before, the self-assemblies remained stable with temperature due to the strategic incorporation of PEG, PCL, and P(AAm-co-AN). This design prevents NP disassembly, which could potentially reduce the chances of burst release while allowing multiple thermal activations for more precise cargo release. CUR was used as a model drug to evaluate temperature-controlled release through morphological changes in the NPs. The photophysical properties of CUR are well documented, which gives us a good handle in using it as a probe to understand the morphological transitions occurring in T7NPs.<sup>61, 62</sup> Drug-loaded NPs were prepared at 5.0 mg mL<sup>-1</sup>. DL% and EE% were determined by UV-Vis as 3.4 ± 0.6% and 40.8 ± 6.4%, respectively. The CUR-loaded T7NPs (CUR-NPs) were analyzed by DLS and TEM (Figure 4. 4, Figure 4. 19). With the introduction of CUR, the NPs reduced in size from 217 nm to 178 nm. Additionally, the NPs became more monodispersed, as evidenced by the reduced peak widths in the hydrodynamic diameter distribution (Figure 4. 4A). Hydrophobic drugs such as CUR can provide additional driving force for self-assembly to give denser and smaller micelles, which explains the smaller size observed.<sup>82</sup>

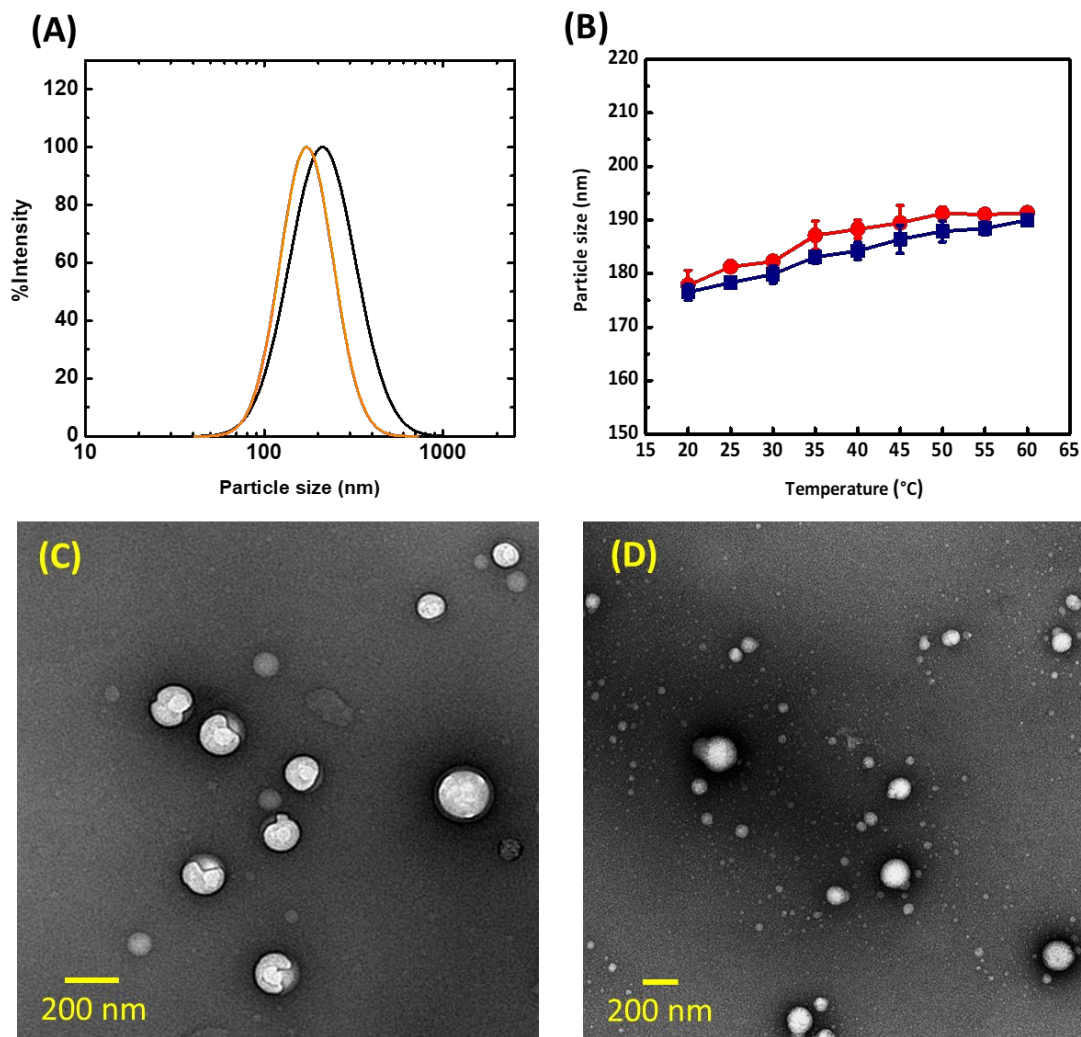


**Figure 4. 4:** (A) DLS distribution curves of T7NPs (black) and CUR-loaded T7NPs (CUR-NPs, orange), (B) DLS analyses of CUR-NPs with temperature, (C) TEM image of CUR-NPs before heating (20 °C), and (D) after heating (40 °C). Samples were stained with 2% uranyl acetate solution prior to analysis.

Subsequently, we analyzed the particle size change of T7NPs with respect to temperature. To ensure the stability of CUR throughout the experiment, temperatures ranging from 20-60 °C were employed. In general, CUR's stability with temperature varies depending on the solvent. For instance, CUR remains stable in methanol up to 80 °C.<sup>83</sup> However, when introduced into aqueous

buffer/ methanol mixtures (50:50 (v/v), pH 8.0) between 37-60 °C, CUR undergoes rapid degradation.<sup>84</sup> Nevertheless, encapsulation of CUR into NPs has been proven to improve its thermal stability.<sup>85-87</sup> Upon heating, T7NPs gradually increased in size, reaching 191 nm when heated to 60 °C (Figure 4. 4B). The NPs then decreased back to approximately the same size upon cooling (177 nm). This trend was consistent across three cycles of heating-cooling, demonstrating the stability and reversibility of the CUR-NPs with temperature variations. Our design strategy with the composition in the model ABC polymer [P(AAm-*co*-AN), PEG, and PCL] seems to confer stability to the NPs over a range of temperatures. This design could potentially result in drug delivery systems with reduced accumulation of drug at unintended sites.

To ascertain the morphology and stability in detail, we performed TEM studies to visualize changes in CUR-NPs. The NPs were analyzed before (Figure 4. 4C, Figure 4. 19) and after heating (Figure 4. 4D). As seen in Figure 4. 4C, CUR-NPs formed spherical particles, with diameters of approximately 148 nm. Interestingly, the NPs showed microphase separation within the core, albeit being less distinct as compared to the blank counterpart. This observation suggests that CUR induces reorganization of the internal structure of NPs. Similar observations have been reported by Schulz et al., who noted a drug-induced morphological switch in poly(2-oxazoline)-based micelles.<sup>88</sup> In their study, they found that aggregation of an ABA (A = poly(2-methyl-2-oxazoline), B = poly(2-n-butyl-2-oxazoline)) triblock copolymer changed from worm-like to spherical micelles when paclitaxel was added. We then examined TEM images of CUR-NPs upon heating (Figure 4. 4D), using the same procedure as outlined for T6NPs, and noticed that CUR-NPs had an approximate size of 160 nm. Similar to what was observed with empty NPs, more uniform structures were seen, which suggests morphological transition of NPs with temperature. It suggests retention of micellar structure from strategically incorporated P(AAm-*co*-AN), PEG, and PCL segments, and offers avenues in introducing stable temperature-mediated morphology changes.

### Evaluation of CUR-NPs morphology changes using UV-Vis

To further understand the microenvironments of CUR-NPs, we turned to UV-Vis to carry out a detailed evaluation using the emission spectra of CUR at varied temperatures. Since CUR has photophysical properties sensitive to its environment, the absorption profiles serve as an indication of the hydrophilic or hydrophobic environment. For instance, CUR absorption shows a notable shift to longer wavelengths with an increase in solvent polarity, such as 406 nm in hexane and 420 nm in methanol.<sup>89</sup> As shown in Figure 4. 5A, CUR-NPs showed an absorption peak at approximately 425 nm, which is slightly red-shifted from well-solvated conditions (methanol). The appearance of a vibronic structure as indicated by the shoulder at 457 nm implies crystallization within the NP. In addition, the absorption profile is different from CUR in water, which shows low intensity peaks at 237, 345, and 419 nm at room temperature.<sup>90</sup> These observations suggest that CUR is in a favorable environment promoted by encapsulation in T7NPs.

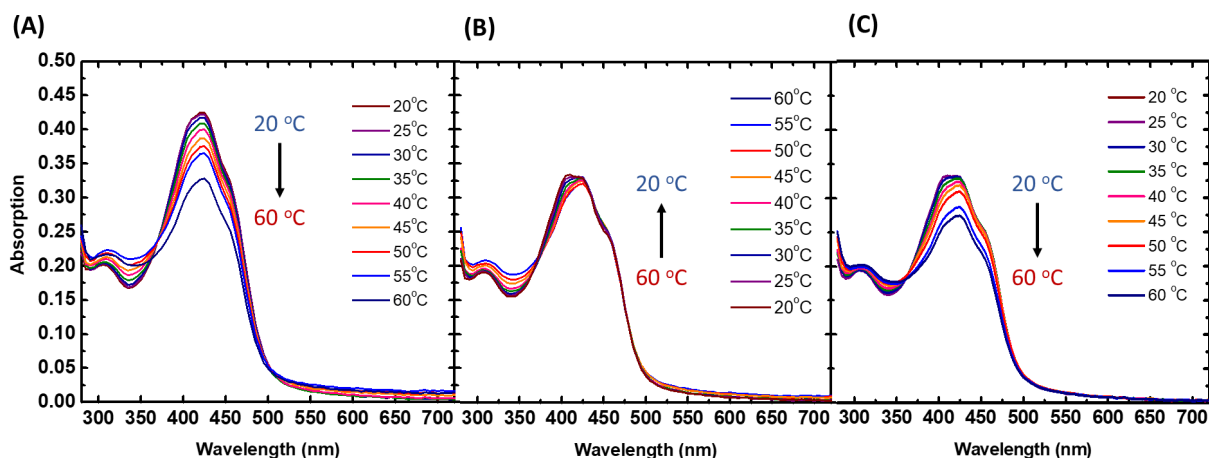


**Figure 4. 5:** UV-Vis spectra of CUR-loaded T7NP ( $c = 5.0 \text{ mg mL}^{-1}$ ) (A) heated from 20 to 60 °C, (B) subsequently cooled from 60 to 20 °C, and (C) heated again to 60 °C.

We subsequently examined the absorption spectra of CUR-NPs at different temperatures. In general, CUR's absorption spectra with temperature varies depending on the solvent. For instance, CUR in methanol exhibits no significant change when heated, whereas in water, the absorption intensities of CUR at 237, 345, and 419 nm increase at higher temperature due to enhanced aqueous

solubility.<sup>62</sup> When CUR-NPs were first heated from 20-60 °C, we observed decreasing absorption intensities with temperature (Figure 4. 5A). This may be due to the increased solubility of P(AAm<sub>111</sub>-*co*-AN<sub>70</sub>)-*b*-PEG<sub>90</sub>-PCL<sub>25</sub> that promotes micelle transition to form a smaller core size that is able to retain CUR. This reorganization will promote CUR movement, as reflected in the lower intensities observed. When the system was cooled back to 20 °C, we saw insignificant changes to the peak intensity at 425 nm (Figure 4. 5B). This attenuation in CUR is likely due to the decrease in P(AAm<sub>111</sub>-*co*-AN<sub>70</sub>)-*b*-PEG<sub>90</sub>-*b*-PCL<sub>25</sub> solubility that induced a reorganization of the NP, which can impede CUR mobility. When the system was reheated to 60 °C, CUR absorption intensity reduced further, suggesting a second transition of the system that influences CUR distribution (Figure 4. 5C). These observations are in line with what we expect of the CUR reorganization with respect to the NP morphology transitioning with temperature. As the morphology changes, the increased or decreased solubility of P(AAm-*co*-AN) leads to core size and packing differences that affect CUR distribution. These results highlight the substantial potential in utilizing CUR-NPs as nanocarriers for spatiotemporal control over drug release.

#### Analysis of CUR-NP morphology changes through fluorescence studies

We explored using CUR as a fluorescent probe to investigate the environment it is in when encapsulated in NPs. It is known that CUR's fluorescence shows solvent-dependent shifts in the emission maxima, exhibiting a red shift with increasing solvent polarity.<sup>91</sup> For instance, the observed fluorescence maxima are 439 nm (hexane), 540 nm (methanol), and 550 nm (water).<sup>62</sup> The change in CUR emission profiles in different environments makes it a valuable tool for examining the environment of NPs, and this was utilized to evaluate potential NP morphological changes from a flower-to-star-like structure. The absorption profiles could provide information about the microenvironment of CUR within the NP. Initially, CUR is encapsulated in a hydrophobic core formed from both P(AAm-*co*-AN) and PCL, whereas upon heating, the core is formed solely from PCL. Consequently, we expect the differing core environments to be reflected in the emission spectra.

CUR-NPs ( $c = 5.0 \text{ mg mL}^{-1}$ ) were excited at  $\lambda_{\text{ex}} = 420 \text{ nm}$  in the emission range of 450–700 nm, and the fluorescence spectra at each temperature point were collected when the solution was heated from 20 to 60 °C (Figure 4. 6A), and then subsequently cooled from 60 to 20 °C (Figure 4. 6B). Prior to heating, we observed peak maxima at 533 and 582 nm, suggesting CUR encapsulation in two different environments. This observation (as noted using TEM analyses) suggests that immiscibility of P(AAm-co-AN) and PCL would place CUR in different NP environments. When the solution was heated to 60 °C, a reduction in both peak intensities was noted, suggesting diffusion of CUR from the NP. Upon cooling, the intensity of both peaks increased, indicating re-distribution of CUR within the NP. The reversible nature of this transition suggests that temperature can be utilized to control CUR mobility in CUR-NPs. Furthermore, two noteworthy observations were made. Firstly, the peak at 582 nm was initially higher in intensity compared to 533 nm. However, upon heating, the intensity diminished to nearly match that of 533 nm; upon cooling, while the intensity increased, it did not fully restore to surpass that of 533 nm. This implies that the reorganization of the NP resulted in CUR being re-distributed in the core-shell structures. The second interesting observation was the absence of any shift in both peak maxima, suggesting CUR environment remained largely unchanged throughout the temperature cycling process, highlighting the stability provided to CUR by these environments. Additional experiments, such as small-angle x-ray scattering studies, could provide invaluable insights into changes in NP core/shell size and a detailed understanding of these transitions.

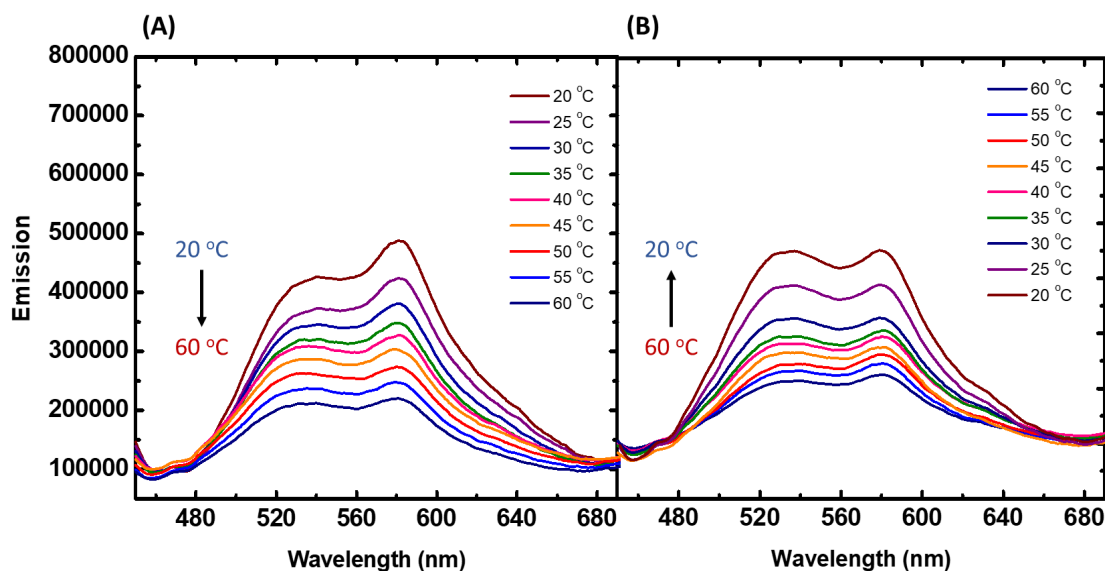


**Figure 4. 6:** Fluorescence spectrum of CUR-loaded T7NP with temperature ( $c = 5.0 \text{ mg mL}^{-1}$ ) (A) heated from 20 to 60 °C and (B) subsequently cooled from 60 to 20 °C.

#### Evaluation of drug release under physiological conditions

CUR release studies were subsequently conducted in phosphate buffer saline (PBS, 0.01 M, pH 7.4) under three different conditions: 25 °C, 37 °C, and alternating between the two (Figure 4. 7). When comparing the release profiles at 25 °C and 37 °C, we observed a temperature-dependent behavior, with a 19-38% increase in CUR release at the higher temperature. For instance, CUR release reached 48% in 2 h at 25 °C, and increased to 69% at 37 °C. At 4 h, the release was 59% (25 °C)/ 83% (37 °C); 63% (25 °C)/ 91% (37 °C) in 6 h, 64% (25 °C)/ 92% (37 °C) in 8 h, 69% (25 °C)/ 93% (37 °C) in 12 h, 74% (25 °C)/ 97% (37 °C) in 24 h, 76% (25 °C)/ 97% (37 °C) in 32 h, and 80% (25 °C)/ 99% (37 °C) in 50 h. Additionally, there was a significant release of CUR under physiological conditions (mimicked during drug release studies). It is possible that CUR release that was subjected to large volume of PBS (140 mL) promoted its diffusion to the external medium to satisfy the concentration equilibrium, resulting in rapid release of drug.<sup>92</sup> We also examined CUR release at alternating temperatures to assess any controllable release patterns. The temperature was changed as follows: 0-4 h: 25 °C, 4-8 h: 37 °C, 8-12 h: 25 °C, 12-24 h: 37 °C, 24-32 h: 25 °C, 32-50 h: 37 °C. While we were able to change temperature periodically and modulate

CUR release, it was challenging to ascertain controlled release with temperature variations as CUR release remained consistently high under sink conditions. Specifically, CUR release reached 58% in 2 h, 75% in 4 h, 80% in 6 h, 81% in 8 h, 86% in 12 h, 91% in 24 h, 94% in 32 h, and 98% in 50 h.

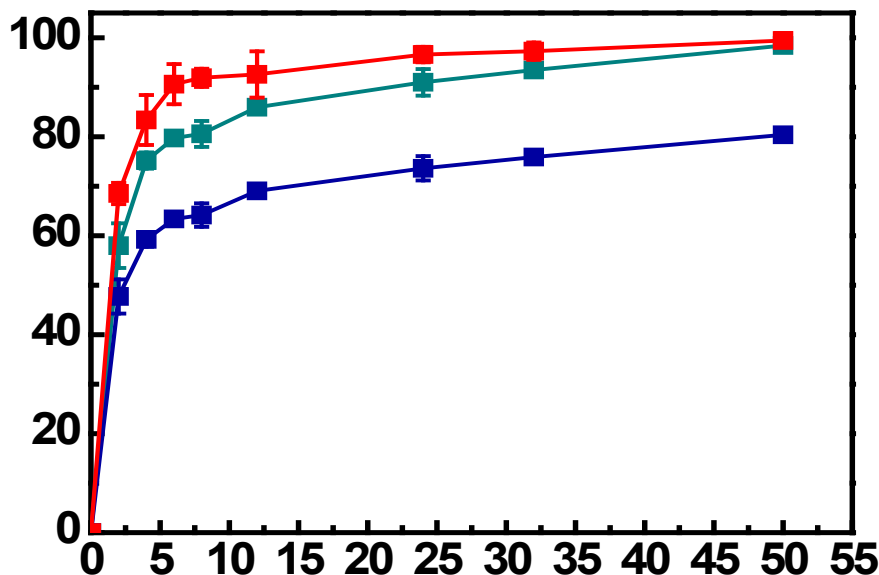


**Figure 4. 7:** Drug release of CUR-NP at different temperatures: 25 °C (blue), 37 °C (red), and alternating temperatures (green, 0-4 h: 25 °C, 4-8 h: 37 °C, 8-12 h: 25 °C, 12-24 h: 37 °C, 24-32 h: 25 °C, 32-50 h: 37 °C). All drug release studies were conducted in PBS buffer (pH 7.4, 0.01 M) with 1 wt% Tween 80 added.

#### 4.6. Conclusions

A triblock copolymer with strategic spatial location of individual polymer fragments with pre-defined tasks, P(AAm<sub>111</sub>-*co*-AN<sub>70</sub>)-*b*-PEG<sub>90</sub>-*b*-PCL<sub>25</sub>, offers a versatile platform in designing soft NPs that can undergo thermoresponsive phase transitions for sustained and controlled cargo release. Leveraging the UCST behavior of P(AAm-*co*-AN), it was conjugated to hydrophilic PEG and hydrophobic PCL, in this sequence, to design NPs that could undergo reversible morphological transitions. P(AAm-*co*-AN) retains its inherent UCST characteristics in the triblock copolymer, as

evidenced by cloud point measurements, which showed concentration-dependent phase transitions influenced by chain-chain interactions within the polymer. The cloud point of the triblock copolymer ( $c = 5.0 \text{ mg mL}^{-1}$ ) was  $39 \text{ }^{\circ}\text{C}$  (heating)/  $37 \text{ }^{\circ}\text{C}$  (cooling), close to the desired physiological conditions. The strategic placement of each fraction in P(AAm-co-AN)-PEG-PCL facilitates formation of self-assembled NPs capable of undergoing stable, temperature-directed morphological transformations. Upon loading CUR into these UCST-responsive NPs, CUR undergoes temperature-controlled core-shell redistribution driven by these morphological transitions, which are triggered by temperature variations. CUR release is controlled by temperature-dependent NP transformations, demonstrating the potential of these NPs as versatile drug delivery nanocarriers with tunable cargo release profiles. Our results highlight the importance of structural design in enabling temperature-sensitive nanocarriers, and expanding the scope of UCST-based morphological transformations in nanomedicine.

#### 4.7. References

1. Shymborska, Y.; Budkowski, A.; Raczkowska, J.; Donchak, V.; Melnyk, Y.; Vasiichuk, V.; Stetsyshyn, Y. Switching It Up: The Promise of Stimuli-Responsive Polymer Systems in Biomedical Science. *Chem. Rec.* **2024**, *24* (2), e202300217.
2. Singh, D.; Sharma, Y.; Dheer, D.; Shankar, R. Stimuli Responsiveness of Recent Biomacromolecular Systems (Concept to Market): A Review. *Int. J. Biol. Macromol.* **2024**, *261*, 129901.
3. Wu, W.; Mitra, N.; Yan, E. C. Y.; Zhou, S. Multifunctional Hybrid Nanogel for Integration of Optical Glucose Sensing and Self-Regulated Insulin Release at Physiological pH. *ACS Nano* **2010**, *4* (8), 4831-4839.
4. Zhang, Q. M.; Berg, D.; Duan, J.; Mugo, S. M.; Serpe, M. J. Optical Devices Constructed from Ferrocene-Modified Microgels for  $\text{H}_2\text{O}_2$  Sensing. *ACS Appl. Mater. Interfaces* **2016**, *8* (40), 27264-27269.

5. Kolouchova, K.; Sedlacek, O.; Jirak, D.; Babuka, D.; Blahut, J.; Kotek, J.; Vit, M.; Trousil, J.; Konefał, R.; Janouskova, O.; et al. Self-Assembled Thermoresponsive Polymeric Nanogels for  $^{19}\text{F}$  MR Imaging. *Biomacromolecules* **2018**, *19* (8), 3515-3524.
6. Fu, C.; Tang, J.; Pye, A.; Liu, T.; Zhang, C.; Tan, X.; Han, F.; Peng, H.; Whittaker, A. K. Fluorinated Glycopolymers as Reduction-Responsive  $^{19}\text{F}$  MRI Agents for Targeted Imaging of Cancer. *Biomacromolecules* **2019**, *20* (5), 2043-2050.
7. Duan, Z.; Cai, H.; Zhang, H.; Chen, K.; Li, N.; Xu, Z.; Gong, Q.; Luo, K. PEGylated Multistimuli-Responsive Dendritic Prodrug-Based Nanoscale System for Enhanced Anticancer Activity. *ACS Appl. Mater. Interfaces* **2018**, *10* (42), 35770-35783.
8. Feng, Q.; Xu, J.; Liu, X.; Wang, H.; Xiong, J.; Xiao, K. Targeted Delivery by pH-Responsive mPEG-S-PBLG Micelles Significantly Enhances the Anti-Tumor Efficacy of Doxorubicin with Reduced Cardiotoxicity. *Drug Deliv.* **2021**, *28* (1), 2495-2509.
9. Willott, J. D.; Nielen, W. M.; de Vos, W. M. Stimuli-Responsive Membranes through Sustainable Aqueous Phase Separation. *ACS Appl. Polym. Mater.* **2020**, *2* (2), 659-667.
10. Karimi, M.; Sahandi Zangabad, P.; Ghasemi, A.; Amiri, M.; Bahrami, M.; Malekzad, H.; Ghahramanzadeh Asl, H.; Mahdieh, Z.; Bozorgomid, M.; Ghasemi, A.; et al. Temperature-Responsive Smart Nanocarriers for Delivery of Therapeutic Agents: Applications and Recent Advances. *ACS Appl. Mater. Interfaces* **2016**, *8* (33), 21107-21133.
11. Kim, Y.-J.; Matsunaga, Y. T. Thermo-Responsive Polymers and Their Application as Smart Biomaterials. *J. Mater. Chem. B* **2017**, *5* (23), 4307-4321.
12. Alavi, S. E.; Alavi, S. Z.; Nisa, M. u.; Koohi, M.; Raza, A.; Ebrahimi Shahmabadi, H. Revolutionizing Wound Healing: Exploring Scarless Solutions through Drug Delivery Innovations. *Mol. Pharm.* **2024**, *21* (3), 1056-1076.

13. Vanparijs, N.; Nuhn, L.; De Geest, B. G. Transiently Thermoresponsive Polymers and Their Applications in Biomedicine. *Chem. Soc. Rev.* **2017**, *46* (4), 1193-1239.
14. Fan, X.; Cheng, H.; Wang, X.; Ye, E.; Loh, X. J.; Wu, Y.-L.; Li, Z. Thermoresponsive Supramolecular Chemotherapy by “V”-Shaped Armed  $\beta$ -Cyclodextrin Star Polymer to Overcome Drug Resistance. *Adv. Healthcare Mater.* **2018**, *7* (7), 1701143.
15. Xu, X.; Bizmark, N.; Christie, K. S. S.; Datta, S. S.; Ren, Z. J.; Priestley, R. D. Thermoresponsive Polymers for Water Treatment and Collection. *Macromolecules* **2022**, *55* (6), 1894-1909.
16. Sharma, R.; Ungar, D.; Dyson, E.; Rimmer, S.; Chechik, V. Functional Magnetic Nanoparticles for Protein Delivery Applications: Understanding Protein–Nanoparticle Interactions. *Nanoscale* **2024**, *16* (5), 2466-2477.
17. Zeqiri, E.; da Silva, M. A.; Aspinall, S. R.; Hoffman, E.; Hutter, V.; Cook, M. T. Thermoreversible Gels for the Encapsulation of Macrophages: Evaluation of Polymer Type on Rheology and Cytocompatibility. *RSC Appl. Polym.* **2024**, *2* (1), 32-46.
18. Doberenz, F.; Zeng, K.; Willems, C.; Zhang, K.; Groth, T. Thermoresponsive Polymers and Their Biomedical Application in Tissue Engineering – a Review. *J. Mater. Chem. B* **2020**, *8* (4), 607-628.
19. Cook, M. T.; Haddow, P.; Kirton, S. B.; McAuley, W. J. Polymers Exhibiting Lower Critical Solution Temperatures as a Route to Thermoreversible Gelators for Healthcare. *Adv. Funct. Mater.* **2021**, *31* (8), 2008123.
20. Nakamura, M.; Nishimura, S.-n.; Higashi, N.; Koga, T. Thermo-Responsive Injectable Hydrogels from Linear and Star-Shaped Block Copolymers Composed of Amino Acid-Derived Vinyl Polymer and Poly(ethylene glycol) for Biomedical Applications. *Mater. Adv.* **2024**, *5* (2), 665-674.

21. Mairal, A.; Mehrotra, S.; Kumar, A.; Maiwal, R.; Marsal, J.; Kumar, A. Hyaluronic Acid-Conjugated Thermoresponsive Polymer-Based Bioformulation Enhanced Wound Healing and Gut Barrier Repair of a TNBS-Induced Colitis Injury *Ex Vivo* Model in a Dynamic Perfusion Device. *ACS Appl. Mater. Interfaces* **2024**, *16* (5), 5382-5400.
22. Stetsyshyn, Y.; Raczowska, J.; Harhay, K.; Gajos, K.; Melnyk, Y.; Dąbczyński, P.; Shevtsova, T.; Budkowski, A. Temperature-Responsive and Multi-Responsive Grafted Polymer Brushes with Transitions Based on Critical Solution Temperature: Synthesis, Properties, and Applications. *Colloid. Polym. Sci.* **2021**, *299* (3), 363-383.
23. Luo, G.-F.; Chen, W.-H.; Zhang, X.-Z. 100<sup>th</sup> Anniversary of Macromolecular Science Viewpoint: Poly(N-isopropylacrylamide)-Based Thermally Responsive Micelles. *ACS Mater. Lett.* **2020**, *9* (6), 872-881.
24. Narumi, A.; Sato, S.-i.; Shen, X.; Kakuchi, T. Precision Synthesis for Well-Defined Linear and/or Architecturally Controlled Thermoresponsive Poly(N-substituted acrylamide)s. *Polym. Chem.* **2022**, *13* (10), 1293-1319.
25. Goyal, R.; Sahu, S.; Mitra, S.; Niranjana, R.; Priyadarshini, R.; Yadav, R.; Lochab, B. Nanocellulose-Reinforced 4D Printed Hydrogels: Thermoresponsive Shape Morphing and Drug Release. *ACS Appl. Polym. Mater.* **2024**, *6* (2), 1348-1361.
26. Yang, L.; Ren, P.; Wei, D.; Liang, M.; Xu, L.; Tao, Y.; Jiao, G.; Zhang, T.; Zhang, Q. Temperature-Controlled Screening of Catechol Groups in Poly(N-isopropylacrylamide-co-dopamine methacrylamide) for Cell Detachment. *ACS Appl. Polym. Mater.* **2024**, *6* (4), 2061-2075.
27. Zhang, X.; Ding, H.; Li, Z.; Bai, Y.; Zhang, L. A “Mesh Scaffold” That Regulates the Mechanical Properties and Restricts the Phase Transition-Induced Volume Change of the PNIPAM-Based Hydrogel for Wearable Sensors. *Mater. Horiz.* **2024**, *11* (3), 835-846.

28. Yuan, Y.; Raheja, K.; Milbrandt, N. B.; Beilharz, S.; Tene, S.; Oshabaheebwa, S.; Gurkan, U. A.; Samia, A. C. S.; Karayilan, M. Thermoresponsive Polymers with LCST Transition: Synthesis, Characterization, and Their Impact on Biomedical Frontiers. *RSC Appl. Polym.* **2023**, *1* (2), 158-189.
29. Zhang, G.; Wang, Y.; Liu, G. Poly(3-imidazolyl-2-hydroxypropyl methacrylate) – a New Polymer with a Tunable Upper Critical Solution Temperature in Water. *Polym. Chem.* **2016**, *7* (43), 6645-6654.
30. Liu, F.; Seuring, J.; Agarwal, S. Controlled Radical Polymerization of N-Acryloylglycinamide and UCST-Type Phase Transition of the Polymers. *J. Polym. Sci., Part A: Polym. Chem.* **2012**, *50* (23), 4920-4928.
31. Lan, H.; Liu, Y.; Mao, Y.; Han, J.; Wang, Y.; Wang, Y.; Wang, L. Rational Design of Hydrogen Bonds for Driving Thermo-Responsive Phase Transition and Assembly Behavior of Block Copolymer in Water. *Polym. Chem.* **2022**, *13* (18), 2674-2684.
32. Shimada, N.; Nakayama, M.; Kano, A.; Maruyama, A. Design of UCST Polymers for Chilling Capture of Proteins. *Biomacromolecules* **2013**, *14* (5), 1452-1457.
33. Le, M.; Huang, W.; Chen, K.-F.; Lin, C.; Cai, L.; Zhang, H.; Jia, Y.-G. Upper Critical Solution Temperature Polymeric Drug Carriers. *Chem. Eng. J.* **2022**, *432*, 134354.
34. Deng, Y.; Käfer, F.; Chen, T.; Jin, Q.; Ji, J.; Agarwal, S. Let There Be Light: Polymeric Micelles with Upper Critical Solution Temperature as Light-Triggered Heat Nanogenerators for Combating Drug-Resistant Cancer. *Small* **2018**, *14* (37), 1802420.
35. Hu, W.; Bai, X.; Wang, Y.; Lei, Z.; Luo, H.; Tong, Z. Upper Critical Solution Temperature Polymer-Grafted Hollow Mesoporous Silica Nanoparticles for Near-Infrared-Irradiated Drug Release. *J. Mater. Chem. B* **2019**, *7* (38), 5789-5796.

36. Fu, W.; Luo, C.; Morin, E. A.; He, W.; Li, Z.; Zhao, B. UCST-Type Thermosensitive Hairy Nanogels Synthesized by RAFT Polymerization-Induced Self-Assembly. *ACS Mater. Lett.* **2017**, *6* (2), 127-133.
37. Lim, J.; Matsuoka, H.; Yusa, S.-i.; Saruwatari, Y. Temperature-Responsive Behavior of Double Hydrophilic Carboxy-Sulfobetaine Block Copolymers and Their Self-Assemblies in Water. *Langmuir* **2019**, *35* (5), 1571-1582.
38. Ohshio, M.; Ishihara, K.; Maruyama, A.; Shimada, N.; Yusa, S.-i. Synthesis and Properties of Upper Critical Solution Temperature Responsive Nanogels. *Langmuir* **2019**, *35* (22), 7261-7267.
39. Sponchioni, M.; Rodrigues Bassam, P.; Moscatelli, D.; Arosio, P.; Capasso Palmiero, U. Biodegradable Zwitterionic Nanoparticles with Tunable UCST-Type Phase Separation under Physiological Conditions. *Nanoscale* **2019**, *11* (35), 16582-16591.
40. Zhu, Y.; Noy, J.-M.; Lowe, A. B.; Roth, P. J. The Synthesis and Aqueous Solution Properties of Sulfobutylbetaine (co)Polymers: Comparison of Synthetic Routes and Tuneable Upper Critical Solution Temperatures. *Polym. Chem.* **2015**, *6* (31), 5705-5718.
41. Vishnevetskaya, N. S.; Hildebrand, V.; Niebuur, B.-J.; Grillo, I.; Filippov, S. K.; Laschewsky, A.; Müller-Buschbaum, P.; Papadakis, C. M. Aggregation Behavior of Doubly Thermoresponsive Polysulfobetaine-*b*-Poly(N-isopropylacrylamide) Diblock Copolymers. *Macromolecules* **2016**, *49* (17), 6655-6668.
42. Zhang, H.; Tong, X.; Zhao, Y. Diverse Thermoresponsive Behaviors of Uncharged UCST Block Copolymer Micelles in Physiological Medium. *Langmuir* **2014**, *30* (38), 11433-11441.
43. Bhadran, A.; Shah, T.; Babanyinah, G. K.; Polara, H.; Taslimy, S.; Biewer, M. C.; Stefan, M. C. Recent Advances in Polycaprolactones for Anticancer Drug Delivery. *Pharmaceutics* **2023**, *15* (7), 1977.

44. Pranav, U.; Malhotra, M.; Pathan, S.; Jayakannan, M. Structural Engineering of Star Block Biodegradable Polymer Unimolecular Micelles for Drug Delivery in Cancer Cells. *ACS Biomater. Sci. Eng.* **2023**, *9* (2), 743-759.
45. Ziolo, A.; Mossety-Leszczak, B.; Walczak, M.; Strachota, B.; Strachota, A.; Awsiuk, K.; Janiszewska, N.; Raczowska, J. Synthesis and Morphology Characteristics of New Highly Branched Polycaprolactone PCL. *Molecules* **2024**, *29* (5), 991.
46. Karmegam, V.; Kuruppu, S. S.; Udamulle Gedara, C. M.; Biewer, M. C.; Stefan, M. C. Enhanced DOX Loading in Star-Like Benzyl Functionalized Polycaprolactone Micelles. *J. Polym. Sci.* **2021**, *59* (23), 3040-3052.
47. Kadam, V. S.; Nicol, E.; Gaillard, C. Synthesis of Flower-Like Poly(ethylene oxide) Based Macromolecular Architectures by Photo-Cross-Linking of Block Copolymers Self-Assemblies. *Macromolecules* **2012**, *45* (1), 410-419.
48. Li, S.; He, J.; Zhang, M.; Wang, H.; Ni, P. Multicompartment Morphologies Self-Assembled from Fluorinated ABC Triblock Terpolymers: The Effects of Flexible and Rigid Hydrophobic Moieties. *Polym. Chem.* **2016**, *7* (9), 1773-1781.
49. Baulin, V. A. Topological Changes in Telechelic Micelles: Flowers Versus Stars. *Macromolecules* **2022**, *55* (2), 517-522.
50. Mizoue, Y.; Onodera, E.; Haraguchi, K.; Yusa, S.-i. Association Behavior of Amphiphilic ABA Triblock Copolymer Composed of Poly(2-methoxyethyl acrylate) (A) and Poly(ethylene oxide) (B) in Aqueous Solution. *Polymers* **2022**, *14* (9), 1678.
51. Yang, Y.; Hua, C.; Dong, C.-M. Synthesis, Self-Assembly, and *In Vitro* Doxorubicin Release Behavior of Dendron-Like/Linear/Dendron-Like Poly( $\epsilon$ -caprolactone)-*b*-Poly(ethylene glycol)-*b*-Poly( $\epsilon$ -caprolactone) Triblock Copolymers. *Biomacromolecules* **2009**, *10* (8), 2310-2318.

52. Sun, L.; Shen, L.-J.; Zhu, M.-Q.; Dong, C.-M.; Wei, Y. Synthesis, Self-Assembly, Drug-Release Behavior, and Cytotoxicity of Triblock and Pentablock Copolymers Composed of Poly( $\epsilon$ -caprolactone), Poly(L-lactide), and Poly(ethylene glycol). *J. Polym. Sci., Part A: Polym. Chem.* **2010**, *48* (20), 4583-4593.
53. Lee, E. S.; Oh, K. T.; Kim, D.; Youn, Y. S.; Bae, Y. H. Tumor pH-Responsive Flower-Like Micelles of Poly(L-Lactic Acid)-*b*-Poly(ethylene glycol)-*b*-Poly(L-histidine). *J. Controlled Release* **2007**, *123* (1), 19-26.
54. Oh, K. T.; Oh, Y. T.; Oh, N.-M.; Kim, K.; Lee, D. H.; Lee, E. S. A Smart Flower-Like Polymeric Micelle for pH-Triggered Anticancer Drug Release. *Int. J. Pharm.* **2009**, *375* (1), 163-169.
55. Liu, B.; Chen, H.; Li, X.; Zhao, C.; Liu, Y.; Zhu, L.; Deng, H.; Li, J.; Li, G.; Guo, F.; et al. pH-Responsive Flower-Like Micelles Constructed via Oxime Linkage for Anticancer Drug Delivery. *RSC Adv.* **2014**, *4* (90), 48943-48951.
56. Nekoueyfard, E.; Radmanesh, F.; Baharvand, H.; Mahdieh, A.; Sadeghi-Abandansari, H.; Dinarvand, R. Reduction-Sensitive Flower-Like Magnetomicelles Based on PCL-SS-PEG-SS-PCL Triblock Copolymer as Anti-Cancer Drug Delivery System. *Eur. Polym. J.* **2023**, *189*, 111978.
57. Yang, Q.; He, C.; Zhang, Z.; Tan, L.; Liu, B.; Zhu, Z.; Shao, Z.; Gong, B.; Shen, Y.-M. Redox-Responsive Flower-Like Micelles of Poly(L-lactic Acid)-*b*-Poly(ethylene glycol)-*b*-Poly(L-lactic Acid) for Intracellular Drug Delivery. *Polymer* **2016**, *90*, 351-362.
58. Zhao, C.; Shuai, S.; Zhou, S.; Liu, Y.; Huo, W.; Zhu, H.; Rao, Z.; Li, Y.; Zhou, K.; Ge, W.; et al. Synthesis and Characterization of Photo-Responsive Flower-Like Copolymer Micelles with O-Nitrobenzyl as the Junction Point. *Mater. Lett.* **2020**, *261*, 127151.
59. Lin, S.; Shang, J.; Theato, P. CO<sub>2</sub>-Triggered UCST Transition of Amphiphilic Triblock Copolymers and Their Self-Assemblies. *Polym. Chem.* **2017**, *8* (17), 2619-2629.

60. Sahu, A.; Kasoju, N.; Bora, U. Fluorescence Study of the Curcumin–Casein Micelle Complexation and Its Application as a Drug Nanocarrier to Cancer Cells. *Biomacromolecules* **2008**, *9* (10), 2905-2912.
61. Manasa, P. S. L.; Kamble, A. D.; Chilakamarthi, U. Various Extraction Techniques of Curcumin—a Comprehensive Review. *ACS Omega* **2023**, *8* (38), 34868-34878.
62. Jagannathan, R.; Abraham, P. M.; Poddar, P. Temperature-Dependent Spectroscopic Evidences of Curcumin in Aqueous Medium: A Mechanistic Study of Its Solubility and Stability. *J. Phys. Chem. B* **2012**, *116* (50), 14533-14540.
63. Banerjee, C.; Maiti, S.; Mustafi, M.; Kuchlyan, J.; Banik, D.; Kundu, N.; Dhara, D.; Sarkar, N. Effect of Encapsulation of Curcumin in Polymeric Nanoparticles: How Efficient to Control Esipt Process? *Langmuir* **2014**, *30* (36), 10834-10844.
64. Bhopate, D. P.; Mahajan, P. G.; Garadkar, K. M.; Kolekar, G. B.; Patil, S. R. A Highly Selective and Sensitive Single Click Novel Fluorescent Off–On Sensor for Copper and Sulfide Ions Detection Directly in Aqueous Solution Using Curcumin Nanoparticles. *New J. Chem.* **2015**, *39* (9), 7086-7096.
65. Hakeem, A.; Zahid, F.; Duan, R.; Asif, M.; Zhang, T.; Zhang, Z.; Cheng, Y.; Lou, X.; Xia, F. Cellulose Conjugated FITC-Labelled Mesoporous Silica Nanoparticles: Intracellular Accumulation and Stimuli Responsive Doxorubicin Release. *Nanoscale* **2016**, *8* (9), 5089-5097.
66. Yong, H. W.; Ferron, M.; Mecteau, M.; Mihalache-Avram, T.; Lévesque, S.; Rhéaume, É.; Tardif, J.-C.; Kakkar, A. Single Functional Group Platform for Multistimuli Responsivities: Tertiary Amine for CO<sub>2</sub>/pH/ROS-Triggered Cargo Release in Nanocarriers. *Biomacromolecules* **2023**, *24* (9), 4064–4077.
67. Perrier, S. 50th Anniversary Perspective: RAFT Polymerization—a User Guide. *Macromolecules* **2017**, *50* (19), 7433-7447.

68. Niskanen, J.; Tenhu, H. How to Manipulate the Upper Critical Solution Temperature (UCST)? *Polym. Chem.* **2017**, *8* (1), 220-232.
69. Seuring, J.; Agarwal, S. First Example of a Universal and Cost-Effective Approach: Polymers with Tunable Upper Critical Solution Temperature in Water and Electrolyte Solution. *Macromolecules* **2012**, *45* (9), 3910-3918.
70. Chen, L.; Yang, T.; Niu, Y.; Mu, X.; Gong, Y.; Feng, Y.; de Rooij, N. F.; Wang, Y.; Li, H.; Zhou, G. Building a Smart Surface with Converse Temperature-Dependent Wettability Based on Poly(acrylamide-*co*-acrylonitrile). *Chem. Commun.* **2020**, *56* (19), 2837-2840.
71. Du, Y.; Liu, D.; Sun, M.; Shu, G.; Qi, J.; You, Y.; Xu, Y.; Fan, K.; Xu, X.; Jin, F.; et al. Multifunctional Gd-CuS Loaded UCST Polymeric Micelles for MR/PA Imaging-Guided Chemo-Photothermal Tumor Treatment. *Nano Research* **2022**, *15* (3), 2288-2299.
72. Otsuka, C.; Wakahara, Y.; Okabe, K.; Sakata, J.; Okuyama, M.; Hayashi, A.; Tokuyama, H.; Uchiyama, S. Fluorescent Labeling Method Re-Evaluates the Intriguing Thermoresponsive Behavior of Poly(acrylamide-*co*-acrylonitrile)s with Upper Critical Solution Temperatures. *Macromolecules* **2019**, *52* (20), 7646-7660.
73. Hei, M.; Wang, J.; Wang, K.; Zhu, W.; Ma, P. X. Dually Responsive Mesoporous Silica Nanoparticles Regulated by Upper Critical Solution Temperature Polymers for Intracellular Drug Delivery. *J. Mater. Chem. B* **2017**, *5* (48), 9497-9501.
74. Audureau, N.; Coumes, F.; Guigner, J.-M.; Nguyen, T. P. T.; Ménager, C.; Stoffelbach, F.; Rieger, J. Thermoresponsive Properties of Poly(acrylamide-*co*-acrylonitrile)-Based Diblock Copolymers Synthesized (by PISA) in Water. *Polym. Chem.* **2020**, *11*, 5998-6008.
75. Hou, L.; Wu, P. Understanding the UCST-Type Transition of P(AAm-*co*-AN) in H<sub>2</sub>O and D<sub>2</sub>O: Dramatic Effects of Solvent Isotopes. *Soft Matter* **2015**, *11* (35), 7059-7065.

76. Li, Y.; Zhang, T.; Liu, Q.; He, J. PEG-Derivatized Dual-Functional Nanomicelles for Improved Cancer Therapy. *Front. Pharmacol.* **2019**, *10*, 1-14.
77. Huang, G.; Li, H.; Feng, S.-T.; Li, X.; Tong, G.; Liu, J.; Quan, C.; Jiang, Q.; Zhang, C.; Li, Z. Self-Assembled UCST-Type Micelles as Potential Drug Carriers for Cancer Therapeutics. *Macromol. Chem. Phys.* **2015**, *216* (9), 1014-1023.
78. Bajaj, P.; Padmanaban, M. Copolymerization of Acrylonitrile with 3-Chloro, 2-Hydroxy-Propyl Acrylate and Methacrylate. *J. Polym. Sci., Polym. Chem. Ed.* **1983**, *21* (8), 2261-2270.
79. Li, W.; Huang, L.; Ying, X.; Jian, Y.; Hong, Y.; Hu, F.; Du, Y. Antitumor Drug Delivery Modulated by a Polymeric Micelle with an Upper Critical Solution Temperature. *Angew. Chem. Int. Ed.* **2015**, *54* (10), 3126-3131.
80. Wu, B.; Huang, W.-Q.; Nie, X.; Zhang, Z.; Chen, G.; Wang, H.-L.; Wang, F.; Ding, S.-G.; Hao, Z.-Y.; You, Y.-Z. The Effect of Topology of PEG Chain on the Stability of Micelles in Brine and Serum. *Colloid Interface Sci. Commun.* **2021**, *41*, 100386.
81. Liu, H.; Feng, Y. Flower-Like Multicompartment Micelles with Janus-Core Self-Assembled from Fluorocarbon-Terminated Pluronics. *Macromol. Chem. Phys.* **2018**, *219* (8), 1700558.
82. Basak, R.; Bandyopadhyay, R. Encapsulation of Hydrophobic Drugs in Pluronic F127 Micelles: Effects of Drug Hydrophobicity, Solution Temperature, and pH. *Langmuir* **2013**, *29* (13), 4350-4356.
83. Peram, M. R.; Jalalpure, S. S.; Palkar, M. B.; Diwan, P. V. Stability Studies of Pure and Mixture Form of Curcuminoids by Reverse Phase-HPLC Method under Various Experimental Stress Conditions. *Food Sci. Biotechnol.* **2017**, *26* (3), 591-602.

84. Naksuriya, O.; van Steenberg, M. J.; Torano, J. S.; Okonogi, S.; Hennink, W. E. A Kinetic Degradation Study of Curcumin in Its Free Form and Loaded in Polymeric Micelles. *The AAPS Journal* **2016**, *18* (3), 777-787.
85. Lin, D.; Xiao, L.; Qin, W.; Loy, D. A.; Wu, Z.; Chen, H.; Zhang, Q. Preparation, Characterization and Antioxidant Properties of Curcumin Encapsulated Chitosan/Lignosulfonate Micelles. *Carbohydr. Polym.* **2022**, *281*, 119080.
86. Wang, Z.; Xu, J.; Ji, F.; Liu, H.; Wang, C.; Luo, S.; Zheng, Z. Glycated Soy  $\beta$ -Conglycinin Nanoparticle for Efficient Nanocarrier of Curcumin: Formation Mechanism, Thermal Stability, and Storage Stability. *Foods* **2022**, *11* (22), 3703.
87. Liu, M.; Peng, S.; McClements, D. J.; Chen, L.; Lin, S.; Wang, W. Enhancing Stability of Curcumin-Loaded Casein Nanoparticles by Adding Liposomal Nanoparticles. *LWT* **2023**, *189*, 115405.
88. Schulz, A.; Jaksch, S.; Schubel, R.; Wegener, E.; Di, Z.; Han, Y.; Meister, A.; Kressler, J.; Kabanov, A. V.; Luxenhofer, R.; et al. Drug-Induced Morphology Switch in Drug Delivery Systems Based on Poly(2-oxazoline)s. *ACS Nano* **2014**, *8* (3), 2686-2696.
89. Singh, P. K.; Wani, K.; Kaul-Ghanekar, R.; Prabhune, A.; Ogale, S. From Micron to Nano-Curcumin by Sophorolipid co-Processing: Highly Enhanced Bioavailability, Fluorescence, and Anti-Cancer Efficacy. *RSC Adv.* **2014**, *4* (104), 60334-60341.
90. Ucisik, M. H.; Küpcü, S.; Schuster, B.; Sleytr, U. B. Characterization of Curcuemulsomes: Nanoformulation for Enhanced Solubility and Delivery of Curcumin. *J. Nanobiotechnol.* **2013**, *11* (1), 37.
91. Patra, D.; Barakat, C. Synchronous Fluorescence Spectroscopic Study of Solvatochromic Curcumin Dye. *Spectrochim. Acta, Part A* **2011**, *79* (5), 1034-1041.

92. Liu, P.; De Wulf, O.; Laru, J.; Heikkilä, T.; van Veen, B.; Kiesvaara, J.; Hirvonen, J.; Peltonen, L.; Laaksonen, T. Dissolution Studies of Poorly Soluble Drug Nanosuspensions in Non-Sink Conditions. *AAPS PharmSciTech* **2013**, *14* (2), 748-756.

#### 4.8. Appendix C: Supporting Information for Chapter 4

##### Characterization

All NMR spectra were recorded on a Bruker AVIIIHD 500 MHz spectrometer at ambient temperature. The spectra were calibrated at 2.50 ppm and 7.26 ppm for deuterated dimethyl sulfoxide (DMSO- $d_6$ ) and deuterated chloroform ( $CDCl_3$ ), respectively. The IR spectra were recorded on a Bruker ATR-FTIR infrared spectrometer Alpha II equipped with a single bounce diamond crystal and a  $LiTaO_3$  detector. Measurements were conducted from 400 to 4000  $cm^{-1}$  with a resolution of 4  $cm^{-1}$  at room temperature. Turbidity measurements, variable temperature UV-Vis, and drug release studies were recorded on a Cary50 Bio UV-Vis spectrophotometer operating with a Xenon lamp and equipped with a temperature-controlling unit. All turbidity measurements were conducted at a heating/ cooling rate of 5  $^{\circ}C\ min^{-1}$  and the optical transmittance was recorded at 670 nm. CUR release studies were measured at ambient temperatures and recording CUR absorption at 426 nm. Variable temperature UV-Vis studies were conducted at a heating/ cooling rate 5  $^{\circ}C\ min^{-1}$  and the spectra were collected from 200-800 nm. To obtain the particle sizes of NPs, a Brookhaven Instrument NanoBrook Omni installed with a 40 mW diode laser operating at 640 nm was used. The temperature-dependent measurements were conducted at a heating/ cooling rate of 5  $^{\circ}C\ min^{-1}$ . The solutions were allowed to equilibrate at each temperature point for 3 min prior to analysis. A FEI Tecnai 12 BioTwin 120 kV TEM equipped with an AMT XR80 CCD Camera System was used to investigate the morphologies of NPs. The solutions were stained with 2% uranyl acetate before imaging. The variable temperature fluorescence studies were conducted using a PTI QM4 fluorometer equipped with a rapid Peltier temperature controlled multiple position sample holder.

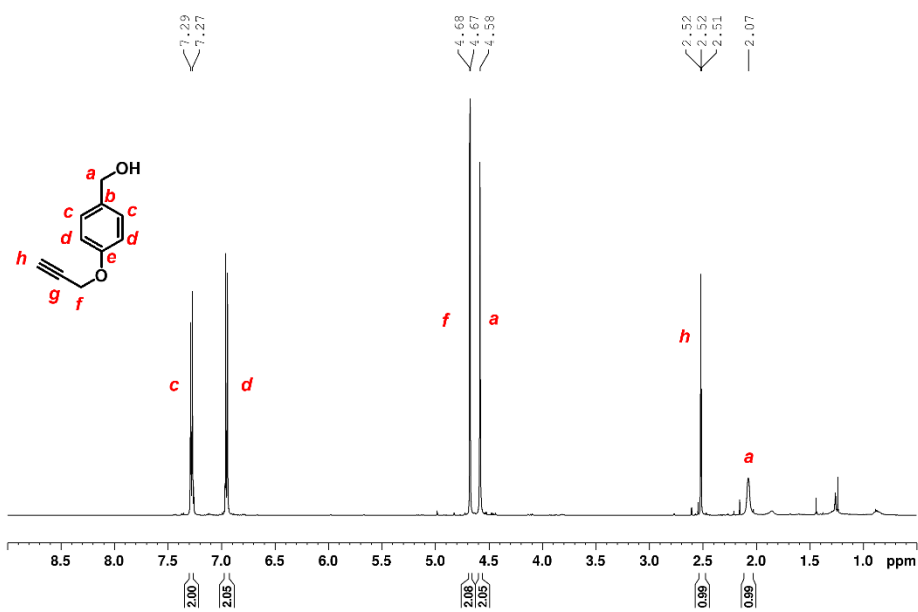
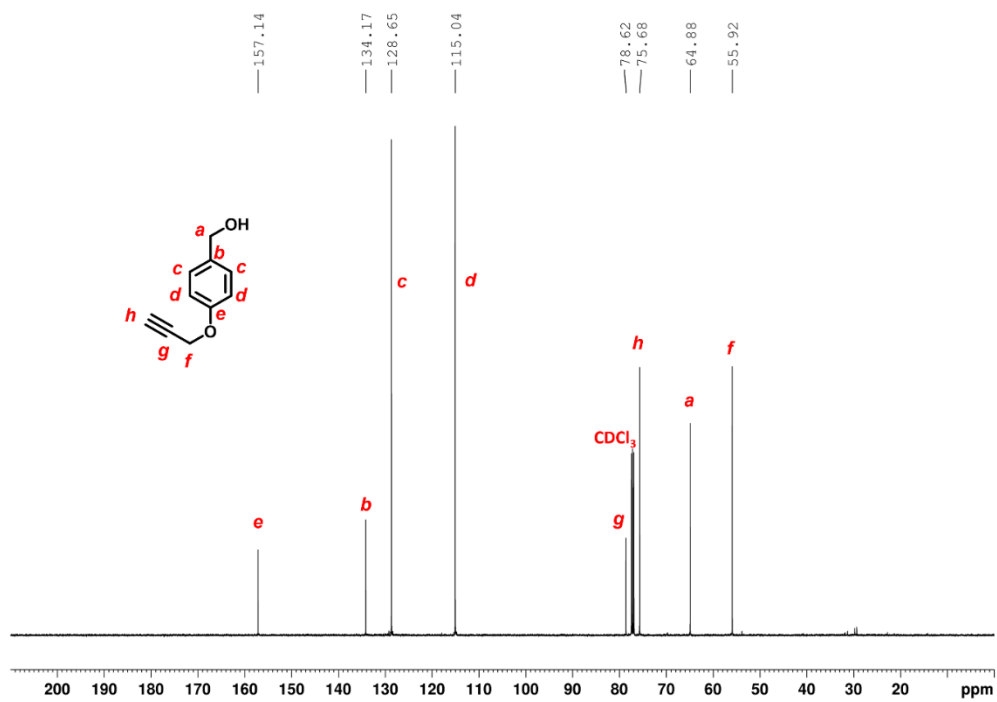
SynthesisSynthesis of 4-(prop-2-yn-1-yloxy)phenyl)methanol (4PBA)

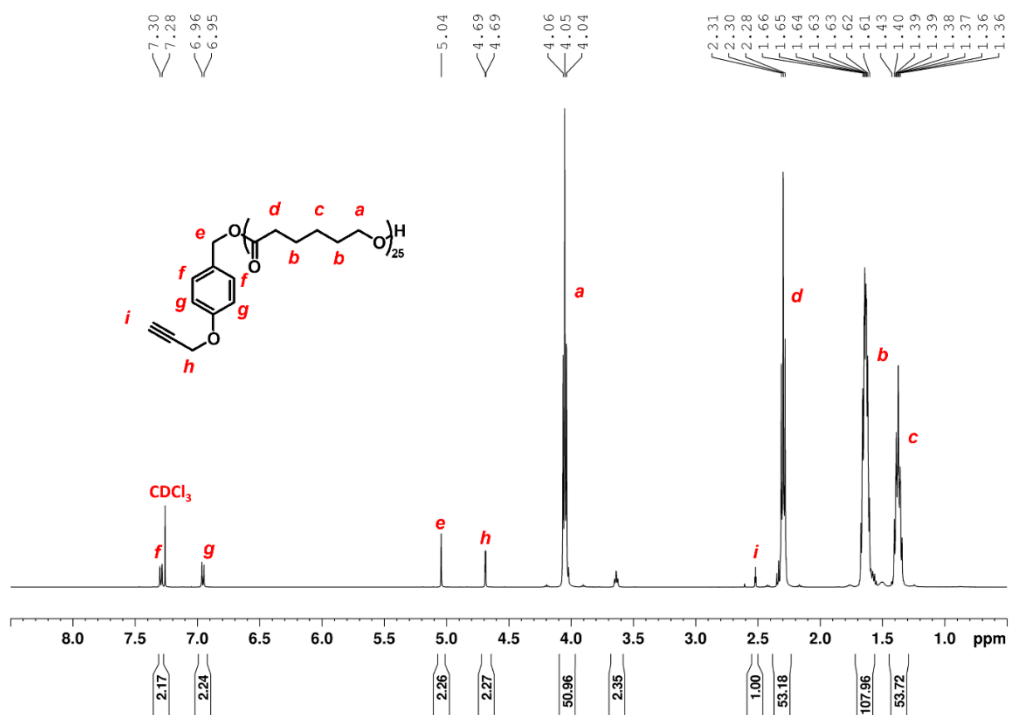
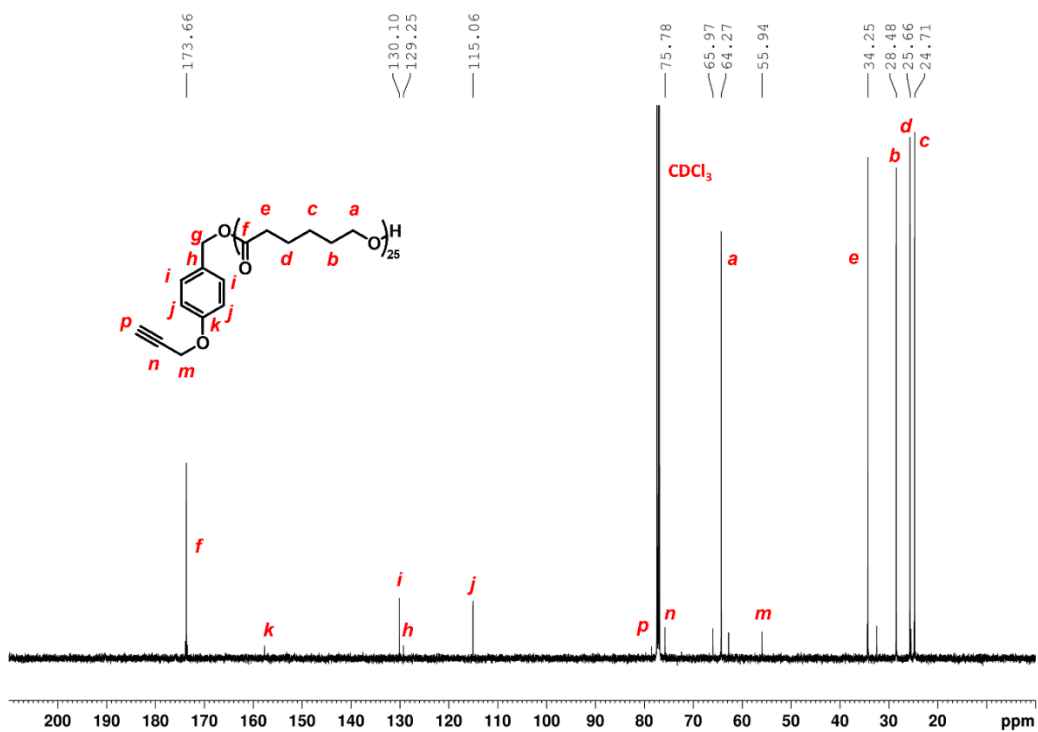
To a stirred solution of propargyl bromide (0.540 mL, 6.04 mmol, 1.5 eq) and 4-hydroxybenzyl alcohol (0.5 g, 3.93 mmol, 1 eq) in acetone (22 mL),  $K_2CO_3$  (0.724 g, 5.24 mmol, 1.3 eq) and 18-crown-6 (0.043 g, 0.163 mmol, 0.04 eq) were added and the reaction mixture was refluxed at 65 °C under nitrogen for 24 h with magnetic stirring. After cooling down to room temperature, any residue from the reaction mixture was removed by vacuum filtration. The filtrate was then evaporated to dryness under reduced pressure and partitioned between water and dichloromethane (DCM). The aqueous layer was extracted with dichloromethane (3 x 50 mL) and the combined organic extracts were dried with anhydrous  $MgSO_4$  and then dried under reduced pressure. The crude product was purified by column chromatography using 1:1 hexane and ethyl acetate. After evaporation of solvents, the product was recovered as a brown oil. Yield: 87% (2.69 g).  $^1H$  NMR (500 MHz,  $CDCl_3$ ):  $\delta$  (ppm) 2.07 (br s, 1H, -OH), 2.53 (t, 2H,  $-C\equiv CH$ ), 4.58 (s, 2H,  $-CH_2OH$ ), 4.67 (d, 2H,  $-OCH_2$ ), 7.27 (d, 2H, Ar-H), 7.29 (d, 2H, Ar-H).  $^{13}C$   $\{^1H\}$  NMR ( $CDCl_3$ , 125 MHz):  $\delta$  (ppm) 55.9, 64.9, 75.7, 78.6, 115.0, 128.7, 134.2, 157.1.

Synthesis of 4-(prop-2-ynyloxy)benzyl polycaprolactone (4PB-PCL)

T1 (0.15 g, 0.926 mmol, 1 eq) was dissolved in dry toluene and heated to 100 °C under nitrogen with magnetic stirring.  $\epsilon$ -caprolactone (2.88 mL, 25.9 mmol, 28 eq) was subsequently added to the mixture and heated to 110 °C. Tin(II) 2-ethyl hexanoate (0.03 mL, 0.09 mmol, 0.1 eq) was then added and the reaction mixture was refluxed at 115 °C for 24 h. After cooling down to room temperature, the solvent was removed under reduced pressure. The crude product was purified by dissolving in minimal DCM and precipitated in ice cold methanol. The product was collected under vacuum filtration and dried in the desiccator. Yield= 88% (1.8 g).  $^1H$  NMR (500 MHz,  $CDCl_3$ ):  $\delta$  (ppm) 1.36- 1.43 (m, 54H,  $(-OC-CH_2-CH_2-CH_2-CH_2-CH_2-O)_{27}$ ), 1.61- 1.66 (m, 108H,  $(-OC-CH_2-CH_2-CH_2-CH_2-CH_2-O)_{27}$ ), 2.30 (t, 53H,  $(-OC-CH_2-CH_2-CH_2-CH_2-CH_2-O)_{27}$ ), 2.52 (t, 2H,  $-C\equiv CH$ ), 4.05 (t, 51H,  $(-OC-CH_2-CH_2-CH_2-CH_2-CH_2-O)_{27}$ ), 4.69 (d, 2H,  $CH_2-C\equiv C$ ), 5.04 (s, 2H,  $CH_2-OH$ ), 6.95 (d, 2H, Ar-H), 7.29 (d, 2H, Ar-H).  $^{13}C$   $\{^1H\}$  NMR ( $CDCl_3$ , 125 MHz):  $\delta$  (ppm) 24.7, 25.7, 28.5, 34.3, 55.9, 64.3, 65.9, 75.8, 115.1, 129.25, 130.10, 173.7. MS: MALDI-TOF  $M_n = 3143.20$ ;  $M_w = 3351.84$ ; PDI = 1.07; DP = 27.

## Supplementary figures

Figure 4. 8:  $^1\text{H}$  NMR spectrum of 4PBA.Figure 4. 9:  $^{13}\text{C}$  NMR spectrum of 4PBA.

Figure 4. 10:  $^1\text{H}$  NMR spectrum of 4PB-PCL.Figure 4. 11:  $^{13}\text{C}$  NMR spectrum of 4PB-PCL.

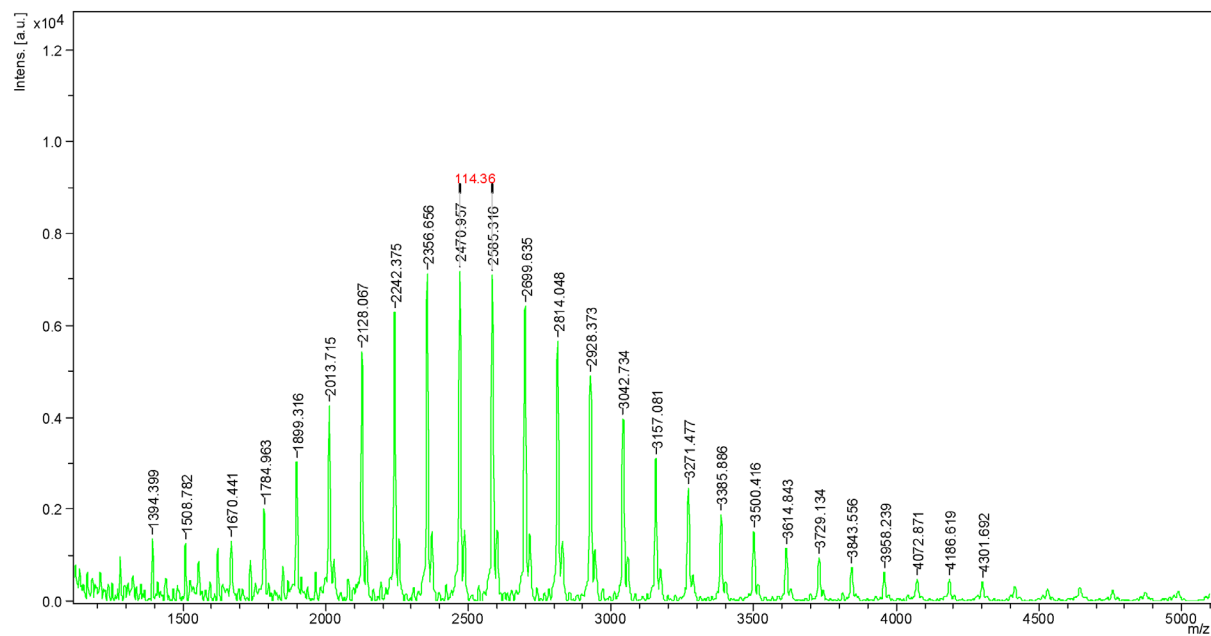


Figure 4. 12: MALDI-ToF MS spectrum of 4PB-PCL.

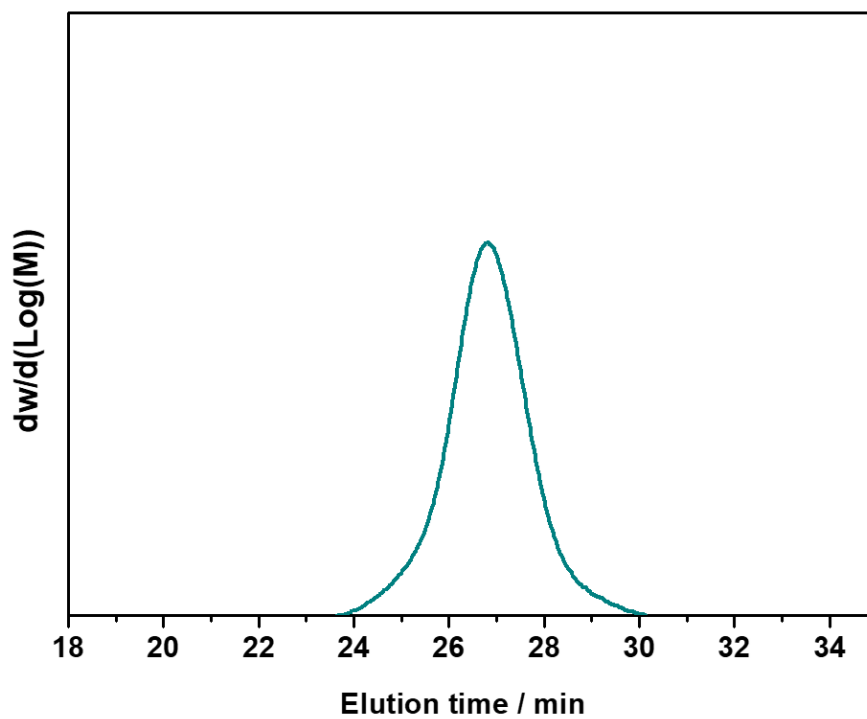


Figure 4. 13. THF GPC traces of 4PB-PCL ( $D=1.20$ ).

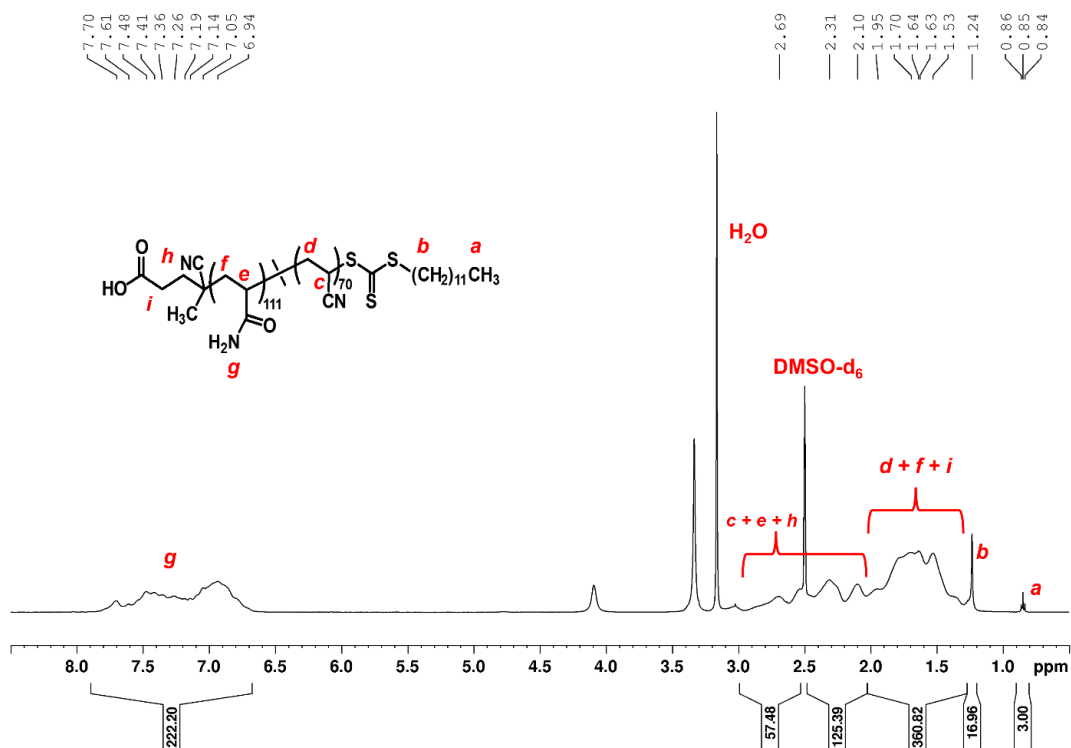


Figure 4. 14:  $^1\text{H}$  NMR spectrum of P(AAm<sub>111</sub>-co-AN<sub>70</sub>).

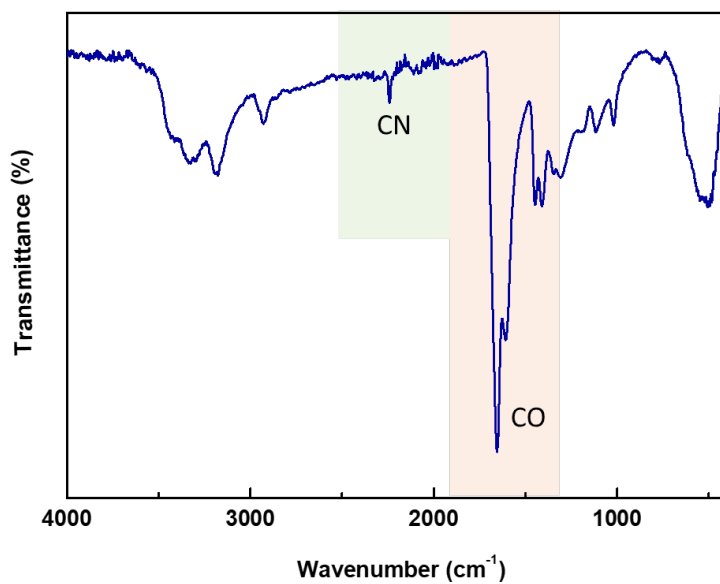


Figure 4. 15. FT-IR spectrum of P(AAm<sub>111</sub>-co-AN<sub>70</sub>).

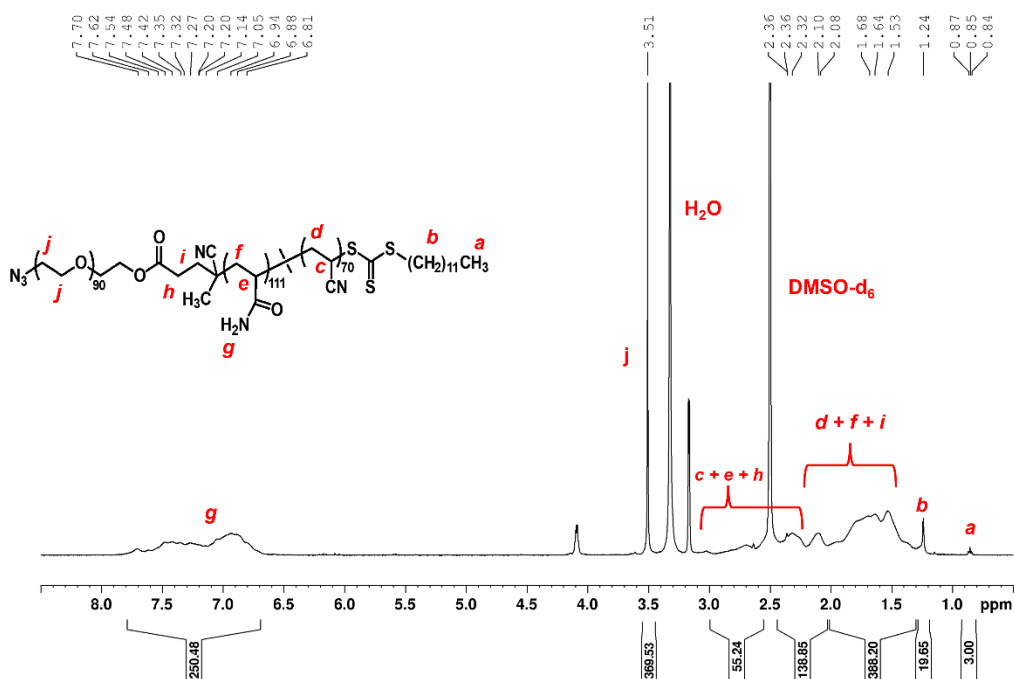


Figure 4. 16:  $^1\text{H}$  NMR spectrum of  $P(\text{AAm}_{111}\text{-co-AN}_{70})\text{-b-PEG}_{90}$ .

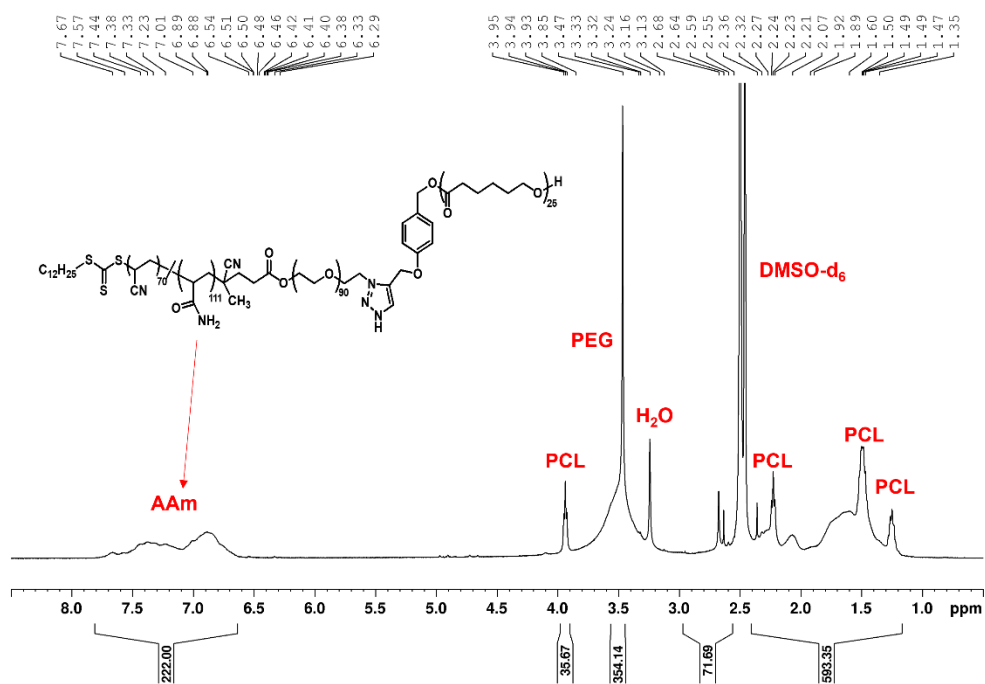
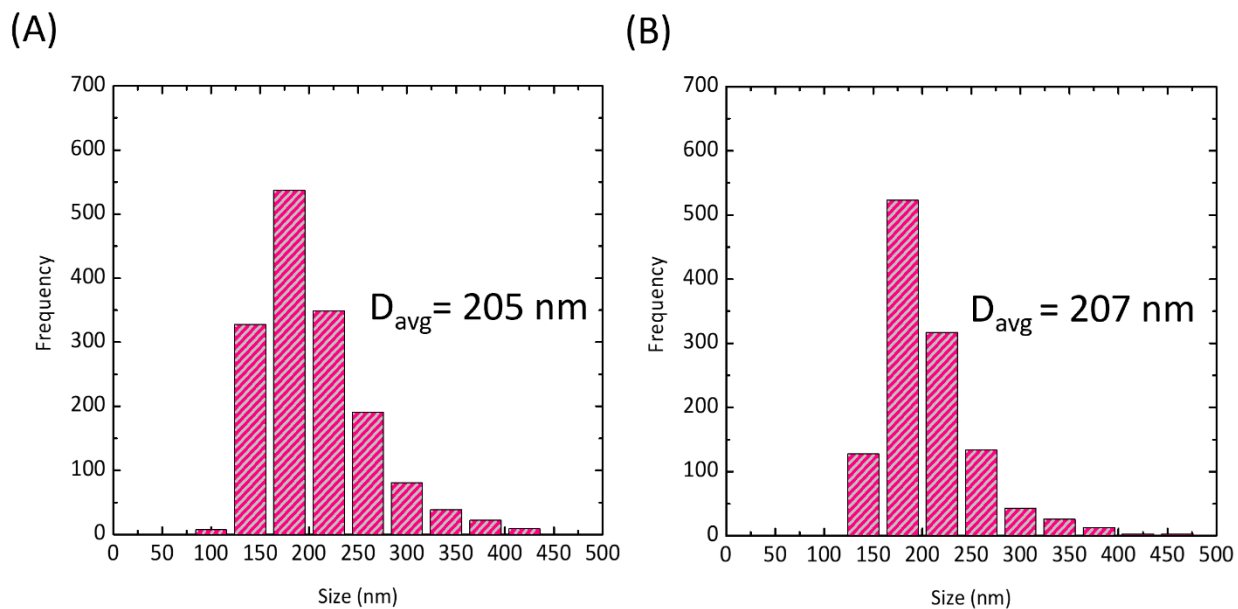
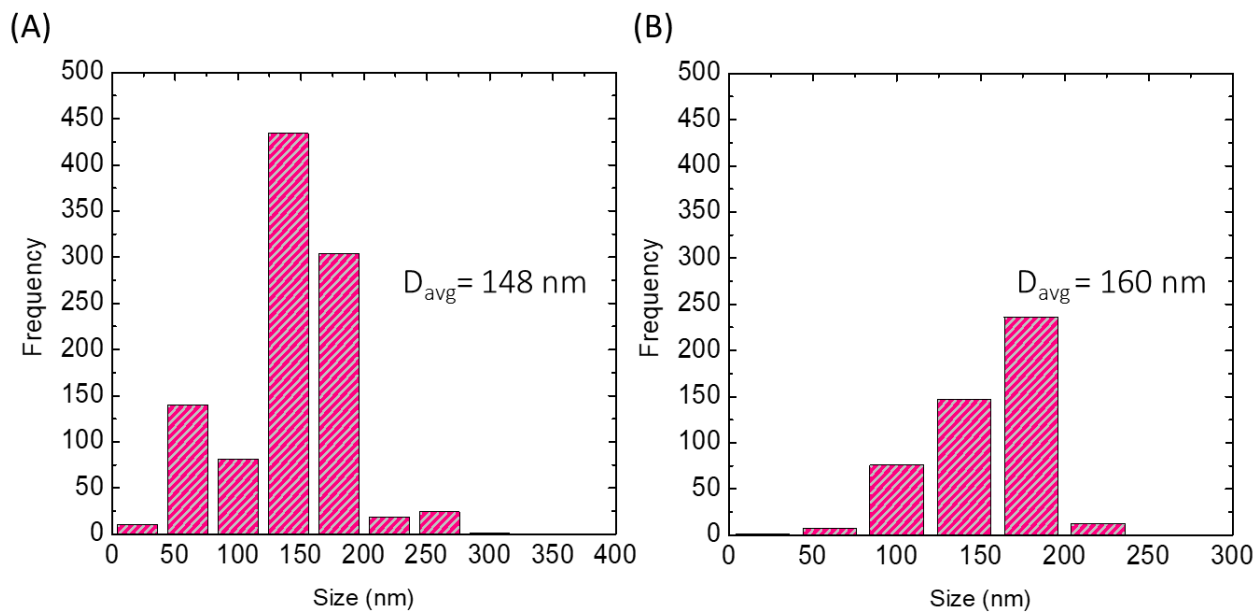


Figure 4. 17:  $^1\text{H}$  NMR spectrum of  $P(\text{AAm}_{111}\text{-co-AN}_{70})\text{-b-PEG}_{90}\text{-b-PCL}_{25}$ .



**Figure 4.18:** TEM analyses of T7NPs (A) before and (B) after heating.



**Figure 4.19:** TEM analyses of CUR-NPs (A) before and (B) after heating.

## Chapter 5: Conclusions and Outlook

### 5.1. Conclusions

This thesis contributes to the field of nanomedicine by leveraging techniques in polymer synthesis to engineer functional soft nanoparticles. It demonstrates the utility of polymerization methodologies including ring-opening polymerization (ROP) and reversible addition-fragmentation-chain transfer (RAFT); efficient post-polymerization strategies including bromination, selective monotosylation, azidation etc.; and polymer stitching methods such as copper-catalyzed alkyne-azide cycloaddition (or ‘click chemistry’), in facilitating the design and synthesis of amphiphilic miktoarm star and triblock copolymers. Such synthetic design of polymer precursors is essential in controlling desired characteristics of their aqueous self-assemblies including nanoparticle size, surface entities, and morphologies to suit diverse biomedical applications. The potential of our design strategy is elaborated specifically through: (1) core forming hydrophobic polycaprolactone (PCL) end-group functionalization with tertiary amines in branched miktoarm star polymers. It simplifies fabrication of nanoformulations that respond to multiple biological stimuli using a single chemical entity, expanding the scope of polymeric particles in nanomedicine; (2) incorporation of charged amine groups at the hydrophilic shell forming PEG termini, which leads to intrinsically active antimicrobial core-shell nanoparticles upon self-assembly. These nanoformulations concurrently provide an additional function of delivering antibacterial agents for combination therapy; and (3) design of ABC copolymers containing UCST responsive polymer strategically located in amphiphilic triblock (P(AAm-*co*-AN)-*b*-PEG-*b*-PCL) polymer. A detailed evaluation of this model system provides a platform in assembling temperature-responsive formulations which transition between two distinct and stable morphologies for controlled and sustained delivery of their cargo.

The design of nanocarriers that could collectively exploit several endogenous stimuli holds great potential in nanomedicine. However, complexity in synthetic approaches to confer multiple chemical units for responsivity has resulted in poor clinical translation of such technologies. Our research has helped simplify the design of polymer precursors to obtain nanocarriers that are responsive to multiple endogenous stimuli, including CO<sub>2</sub>, pH, ROS, and CO<sub>2</sub> + ROS. This was

achieved through incorporation of a single tertiary amine at the PCL block terminus within an AB<sub>2</sub> (A = PCL, B = PEG) miktoarm polymer. Upon self-assembly, tertiary amine formed an integral part of the hydrophobic core of the resulting spherical micelles. These nanoparticles exhibited low critical micelle concentrations, suitable hydrodynamic diameters (<200 nm), and excellent drug loading efficiencies. Drug-loaded and stable nanoformulations provided environment-selective release profiles based on the multiple stimuli at disease sites such as, dissolved CO<sub>2</sub> concentrations, variable pH; ROS, and CO<sub>2</sub> + ROS combination. *In vitro* evaluation demonstrated that curcumin loading suppresses drug toxicity at high concentrations without compromising its inhibitory efficacies. This research contributed a simple-by-design strategy in designing stimuli-responsive polymeric nanoparticles in drug delivery.

Antimicrobial drug resistance continues to pose significant challenges. We have contributed a macromolecular platform in which incorporation of surface positive charge on the shell of soft nanoparticles imparted intrinsic antimicrobial properties, as well as provided opportunities to encapsulate a desired small molecular antimicrobial agent. This dual functional antimicrobial system could be easily assembled through i) an elaboration of our methodology to synthesize miktoarm polymers with charged amino groups at the hydrophilic termini; and ii) their subsequent aqueous self-assembly. Cationic nanoparticles demonstrated intrinsic antimicrobial properties, which were shown to inhibit bacterial (*E. coli* and *B. subtilis*) growth. Introduction of the positive charge on the surface of the micelle did not impede drug delivery, and curcumin and terbinafine loaded formulation exhibited their inhibitory activity. These results expand the utility of soft nanoparticles in designing multifunctional formulations for better efficacy: antimicrobial agent (for rapid, direct inhibition) and a nanocarrier for bactericidal agent delivery (for extended inhibitory activity). Our system offers new avenues for combination therapy and combating antimicrobial resistance.

In our continued pursuit in designing stimuli-responsive polymeric precursors to cutting-edge biomedical applications, we further expanded our simple-by-design strategy in developing thermoresponsive nanoformulations that could undergo temperature-induced morphological transformations while keeping their overall structural integrity intact. We have demonstrated that one could achieve this by strategically introducing UCST thermoresponsive block, P(AAm-co-

AN) into an ABC triblock copolymer (A = PCL, B = PEG, C = P(AAm-co-AN)) triblock copolymers. The triblock copolymer showed thermoresponsive behavior, transitioning reversibly between insoluble-to-soluble states induced by temperature. Below the cloud point temperature of 39 °C, spherical micelles were formed, potentially adopting a flower-like structure with PEG in the outer shell and P(AAm-co-AN) and PCL constituting the core. When the temperature was raised above the cloud point, a morphological change was observed, likely consisting of PEG and P(AAm-co-AN) as the shell, and PCL the core. We have examined this behavior on a model ABC block copolymer utilizing DLS and TEM, which clearly established stability of nanoparticles across a range of measured temperatures (20-60 °C). UV-Vis and fluorescence spectra of the CUR-loaded nanoparticles revealed temperature-controlled drug mobility dynamics. Nanoformulations responded to temperature and drug release was accelerated at higher temperatures. It represents, to the best of our knowledge, the first example of a UCST responsive P(AAm-co-AN)-based nanoparticle which exhibits stable and reversible morphological transitions.

## 5.2. Outlook

This thesis contributes to the field of nanomedicine through polymer micelle core- and shell-functionalization strategies. However, there still remains a substantial amount of work to facilitate their bench-to-bedside transition. This thesis research has contributed a simple-by-design strategy in fabricating smart soft nanoparticles, but a detailed biological evaluation is critical and necessary to advance these innovations into pre-clinical and clinical trials. We evaluated their *in vitro* performance through limited drug and cell lines selection. It establishes their scope, which can be easily expanded to include varied pharmaceutical agents and cell lines.

As part of our ongoing collaboration with the Montréal Heart Institute, we have also initiated *in vivo* studies in mice. In this preliminary investigation, we observed that the multistimuli-responsive nanocarrier (TA-MP2, noted in Chapter 2) primarily accumulates in the kidney, liver, salivary glands, and to a certain extent, in the heart, brain, and lungs. Given that the latter areas are difficult to target with conventional drugs, these results are promising, as one could potentially deliver therapeutics for cardiovascular diseases such as olmesartan medoxomil ( $\log P=4.31$ , treats hypertension) and andrographolide ( $\log P=2.62$ , regulates inflammation due to atherosclerosis).<sup>1-3</sup> One could also transport drugs across the blood-brain barrier for treatment of neurological

disorders such as Alzheimer's disease with rivastigmine ( $\log P= 2.1$ ) and schizophrenia with aripiprazole ( $\log P= 4.55$ ).<sup>4-7</sup> As each drug and nanocarrier is unique, similar self-assemblies should be carefully examined with the appropriate drugs to work towards these therapeutic goals. Even with the same nanocarrier, the size, stability, drug loading and release rates are expected to be different depending on the aqueous solubility, size, and structure of the desired drug, as well as the drug-polymer interactions. Further *in vitro* and *in vivo* studies are warranted to ascertain the efficacy of these new drug-nanocarrier combinations. This broader exploration will enhance our understanding of the therapeutic potential of our system to advance it from bench-to-bedside.

Conventional procedures to identify suitable drug-nanocarrier combinations require a trial and error approach. Extensive time and resources are needed in adjusting parameters such as molecular weight, size, charge, and drug loading to obtain systems that are suitable for nanomedicine. These studies are typically preceded by biological evaluations to determine their efficacy in various cell lines before moving into *in vivo* experiments. It is evident that the design of nanoformulations is a complex endeavor, often lacking guaranteed success. Traditionally, the Hansen solubility parameter (HSP) and Flory-Huggins interaction parameter ( $\chi$ ) have been used in predicting the solubility and miscibility of drug-polymer mixtures.<sup>8</sup> However, HSP calculations are biased towards non-polar interactions, diminishing specific drug-polymer interactions and yielding inaccurate predictions.<sup>9</sup> In addition,  $\delta_t$  calculations rely on the group contribution method (GCM), which is severely restricted to the most common chemical moieties.<sup>10</sup> Moreover, the additive nature of GCM fails to account for geometric variations such as branched polymers.<sup>11</sup> To address these limitations, *in silico* approaches provide a more precise and rational prediction into formulation design. It has been shown that  $\chi$  obtained from molecular dynamics (MD) simulation is more accurate than  $\chi$  obtained from GCM.<sup>12</sup> When simulating the intermolecular interactions between drug and carriers, MD studies consider the local molecular arrangement in calculating the interaction energy, which is a more accurate estimation of the solvation process. Therefore, MD simulation is crucial in understanding drug-polymer solubility and miscibility before investing extensive efforts in evaluating new nanoformulations.

In addition to understanding drug-polymer interactions, it is crucial to explore potential nanoparticle behavior in biological fluids. Nanoparticles have been shown to spontaneously interact with biological molecules in the bloodstream, including lipids, proteins, and nucleic acids.

<sup>13, 14</sup> Among these biomolecules, the protein corona is one of the most extensively studied due to its significant impact on nanoparticle properties such as size, shape, and surface characteristics. <sup>15,</sup>  
<sup>16</sup> This modification can impact the distribution of nanoparticles, their interactions with cell membranes, cellular uptake, toxicity, and clearance. <sup>17, 18</sup> Furthermore, the protein corona can also act as a barrier that impacts drug release, introducing an additional layer of complexity in drug delivery systems. <sup>19</sup> Consequently, nanoparticles may exhibit behavior in biological systems that deviates from their intended design. In our studies, we utilized PEG to leverage its stealth effect and enhance the delivery of water-insoluble drugs. PEGylation has been shown to decrease protein adsorption, minimize uptake by macrophages, and prolong the circulation time of nanoparticles compared to bare nanoparticles. <sup>20</sup> However, it is important to note that PEG cannot entirely prevent the formation of protein coronas. <sup>21</sup> The stealth effect provided by PEG is influenced by factors including PEG chain length and density. <sup>22</sup> These variables play a critical role in the drug loading, release kinetics, and circulation time of nanoparticles. It would be of interest to deliberately incorporate protein coronas onto our nanoparticles to examine their self-assembly properties and drug delivery capabilities. This approach will enhance our understanding of how the protein corona affects nanoparticle functionality in complex biological environments and improve the prediction of nanoparticle performance *in vivo*.

The antibacterial nanoparticles developed in this thesis offer great potential which needs to be further explored. Intrinsic antimicrobial activity of these formulations against *E. coli* (Gram negative) and *B. subtilis* (Gram positive), as well as their prospect as delivery agents has been evaluated here for potential drug-nanocarrier synergistic effects. SEM images suggest that P7-micelles inhibit the growth of both bacterial strains through cell membrane disruption. It would be of interest to further elucidate the mode of antibacterial action with mechanistic studies. For example, Hoque et al. utilized 3,3'-dipropylthiadicarbocyanine iodide (diSC<sub>3</sub>(5)) as a fluorescence dye to track its accumulation in the membranes of *S. aureus* and *E. coli*. <sup>23</sup> They observed an increase in fluorescence intensity when the membrane potential was disrupted as the dye was released into solution, complementing their results obtained from SEM and fluorescence microscopy. Applying the same dye to our systems would provide a more comprehensive understanding of the inhibition mechanism. Additionally, Hoque et al. studied the antifungal activity of their cationic polymers. In general, antifungal activity studies are performed similarly

to antibacterial activity studies, where the OD<sub>600</sub> of the fungal cells ( $\pm$  samples) in a 96-well plate is recorded over a certain period of time. This data can then be used to interpret cell growth, death, or inhibition. The mechanism of action can also be evaluated similarly by using SEM to observe structural changes, diSC<sub>3</sub>(5) to detect loss in membrane potential, and propidium iodide to examine a fluorescence-based LIVE/ DEAD assay.<sup>24-26</sup> In essence, we can apply the results from our antibacterial studies to guide the analysis of our system's potential antifungal properties, and potentially expand the scope to biofilm eradication.

Utilizing miktoarm star polymers also gives us flexibility in customizing nanoparticle topology. By synthesizing P7-derivatives with varying number of polymeric arms, we can correspondingly alter the charge density and amphiphilicity of derived micelles to determine their structure-property relationships. Previously, Laroque et al. compared the antibacterial activity of several amphiphilic star copolymers to their linear counterparts.<sup>27</sup> They showed that star architectures significantly reduce *P. aeruginosa* PA14 growth in contrast to its linear copolymer equivalent. Zhao et al. also showed the interplay between charge density and amphiphilicity in promoting the additive effects of polysulfoniums and the antibiotic rifampicin.<sup>28</sup> Although they could accurately alter the charge density and amphiphilicity, they found that a balance between the two is necessary for combination treatment. It is of interest to conduct a systematic study to explore the influence of polymer branching on antimicrobial activity. As the charge densities and hydrophilic/hydrophobic balance is different, the antibacterial potency and biocompatibility is expected to differ—using miktoarm polymers allows us to explore such variations. Exploring such structure-property relationships will benefit the scientific community and inform the design of nanoparticles for biomedical applications.

The move towards personalized nanomedicine may especially benefit from the UCST-responsive system reported here, owing to its stable reversible morphological transitions. It is of interest to delve deeper into the morphology transition using various experimental techniques. For instance, de Graaf et al. utilized <sup>1</sup>H NMR relaxometry to distinguish flower- and star-like micelles formed from PNIPAM-PEG-PNIPAM and mPEG-PNIPAM, respectively.<sup>29</sup> Their observations highlighted several distinguishing features of the looped structure, including rigid PEG segments near the core and less flexible PEG distal segments. Static light scattering measurements also revealed lower PEG surface density in the flower-like configuration. Both methodologies serve as

robust tools for discerning the morphology transitions in our nanoparticles. Employing similar strategies with varying temperatures is of keen interest. To achieve this, it would be essential to examine P(AAm<sub>111</sub>-*co*-AN<sub>70</sub>)-*b*-PEG<sub>90</sub>-*b*-PCL<sub>25</sub> and its corresponding self-assemblies in D<sub>2</sub>O, akin to those performed in H<sub>2</sub>O, as documented in Chapter 4. Differences in transmission profiles, cloud points, and nanoparticle morphology are expected due to varied interactions with deuterated solvents.<sup>30</sup> In 2015, Hou and Wu explored the effects of solvent isotopes on the UCST behavior of P(AAm-*co*-AN). They reported a 10 °C increase in transition temperature of the same polymer at the same concentration in D<sub>2</sub>O than in H<sub>2</sub>O, suggesting stronger polymer-polymer interactions than polymer-solvent interactions in deuterated solvents. This result was complemented with their FTIR spectra and DLS analyses that suggested stronger polymer-polymer interactions in D<sub>2</sub>O. Therefore, prior to any relaxometry studies, it is imperative to assess the changes in transmission with varying temperatures and concentrations, alongside examining nanoparticle morphology using both DLS and TEM. Additionally, it is of significant interest to establish an intricate structure-property relationship for the P(AAm-*co*-AN)-*b*-PEG-*b*-PCL triblock copolymer. Currently, the nanoparticles derived from P(AAm<sub>111</sub>-*co*-AN<sub>70</sub>)-*b*-PEG<sub>90</sub>-*b*-PCL<sub>25</sub> slightly surpass the size threshold preferred for efficient nanocarriers (obtained: 209 nm, preferred: <200 nm). While the incorporation of CUR reduced the particle size below this guideline, it is advantageous to design nanoparticles that are consistently below this threshold to optimize their blood circulation and tissue penetration. A comprehensive exploration encompassing statistical analyses of the copolymer with different molecular weights, varying AN content, concentration, and exploring their associated self-assembly characteristics is instrumental in understanding the correlation between polymer composition and resulting self-assembly characteristics. By systematically varying these parameters, we can optimize the nanoparticles to meet specific demands, even beyond the realm of drug delivery.

### 5.3. References

1. El-Gendy, M. A.; El-Assal, M. I. A.; Tadros, M. I.; El-Gazayerly, O. N. Olmesartan Medoximil-Loaded Mixed Micelles: Preparation, Characterization and *In-Vitro* Evaluation. *Futur. J. Pharm. Sci.* **2017**, 3 (2), 90-94.

2. Wu, T.; Chen, X.; Wang, Y.; Xiao, H.; Peng, Y.; Lin, L.; Xia, W.; Long, M.; Tao, J.; Shuai, X. Aortic Plaque-Targeted Andrographolide Delivery with Oxidation-Sensitive Micelle Effectively Treats Atherosclerosis via Simultaneous ROS Capture and Anti-Inflammation. *Nanomed. Nanotechnol. Biol. Med.* **2018**, *14* (7), 2215-2226.
3. Loureiro Damasceno, J. P.; Silva da Rosa, H.; Silva de Araújo, L.; Jacometti Cardoso Furtado, N. A. Andrographis Paniculata Formulations: Impact on Diterpene Lactone Oral Bioavailability. *Eur. J. Drug Metab. Pharmacokinet.* **2022**, *47* (1), 19-30.
4. Tannergren, C.; Bergendal, A.; Lennernäs, H.; Abrahamsson, B. Toward an Increased Understanding of the Barriers to Colonic Drug Absorption in Humans: Implications for Early Controlled Release Candidate Assessment. *Mol. Pharm.* **2009**, *6* (1), 60-73.
5. Scialabba, C.; Rocco, F.; Licciardi, M.; Pitarresi, G.; Ceruti, M.; Giammona, G. Amphiphilic Polyaspartamide Copolymer-Based Micelles for Rivastigmine Delivery to Neuronal Cells. *Drug Deliv.* **2012**, *19* (6), 307-316.
6. Casey, A. B.; Canal, C. E. Classics in Chemical Neuroscience: Aripiprazole. *ACS Chem. Neurosci.* **2017**, *8* (6), 1135-1146.
7. Patil, P. H.; Wankhede, P. R.; Mahajan, H. S.; Zavar, L. R. Aripiprazole-Loaded Polymeric Micelles: Fabrication, Optimization and Evaluation Using Response Surface Method. *Recent Pat. Drug Delivery Formulation* **2018**, *12* (1), 53-64.
8. Liu, S.; Li, M.; Jia, L.; Chen, M.; Du, S.; Gong, J. Investigation of Drug-Polymer Miscibility, Molecular Interaction, and Their Effects on the Physical Stabilities and Dissolution Behaviors of Norfloxacin Amorphous Solid Dispersions. *Cryst. Growth Des.* **2020**, *20* (5), 2952-2964.
9. Venkatram, S.; Kim, C.; Chandrasekaran, A.; Ramprasad, R. Critical Assessment of the Hildebrand and Hansen Solubility Parameters for Polymers. *J. Chem. Inf. Model.* **2019**, *59* (10), 4188-4194.

10. Mathieu, D. Pencil and Paper Estimation of Hansen Solubility Parameters. *ACS Omega* **2018**, *3* (12), 17049-17056.
11. Faasen, D. P.; Jarray, A.; Zandvliet, H. J. W.; Kooij, E. S.; Kwiecinski, W. Hansen Solubility Parameters Obtained Via Molecular Dynamics Simulations as a Route to Predict Siloxane Surfactant Adsorption. *J. Colloid Interface Sci.* **2020**, *575*, 326-336.
12. Patel, S.; Lavasanifar, A.; Choi, P. Application of Molecular Dynamics Simulation to Predict the Compatability between Water-Insoluble Drugs and Self-Associating Poly(ethylene oxide)-*b*-Poly( $\epsilon$ -caprolactone) Block Copolymers. *Biomacromolecules* **2008**, *9* (11), 3014-3023.
13. Mahmoudi, M.; Landry, M. P.; Moore, A.; Coreas, R. The Protein Corona from Nanomedicine to Environmental Science. *Nat. Rev. Mat.* **2023**, *8* (7), 422-438.
14. Papafilippou, L.; Nicolaou, A.; Kendall, A. C.; Camacho-Muñoz, D.; Hadjidemetriou, M. The Lipidomic Profile of the Nanoparticle-Biomolecule Corona Reflects the Diversity of Plasma Lipids. *Nanoscale* **2023**, *15* (26), 11038-11051.
15. Ke, P. C.; Lin, S.; Parak, W. J.; Davis, T. P.; Caruso, F. A Decade of the Protein Corona. *ACS Nano* **2017**, *11* (12), 11773-11776.
16. Schöttler, S.; Landfester, K.; Mailänder, V. Controlling the Stealth Effect of Nanocarriers through Understanding the Protein Corona. *Angew. Chem. Int. Ed.* **2016**, *55* (31), 8806-8815.
17. Li, H.; Wang, Y.; Tang, Q.; Yin, D.; Tang, C.; He, E.; Zou, L.; Peng, Q. The Protein Corona and Its Effects on Nanoparticle-Based Drug Delivery Systems. *Acta Biomater.* **2021**, *129*, 57-72.
18. Friedl, J. D.; Nele, V.; De Rosa, G.; Bernkop-Schnürch, A. Bioinert, Stealth or Interactive: How Surface Chemistry of Nanocarriers Determines Their Fate *In Vivo*. *Adv. Funct. Mater.* **2021**, *31* (34), 2103347.
19. Sharifi, S.; Caracciolo, G.; Mahmoudi, M. Biomolecular Corona Affects Controlled Release of Drug Payloads from Nanocarriers. *Trends Pharmacol. Sci.* **2020**, *41* (9), 641-652.

20. Suk, J. S.; Xu, Q.; Kim, N.; Hanes, J.; Ensign, L. M. PEGylation as a Strategy for Improving Nanoparticle-Based Drug and Gene Delivery. *Adv. Drug Del. Rev.* **2016**, *99*, 28-51.
21. Gref, R.; Lück, M.; Quellec, P.; Marchand, M.; Dellacherie, E.; Harnisch, S.; Blunk, T.; Müller, R. H. 'Stealth' Corona-Core Nanoparticles Surface Modified by Polyethylene Glycol (PEG): Influences of the Corona (PEG Chain Length and Surface Density) and of the Core Composition on Phagocytic Uptake and Plasma Protein Adsorption. *Colloids Surf., B* **2000**, *18* (3), 301-313.
22. Li, M.; Jiang, S.; Simon, J.; Paßlick, D.; Frey, M.-L.; Wagner, M.; Mailänder, V.; Crespy, D.; Landfester, K. Brush Conformation of Polyethylene Glycol Determines the Stealth Effect of Nanocarriers in the Low Protein Adsorption Regime. *Nano Lett.* **2021**, *21* (4), 1591-1598.
23. Hoque, J.; Akkapeddi, P.; Yadav, V.; Manjunath, G. B.; Uppu, D. S. S. M.; Konai, M. M.; Yarlagadda, V.; Sanyal, K.; Halder, J. Broad Spectrum Antibacterial and Antifungal Polymeric Paint Materials: Synthesis, Structure–Activity Relationship, and Membrane-Active Mode of Action. *ACS Appl. Mater. Interfaces* **2015**, *7* (3), 1804-1815.
24. Zhang, Y.; Chen, Y.-y.; Huang, L.; Chai, Z.-g.; Shen, L.-j.; Xiao, Y.-h. The Antifungal Effects and Mechanical Properties of Silver Bromide/Cationic Polymer Nano-Composite-Modified Poly-Methyl Methacrylate-Based Dental Resin. *Sci. Rep.* **2017**, *7* (1), 1547.
25. Mukherjee, A.; Barman, R.; Das, B.; Ghosh, S. Highly Efficient Biofilm Eradication by Antibacterial Two-Dimensional Supramolecular Polymers. *Chem. Mater.* **2021**, *33* (22), 8656-8665.
26. Yeung, C. W. S.; Periyah, M. H.; Teo, J. Y. Q.; Goh, E. T. L.; Chee, P. L.; Loh, W. W.; Loh, X. J.; Lakshminarayanan, R.; Lim, J. Y. C. Transforming Polyethylene into Water-Soluble Antifungal Polymers. *Macromolecules* **2023**, *56* (3), 815-823.
27. Laroque, S.; Garcia Maset, R.; Hapeshi, A.; Burgevin, F.; Locock, K. E. S.; Perrier, S. Synthetic Star Nanoengineered Antimicrobial Polymers as Antibiofilm Agents: Bacterial Membrane Disruption and Cell Aggregation. *Biomacromolecules* **2023**, *24* (7), 3073-3085.

28. Zhao, Y.; Wang, X.; Hu, Y.; Zhao, J.; Sun, M.; Yang, M.; Xuan, H.; Wang, X.; Zhang, J.; Zhu, Z.; et al. Enhanced Synergistic Antibacterial and Antibiofilm Efficacy of Main-Chain Polysulfoniums with Antibiotics by Balancing Charge Density and Amphiphilicity. *ACS Appl. Polym. Mater.* **2023**, *5* (6), 4437-4447.
29. de Graaf, A. J.; Boere, K. W. M.; Kemmink, J.; Fokkink, R. G.; van Nostrum, C. F.; Rijkers, D. T. S.; van der Gucht, J.; Wienk, H.; Baldus, M.; Mastrobattista, E.; et al. Looped Structure of Flowerlike Micelles Revealed by <sup>1</sup>H NMR Relaxometry and Light Scattering. *Langmuir* **2011**, *27* (16), 9843-9848.
30. Hou, L.; Wu, P. Understanding the UCST-Type Transition of P(AAm-co-AN) in H<sub>2</sub>O and D<sub>2</sub>O: Dramatic Effects of Solvent Isotopes. *Soft Matter* **2015**, *11* (35), 7059-7065.